Transactions of the ASME®

Transactions of the ASME, Journal of Heat Transfer (ISSN 0022-1481) is published bi-monthly (Feb., Apr., June, Aug., Oct., Dec.) by The American Society of Mechanical Engineers, Three Park Avenue, New York, NY 10016. Periodicals postage paid at New York, NY and additional mailing offices. POSTMASTER: Send address changes to Transactions of the ASME, Journal of Heat Transfer, c/o THE AMERICAN SOCIETY OF MECHANICAL ENGINEERS, 22 Law Drive, Box 2300, Fairfield, NJ 07007-2300. **CHANGES OF ADDRESS** must be received at Society headquarters seven weeks before they are to be effective. Please send old label and new address. **STATEMENT from By-Laws.** The Society shall not be responsible for statements or opinions advanced in papers or ... printed in its publications (B7.1, Para. 3), **COPYRIGHT** © **2003** by The American Society of Mechanical Engineers. For authorization to photocopy material for internal or personal use under those circumstances not falling within the fair use provisions of the Copyright Act, contact the Copyright Clearance Center (CCC), 222 Rosewood Drive, Danvers, MA 01923, tel: 978-750-8400, *www.copyright.com.* Request for special permission or bulk copying should be addressed to Reprints/Permission Department. **INDEXED** by Applied Mechanics Reviews and Engineering Information, Inc. Canadian Goods & Services Tax Registration #126148048.

Journal of Heat Transfer

Published Bimonthly by The American Society of Mechanical Engineers

VOLUME 125 • NUMBER 3 • JUNE 2003

TECHNICAL PAPERS

(Contents continued on inside back cover)

This journal is printed on acid-free paper, which exceeds the ANSI Z39.48-1992 specification for permanence of paper and library materials. ♾™
♻ 85% recycled content, including 10% post-consumer fibers.

TECHNICAL NOTES

ERRATA

ANNOUNCEMENT

The ASME Journal of Heat Transfer is abstracted and indexed in the following:

Applied Science and Technology Index, AMR Abstracts Database, Chemical Abstracts, Chemical Engineering and Biotechnology Abstracts (Electronic equivalent of Process and Chemical Engineering), Civil Engineering Abstracts, Compendex (The electronic equivalent of Engineering Index), Corrosion Abstracts, Current Contents, E & P Health, Safety, and Environment, Ei EncompassLit, Engineered Materials Abstracts, Engineering Index, Enviroline (The electronic equivalent of Environment Abstracts), Environment Abstracts, Environmental Engineering Abstracts, Environmental Science and Pollution Management, Fluidex, Fuel and Energy Abstracts, Index to Scientific Reviews, INSPEC, International Building Services Abstracts, Mechanical & Transportation Engineering Abstracts, Mechanical Engineering Abstracts, METADEX (The electronic equivalent of Metals Abstracts and Alloys Index), Petroleum Abstracts, Process and Chemical Engineering, Referativnyi Zhurnal, Science Citation Index, SciSearch (The electronic equivalent of Science Citation Index), Theoretical Chemical Engineering

Numerical Analysis of the Transverse Thermal Conductivity of Composites With Imperfect Interfaces

Samuel Graham
e-mail: sgraham@sandia.gov
Member of ASME
Senior Member of Technical Staff,
PO Box 969, MS 9404,
Sandia National Laboratories,
Livermore, CA 94568

David L. McDowell
e-mail: david.mcdowell@me.gatech.edu
Professor and ASME Fellow
Woodruff School of Mechanical Engineering,
Georgia Institute of Technology,
Atlanta, GA 30332-0405

Estimation of the transverse thermal conductivity of continuous fiber reinforced composites containing a random fiber distribution with imperfect interfaces was performed using finite element analysis. FEA results were compared with the classical solution of Hasselman and Johnson to determine limits of applicability. The results show that the Hasselman and Johnson model predicts the effective thermal conductivity within 3 percent of the numerical estimates for interfacial conductance values of $1\times10^{-2}-1\times10^{3}$ *W/m*^{2}*K, fiber-matrix conductivity ratios between 1 and 100, and fiber volume fractions up to 50 percent which are properties typical of ceramic composites. The results show that the applicability of the classical dilute concentration model can not be determined by constituent volume fraction, but by the degree of interaction between the microstructural heterogeneities.* [DOI: 10.1115/1.1561814]

Keywords: Composites, Conduction, Finite Element, Heat Transfer, Properties, Thermophysical

Introduction

The prediction of effective thermal conductivity is important for materials requiring thermal dissipation such as thermal interface materials, printed circuit boards, and ceramic matrix composites. For these material systems, the integrity of the constituent interface plays an important role in determining the effective thermal conductivity. For heterogenous materials, interfacial thermal conductance values, H_i, are often indirectly determined from effective thermal conductivity measurements through correlations with analytical models. Since both the longitudinal and transverse effective thermal conductivities of composites depend greatly upon the interfacial thermal conductance, knowledge of this parameter is very critical to the prediction of effective thermal conductivity and tailoring its value. The accuracy of determining interfacial conductance values from effective property data will depend on the accuracy of the measurements and the validity of the model employed. For the transverse thermal conductivity of composites, the Hasselman-Johnson model [1] is one of the most widely used, and was one of the first to incorporate effects of imperfect thermal interface between constituents. Other modeling approaches have used micromechanics based theories to address the effective thermal conductivity of composites with imperfect thermal interfaces, but have resulted in essentially the same expression given by Hasselman-Johnson [cf. 2]. Thus, to minimize redundancy, the Hasselman-Johnson model will be used to describe this group of models. The Hasselman-Johnson model (Eq. 1) is a modification of the Rayleigh effective medium theory [3] which assumes no interaction between second phase constituents. Therefore, the basis of the model assumes a dilute concentration of a second phase which may not be realized in some composite systems. Much research effort has gone into improving the prediction of effective material properties for composites containing non-dilute, interacting reinforcement phase. Since imperfect thermal interfaces may alter the nature of interaction between inclusions in composites, it may be possible to extend models like Hasselman-Johnson to composites where the classification of dilute fiber concentration is not commonly used (e.g., fiber volume fractions >30 percent). An assessment of the applicability of the Hasselman-Johnson model is necessary in order to better interpret data obtained through its use and to determine a range of volume fractions and thermal interface conditions under which it provides reasonable predictions.

$$K=K_m\frac{\left[\left(\frac{K_f}{K_m}-1-\frac{K_f}{r_fH_i}\right)V_f+\left(1+\frac{K_f}{r_fH_i}+\frac{K_f}{K_m}\right)\right]}{\left[\left(1+\frac{K_f}{r_fH_i}+\frac{K_f}{K_m}\right)V_f+\left(1+\frac{K_f}{r_fH_i}+\frac{K_f}{K_m}\right)\right]} \quad (1)$$

Due to the difficulty in treating the effects of fiber interactions on local field responses, numerical techniques are often used to determine effective properties of materials. Previous studies on effective thermal conductivity have used the concept of unit cell methods which assumes a periodic microstructure. These results have shown that the Hasselman and Johnson model is exact up to fiber volume fractions of 50 percent and is within 5 percent up to $V_f=70$ percent [2,4]. However, not all composite microstructures are amenable to unit cell analysis and may contain stronger fiber interactions effects which can place additional limitations on the applicability of the Hasselman-Johnson predictions. An example of such a case is unidirectional or cross-ply laminate composites where fiber reinforcement is not uniformly or periodically spaced within the matrix material. In these composite microstructures, assuming a random fiber arrangement may better account for fiber interaction effects as compared to periodic arrays of reinforcement. It is the intention of this work to address the problem of transverse thermal conductivity of continuous fiber reinforced ceramic matrix composites (CFCCs) containing a random fiber distribution and interfacial thermal resistance. This approach will involve a parametric study utilizing finite elements to analyze the effects of spatial randomness, differences of the fiber and matrix conductivities, and interfacial integrity. These results will be used to assess the range of applicability of closed form analytical solutions like the Hasselman-Johnson model for determining the effective transverse thermal conductivity of composites. Special at-

Contributed by the Heat Transfer Division for publication in the JOURNAL OF HEAT TRANSFER. Manuscript received by the Heat Transfer Division December 19, 2001; revision received November 12, 2002. Associate Editor: H. S. Lee.

tention will be given to ensure that the numerical treatment of the problem is reflective of the response expected from a representative volume element of material [5].

Finite Element Modeling. A finite element study was performed on random fiber distributions limited to 50 percent fiber volume fraction. Above 50 percent fiber volume fraction, the percolation threshold is approached and thermal conductivity changes rapidly with increasing fiber volume fraction [6]. Significant fiber interactions occur at these high volume fractions in the form of conductive chain formations. This type of interaction is not considered by the Hasselman-Johnson model and will not be addressed here. Fiber-matrix conductivity ratios, K_f/K_m, of 1, 10, and 100 were studied. These values were chosen in consideration of CFCCs where conductivity ratios do not vary far from this range of values. The simulations involved the use of a commercially available finite element code ABAQUS. The mesh was created using two-dimensional, eight-node heat transfer elements (DC2D8) within the fiber and matrix and six-node interface elements (DINTER3) along the fiber-matrix interface to simulate interfacial conditions. Interface elements allow the specification of an interfacial thermal conductance value as given by the thermal boundary condition:

$$K_f \nabla T_f = K_m \nabla T_m \tag{2}$$

$$K_m \nabla T_m = H_i (T_f - T_m) \tag{3}$$

Temperature boundary conditions were employed along the top and bottom faces of the unit cell while lateral sides were held adiabatic. The effective thermal conductivity was determined by:

$$\overline{q} = -K\overline{\nabla T} \tag{4}$$

where the average heat flux and temperature gradient are evaluated along the model boundary S by

$$\overline{q} = \frac{1}{L_w}\int_0^{L_w} q\,dS \tag{5}$$

$$\overline{\nabla T} = \frac{1}{L_w}\int_0^{L_w} \nabla T\,dS \tag{6}$$

Since the use of random fiber models preclude the use of unit cell concepts, issues concerning statistical homogeneity and scale effects are raised. In a classical continuum limit, there exists a representative volume element (RVE) which contains a statistical representation of all local heterogeneities [5]. This volume may be represented by a cube of material whose sides are of length L_w and is such that volume averaged material responses should be the same whether temperature or heat flux boundary conditions are applied [5,7–8]. For the case of material responses transverse to the axis of randomly distributed fibers, the RVE may be simulated by a square window placed on the cross section of the microstructure with the following relative scale dimensions (Fig. 1):

$$\kappa = \frac{L_w}{d_f} \tag{7}$$

where L_w is the length of the side of the window, and d_f is the fiber diameter [9]. This scale defines the relative window size with respect to the scale of microstructural dimensions. It can also be viewed as the relative scale of the periodicity of the response of local field variables with respect to the scale of the microstructural dimensions. Since the window can be placed randomly within the composite cross section, statistical homogeneity requires that volume averaged material response functions should be invariant with respect to the position of the RVE window [7–8,10]. A true RVE exists only when $L_w \gg d_f$, which is difficult to model even using finite element approaches. Attempts are made to approximate an RVE by choosing a suitable window size of scale dimension κ; this will be referred to as a pseudo-RVE. For this simulation, random-periodic arrangements were used which are doubly

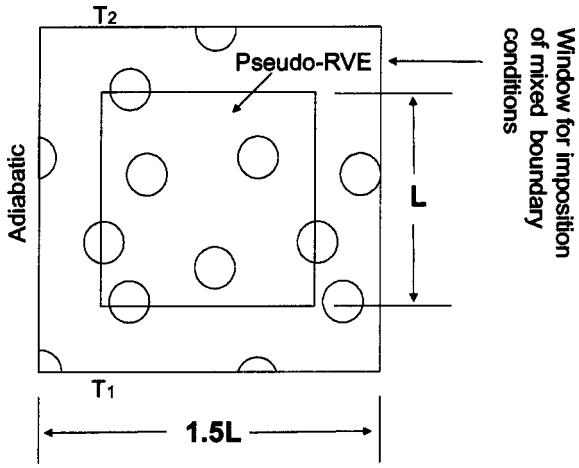

Fig. 1 Depiction of pseudo-RVE and doubly periodic region which was modeled by finite elements. The characteristic dimension of the outer boundary is 1.5 times larger than the pseudo-RVE on which calculations were made for effective conductivity. Periodic boundary conditions were prescribed on the outer boundary.

periodic over the length L, but random within the pseudo-RVE window. The placement of fibers along the pseudo-RVE boundary serves to induce periodicity of field quantities along the boundary and to minimize fiber interaction with overall model boundaries [10]. The advantage of this approach is that the effective properties determined by this methodology are much closer to ones for a true RVE of a random heterogeneous material. In addition, the use of random-periodic boundary conditions has been shown to be bounded by the responses obtained from temperature (essential) and heat flux (natural) boundary conditions [11]. Therefore, the use of appropriate random-periodic boundary conditions provides a faster convergence to homogenization for a given scale dimension κ. For this study, the scale dimension was taken to be $\kappa = 7$.

In order to induce random-periodic boundary conditions on the pseudo-RVE window using ABAQUS, reflections were made outside the window on which temperature boundary conditions were specified as shown in Fig. 1. Based on previous studies on the growth of cracks in a brittle medium, the length of the outer boundary was taken to be $1.5L_w$ [10]. This removes the interior window of interest from the effects of the boundary conditions applied in the models. In addition, the reflections were necessary to induce random-periodic boundary conditions on the inner window which cannot be prescribed in ABAQUS, but approximated [10]. Figure 2 depicts a typical finite element mesh of the random-periodic geometries analyzed in this study.

Results

Figures 3–5 present the finite element results along with comparisons to the Hasselman-Johnson model for K_f/K_m ratios of 1, 10, and 100, respectively. In order to apply the results to diverse material systems, the results are presented as a function of interfacial Biot number, B_i. The interfacial Biot number was defined by multiplying the interfacial conductance values (H_i) by the fiber radius and dividing by the fiber conductivity ($H_i r_f/K_f$). Cases of perfect bonding and insulated particles were simulated by using conductance values of 1×10^4 and 1×10^{-3}, respectively. The finite element results show a nonlinear decrease in effective thermal conductivity values with decreasing interfacial thermal conductance. As shown by the results, all effective conductivity values decrease asymptotically to the same level for a given volume fraction, regardless of the initial K_f/K_m. At sufficiently low values of H_i, the composite behaves simply as a material containing voids as the fibers contribute less to thermal conduction as predicted by

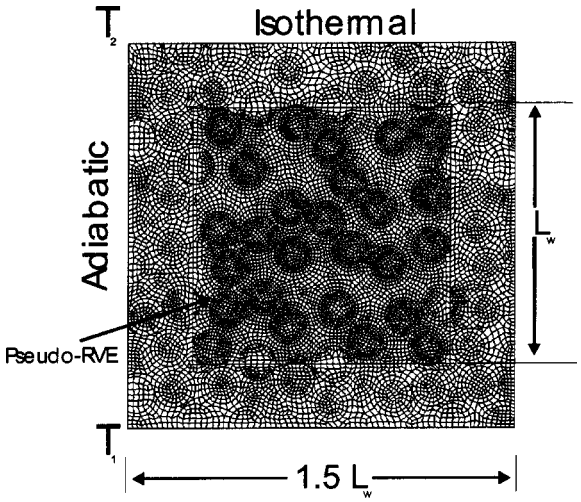

Fig. 2 Finite element mesh depicting the doubly-periodic region which is 1.5 times the characteristic dimension of the pseudo-RVE. Fiber volume fraction shown is 50 percent.

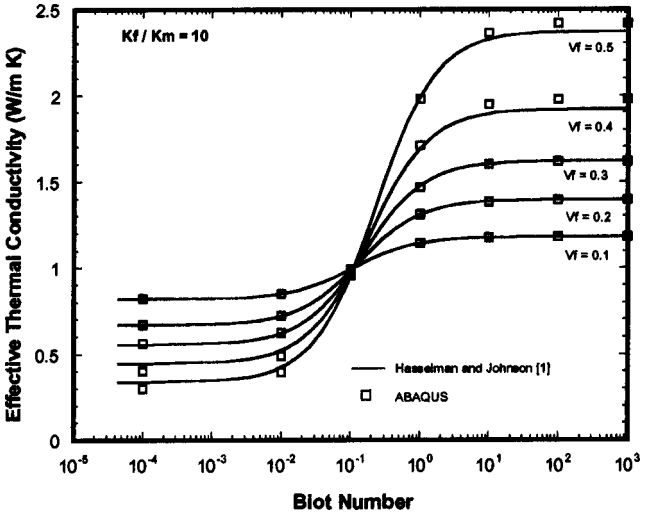

Fig. 4 Comparison of the finite element results for effective thermal conductivity with the analytical solution of Hasselman and Johnson. Results are for random-periodic distributions containing up to 50 percent fiber volume fraction and a K_f/K_m ratio of 10.

Eq. 1. The decrease in fiber contribution to thermal conduction leads to a decrease in the heterogeneity contrast between the fiber and matrix as seen in Fig. 3–4. The results also show that for $K_f/K_m>1$, the effective thermal conductivity solutions converge at a single Biot number, irrespective of the volume fraction. This result is in accordance with the Hasselman-Johnson model which predicts that convergence will occur when the following relationship is satisfied:

$$B_i=\frac{H_i r_f}{K_f}=\frac{1}{K_{\text{ratio}}-1}; \quad K_{\text{ratio}}=\frac{K_f}{K_m} \tag{8}$$

This value of interfacial thermal conductance will be referred to as the homogenizing value, since the effective thermal conductivity of the composite is the same as the matrix ($K_m=1$ W/mK for all cases. It can be postulated for all $K_f/K_m>1$, there exists an imperfect interfacial condition which balances out the effects of the higher fiber conductivity and causes the material to behave homogeneously globally and locally. Thus, as the interfacial thermal conductance decreases towards the homogenization value, the perturbation of the thermal field variables around fibers becomes smaller and fewer interaction effects are realized. Once B_i decreases beyond this homogenizing value, the heterogeneous nature of the microstructure is again manifested in terms of significant fiber (or void) interaction effects.

Comparison of the results in Fig. 3–5 show excellent agreement with the Hasselman-Johnson model for all K_f/K_m ratios when $V_f \leqslant 0.3$. Agreement is expected between model and data for low fiber volume fractions due to the negligible fiber interaction effects. Differences between the model and finite element calculations are less than 0.6 percent for $V_f \leqslant 0.3$ for all K_f/K_m ratios and thermal conductance values used in this study. Once the fiber volume fraction is increased above 30 percent, significant deviations between the model and finite element data are observed, and occurs at volume fractions much lower than reported with the use of

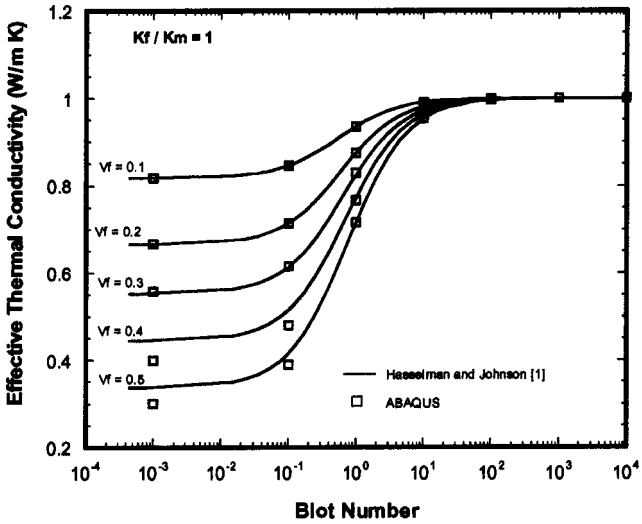

Fig. 3 Comparison of the finite element results for effective thermal conductivity with the analytical solution of Hasselman and Johnson. Results presented are for random-periodic distributions containing up to 50 percent fiber volume fraction and a K_f/K_m ratio of 1.

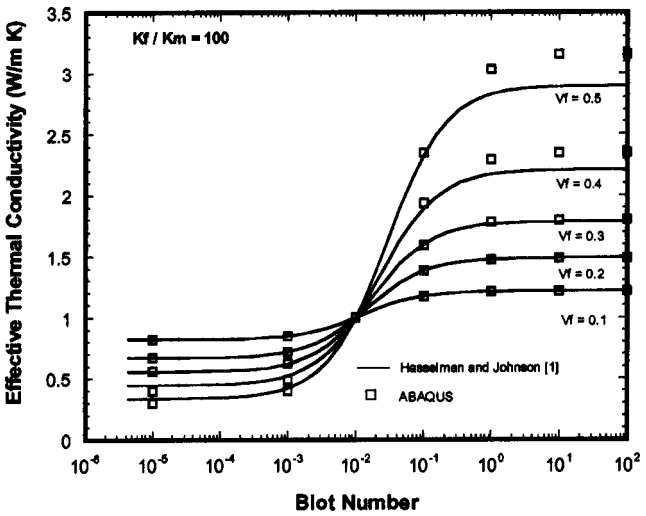

Fig. 5 Comparison of the finite element results for effective thermal conductivity with the analytical solution of Hasselman and Johnson. Results are for random-periodic distributions containing up to 50 percent fiber volume fraction and a K_f/K_m ratio of 100.

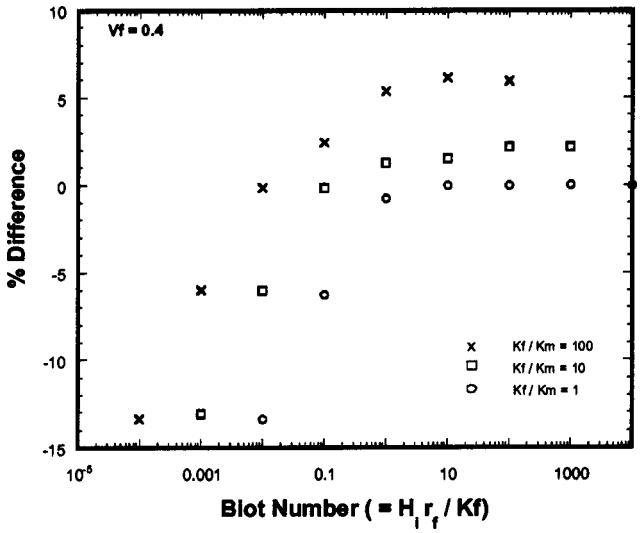

Fig. 6 Nondimensional plot of the difference between the finite element results and the Hasselman-Johnson model for K_f/K_m=1,10,100, and V_f=0.4

unit cell analysis [4]. For $K_f/K_m \geq 10$, the Hasselman-Johnson model under predicts thermal conductivity for conditions of nearly perfect interfacial bonding ($B_i = 10000$). The severity of this under prediction increases with increasing volume fraction and fiber-matrix conductivity ratio as shown in Fig. 4–5. For all K_f/K_m, the model over predicts the value of thermal conductivity for conditions of nearly insulated interfaces ($B_i = 0.001$). However, these two interfacial conditions are extreme cases which bring out the peak differences in heterogeneous responses on the material mesoscale. This is evident through an analysis of the differences between the model and finite element results (Fig. 6–7) which show a nonlinear variation between the model and numerical predictions as a function of interfacial conductance. Significant differences of up to 10 percent exist between the model and finite element data for conditions of perfect interfacial bonding and $K_f/K_m > 1$. These differences vanish as the interfacial thermal conductance approaches the homogenizing value. As the equality in Eq. 8 is approached, differences between the model and finite element results are also reduced and properties can be better estimated by the dilute concentration method. Further decreasing B_i results in increased differences between the model and results as the material begins to simulate a material containing voids. This can be seen since the differences between the model and numerical results converge to a value on the order of 15 percent (for a fixed volume fraction) once B_i is less than the homogenizing value.

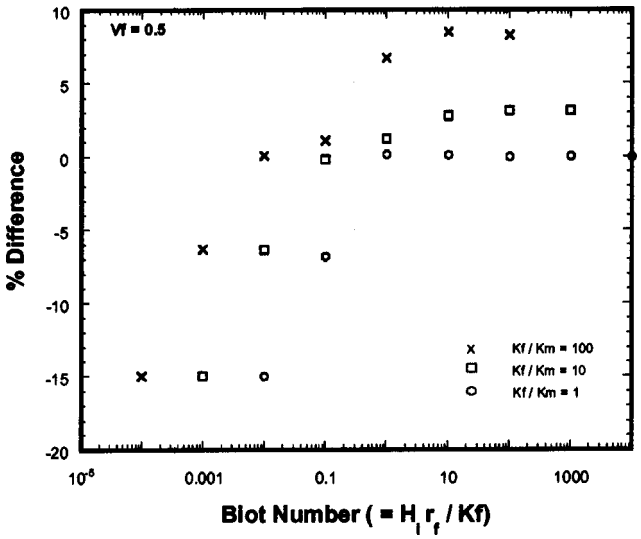

Fig. 7 Nondimensional plot of the difference between the finite element results and the Hasselman-Johnson model for K_f/K_m=1,10,100, and V_f=0.5

The finite element results and model comparisons suggest that there exists a region of composite material parameters for which the Hasselman-Johnson model can be used successfully to predict the effective thermal conductivity transverse to the fiber axis or to correlate the interfacial thermal conductance values. This conclusion may also be extended to analytical predictions of effective thermal conductivity of heterogenous media containing particulates (spheres, short fibers, etc.) as well, since the interfacial conductance will have a similar effect on particle contribution to conduction as shown in this analysis. Since the majority of numerical analyses and analytical works have focused on the condition of perfect thermal interfaces, much research has gone into improving the prediction capabilities for effective thermal conductivity of composites with fiber interactions [11–15]. Many of the improvements in model predictions rely on the aid of numerical schemes or detailed statistical information about the microstructure. However, perfect interfaces are not physically realized in all composite media. By introducing the concept of the imperfect interface, the level of interaction between the second phase may be reduced to the point where materials become amenable to closed form models such as Eq. 1. Such is the case for many CFCCs where a significant interfacial thermal resistance exists as a result of material processing. Fiber volume fractions in CFCCs typically range between 30–50 percent, which results in non-negligible fiber interactions under conditions of perfect or insulated thermal interfaces. In glass-ceramic composites, thermal residual stresses may cause interfacial debonding after cool down from hot-pressing temperatures. For CFCCs manufactured by chemical vapor deposition and reaction bonding processes, imperfect thermal interfaces have also been shown to develop [16]. Interfacial thermal conductance values have been shown to range from 4×10^6 to 1×10^4 W/m^2 K for composites containing Nicalon and SCS-6 reinforcement [16–19]. Including the effect of fiber dimension by using the Biot number ($H_i\ r_f/K_f$), these conductance values correspond to $B_i = 0.35-280$. This assumes a fiber radius of 70 μm and a transverse conductivity of 1 W/mK when calculating B_i for SCS-6 fibers. Figure 7 displays the largest differences between the model and finite element data versus the Biot number. Based on the expected range of $B_i = 0.35-280$ and $K_f/K_m \leq 10$ for ceramic composites, negligible errors between the Hasselman-Johnson model and the actual value of thermal conductivity are expected for $V_f \leq 0.5$. Most glass-ceramic composites reinforced with Nicalon fibers, SiC/SiC, silicon nitride, and oxide-oxide composites have K_f/K_m values on the order of 1. Thus, the use of the Hasselman-Johnson model for these classes of materials should provide predictions within 1 percent of the actual composite value for the range of Biot numbers and fiber volume fractions given.

Conclusions

Approximate random-periodic finite element results suggest that the Hasselman-Johnson model may be applied heterogenous materials with an imperfect thermal interface between the constituent phases. There appears to be a range of interface resistance values which attenuate the interaction of the second phases, thus, yielding a material which is amenable to dilute concentration models. Based on the results in this study, the Hasselman-Johnson model gives reasonably good predictions for composites with interfacial Biot numbers between 0.1–1000, fiber-matrix conductivity ratios up to 10, and fiber volume fractions up to 50 percent. This result shows that the description of dilute fiber reinforcement should be based not on fiber volume fraction and fiber distribution

alone, but also include the boundary condition at the reinforcement interface which controls the level of interaction between constituents. These results also place more restrictions on the applicability of the Hasselman-Johnson model compared to the analysis of unit cell models [2,4]. Thus, interaction effects in composites not having a regular array of reinforcement are expected to be much higher and yield effective properties different from unit cell models under conditions outside of the restrictions stated above. While additional research is needed to address effective property predictions for non-dilute composite materials, it is expected that more complex numerical solutions will be needed. Micromechanics-based solutions to address reinforcement interaction effects in the presence of imperfect thermal interfaces have converged to single solutions based on dilute reinforcement analysis for both spherical [20] and cylindrical fiber reinforcement [2]. While these micromechanics-based solution approaches provide closed-form analytical expressions, they are limited in their ability to account for fiber interaction effects in the presence of imperfect interfaces.

Nomenclature

CFCC = Continuous Fiber Reinforced Ceramic Composite
RVE = Representative Volume Element
B_i = Biot Number at fiber-matrix interface; $d_f H_i / K_f$
d_f = fiber diameter
H_i = interfacial thermal conductance across fiber-matrix interface
K = effective thermal conductivity
K_f = fiber conductivity
K_m = matrix conductivity
K_{ratio} = ratio of fiber to matrix thermal conductivities
L_w = characteristic length of the pseudo-RVE window
pseudo-RVE = Approximation of an RVE used in finite element modeling
$\overline{q}$ = average heat flux
q = heat flux
r_f = fiber radius
∇T = temperature gradient
$\overline{\nabla T}$ = average temperature gradient
V_f = fiber volume fraction
κ = relative scale dimension of the pseudo-RVE compared to the fiber diameter

References

[1] Hasselman, D. P. H., and Johnson, L. F., 1987, "Effective Thermal Conductivity of Composites with Interfacial Thermal Barrier Resistance," J. Compos. Mater., **21**, pp. 508–515.

[2] Graham, S., 1999, "The Effective Thermal Conductivity of Damaged Composites," Ph.D. thesis, Georgia Institute of Technology, Atlanta, GA.

[3] Lord Rayleigh, W. 1892, "On the Influence of Obstacles Arranged in Rectangular Order Upon the Properties of a Medium," Philos. Mag., **34**, pp. 481–502.

[4] Cha, W., and Beck, J. V., 1989, "Numerical Study of Thermal Conductivity of Fiber-Matrix Composite Materials," in *Design and Manufacturing of Advanced Composites*, ASM International, pp. 219–225.

[5] Hill, R., 1967, "The Essential Structure of Constitutive Laws for Metal Composites and Polycrystals," J. Mech. Phys. Solids, **15**, pp. 79–95.

[6] Donaldson, K. Y., Bhatt, H., and Hasselman, D. P. H., 1993, "Role of Interfacial Gaseous Heat Transfer and Percolation in the Effective Thermal Conductivity of Two Uniaxial Carbon-Fiber-Reinforced Glass Matrix Composites," *Ceramic Engineering and Science Proceedings*, **14**, published by The American Ceramic Society, Westerville, OH, pp. 335–340.

[7] Hashin, Z., 1983, "Analysis of Composite Materials-A Survey," ASME J. Appl. Mech., **50**, pp. 481–505.

[8] Alzebdeh, K., Jasiuk, I., and Ostoja-Starzewski, M., 1998, "Scale and Boundary Condition Effects in Elasticity and Damage Mechanics," in *Damage Mechanics Studies in Applied Mechanics*, J. W. Ju, J.-L. Chaboche, and G. Voyiadjis, eds., Elsevier Science, pp. 65–80.

[9] Ostoja-Starzewski, M., 1998, "Random Field Models of Heterogeneous Materials," Int. J. Solids Struct., **35**, pp. 2429–2455.

[10] Lacy, T., 1998, "Distribution Effects In Damage Mechanics," Ph.D. thesis, Georgia Institute of Technology, Atlanta, GA.

[11] Ostoja-Starzewski, M., and Schulte, J., 1996, "Bounding of Effective Thermal Conductivities of Multiscale Materials by Essential and Natural Boundary Conditions," Phys. Rev. B, **54**, pp. 278–285.

[12] Ostoja-Starzewski, M., Jasiuk, I., Wang, W., and Alzebdeh, K., 1996, "Composites With Functionally Graded Interphases: Mesocontinuum Concept and Effective Transverse Conductivity," Acta Mater., **44**, pp. 2057–2066.

[13] Torquato, S., 1987, "Thermal Conductivity of Disordered Heterogeneous Media From the Microstructure," Reviews in Chemical Engineering, **4**, pp. 151–204.

[14] Torquato, S., 1991, "Random Heterogeneous Media. Microstructures and Improved Bounds on Effective Properties," Appl. Mech. Rev., **44**, pp. 37.

[15] Pitchumani, R., and Yao, S., 1991, "Correlation of Thermal Conductivities of Unidirectional Fibrous Composites Using Local Fractal Techniques," ASME J. Heat Transfer, **113**, pp. 788–796.

[16] Bhatt, H., Donaldson, K., and Hasselman, D. P. H., 1990, "Role of the Interfacial Thermal Barrier in the Effective Thermal Diffusivity/Conductivity of SiC-Fiber-Reinforced Reaction-Bonded Silicon Nitride," J. Am. Ceram. Soc., **73**, pp. 312–316.

[17] Bhatt, H., Donaldson, K., Hasselman, D. P. H., and Bhatt, R., 1992, "Role of Interfacial Carbon Layer in the Thermal Diffusivity/Conductivity of Silicon Carbide Fiber-Reinforced Reaction-Bonded Silicon Nitride Matrix Composites," J. Am. Ceram. Soc., **75**, pp. 334–340.

[18] Depalma, C. M., Bhatt, H., Donaldson, K. Y., Hasselman, D. P. H., Thomas, J. R., and Hurst, E. P., 1994, "Role of Interfacial Thermal Barrier in the Measurement of the Longitudinal Thermal Conductivity of a Uniaxial Fiber-Reinforced Composite by the Flash Method," *Thermal Conductivity 22*, T. Tong, ed., Technomic Publishing Co., Lancaster, PA.

[19] Hasselman, D. P. H., Donaldson, K., Thomas, J., and Brennan, J., 1996, "Thermal Conductivity of Vapor-Liquid-Solid and Vapor-Solid Silicon Carbide Whisker-Reinforced Lithium Aluminosilicate Glass-Ceramic Composites," J. Am. Ceram. Soc., **79**, pp. 742–748.

[20] Benveniste, Y., 1987, "A New Approach to the Application of Mori-Tanaka $=s$ Theory in Composite Materials," Mech. Mater., **6**, pp. 147–157.

Influence of Flatness and Waviness of Rough Surfaces on Surface Contact Conductance

S. Sunil Kumar

K. Ramamurthi

Propulsion Research and Studies Group,
Liquid Propulsion System Centre,
Trivandrum,
India 695547

The effect of surface roughness, waviness and flatness deviations on thermal contact conductance is predicted. Threshold values of the surface parameters which do not adversely influence thermal contact conductance are determined. Flatness deviations less than ten times the average roughness and waviness less than about four times the average roughness do not significantly affect the contact conductance. A correlation is developed for contact conductance in terms of the surface parameters, the material properties and the contact pressure at the joint. Experiments are conducted in vacuum with rough, non-flat and wavy surfaces and the experimental results are demonstrated to agree well with the predictions. [DOI: 10.1115/1.1565093]

Keywords: Contact Resistance, Heat Transfer, Roughness, Thermal, Wavy

Introduction

A large number of theoretical and experimental studies have been carried out to estimate the thermal surface contact conductance between joints formed by rough but conforming flat surfaces [1–5]. A surface is characterized not only by the roughness but also by its flatness and waviness. The influence of the flatness and waviness of surfaces on the contact conductance has not been rigorously analyzed, partly due to difficulty of describing the three dimensional topography of surface flatness and waviness in a physical model. The importance of maintaining flat surfaces at the joint has, however, been recognized [1]. Deviations in flatness and waviness would depend on the speed of machining the surface, the depth of cut and the hardware material. The emergence of modern machining techniques makes it possible to achieve high levels of surface finish, flatness and non-waviness since the feed and depth of cut are controlled within a few microns. It is, however, far from clear whether very high levels of surface flatness and waviness, such as can be generated by the advanced manufacturing processes, are necessary to give good surface contact conductance especially when the characteristic surface roughness is typically of the order of a few microns.

Clausing and Chao [1] have suggested that the deviations in the flatness can be accounted for by means of a ''spherical cap'' model. Here, the apparent contact area is divided into a non-contact region that contains few or no microscopic contact areas and a contact region where the density of micro contacts is high. The flow of heat is constrained in the model to the large scale contact areas. The macroscopic constriction was seen to have a significant influence on the conductance.

Yovanovich [6] extended the theory of Clausing and Chao [1] to predict the conductance of rough wavy surfaces. The macroscopic contact areas were termed as ''contour areas.'' The study, however, did not quantify the explicit influence of waviness or deviations in flatness on thermal contact conductance.

Thomas and Sayles [7] characterized a surface as comprising of a continuous spectrum of wavelengths. The largest wavelengths with large amplitude deviations, corresponding to large-scale errors of form, were termed as flatness deviations. Smaller wavelengths were taken to constitute the waviness. The smallest waviness represented the roughness. The thermal contact conductance was shown to be proportional to $P^{1/3}$ where P is the contact pressure when the surface is characterized by waviness alone. Similar results were obtained by Madhusudana [8]. If surface roughness is the only consideration, the conductance would be proportional to $P^{0.94}$ [8]. It may be noted that the majority of experimental results obtained with different materials in contact show the exponent of the contact pressure to be between these two values of 1/3 and 0.94. Madhusudana [9] observed the flatness deviations to be important at low contact pressures even when the magnitudes of the deviations are comparable to mean surface roughness.

A detailed review of the different models and their predictions of thermal contact conductance of metallic surfaces carried out by Lambert and Fletcher [10] showed that most of the empirical and semi-empirical correlations have very limited applicability when contacting surfaces are wavy and non-flat. Marotta et al. [11] used a thermo-mechanical model that combined both microscopic and macroscopic thermal resistances. A macroscopic thermal constriction resistance from Hertzian contact theory was employed after due modifications for rough surfaces.

Lambert and Fletcher [12] in a recent work modified a semi-empirical model developed by Mikic [13] for non-flat rough metal surfaces and employed it to predict the conductance of metallic coated surfaces. They considered the distribution of pressure in the contact region. The predictions were demonstrated to compare well with experimental data.

Machining techniques have advanced to a level wherein high degree of surface finish can be achieved. Inspection procedures using stylus based and non-contact measurements can also measure the high degree of surface finish. The requirement for the cost-intensive high accuracy machining and the inspection procedures to ascertain the surface finish cannot be justified if their contribution to improve the thermal contact at the joints is not substantial. It is the intention of the present study to determine the effect of waviness and flatness deviation on otherwise conforming rough surfaces and to determine whether there exist threshold values of surface parameters below which thermal contact conductance is not significantly influenced. The surface characteristics are theoretically modeled, their contact conductance predicted and experiments conducted to verify the predictions.

Theoretical Formulation

Energy transfer across a pressed contact occurs by radiation and conduction through interstitial medium and by conduction through micro-contacts. At relatively low temperatures and pressures, the heat transfer across pressed contacts would be dominated by conduction through actual contact area. Convection would be negli-

Contributed by the Heat Transfer Division for publication in the JOURNAL OF HEAT TRANSFER. Manuscript received by the Heat Transfer Division March 19, 2002; revision received December 5, 2002. Associate Editor: G. Chen.

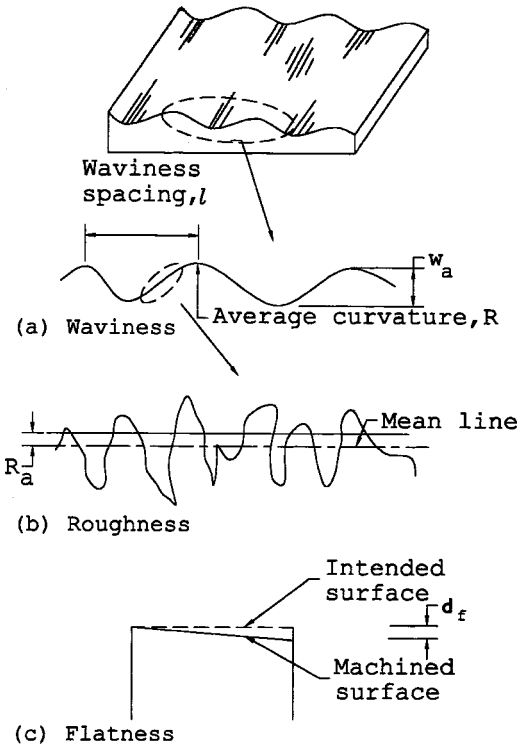

Fig. 1 Representation of surface characteristics

gible for small interfacial clearances, especially at low ambient pressures. In order to model the heat transfer, the contact between the surfaces at the joint needs to be determined. The modeling for the surface contact is given below and is followed by the modelling for the thermal contact conductance.

Model for Surface Roughness, Flatness, and Waviness. A magnified schematic view of a machined surface is shown in Fig. 1. The distribution of asperities is usually not random, but exhibits a preferred direction or lay [6]. The lay contributes to surface waviness. The waviness is represented by the peak to valley height of the measured profile from which roughness is removed by suitable filtering and is represented by an average value w_a [14] (Fig. 1). The average distance between the peaks is represented by waviness spacing length, l. The average curvature of the waviness peak is denoted by R [14,15]. A single value of spacing and curvature is generally used to characterize waviness. Sengupta and Lekoudis [16] use such a description to represent wavy surfaces in their studies of flow in boundary layer. The average surface roughness in Fig. 1 is quantified by a roughness parameter, R_a which is the average height of the profile above and below a mean line as shown. Flatness is defined [15] as the departure of the surface from true flatness and is represented as the maximum deviation of the machined plane from the intended plane. In the particular case of two surfaces under consideration, the deviation d_f corresponds to the sum of deviation obtained for the two mating surfaces and this is schematically shown in Fig. 1. The measurement of the deviation is given subsequently. The modelling of each of these three surface parameters is outlined below.

(a) Surface Roughness. The interaction of asperities from the two rough surfaces leads to individual microscopic contacts at a joint. The modelling comprises of estimating the contact area and is dealt with by Sunil Kumar and Ramamurthi [5]. The surface roughness is described by a standard deviation of combined height distribution (σ) and an average absolute slope (m) for the asperities. The distribution of the asperity heights is assumed to be Gaussian, viz.,

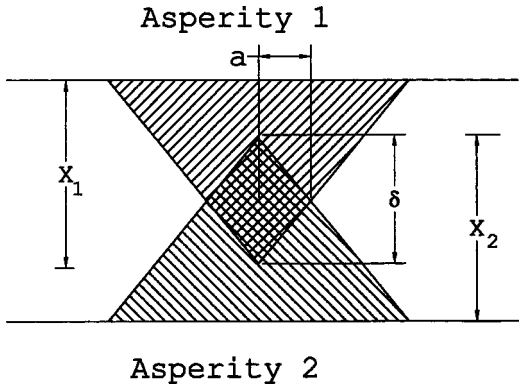

Fig. 2 Physical model of a single asperity contact

$$f(x)=\frac{1}{\sqrt{2\pi}\sigma}\exp\left[-\frac{1}{2}\left\{\frac{x-R_a}{\sigma}\right\}^2\right] \tag{1}$$

Here $f(x)$ denotes the distribution of asperity heights. The asperity height distribution leads to the determination of the number of asperities per unit area and their height [4] as given below. The number of asperities per unit area is determined as:

$$N=(m/7.308\sigma)^2 \tag{2}$$

The maximum summit height is:

$$x_{\max}=8\sigma \tag{3}$$

The mean summit height is given by:

$$R_a=4\sigma \tag{4}$$

The maximum and mean summit heights and the number of asperities per unit area are used to model the actual area of contact for non-flat wavy surfaces as detailed in reference [5]. When two opposing asperities come into contact with each other, as shown in Fig. 2, the asperity summit undergoes a plastic deformation. A contact spot radii, a is formed and is given by:

$$a=0 \quad \text{if} \quad \delta\leqslant 0 \tag{5a}$$

$$a=\delta/2m \quad \text{if} \quad \delta>0 \tag{5b}$$

Here δ is the summit penetration depth and is sketched in Fig. 2. A value of δ less than zero implies that the two asperities are not in contact.

The separation distance or clearance between the reference planes of the two conforming rough surfaces is given by [8]:

$$\varepsilon=\sqrt{2}\sigma\,\mathrm{erfc}^{-1}\left[\frac{2P_j}{P_j+H}\right] \tag{6}$$

The above expression for clearance takes into account the material hardness (H), the surface roughness (σ) and the contact pressure (P_j) in the contact zone. For conforming flat surfaces, the pressure term in Eq. (6) corresponds to the overall contact pressure based on the apparent area of contact. However, for non-flat surfaces, the pressure would vary in the different contact zones. The contact region is therefore subdivided into large number of elemental areas within which the pressure is assumed to be same. This is dealt with subsequently.

(b) Flatness. The deviation in flatness reduces the macroscopic contact region over and above the reduction caused by the microscopic asperity contact. Figure 3 illustrates the modeling procedure of the contact region for two surfaces A and B. The surface A has a high degree of flatness, whereas B has a flatness deviation of d_f. Only part of the surface facing each other comes into contact as represented by the shaded region shown in Fig. 3(b). This area is referred as the contour area of contact (A_f)

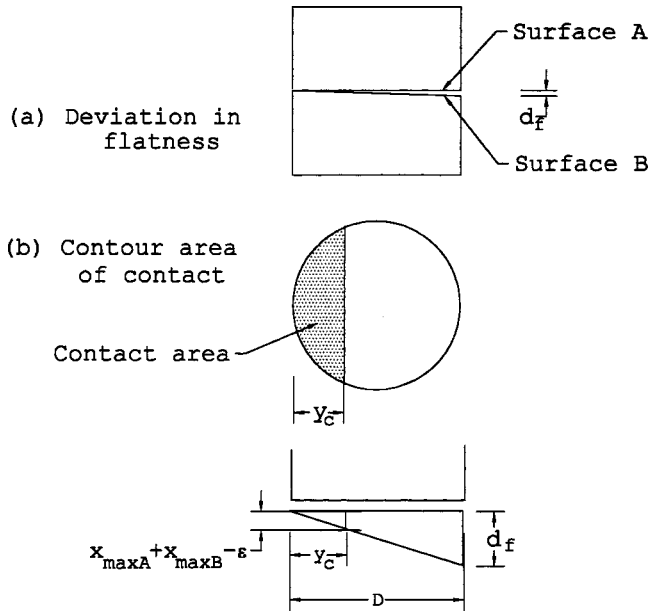

Fig. 3 Physical representation of non-flat rough contact

formed due to flatness deviation [11]. The area would change as the clearance between the contacting surfaces changes. A simple two-dimensional geometrical representation of the surfaces, shown in Fig. 3(*b*), is used to determine the extent y_c over which the surfaces are in contact. This is given by:

$$\frac{y_c}{D}=\frac{x_{\max A}+x_{\max B}-\varepsilon_{\min}}{d_f} \tag{7}$$

Here $x_{\max A}$ and $x_{\max B}$ represent the maximum asperity height of surface *A* and surface *B*, respectively. *D* is the diameter of the surface. The above expression assumes that the surfaces are in contact up to a limit wherein their respective surface asperities can touch each other. The contact area will depend on the applied pressure. In order to determine the contact area and its variation with pressure, the surface is divided into a number of zones of width dy as illustrated in Fig. 4. The maximum pressure and therefore the minimum clearance ($\varepsilon_{\min}$) would occur at zone $j=1$ for a

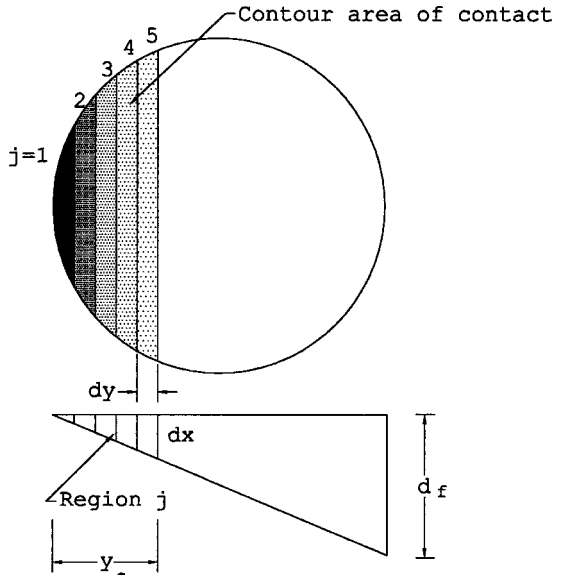

Fig. 4 Descretization of the contact zone

given applied load. The pressure at this zone could be approximated as the ratio of the load to the elemental area. The pressure in each zone will vary along y_c. The pressure is considered to be constant in each of the elemental zones. Knowing the maximum pressure at zone $j=1$, the pressure at subsequent elements is deduced from the following expression [17].

$$P_j=P_1\left[1-\left(\frac{j\times dy}{y_c}\right)^2\right]^{1/2} \tag{8}$$

Here P_1 corresponds to the pressure at zone $j=1$. The width *dy* of the element is so chosen that the estimated total contact area does not differ more than 2% when the width is halved. The zone $j=1$ is in contact when a small value of pressure is applied at the interface. As pressure is increased additional zones get into contact. The number density of contacting asperities in zone $j=1$ are higher compared to new zones which come into contact as applied pressure is increased. The additional clearance (dx_j) at the boundaries of each discretized zone is given by:

$$dx_j=1/2[j.dyd_f/D+(j+1)dyd_f/D] \tag{9}$$

The separation distance is enhanced by the above magnitude over that estimated for rough but conforming flat surfaces. The net clearance for a rough non-flat surface is given by:

$$\varepsilon_j=\varepsilon_{\min}+dx_j \tag{10}$$

(c) Waviness. The waviness is quantified in terms of the average waviness height w_a, average spacing *l*, and average slope or curvature of (*R*). The macro contact zone of two wavy surfaces could either be in the zones of their respective peaks or between the peaks and valleys. The former would give a small macro contact area whereas the latter would provide substantially larger contact. A large number of combinations of peak and valley contact between the surfaces are theoretically feasible. For joints prepared by turning in a lathe, peak to valley contact at the interface is not probable considering the changes of the depth in the azimuthal direction. The contact zone with waviness is modelled as the sum of the contour area of each contacting waviness peak based on the two-dimensional representation of average waviness height, spacing and curvature. The clearances between the wavy surfaces in contact are determined based on averages unlike in the case of roughness and flatness deviations. The width of the contact zone (*w*) when two peaks of radii if curvature R_1 and R_2 meet is given by Hertzian contact theory [17] as:

$$w=\left[\frac{3\pi(K_1+K_2)}{2\left(\frac{1}{R_1}+\frac{1}{R_2}\right)}P\right]^{1/3} \tag{11}$$

where,

$$K_1=\frac{1-\nu_1^2}{\pi E_1}\quad\text{and}\quad K_2=\frac{1-\nu_2^2}{\pi E_2} \tag{12}$$

R_1 and R_2 are macro parameters and the material properties which influence the deformation are the Young's modulus (*E*) and Poisson's ratio (ν). The contour contact area is found for each of the contacting waviness peaks. The microscopic contact region within this macro area is determined using the roughness parameter (R_a) detailed earlier.

The number of wavy peaks (n_f) in contact is determined from measured values of waviness and flatness parameters. The extent y_c over which the surfaces are in contact is based on waviness height and not on the maximum asperity heights.

Model for Thermal Contact Conductance. The heat flow is constrained at macro level through the contour zones corresponding to the macro constrictions from non-planarity and waviness before being further constrained through the individual micro contacts. In addition to the microscopic constriction resistance (R_s) there are therefore two additional macroscopic constriction resis-

tances [6,7] (R_f and R_w) formed by the area contours due to waviness and flatness deviation. The total constriction resistance (R_t) is therefore given by:

$$R_t = R_s + R_f + R_w \tag{13}$$

The total contact conductance h_t is determined as:

$$h_t = 1/R_t A_a \tag{14}$$

The resistance due to surface roughness (R_s) is determined following Mikic [2] using two flat conforming rough surfaces. The heat flow rate for each individual contact is written as,

$$Q_i = 2ka_i \Delta T_c ./ \psi_{si} \tag{15}$$

Here ΔT_c is the temperature drop across the interface. The individual constriction alleviation parameter ψ_{si} in the above equation is defined by:

$$\psi_{si} = (1 - (P_j/H)^{1/2})^{1.5} \tag{16}$$

The constriction parameter is considered to be same ($\psi_s = \psi_{si}$) for all contacting asperities in an elemental zone following [4]. If there are n_c contacting asperities over an apparent area A_a, the total heat flow across the joint is given as:

$$Q = \sum_1^{n_c} Q_i = \frac{2k\Delta T_c}{\psi_s} \sum_1^{n_c} a_i \tag{17}$$

The thermal contact resistance due to surface roughness alone can be calculated from the above equation as:

$$R_s = \frac{\Delta T_c}{Q} = \frac{\psi_s}{2k \sum_{n_c} a_i} \tag{18}$$

Here n_c represents the number of contacting asperities, a_i is the radius of each individual contact circle formed by the two contacting asperities (Fig. 2) and k is the harmonic mean of the conductivities of the two contacting materials. The values of a_i are obtained from the surface roughness parameter using Monte-Carlo simulation of contacting asperities and is detailed in Reference [5].

The macro resistances due to flatness deviation and waviness (R_f and R_w) is written following [8] as:

$$R_f = \frac{\psi_f}{2ka_f} \tag{19}$$

and

$$R_w = \frac{\psi_w}{2ka_w} \tag{20}$$

The macroscopic constriction parameters ψ_f and ψ_w in the above equation are estimated using the expression developed by Roess [11] which gives:

$$\psi_{f,w} = 1 - 1.4093(x_{f,w}) + 0.2959(x_{f,w})^3 + 0.0525(x_{f,w})^5 \tag{21}$$

where

$$x_f = \frac{a_f}{r_a} \quad \text{and} \quad x_w = \frac{a_w}{r_a} \tag{22}$$

Here, a_f and a_w represent the equivalent radius of the contour area formed respectively by flatness deviation and waviness. r_a is the radius of the apparent area of contact. The total contact conductance can be written from Eq. (14) as:

$$h_t = \frac{1}{\left[\dfrac{\psi_s}{2k \sum_{n_c} a_i} + \dfrac{\psi_f}{2ka_f} + \dfrac{\psi_w}{2ka_w} \right] A_a} \tag{23}$$

Contact Area Due to Roughness, Waviness, and Deviation in Flatness

The number of contacting asperities (n_c) within the macro contact zone and their respective contact spot radii, a_i are determined using Monte-Carlo simulation technique [5]. For two contacting surfaces of a given surface texture, the number of asperities in a discretised contact zone of area A_j is given following Eq. (2) as:

$$N_j = NA_j \tag{24}$$

If $x_{\max 1}$ and $x_{\max 2}$ are the respective maximum asperity heights due to roughness of surfaces 1 and 2, respectively, and if one asperity each is randomly chosen on either surface of height x_1 and x_2 then:

$$\frac{x_1}{x_{\max 1}} \leqslant 1 \quad \text{and} \quad \frac{x_2}{x_{\max 2}} \leqslant 1 \tag{25}$$

The individual asperity heights could be assumed to follow Gaussian distribution, and the above equation can be re-written as:

$$\frac{x_1}{x_{\max 1}} \leqslant U_{x1} \quad \text{and} \quad \frac{x_2}{x_{\max 2}} \leqslant U_{x2} \tag{26}$$

Here U_x represents Gaussian random numbers between 0 and 1. By randomly assigning values to U_{x1} and U_{x2}, the individual asperity heights can be estimated. If the combined height of the asperities is larger than the clearance, ε calculated earlier for a region j by Eq. (10), then these asperities will touch each other.

The penetration depth of the asperity is given by;

$$\delta = x_1 + x_2 - \varepsilon_j \tag{27}$$

Here ε_j is the clearance for the discretized zone j and considers the cumulative effect of roughness, deviations in flatness and waviness. Once δ is known, the spot contact radii, a_i can be calculated from Eq. (5) derived earlier. The analysis is repeated for all the asperities in all the descretised zones and covers the entire asperities in the contact region. The total number of contact spots (n_c) and their respective contact radii are thus determined.

Predicted Results and Discussions

The micro and macro contact areas derived in the last section are substituted in Eqs. (18, 19, and 20) to determine micro constriction resistance R_s and macro constriction resistance R_f and R_w. The total surface contact conductance is determined from Eq. (23). A flow chart for the computation is given in Fig. 5. A Microsoft Fortran uniform random number generator subroutine RANDOM is used for generating Gaussian random numbers. The subroutine returns a value between 0 and 1 for an input seed value. For the same input seed value repeated computations reproduced results within 0.23%. When the number of random numbers used for the generation of Gaussian random number was doubled, the deviations were found to reduce further. The estimated conductance values differed only by 0.16% between double precision and single precision computations.

The random model was validated by predicting the results for the limiting case of conforming flat and non-wavy surfaces i.e.; $w_a = 0$ and $d_f = 0$. Predictions were done for varying surface roughness and pressure for different materials. The results are compared in Fig. 6 with those obtained for flat surface joints given in Reference [5] as dimensionless contact conductance h^* and pressure P^*. It is seen that almost identical values are obtained over a wide range of contact pressures confirming the basic model to be valid. A large number of computations were carried out by

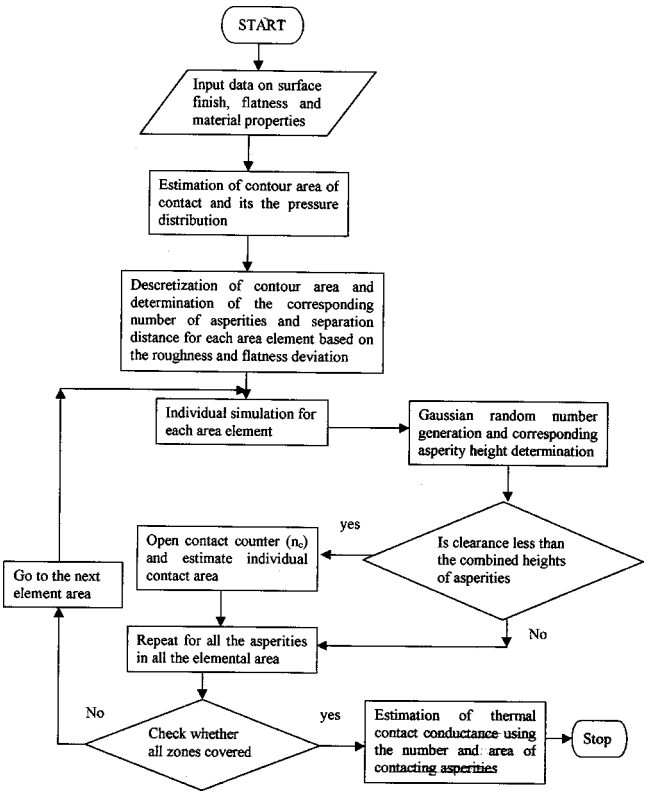

Fig. 5 Computational flow diagram

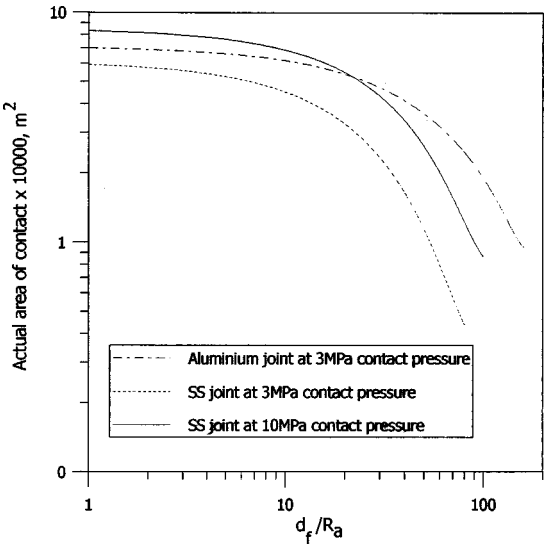

Fig. 7 Effect of flatness deviation on actual area of contact for stainless steel and aluminum joints

varying the values of surface parameters, interfacial contact pressure and materials of contacting surfaces. The predictions are discussed below.

Influence of Flatness Deviations. A typical result showing the reduction in actual contact area for a stainless steel joint due to deviation in flatness is illustrated in a log-log plot in Fig. 7 for two different values of contact pressures of 3MPa and 10MPa. The surface roughness parameter, R_a considered is 1.0 μm. It can be seen that higher contact area persists when the ratio of the flatness deviation to average roughness, (d_f/R_a) is less than about 10. For values of the ratio greater than about 10, rapid decrease of the contact area is observed. It is also noted from the figure that a higher contact pressure yields higher contact surface area and this is to be anticipated.

A second set of predictions, carried out for an aluminum/aluminum joint at 3MPa contact pressure yielded similar trends and is also included in Fig. 7. The chain-dotted line shows the predictions. For the softer material, the contact area is large and is less influenced by deviation in the flatness.

The variation of contact conductance with changes in flatness is shown in Fig. 8 for aluminum/aluminum joint at a contact pressure of 3MPa. The results are qualitatively similar to the changes in contact area and the conductance values are seen to be higher for lower degree of flatness deviation. As the deviation in flatness increases, the number of contact spots reduces resulting in lower values of thermal contact conductance. There exists a region of $d_f/R_a \leqslant 10$ wherein the contact conductance values remains fairly unaffected by the changes in flatness. The results suggest that for two surfaces in contact with each other, it is adequate to maintain the surface flatness deviations within approximately 10 times the

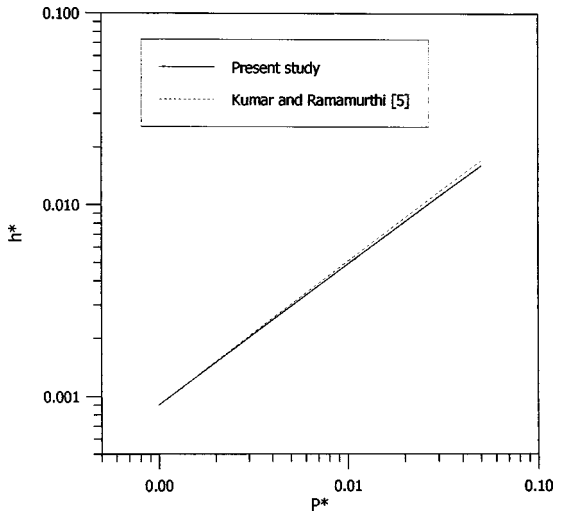

Fig. 6 Comparison with earlier literature for non-wavy flat surfaces

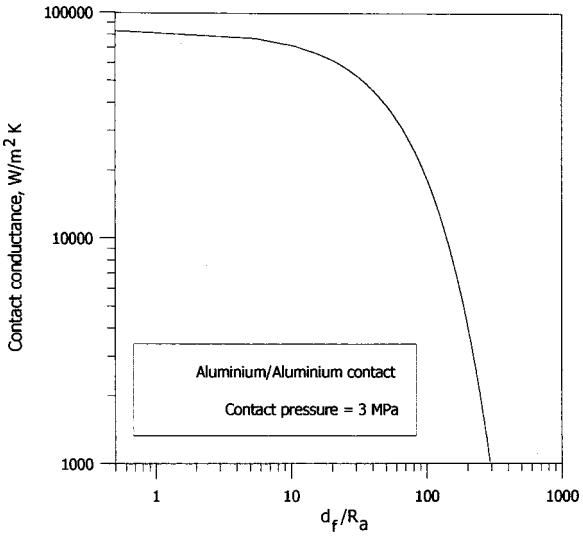

Fig. 8 Influence flatness deviations on thermal contact conductance

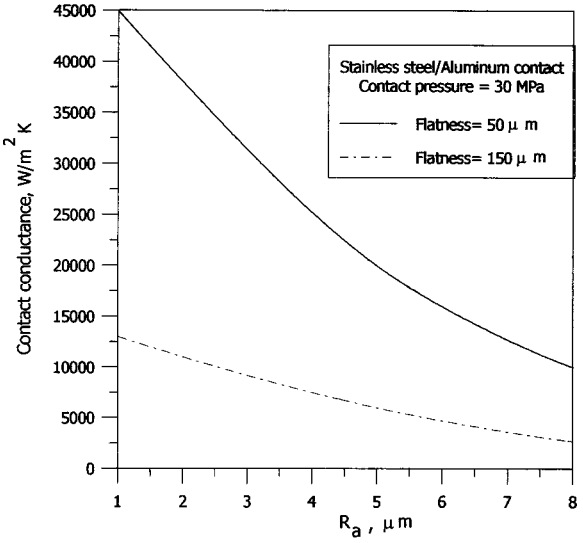

Fig. 9 Inter-dependence of flatness and mean surface roughness

average surface roughness values in order to achieve good thermal contact conductance. Extremely high levels of flatness do not significantly contribute to improvement of the thermal contact conductance.

The variation of the estimated contact conductance values when the average surface roughness is varied for two values of flatness deviations of 50 μm and 150 μm is shown in Fig. 9. Very significant changes in contact conductance values are observed with changes in roughness for the surface having lower flatness deviation. When the magnitude of flatness deviations are comparable with that of surface roughness, the later would influence the contact area and hence affect the values of thermal contact conductance. Flatness deviations of 50 μm and 150 μm, considered in Fig. 9 are very much higher than surface roughness parameter R_a. As the surface roughness parameter R_a increases, the difference in the conductance values between the two non-flat surfaces becomes smaller. For large values of surface roughness, the influence of flatness deviation on thermal contact conductance is small.

Influence of Waviness. The influence of waviness on thermal contact conductance is shown in Fig. 10. A stainless steel/aluminum joint with varying waviness heights for a specified waviness spacing of 80 μm and an average radius of curvature for wavy peaks of 3 μm is considered. This corresponds to specimens obtained by machining in a conventional lathe. A constant value of surface flatness deviation of 6 μm and an overall contact pressure of 30 MPa is assumed. Two sets of data are shown in the figure corresponding to surface roughness (R_a) values of 1 μm and 2 μm. The thermal contact conductance is seen to be relatively unaffected by changes in the value of waviness of about 4 times the average roughness. This value is much smaller compared to the value of 10 obtained in the case of flatness. Though, flatness is the larger macro surface parameter compared to waviness, the contact conductance at a joint is more strongly influenced by waviness. The stronger dependence is attributed to the large decrease in contact area with increasing waviness heights for a specified value of waviness spacing.

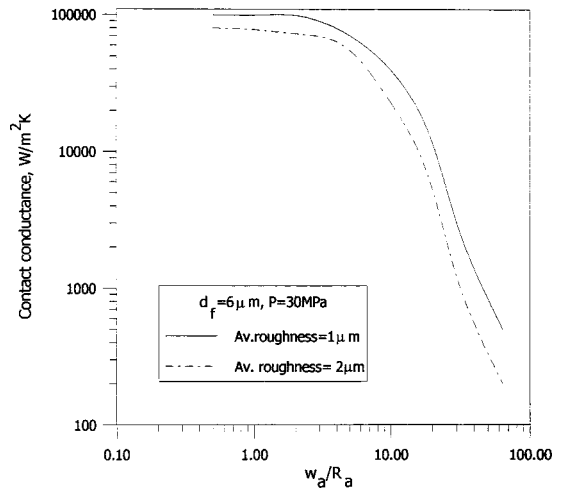

Fig. 10 Surface waviness influence on thermal contact conductance

Generalized Results. A large number of predictions of the contact conductance were carried out by varying the surface roughness, R_a, waviness height, w_a and flatness deviation, d_f at different contact pressures for different materials. These predictions were fitted by general correlation which would bring out the relative influence of each of the variables on the thermal contact conductance. Such a correlation could be useful for a designer to fix acceptable limits for the surface finish, waviness, and flatness deviations. The regression analysis procedure of using a dimensionless pressure and contact conductance term [5] in addition to a newly introduced non-dimensional term, K was followed to fit the predicted values. The term K considered the influence of roughness, waviness, and flatness deviations. A least square fit of the results gives the following:

$$h^* = 0.14(P^*)^{0.61} e^{-1/K} \tag{28}$$

where

$$h^* = \frac{h\sigma}{mk}; \quad P^* = \frac{P}{H}; \quad \text{and} \quad K = 3.8\sigma\left(\frac{2}{d_f + \dfrac{w_a l}{R_{av}}}\right) \tag{29}$$

Here, R_{av} denotes the harmonic mean of the average curvatures of the waviness peaks of the two surfaces. The above correlation is valid over the range of dimensionless loading parameter between 0.0014 and 0.1. The value of K is varied between 0.13 and 5. The standard error in the h^* estimate is 0.0074. The exponent of pressure load is found to be 0.61 which is very close to the values reported by Leung et al. [4], Sunil Kumar and Ramamurthi [5] and Madhusudana [8]. The additional term, K has a negative exponent and brings down the value of contact conductance. The macro surface properties are therefore important. For the limiting case of non-wavy conforming flat surfaces (w_a and d_f tending to very small values), close match is seen between the present correlation and that reported in reference [5].

Experiments

Test Specimen. Stainless steel and aluminum rods 7 cm long and 3 cm in diameter were used for the experiments. These two materials were chosen as they are widely used in different applications and their mechanical and thermal properties are well known. Rough surfaces with flatness deviation were prepared in a conventional milling machine. The preparation of wavy surfaces was more involved and a lathe was programmed for the movement of the cutting tool at speeds between 0.3 mm/rev and 1.8 mm/rev.

The surface finish, waviness, and flatness deviations of the surfaces were evaluated from two-dimensional measurements of surface topography. A Form Talysurf with digital readout facility which uses a position sensitive variable inductance transducer was used to measure the surface characteristics. The transducer converts the small vertical movements of a diamond stylus into proportional variation of electrical signal. The transducer had a sen-

Table 1 Details of test specimens

Test pair	Specimen	R_a (μm)	d_f (μm)	w_a (μm)	1 (μm)
1	SS 304	1.3	17	—	—
2	Aluminum	1.5	17	—	—
3	SS 304	0.6	10	4	980
4	Aluminum	0.6	10	3	700

sitivity of 0.01 μm. Surface roughness and waviness were determined over an evaluation length of 2.5 cm. The signals obtained over the evaluation length were analyzed for cut-off length as per International Standards Organization (ISO). The cut-off length is the minimum length required to give valid measurement of microscopic irregularities. A cut off length of 0.8 mm was chosen for turned surfaces [14]. The distribution of surface heights determined within the cut-off length corresponded to surface roughness and gave the roughness profile. The average surface roughness R_a was obtained the measurements over the entire evaluation length.

The waviness was determined by filtering the roughness from the profile obtained over the evaluation length. The macroscopic undulations obtained after the filtering constitute the waviness and were fitted in the Talydata-2000 software for average surface parameters w_a, l, and R. The above representation of waviness using averages for depth, spacing and curvature is done following the procedure of Dagnall [14].

The flatness deviation d_f of each surface is obtained by filtering out the surface roughness and waviness in the Talysurf measurements. The instrument had a measurement accuracy of $\pm 2\%$ over the specified range of 0 to 20 μm.

A total of 8 test specimens, 4 each of stainless steel and aluminum were made. The range of surface finish, waviness and flatness deviations in the specimen is given in Table 1 given below. The ratio of d_f/R_a varied between 13 and 16 and the ratio w_a/R_a varied between 5 to 6.7 in the specimens. These values are seen from the prediction to be in the region where waviness and flatness do influence the contact conductance.

Experimental Setup. The surface contact conductance was measured in an axial heat flow apparatus. A sketch of the test apparatus is shown in Fig. 11. Test coupons were heated by a heat flux standard (heater). These standards generate a specified value of one-dimensional heat flux. The power input to the heat flux standard was controlled by a variac and measured through a precision digital wattmeter. The contact pressure at the interface was varied by tightening the loading bolt. A load cell placed between the heater and the loading bolt was used for the measurements. The contact pressure was varied between 5 MPa and 70 MPa.

An insulator (Fig. 11) was used to reduce the heat transferred through the loading bolt. The insulator was made out of Vespel, a material possessing an extremely low thermal conductivity ($\approx$0.02 W/mK). Six thermocouple junctions of *T*-type were attached to the surface of the test specimen 7 mm apart. The thermocouples were welded to the test specimen using a discharge type thermocouple welding machine. The load cell and thermocouple outputs were connected to a Fluke Hydra series digital multimeter (DMM) with scanner.

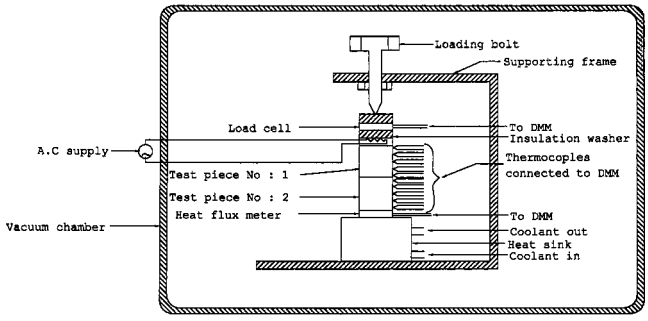

Fig. 11 Experimental set-up

The set-up was placed inside the vacuum chamber of approximately 180 litres capacity. Vacuum was achieved using a two-stage rotary vane vacuum pump. The level of vacuum was measured using a Pirani gauge with readout facility. All experiments were conducted at vacuum better than 10^{-3} mbar. A heat flux gauge was placed below the bottom sample, as shown in Fig. 11, to assess the heat transfer rate through the sink.

The heat flow through the specimen was maintained at about 5.0 watts for the experiments. The thermal path through the specimen showed a much smaller thermal resistance than the thermal path through the pointed loading bolt. The heat transfer through the specimen was determined with the measured temperature gradients. These values were about the same as the power input to the heater indicating that transverse and upward heat flow through the loading mechanism were negligibly small. The radiation loss to the surrounding was minimized by covering the test pieces by a bright aluminum foil. The maximum value of the measured total heat loss was within 9%.

The assumption of steady state was taken to correspond to a situation when maximum temperature change over a period of 5 minutes was less than 0.1°C. In practice, steady state conditions were reached within 40 minutes. However, for the first set of experiments involving initiation from cold conditions, the transients were much longer (almost 190 minutes).

Uncertainty in Measurements. A key factor affecting contact heat transfer measurements is the heat loss. The heat loss was ensured to be small by maintaining the resistance of heat flow to the surrounding to be sufficiently large compared to the contact resistance at the interface. Since the experiments were done in a vacuum chamber, the major source of heat loss to the surrounding is by radiation. The measurement of the temperature differences and the error in locating the thermocouples also contributed to the uncertainties in measurement. All the thermocouples were fabricated in the laboratory and were calibrated using high accuracy microprocessor-controlled temperature bath with an accuracy of ± 0.1°C prior to use. The interfacial temperature difference in the experiments varied between 2°C and 18°C and the mean interfacial temperature varied from 50°C to 73°C.

The maximum uncertainty is associated with experiments having highest load across the joint and for specimens of smoothest surface having least surface waviness and flatness deviations. This condition results in the smallest temperature drop across the interface. The maximum uncertainty in the differential temperature measurement is ± 0.3°C for the smallest temperature difference of 2°C and corresponds to 15% uncertainty. With heat conduction through the specimens known within 9%, the largest uncertainty in measured thermal contact conductance was therefore $[0.09^2 + 0.15^2]^{0.5} = 17.5\%$. The accuracy of measurements was much better for wavy and non-flat surfaces and for test coupons with larger values of surface roughness. The pressure and load measurements were accurate within 2% of the nominal.

Experimental Results and Comparison. Experiments were first done for non-flat and non-wavy surface contacts formed by stainless steel joints and aluminum joints and then repeated with wavy and non-flat surfaces given in Table 1. All experiments were carried at different values of interface contact pressures. Figure 12 gives a comparison of the measured values with the values obtained from prediction and from the generalized correlation given by Eq. (28).

The measured values are seen to be in excellent agreement with the predictions and the correlation. Higher values of contact conductance for aluminum/aluminum contact is to be anticipated due to its lower material hardness. Under pressure, aluminum flows

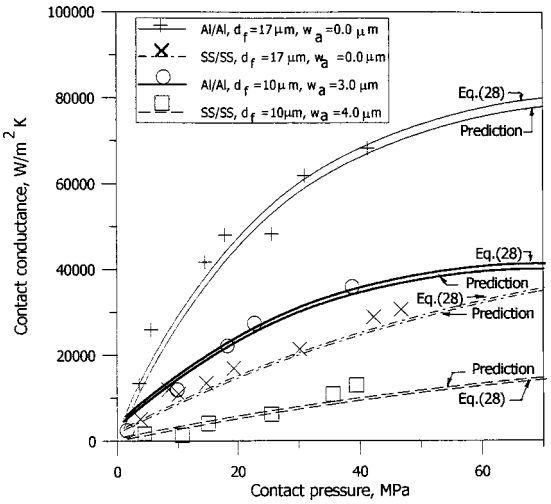

Fig. 12 Comparison of experimental results with predictions and generalized correlation

easier leading to higher values of contact area and hence the contact conductance. A few points in both aluminum and stainless steel joints show deviations which are well within the measurement accuracy of the experiments. Waviness drastically brings down the contact conductance in both stainless steel and aluminum samples confirming that waviness is indeed a very strong surface parameter in the determination of contact conductance. For wavy samples at lower contact pressures, the measured values were observed to be lower than predictions. This could be attributed to the assumption of perfect peak to peak contact in the model. The correlation matches with most of the experimental data within 17%.

Conclusions

The influence of the roughness, waviness and flatness of surfaces on contact conductance is determined. The macro contact area corresponding to deviation in flatness and waviness and the micro contact area for surface roughness is modeled and the surface contact conductance predicted. Experiments are also done with stainless steel and aluminum samples having different levels of waviness, flatness and roughness. The results of the experiments are demonstrated to match closely with the theoretical predictions.

The surface waviness is observed to influence surface contact conductance more strongly compared to flatness deviations. Deviation in flatness less than about 10 times the surface roughness and waviness less than about 4 times the surface roughness do not strongly influence the thermal contact conductance. Flatness is the larger macro surface parameter compared to waviness and the contact conductance is consequently less strongly influenced by waviness. The influence of waviness and flatness is particularly pronounced at smaller values of contact pressures and for harder materials of construction.

A generalized correlation is developed for contact conductance to include the effect of surface roughness, waviness and flatness deviations. The influence of contact pressures and material properties are included in the correlation. The correlation matches with the experimental results within about 17%.

Acknowledgment

The authors thank Mr. Abhilah, P.M for the assistance in conducting the experiments. The helpful discussions with Professor C.V. Madhusudana of University of New South Wales are gratefully acknowledged. The comments and suggestions of the anonymous reviewers helped in revising the manuscript. Their suggestions are also acknowledged.

Nomenclature

a = radius of contact spot/contour, m
A = area, m^2
D = diameter of the sample, m
d_f = deviation in flatness, μm
E = Young's modulus, Pa
h_t = total thermal contact conductance, W/m^{2}K
h^* = dimensionless contact conductance
H = micro hardness of the softer material, Pa
j = number of the discretized region
K = dimensionless surface parameter
k = harmonic mean of thermal conductivities, W/mK
l = waviness spacing, μm
m = slope of the asperity
N = density of asperities, per m^2
n = number of contacting asperities
P = overall contact pressure, Pa
P_j = contact pressure for zone j, Pa
P^* = dimensionless pressure
Q = heat flow rate, W
R = radius of curvature of waviness peak, m
R_a = mean surface roughness, μm
$R_{f,s,w,tt}$ = resistance due to flatness, roughness, waviness and total, K/W
ΔT = temperature difference
U_x = Gaussian random number
w = width of area of contacting wavy peaks, m
w_a = average waviness height, μm
x = summit heights, m
δ = summit penetration depth, m
ε = clearance between the surfaces, m
ν = Poisson's ratio
σ = standard deviation in summit heights, m
$\psi_{f,s,w}$ = constriction alleviation factor due to flatness, roughness, and waviness

Subscripts

a = apparent
av = average
c = asperity contact
i = ith asperity
j = jth discretized region
max = maximum
r = real
w = contour contacts due to waviness
1,2 = surfaces 1 and 2

References

[1] Clausing, A. M., and Chao, B. T., 1965, "Thermal Contact Resistance in Vacuum Environment," ASME J. Heat Transfer, **87**, pp. 243–251.
[2] Mikic, B. B., 1974, "Thermal Contact Conductance; Theoretical Considerations," Int. J. Heat Mass Transf., **17**, pp. 205–214.
[3] McWAID, T., and Marschall, E., 1992, "Thermal Contact Resistance Across Pressed Metal Contacts In Vacuum Environment," Int. J. Heat Mass Transf., **35**, pp. 2911–2920.
[4] Leung, M., Hsieh, C. K., and Goswami, D. Y., 1998, "Prediction of Thermal Contact Conductance in Vacuum by Statistical Mechanics," ASME J. Heat Transfer, **120**, pp. 51–57.
[5] Sunil Kumar, S., and Ramamurthi, K., 2001, "Prediction Of Thermal Contact Conductance In Vacuum Using Monte-Carlo Simulation," J. Thermophys. Heat Transfer, **15**, pp. 27–33.
[6] Yovanovich, M. M., 1969, "Overall Constriction Resistance Between Contacting Rough, Wavy Walls," Int. J. Heat Mass Transf., **12**, pp. 1517–1520.
[7] Thomas, T. R., and Sayles, R. S., 1975, "Random Process Analysis Of The Effect Of Waviness On Thermal Contact Resistance," Prog. Astronaut. Aeronaut., **39**, pp. 3–20.
[8] Madhusudana, C. V., 1996, *Thermal Contact Conductance*, Mechanical Engineering Series, Springer-Verlag, New York, pp. 35.
[9] Madusudana, C. V., 2000, "Accuracy In Thermal Contact Conductance

Experiments—The Effect Of Heat Losses To The Surroundings,'' Int. Commun. Heat Mass Transfer, **27**, pp. 877–891.
[10] Lambert, M. A., and Fletcher, L. S., 1996, ''A Review Of Thermal Contact Conductance Of Metals,'' AIAA Paper 96-0239.
[11] Marotta, E. E., and Fletcher, L. S., 2001, ''Thermal Contact Resistance Models Of Non-Flat, Roughened Surfaces With Non-Metallic Coatings,'' ASME J. Heat Transfer, **123**, pp. 11–23.
[12] Lambert, M. A., and Fletcher, L. S., 2002, ''Thermal Contact Conductance Of Non-Flat, Rough, Metallic Coated Metals,'' ASME J. Heat Transfer, **124**, pp. 405–412.
[13] Mikic, B., 1970, ''Thermal Constriction Resistance Due To Non-Uniform Surface Conditions; Contact Resistance At Non-Uniform Interface Pressure,'' Int. J. Heat Mass Transf., **13**, pp. 1497–1500.
[14] Dagnall, H., 1986, *Explaining Surface Texture*, Rank Taylor Hobson Ltd., UK
[15] Whitehouse, D. J., 1994, *Handbook of Surface Metrology*, IOP Ltd, UK, Chap. 2.
[16] Sengupta, T. K., and Lekoudis, S. G., 1985, ''Calculation of Turbulent Boundary Layer Over Moving Wavy Surfaces,'' AIAA J., **23**(4), pp. 530–536.
[17] Seely, F. B., and Smith, J. O., 1963, *Advances in Mechanics of Materials*, Wiley, NY, Chap. 11.

Numerical Simulation of Reciprocating Flow Forced Convection in Two-Dimensional Channels

Cuneyt Sert

Ali Beskok
e-mail: abeskok@mengr.tamu.edu

Mechanical Engineering Department,
Texas A&M University,
College Station, TX 77840-3123

Numerical simulations of laminar, forced convection heat transfer for reciprocating, two-dimensional channel flows are performed as a function of the penetration length, Womersley (α) and Prandtl (Pr) numbers. The numerical algorithm is based on a spectral element formulation, which enables high-order spatial resolution with exponential decay of discretization errors, and second-order time-accuracy. Uniform heat flux and constant temperature boundary conditions are imposed on certain regions of the top surface, while the bottom surface is kept insulated. Periodicity of velocity and temperature fields is imposed on the side boundaries, while the flow is driven by an oscillating pressure gradient. These sets of boundary conditions enable time-periodic solution of the problem. Instantaneous and time-averaged surface and bulk temperature distributions, and Nusselt number variations are presented. For high α flows, the temperature field is significantly affected by the Richardson's annular effect. Overall, forced convection increases by increasing the penetration length, α and Pr. Corresponding steady-flow simulations are performed by matching the volumetric flowrate. For the limited parameter space investigated in this paper, steady unidirectional forced convection is more effective than the reciprocating flow forced convection. [DOI: 10.1115/1.1565092]

Keywords: Channel Flow, Computational, Forced Convection, Heat Transfer, Pulsating

Introduction

Fluid flow and heat transfer in circular tubes, ducts and channels have extensive engineering applications, including heat exchanger design, biomedical engineering and micro-fluidics. Steady forced convection heat transfer in channels and tubes is well understood. Simple geometry and steady flow conditions enable analytical solutions and collection of reliable experimental data. This results in analytical and empirical relations for the Nusselt number variations in terms of the flow parameters (Shah and London [1]). However, there are relatively fewer investigations of oscillatory-flow heat transfer, which has more stringent time and spatial resolution requirements. Oscillatory flows can be grouped into two categories: pulsating (modulated) and reciprocating (fully reversing) flows. Pulsating flows are always unidirectional and can be decomposed into steady and unsteady components, such as in the case of blood flow in arteries (Zamir [2]). For reciprocating flows, the flow direction changes cyclically. Hence, these flows convect zero net mass. With the advent of micro-electromechanical systems (MEMS) and micro-fluidics, pulsating and reciprocating flows are finding more engineering applications. For example, membrane driven micro-pumps and peristaltic micro-mixers result in pulsating flows (Beskok and Warburton [3], Yi et al. [4]). Several novel heat exchanger devices for electronic cooling applications utilize reciprocating flow and heat transfer (Liao et al. [5], Sert and Beskok [6]). Reciprocating flows are also utilized to enhance mixing in micro-scales (Oddy et al. [7], Dutta and Beskok [8]).

Analyses of pulsating and reciprocating flow heat transfer differ from each other, mainly due to the thermal and velocity boundary conditions. Pulsating flows are unidirectional. Hence, they have permanent inflow and outflow regions, where one can easily define the inlet velocity and temperature boundary conditions. Reciprocating flows require interchange between the inflow and outflow boundaries during a cycle. For most applications, it is difficult to determine the inflow/outflow boundary conditions, since fluid particles exiting the flow domain during a part of the cycle are fed back into the domain, later in the cycle. Although the momentum equation yields an analytical solution for two-dimensional fully developed reciprocating channel flows, analytical solution of the heat transfer problem is not possible, unless the thermal boundary conditions are simplified. In this paper, we mainly concentrate on reciprocating flow heat transfer. Hence, we will discuss the previous work on reciprocating flow heat transfer in detail. Some experimental, numerical and analytical studies on pulsating flow heat transfer can be found in (Siegel and Perlmutter [9]; Siegel [10]; Kim et al. [11]; Moschandreou and Zamir [12]; Zhao and Cheng [13]; Greiner et al. [14]).

A literature survey on reciprocating flow heat transfer shows two different categories of investigations. The first one is focused on heat conduction enhancement with high frequency, low amplitude oscillations, while the second one is focused on forced convection with low frequency, large amplitude oscillations in relatively short channels. One of the early studies of the former category is due to Chatwin [15], who showed enhancement of species diffusion under high frequency oscillations. Later this phenomenon was applied to enhance heat transfer, where effective thermal diffusivities, that are about three orders of magnitudes higher than the values due to molecular thermal diffusion, are achieved (Kurzweg and Zhao [16]; Kurzweg [17]).

Regarding the second category, Li and Yang [18] investigated heat transfer in reciprocating flows at low frequencies and large amplitudes by numerical simulations. They showed heat transfer enhancement due to the intra-cycle oscillations, which were caused by ''sudden changes of the inlet and exit boundary conditions.'' Liao et al. [5] performed forced-convection experiments

Contributed by the Heat Transfer Division for publication in the JOURNAL OF HEAT TRANSFER. Manuscript received by the Heat Transfer Division January 14, 2002; revision received December 4, 2002. Associate Editor: S. P. Vanka.

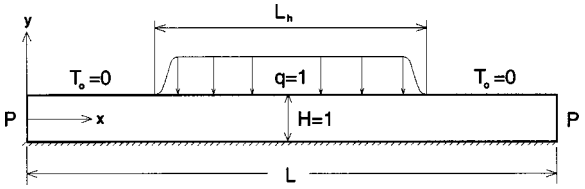

Fig. 1 The geometry and thermal boundary conditions used in this study. On the top surface, uniform heat flux of $q=1$ is specified at $5 \leqslant x \leqslant 15$. For $4 \leqslant x \leqslant 5$ and $16 \geqslant x \geqslant 15$, the heat flux varies from zero to unity sinusoidally. Zero wall temperature is specified for $x \leqslant 4$ and $x \geqslant 16$. Bottom wall is insulated, while side surfaces are periodic (cyclic/repeating).

on microprocessor chips by means of channeled zero-mean oscillatory air flow. They measured the surface temperature of several power generating components in a typical personal computer, and reported heat transfer enhancement by oscillatory forced convection, compared to the conventional fan cooling. Based on the Reynolds number (Re), Liao et al. [5] distinguished two different heat transfer enhancement mechanisms. In the low Re regime, heat transfer enhancement was observed due to the reduction in the Stokes layer thickness with increased flow frequency. While for the high Re regime, heat transfer enhancement was observed due to the presence of ''higher-order harmonics of imposed flow frequency.'' Cooper et al. [19] investigated forced convection heat transfer by heating the bottom wall section of a rectangular duct. Experiments were performed at low frequencies with large tidal displacements. The results showed enhanced heat transfer rates for increased oscillation frequencies and tidal displacements, and decreased duct heights. Chou et al. [20] used oscillatory flow to cool electronic devices. Their idea was to carry the heat away from the source using bubbles oscillating in a micro channel. Preliminary results show heat transfer enhancement caused by the oscillatory flow.

In this study, we present numerical solutions of reciprocating fluid flow and heat transfer in two-dimensional channels. This paper is organized as follows. First, we further define the problem, and state the boundary conditions. Then the governing equations are presented, followed by the exact solution of the fluid flow problem and demonstration of numerical convergence characteristics of our scheme for high Womersley number flows. Finally, the temperature field results are presented and the effects of various flow and heat transfer parameters on time-periodic oscillatory forced convection are discussed.

Problem Definition and Important Parameters

A schematic view of the computational domain along with the associated boundary conditions is shown in Fig. 1. We consider fully reversing flow driven by an oscillatory pressure gradient. The middle portion of the top plate is uniformly heated, while its two sides are kept at constant temperature, and the bottom plate is insulated. The presence of constant temperature zones allows a time-periodic solution for the heat transfer problem. Periodic (cyclic/repeating) boundary conditions are specified at the two ends. The periodicity condition is such that fluid coming out of one side enters through the other side. Therefore, the velocity and temperature values are always the same at both ends. For a better understanding of the periodic boundary conditions, this problem can be visualized as a portion of an infinitely long channel with repeated constant temperature and constant heat flux sections as shown in Fig. 2. Such a configuration can be observed in electronic cooling applications, where the IC boards usually have a repeating pattern. For this application, our analysis would be valid sufficiently away from the device inlet/exit regions, where flow development effects are negligible.

In our simplified two-dimensional model, there are four important geometric length scales: channel height H^*, total channel length L^*, length of the heated portion of the channel L_h^*, where heat flux is applied, and the penetration length L_p^* (tidal displacement). Penetration length is the average distance traveled by fluid particles during one-half of an oscillation period ($\tau^*/2$). Considering sinusoidal oscillations, the penetration length is defined as

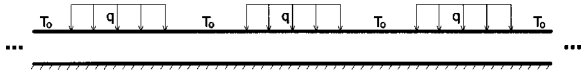

Fig. 2 Schematic view of a hypothetical problem that consists of a channel with repeating heated and constant temperature boundaries

$$L_p^* = \bar{u}^* \frac{\pi}{\omega^*}, \tag{1}$$

where $\omega^* = 2\pi/\tau^*$ is the oscillation frequency and $\bar{u}^*$ is the time and cross-channel averaged axial velocity. The parameter L_p^* is a practical measure of the oscillation amplitude. For efficient cooling, L_p^* should be large enough so that the heated fluid under the constant heat-flux region will travel towards the constant temperature boundaries, where efficient heat transfer to the surroundings can take place.

For oscillatory flows the Womersley number is an important non-dimensional parameter, defined as

$$\alpha = \sqrt{\frac{\omega^* H^{*2}}{\nu^*}}. \tag{2}$$

The Womersley number determines the velocity profile. Small α values result in a quasi-steady flow with oscillatory parabolic velocity profiles. However, large α values lead to the well-known ''Richardson's annular effect'' that results in near-wall velocity overshoots, where the maximum velocity no longer occurs at the symmetry plane (Zhao and Cheng [13]; Richardson and Tyler [21]). This has direct effects on heat transfer, since high velocities with large gradients increase the heat removal rate from the surfaces. Zhao and Cheng reported observing annular effects in the temperature profiles [13]. This is also verified in our current study. The Womersley number is sometimes called the ''kinetic Reynolds number'' because it plays the same role as the Reynolds number in unidirectional steady flows. The Prandtl number (ratio of momentum and thermal diffusivities) is also important in heat transfer. For reciprocating flows, the thermal boundary layer thickness is determined by both the Prandtl and Womersley numbers.

Selecting the channel height H^* as the characteristic length scale, the important nondimensional parameters are L ($=L^*/H^*$), L_h ($=L_h^*/H^*$), L_p ($=L_p^*/H^*$), α and Pr. This five-parameter space makes it difficult to study the importance of every parameter in detail. Therefore, we fixed the normalized channel length L and the heated region length L_h, and varied L_p, α, and Pr, by using two different values for each of these parameters. This results in eight different conditions, which are summa-

Table 1 Non-dimensional parameters used in the simulations

Case no.	L	L_h	L_p	α	Pr	Re′
1	20	12	5	1	1	$5/\pi$
2	20	12	5	1	10	$5/\pi$
3	20	12	5	10	1	$500/\pi$
4	20	12	5	10	10	$500/\pi$
5	20	12	10	1	1	$10/\pi$
6	20	12	10	1	10	$10/\pi$
7	20	12	10	10	1	$1000/\pi$
8	20	12	10	10	10	$1000/\pi$

rized in Table 1. The parameters appearing in Table 1 are all nondimensional.

In our simulations the input parameters are L_p, α, and Pr. The flow is driven by an oscillatory pressure gradient given by,

$$\frac{\partial p^*}{\partial x^*} = -A^* \cos(\omega^* t^*), \tag{3}$$

where p^*, A^*, and t^* are the pressure, pressure gradient amplitude and time, respectively. The amplitude A^* is directly related to $\bar{u}^*$ introduced in Eq. (1). Its value is calculated using the analytical velocity profile, which will be demonstrated in the forthcoming sections.

Nondimensionalization and Governing Equations

Numerical simulations are performed using nondimensional parameters. The length, time, velocity, pressure, temperature and heat flux are normalized as follows:

$$x = \frac{x^*}{H^*} \qquad y = \frac{y^*}{H^*} \qquad t = \frac{t^*}{1/\omega^*} \qquad u = \frac{u^*}{\omega^* H^*}$$

$$p = \frac{p^*}{\rho^*(\omega^* H^*)^2} \qquad T = \frac{T^* - T_o^*}{\Delta T^*} \qquad q = \frac{q^*}{k^* \Delta T^*/H^*} = 1, \tag{4}$$

where the velocity is normalized by $\omega^* H^*$ due to the lack of a characteristic velocity scale in the problem. In Eq. (4), T^* and q^* represent the temperature and heat flux, respectively, while the specified wall temperature is T_o^*, and ΔT^* is a reference temperature difference in the domain. Since there is only one reference temperature value on the wall (T_o^*) and uniform or zero heat flux conditions are specified on the rest of the boundary, ΔT^* is determined in the *post-processing stage*. We calculate the appropriate value for ΔT^* using the maximum allowable temperature difference in the flow domain (based on the design considerations) and the calculated maximum nondimensional temperature ($T_{\max}$). As an example, lets consider an electronic cooling application, where the maximum temperature difference between the ambient and the chip surface is 30°C. If our simulation results in $T_{\max} = 2$, then $\Delta T^* = 15$°C. We can calculate the maximum possible heat dissipation (q^*) from the system using $q^* = qk\Delta T^*/H^*$. Alternatively, one can select the desired heat flux (q^*), and calculate ΔT^* to find the maximum surface temperature. This normalization makes it easier to utilize *dynamic similarity* for obtaining the dimensional temperature and heat flux values.

Governing equations are the conservation of mass, incompressible Navier-Stokes and heat transport equations, presented in the following nondimensional form,

$$\nabla . \vec{u} = 0, \tag{5}$$

$$\frac{\partial \vec{u}}{\partial t} + (\vec{u}.\nabla)\vec{u} = -\nabla p + \frac{1}{\mathrm{Re}} \nabla^2 \vec{u}, \tag{6}$$

$$\frac{\partial T}{\partial t} + (\vec{u}.\nabla) T = \frac{1}{\mathrm{Pe}} \nabla^2 T, \tag{7}$$

where $\mathrm{Re} = \alpha^2$ for oscillatory flows. Thermal conduction coefficient and viscosity are assumed to be constant and the viscous heating terms in the heat transport equation are neglected. These assumptions and approximations are consistent with the previous analytical and numerical studies.

At this point it is worthwhile to mention that the flow inside the channel is hydrodynamically fully developed (i.e., the streamwise gradient of the velocity vector is zero) at all times. Based on Fig. 2 and the discussion about the periodic end conditions, fully-developed flow is automatically satisfied. Therefore, the entry and flow development effects are excluded in the current study.

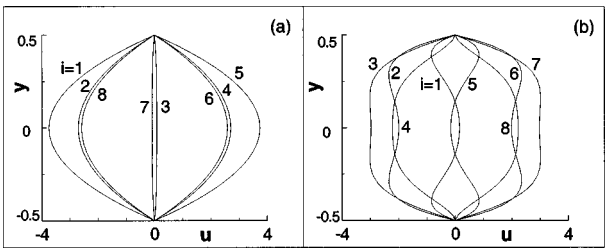

Fig. 3 Analytical solution of the velocity profiles at various times during a cycle for (*a*) $\alpha = 1$, and (*b*) $\alpha = 10$ flow. Index *i* represents time within a period of the pressure pulse ($t = i - 1/8\ \tau$).

Analytical Solution of the Velocity Field

The analytical solution of reciprocating flows in a two-dimensional channel is known. Consider the flow between two parallel plates, driven harmonically in time with a pressure gradient of the following form,

$$-\frac{\partial p}{\partial x} = A e^{-it}, \tag{8}$$

where A is the pressure gradient normalized with $(\rho^* \omega^{*2} H^{*3})$, and $i = \sqrt{-1}$. The velocity profile for this flow is given by (Landau and Lifshitz [22])

$$u(y,t) = \mathrm{Real}\left\{ iAe^{-it}\left[1 - \frac{\cos\left(\frac{(i+1)\sqrt{2}}{\alpha} y \right)}{\cos\left(\frac{(i+1)}{\sqrt{2}\alpha} \right)} \right] \right\}, \tag{9}$$

where y is the cross channel distance normalized by the channel height H^*. Figure 3 shows the velocity profiles at various instances during a cycle for $\alpha = 1$ and $\alpha = 10$ flows. Quasi-steady flow behavior is observed for $\alpha = 1$ flow, while the Richardson's annular effect is present for $\alpha = 10$.

The time and cross-channel-averaged velocity ($\bar{\bar{u}}$) is obtained by integrating Eq. (9) as follows,

$$\bar{\bar{u}} = \frac{1}{\tau H} \int_0^\tau \int_{-H/2}^{H/2} u(y,t)\, dy\, dt, \tag{10}$$

where $\tau = 2\pi$ (radians) is the normalized oscillation period, and $H = 1$ is the normalized channel height. This integral is evaluated numerically, and $\bar{\bar{u}} = 0.0528A$ and $\bar{\bar{u}} = 0.5647A$ are obtained for $\alpha = 1$ and $\alpha = 10$, respectively. For a desired tidal displacement L_p, we calculate the corresponding pressure amplitude A, using $\bar{\bar{u}} = L_p/\pi$, which is a nondimensional form of Eq. (1).

Numerical Accuracy and Convergence

Our numerical algorithm utilizes spectral element discretization of two-dimensional, unsteady Navier-Stokes and heat transport equations (Eqs. (5–7)). Time integration is handled by a second-order accurate, stiffly stable time integration scheme. In this section, we demonstrate the space and time accuracy of our numerical solution by comparisons with the analytical solution of the reciprocating flow velocity profile. Simulations were performed using 104 elements, where 26 elements were employed in the streamwise direction and 4 elements were employed in the cross flow direction, as shown in Fig. 4 (top). In the spectral element method, we keep the elemental discretization of the domain fixed, and refine our solution by increasing the expansion order within each element (*p*-type refinement). In Fig. 4 (bottom), we show quadrature points obtained by *p*-type refinements, which result in 16, 49, 100, and 169 collocation points for 3rd, 6th, 9th, and 12th order spectral expansions, respectively. The spectral element

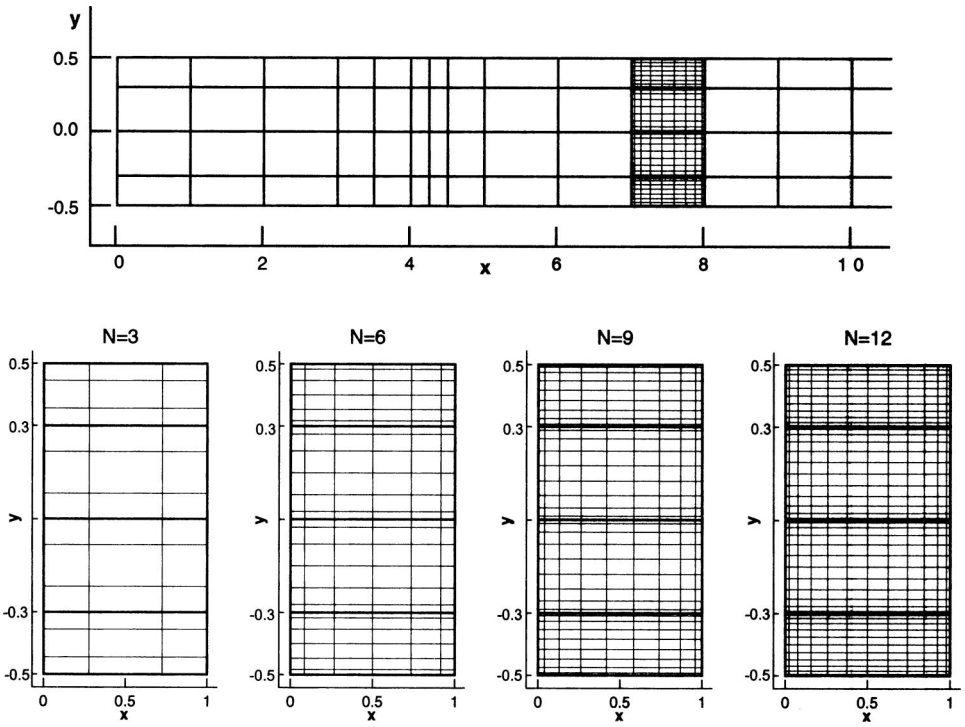

Fig. 4 ***Top*: Half of the actual mesh used in the simulations. Quadrature points for a 9th-order expansion are also shown for selected elements. A finer mesh is used at the Neumann/Dirichlet boundary interface on the top wall ($4<x<4.5$) to resolve large temperature variations.** ***Bottom*: A portion of the spectral element mesh showing only cross-channel discretization with different expansion orders (N). Thick lines show the elements, while thin lines show the collocation points. Progressively increasing the element order (N) by keeping the total number of elements fixed is known as *p*-type refinement.**

method *exhibits exponential reduction of discretization errors* for sufficiently smooth (C^{∞}) problems upon *p*-type mesh refinement (Karniadakis and Sherwin [23]). The method also features small dispersion errors for long time integration of unsteady flow problems (Beskok and Warburton [24]).

We demonstrate the convergence characteristics of our method for $\alpha=10$ flow, which exhibits rather complex velocity profiles with large localized gradients. In Fig. 5(*a*), we show the variation of L_{∞} error norm (maximum error) as a function of the elemental expansion order N. The L_{∞} error is calculated using the numerical solution and the exact solution given in Eq. (9). The discretization error is evaluated by solving the unsteady problem with various spectral expansion orders, until a predetermined absolute time is reached. We utilized a very small time-step ($\Delta t=10^{-5}$) in order to ensure that the leading order errors are due to spatial discretization. The results shown in Fig. 5(*a*) clearly indicate the spectral accuracy of the algorithm. Decrease of the discretization error by several orders-of-magnitude with *p*-type refinements is an important aspect of the spectral element method. For example in Fig. 5(*a*), the discretization errors of the 6th and 12th order expansions are about 10^{-4} and 10^{-9}, respectively. This shows a reduction in the discretization error by five orders-of-magnitude, while the number of collocation points per direction is increased approximately by a factor of two (from 7 to 13 between the 6th and 12th order discretizations). Exponential decay of discretization errors by *p*-type refinements is a great advantage of spectral element methods over lower-order schemes, where grid independent solutions can be achieved more effectively.

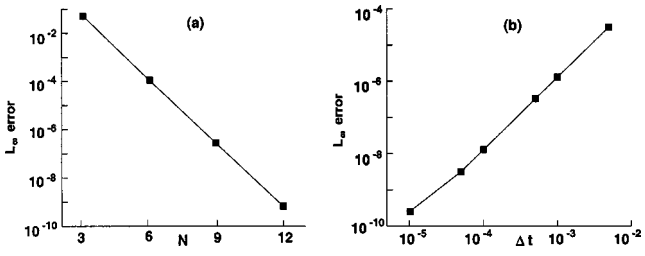

Fig. 5 Space and time accuracy for $\alpha=10$ flow. (*a*) Variation of L_{∞} error as a function of the expansion order N (obtained using $\Delta t=10^{-5}$). Exponential decay of the discretization error indicates spectral convergence. (*b*) Variation of L_{∞} error as a function of the time step (obtained using 12th order elements). Shows second-order time accuracy.

Since we are solving a transient problem, time accuracy of the numerical algorithm also plays a significant role. Time accuracy is verified using controlled sets of simulations, in which, we employed 12th order spectral elements to ensure that the leading-order error in our solution is due to the time discretization. We integrated the transient problem with various time steps until a predetermined absolute time is reached. In Fig. 5(*b*), we show L_{∞} error variation as a function of the time step Δt. The slope of this Log-Log plot is 2, verifying that time accuracy of the algorithm is second-order. Since we do not have an analytical solution for the temperature field, we verified convergence of our numerical results by *p*-type mesh refinements, until grid independent solutions are obtained. The forthcoming results are obtained using polynomial orders of $7\sim9$ and $8\sim11$, for $\alpha=1$ and $\alpha=10$ cases, respectively.

Results

In this section we present detailed analyses of temperature field and heat transfer results for the cases presented in Table 1. We

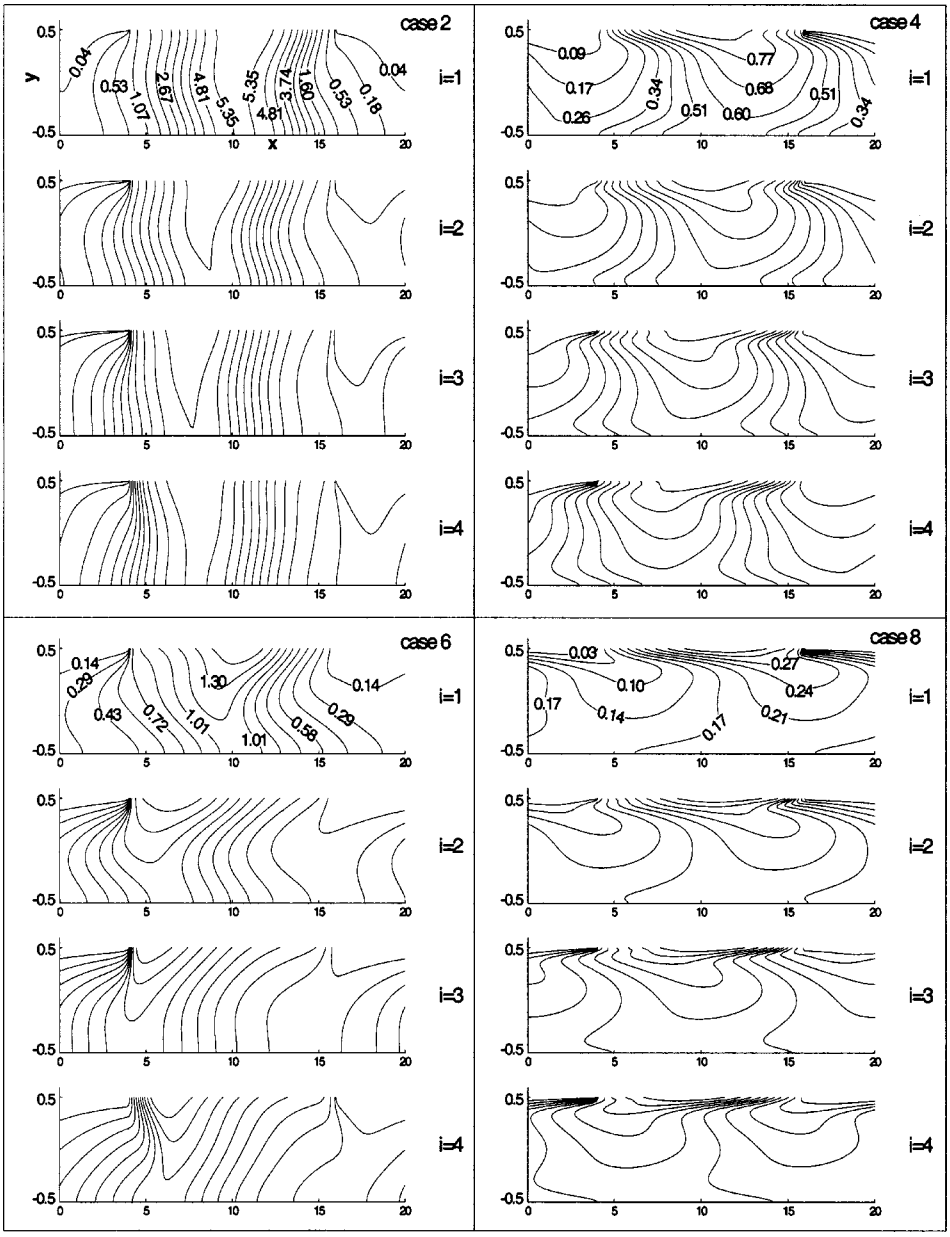

Fig. 6 Instantaneous temperature contours for cases 2, 4, 6, and 8. Index *i* represents time within half a period of the pressure pulse ($t=(i-1)\tau/8$). The flow and thermal conditions are presented in Table 1.

examine the effects of the Prandtl and the Womersley numbers as well as the tidal displacement on heat transfer. The results presented in the following sections are obtained after the simulations have reached their corresponding time-periodic states.

Temperature Contours. We present snapshots of temperature contours for cases 2, 4, 6, and 8 ($\mathrm{Pr}=10$) in Fig. 6. These snapshots are synchronized with the pressure pulse, and they are obtained at 0τ, $1/8\tau$, $1/4\tau$, and $3/8\tau$. Comparisons of cases in the horizontal and vertical directions indicate the effects of α and L_p, respectively. The left column (cases 2 and 6) shows temperature contours oscillating back and forth with rather monotonic shapes. Especially for case 2, temperature contours across the channel are almost uniform at any time. Small L_p and α values for case 2 result in the lowest axial velocities. Hence, conduction (in the axial direction) dominates over convection, as can be deduced from the temperature contours. For case 2, the hot fluid pocket under the heat source is not effectively convecting towards the cold walls. Case 6 has twice the tidal displacement of case 2, and it shows stronger cross-channel temperature variations. Values of the normalized temperature are significantly reduced from case 2 to case 6, indicating increased convective cooling with increased tidal displacement L_p. Large cross-channel temperature variations are observed for cases 4 and 8, which correspond to $\alpha=10$ flows. Case 8 has the highest L_p and α values used in this work. Temperature contours for this case concentrate near the top surface, which indicates thin thermal boundary layers and enhanced forced convection. Temperature values are also significantly lower than the other cases. Our overall observation from Fig. 6 is that the normalized fluid temperature in the channels are decreased with increased tidal displacement L_p and Womersley number α, and the temperature distribution in the channel is highly affected by the velocity profile.

Temperature Profiles. Detailed descriptions of temperature profiles for reciprocating flows are not common in the literature.

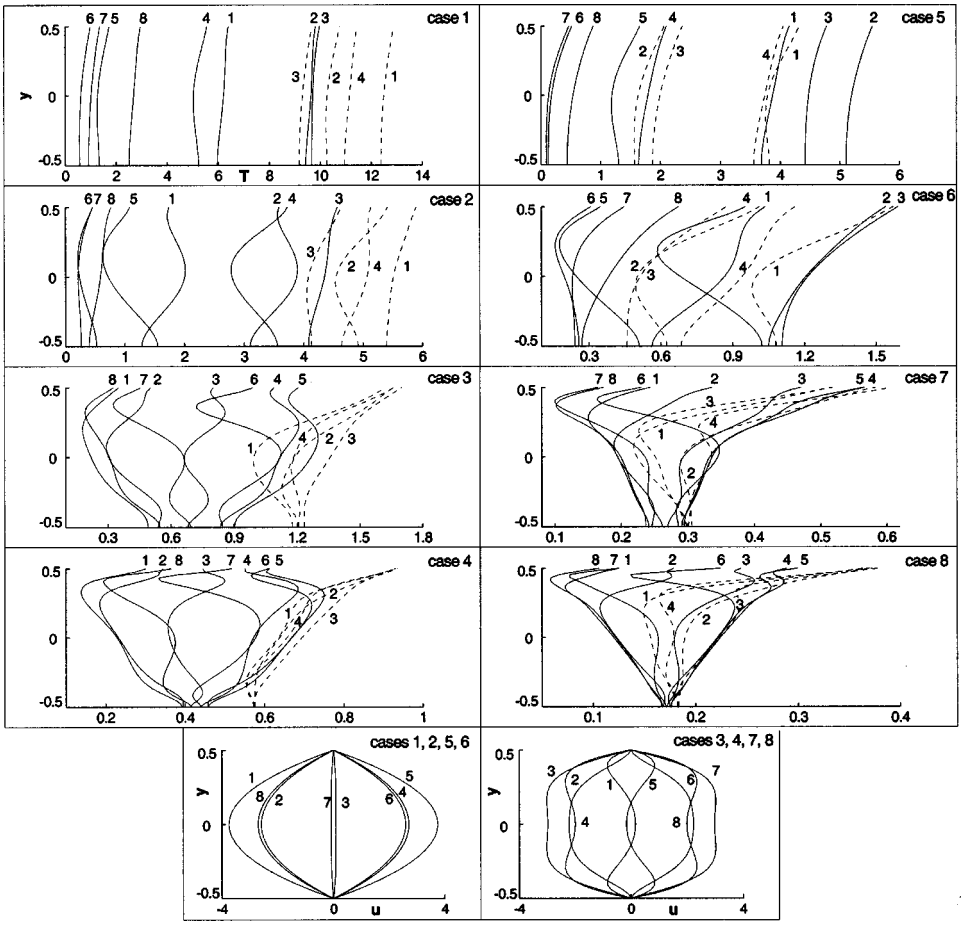

Fig. 7 Instantaneous temperature and velocity profiles at axial locations of $x=5$ (solid-lines) and $x=10$ (dashed-lines). Index i represents time within a period of the pressure pulse ($t=(i-1)\pi/8$). Simulation parameters are presented in Table 1.

In Fig. 7, we present the temperature distribution at $x=5$ (solid-lines) and $x=10$ (dashed-line) for all cases. Each figure shows the temperature profiles obtained at eight different instances. These snapshots are synchronized with the velocity profiles, which are shown at the bottom of the figure. The abscissa shows the temperature value, while the ordinate shows the cross-channel coordinate. The location $x=10$ corresponds to the geometric center of the channel, where non-dimensional heat flux of $q=1$ is imposed on the top wall. Due to the symmetry plane at $x=10$, temperature profiles at this location repeat twice cyclically from $i=1$ to 4, while the temperature profiles at $x=5$ cycle from $i=1$ to 8. In Fig. 7, the top four cases (1, 2, 5, and 6) are obtained under oscillatory parabolic velocity profiles ($\alpha=1$), while the bottom four cases (3, 4, 7, and 8) are obtained for $\alpha=10$ flow. For $\alpha=10$ cases, sharp velocity gradients near the walls result in enhanced oscillations in the temperature profiles. For example, the temperature profile in case 7 has as many as five inflection points at times $i=2$, 3, 5, 6. It is clear from these results that the Richardson's annular effect, which exists in the velocity profiles at large frequencies, affects the temperature profiles. For case 1, temperature profiles are almost uniform at all times. An increase in the tidal displacement L_p results in monotonic temperature variations, as shown in case 5. In cases 1 and 2, temperature values at $x=10$ are higher than the values at $x=5$, which is an indication of hot fluid being stuck under the heated region. The comparison of cases 6 and 7 in Fig. 7 shows that an increased Womersley number results in localized temperature gradients near the top wall with sudden temperature fluctuations. An increase in the Prandtl number creates sharper temperature variations in the cross-flow direction, as can be seen by a comparison of cases 7 and 8. It is interesting to note that for a given axial location, the bottom wall temperature for cases 4, 7, and 8 remains almost constant throughout the cycle. All of these cases have a large α value, which corresponds to a large Re and enhanced convection. Heat supplied from the top plate rapidly convects along the channel and most of the thermal activity is occurring near the top wall. These cases result in bulk temperatures that are significantly lower than the surface temperatures, which results in high Nusselt numbers, as discussed in detail in the following sections.

Top-Wall Temperature Variations. In electronic cooling applications, exceeding a certain temperature may result in chip failure. Therefore, the maximum surface temperature is an important design parameter. In addition to the maximum surface temperature, the time of exposure to high temperatures also plays an important role. Figure 8 shows top wall temperatures at five different instances during half a cycle. Comparison of the left ($L_p=5$) and right ($L_p=10$) columns shows that the maximum top wall temperature for low penetration length simulations occurs in a narrowly bounded region near the channel center. However, for $L_p=10$, the location of the maximum surface temperature is oscillating throughout the entire heated region. Comparisons of all eight cases show that the maximum surface temperature decreases with increased L_p, α, and Pr.

Bulk Temperature and the Nusselt Number. Bulk temperature is an important parameter, used in the calculation of the Nusselt number. Classical definition of the bulk temperature is

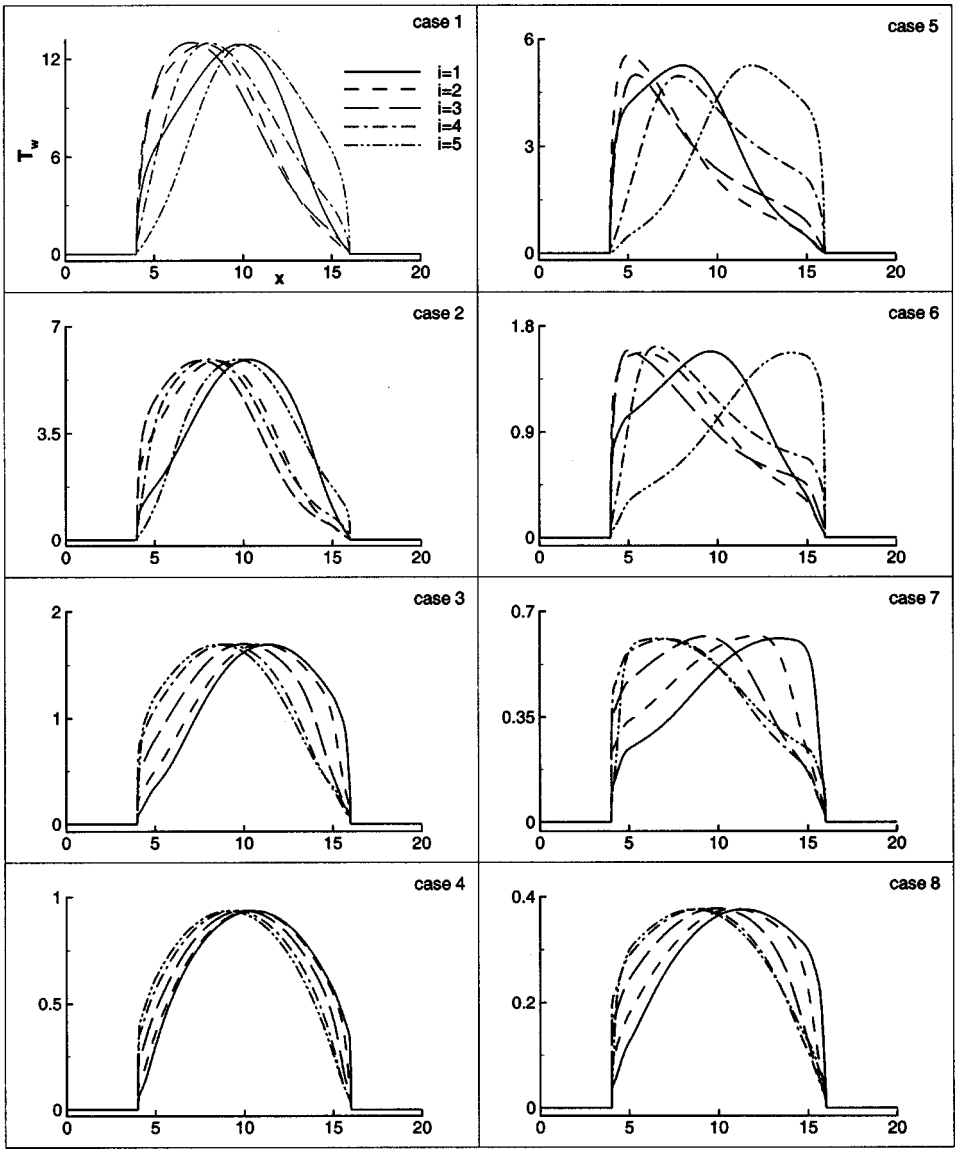

Fig. 8 Instantaneous top-wall temperatures. Index *i* represents time within half a period of the pressure pulse ($t=(i-1)\tau/8$). Simulation parameters are presented in Table 1.

$$T_b(x,t)=\frac{\frac{1}{H}\int_{-H/2}^{H/2}u(y,t)T(x,y,t)dy}{\frac{1}{H}\int_{-H/2}^{H/2}u(y,t)dy}. \tag{11}$$

This definition is not preferred in a reciprocating flow, because the denominator becomes zero twice during a cycle. To overcome this difficulty, we defined a time-averaged bulk temperature in the following form,

$$\overline{T}_b(x)=\frac{\frac{1}{\tau H}\int_0^{\tau}\int_{-H/2}^{H/2}|u(y,t)|T(x,y,t)dydt}{\bar{\bar{u}}}. \tag{12}$$

The absolute value in the numerator is used in order to avoid negative bulk temperatures during the flow reversal. An alternative definition can utilize time integration over a half cycle rather than a full cycle, which will yield the same result due to the half-period symmetry of the velocity and temperature fields.

Figure 9 shows axial variations of time-averaged top-wall (solid lines) and bulk (dashed lines) temperatures. The dashed-dotted and dashed-dotted-dotted lines in the figure correspond to unidirectional steady forced convection cases, which will be discussed in the next section. This figure shows that both the time-averaged wall temperature and bulk temperature decrease with increasing L_p, α, and Pr. For $\alpha=1$ cases (top four plots), the bulk temperature values are close to the time-averaged wall temperature at $5<x<15$. This is especially noticeable for cases 1 and 2. On the other hand, bulk temperatures for cases 7 and 8 are almost half of the time-averaged wall temperatures at $5<x<10$. Here we mention that cases 7 and 8 are the most effective in evenly spreading heat to the entire channel, as can be seen from their almost flat bulk temperature distributions. This also shows enhanced forced convection cooling for these cases.

In the simulations we specified a nondimensional constant heat flux value of unity in the region $5<x<15$. For $q=1$, the time-averaged Nusselt number can be calculated as (Sert and Beskok [6]),

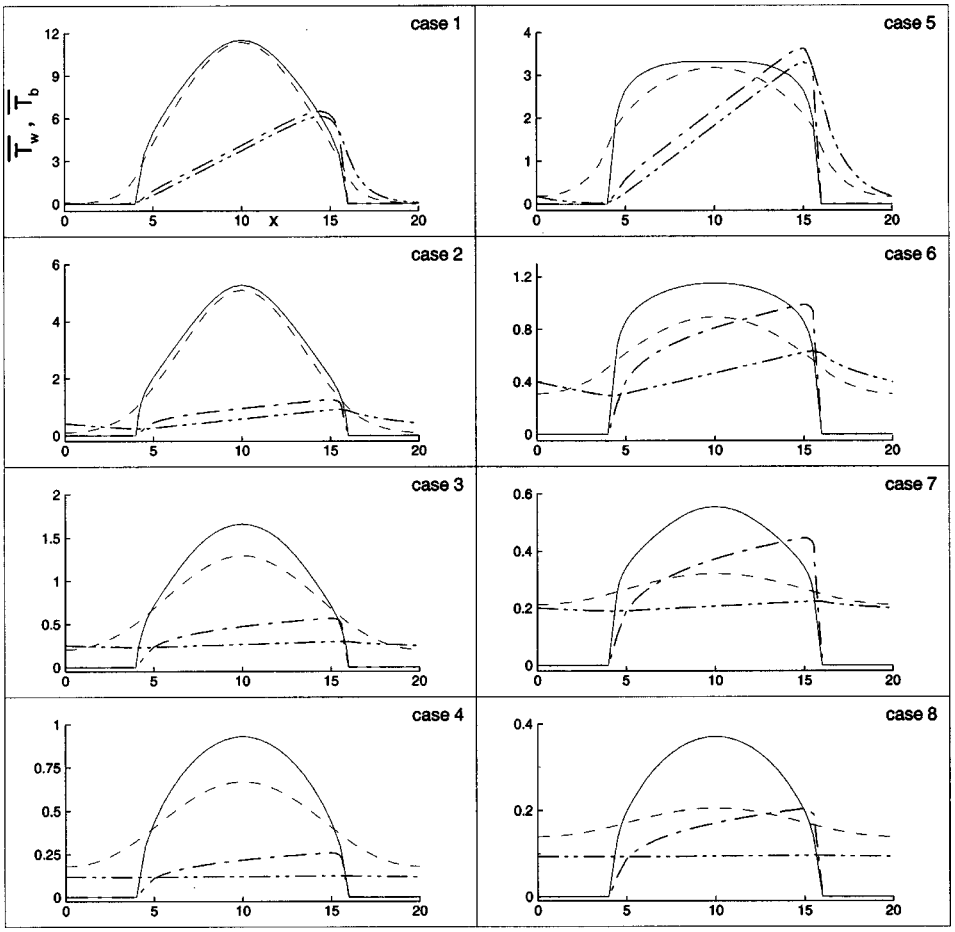

Fig. 9 Time-averaged wall-temperature (solid lines) and time-averaged bulk temperature (dashed-lines) variations for reciprocating flows. Wall temperature (dashed-dotted lines) and bulk temperature (dashed-dotted-dotted lines) variations for unidirectional steady flows are also shown. Simulation parameters are presented in Table 1.

$$\overline{\mathrm{Nu}}(x)=\frac{2}{\overline{T}_w-\overline{T}_b}. \tag{13}$$

Variations of time-averaged Nusselt number along the heated portion of the channel are shown in Fig. 10(*a*). We separated the low and high Womersley number cases. For $\alpha=1$ (cases 1, 2, 5, and 6), the maximum $\overline{\mathrm{Nu}}$ occurs at the middle of the channel ($x=10$). For these cases, slight increases at $x=5$ and $x=15$ are due to the change in the boundary conditions (See Fig. 1). Specifically, the wall temperature suddenly drops to zero at $x=4$ and $x=16$, while the bulk temperature is decreasing gradually. These variations in the boundary conditions result in localized increases in the Nusselt number. It is interesting to notice that the tidal displacement and Prandtl number are both important here. Case 6 shows an almost uniform time averaged Nusselt number in the heated zone, which is an indication of effective heat transfer. The results for $\alpha=10$ are shown on the top left figure. For cases 3, 4, 7, and 8, the maximum $\overline{\mathrm{Nu}}$ occurs at both ends of the heated region, whereas the minimum $\overline{\mathrm{Nu}}$ occurs at the channel center. Comparing case 3 with case 4 (or case 7 with case 8), we observe that the time averaged Nusselt number is increased by increasing the Prandtl number. Comparing case 3 with case 7 (or case 4 with case 8) shows that increasing the tidal displacement increases the Nusselt number. Finally, comparing cases 6 and 8 shows that $\overline{\mathrm{Nu}}$ increases with the Womersley number.

Steady Unidirectional Forced Convection. In this section, previously obtained oscillatory flow temperature and Nusselt number results are compared against the steady, unidirectional forced convection. We match the oscillatory and unidirectional flows by matching the time-averaged flowrate. Reynolds number of the corresponding unidirectional flows is calculated by

$$\mathrm{Re}'=\frac{\bar{u}^*H^*}{v^*}=\frac{\alpha^2L_p^*}{\pi H^*}, \tag{14}$$

which is presented in Table 1. The velocity and temperature boundary conditions at the channel ends are periodic. Flow is from left to right, and it is maintained by a constant pressure gradient. The resultant velocity profiles are parabolic, typical of pressure driven laminar flows. Due to the periodic temperature boundary conditions, fluid leaving from the right boundary is entering from the left with a temperature equal to the exit temperature. Numerical results correspond to the steady state conditions.

Bulk and wall temperature variations along the channel are shown in Fig. 9 using dashed-dotted-dotted and dashed-dotted lines, respectively. For cases 1, 2, and 5, bulk and wall temperatures increase linearly with the same slope in most of the heated region, indicating thermally developed flow. We also observe that case 6 is *almost* thermally developed. Cases 1, 2, 5, and 6 correspond to low Reynolds numbers ($\mathrm{Re}'<4$), resulting in relatively small Peclet numbers. Cases 3, 4, 7, and 8 correspond to Reynolds numbers that are two orders-of-magnitude higher than the corresponding low Reynolds number cases (See Table 1). This is due to the quadratic dependence of the Reynolds number on the Womer-

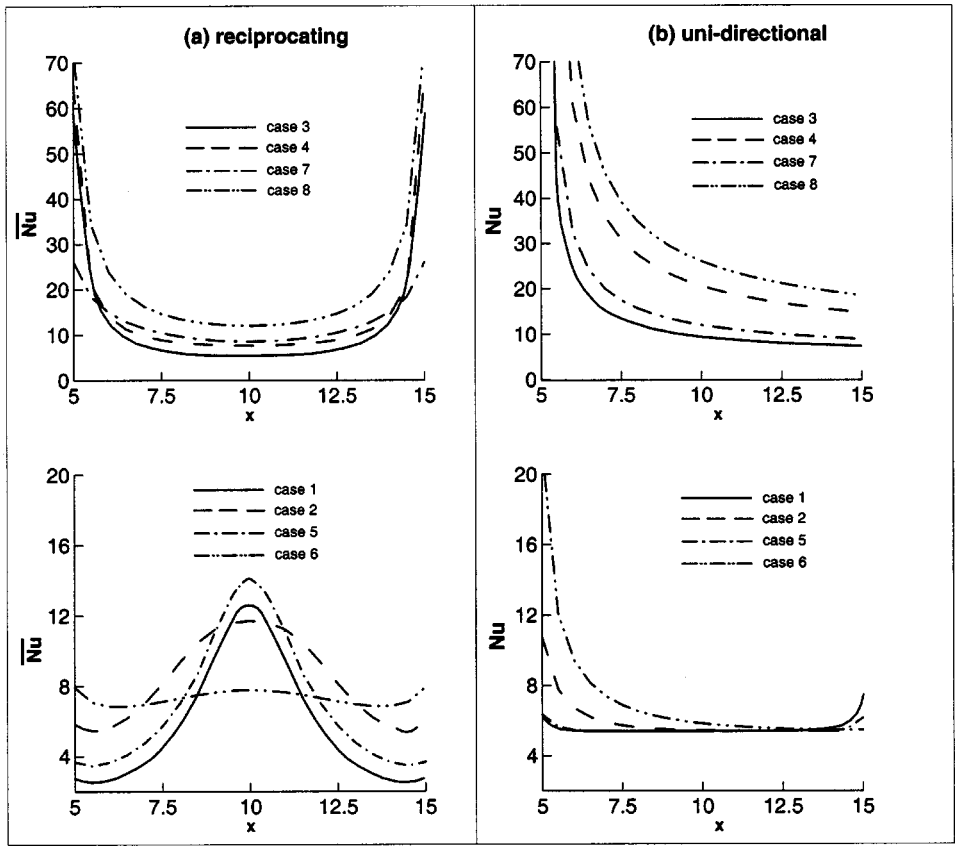

Fig. 10 Axial distribution of time-averaged Nusselt number for (*a*) reciprocating, (*b*) unidirectional steady flows. Simulation parameters are presented in Table 1.

sley number, given by Eq. (14). For these cases, thermally developed conditions are not observed. In all of the cases, unidirectional forced convection results in smaller bulk and surface temperatures than the reciprocating flow, with the exception of case 5. In addition, we note that time-averaged top wall temperatures in Fig. 9 are less than the instantaneous maximum wall temperature shown in Fig. 8. Low L_p cases (cases 1, 2, 3, and 4) give considerably higher maximum wall temperatures than their unidirectional flow counterparts. For cases 4 and 8, the bulk temperature of the unidirectional flows are almost uniform throughout the channel, and these cases correspond to the maximum Peclet numbers simulated in our work. Unidirectional flows result in increasing surface temperatures in the downstream direction, where oscillatory flows experience oscillating temperature maxima, as can be seen from Figs. 9 and 8, respectively. This basic difference may become important for various applications. Nusselt number variations of unidirectional steady flows in the heated region are shown in Fig. 10(*b*). Maximum Nusselt number is observed at the entrance of the heated region and decreases continuously. Two exceptions are the slight increases seen at $x=15$ for cases 1 and 5. These cases have the lowest Pe, and local increase in the Nusselt number is due to noticeable heat conduction in the upstream direction. Cases 1, 2, and 5 have reached thermally developed conditions with constant Nusselt number of 5.387, a value very close to 5.3846 given by Shah and London [1]. Cases 3, 4, 7, and 8 correspond to high Peclet numbers. For these cases, high Nusselt numbers are observed due to the thermally developing flow conditions.

Discussion and Conclusions

Motivated by its potential in electronic cooling and microfluidics applications, we simulated reciprocating flow forced convection in two-dimensional channels, and compared our results with the corresponding unidirectional flows. We assumed a cyclically repeating flow section and imposed periodicity of velocity and temperature fields at the sides of the computational domain. To our knowledge, periodic thermal boundary conditions in reciprocating flows have not been investigated before. Simulation results indicate that the instantaneous and time-averaged surface temperatures, and the time-averaged bulk temperature are reduced by increasing the penetration length, Womersley and Prandtl numbers. Therefore, it is possible to determine a combination of L_p, α, and Pr that will keep the maximum surface temperature below a desired value, which is important for cooling applications. Unlike unidirectional flows, reciprocating flows convect heat to both sides of the heated region. This results in oscillation of the maximum surface temperature along the heated region of the channel, which may be advantageous over unidirectional forced convection, where the maximum surface temperature occurs at the exit of the heated region.

Numerical simulations show an increase of the time-averaged Nusselt number with increasing α, Pr, and L_p. Variation of the time-averaged Nusselt number along the heated region of the channel shows different trends for $\alpha=1$ and $\alpha=10$ flows, indicating that velocity profiles have strong influences on the heat transfer characteristics. Richardson's annular effect, observed in the velocity profiles for high frequency oscillatory flows, affects the temperature profiles and heat transfer characteristics, as shown by the instantaneous temperature contours and profiles. Unidirectional flows corresponding to $\alpha=1$ cases show thermally fully developed conditions towards the downstream portion of the channel. For these cases, the reciprocating flow Nusselt numbers is comparable to or higher than the corresponding unidirectional flow cases. Overall unidirectional flows resulted in smaller surface

temperatures than the reciprocating flows. However, we believe that with proper combinations of the parameters, heat transfer rates higher than the corresponding unidirectional flows can be achieved. In future studies, a larger parameter space will be explored by varying the heated length (L_h) and the total length (L) of the channel.

Finally, temperature dependence of fluid properties, viscous heating and three-dimensionality effects are not considered in the current study. Temperature dependence of fluid properties is significant for large temperature variations. This may be checked by calculating the maximum temperature difference ΔT^* obtained for a desired heat flux value. Viscous heating may become important for high Re flows. Three-dimensionality effects are important for turbulent channel flows; but all cases studied here, including the steady unidirectional flows, fall into the laminar flow regime.

Acknowledgments

This work was funded by Texas Higher Education Council, Advanced Research Program, Grant Number: 000512-0418-1999. The computational facilities provided by Dell STAR Grant are appreciated.

Nomenclature

A = pressure gradient amplitude
C_p = specific heat at constant pressure
H = channel height
k = heat conduction coefficient
L = total channel length
L_p = penetration length
L_h = heated channel length
Nu = Nusselt number
Pe = Peclet number (Re×Pr)
Pr = Prandtl number ($\rho^* v^* C_p^*/k^*$)
q = heat flux
Re = Reynolds number for oscillatory flows ($\omega^* H^{*2}/v^* \equiv \alpha^2$)
Re′ = Reynolds number based on volumetric flowrate per channel width ($\bar{u}^* H^*/v^*$)
t = time
u = axial velocity
x = streamwise direction
y = cross-flow direction

Greek

α = Womersley number ($\sqrt{\omega^* H^{*2}/v^*}$)
ν = kinematic viscosity
τ = period
ω = frequency

Subscript and Superscript

b = bulk quantity
o = reference value, side-wall value
$-$ = time-averaged quantity, used for top wall and bulk temperatures and Nu
$=$ = time and space averaged quantity
$*$ = dimensional quantity

References

[1] Shah, R. K., and London, A. L., 1978, "Laminar Flow Forced Convection in Ducts," *Advances in Heat Transfer*, Irvine, T. F., Jr., and Hartnett J. P., eds., Academic Press, New York, NY.
[2] Zamir, M., 2000, *The Physics of Pulsatile Flow*, Springer-Verlag, New York, NY.
[3] Beskok, A., and Warburton, T. C., 2001, "Arbitrary Lagrangian Eulerian Analysis of a Bidirectional Micro-Pump Using Spectral Elements," Int. J. Comput. Eng. Sci. **2**(1), pp. 43–57.
[4] Yi, M., Bau, H. H., and Hu, H., 2000, "A Peristaltic Meso-Scale Mixer," in *Proceedings of ASME IMECE Meeting*, MEMS, **2**, pp. 367–374.
[5] Liao, Q. D., Yang, K. T., and Nee, V. W., 1995, "Microprocessor Chip Cooling by Channeled Zero-Mean Oscillatory Air Flow," *Advances in Electronics Packaging*, EEP-Vol. 10-2, pp. 789–794.
[6] Sert, C., and Beskok, A., 2002, "Oscillatory Flow Forced Convection in Micro Heat Spreaders," Numer. Heat Transfer, Part A. **42**(7), pp. 685–705.
[7] Oddy, M. H., Santiago, J. G., and Mikkelsen, J. C., 2001, "Electrokinetic Instability Micromixing," Anal. Chem., **73–24**, pp. 5822–5832.
[8] Dutta, P., and Beskok, A., 2001, "Time Periodic Electroosmotic Flows: Analogies to Stokes' Second Problem," Anal. Chem., **73**(21), pp. 5097–5102.
[9] Siegel, R., and Perlmutter, M., 1962, "Heat Transfer for Pulsating Laminar Duct Flow," ASME J. Heat Transfer, **84**, pp. 111–123.
[10] Siegel, R., 1987, "Influence of Oscillation-Induced Diffusion on Heat Transfer in a Uniformly Heated Channel," ASME J. Heat Transfer, **109**, pp. 244–247.
[11] Kim, S. Y., Kang, B. H., and Hyun, J. M., 1993, "Heat Transfer in the Thermally Developing Region of a Pulsating Channel Flow," Int. J. Heat Mass Transf., **36**, pp. 4257–4266.
[12] Moschandreou, T., and Zamir, M., 1997, "Heat Transfer in a Tube with Pulsating Flow and Constant Heat Flux," Int. J. Heat Mass Transf., **40**, pp. 2461–2466.
[13] Zhao, T., and Cheng, P., 1995, "A Numerical Solution of Laminar Forced Convection in a Pipe Subjected to a Reciprocating Flow," Int. J. Heat Mass Transf., **38**, pp. 3011–3022.
[14] Greiner, M., Fischer, P. F., and Tufo, H., 2001 "Numerical Simulations of Resonant Heat Transfer Augmentation at Low Reynolds Numbers," in *Proceedings of ASME International Mechanical Engineering Congress and Exposition*, IMECE2001/HTD-24100, November 11–16, 2001, New York, NY.
[15] Chatwin, P. C., 1975, "The Longitudinal Dispersion of Passive Contaminant in Oscillating Flow in Tubes," J. Fluid Mech., **71**, pp. 513–527.
[16] Kurzweg, U. H., and Zhao, L., 1984, "Heat Transfer by High-Frequency Oscillations: A New Hydrodynamic Technique For Achieving Large Effective Thermal Conductivities," Phys. Fluids, **27**, pp. 2624–2627.
[17] Kurzweg, U. H., 1985, "Enhanced Heat Conduction in Oscillating Viscous Flows Within Parallel-Plate Channels," J. Fluid Mech., **156**, pp. 291–300.
[18] Li, P., and Yang, K. T., 2000, "Mechanisms for the Heat Transfer Enhancement in Zero-Mean Oscillatory Flows in Short Channels," Int. J. Heat Mass Transf., **43**, pp. 3551–3566.
[19] Cooper, W. L., Nee, V. W., and Yang, K. T., 1994, "An Experimental Investigation of Convective Heat Transfer From the Heated Floor of a Rectangular Duct to a Low Frequency Large Tidal Displacement Oscillatory Flow," Int. J. Heat Mass Transf., **37**, pp. 581–592.
[20] Chou, F-C., Weng, J-G., and Tien, C-L., 1998, "Cooling of Micro Hot Spots by Oscillatory Flow," *Proceedings of the 11th International Symposium on Transport Phenomena*, Hsinchu, Taiwan, pp. 324–329.
[21] Richardson, E. G., and Tyler, E., 1929, "The Transverse Velocity Gradient Near The Mouths of Pipes in Which An Alternating or Continuous Flow of Air is Established," Proc. Phys. Soc. London, **42**, pp. 1–15.
[22] Landau, L. D., and Lifshitz, E. M., 1987, *Course of Theoretical Physics Volume 6-Fluid Mechanics*, 2nd ed., Pergamon Press.
[23] Karniadakis, G. M., and Sherwin, S. J., 1999, *Spectral/hp Element Methods for CFD*, Oxford University Press, New York.
[24] Beskok, A., and Warburton, T. C., 2001, "An Unstructured H/P Finite Element Scheme for Fluid Flow and Heat Transport in Moving Domains," J. Comput. Phys., **174**, pp. 492–509.

Numerical Prediction of Flow and Heat Transfer in a Rectangular Channel With a Built-In Circular Tube

S. Tiwari

G. Biswas
e-mail: gtm@iitk.ac.in
Mem. ASME

P. L. N. Prasad

Sudipta Basu

Department of Mechanical Engineering,
Indian Institute of Technology,
Kanpur-208016, India

A numerical investigation of flow and heat transfer in a rectangular duct with a built-in circular tube was carried out for moderate Reynolds numbers and varying blockage ratios. Since the heat transfer in the duct is dictated by the flow structure, the study was directed towards characterization of the flow. To this end, the topological theory shows promise of becoming a powerful tool for the study of flow structures. The limiting streamlines on the tube and the bottom plate reveal a complex flow field. The separation lines and points of singularity (saddle points and nodal points) were investigated. The iso-Nusselt number contours and span-averaged Nusselt number distribution in the flow passage shed light on the heat transfer performance in the duct. The investigation was necessitated by the need to enhance heat transfer in fin-tube heat exchangers through identification of the zones of poor heat transfer. The predicted results compare well with the well documented experimental results available in the literature. In the range of Reynolds numbers considered for the present case, no need is felt to employ any turbulence model in order to describe the heat transfer behavior. Time series signals of the transverse velocity component in the wake zone are presented with their FFT and time-delay plots. The onset of turbulence is not observed up to the highest value of the Reynolds number considered in the present case. This confirms that the transition to turbulence is delayed in the present case compared with that observed for flow past a circular tube placed in an infinite medium. The reason may be attributed to the narrow gap between the no-slip channel walls. [DOI: 10.1115/1.1571087]

Keywords: Forced Convection, Heat Transfer, Heat Exchangers, Tubes, Unsteady, Vortex

Introduction

In gas-liquid crossflow heat exchangers, fin-tubes are commonly used. The gas generally flows across the tubes and the liquid flows inside the tubes. Figure 1 shows a schematic diagram of the core region of a fin-tube heat exchanger. The purpose of the fin is to enhance the heat transfer rate on the gas side, since the transport coefficient on the gas side is usually much smaller than that on the liquid side, see Fiebig et al. [1] and Jacobi and Shah [2]. The various fin configurations are characterized as plain, corrugated and wavy (Wang et al. [3]). Although fin-tube heat exchangers are the most widely used heat exchangers, no experimental method has successfully measured the accurate local heat transfer. Rosman et al. [4] investigated numerically and experimentally one and two-row fin-tube heat exchangers. They used isothermal fins for their calculations, the reason being the narrow space between the two adjacent fins. Two-dimensional simulations of flow past a tube bundle have been reported by Launder and Massey [5] and Wung and Chen [6]. In recently published papers, it has been observed that slender vortex generators can improve the heat transfer coefficient, keeping the pressure penalty at a modest level. Biswas et al. [7] and Tsai et al. [8] reported numerical investigations on related topics. In the above investigations the enhancement of heat transfer from the fin surfaces was achieved by disrupting the growth of thermal boundary layer. Biswas et al. [7] introduced longitudinal (streamwise) vortices in the flow field by placing delta winglet-type vortex generators on the flat surface. Fiebig et al. [9] showed the promise of longitudinal vortices in enhancement of heat transfer through a detailed numerical investigation. Pauley and Eaton [10] used longitudinal vortices for the enhancement of heat transfer in turbulent flows. Longitudinal vortices are developed owing to the difference in pressure between the front surface of the delta winglets facing the flow and the back surface.

Existing air-cooled condensers in geothermal power plants consist of the same fin-tube arrangement as in Fig. 1. Air is forced through several rows of the fins by large fans. The fins act as extended surfaces, providing a larger surface area of heat transfer on the air side. Even with the extended surfaces, dominant thermal resistance is on the air side, since condensation phase-change heat transfer takes place inside the tubes. The condenser units can be very large, consuming a large fraction of the overall capital cost of these plants. In addition, the power required to operate the fans represents a significant parasitic house load, reducing the net power production of the plant. In order to analyze the mechanism involved in the heat transfer and flow behavior in such heat exchangers, a detailed investigation on a heat exchanger module is necessary. Such a module is shown in Fig. 2.

To achieve significant heat transfer enhancement, novel techniques need to be developed. In the region near the fin-tube junction, high heat transfer coefficients exist owing to formation of horseshoe vortices. However, low heat transfer coefficients are observed on the fin surfaces in the near-wake region directly downstream of the circular tubes. This region is therefore a prime focus area for transport enhancement. In the present study, a detailed three-dimensional numerical model has been formulated to provide a better understanding of the flow physics. In the numeri-

Contributed by the Heat Transfer Division for publication in the JOURNAL OF HEAT TRANSFER. Manuscript received by the Heat Transfer Division February 26, 2002; revision received February 13, 2003. Associate Editor: S. P. Vanka.

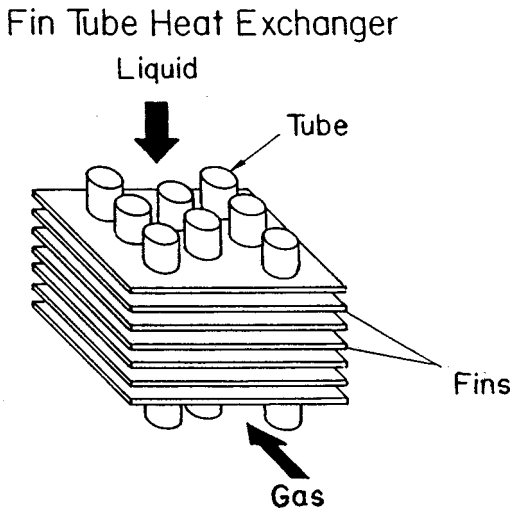

Fig. 1 Schematic diagram of the core region of a fin-tube heat exchanger

cal model, the Navier-Stokes equations together with the governing equation of energy were solved in a rectangular channel with a built-in circular tube.

Statement of the Problem

Figure 2 also represents the computational domain. Two neighboring fins form a channel of height H, width $B=11.25H$ and length $L=25H$. Circular tubes of various diameters are located at a distance $L_1=L/4$ from the inlet. The blockage ratio, D/B, was varied using the values of 0.267, 0.444, and 0.533. Air was used as the working fluid, hence the Prandtl number of the study is 0.7.

The three-dimensional Navier-Stokes equations for laminar flow of an arbitrary spatial control volume V, bound by a closed surface S, can be expressed in the following general convection-diffusion-source integral form:

$$\frac{\partial}{\partial t}\int_V \rho\phi dV+\int_S (\rho\vec{u}\phi-\Gamma_\phi\nabla\phi)\cdot d\vec{S}=\int_V S_\phi dV \qquad (1)$$

where ρ represents the fluid density, $\vec{u}$ is the fluid velocity, ϕ is any vector component or scalar quantity and S_ϕ is the volumetric source term. For incompressible flow of a Newtonian fluid, the equation takes the form

$$\frac{\partial}{\partial t}\int_V \phi dV+\int_S\left(\vec{u}\phi-\frac{\Gamma_\phi}{\rho}\nabla\phi\right)\cdot d\vec{S}=\frac{1}{\rho}\int_V S_\phi dV \qquad (2)$$

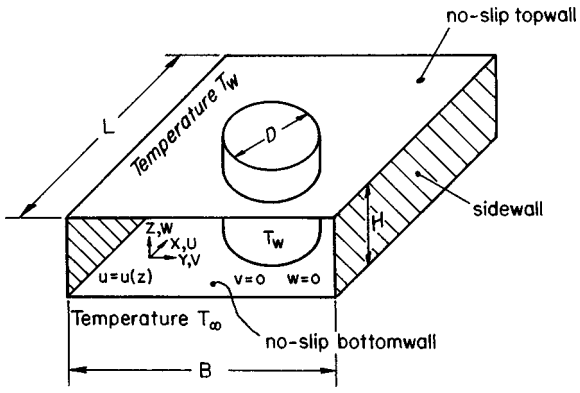

Fig. 2 The module of the heat exchanger

Table 1

Equation	ϕ	Γ_ϕ	S_ϕ
Continuity	1	0	0
Momentum	u, v, w	μ	$\frac{\partial p}{\partial x},\frac{\partial p}{\partial y},\frac{\partial p}{\partial z}$
Energy	T	$\frac{k}{C_p}$	0

and the source term for the momentum equation becomes $-1/\rho\int pI.d\vec{S}$, where I is the unit tensor. In this formulation, we work with Cartesian components of velocity. The quantity ϕ can be the three Cartesian components of velocity u, v, and w and also any scalar, e.g., temperature T which needs to be determined. The variables of the general transport equation (2) are given in Table 1.

Boundary Conditions

- Top and bottom plates

$u=v=w=0$ (no-slip boundary condition) and $\partial p/\partial z=0$

$T=T_w$ (T_w represents wall temperature)

- Side walls

$\partial u/\partial y=\partial w/\partial y=0$, $v=0$ (free-slip boundary condition) and $\partial p/\partial y=0$

$\partial T/\partial y=0$

- Channel inlet

$u=U_\infty$, $v=w=0$ and $\partial p/\partial x=0$

$T=T_\infty$

- Channel exit

$\partial\phi/\partial t+U_{av}\partial\phi/\partial x=0$ (Orlanski [11] boundary condition)

(where ϕ represents either of u, v, w or T)

$p=p_\infty$

- Obstacles (surface of the circular tube)

$u=v=w=0$ and $\partial p/\partial n=0$ (where n signifies the normal direction)

$T=T_w$

Grid Generation

Figure 3 shows a schematic representation of the three-dimensional grid used for the present computation. The initial grid is generated by the method of transfinite interpolation. This method essentially uses a linear interpolation scheme to compute the interior points by using the coordinate values from the boundaries. The grid obtained by algebraic mapping is further improved by the use of the partial differential equations technique. The two-dimensional grids on the x-y plane are stacked in the z direction with constant Δz.

Solution Technique

A finite-volume method due to Eswaran and Prakash [12] has been used to discretize and solve the governing conservation equations. The pressure-velocity iterations follow the method due to Harlow and Welch [13]. The procedure of Eswaran and Prakash [12] has been documented in the recent work of Prabhakar et al. [14].

Results and Discussion

A $69\times49\times23$ grid-mesh is used in the present computation. The divergence-free criterion is satisfied using an upper bound of 10^{-4}. Computations are carried out for three blockage ratios, 0.267, 0.444, and 0.533, and three Reynolds numbers, 500, 1000,

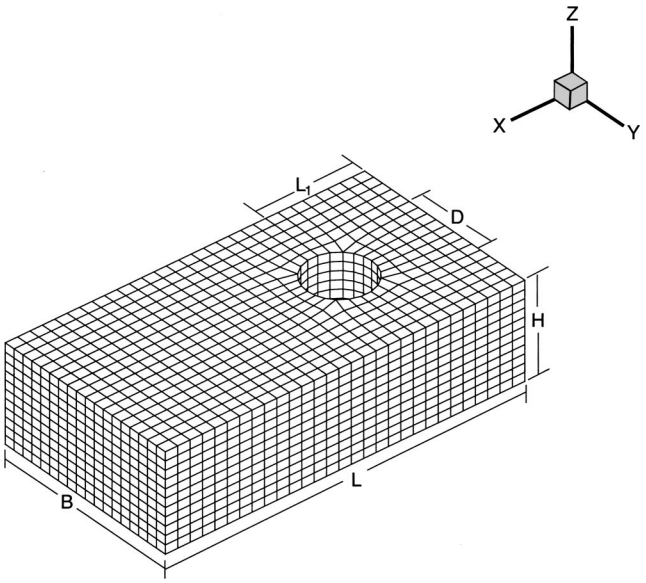

Fig. 3 Schematic representation of the three-dimensional grid

and 1400. Air is used as the working fluid, hence the Prandtl number is 0.7. The span-averaged Nusselt number is calculated on the basis of the bulk-mean temperature.

Flow Characteristics. In this section a detailed investigation of the flow structure in the passage of a fin-tube element is presented. For a three-dimensional flow simulation, it becomes difficult to handle the huge amount of data and only the effective use of some approaches proposed in the literature can depict the flow structure. Of the possible methodologies that enable us to explore the kinematics of complex flows, the method of topological study of limiting streamlines is the most preferred one because the flow structure is best described by the topological properties inferred from computed streamlines. According to Legendre [15], the topology of three-dimensional streamlines projected on a no-slip body surface is analogous to the experimental surface flow visualization. The skin-friction lines, according to Lighthill [16], can be regarded as the projection of the three-dimensional streamline field on the body surface.

Figure 4 shows a schematic representation of various singular points which may appear in a flow field. At the singular points in a flow field, the velocity vectors have zero magnitude, but indeterminate direction. In the vicinity of these singular points, the dynamic characteristics of the flow depend on the eigenvalues of the Jacobian of the field. Corresponding to each eigenvalue, there exists an eigenvector specifying the principal value of the field component with vanishing cross components. The dynamic character of the singular points, defined as saddle points or nodal points, also depends on the divergence of the shear-stress vector. Thus, the field Jacobian and the divergence of the shear stress vector, together establish the criteria for complete characterization of the singular points or critical points associated with the flow field. We may mention that a focus is a spiral node and a sink is a stable node. Through the nodal points, an infinite number of shear-stress lines pass. Nodal points of attachment act as sources of skin-friction lines from the point, and the nodal points of separation act as sinks, where the skin-friction lines meet. For a singular point, defined as a spiral node, all shear stress lines spiral on to, or out of, this point.

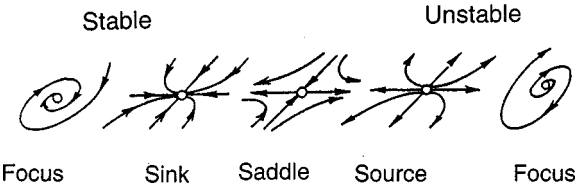

Fig. 4 Schematic representation of the singular points

Through a saddle point only two sets of shear-stress lines pass. On each of these lines, the skin-friction behaves as a vector field. Shear stress in a three-dimensional flow field is brought about by each of the two independent flow velocity components (on a two-dimensional two-dimensional projection). On a two-dimensional plane, in the vicinity of a solid surface, say on either of the no-slip surfaces of the channel walls, the direction of skin-friction vector field is dictated by its associated direction ratios $[\mu\partial u/\partial z, \mu\partial v/\partial z]$. The direction keeps on changing depending on the relative magnitudes of the two direction ratios. Here, the direction z is the direction normal to the surface containing the skin-friction lines of interest. For any general surface, we may use the symbol S to show the perpendicular direction to the plane of interest.

The saddle points describe either separation or attachment. For a saddle point of separation, the skin-friction directions are towards the critical point, and for a saddle point of attachment, these directions are away from the point. In a two-dimensional flow, there exist special streamlines, called separation lines, which conveniently divide the flow into two distinct regions. Such streamlines originate at the saddle points. The three-dimensional counterpart to these separation lines is special stream surfaces.

Flow Topology on the Horizontal and the Vertical Planes. Figure 5 presents the streamline plots on the horizontal midplane of the channel corresponding to the instantaneous flow field and the time-averaged flow field. It can be observed that the instantaneous flow field illustrates vortex shedding. However, this asymmetry is suppressed when the time-averaged flow field is viewed on the horizontal midplane. The asymmetry in the wake zone of Fig. 5(a) is time dependent and possesses an unsteady periodic nature. Such a flow structure may be observed in a flow field only beyond a critical Reynolds number. Below this Reynolds number, the flow field is steady in nature. For the present case, the shedding pattern corresponds to Re=1000. The flow field, shown in Fig. 5(b), is averaged over a large span of time (typically a few shedding cycles) so that the asymmetry in the wake zone disap-

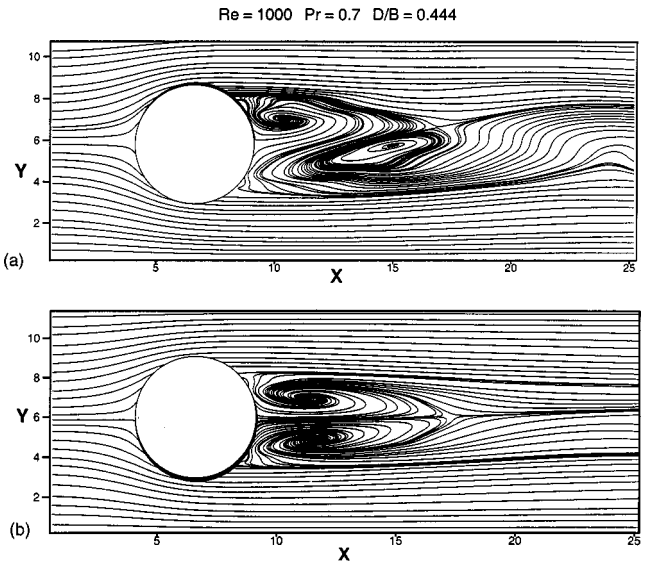

Fig. 5 Streamline representation of the flow past a circular tube placed in a channel on the horizontal midplane for (a) instantaneous flow field and (b) time-averaged flow field

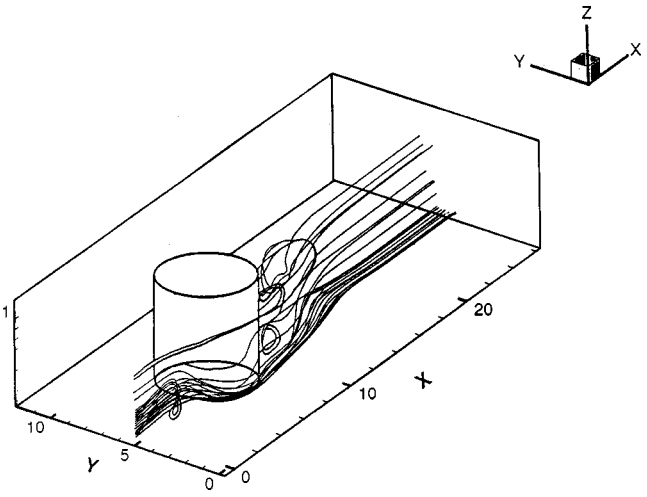

Fig. 6 Structure of three-dimensional flow (particle path)

pears and a symmetrical field pattern is discerned. It may be mentioned that the averaged flow field is an abstract construct that reveals a pseudo-steady-state behavior.

Figure 6 illustrates the particle traces for an instantaneous flow field, showing the paths followed by the fluid particles during the course of their travel through the channel. The flow pattern clearly shows the existence of a screw-like helical vortex motion in the region close to the circular tube. The wake zone of the tube exhibits a strong three-dimensional behavior. The significant normal velocity component in the wake zone, w, is due to the pressure gradient in the direction normal to the no-slip walls towards the midplane.

Limiting Streamlines on the Tube Surface and the Bottom Plate. The structure of the wall streamlines or limiting streamlines on the tube surface was investigated. These streamlines consist of only the tangential component of velocity near the surface of the tube. Figure 7 shows such streamlines corresponding to the time-averaged velocity field. It is seen that the surface streamlines are symmetrically distributed about the midplane of the channel. These surface streamlines reveal bifurcation. The bifurcation may be either a positive bifurcation or a negative bifurcation. A streamline which eventually bifurcates into two or more streamlines follows a positive bifurcation (Fig. 8). On the other hand, two or more streamlimes merging into a single streamline show the behavior of a negative bifurcation (Fig. 8). In Fig. 7, a positive bifurcation is observed near the forward stagnation line of the tube surface ($\theta=0$ or $\theta=2\pi$). The line of reattachment at $\theta=\pi$ is

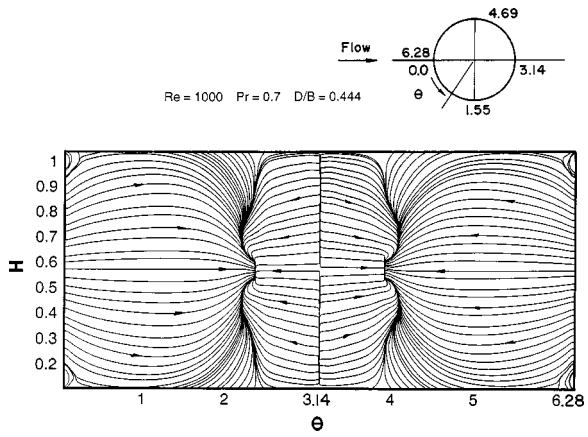

Fig. 7 Limiting streamlines on the tube surface

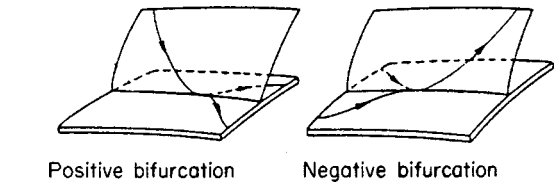

Fig. 8 Positive and negative bifurcation lines

also clearly observed in this figure. Two other lines are also seen having their locations at an angle $0.7\pi<\theta<0.8\pi$ and $1.2\pi<\theta<1.3\pi$, respectively. Near these lines, the tangential components of the shear stress vector vanish. Hornung and Perry [17] called this a negative stream surface bifurcation. The streamlines combine to form a single streamline along the negative bifurcation line. These lines can be termed separation lines, along which the boundary layer separates from the tube surface. In Fig. 7, the separation angle shows a symmetric variation about the midplane. The values of the separation angle at four different heights from the bottom plane, $z=0.1H$, $0.2H$, $0.43H$ and $0.5H$, are $\theta=0.75\pi$, 0.74π, 0.68π, and 0.73π, respectively. This shows that the separation angle is large in the vicinity of the midplane of the tube and near the channel walls, and is relatively smaller at an intermediate height close to the midplane.

Figure 9 shows the streamlines in the region close to the bottom wall corresponding to the instantaneous field and the time-averaged field. A great deal of information about the flow and heat transfer characteristics can be extracted from these figures. The asymmetry due to vortex shedding is apparent in the instantaneous field (Fig. 9(a)) while the time-averaged field (Fig. 9(b)) is almost symmetrical. A saddle point of separation and a horseshoe vortex system are seen in Fig. 9(b). The incoming flow does not separate in the traditional sense but reaches a stagnation or saddle point of separation (A) and goes around the body. The nodal point of attachment (C), and the separation lines which form circular arcs across the tube, are also shown. The flow away from no-slip top and bottom walls, after it hits the forward stagnation line of the tube, moves towards the walls due to normal pressure gradient and creates a small region of reversed flow. On each side of the tube, one finds a region of converging streamlines (G). These are

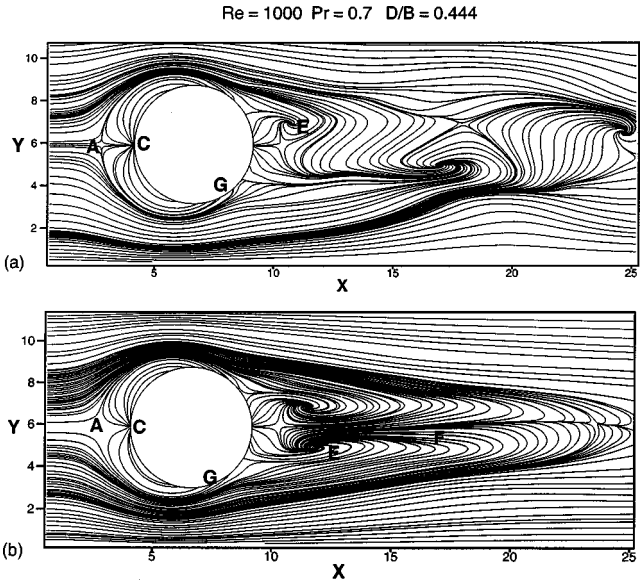

Fig. 9 Limiting streamlines of the flow past a built-in circular tube in a channel at the bottom plate corresponding to (*a*) instantaneous flow field and (*b*) time-averaged flow field

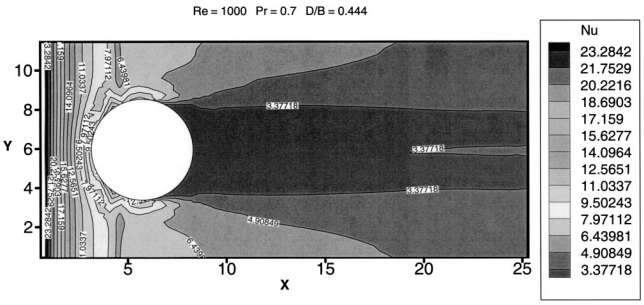

Fig. 10 Iso-Nusselt number distribution on the bottom wall

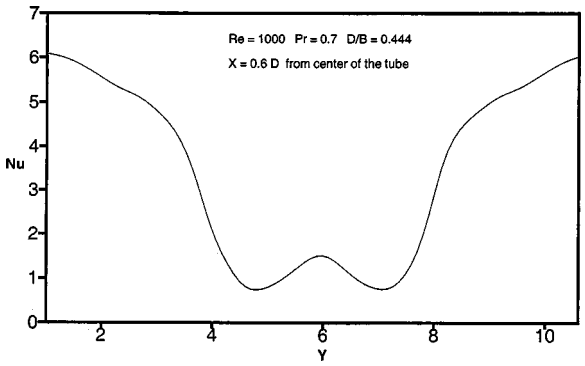

Fig. 12 Transverse variation of local Nusselt number

the foot prints of the horseshoe vortex system. Behind the tube, in the wake zone, two areas of swirling flow (E) are seen. A wake stagnation point (F) downstream of the tube is also shown, which, together with the swirls E, constitutes a saddle zone.

Heat Transfer Characteristics. Figure 10 shows the isolines of local Nusselt number obtained from the time-averaged flow field and temperature field on the bottom plate. Several interesting features may be observed from the figure. At the leading edge of the channel walls, the Nusselt number has a large value and then decreases gradually. At the leading edge, the cooler fluid comes in contact with the hot solid wall for the first time, as a result of which the convection heat transfer is large. A gradual decrease in the Nusselt number is attributed to the development of the thermal boundary layer on the channel wall. In fact, the inlet condition is one of uniform velocity as well as uniform temperature. Therefore, both the velocity and the thermal boundary layers are developing at the channel leading edge. The region that follows the leading edge of the channel is the combined-entrance region. A significant increase in Nusselt number is observed in front of the tube which results from the formation of a horseshoe vortex system that consists of two counter-rotating longitudinal vortices. As the fluid approaches the stagnation line of the circular tube, it slows and its pressure increases. The smaller velocity in the boundary layer, in the vicinity of the channel walls, leads to a smaller pressure increase compared with the midplane. This induces a pressure gradient normal to the no-slip walls and the pressure gradient-driven flow is directed from the midplane towards the wall. Hence the induced pressure gradient along the stagnation line induces the flow towards the no-slip walls that interacts with the main stream. The fluid rolls up, forming vortices, which finally wrap around the front half of the tube and extend to the rear of the tube [18]. Figure 6 explains the formation of a critical point and initiation of the spiralling motion adjacent to the critical point. The spiralling motion of the horseshoe vortices brings about better mixing, and the heat transfer in this region is significantly enhanced. The Nusselt number is low in the wake region, as shown in Fig. 10. The poor heat transfer in this region is attributed to the separated dead water zone with fluid recirculating at a low velocity. This trend matches qualitatively well the experimental results of O'Brien and Sohal [19].

Figure 11 shows the distribution of the time-averaged and span-averaged Nusselt number in the streamwise direction for three Reynolds numbers, 600, 1000, and 1400, corresponding to a blockage ratio of 0.444. In each case, at the leading edge of the fin, the Nusselt number is high and then it decreases gradually, showing a local maximum in front of the tube. The reasons for this increase in the Nusselt number in front of the tube have been explained earlier. In the developing region of the flow, the span-averaged Nusselt number shows a significant increase in value with increasing Reynolds number. As the flow develops in the downstream, this increase is not very significant.

The variation of span-averaged Nusselt number along the length of the channel does not convey any information about the spanwise variation of local Nusselt number on the channel walls. For the time-averaged field, the variation of local Nusselt number in the spanwise direction at any axial location is expected to be symmetric about the midpoint on the span of the channel. Figure 12 shows the spanwise variation of the local Nusselt number in the wake region at an axial distance of $x/R=1.2$ from the center of the tube. The two peaks in the figure result from almost symmetric swirls generated by the longitudinal horseshoe vortices. The poor heat transfer in the dead-water region ($-0.5<y/R<0.5$) is evident.

Figure 13 shows variation of the time-averaged and span-averaged Nusselt number along the channel length for three blockage ratios (D/B), 0.267, 0.444, and 0.533, at a Reynolds number of 1000. It may be observed that with increasing blockage

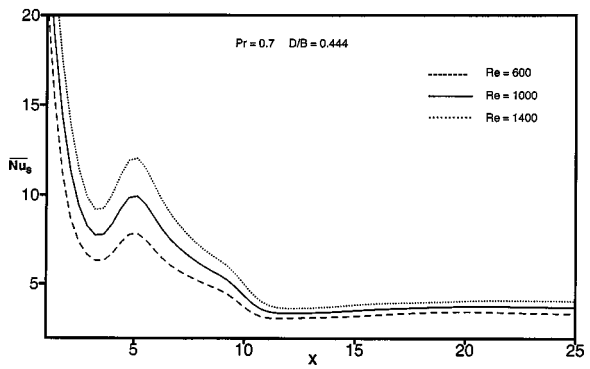

Fig. 11 Variation of span-averaged Nu with Reynolds number ($D/B=0.444$)

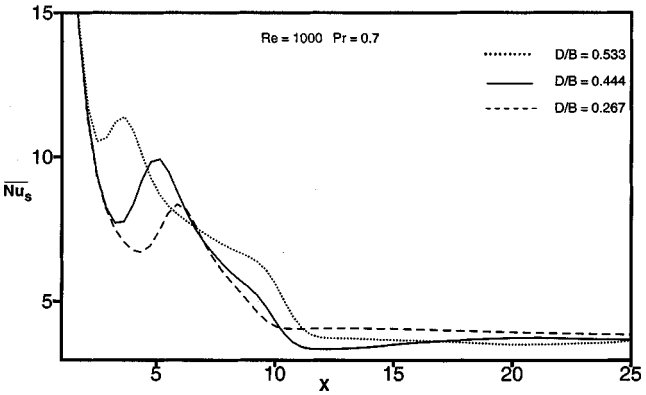

Fig. 13 Variation of span-averaged Nu with blockage ratio (Re=1000)

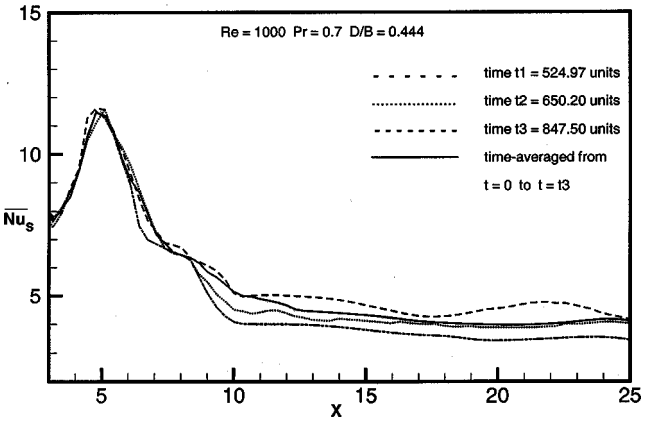

Fig. 14 Comparison of span-averaged Nusselt number at three different time instants with the time-averaged span-averaged Nusselt number

ratio, the location of the maximum value of the span-averaged Nusselt number shifts more towards the upstream side. The reason for this may be attributed to an earlier onset of formation of the horseshoe vortices with increasing radius of the circular tube, for a fixed location of the center of the tube. The maximum value of the span-averaged Nusselt number is also observed to be higher for higher blockage ratios. The increased constriction in the passage causes more acceleration in the flow, and the acceleration-driven steeper temperature gradients contribute to a larger span-averaged Nusselt number.

In addition to the heat transfer behavior corresponding to the time-averaged field, the heat transfer characteristics corresponding to the instantaneous field bear special significance. In design considerations, this aspect plays a very important role. Figure 14 shows the distribution of the span-averaged Nusselt number on the bottom wall at three arbitrary time instants, say non-dimensional times of 525.97, 650.20, and 847.50 units. The Reynolds number for this computation is 1000 and the blockage ratio is $D/B=0.444$. This figure shows very little difference in the distribution pattern. The flow fluctuates with a low-frequency oscillation (this will be discussed in a subsequent section). The difference appears mainly in the wake zone, as expected. This figure also reveals that the amplitude of the oscillations is not very large. The increase in the value of the span-averaged Nusselt number in the downstream section, at larger time instants, is mainly attributable to the development of the flow in that section with passage of time. The effect of mild oscillations on heat transfer becomes apparent when the results are compared with those for the time-averaged field presented in the same plot.

Figure 15 represents the pressure variation along the length of channel. The variation of pressure is considered for three Reynolds numbers, 600, 1000, and 1400, with a blockage ratio of 0.444. The cross-stream averaged pressure distribution, $(p/\rho U_\infty^2)$ Re, along the channel length is shown as a function of the Reynolds number. The dimensionless pressure drop in Fig. 15 has been scaled with the Reynolds number entailing the matching points at the entry plane of the channel over the entire range of Reynolds number.

Validation of Results and Grid Independence. The model validation was performed through comparison with the experimental results of O'Brien and Sohal [19]. Figure 16 shows a comparison between the predicted and the experimentally obtained variation of the local Nusselt number in the spanwise direction at an axial location $x/D=1.38$ from the center of the tube. The geometric parameters were described by O'Brien and Sohal [19]. In the experiment, an unheated channel length was provided to ensure a hydrodynamically developed condition at the test section. In the numerical simulation used for the comparison, we used a hydrodynamically fully developed velocity profile at the inlet of the channel. O'Brien and Sohal [19] used infrared thermography to measure the heat transfer characteristics. The predicted values compare fairly well with their experimental counterparts.

The grid independence was confirmed rigorously. The variation

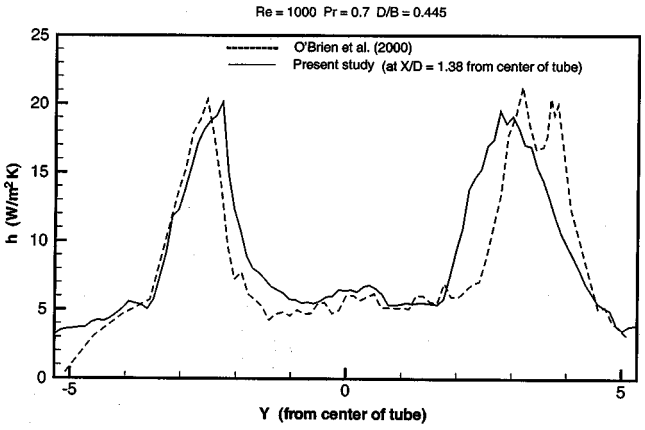

Fig. 16 Comparison of transverse variation of heat transfer coefficient in the wake region

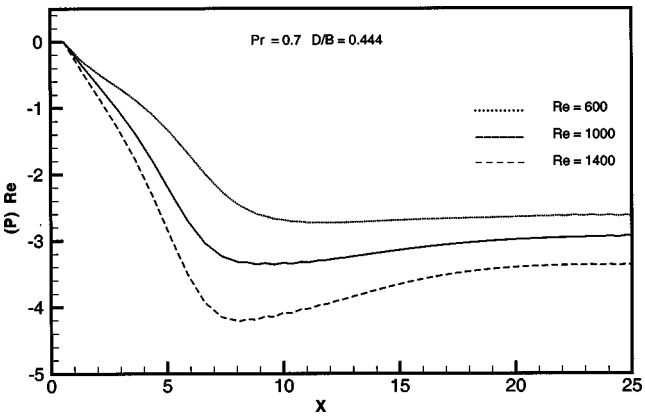

Fig. 15 Pressure variation along the length of the channel for different values of Reynolds number

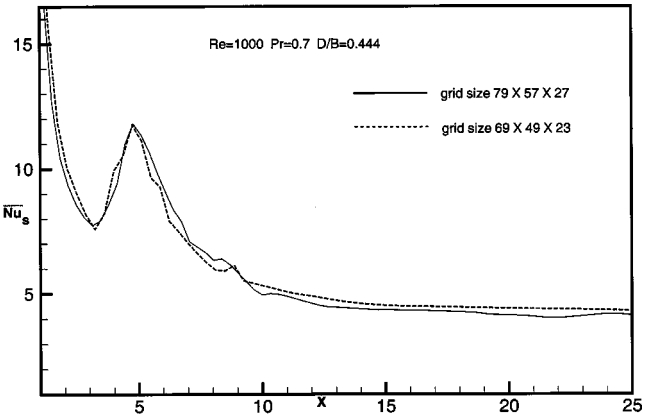

Fig. 17 Comparison of span-averaged Nusselt number for two different grids (time-averaged plots)

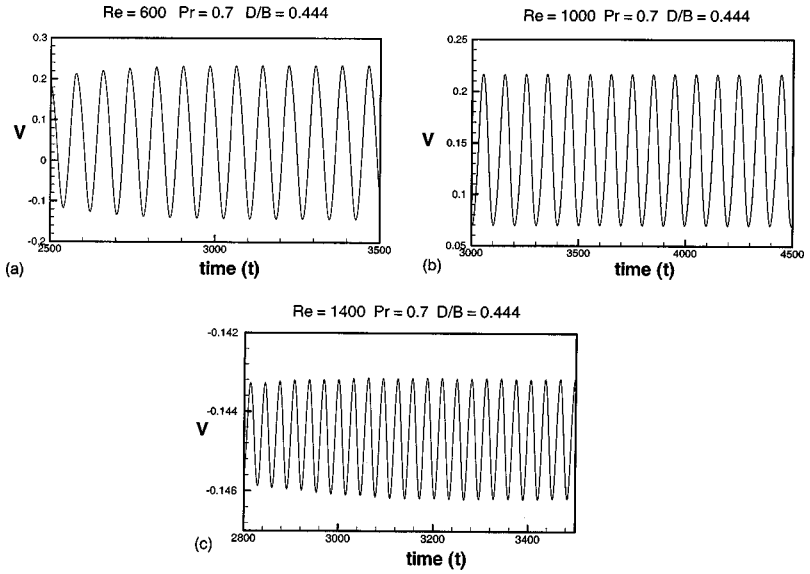

Fig. 18 Time series signal of transverse velocity at a point in the wake of circular tube

of the span-averaged Nusselt number for two grid sizes, $79\times57\times27$ and $69\times49\times23$, corresponding to Re$=1000$ and $D/B=0.444$ is shown in Fig. 17. It is observed that the time and space averaged Nusselt number, for the channel, differs from the projected grid-independence situation by less than 3%. All the computations in the present case were conducted on a grid-mesh of $69\times49\times23$ to save some computation time.

Time Series Analysis. The flow and heat transfer results discussed so far have been presented by assuming a laminar nature of the flow field. The assumption simplifies the present analysis and avoids the use of any turbulence model. To confirm the validity of this presumption, a time series analysis was carried out. The signal traces were obtained from the transverse component of velocity (v) of a fluid particle located at a point in the wake region. The point of interest in the wake region of the circular tube was chosen at a location of twice the diameter of the tube downstream from center of the circular tube. The time series data for transverse velocity are collected for three Reynolds numbers, 600, 1000, and 1400, and a blockage ratio of $D/B=0.444$. Figure 18 presents the time series signal of the transverse velocity for the three cases. It is observed that the amplitude of the oscillations decreases with increase in the Reynolds number. Figure 19 presents the FFT (fast Fourier transform) of the signal for the same three cases. With increase in Reynolds number, a decrease in the magnitude of power peak of the FFT is seen. The FFT corresponding to Re $=1400$ shows the appearance of an extra peak of very low frequency and relatively much smaller power. This reveals that at a Reynolds number between 1000 and 1400, a Hopf bifurcation takes place in the temporal characteristic of the signal. In the present situation of the flow, confined in a channel, the Reynolds number considered for computations is below the critical Reynolds number corresponding to chaotic transitions of the flow.

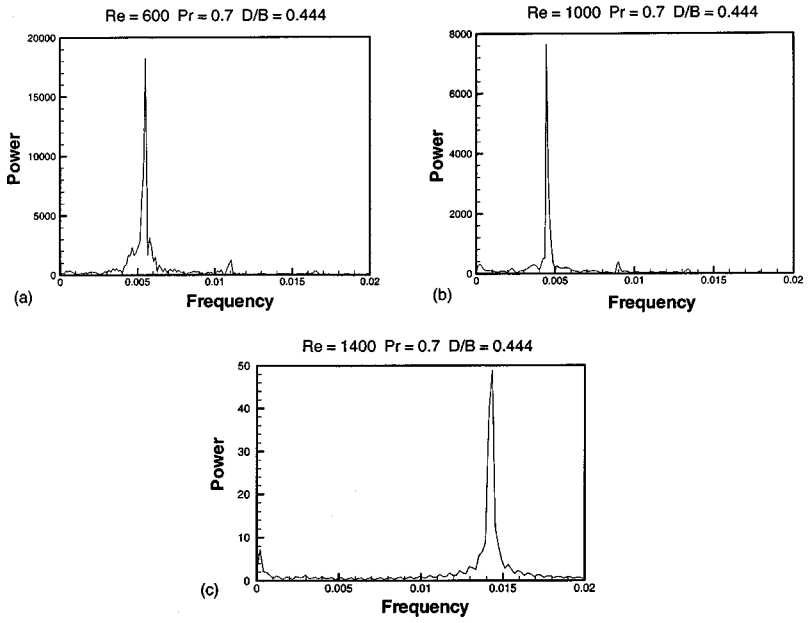

Fig. 19 FFT of the time series of transverse velocity signal

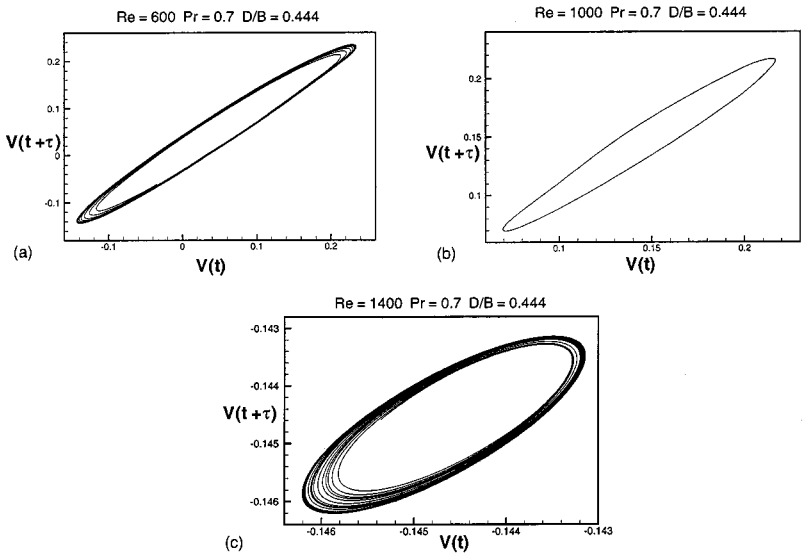

Fig. 20 Time-delay reconstructions of the transverse velocity signal

From the consideration of channel flows, the Reynolds numbers of interest are well below the transitional Reynolds number and the flow in the channel is supposed to be laminar. However, the Reynolds numbers based on the tube diameters are fairly large (for example, Re_D for the case of $Re=600$ is 2997 and for the case of $Re=1400$ it is 6993). The laminar vortex shedding, in the case of a circular tube in an infinite medium, is observed at $50<Re_D<190$. With the increasing Reynolds number, the three-dimensional wake becomes more chaotic. The shear layers separating from the cylinder become unstable at a Reynolds number around 1200 (Prasad and Williamson [20]). Therefore, identification of the nature of the flow becomes a challenging task in our geometry. The single dominant frequency in the power spectrum of Fig. 19(a) indicates the presence of one dominant shedding frequency at a Reynolds number $Re=600$. Even at $Re=1400$, only one extra subharmonic frequency is observed (Fig. 19(c)) in the power spectrum, which means that the flow has not yet encountered a chaotic transition. The important point to observe is that the amplitude of the oscillations keeps on decreasing with increasing Reynolds number. Karniadakis and Triantafyllou [21] carried out investigations on three-dimensional dynamics and transition to turbulence in the wake of bluff bodies. Vittori and Blondeaux [22] found the route to chaos in the two-dimensional oscillatory flow around a circular cylinder (placed in an infinite medium). The value of the critical Reynolds number is higher in the present computations than their result. The delay in the critical Reynolds number to cause the flow transition, in the present case, may be attributed to the following reason. The gap between the no-slip channel walls in the present study is small and, as a consequence, the strong viscous effect appearing therein constrains the transitional limits of the flow.

Williams-Stuber and Gharib [23] and Pulliam and Vastano [24] carried out transitional studies from order to chaos in the wake of an airfoil. Both studies recommend strongly that a good confirmation of transitional scenario can be made by analysing the time-delay reconstructions. For this, the transverse velocity at any instant of time ($v(t)$) is independently contrasted with that at a delayed time (say $v(t+\tau)$). Figure 20 gives the plots of time-delay reconstructions for the three cases having their time-signal and FFT as shown in Figs. 18 and 19, respectively. At higher Re value, the spreading of the time-delay plot in a small region demonstrates the tendency of subharmonic bifurcations in the transitional regime.

Conclusion

A three-dimensional numerical study on the flow and heat transfer characteristics in a narrow rectangular duct with a built-in circular tube in a cross-flow configuration has been performed. The duct was designed to simulate a passage formed by any two neighboring fins in a fin-tube heat exchanger. The flow-field is different from two-dimensional flows. At the rear of the tube, it leads to a screw-like motion of a helical vortex tube. Limiting streamlines on the tube surface showed typical separation lines. Limiting streamlines on the bottom wall clearly established the presence of a saddle point of separation, a nodal point of attachment in front of the tube and bottom wall junction and a horseshoe vortex system that wraps around the tube and extends to the rear of the tube. The span-averaged Nusselt number distribution and the iso-Nusselt number distribution clearly establish the high heat transfer near the leading edge of the fins and in the region influenced by the horseshoe vortex system. Poor heat transfer in the dead water zone is observed. The heat transfer enhancement caused by the horseshoe or necklace vortices around the fore-root of the tube is unable to offset the poor heat transfer in the near-wake region. The zone of poor heat transfer can possibly be removed by inducing swirling motion in the wake region. This study confirmed that in the range of Re considered, onset of turbulence is not brought about. As a consequence, the predicted heat transfer results, without using any turbulence model, are a meaningful numerical approximation of the physical situation.

Acknowledgment

This investigation was sponsored by the New Energy and Industrial Development Organization (NEDO), Japan.

Nomenclature

B = channel width
CV = control volume
D = diameter of the cylinder
F = mass flux through a cell face
H = channel height
I = unit tensor
L_1 = distance of center circular tube from the channel inlet
Nu = local Nusselt number, $(1/1-\theta_b)\ (\partial\theta/\partial Z)_{Z=0}$

$\overline{\mathrm{Nu}_s}$ = span-wise averaged Nusselt number, $\int_0^B \mathrm{Nu}.dy/\int_0^B dy$
P = non-dimensional static pressure, $p/\rho U_\infty^2$
Pr = Prandl number
Re = Reynolds number based on channel height $=\rho U_\infty H/\mu$
Re_D = Reynolds number based on tube diameter $=\rho U_\infty D/\mu$
S = surface area of a cell face
T = temperature
k = thermal conductivity
p = static pressure
t = time
u = axial velocity
v = spanwise velocity
w = normal or vertical velocity
x = axial dimension of coordinates
y = spanwise dimension of coordinates
z = normal or vertical dimension of coordinates

Greek Letters

α_1, α_2, α_2 = coefficients of linearly independent unit vectors
ρ = density of the fluid
θ = nondimensional temperature $(T-T_\infty)/(T_w-T_\infty)$

References

[1] Fiebig, M., Chen, Y., Grosse-Gorgemann, A., and Mitra, N. K., 1995, ''Conjugate Heat Transfer of a Finned Tube Part A: Heat Transfer Behavior and Occurrence of Heat Transfer Reversal,'' Numer. Heat Transfer, Part A, **28**, pp. 133–146.

[2] Jacobi, A. M., and Shah, R. K., 1995, ''Heat Transfer Surface Enhancement Through the Use of Longitudinal Vortices: A Review of Recent Progress,'' Exp. Therm. Fluid Sci., **11**, pp. 295–309.

[3] Wang, C. C., Lo, J., Lin, Y. T., and Wei, C. S., 2002, ''Flow Visualization of Annular and Delta Winglet Vortex Generators in Fin-and-Tube Heat Exchanger Application,'' Int. J. Heat Mass Transf., **45**, pp. 3803–3815.

[4] Rosman, E. C., Carajilescov, P., and Saboya, F. E. M., 1984, ''Performance of One and Two-Row Tube and Plate Fin Heat Exchangers,'' J. Heat Transfer , **106**, pp. 627–632.

[5] Launder, B. E., and Massey, T. H., 1978, ''The Numerical Prediction of Viscous Flow and Heat Transfer in Tube Banks,'' J. Heat Transfer , **100**, pp. 565–571.

[6] Wung, T. S., and Chen, C. J., 1989, ''Finite Analytic Solution of Convective Heat Transfer for Tube Arrays in Cross Flow, Part I and Part II,'' J. Heat Transfer , **111**, pp. 633–648.

[7] Biswas, G., Mitra, N. K., and Fiebig, M., 1994, ''Heat Transfer Enhancement in Fin-tube Heat Exchangers by Winglet-type Vortex Generators,'' Int. J. Heat Mass Transf., **35**, pp. 283–291.

[8] Tsai, S. F., Sheu, T. W. H., and Lee, S. M., 1999, ''Heat Transfer in a Conjugate Heat Exchanger with a Wavy Fin Surface,'' Int. J. Heat Mass Transf., **42**, pp. 1735–1745.

[9] Fiebig, M., Brockmeier, U., Mitra, N. K., and Guntermann, T., 1989, ''Structure of Velocity and Temperature Fields in Laminar Channel Flows with Longitudinal Vortex Generators,'' Numer. Heat Transfer, Part A, **15**, pp. 281–302.

[10] Pauley, W. R., and Eaton, J. K., 1988, ''Experimental Study of the Development of Longitudinal Vortex Pairs Embedded in a Turbulent Boundary Layer,'' AIAA J., **26**, pp. 816–823.

[11] Orlanski, I., 1976, ''A Simple Boundary Condition for Unbounded Flows,'' J. Comput. Phys., **21**, pp. 251–269.

[12] Eswaran, V., and Prakash, S., 1998, ''A Finite Volume Method for Navier-Stokes Equations,'' in *Proceedings of the Third Asian CFD Conference*, Bangalore, **1**, pp. 251–269.

[13] Harlow, F. H., and Welch, J. E., 1965, ''Numerical Calculation of Time-Independent Viscous Incompressible Flow of Fluid With Free Surface,'' Phys. Fluids, **8**, pp. 2182–2188.

[14] Prabhakar, V., Biswas, G., and Eswaran, V., 2002, ''Numerical Prediction of Heat Transfer in a Channel With a Built-in Tube and Two Different Shaped Vortex Generators,'' Numer. Heat Transfer, Part A, **41**, pp. 307–329.

[15] Legendre, R., 1956, ''Separation de Courant Lecoulement Laminaire Tridimensional,'' Rech. Aerosp., **54**, pp. 3–8.

[16] Lighthill, M., 1963, ''Attachment and Separation in Three-Dimensional Flow,'' in *Laminar Boundary Layers*, L. Rosenhead Ed., **2**, Oxford University Press, Oxford, pp. 72–82.

[17] Hornung, H., and Perry, A. E., 1984, ''Some Aspects of Three-Dimensional Separation,'' Z. Flugwiss. Weltraumforsch., **8–2**(3), pp. 77–87 and 155–160.

[18] Goldstein, R. J., and Karni, J., 1984, ''The Effect of a Wall Boundary Layer on a Local Mass Transfer From a Cylinder in Crossflow,'' ASME J. Heat Transfer, **106**, pp. 260–267.

[19] O'Brien, J. E., and Sohal, M. S., 2000, ''Local Heat Transfer for Finned-Tube Heat Exchangers using Oval Tubes,'' *Proceedings of NHTC'00 34th National Heat Transfer Conference*, Pittsburgh, PA, NHTC 2000-12093.

[20] Prasad, A., and Williamson, C. H. K., 1997, ''The Instability of the Shear Layer Separating from a Bluff Body,'' J. Fluid Mech., **333**, pp. 375–402.

[21] Karniadakis, G. E., and Triantafyllou, G. S., 1992, ''Three-Dimensional Dynamics and Transition to Turbulence in the Wake of Bluff Objects,'' J. Fluid Mech., **238**, pp. 1–30.

[22] Vittori, G., and Blondeaux, P., 1993, ''Quasiperiodicity and Phase Locking Route to Chaos in the 2-D Oscillatory Flow Around a Circular Cylinder,'' Phys. Fluids A, **5**, pp. 1866–1868.

[23] Williams-Stuber, K., and Gharib, M., 1990, ''Transition From Order to Chaos in the Wake of an Airfoil,'' J. Fluid Mech., **213**, pp. 29–57.

[24] Pulliam, T. H., and Vastano, J. A., 1993, ''Transition to Chaos in an Open Unforced 2D Flow,'' J. Comput. Phys., **105**, pp. 133–149.

Reattachment of Three-Dimensional Flow Adjacent to Backward-Facing Step

J. H. Nie

B. F. Armaly

Department of Mechanical and Aerospace Engineering, and Engineering Mechanics, University of Missouri-Rolla, Rolla, MO 65401

Numerical simulations for incompressible three-dimensional laminar forced convection flow adjacent to backward-facing step in rectangular duct are performed to examine the reattachment region of the separated flow on the stepped wall. The feasibility of utilizing the two-dimensional flow definition and the limiting streamline definition for identifying the reattachment line/region was examined. The downwash and the "jet-like" flow that develops near the sidewall creates significant spanwise flow adjacent to the stepped wall, making it difficult to identify a reattachment line/region both numerically and experimentally. The use of the line/region that identifies the location on a plane adjacent to the stepped wall where the gradient of the mean streamwise velocity component is zero $(\partial u/\partial y|_{y=0}=0)$ *is recommended for code and apparatus validation of three-dimensional separated flow.* [DOI: 10.1115/1.1571091]

Keywords: Convection, Heat Transfer, Reattachment, Recirculating, Three-Dimensional

1 Introduction

Separated and reattached flow occurs in many heat transfer-exchanging devices, such as electronic and power generating equipment and dump combustors. A great deal of mixing of high and low energy fluid occurs in the reattached flow region, thus impacting significantly the heat transfer performance of these devices. Studies of separated flow have been conducted extensively during the past decades, and the backward-facing step geometry received most of the attention ([1–3] and the references cited therein). In particular, the heat transfer rate changes rapidly and reaches its maximum value near the reattachment region. The reattachment length has been identified as a parameter for characterizing the global features of such flow, and it has been measured [1,4] and used to validate/compare two-dimensional numerical flow simulation codes [5–8] and measurements.

Measurements of reattachment in two-dimensional separated flow have been performed by using laser Doppler velocimeter (LDV) [1], hot-wire anemometer [9], particle image velocimeter [10], wall probes [11], and oil-film dispersion technique [12]. The oil-film dispersion technique relies on visualization and could not be used simultaneously while measuring heat transfer. The other methods rely on locating the point/region where the wall shear stress is zero ($\tau_w=\mu\partial u/\partial y|_{y=0}=0$, where μ is dynamic viscosity, u is the streamwise velocity component, and y is the direction normal to the wall). This is accomplished by measuring the mean streamwise velocity component (u) on a plane that is adjacent to the wall, and determining from that data the locations (reattachment points) where the mean streamwise velocity component (u) is either zero or is changing its direction (sign) from positive to negative [1]. Most of the published work dealt with two-dimensional separated flow and relatively little is published about three-dimensional flow ([13] and the references cited therein). For two-dimensional flow, the reattachment point/region on the stepped wall is a one-dimensional region where the shear stress ($\mu\partial u/\partial y|_{y=0}$) is zero. But for three-dimensional flow, reattachment on the stepped wall is a two-dimensional line/region and the wall shear stress ($\tau_w=\mu\sqrt{(\partial u/\partial y)^2+(\partial w/\partial y)^2}|_{y=0}$, where w is the spanwise velocity component) is equal to zero only at one point on the stepped wall. The location where the shear stress is minimum does not correspond to the reattachment line in three-dimensional flow. To the authors' knowledge, methods for numerically and/or experimentally identifying the reattachment region in three-dimensional flow adjacent to backward-facing step have not appeared in the literature. The two-dimensional flow definition for identifying reattachment has been applied [14,15] to three-dimensional flow, but as will be shown later that definition is not appropriate for three-dimensional flow. A topological sketch of three-dimensional flow structures was presented based on the reattachment length located experimentally using the two-dimensional definition [14]. The present work utilizes numerical simulations to examine the flow in the reattachment region for the purpose of identifying a method, if possible, for locating the reattachment line/region or other similar criterion that can be employed experimentally and numerically for validating and comparing three-dimensional simulation codes and measurements, similar to what has been done for two-dimensional flow [7,8].

2 Model Description and Simulation

Three-dimensional laminar forced convection flow in a heated duct with a backward facing step is numerically simulated, and a schematic of the computation domain is shown in Fig. 1. The upstream height of the duct (h) is 0.01 m, its downstream height (H) is 0.02 m, and its width (W) is 0.08 m. This geometry provides a backward facing step height of $S=0.01$ m, an expansion ratio of $ER=H/(H-S)=2$, and an aspect ratio of $AR=W/S=8$. By exploiting the symmetry of the flow field in the spanwise direction, the width of the computation domain is reduced to half of the actual width of the duct ($L=0.04$ m). The length of the computation domain is 0.02 m and 0.5 m upstream and downstream of the step respectively, i.e., $-2\leqslant x/S\leqslant 50$. This choice is made to insure that the flow at the inlet section of the duct ($x/S=-2$) is not affected significantly by the sudden expansion in the geometry at the step, and the flow at the exit section ($x/S=50$) is fully developed. Measurements for the same geometry show that the flow is fully developed at these planes [16]. It was also confirmed that the use of a longer computational domain did not change the flow behavior in the region close to the backward-facing step ($x/S<15$). The origin of the coordinate system is located at the bottom corner of the step as shown in Fig. 1. Velocity measurements in the same geometry, using laser Doppler velocimeter,

Contributed by the Heat Transfer Division for publication in the JOURNAL OF HEAT TRANSFER. Manuscript received by the Heat Transfer Division July 5, 2002; revision received February 13, 2003. Associate Editor: V. Prasad.

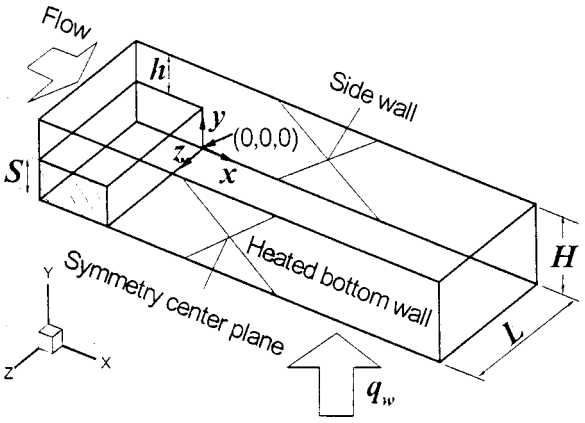

Fig. 1 Schematic of the computation domain

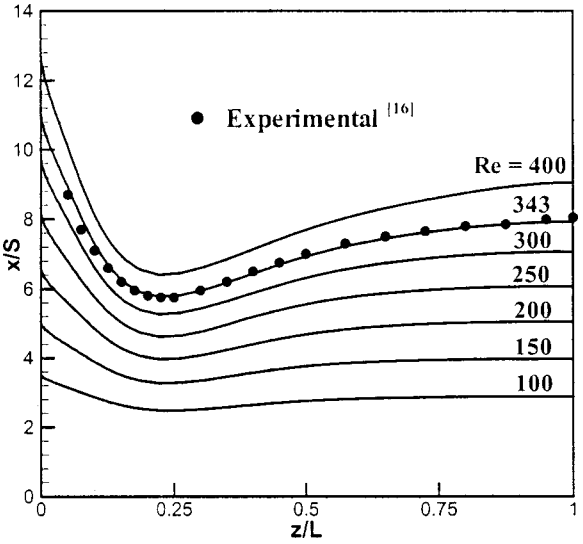

Fig. 2 Lines where the gradient of the mean streamwise velocity on the stepped wall ($\partial u/\partial y|_{y=0}$) is zero

show that the flow is laminar and steady for Reynolds number smaller than 600 [16]. The steady laminar three-dimensional Navier-Stokes and energy equations are solved numerically (using finite difference scheme) together with the continuity equation to simulate the thermal and the flow fields.

Continuity equation:

$$\frac{\partial}{\partial x}(\rho u)+\frac{\partial}{\partial y}(\rho v)+\frac{\partial}{\partial z}(\rho w)=0 \tag{1}$$

Momentum equations:

$$\frac{\partial}{\partial x}(\rho u^2)+\frac{\partial}{\partial y}(\rho uv)+\frac{\partial}{\partial z}(\rho uw)=-\frac{\partial p}{\partial x}+\mu\left(\frac{\partial^2 u}{\partial x^2}+\frac{\partial^2 u}{\partial y^2}+\frac{\partial^2 u}{\partial z^2}\right) \tag{2}$$

$$\frac{\partial}{\partial x}(\rho uv)+\frac{\partial}{\partial y}(\rho v^2)+\frac{\partial}{\partial z}(\rho vw)=-\frac{\partial p}{\partial y}+\mu\left(\frac{\partial^2 v}{\partial x^2}+\frac{\partial^2 v}{\partial y^2}+\frac{\partial^2 v}{\partial z^2}\right) \tag{3}$$

$$\frac{\partial}{\partial x}(\rho uw)+\frac{\partial}{\partial y}(\rho vw)+\frac{\partial}{\partial z}(\rho w^2)=-\frac{\partial p}{\partial z}+\mu\left(\frac{\partial^2 w}{\partial x^2}+\frac{\partial^2 w}{\partial y^2}+\frac{\partial^2 w}{\partial z^2}\right) \tag{4}$$

Energy equation:

$$\frac{\partial}{\partial x}(\rho C_p uT)+\frac{\partial}{\partial y}(\rho C_p vT)+\frac{\partial}{\partial z}(\rho C_p wT)=k\left(\frac{\partial^2 T}{\partial x^2}+\frac{\partial^2 T}{\partial y^2}+\frac{\partial^2 T}{\partial z^2}\right) \tag{5}$$

where T is temperature and u, v, w are velocity components in coordinate directions of x, y, and z as shown in Fig. 1. The physical properties are treated as constants in the simulation and evaluated for air at the inlet temperature of $T_0=20°C$ (i.e., density (ρ) equals to 1.205 kg/m^3, dynamic viscosity (μ) is 1.81×10^{-5} kg/m·s, thermal conductivity (k) is 0.0259 W/m·°C, and specific heat (C_p) is 1005 J/kg·°C). The boundary conditions are treated as no slip conditions (zero velocities) at the solid walls, and thermally adiabatic at all the walls with the exception of the downstream stepped wall ($y/S=0.0$, for $0.0\leqslant x/S\leqslant 50$, and all z) that was treated as having a fixed and uniform heat flux ($q_w=-k\partial T/\partial y|_{y=0}$) that is equal to $q_w=50$ W/m^2. The flow rate was varied to cover a Reynolds number range from 100 to 400. The flow conditions at the upstream inlet section of the duct ($x/S=-2$, $1\leqslant y/S\leqslant 2$, for all z) are considered to be hydrodynamically steady and fully developed, and having uniform temperature profile ($T_0=20°C$). Distribution of the mean streamwise velocity component (u) is considered to be equivalent to the one described by Shah and London [17], while the other velocity components (v and w) are set equal to zero at that inlet section ($x/S=-2$). Symmetry conditions were imposed at the center width of the duct ($z/L=1$, for all x and y), and fully developed conditions were imposed at the outlet section ($x/S=50$, for all y and z).

Hexahedron volume elements and non-uniform staggered grid arrangement are employed in the simulation. SIMPLE algorithm [18] is utilized for the pressure correction in the iteration procedure. Power-law scheme is used for the convection terms and central difference scheme is used for the diffusion terms. The resulting finite difference equations are solved numerically by making use of a line-by-line method combined with ADI scheme. The grid is highly concentrated close to the step and near the corners, in order to insure the accuracy of the numerical simulation. Grid independence tests were performed using several grid densities and distributions for Re=343, and the line designating the locations where the mean streamwise velocity component (u) is zero on a plane adjacent to the stepped wall, was used as the criteria for grid independence solution. A grid of $180\times36\times36$ downstream from the step was selected for this simulation. Using a larger grid $200\times42\times42$ downstream from the step resulted in less than 2 percent difference in the predicted locations where the mean streamwise velocity component (u) is zero on a plane adjacent to the stepped wall. The residual sum for each of the conserved variables is computed and stored at the end of each iteration, thus recording the convergence history. The convergence criterion required that the maximum relative mass residual based on the inlet mass be smaller than 10^{-6}. All calculations were performed on Hewlett Packard Visualize B1000 workstations along with the HP-UX FORTRAN 77 compiler. One iteration required approximately 68.21 s when the total number of grid points was about 2.5×10^5. Predictions of the locations where the mean streamwise velocity component (u) is zero on a plane adjacent to the stepped wall (line (x_u)) compare very well with measured results [16] for Re=343, as shown in Fig. 2, and that provides code validation. Predictions for other Reynolds numbers are also presented in Fig. 2.

3 Results and Discussions

The general behavior of the three-dimensional flow at Re =400 is presented in Fig. 3 through the presentations of stream-

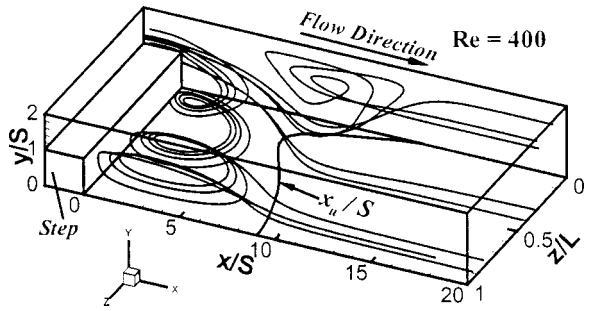

Fig. 3 General flow patterns adjacent to backward-facing step

lines that trace the paths of hypothetical massless particles placed in the flow field. Due to space limitations, most of the results that illustrate general flow features are presented only for a Reynolds number of 400, and similar behavior develops for different Reynolds numbers in the range of $100<\mathrm{Re}<400$. The separated flow develops a primary recirculation flow region that is attached to the step, and several significant flow features appear downstream from the step as can be seen in that figure.

1. A downwash that develops adjacent to the sidewall with a vortex flow that moves in the spanwise direction inside the primary recirculation flow region can be seen in Fig. 3, and a more detailed view is shown in Fig. 4 for a selected spanwise plane of $z/L=0.025$. The streamlines that are displayed in this figure start at the inlet plane of the duct from 21 points that are between $y/S=1.01$ and 1.99. Fluid originating at the inlet plane of the duct in the region between $0<z/L<0.03$ flows (downwash) into the primary recirculation region in a manner similar to what is shown in Fig. 4.

2. A ''jet-like'' flow that moves toward the stepped wall and rebounds towards the sidewall as can also be seen in Fig. 3. Fluid originating at the inlet plane of the duct in the region between $0.03<z/L<0.5$ will generate similar flow features, and a more detailed view is shown in Fig. 5 at a selected spanwise plane of $z/L=0.075$. The streamlines that are displayed in this figure start from identical transverse locations as those shown in Fig. 4. Fraction of the incoming fluid from that region flows directly into the primary recirculation flow region and the remaining portion flows towards what appears to be a reattachment on the stepped wall. A fraction of that fluid rebounds and moves sharply toward the upper region of the sidewall and splits with a portion flowing upstream toward the step (forming a reverse flow region adjacent to the sidewall) and another portion flows directly downstream.

3. Fluid originating at the inlet plane of the duct in the region between $0.5<z/L<1$ flows directly downstream after approaching the stepped wall and does not appear to contribute to the primary recirculation flow region as shown in Fig. 6. The effects of the spanwise flow can be seen in all of these figures in planes that are below and above the step. The impact of the spanwise flow at the selected plane of $z/L=0.6$ can be seen more clearly from the top view that is presented in Fig. 6. The side-view in Fig. 6 shows that the fluid in this region does not reattach directly to the stepped wall.

4. A recirculation flow region develops adjacent to the sidewall producing a ''jet-like'' flow that reattaches to the stepped wall as shown in Fig. 7. It has a shape of a teardrop with thin upper section and relatively thick lower section as shown from the projection viewed from the exit section in Fig. 7. Fluid from that ''jet-like'' flows in all directions upstream into the primary recirculation flow region, and downstream as shown in Fig. 7. The impingement of this ''jet-like'' flow on the stepped wall is responsible for the maximum Nusselt number that develops in that region.

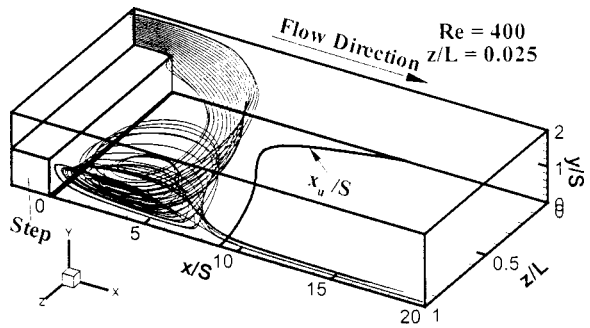

Fig. 4 Streamlines starting from the spanwise plane of $z/L=0.025$

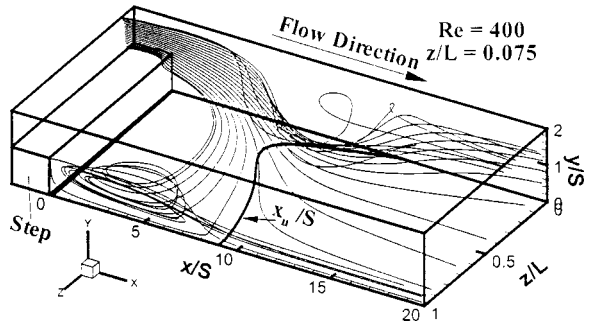

Fig. 5 Streamlines starting from the spanwise plane of $z/L=0.075$

Distributions of the three velocity components on a plane adjacent to the stepped wall ($y/S=0.01$) along the x-plane and the z-plane that intersect at the ''jet-like'' impingement location are shown in Figs. 8(a) and 8(b). The ''jet-like'' impingement location is determined as the point on a y-plane adjacent to the wall ($y/S=0.01$) where both the streamwise and the spanwise velocity components are equal to ''zero.'' These two planes intersect at $x/S=6.6$ and $z/L=0.18$ for Reynolds number of 400. The Nusselt number distributions along these two planes on the stepped wall are also presented in these figures. The circle symbol, where both the streamwise velocity component (u) and the spanwise velocity component (w) are zero, represents the location where the ''jet-like'' flow impinges on the stepped wall. Another sample of velocity distributions are presented in Fig. 9 on the transverse plane of $y/S=0.4$ for the selected planes of $x/S=5.61$ and $z/L=0.16$. These planes were selected to illustrate the various reverse flow regions that develop in this flow. Additional details about the flow behavior in this geometry can be found in reference [19].

Some studies [14,15] have used the two-dimensional definition of reattachment (x_u-line, the location at the stepped wall where the streamwise shear stress component is zero, or where $\partial u/\partial y|_{y=0}=0$) to identify reattachment in three-dimensional separated flow adjacent to backward-facing step. A sample of such effort is illustrated in Fig. 2 for different Reynolds numbers. The limiting streamlines method has also been explored as a method for identifying reattachment in three-dimensional flow. Limiting streamlines on a y plane ($y/S=0.01$) adjacent to the stepped wall, on a y plane ($y/S=1.99$) adjacent to the flat wall, and on a z plane ($z/L=0.01$) adjacent to the sidewall, are presented in Fig. 10. The reverse flow regions adjacent to both the sidewall and to the upper flat wall can be clearly seen in this figure. Streamlines projected onto a no-slip surface are the computational analogy to the experimental surface flow visualization [20]. The bold solid line that is shown on the stepped wall identifies the locations (x_u) where the mean streamwise velocity component (u) and the streamwise wall shear stress component ($\partial u/\partial y|_{y=0}$) are zero on that plane.

Figure 11 illustrates the limiting streamlines that originate from

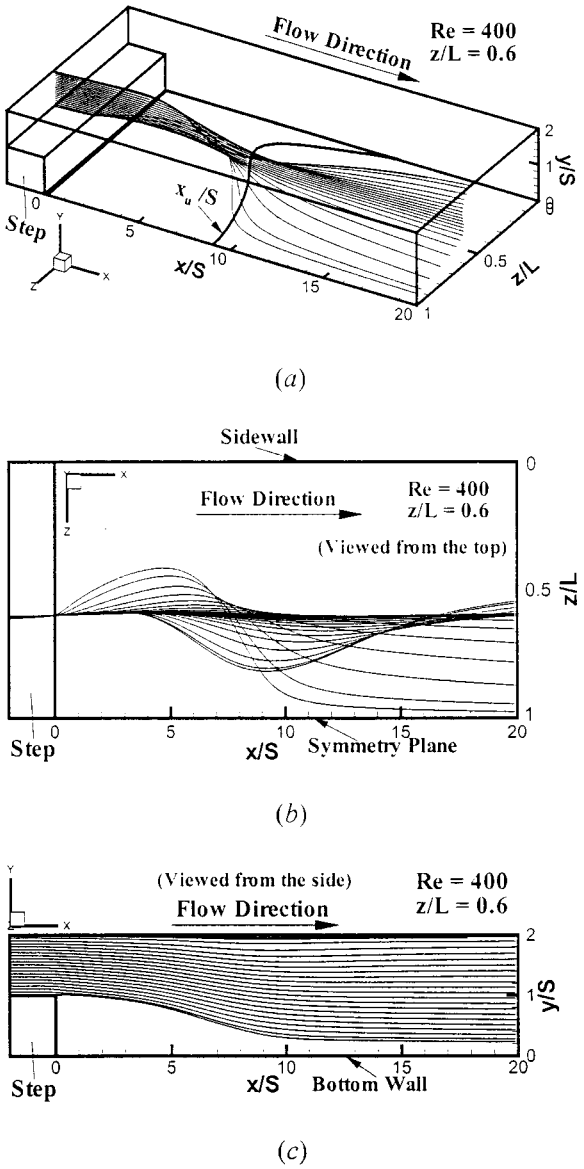

Fig. 6 Streamlines starting from the spanwise plane of $z/L = 0.6$

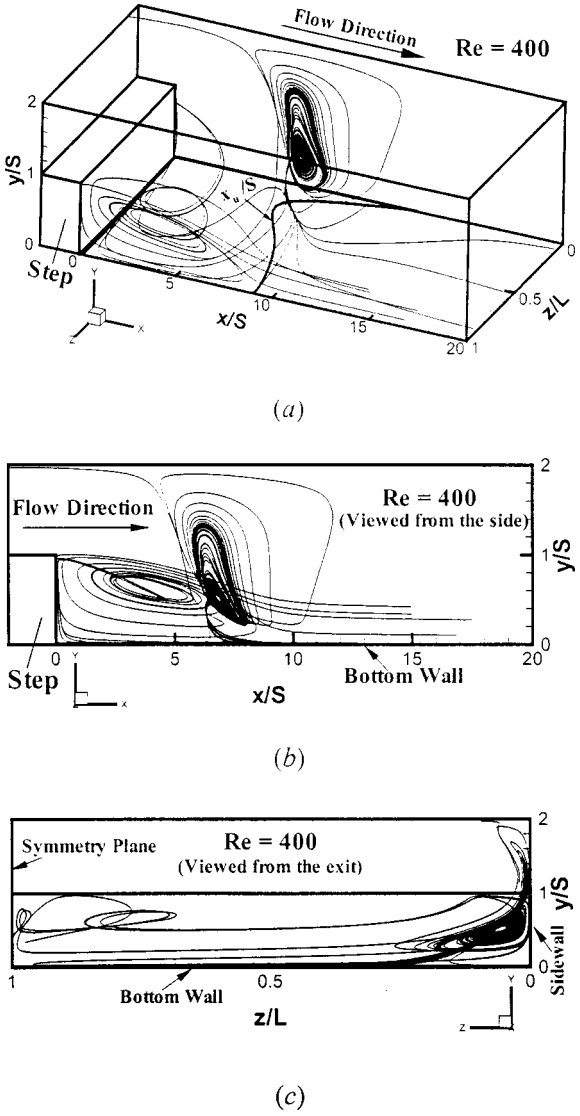

Fig. 7 The "jet-like" flow and the recirculation region that develops adjacent to the sidewall

the "jet-like" flow (see also Fig. 7) along with the line that designates the locations where the mean streamwise velocity component is zero (x_u-line) on a plane adjacent to the stepped wall. These limiting streamlines are used to identify the outer boundary of the primary recirculation flow region (x_b), and that is presented as dashed line in the figure. This boundary, (x_b), is determined by the criterion that the streamlines on both sides of this boundary line move in opposite directions: the streamlines upstream from this line flow upstream toward the step, and the streamlines downstream from this line flow downstream and away from the step. Sample of the streamlines that are used to determine the boundary line (x_b), by interpolation, are shown as darker lines in the figure. This boundary line (x_b) is different from the zero mean streamwise velocity line (x_u) for three-dimensional flow but they are identical to each other for the two-dimensional flow (i.e., at the center of the duct with a large aspect ratio).

Distributions of velocity components (v and w) along the x_u-line, that are presented in Fig. 12, show a region close to the sidewall with positive mean transverse velocity component (v). That region is part of the sidewall recirculation flow region that develops in this geometry. The wall shear stress is zero only at the point where the dimensionless gradient of the mean spanwise velocity component ($\partial w/\partial y|_{y=0} \cdot (S/u_0)$) line and the x_u-line (where $\partial u/\partial y|_{y=0} = 0$) intersect as shown in Fig. 12. That point is the impingement location of the "jet-like" flow that develops adjacent to the sidewall, and the peak (absolute value) of the transverse velocity component (v) develops in the same region. The results in Fig. 13 represent the velocity field on a plane adjacent to the stepped wall ($y/S = 0.01$), and the color in that figure designates the magnitude of the mean transverse velocity component (v) on that plane. Regions with positive and negative mean transverse velocity component can be easily identified in that figure. Lines identifying the locations where (a) the mean transverse velocity component is zero ($v = 0$); (b) the gradient of the mean streamwise velocity component is zero ($\partial u/\partial y|_{y=0} = 0$, the x_u-line); and (c) the gradient of the mean spanwise velocity component is zero ($\partial w/\partial y|_{y=0} = 0$, the x_w-line), are shown in this figure. The significant spanwise flow that develop in the primary recirculation flow region and in the region of the "jet-like" flow can be seen clearly from that figure. The swirling flow, the spanwise flow, and the "jet-like" flow that develop in this geometry adjacent to the stepped wall make it very difficult to identify numerically and/or experimentally a reattachment line/region that can be used for code and apparatus validation.

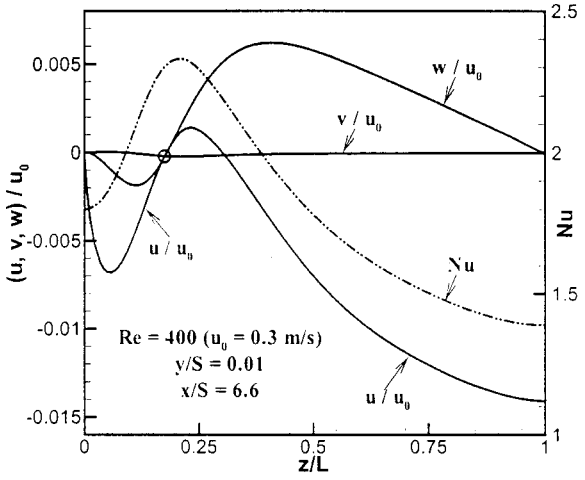

(a)

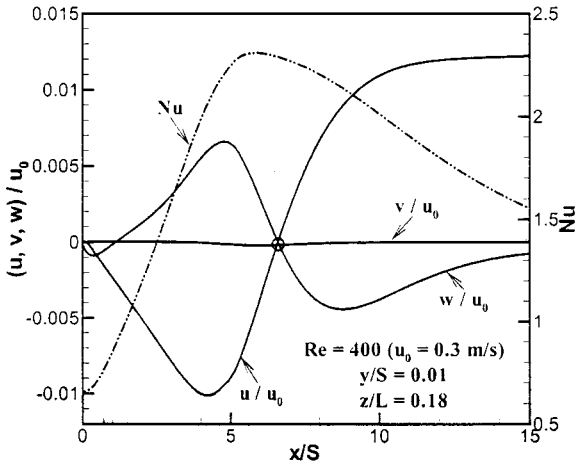

(b)

Fig. 8 Distributions of the velocity components on the planes intersecting at the "jet-like" flow impingement location ($y/S = 0.01$)

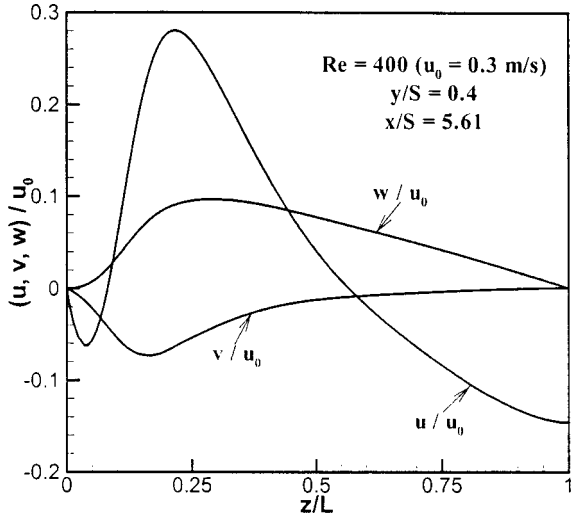

(a) as a function of x/S at the $z/L = 0.16$ plane

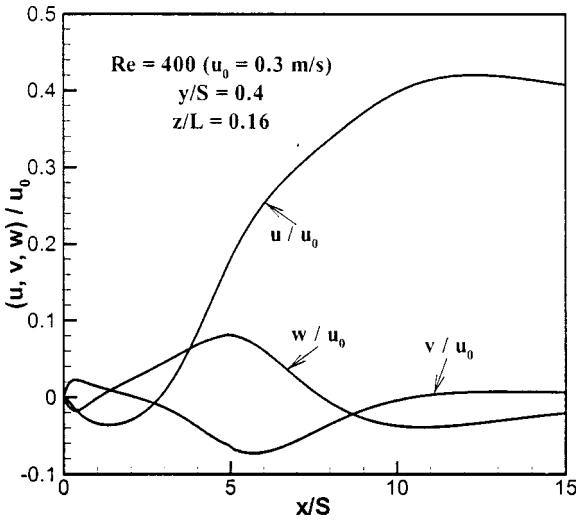

(b) as a function of z/L at the $x/S = 5.61$ plane

Fig. 9 Distributions of the velocity components on the $y/S = 0.4$ plane

The two lines that have been identified in Fig. 11 adjacent to the stepped wall (one line identifies the location where $\partial u/\partial y|_{y=0}$ is zero (x_u-line), and the other line identifies the boundary of the primary recirculation region (x_b-line) as determined from the limiting streamlines) do not identify the location of reattachment for this three-dimensional flow. This conclusion was reached from examining the results presented in Figs. 12 and 13. These figures show that a region near the sidewall ($z/L < 0.15$) has a positive mean transverse velocity component (v), i.e., velocity is moving away from the stepped wall. Hence, the segments of the x_u-line and the x_b-line that are inside this region are not part of the reattachment line/region. Part of the boundary of the primary recirculation region (x_b-line) that is downstream from the x_u-line develop from the "jet-like" flow impingement and that fluid ends up flowing upstream toward the step as shown in Fig. 11.

Lines designating the locations on a plane adjacent to the stepped wall ($y/S = 0.01$) where (a) the mean transverse velocity component is zero ($v = 0$); (b) the mean transverse velocity component is maximum (absolute value of v); (c) the gradient of the mean streamwise velocity component is zero ($\partial u/\partial y|_{y=0} = 0$, the x_u-line); (d) the gradient of the mean spanwise velocity component is zero ($\partial w/\partial y|_{y=0} = 0$, the x_w-line); (e) the boundary of primary recirculation region on the stepped wall (the x_b-line); and (f) the Nusselt number is maximum ($\mathrm{Nu} = q_w S/k(T_w - T_0)$, where T_w is the wall temperature), are presented in Fig. 14. A line identifying the locations where the wall shear stress is minimum is also presented in this figure, but the x_u-line ($\partial u/\partial y|_{y=0} = 0$), is almost identical to this line because the magnitude of $(\partial w/\partial y)^2$ is much smaller than that of $(\partial u/\partial y)^2$ in that region. These lines/regions can be located by using simulated flow and thermal fields and can also be measured. Any one of these lines can be used for code and apparatus validation. The easiest one of these to measure, however, is the location where the gradient of the mean streamwise velocity component is zero ($\partial u/\partial y|_{y=0} = 0$) and for that reason it is recommended for use.

Conclusions

Results from numerical simulations of three-dimensional laminar forced convection flow adjacent to backward-facing step in a rectangular duct are used to examine the flow and heat transfer in the neighborhood of the reattachment region. The impingement of the "jet-like" flow on the stepped wall is responsible for the maxi-

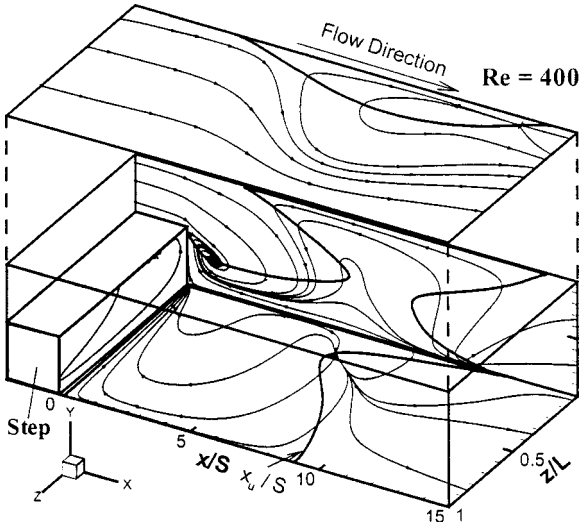

Fig. 10 Limiting streamlines adjacent to the stepped wall, the sidewall, and the upper flat wall

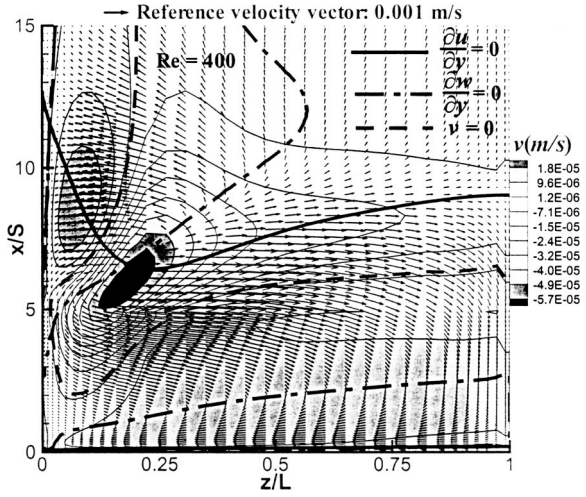

Fig. 13 Velocity field on a *y*-plane adjacent to the stepped wall ($y/S = 0.01$) for Re=400

mum Nusselt number that develops in that region. The two-dimensional flow definition for the reattachment (x_u-line) and the limiting streamlines definition for identifying the boundary of the primary recirculation region (x_b-line) were examined for possible use in determining the reattachment line/region in this three-dimensional flow. Unfortunately, neither one of these definitions is appropriate for use in determining the reattachment line/region in this three-dimensional flow. The strong spanwise flow that develops in both the negative and positive directions adjacent to the stepped wall in the reattachment region makes it very difficult to quantify from measurements or from simulations the location of the reattachment line. For that reason, the two-dimensional flow

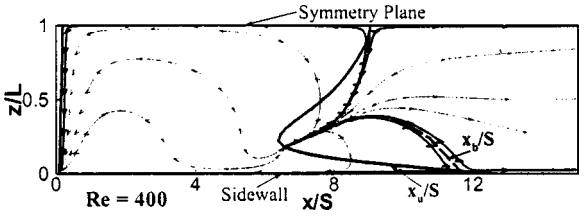

Fig. 11 Boundaries of the primary recirculation region on the stepped wall

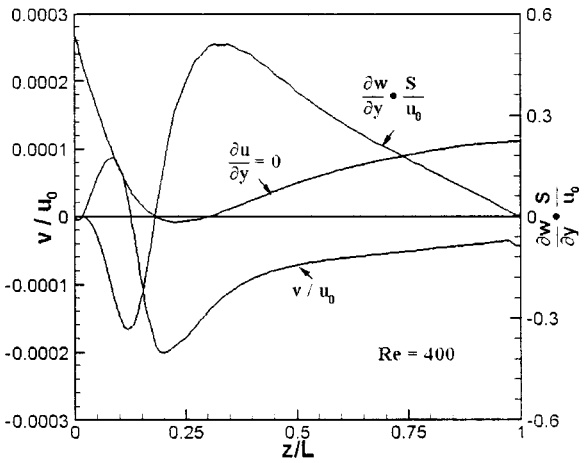

Fig. 12 Distributions of velocity component (v) and velocity gradients along the x_u-line

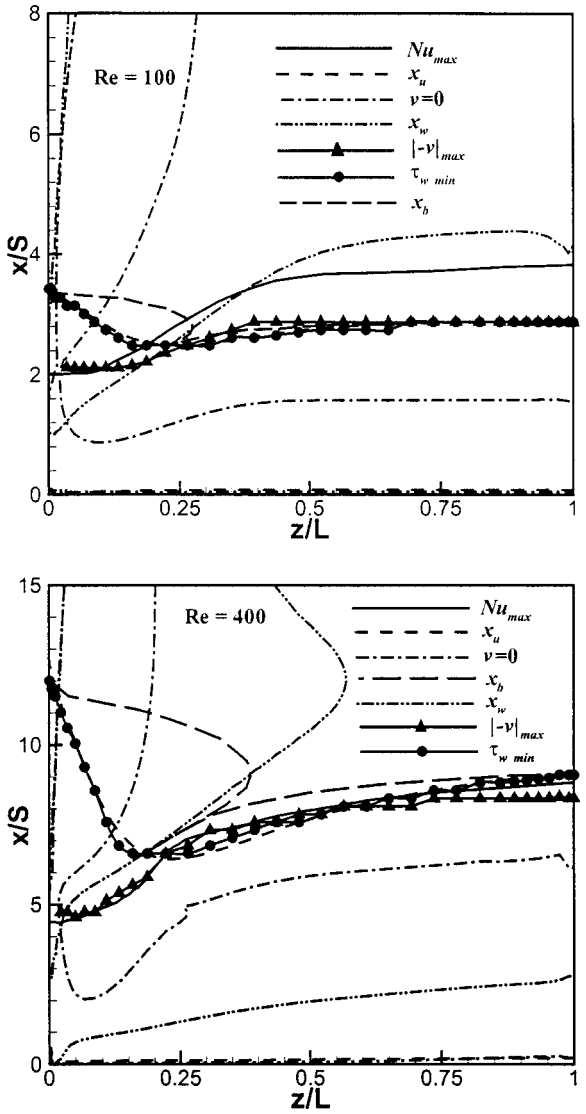

Fig. 14 Distributions of several lines adjacent to the stepped wall

definition for reattachment, (i.e., the location where the gradient of the mean streamwise velocity component is zero ($\partial u/\partial y|_{y=0} = 0$, the x_u-line)), that does not identify reattachment in three-dimensional flow), is recommended for use as the criterion for codes and apparatus validations due to the ease of its measurements and its evaluation from numerical simulations.

Acknowledgments

This work was supported in part by the National Science Foundation (NSF) under Grants CTS-9906746 and CTS-9818203.

Nomenclature

AR = aspect ratio $= W/S$
C_f = skin friction coefficient $= 2\tau_w/\rho u_0^2$
C_p = specific heat
ER = expansion ratio $= H/(H-S)$
H = duct height downstream from the step
h = duct height upstream from the step
k = thermal conductivity
L = half width of the duct
Nu = Nusselt number $= q_w S/k(T_w - T_0)$
p = pressure
q_w = wall heat flux $= -k\partial T/\partial n$ at the wall
Re = Reynolds number $= 2\rho u_0 h/\mu$
S = step height
T = temperature
T_0 = inlet temperature
T_w = wall temperature
u = velocity component in the x-coordinate direction
u_0 = average inlet velocity
v = velocity component in the y-coordinate direction
W = width of the duct
w = velocity component in the z-coordinate direction
x = streamwise coordinate
x_b = outer boundary of the primary recirculation region
x_u = locations where the streamwise velocity gradient is zero ($\partial u/\partial y = 0$)
x_w = locations where the spanwise velocity gradient is zero ($\partial w/\partial y = 0$)
y = transverse coordinate
z = spanwise coordinate
μ = dynamic viscosity
ρ = density
τ_w = wall shear stress, for three-dimensional flow $\tau_w = \mu\sqrt{(\partial u/\partial y)^2 + (\partial w/\partial y)^2}$

References

[1] Armaly, B. F., Durst, F., Pereira, J. C. F., and Schonung, B., 1983, "Experimental and Theoretical Investigation of Backward-Facing Step Flow," J. Fluid Mech., **127**, pp. 473–496.
[2] Simpson, R. L., 1996, "Aspects of Turbulent Boundary-Layer Separation," Prog. Aerosp. Sci., **32**(5), pp. 457–521.
[3] Eaton, J. K., and Johnson, J. P., 1981, "A Review of Research on Subsonic Turbulent Flow Reattachment," AIAA J., **19**(9), pp. 1093–1100.
[4] Jovic, S., and Driver, D. M., 1994, "Backward-Facing Step Measurements at Low Reynolds Number, Re_h=5000," *NASA Technical Memorandum 108807*, National Aeronautics and Space Administration.
[5] Sohn, J. L., 1988, "Evaluation of FIDAP on Some Classical Laminar and Turbulent Benchmarks," Int. J. Numer. Methods Fluids, **8**(5), pp. 1469–1490.
[6] Khadra, K., Angot, P., Parneix, S., and Caltagitone, J. P., 2000, "Fictitious Domain Approach for Numerical Modeling of Navier-Stokes Equations," Int. J. Numer. Methods Fluids, **34**(8), pp. 651–684.
[7] Blackwell, B. F., and Pepper, D. W., eds., 1992, "Benchmark Problems for Heat Transfer Codes," *HTD-Vol. 222*, American Society of Mechanical Engineers, New York, NY.
[8] Blackwell, B. F., and Armaly, B. F., eds., 1993, "Computational Aspects of Heat Transfer-Benchmark Problems," *HTD-Vol. 258*, American Society of Mechanical Engineers, New York, NY.
[9] Otugen, M. V., and Muckenthaler, G., 1992, "Study of Separated Shear Layer in Moderate Reynolds Number Plane Sudden Expansion Flows," AIAA J., **30**(7), pp. 1808–1814.
[10] Shen, G. X., and Ma, G. Y., 1996, "The Investigation on the Properties and Structures of Starting Vortex Flow Past a Backward-Facing Step by WBIV Technique," Exp. Fluids, **21**(1), pp. 57–65.
[11] Vogel, J. C., and Eaton, J. K., 1985, "Combined Heat Transfer and Fluid Dynamics Measurements Downstream of a Backward-Facing Step," J. Heat Transfer. **107**(4), pp. 922–929.
[12] Settles, G. S., 1986, "Modern Developments in Flow Visualization," AIAA J., **24**(8), pp. 1313–1323.
[13] Carrington, D. B., and Pepper, D. W., 2002, "Convective Heat Transfer Downstream of a 3-D Backward-Facing Step," Numer. Heat Transfer, Part A, **41** (6-7), pp. 555–578.
[14] Shih, C., and Ho, C. M., 1994, "Three-Dimensional Recirculation Flow in a Backward Facing Step," ASME J. Fluids Eng., **116**(2), pp. 228–232.
[15] Li, A., and Armaly, B. F., 2000, "Convection Adjacent to a 3-D Backward-Facing Step," NHTC 2000-12301, *Proceedings of the ASME/AIChE National Heat Transfer Conference*, S. C. Yao and Allan Jones, eds., August 20–22, Pittsburgh, PA.
[16] Li, A., 2001, "Experimental and Numerical Study of Three-Dimensional Laminar Separated Flow Adjacent to Backward-Facing Step," Ph.D. thesis, University of Missouri, Rolla, MO.
[17] Shah, R. K., and London, A. L., 1978, *Laminar Forced Convection in Ducts*, Academic Press, New York.
[18] Patankar, S. V., 1980, *Numerical Heat Transfer and Fluid Flow*, Hemisphere, New York.
[19] Armaly, B. F., Li, A., and Nie, J. H., 2002, "Three-Dimensional Forced Convection Flow Adjacent to Backward-Facing Step," J. Thermophys. Heat Transfer, **16**(2), pp. 222–227.
[20] Perry, A. E., and Chong, M. S., 2000, "Interpretation of Flow Visualization," in *Flow Visualization: Techniques and Examples*, A. J. Smits and T. T. Lim, ed., Imperial College Press, London, UK, pp. 1–26.

Quasi-Steady State Natural Convection in Laser Chemical Vapor Deposition With a Moving Laser Beam

Yuwen Zhang
Department of Mechanical Engineering,
New Mexico State University,
Las Cruces, NM 88003

Numerical analysis of laser chemical vapor deposition (LCVD) of titanium nitride by a moving laser beam is presented. The effect of natural convection due to temperature and concentration differences in the gaseous mixture is modeled and implemented into thermal model of LCVD by a moving laser beam. The problem is formulated in a coordinate system that moves with the laser beam and therefore, the problem is a quasi-steady state problem. The results show that the effect of natural convection on the shape of deposited film is very insignificant for cases with a laser power of 300 W but becomes important when the laser power is increased to 360 W. [DOI: 10.1115/1.1565088]

Keywords: Heat Transfer, Laser, Mass Transfer, Natural Convection, Vapor Deposition

Introduction

Solid Freeform Fabrication (SFF) is an emerging manufacturing technology that directly creates three-dimensional parts from a Computer Aided Design (CAD) [1,2]. The CAD data are transferred to an STL (stereolithography format) computer file, which is then sliced to generate two-dimensional sections of the virtual product. The physical product is built by layering two-dimensional sections of finite thickness. An extremely wide array of SFF technologies has been proposed for purposes of providing physical three-dimensional renderings of CAD data. However, only a few have been extended to build structurally-sound parts of near full density. Almost always, the SFF technologies that fit into the latter group are powered by thermal fabrication of three-dimensional objects from powders or gases. To produce fully functional structural components, gas based approaches to SFF such as Selective Area Laser Deposition (SALD) seem to be very promising [3–5]. SALD utilizes the Laser Chemical Vapor Deposition (LCVD) technique, which can be based on reactions initiated pyrolytically, photolytically or a combination of both [2], to deposit the film at a desired location on the substrate. LCVD is also applicable on thin film coating and the growth of semiconductor.

A very detailed literature review on Chemical Vapor Deposition (CVD) is given by Mahajan [6]. The difference between LCVD and CVD is that only a very small spot on the substrate is heated by the laser beam and vapor deposition occurs only on the heated spot in the LCVD process. Mazumder and Kar [7] reviewed the theoretical and experimental aspects on LCVD up to 1995. More recently, Duty et al. have thoroughly reviewed materials, modeling and process control of LCVD [8]. Jacquot et al. [9] proposed a thermal model of the SALD process using acetylene (C_2H_2) as the source gas. Various phenomena, which include heat conduction in the substrate, chemical reaction during carbon deposition, and mass diffusion of acetylene in the chamber are taken into account. The effect of chemical reaction heat on the heat conduction of the substrate was also taken into account. The temperature of the gases was, however, assumed to be uniform and therefore heat transfer in the gas phase was neglected. Zhang and Faghri [10] developed a very detailed model of the SALD, which includes the submodels of heat transfer, chemical reaction and mass transfer. This model was employed to simulate LCVD of TiN films on a finite slab with stationary and moving laser beams. The results showed that the effect of chemical reaction heat on the shape of the deposited film was negligible.

In LCVD, the spot on the substrate under laser irradiation is at a very high temperature (1200 K or higher). Temperature gradients in the source gases will cause natural convection in the chamber. The concentration of the gas mixture near the hot spot on the substrate is affected by the chemical reaction taking place on the substrate. Concentration differences in the chamber become another driving force for natural convection in the chamber. For the case of LCVD by a stationary laser beam, Lee et al. [11] concluded that the effect of natural convection on the thin film deposition rate was negligible and the heat and mass transfer in the gases were dominated by diffusion. In the SALD process, the laser beam scans the substrate and the product of the chemical reaction forms a line on the substrate. These lines, formed by multiple laser scans, are subsequently interwoven to form a part layer. In order to thoroughly understand the effects of various physical phenomena, including natural convection, on the SALD process, natural convection during LCVD with a moving laser beam is investigated in this paper.

Physical Model

The physical model of LCVD under consideration is illustrated in Fig. 1. A substrate made of Incoloy 800 with a thickness of h is located in the bottom of a chamber. Before the vapor deposition is started, the chamber is evacuated and then filled with a mixture of H_2, N_2, and $TiCl_4$. A laser beam moves along the surface of the substrate with a constant velocity, u_b. The initial temperature of the substrate, T_i, is below the chemical reaction temperature. Vapor deposition starts when the surface temperature reaches the chemical reaction temperature. The chemical reaction that takes place on the top substrate surface absorbs part of the laser energy and consumes the $TiCl_4$ near the substrate surface. A concentration difference is therefore established and becomes the driving force for mass transfer. The physical model of the LCVD process includes: natural convection, heat transfer in the substrate and gases, chemical reaction, as well as mass transfer in the gases.

The laser beam travels with a constant velocity, u_b, along the surface of the substrate, which is a typical moving heat source problem [12]. If the substrate is sufficiently large compared to the

Contributed by the Heat Transfer Division for publication in the JOURNAL OF HEAT TRANSFER. Manuscript received by the Heat Transfer Division April 23, 2002; revision received November 15, 2002. Associate Editor: K. S. Ball.

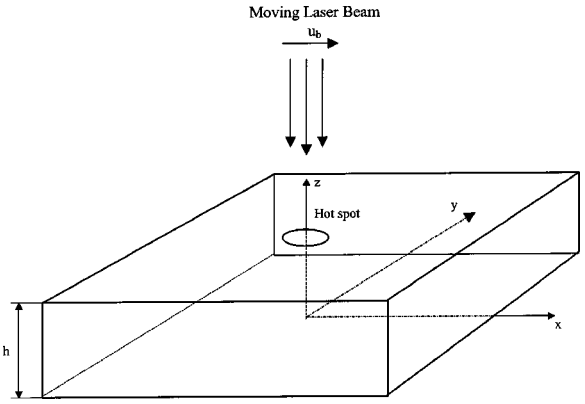

Fig. 1 Physical model of laser chemical vapor deposition

diameter of the laser beam, which has an order of magnitude of 10^{-3} m, a quasi-steady state occurs. The system appears to be in steady state from the stand-point of the observer located in and traveling with the laser beam. By simulating LCVD with a moving laser beam in the moving coordinate system, the computational time will be substantially shortened, making possible numerical simulation for a significant number of cases.

Since the temperature of the substrate undergoes a significant change under laser irradiation, the constant thermal properties assumption does not apply [9–11]. Heat transfer in the substrate and gases is modeled as one problem with different thermal properties in each region. In the substrate region, the velocity is set to zero in the numerical solution. The advantage of modeling the heat and mass transfer problem in the substrate and the gases as one problem is that the temperature distribution in the substrate and gases can be obtained by solving one equation, and the iteration procedure to match the boundary condition at the substrate-gas interface can therefore be eliminated. Since the model geometry is symmetric about the *xz* plane, only half of the problem needs to be investigated. For a coordinate system moving with the laser beam as shown in Fig. 1, the laser beam is stationary but the substrate and the chamber move with a velocity $-u_b$. The heat and mass transfer in the substrate and gases are modeled with the following equations:

$$\frac{\partial u}{\partial x}+\frac{\partial v}{\partial y}+\frac{\partial w}{\partial z}=0 \tag{1}$$

$$u\frac{\partial u}{\partial x}+v\frac{\partial u}{\partial y}+w\frac{\partial u}{\partial z}=-\frac{1}{\rho}\frac{\partial p}{\partial x}+\nu\left(\frac{\partial^2 u}{\partial x^2}+\frac{\partial^2 u}{\partial y^2}+\frac{\partial^2 u}{\partial z^2}\right) \tag{2}$$

$$u\frac{\partial v}{\partial x}+v\frac{\partial v}{\partial y}+w\frac{\partial v}{\partial z}=-\frac{1}{\rho}\frac{\partial p}{\partial y}+\nu\left(\frac{\partial^2 v}{\partial x^2}+\frac{\partial^2 v}{\partial y^2}+\frac{\partial^2 v}{\partial z^2}\right) \tag{3}$$

$$u\frac{\partial \psi}{\partial x}+v\frac{\partial w}{\partial y}+w\frac{\partial w}{\partial z}=-\frac{1}{\rho}\frac{\partial p}{\partial z}+\nu\left(\frac{\partial^2 w}{\partial x^2}+\frac{\partial^2 w}{\partial y^2}+\frac{\partial^2 w}{\partial z^2}\right)-g\beta(T-T_\infty)-g\beta_c(C-C_\infty) \tag{4}$$

$$\rho\left(\frac{\partial(uc_pT)}{\partial x}+\frac{\partial(vc_pT)}{\partial y}+\frac{\partial(wc_pT)}{\partial z}\right)=\frac{\partial}{\partial x}\left(k\frac{\partial T}{\partial x}\right)+\frac{\partial}{\partial y}\left(k\frac{\partial T}{\partial y}\right)+\frac{\partial}{\partial z}\left(k\frac{\partial T}{\partial z}\right)+S \tag{5}$$

$$\frac{\partial(uC)}{\partial x}+\frac{\partial(vC)}{\partial y}+\frac{\partial(wC)}{\partial z}=D\left(\frac{\partial^2 C}{\partial x^2}+\frac{\partial^2 C}{\partial y^2}+\frac{\partial^2 C}{\partial z^2}\right)+S_c \tag{6}$$

where β and β_c are respectively the coefficients of thermal expansion and concentration expansion coefficient, and the Boussinesq approximation is applied.

For the substrate region, the thermal properties are those of Incoloy 800, the substrate material. For the gaseous region, the thermal properties are determined by the individual thermal properties of H_2, N_2, and $TiCl_4$ as well as their molar fractions [13]. The mass diffusivity of $TiCl_4$ in the gas mixture is determined by the Stefan-Maxwell equation [13] using the binary diffusivity of $TiCl_4$ with respect to all other species, which is calculated using the hard sphere model [13].

The source term in Eq. (5) deals with the effects of laser beam heating and chemical reaction. The source term will be zero everywhere except at the substrate-gas interface under the laser spot. The heat flux at the substrate surface due to laser beam irradiation and chemical reaction is expressed as

$$q''=\frac{2P\alpha_a}{\pi r_0^2}\exp\left[-\frac{2(x^2+y^2)}{r_0^2}\right]-\varepsilon\sigma(T^4-T_\infty^4)-\rho_{\mathrm{TiN}}\Delta H_R\frac{d\delta}{dt},\quad z=h \tag{7}$$

where $d\delta/dt$ is the deposit rate, For a chemical reaction in the order of unity, the deposition rate is expressed as [10]

$$\frac{d\delta}{dt}=\frac{\dot{m}}{\rho_{\mathrm{TiN}}}=\frac{\gamma_{\mathrm{TiN}}K_0}{\rho_{\mathrm{TiN}}}\exp\left(-\frac{E}{R_uT_s}\right)C_s \tag{8}$$

where C_s represents the concentration of $TiCl_4$ at the surface of the substrate. The constant, K_0, in Eq. (8) is defined as

$$K_0=(C_{H_2})_i(C_{N_2})_i^{1/2}K_0' \tag{8a}$$

The coefficient γ_{TiN} in Eq. (8) is sticking coefficient defined as [14]

$$\gamma_{\mathrm{TiN}}=\begin{cases}1 & T<T_m\\ 1+(T_m-T_s)/(T_M-T) & T_m\leqslant T\leqslant T_M\\ 0 & T>T_M\end{cases} \tag{8b}$$

which means that the product of chemical reaction can be fully stuck on the substrate only if the surface temperature is below T_m. If the surface temperature is between T_m and T_M, the product of chemical reaction can only be partially stuck on the substrate. No product of chemical reaction can be stuck on the substrate if the substrate surface temperature is higher than T_M. The sticking coefficient model defined in Eq. (8*b*) has been applied to model volcano-like profiles of deposited film for LCVD with stationary laser beam and the agreement with experimental results were satisfactory [10,14]. The values of T_m and T_M are chosen to be 1473 K and 1640 K, respectively [14].

The LCVD problem under investigation is steady in the moving coordinate system and therefore, the deposition height, δ, is not a function of time. The scanning time is translated into the spatial variable x by

$$\frac{dx}{dt}=-u_b \tag{9}$$

Substituting Eq. (9) into Eq. (8), an equation concerning the profile of the deposited film can be obtained.

$$\frac{d\delta}{dx}=-\frac{\gamma_{\mathrm{TiN}}K_0}{u_b\rho_{\mathrm{TiN}}}\exp\left(-\frac{E}{R_uT_s}\right)C_s \tag{10}$$

In order to use Eq. (7) to determine the source term in Eq. (5), the heat flux is treated as an internal heat source in the grid near the surface of the substrate, i.e.,

$$S=\frac{q''\Delta x\Delta y}{\Delta V}=\frac{q''}{\Delta z} \tag{11}$$

where, Δx, Δy, Δz represent the dimensions of the control volume cell in the substrate near its surface.

The effect of the chemical reaction on the mass transfer is accounted for by a source term in Eq. (6). The mass flux rate of $TiCl_4$ at the substrate is expressed as

$$\dot{m}_{TiCl_4} = \rho_{TiN} \frac{d\delta}{dt} \frac{M_{TiCl_4}}{M_{TiN}} \tag{12}$$

The source term in Eq. (6) is then expressed as

$$S_c = -\frac{\dot{m}_{TiCl_4} \Delta x \Delta y}{\Delta V} = \frac{M_{TiCl_4}}{M_{TiN}} \frac{K_0}{\Delta z} \exp\left(-\frac{E}{R_u T_s}\right) C_s, \quad z = h \tag{13}$$

The boundary conditions of the velocities are

$$u = -u_b, \quad v = w = 0, \quad |x| \to \infty \tag{14a}$$

$$v = \frac{\partial u}{\partial y} = \frac{\partial w}{\partial y} = 0, \quad y = 0 \tag{14b}$$

$$u = -u_b, \quad v = w = 0, \quad y \to \infty \tag{14c}$$

$$u = -u_b, \quad v = w = 0, \quad z = 0, \infty \tag{14d}$$

The boundary conditions for Eqs. (5–6) are

$$T = T_i, \quad C = C_i \quad |x| \to \infty \tag{15a}$$

$$\frac{\partial T}{\partial y} = \frac{\partial C}{\partial y} = 0, \quad y = 0 \tag{15b}$$

$$T = T_i, \quad C = C_i \quad y \to \infty \tag{15c}$$

$$\frac{\partial T}{\partial z} = 0, \quad C = 0, \quad z = 0 \tag{15d}$$

$$\frac{\partial T}{\partial z} = \frac{\partial C}{\partial z} = 0, \quad z \to \infty \tag{15e}$$

Numerical Solution

The problem under investigation is a conjugate natural convection problem driven by temperature and concentration differences. The governing equations are discretized using the finite volume method [15]. The SIMPLEC algorithm [16] was employed to handle the linkage between velocity and pressure. Staggered grid was used to discretize the solution domain. The pressure, temperature, concentration, and all properties are stored on the main grid, which is at the center of the control volume. The velocity components are calculated at points that lie on the faces of the control volumes. The convection-diffusion terms in the momentum, energy and concentration equations are discretized by an exponential scheme. The resulting discretized equations are solved using the ADI (Alternative Directional Implicit) method. The underrelaxation factor for the velocity components is 0.5. Underrelaxation for pressure is not needed in the SIMPLEC algorithm.

The governing equations are written for the entire domain that includes both the substrate and gas. The velocity and concentration in the substrate region should be zero. The algebraic equations resulting from the control volume approach have the following format

$$a_p \phi_p = \sum a_{nb} \phi_{nb} + b \tag{16}$$

By setting $a_p = 10^{30}$ in Eq. (16) at the grid point located in the substrate region for the momentum equations and the mass transfer equation, zero velocity and concentration fields can be achieved [17]. In order to ensure that the velocity field is not altered by the pressure correction, the pressure correction at the points in the substrate region must be zero. The above technique is also applied to achieve zero pressure correction. The coefficients of the algebraic equations are altered before the algebraic equations are solved. The overall solution procedure is similar to that outlined in Ref. [10] and will not be repeated here. The typical number of iterations to get a converged solution is about 6000. In order to accelerate convergence, the initial temperature and concentration distributions for a specific case can be set as the converged temperature distribution for a similar case, which results in a reduction of the iteration number by 50%.

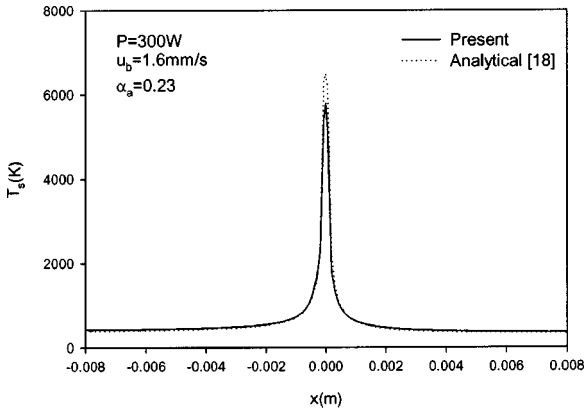

Fig. 2 Comparison between analytical and numerical solutions for pure conduction

In order to simulate LCVD in the moving coordinate system, the computational domain in the x and y directions must be large enough so that the effect of the computational domain on the temperature and concentration distributions can be eliminated. The calculations were carried out for a non-uniform grid of 82 nodes in the x direction, 42 nodes in the y direction, and 82 nodes in the z direction. Finer grid sizes ($122 \times 62 \times 122$) were also used in the calculations, but the difference in the cross-sectional area of the thin film over the present grid size is less than 2%.

Results and Discussion

In order to verify the validity of the code, the calculation is initially made with conduction only in the substrate with a moving laser beam. The conduction problem in the substrate is achieved by setting the thermal conductivity of the gas to zero so that there

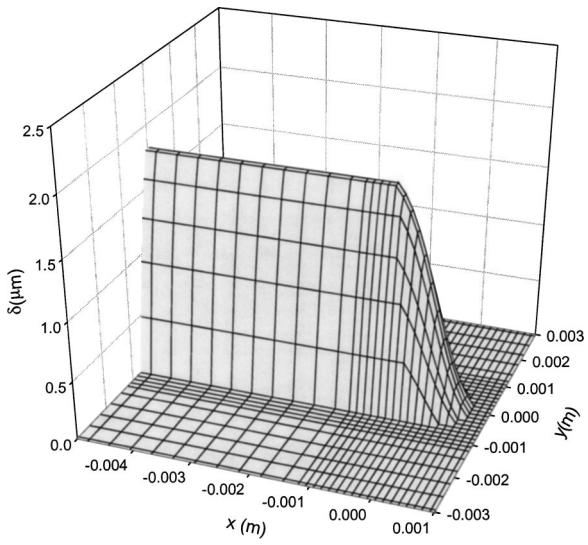

Fig. 3 Shape of the deposited film ($P = 300$ W, $u_b = 1.2$ mm/s)

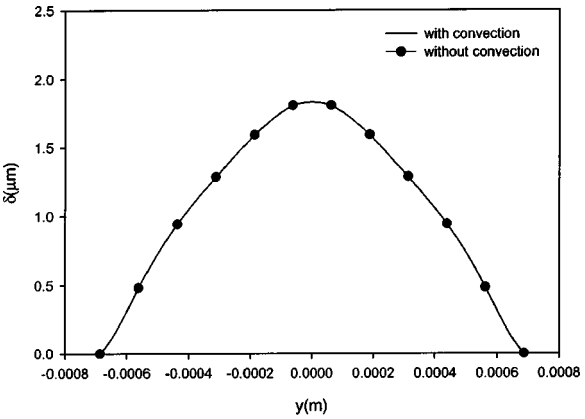

Fig. 4 Comparison of cross section ($P=300$ W, $u_b=1.2$ mm/s)

is no heat conduction in the vapor phase. The steady state surface temperature obtained by numerical solution is compared with the temperature distribution caused by a moving point heat source. The temperature expression of a semi-infinite body with a moving point heat source is [18]

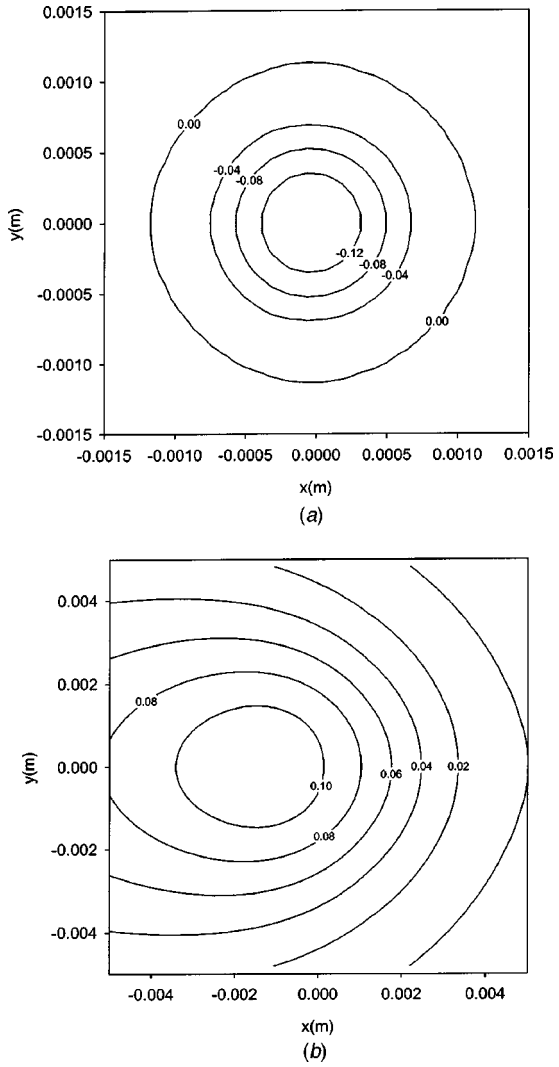

Fig. 5 Contour of velocity component, w[m/s] ($P=300$ W, $u_b=1.2$ mm/s): (a) $z=0.0052$ m; and (b) $z=0.0081$ m

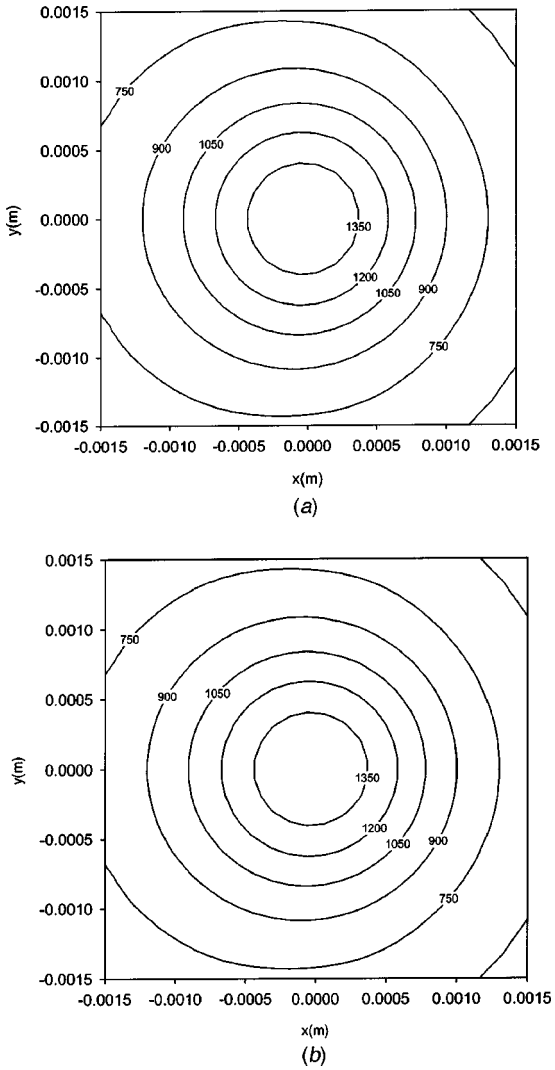

Fig. 6 Comparison of substrate surface temperature, T_s [K] ($P=300$ W, $u_b=1.2$ mm/s): (a) with convection; and (b) without convection

$$T_s - T_i = \frac{P\alpha_a}{2\pi kr}\exp\left[-\frac{u(r+x)}{2\alpha}\right] \tag{17}$$

In order to simulate conduction in the substrate subject to a moving point heat source, the heat flux at the substrate surface due to laser beam irradiation is expressed as

$$q'' = \begin{cases} \dfrac{P\alpha_a}{\pi r_0^2} & r \le r_0 \\ 0 & r > r_0 \end{cases}, \quad z = h \tag{18}$$

where the moving heat source is assumed to be top-hat (uniform distribution) instead of a Gaussian distribution because the latter results in the energy spread in a large spot. Effects of surface radiation and chemical reaction on the surface heat flux are also neglected in Eq. (17) in order to simulate pure conduction in the substrate.

The surface temperatures obtained by both methods are plotted in Fig. 2. The radius of the moving laser beam is $r_0=1.41\times10^{-4}$ mm, which is very small in order to simulate conduction in the substrate subject to a moving point heat source. It is seen that the overall agreement between the two solutions is very good except at the locations near $x=0$. This discrepancy of the two results is due to the nature of the heat source modeled in the

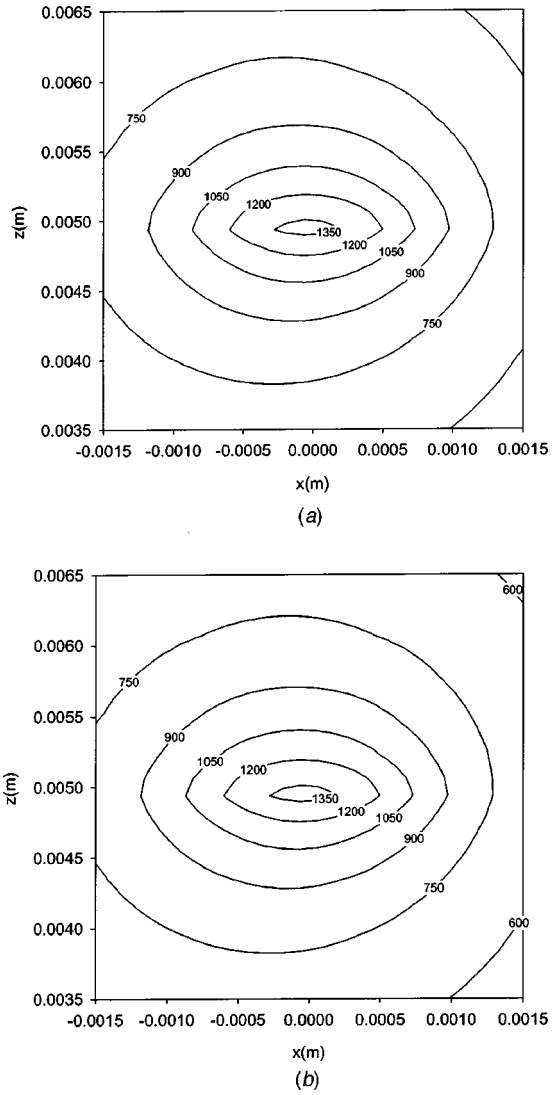

Fig. 7 Contour of temperature, T [K] ($P=300$ W, $u_b=1.2$ mm/s, $y=0$): (*a*) with convection; and (*b*) without convection

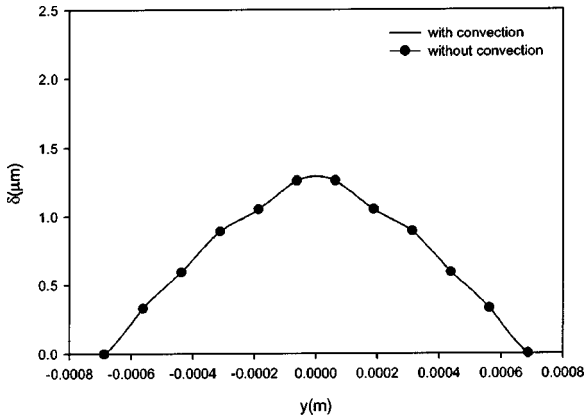

Fig. 8 Comparison of cross section ($P=300$ W, $u_b=1.6$ mm/s)

analytical and numerical solutions. The analytical result is for the temperature distribution caused by an infinitesimal heat source at $x=0$, while the numerical temperature distribution result is for a finite size heat source. Considering the different models, the agreement between the numerical and analytical solutions is very good.

Numerical simulations of LCVD process are performed with parameters similar to those in Ref. [10], [14]. The radius of the laser beam is very small compared with that of the chamber and therefore, the LCVD problem can be modeled as LCVD on a substrate with infinite length and width. The validity of this assumption, of course, depends on the actual size of the substrate. On the other hand, it allows obtaining quasi-steady state solutions and conducting a parametric study. The computational domain (the size of the chamber) used in this paper is $0.5\times0.5\times0.125\ \mathrm{m}^3$ ($x\times y\times z$) to ensure that the effect of the computational domain on the temperature distribution and deposited film can be eliminated. The thickness of the substrate is 5 mm and the bottom of the substrate is assumed to be adiabatic. The radius of the laser beam, which is defined as the radius where the laser intensity is $1/e^2$ of the intensity at the center of the laser beam, is 1.0×10^{-3} m. The absorptivity of the laser beam at the substrate surface is taken to be 0.23 [7,19]. The activation energy of the chemical reaction is taken to be $E=51.02$ kJ/mol. The total pressure in the chamber is 207 torr and the partial pressure of titanium tetrachloride is 7 torr. The partial pressures of N_2 and H_2 are the same. The initial temperature of the substrate and gas is 338 K. The concentrations of different species can be obtained by using

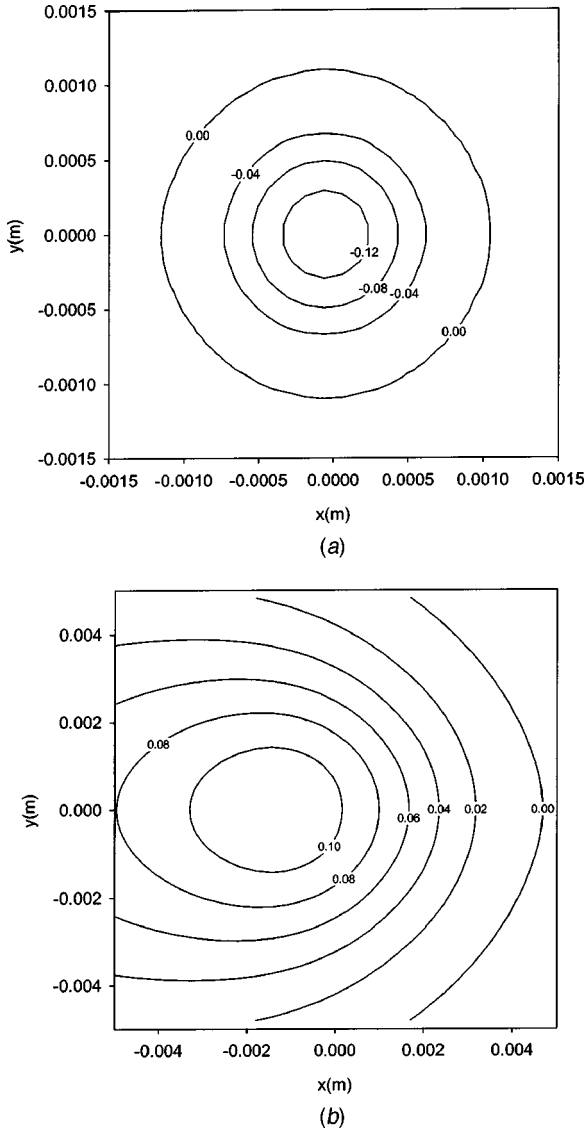

Fig. 9 Contour of velocity component, w [m/s] ($P=300$ W, $u_b=1.6$ mm/s): (*a*) $z=0.0052$ m; and (*b*) $z=0.0081$ m

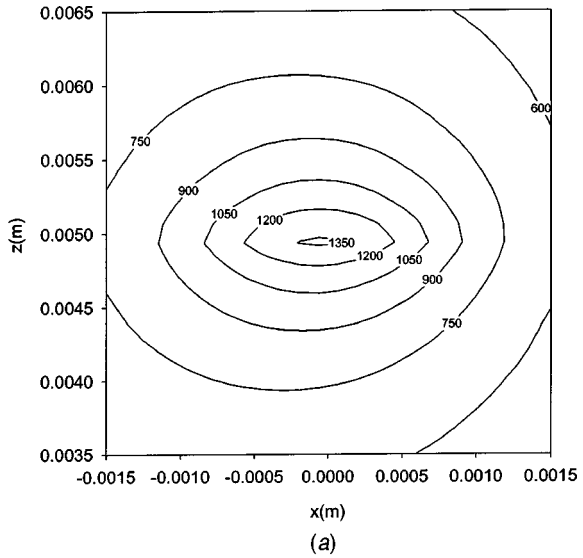

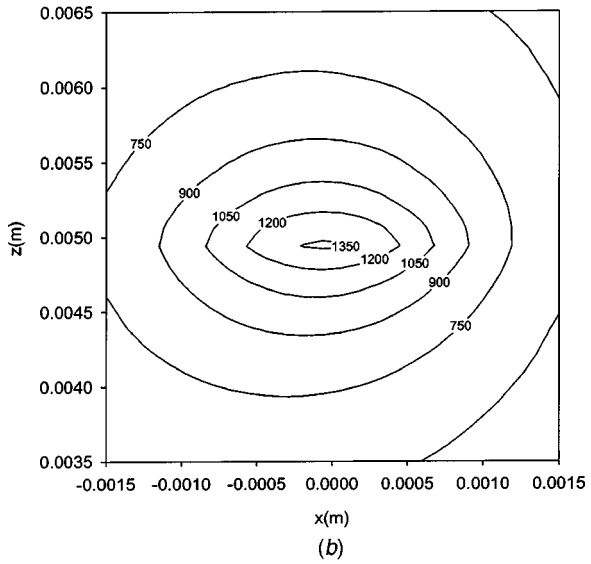

Fig. 10 Contour of temperature, T [K] ($P=300$ W, $u_b=1.6$ mm/s, $y=0$): (*a*) with convection; and (*b*) without convection

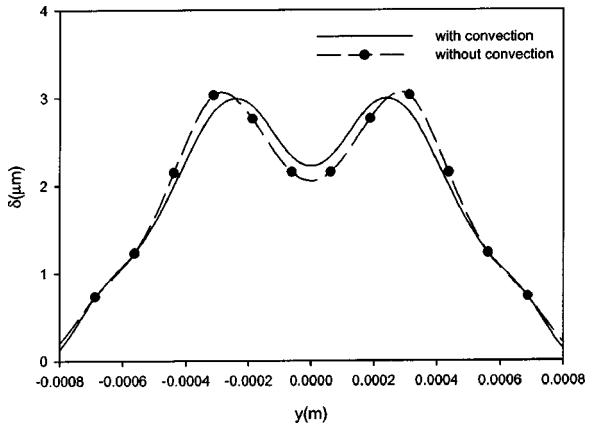

Fig. 11 Comparison of cross section ($P=360$ W, $u_b=1.2$ mm/s)

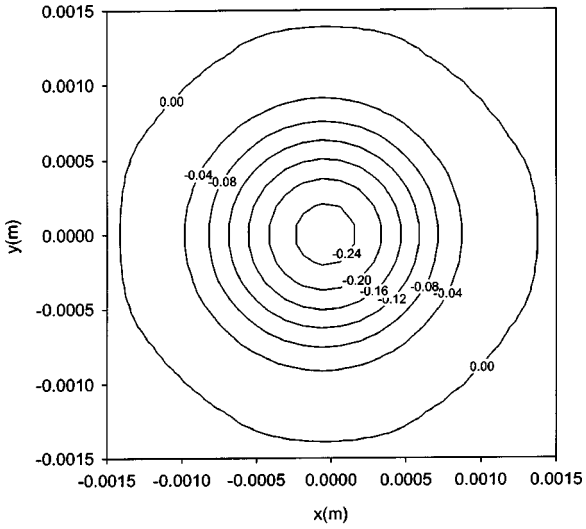

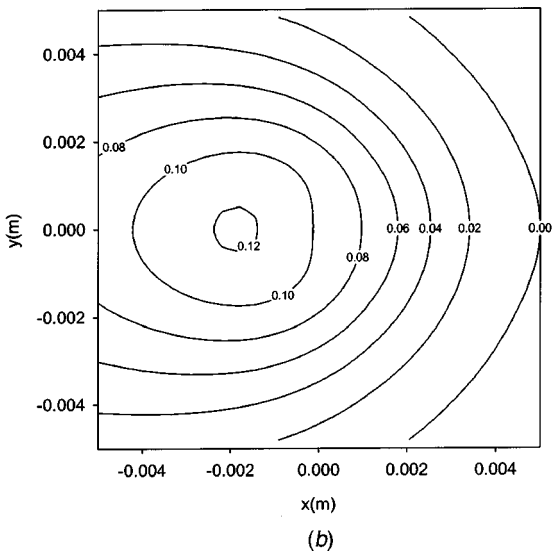

Fig. 12 Contour of velocity component, w [m/s] ($P=360$ W, $u_b=1.2$ mm/s): (*a*) $z=0.0052$ m; and (*b*) $z=0.0081$ m

ideal gas law. With the conditions specified above, the constant K_0, as defined in Eq. (8*a*), is 8.4 m/s [10]. Chemical reaction heat, ΔH_R, as determined by using JANAF thermochemical tables [20], is 5.379×10^6 J/kg.

Figure 3 shows the shape of the deposited TiN film obtained by using a laser power of 300 W and scanning velocity of 1.2 mm/s. It can be seen that the cross sectional area is not a function of x at locations in the wake of the laser beam. The growth of the thin film only occurs in the spot directly under the laser beam irradiation. Figure 4 shows a comparison of the cross-section of the thin film predicted by models with and without convection. The deposited TiN film thicknesses obtained by models with and without convection are very similar: the difference at the top of the thin film is only 0.09%. Figure 5 shows the bulk velocity component in the z direction at different heights, which are chosen so that the characteristics of fluid flow induced by chemical reaction and natural convection can be observed. Since the chemical reaction takes place on the hot spot of the substrate under laser irradiation, gases flow toward the hot spot due to consumption of $TiCl_4$. Therefore, the velocity component in the z direction is negative at

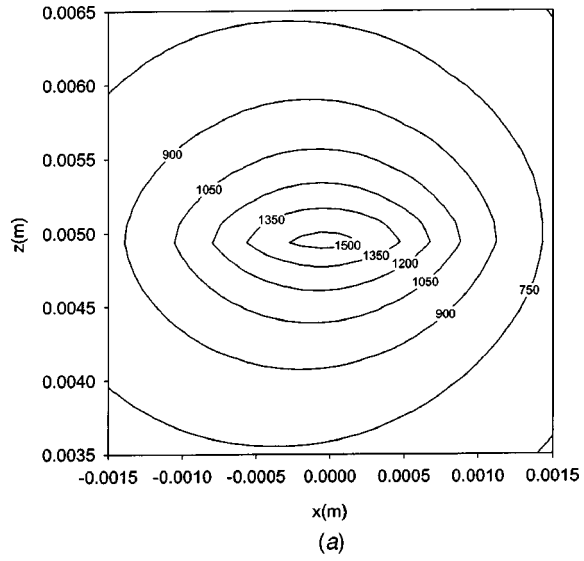

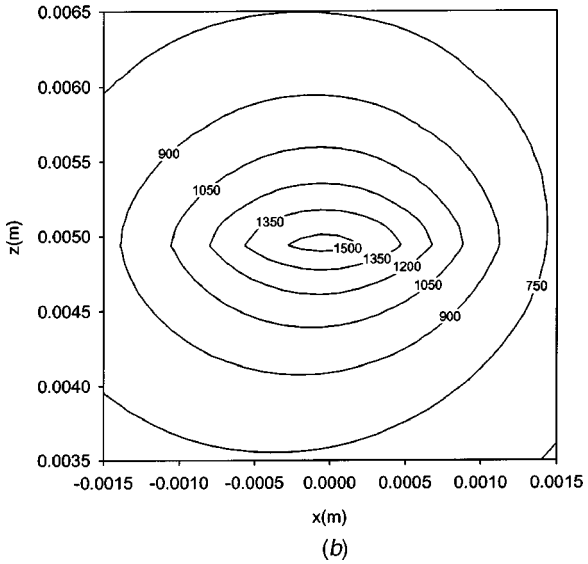

Fig. 13 Contour of temperature, T [K] ($P=360$ W, $u_b=1.2$ mm/s, $y=0$): (*a*) with convection; and (*b*) without convection

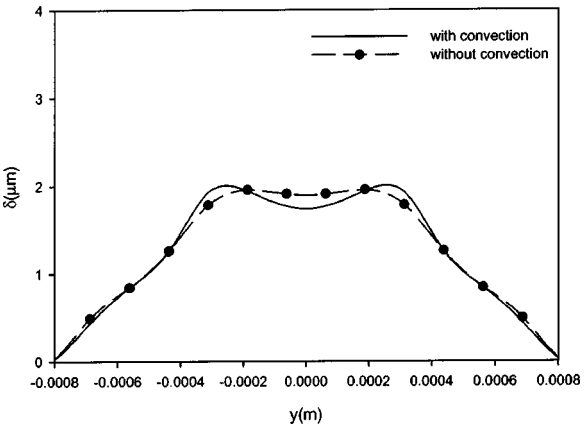

Fig. 14 Comparison of cross section ($P=360$ W, $u_b=1.6$ mm/s)

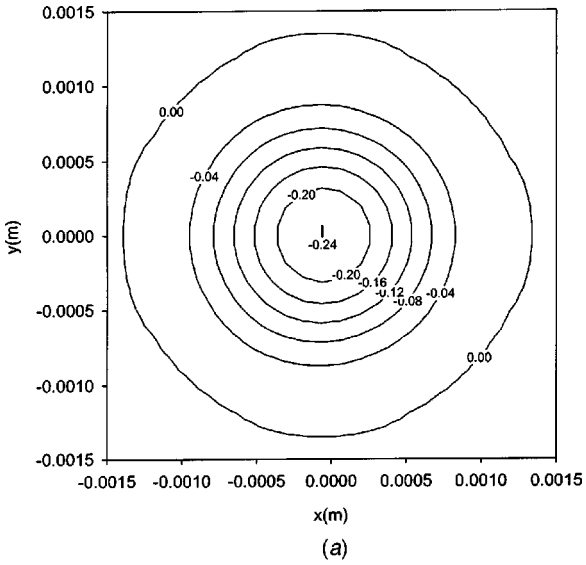

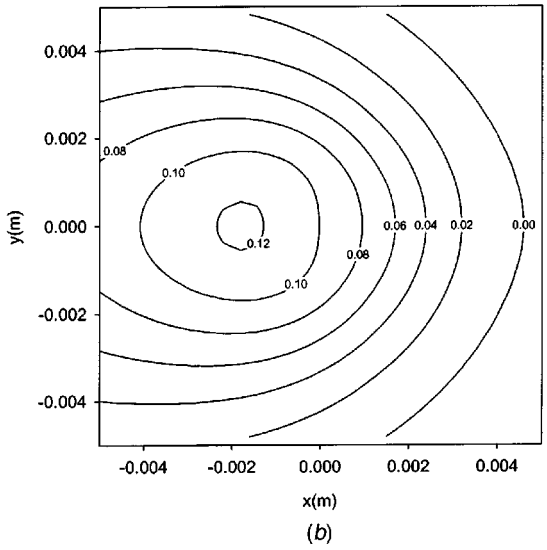

Fig. 15 Contour of velocity component, w [m/s] ($P=360$ W, $u_b=1.6$ mm/s): (*a*) $z=0.0052$ m; and (*b*) $z=0.0081$ m

$z=0.0052$ m, which is at a height 0.2 mm above the top of the substrate surface. The contour of w at this height is nearly circular even though the entire system moves with a velocity of $-u_b$. At another height, $z=0.0081$ m, the velocity component in the z direction near the center of the laser beam is positive due to natural convection. The region affected by natural convection at higher locations is also significantly larger than that at the lower location, which is due to increase of the horizontal cross-sectional area of the plume formed by heating of the small area of substrate. The location with high velocity is shifted toward the negative x direction since the entire system moves with $-u_b$ in the moving coordinate system. Figure 6 illustrates the surface temperature contour on the top of the substrate. The isotherms on the top of the substrate for the models with and without natural convection are almost the same, which means that natural convection has very little effect on substrate surface temperature. As a result, the effect of natural convection on the cross sectional area of the deposited film is negligibly small as indicated in Fig. 4. The temperature contour at $y=0$ is shown in Fig. 7. It is seen that the isotherms in the substrate region ($z<0.005$ m) are almost the same for the cases with and without convection. On the other hand, the isotherms in the gaseous region are slightly shifted down for case with convection because the velocity component in the z direction near substrate surface is negative.

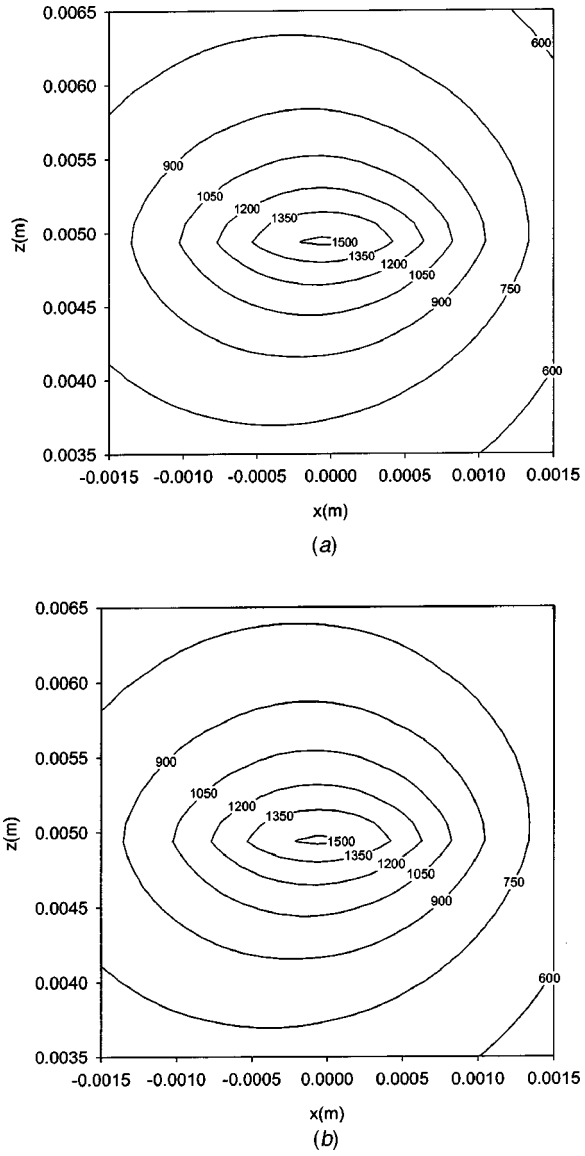

Fig. 16 Contour of temperature, T [K] ($P=360$ W, $u_b=1.6$ mm/s, $y=0$): (*a*) with convection; and (*b*) without convection

Figure 8 shows predicted TiN film thicknesses with the same laser power ($P=300$ W) but a fast scanning velocity of $u_b=1.6$ mm/s. The peak thickness of the deposited thin film is 30% smaller than that for $u_b=1.2$ mm/s because the time for any given spot exposed under laser irradiation is shorter and also the highest surface temperature of the substrate is lowered by 22 K. Similar to the case of $u_b=1.2$ mm/s, the results obtained by models with and without convection are very similar. The velocity components in z direction at different heights are shown in Fig. 9. The contours are similar to the case of $u_b=1.2$ mm/s but the contours for both heights are slightly shifted to the negative x direction due to the higher scanning velocity. Figure 10 shows the temperature contour at $y=0$, which is qualitively similar to that at the lower scanning velocity. However, the contours are shifted to the left compared to that at the lower scanning velocity.

A comparison of cross-sectional areas obtained by models with and without natural convection is shown in Fig. 11, wherein the scanning velocity is the same as that in the case of Fig. 4, but the laser power is increased to 360 W. Compare to the case of 300 W, the film thickness is doubled and the width of the film is increased by 15%. Another phenomenon that can be observed is that a groove exists on the top of the deposited film because the larger laser power causes the top surface temperature of the substrate, in some points, exceed T_m, above which the product of the chemical reaction can not be fully stuck on the substrate surface [14]. The groove is deeper for the case without convection and the effect of natural convection makes the groove shallower. This effect of natural convection on the shape of the deposited film can be explained by the fact that natural convection makes the surface temperature more uniform. However, the overall cross sectional areas for the cases with and without natural convection are almost not affected by natural convection. The velocity components in the z direction at different heights for $P=360$ W and $u_b=1.2$ mm/s are shown in Fig. 12. The velocity at $z=0.0052$ m for the case of $P=360$ W is doubled compared to that of $P=300$ W because more gases are consumed due to chemical reaction. The diameter of the heat affected zone for a laser power of 360 W is about 20% larger then that for a laser power of 300 W. The increase of the velocity at $z=0.0081$ m by increasing laser power is not as much as that at $z=0.0052$ m. For larger laser power, the region affected by natural convection is larger and is shifted to the negative x direction. The comparison of the temperature contour at $y=0$ is shown in Fig. 13. The effect of natural convection on the temperature contour is more significant for the case of larger laser power.

Figure 14 shows predicted deposited TiN film thickness with a fast scanning speed of $u_b=1.6$ mm/s keeping the laser power at 360 W. It can be seen that the thickness of the deposited thin film is reduced by about 30% and the top of the film is nearly flat. There is notable difference between shapes of cross-sections obtained by using models with and without natural convection, which means natural convection still plays an important role for fast scanning. Figure 15 shows the velocity components in the z direction at different heights. The shapes of the contours are very similar to the case of $u_b=1.2$ mm/s, except the contours for both heights are slightly shifted to the negative x direction due to the higher scanning velocity. Figure 16 shows temperature contours at $y=0$. Note that the contours are shifted to the left compared to that at the lower scanning velocity.

Conclusions

Natural convection in the LCVD of TiN films on a substrate with a moving laser beam was investigated numerically. The results show that the effect of natural convection on the shape of deposited films is negligible for a laser power of 300 W. When the laser power is increased to 360 W, a groove is observed on top of the thin film and the effect of natural convection on the shape of the cross sectional area becomes important. The velocity components in the z direction are negative at the locations near the substrate surface under laser irradiation because the chemical reaction consumes $TiCl_4$ at the surface. At the locations far from the substrate surface, the velocity component in the z direction near the center of the laser beam becomes positive due to natural convection driven by the temperature gradient in the gases. Natural convection has very little effect on the temperature contours near the hot spot under laser irradiation.

Nomenclature

C = concentration (kg/m^3)
c_p = specific heat (J/kgK)
D = mass diffusivity (m^2/s)
E = activation energy (kJ/mol)
h = thickness of the substrate (m)
k = thermal conductivity (W/mK)
K_0' = Arrhenius constant
M = molecular weight (g/mol)
m = mass flux (kg/m^2)
P = laser power (W)
p = pressure (Pa)
q'' = heat flux (W/m^2)

r_o = radius of the laser beam (m)
R_u = universal gas constant (=8.314 kJ/kmol)
S = source term in the energy equation
S_c = source term in the mass transfer equation
t = time (s)
T = temperature (K)
u = velocity component in x direction (m/s)
v = velocity component in y direction (m/s)
w = velocity component in z direction (m/s)
x = coordinate in length direction (m)
y = coordinate in width direction (m)
z = coordinate in height direction (m)

Greek Symbols

α = diffusivity (m^2/s)
α_a = absorptivity
β = coefficients of thermal expansion (1/K)
β_c = concentration expansion coefficients (m^3/kg)
γ = sticking coefficient
δ = thickness of the deposited film (m)
ΔH_R = heat of chemical reaction (J/kg)
ε = emissivity
ρ = density (kg/m^3)

Subscripts

g = gas
i = initial value
s = substrate
∞ = infinite

References

[1] Conley, J. G., and Marcus, H. L., 1997, ''Rapid Prototyping and Solid Freeform Fabrication,'' ASME J. Manuf. Sci. Eng., **119**, pp. 811–816.
[2] Marcus, H. L., Zong, G., and Subramanian, P. K., 1993, Residual Stresses in Laser Processed Solid Freeform Fabrication, in *Residual Stresses in Composites: Measurement, Modeling and Effect on Thermomechanical Properties*, E. V. Barrera and I. Dutta, eds., TMS.
[3] Jakubenas, K. J., Birmingham, B., Harission, S., Croker, J., Shaarawi, M. S., Tomkins, J. V., Sanchez, J., and Marcus, H., 1997, ''Recent Advances in SALD and SALDVI,'' Procs. of 7th International Conference on Rapid Prototyping, San Francisco, CA.
[4] Jakubenas, K. J., Lee, Y. L., Shaarawi, M. S., Marcus, H., and Sanchez, J. M., 1997, ''Selective Area Laser Deposition of Titanium Oxide,'' Rapid Prototyping J., **3**, pp. 66–70.
[5] Harrison, S., and Marcus, H. L., 1999, ''Gas-phase Selective Laser Deposition (SALD) Joining of SiC,'' Mater. Des., **20**, pp. 147–152.
[6] Mahajan, R. L., 1996, ''Transport Phenomena in Chemical Vapor-Deposition Systems,'' Adv. Heat Transfer , Academic Press, San Diego.
[7] Mazumder, J., and Kar, A., 1995, *Theory and Application of Laser Chemical Vapor Deposition*, Plenum Publishing Co., New York.
[8] Duty, C. E., Jean, D. L., and Lackey, W. J., 2001, ''Laser Chemical Vapor Deposition: Materials, Modeling, and Process Control,'' Int. Mater. Rev., **46**, pp. 271–287.
[9] Jacquot, Y., Zong, G.-S., and Marcus, H. L., 1995, ''Modeling of Selective Laser Deposition for Solid Freeform Fabrication,'' *Proceedings of Solid Freeform Fabrication Symposium 1995*, pp. 74–82.
[10] Zhang, Y., and Faghri, A., 2000, ''Thermal Modeling of Selective Area Laser Deposition of Titanium Nitride on a Finite Slab with Stationary and Moving Laser Beams,'' Int. J. Heat Mass Transf., **43**, pp. 3835–3846.
[11] Lee, Y. L., Tompkins, J. V., Sanchez, J. M., and Marcus, H. L., 1995, ''Deposition Rate of Silicon Carbide by Selected Area Laser Deposition,'' *Proceedings of Solid Freeform Fabrication Symposium 1995*, pp. 433–439.
[12] Manca, O., Morrone, B., and Naso, V., 1995, ''Quasi-Steady-State Three-Dimensional Temperature Distribution induced by a Moving Circular Gaussian Heat Source in a Finite Depth Solid,'' Int. J. Heat Mass Transf., **38**, pp. 1305–1315.
[13] Bird, R. B., Stewart, W. E., and Lightfoot, E. N., 1960, *Transport Phenomena*, John Wiley & Sons, New York.
[14] Conde, O., Kar, A., and Mazumder, J., 1992, ''Laser Chemical Vapor Deposition of TiN Dot: A Comparison of Theoretical and Experimental Results,'' J. Appl. Phys., **72**, pp. 754–761.
[15] Patankar, S. V., 1980, *Numerical Heat Transfer and Fluid Flow*, Hemisphere, Washington, DC.
[16] Van Doormaal, J. P., and Raithby, G. D., 1984, ''Enhancements of the Simple Method For Predicting Incompressible Fluid Flows,'' Numer. Heat Transfer, **7**, pp. 147–163.
[17] Yang, M., and Tao, W. Q., 1992, ''Numerical Study of Natural Convection Heat Transfer in a Cylindrical Envelop with Internal Concentric Slotted Hollow Cylinder,'' Numer. Heat Transfer, Part A, **22**, pp. 289–305.
[18] Carslaw, H. S., and Jaeger, J. C., 1959, *Conduction of Heat in Solids*, Clarendon, Oxford.
[19] Kar, A., and Mazumder, J., 1989, ''Three-Dimensional Transient Thermal Analysis for Laser Chemical Vapor Deposition on Uniformly Moving Finite Slabs,'' J. Appl. Phys., **65**, pp. 2923–2934.
[20] Chase, W. M., 1986, ''JANAF Thermochemical Tables, 3rd Edition,'' J. Phys. Chem. Ref. Data, **14**, Suppl 1.

Xianchang Li
e-mail: xli8@uno.edu
Energy Conversion and Conservation Center,
University of New Orleans,
New Orleans, LA 70148-2220

J. Leo Gaddis
e-mail: leo.gaddis@ces.clemson.edu
Department of Mechanical Engineering,
Clemson University,
Clemson, SC 29634-0921

Ting Wang
e-mail: twang@uno.edu
Energy Conversion and Conservation Center,
University of New Orleans,
New Orleans, LA 70148-2220

Mist/Steam Heat Transfer With Jet Impingement Onto a Concave Surface

Internal mist/steam blade cooling technology is proposed for the future generation of Advanced Turbine Systems (ATS). Fine water droplets about 5 μm were carried by steam through a slot jet onto a concave heated surface in a confined channel to simulate inner surface cooling at the leading edge of a turbine blade. Experiments covered Reynolds numbers from 7500 to 22,000 and heat fluxes from 3 to 21 kW/m^2. Results indicate that the cooling is enhanced significantly near the stagnation point by the mist, decreasing downstream. Unlike impingement onto a flat target where the enhancement vanished at six jet diameters downstream, the cooling enhancement over a concave surface prevails at all points downstream. Similar to the results of the flat surface, the cooling enhancement declines at higher heat fluxes. Up to 200 % cooling enhancement at the stagnation point was achieved by injecting approximately 0.5 % of mist. [DOI: 10.1115/1.1561813]

Keywords: Mist Cooling, Enhanced Heat Transfer, Impingment Jets.

Introduction

To improve the overall efficiency of gas turbine engines, the turbine inlet temperature and compressor pressure ratio are continuously increasing for the next generation of gas turbine systems. As a result, even with the potential advancement of future high-temperature materials, highly efficient gas turbine engines are expected to continue to operate at temperatures much higher than the allowable metal temperature of the turbine airfoils, which, in turn, makes effective cooling of the airfoils essential.

With recent adoptions of closed-loop steam cooling by two major gas turbine manufacturers (Bannister and Little [1]; Mukavetz [2]) for heavy-frame Advanced Turbine Systems (ATS), a major part of the external cooling load will be replaced by internal steam cooling. Generally, the internal heat transfer coefficient is required to be in the range of 8000~10000 W/m^2 K to replace the cooling load currently shared by external air-film cooling. Liquid water can achieve this goal easily, but problems with instability when boiling occurs have discounted its chances. With the availability of steam from the bottoming cycle of a heavy-frame ATS, mist/steam cooling has been introduced by this research group as a potential means to significantly enhance the internal cooling of turbine airfoils. The advantages and reasons of using mist/steam cooling, a comparison of mist/air and mist/steam cooling, and a review of previous related studies have been presented by Guo et al. [3] and are not repeated here.

Basically, the concept of using mist/steam cooling to enhance cooling effectiveness is based on the following features discussed by Li et al. [4]: (a) single-phase heat transfer improved by increased mixing induced by particle dynamics, additional momentum and mass transfer induced by evaporation of liquid droplets on/near the wall, and increased specific heat, (b) the quenching effect of mist in the superheated boundary layer resulting in a steeper temperature gradient near the wall, and (c) the direct wall-to-droplet heat transfer during impact releasing the latent heat of evaporation.

Wachters et al. [5] considered the impact of droplets about 60 μm onto a heated surface at velocities in the range of 5 m/s. The investigation focused on identifying conditions under which impinging droplets would maintain the spheroidal state and the associated low rates of heat flow. Goodyer and Waterston [6] considered mist/air impingement for turbine blade cooling at surface temperatures above 600°C. They suggested that the heat transfer was dominated by partial contact between the droplets and the target surface, during which the droplets vaporized at least partially. A vapor cushion and the elastic deformation of the droplets were responsible for rejecting the droplets. Addition of 6 % water was found to improve the stagnation point heat transfer by 100 %, diminishing away from the stagnation point. Droplet size was found to have little effect for 30 μm$<d_{32}<$200 μm.

Yoshida et al. [7] focused on the effect on turbulent structure with a suspension of 50-μm glass beads. In the impinging jet region, the gas velocity decreased due to the rebound of beads, accompanied by an increase in the normal direction velocity fluctuations. In the downstream region the effect was slight. The Nusselt number was found to increase by a factor of 2.7 for the relatively high mass flow ratios (solid/gas) of 0.8.

Buyevich and Mankevich [8,9] modeled the particles in the mist as liquid discs separated from the wall by a vapor layer whose thickness is that of the wall roughness. A critical impact velocity was identified to determine whether a droplet rebounds or is captured. They applied the model to dilute mist impingement and reported agreement with experiment.

Fujimoto and Hatta [10] studied deformation and rebound of a water droplet on a high-temperature wall. For Weber numbers of 10 to 60, they computed the distortions of the droplet as it flattened, contracted, and rebounded. They used a simple heat transfer model to confirm that surface tension dominates vapor production in the rebounding process. Hatta et al. [11] gave correlations of contact time and contact area of the droplet with Weber number.

Nirmalan et al. [12] conducted an experimental study of turbine vane heat transfer with water-air mist cooling. Water was pressured inside the vane and broken up into small droplets through many cooling holes on an inner wall inside the vane and impinged on the inner side of the vane's outer wall. Their results showed significant cooling enhancement using water/air mist jets, but they found the jets are difficult to control and resulted in nonuniform overcooling over the target surface.

Guo et al. [3,13] studied the mist/steam flow and heat transfer in a straight tube under highly superheated wall temperatures. It was found that the heat transfer performance of steam could be significantly improved by adding mist into the main flow. An av-

Contributed by the Heat Transfer Division for publication in the JOURNAL OF HEAT TRANSFER. Manuscript received by the Heat Transfer Division May 28, 2002; revision received November 12, 2002. Associate Editor: C. Amon.

erage enhancement of 100 % with the highest local heat transfer enhancement of 200 % was achieved with 5 % mist. Guo et al. [14] performed an experimental study on mist/steam cooling in a highly heated, horizontal 180° tube bend with the same experimental facility as above. Due to the effect of centrifugal force, the outer wall of the test section always exhibited a higher heat transfer than the inner wall. However, the inner wall exhibited higher heat transfer enhancement than the outer wall in most cases. The highest enhancement occurred at about 45° downstream of the inlet of the test section. The overall cooling enhancement of the mist/steam flow ranged from 40 % to 300 % with maximum local cooling enhancement being over 800 %.

Li et al. [15] reported results of a mist/steam slot jet impinging on a heated flat surface. They concluded that stagnation point heat transfer could be enhanced over 200 % by the addition of 1.5 % mist. The mist enhancement was found to decline to near zero by five slot widths downstream. Li et al. [16] compared the results of a slot jet and a row of discrete jets with equal mass flows. The comparison indicates that the slot achieves less cooling effectiveness in steam-only flow but produces superior cooling enhancement in mist/steam flow

If jet impingement cooling on turbine blades is employed, it is likely that the region will be the inner surface corresponding to the external stagnation region (or leading edge of a blade). This region will have the highest amount of thermal challenge. The concave target surface will be characteristic of this region. A concave surface is known to cause flow instability within a boundary layer (Rayleigh [17]). Any fluctuation of fluid velocity will be amplified and result in more mixing. Studies have also been conducted on single-phase jet impingent with concave target surface. Hrycak [18] studied heat transfer and flow characteristics of gaseous jets impinging on a concave hemispherical plate. He discovered that the total heat transfer on the concave surface is higher than that corresponding to a flat surface. Metzger et al. [19] conducted an experiment of impingement cooling on concave surfaces with lines of circular air jets. They reported that the lines of circular jets impinging on concaves surfaces produced higher heat transfer coefficients than comparable two-dimensional jets impinging on plane surfaces.

Regarding droplets in the flow, the effect of concave curvature will cause acceleration in the flow so that droplets tending to lag will be forced toward the surface. Thus, it is anticipated that the augmented mixing on a concave surface could enhance cooling more than its flat counterpart. Also, mist droplets in flows having curvature are constantly being accelerated toward the curve center and the natural lag will result in the particle drifting toward the surface. Particle drift into the heated surface will increase the primary mechanisms responsible for enhancement. To simulate the turbine airfoil leading edge cooling, this paper extends previous studies of mist/steam impinging jet cooling from a flat surface to a concave surface.

Experimental Facility

Experimental System. The overall experimental system is shown in Fig. 1, which consists of four subsystems: steam system, water system, atomizing system and test section. The steam system supplies the main steam flow used in the experimental study. The high-pressure (about 8 bar) steam extracted from the steam pipeline existing in the building becomes clean and dry saturated steam after passing through a strainer, a pressure regulator, a desuperheater and a filter. The saturated steam at about 1.5 bar then enters the mixing chamber and mixes with the mist from the atomizer system. The mist/steam flow enters to the test section through a flexible silicone tube and exits to a condenser. Water at 68 bar and 15°C supplies the atomizer (Mee Industries Inc.) to produce droplets with an average diameter (d_{10}) about 10 μm. In this investigation four nozzles are operated together to provide mist.

Figure 2 shows plan and profile views of the test section with

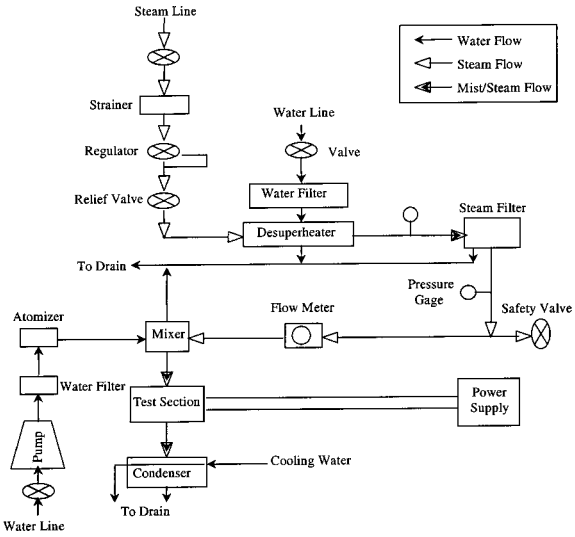

Fig. 1 Schematic diagram of experimental system

concave surface. It is constructed similar in detail to the flat surface of Li et al. [15] to provide the most straightforward comparison and the easiest and most basic isolation of the curvature effect. A 7.5-mm wide slot located in a surface having inner curvature of radius 57 mm directs flow onto the heated surface located 22.5 mm away. The outer (heated surface) radius of curvature is 57.0+22.5=79.5 mm. The depth of flow channel between the flat sidewalls is 100 mm. Five polished heater surfaces preformed to fit the curvature are arranged electrically in series to afford the electrical heating by a DC power supply capable of 750 A. Thin processed mica (Cogebi) sheets are used to insulate the heater backside from the thermocouples and from the adjacent heater. The mica is trimmed flush with the heater surface after installation to provide a smooth joint between the segmented heaters.

The test section is arranged with the sidewalls level with the earth. Flow is admitted downward along the axis of the inner cylinder that contains the slot. The inner cylinder is allowed to have a tiny gap with the bottom plate to pass any liquid which could accumulate but which should not pass a significant amount of vapor. Flow exiting the semi-cylindrical heater is collected and passed to the condenser. Provisions are made to drain any liquid from the apparatus. Different from the flat-wall case, in which the test section can be assessed by laser beams through Pyrex windows on the side walls, no optical penetrations were made in the present test section.

Instrumentation

Temperature Measurement. All temperatures are measured by Omega 30-gage (about 0.25 mm in wire diameter) Chromega/

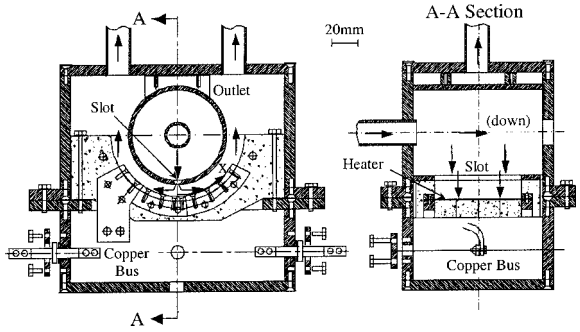

Fig. 2 Details of test section

Alomega (K type) thermocouples with braided fiberglass insulation. A data logger (FLUKE Model 2250) is used to monitor and record the temperature. The thermocouples, along with the data logger, were calibrated against a standard Resistance Temperature Device (RTD) system for nominal temperature uncertainty of 0.3°C. To measure the temperature distribution on the heated surface, thermocouples are strategically placed at the stagnation point and at about 1, 2, 3, 4.5, 6, 8, and 10 slot widths away from the jet center. The temperature at the inlet of the test section and the temperature of water for the atomizer are also measured.

Flow Rate and Others. The heating power to the test section is obtained from the current and the resistance of the heaters in the test section. The current is given by the voltage across the precision shunt (with a resistance of $1.333\times10^{-4}\ \Omega$) of the power supply. The voltage across the test section is measured directly by a voltmeter. Pressure gages before and after the steam filter indicate the pressure of the steam. The mist liquid flow is measured by flow meter. The exiting steam is condensed and measured by catch-and-weigh as are drainages from the mist-steam mixer, from the tube supplying the test section, and from the bottom of the test section itself.

Data Reduction and Uncertainty Analysis

Heat Transfer Coefficient. For jet impingement, the heat transfer coefficient is usually defined as

$$h(x)=\frac{q''(x)}{T_w(x)-T_j} \tag{1}$$

where q'' is the wall heat flux, T_w is the local wall temperature, and T_j is the temperature of the jet. The steam saturation temperature is taken as the jet temperature for the current study. The wall temperatures are measured by thermocouples electrically insulated by mica at the backside of the heater. Since the temperature drop across the heater is less than 1 % of (T_w-T_j), the temperatures of the thermocouples are directly used as the wall temperature.

The heat flux is obtained from the power divided by the area, assuming the heater has a uniform thickness and has uniform current density. The heating power is obtained from the electrical resistance of the heater components and the current passing through the heater as follows.

$$q''=I^2\xi/\delta B^2 \tag{2}$$

where I is the current passing through the heater and ξ is the resistivity of the heater materials. The quantities δ and B are the heater thickness and width, respectively. Calculation by this equation avoids measurement error of the heater length and of the voltage across the test section due to contact resistance. In the current design, the supporting block for the heaters is ceramic with low thermal conductivity and it is surrounded by saturated steam. A simple one-dimensional heat conduction model is used to provide a correction for a small (<5 %) backside heat loss in data processing.

In [15] the trend of heat transfer for pure steam vapor on the flat surface followed the form given in Eq. (3).

$$\mathrm{Nu}_0=0.069\,\mathrm{Re}^{0.75}\,\mathrm{Pr}^{0.4} \tag{3}$$

The power for Reynolds number can range from 0.5 to 0.8 for jet impingement heat transfer (Downs and James [20]). The trend of Eq. (3) is compatible with the results observed herein and is used to correct the flow velocity changes caused by addition of mist into the steam flow.

Uncertainty Analysis. Based on the methodology developed by Moffat [21], the N^{th}-order uncertainty analysis is conducted on both heat transfer and flow rate in this study. The results of uncertainty analysis are summarized in Table 1. It is found that the uncertainty for heat transfer is about 5~7 % and the largest source is the heating current of the power supply. For the flow rate, although the uncertainty for the steam phase is very small, the mist concentration has a large uncertainty, as much as 40 %, and the largest source is Δt (sampling time). The enlarged uncertainty occurs as a result of subtracting the mist-free condenser flow from the mist-laden condenser flow. The uncertainty of Reynolds number is not large and has main sources of steam viscosity, μ_s, and the slot dimension. The detailed uncertainty analysis is documented by Li [22].

Table 1 Results of uncertainty analysis

Resultants	Nominal Value	Nth-order Uncertainty (percent)	Largest Source
m_l/m_s	0.5×10^{-2}	40	Δt
Re	15300	1.65	μ_s
q''	13.4 (kW/m^2)	5.43	V_{shunt}
h	268 (W/m^2 K)	6.27	V_{shunt}
Nu	161	6.50	V_{shunt}

Experimental Results and Discussions

It was known from prior testing (Guo et al. [13]) that the average droplet size distribution of the free jet is about 12 μm. As the (subcooled) droplets are mixed in a chamber with saturated steam, they grow as a result of warming to saturation, but many droplets encounter the walls and stick. Larger droplets are systematically removed in this process so the remaining mist stream has a droplet size distribution averaging 8 μm. As the mist travels down a tube to enter the test section the droplets are further changed to an average size of 3.2 μm (Li et al. [15]). In the curved wall test section, there is an abrupt turn within the test section as the flow entering the cylinder turns by a right angle to pass the slot (see Fig. 2). This maneuver results in the capture on the plenum surfaces of a substantial portion of the mist and results in a selective reduction of larger particles. The mist mass flow rate entering the test section is calculated by mass balance of the entire flow system. However, without provision for optical (PDPA) measurement as it was done in the flat wall test section to crosscheck the mist flow rate, the uncertainty of the mist mass flow rate is as high as 40 %. The mist addition was limited in the current tests to about 0.5 % of the vapor flow, where the flat surface testing [15] was conducted with 1.5 % to 3 % mist mass fraction.

Typical Heat Transfer Result. Figure 3(*a*) shows a typical distribution of wall temperature at a fixed value of flow rate. The Reynolds number, 7500, is based on 2*b*, the hydraulic diameter of a long (100 mm) slot of width 7.5 mm. The heat flux (3350 W/m^2) is the lowest of three values tested at this Reynolds number. On the figure are the temperature distributions for steam alone and steam with 0.5 % mist by mass. The temperature is lowest at the stagnation point, rising to a maximum value at about 8 slot widths downstream and declining at 10 diameters downstream. Relative to the saturation temperature of about 103°C, the mist is shown to reduce the wall temperature excess (or superheat) from about 25 deg to about eight deg at the stagnation point. Farther downstream the mist effect wanes but never vanishes.

Figure 3(*b*) shows the results in terms of a heat transfer coefficient, *h*, defined for both single phase and mist flows according to Eq. (1). In the flat wall test [15] at the same Reynolds number and the same heating rate, the impingement point heat transfer of steam-only was measured to be 2.7 % lower, while the experimental uncertainty for the single phase (steam only) test results is about 5 %. Therefore the results for single-phase heat transfer are identical with the flat surface within experimental uncertainty. A comparison between concave (Fig. 3(*b*)) and flat walls (Fig. 13 in the Appendix) has been made for the distribution of steam-only heat transfer coefficient downstream from the impingement. The distributions are very similar except that the last measuring point

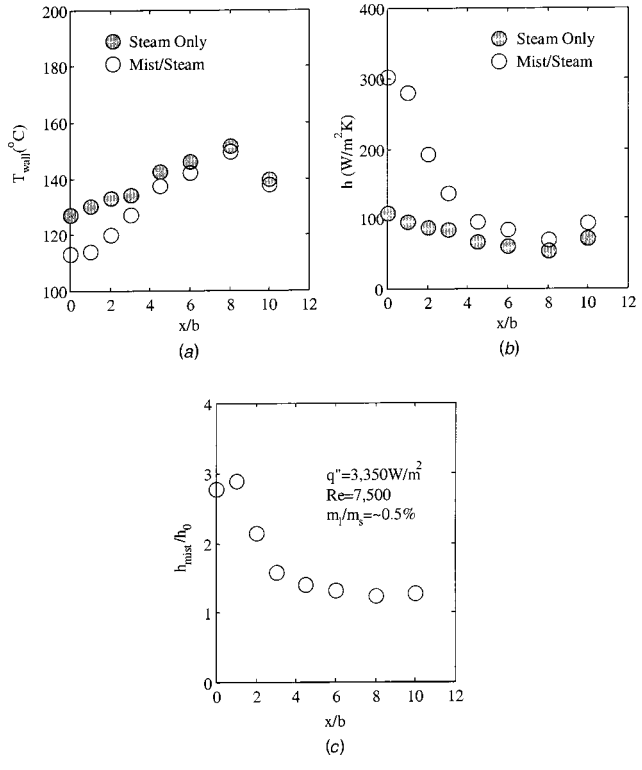

Fig. 3 Heat transfer results at Re=7500 with $q''=3350$ W/m^2 and $m_l/m_s=\sim 0.5$ %: (*a*) wall temperature; (*b*) heat transfer coefficient; and (*c*) ratio of heat transfer coefficient.

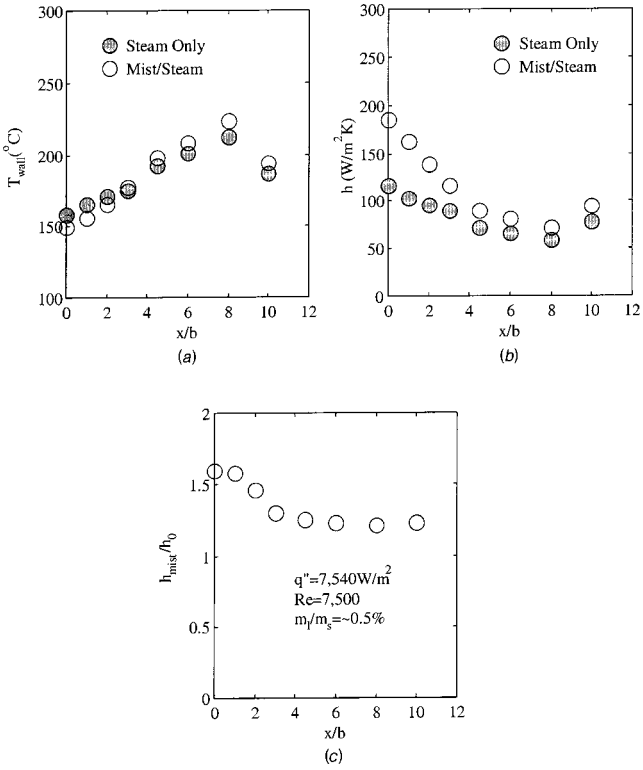

Fig. 4 Heat transfer results at Re=7500 with $q''=7540$ W/m^2 and $m_l/m_s=\sim 0.5$ %: (*a*) wall temperature; (*b*) heat transfer coefficient; and (*c*) ratio of heat transfer coefficient.

of the curved wall section shows a relatively large increase in heat transfer coefficient not seen in the flat section. The increase is considered to be an influence of the exit. As discussed earlier, the jet impingement onto a concave surface may result in a higher heat transfer coefficient than onto a flat surface [18,19] although the current difference is small.

Figure 3(*b*) shows also the heat transfer coefficient with mist. The heat transfer coefficient is magnified by 200 % (factor of three) at the stagnation point. Figure 3(*c*) shows the ratio of h to h_0, the latter being the single-phase value. This ratio, termed the enhancement, is shown to be about three at the stagnation point and declines to about 25 % at eight slot widths downstream. However, there is a contrast with the flat surface results in which the mist effect wanes completely by the exit of the test section. As in many of the flat surface results, the enhancement has a maximum value slightly off the centerline of the impinging jet. However, the actual cooling is greatest at the stagnation point (or stagnation line for a two-dimensional test section).

Heat Transfer Results With Different Heat Fluxes. Figure 4(*a*) presents surface temperature data at the same Reynolds number, 7500, and at a higher heat transfer rate of 7540 W/m^2. As in earlier testing the higher wall temperature results in higher single-phase heat transfer coefficients, attributable to thermal properties. This effect of thermal properties will be discussed later. The resulting heat transfer coefficient is shown in Fig. 4(*b*). The mist effect results in lowering of temperatures near the stagnation point and raising of temperatures downstream. When the heat transfer coefficient is calculated, the mist raises the heat transfer coefficient even at points having raised temperature values. This is because the actual steam flow rates in the mist cases are reduced by amounts that are condensed to raise the subcooled mist to the saturated temperature when subcooled mist is introduced in a steam flow of constant flow rate. The reduction in steam flow reduces the single-phase cooling effect and would, without an independent mist effect, result in a higher temperature. In some cases the independent mist effect is weaker than the effect of reducing the steam flow and the temperature can actually rise with mist addition. To compensate for this effect of condensation, the heat transfer results of the mist cases are corrected for the flow rate variations according to the correlation, Eq. (3), to the nominal values of Re. The modest adjustment increases the measured heat transfer coefficient of the mist cases and the correction procedure results in enhancement at every point even when the temperature experienced during mist is higher than it was with steam alone. The enhancement, shown in Fig. 4(*c*), is 60 % at the stagnation point and decreases to about 20 % at the downstream location. As is the case for all impingement flows, the enhancement factor is inversely related to the total heat flux.

Figure 5 presents the surface temperatures, heat transfer coefficient, and the enhancement for the highest heat transfer rate at 13,400 W/m^2 with the same Reynolds number, 7500. As anticipated, the surface temperatures are reduced by mist, the heat transfer coefficient is increased compared with single-phase data, and the enhancement is less than observed at lower heat transfer rates. Enhancement occurs at all measured positions. Notice again that the steam-only heat transfer coefficient at the stagnation point increases slightly at this heat flux.

From the three figures (3, 4, and 5) it is evident that the mist effect extends beyond $x/b=5$, where on a flat plate in Figs. 13 and 14 the mist effect was found to wane. In fact, a significant enhancement is noted at all points. The lowest enhancement at any point on the surface is 15 %; that being at $x/b=7$ and the highest heat flux. The extension of enhancement beyond that for flat plates is consistent with the enhanced mixing mechanism and droplet lag caused by accelerating flow along the concave wall.

The stagnation point enhancements range from 35 % at high wall heat flux to nearly 200 % at low heat flux. These values are achieved at a low (0.5 %) mist concentration. Comparing these with 60 to 550 % enhancements on flat plates (Fig. 13) with 3.5 % mist concentration at 7500 Reynolds number indicates that the

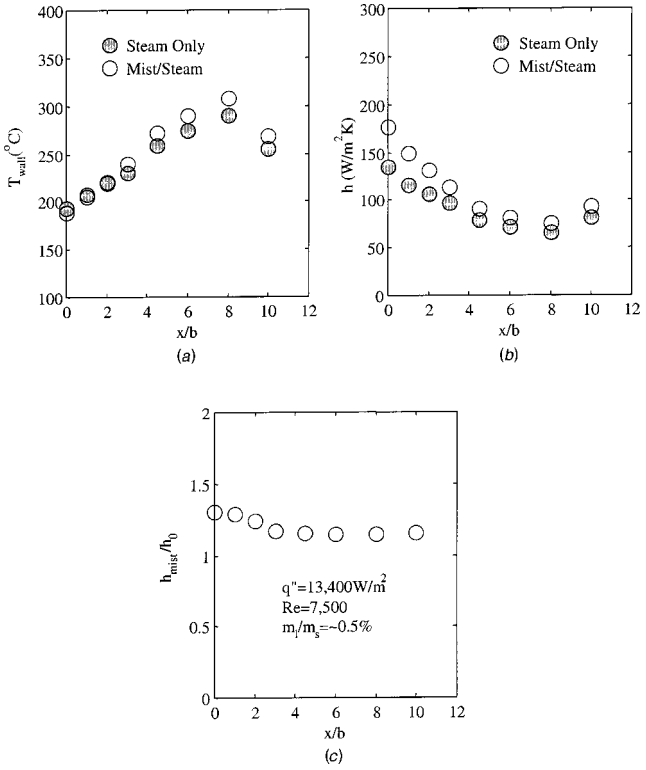

Fig. 5 Heat transfer results at Re=7500 with $q''=13400$ W/m^2 and $m_l/m_s=\sim 0.5$ %: (*a*) wall temperature; (*b*) heat transfer coefficient; and (*c*) ratio of heat transfer coefficient.

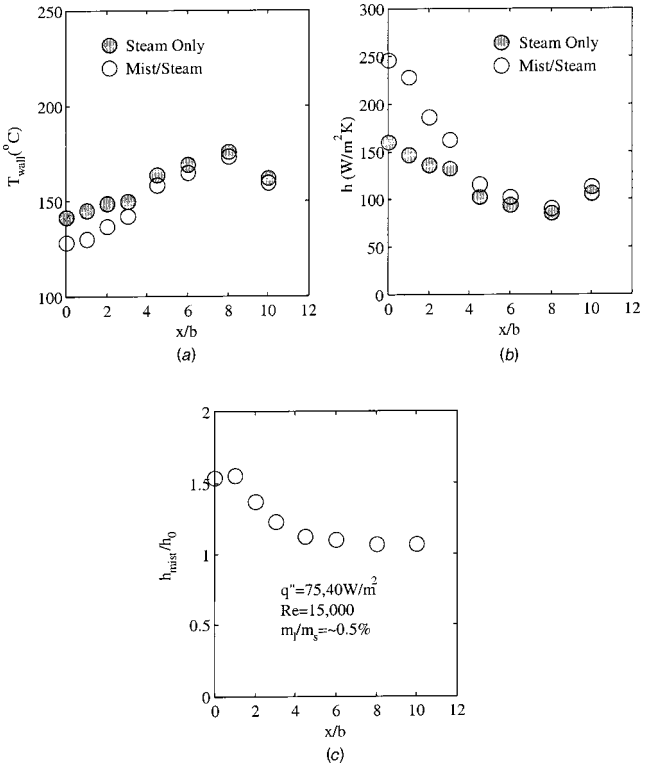

Fig. 6 Heat transfer results at Re=15,000 with $q''=7540$ W/m^2 and $m_l/m_s=\sim 0.5$ %: (*a*) wall temperature; (*b*) heat transfer coefficient; and (*c*) ratio of heat transfer coefficient.

enhancement per unit mass of mist is comparable or even superior with the concave target surface. Direct comparison of equal mist/steam ratio was not obtained in the present case due to the droplet attrition in the curved surface test section as explained previously.

Heat Transfer Results With Different Reynolds Numbers Two more Reynolds numbers (15,000 and 22,500) have been covered in this study. At Re=15,000 three heat flux values were also tested. These results are reported in Figs. 6, 7, and 8. Similar trends to those identified at Re=7500 are evident. However, at the higher steam flow, even more mist attrition occurs. Therefore, the mist/steam mass ratio is believed less than 0.5 % for higher Reynolds number cases.

Comparison of results of higher Reynolds number at 15,000 with the flat wall case can be made between Figs. 6 and 14. Again, clear comparisons with the flat heater surface are difficult because the mist mass in the curved-wall experiment amounted to 1/3 or less of the mass fraction in the flat-walled experiment. The mist effect in the flat experiment (Fig. 14) exceeds the effect reported here on a curved surface (Fig. 6). Still it is clear that the effect per unit mass of mist is comparable. The curved surface enhancement endures downstream, while the flat surface enhancement does not.

The preceding patterns continue to be valid for the data at Reynolds number 22,500; therefore, only the heat transfer coefficients are presented for brevity in Fig. 9. Clearly all the former patterns are intact: the heat transfer coefficients decline generally away from the stagnation point, the enhancement wanes but not to zero, and the enhancement declines with increased heat flux.

As for Re=7500, the heat transfer coefficient at the stagnation point for steam-only flow increases with heat flux at Reynolds numbers 15,000 and 22,500. This effect is partially absorbed by temperature-dependent properties. In Fig. 10 the Nusselt numbers are calculated based on two slot widths and the thermal conductivity at the film (mean of wall and bulk). At higher Reynolds numbers the stagnation Nusselt values coincide with flat plate data correlation Eq. (3) and are almost independent of heat flux. At low Reynolds number (7500), the curved wall results are approximately 20 % above the flat-wall correlation and are scattered within 10 % by heat flux. The effect of Gortler vortices and secondary flow have the potential of affecting the curved-wall results. However, at the Reynolds numbers conducted in the present paper, the effect of Gortler vortices is expected to be reduced since Gortler vorticities are usually seen in the laminar flow. This may explain why the results of the steam-only case on a concave curve in this paper is close to that on flat walls. Weaker secondary flows, which exist in Reynolds number range in the present study, do not seem to affect the steam-only flow although evidence of present results shows that the secondary flows play an important role to affect mist flows. Collective results presented in Nusselt number for each Reynolds number with different heat fluxes can be found in Appendix (Fig. 15). No generalized correlations are derived in this paper to show the effect of mist cooling enhancement.

Comparison of Enhancement Patterns With Slot Jet. Efforts have been made to compare the enhancement patterns between jet impingement with curved target and that with flat target. Figures 11 and 12 illustrate the difference in the patterns of enhancement in the flat and the curved heater cases. The enhancement, defined as h/h_0, is normalized by the value at the central point (stagnation point). Since the value at $x=0$ is forced to be unity, both Figs. 11 and 12 should be used to examine the uniformity and extend of cooling enhancement instead of being used for comparing the enhancement magnitudes. Figure 11, for Re=7500, shows that for the flat surface, particularly at lower heat flux, the maximum enhancement is not at the stagnation line, but occurs at approximately one jet width away from the axis. For the curved surface, this phenomenon is less pronounced. This is speculated as a result of secondary flows which assist in transporting water droplets in the lateral (spanwise) direction and thus avoid the in-

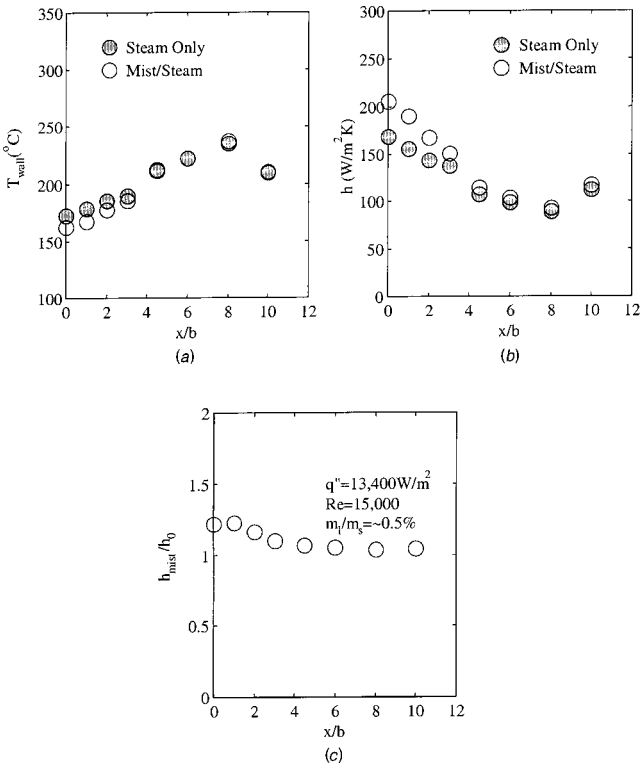

Fig. 7 Heat transfer results at Re=15,000 with q'' =13400 W/m^2 and m_l/m_s=~0.5 %: (*a*) wall temperature; (*b*) heat transfer coefficient; and (*c*) ratio of heat transfer coefficient.

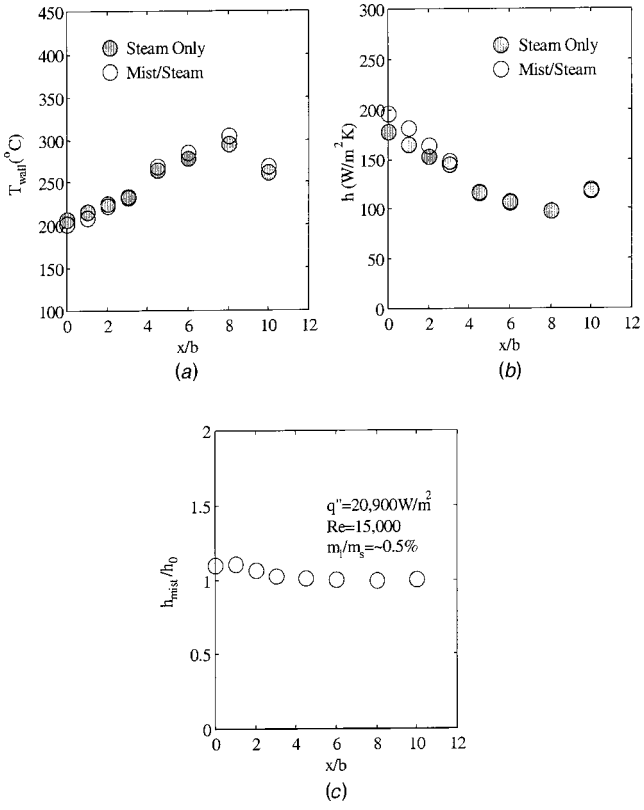

Fig. 8 Heat transfer results at Re=15,000 with q'' =20900 W/m^2 and m_l/m_s=~0.5 %: (*a*) wall temperature; (*b*) heat transfer coefficient; and (*c*) ratio of heat transfer coefficient.

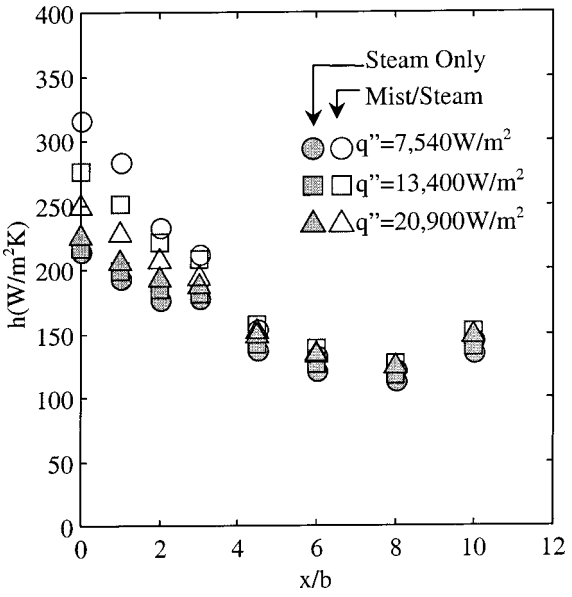

Fig. 9 Heat transfer results for Re=22,500 at various heat fluxes

creased droplet density accumulated near $x/b=1$ on a flat wall. More important is the observation of lengthened enhancement region which extends farther downstream on the curved surface. It is believed that the enhanced mixing and flow instability from curvature and the secondary flows generated from the sidewalls cause the mist to become more effective. The secondary flows and droplet lag seem to lengthen the residence time of mist and results to having more mist impact on downstream region on a concave surface. Furthermore, inertia produced by the stagnation pressure may accelerate the droplets to cross over the curved streamline of the steam resulting to more effective impact on a concave surface than on a flat surface. Figure 12 compares the heat transfer enhancement between flat and concave target surface at Re=22,500 with different heat fluxes. The mist/steam ratio is 1.5 % for flat wall cases and 0.5 % for curved wall cases. Comparisons of cases at 7540 W/m^2 and 13,400 W/m^2 between Fig. 11 and Fig. 12

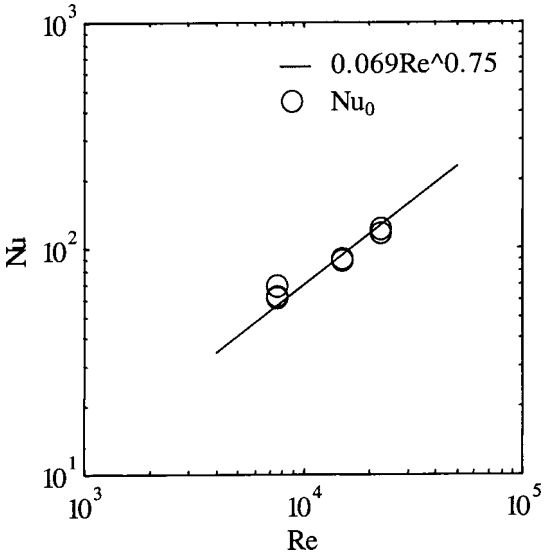

Fig. 10 Comparison of steam alone stagnation heat transfer on concaved surface with flat plate correlation. Two heat fluxes are applied for each Reynolds number.

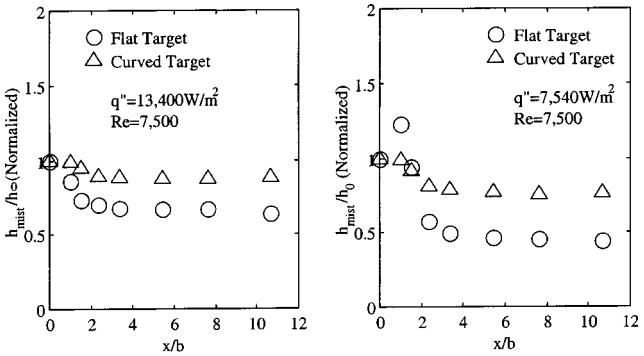

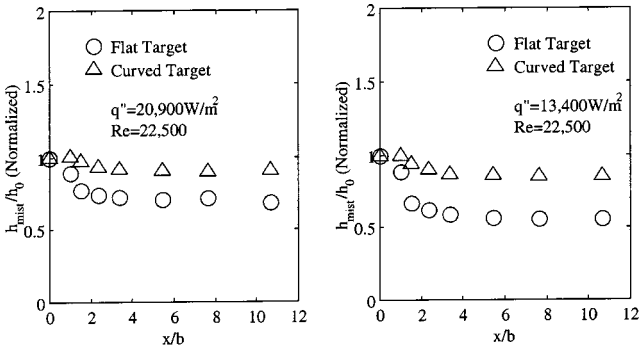

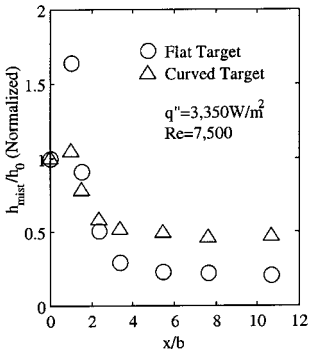

Fig. 11 Comparison of heat transfer enhancement for flat and concave target surfaces at Re=7500 (m_l/m_s=1.5 % for flat case and m_l/m_s=0.5 % for curved case). The enhancement is normalized by the value at the stagnation point.

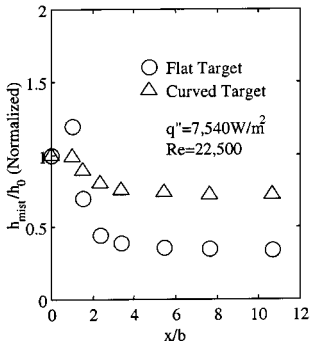

Fig. 12 Comparison of heat transfer enhancement for flat and concave target surfaces at Re=22,500 (m_l/m_s=1.5 % for flat case and m_l/m_s=0.5 % for curved case). The enhancement is normalized by the value at the stagnation point.

indicate that increasing Reynolds number reduces uniformity of enhancement on flat surfaces but did not have much effect on the concave wall cases.

Relevance to Turbine Applications. Actual application is expected at 25~35 bar, and Reynolds number to 400,000. Projections to the higher Reynolds numbers of gas turbine applications will increase the single-phase heat component and improve the mist component, based on the trends herein. At the increased wall superheat values, which may reach 700°C, there may be a decline in the mist effect. But the trends indicate that the mist concentration continues to influence the mist effect and it is expected that the higher fluid density will permit carrying increased mist concentration. More detailed discussion of the relevance of low pressure and low temperature laboratory results to real turbine applications can be found in Guo et al. [14]. Further study is required to establish whether higher pressures and temperatures will support useful mist enhancement.

Conclusions

Experiments have been conducted showing the cooling effect of a mist-laden steam slot jet impinging on a concave surface compared to a single-phase jet and to a mist jet on a flat surface. It can be concluded that

1) The temperature of a surface cooled by steam flow dropped with the addition of a fine mist entrained in the flow. The drop in surface temperature corresponds to an increase, or an enhancement, of the cooling.

2) In terms of heat transfer coefficient, enhancements of 30 to 200 % at the stagnation point have been obtained with an addition of mist 0.5 % or less by mass. The cooling enhancement is greater at lower heat fluxes and at higher Reynolds numbers as has been observed in earlier flat surface studies.

3) The effect of Gortler vortices and secondary flow have the potential of affecting curved-wall results. However, at Reynolds numbers of the present study, the effect of Gortler vorticities is not significant. This may explain why the results of the steam-only case on a concave curve in this paper is identical within experimental uncertainty with that for a flat surface [15]. Weaker secondary flows, which exist in the Reynolds number range in the present study, do not seem to affect the steam-only flow although evidence of present results shows that the secondary flows play an important role to affect mist flows.

4) The enhancement downstream of the stagnation point diminishes, but does not vanish while the flat surface enhancement vanished at $x/b>5$. Presumably this advantage is due to (*a*) the acceleration effect of the curvature on the lagging droplets and (*b*) the lengthened mist residence time resulted from lateral transport of droplets by secondary flows.

5) The maximum cooling enhancement occurs at $x/b=1$ in most of the flat surface cases is not seen on the concave surface cases. This is assumed to be caused by as a result of secondary flows which assist in transporting water droplets in the lateral (spanwise) direction and thus avoid the increased droplet density accumulated near $x/b=1$ on a flat wall.

Acknowledgments

The authors would like to thank Graver Separations (Wilmington, DE) for donating the steam filters for the experiment. We also want to thank Mee Industries Inc. (El Monte, CA) for donating the pressure atomizers and the high-pressure pump. We appreciate the help from Dr. T. Guo in setting up the test facility. This research was sponsored by the U.S. Department of Energy under the contract DOE/AGTSR 95-01-SR-034, and was managed by Dr. N. Holcombe at the Federal Energy Technology Center and by Dr. Larry Golan at the South Carolina Institute for Energy Studies.

Nomenclature

B = width of heater element
b = jet width (7.5 mm)
d = diameter of droplet
d_{10} = arithmetic mean diameter
d_{32} = Sauter mean diameter
h = heat transfer coefficient
I = current through the heater
k = thermal conductivity
m = mass flow rate
Nu = Nusselt number ($h2b/k$)
Pr = Prandtl number
PDPA = phase Doppler particle analyzer
q'' = heat flux
Re = Reynolds number ($\rho_s V_j 2b/\mu_s$)
T = temperature
t = time
V_j = average jet velocity at jet exit
V_{shunt} = voltage cross the shunt
x = streamwise coordinate along the target wall
δ = thickness of heater elements
μ = dynamic viscosity
ρ = density
ξ = resistivity (Ω m)

Subscripts

0 = single phase
j = jet
l = liquid phase
s = steam
w = wall

Appendix

Selected results of a slot jet impinging on a flat surface from Li, et al. [15] are given in Figs. 13 and 14. It can be found that the distribution of steam-only heat transfer coefficient is very similar to the result with concave target surface. It is also shown that the

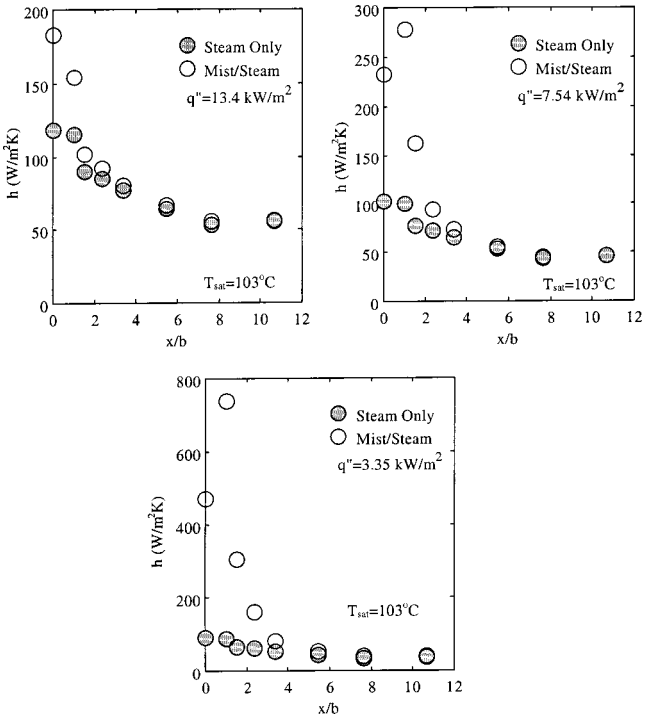

Fig. 13 Heat transfer results for mist/steam slot jet impingement on a flat surface (Re=7500 and m_l/m_s=~3.5 %)

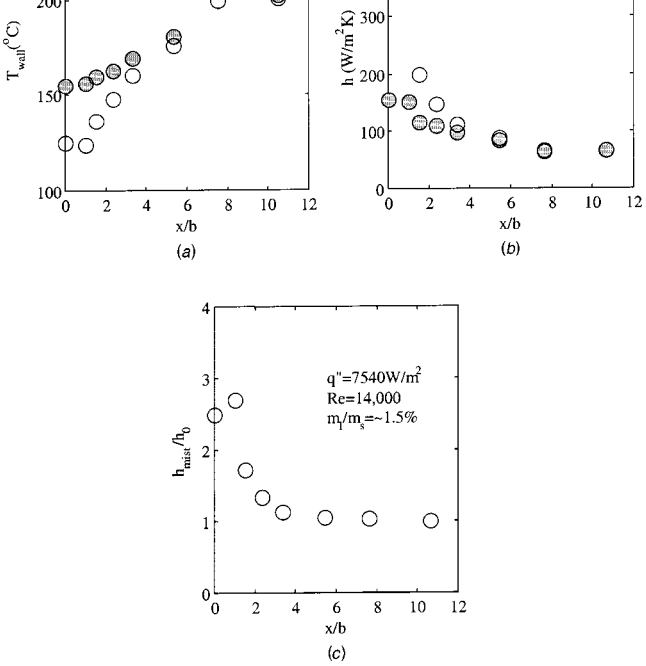

Fig. 14 Heat transfer results for mist/steam slot jet impingement on a flat surface (Re=14,000 and m_l/m_s=~1.5 %)

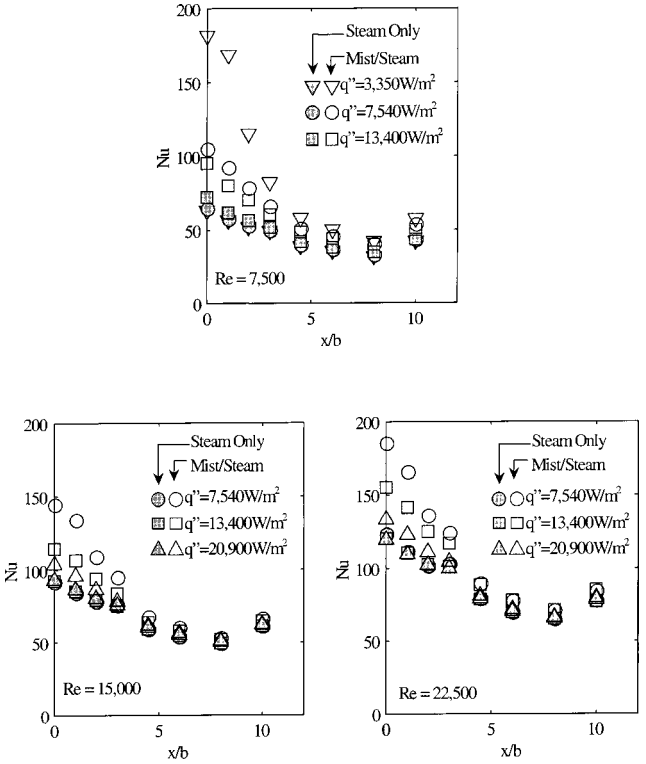

Fig. 15 Heat transfer results in Nusselt number over a concave surface

mist effect in the flat surface heat transfer wanes almost to none by the exit of the test section. The heat transfer coefficient has a maximum value slightly off the centerline of the impinging jet.

The heat transfer results of concave target surface are presented in Nusselt number in Fig. 15. Results under different heat fluxes and Reynolds numbers are included. By using the film temperature to evaluate the thermal conductivity in Nusselt number the stagnation values coincide with each other under different heat fluxes for steam-only flow. The distribution of Nusselt number in each case is identical to the results presented in heat transfer coefficient earlier.

References

[1] Bannister, R. L., and Little, D. A., 1993, ''Development of Advanced Gas Turbine System,'' Proc. of the Joint Contractor Meeting: FE/EE Advanced Turbine System Conference; FE Fuel Cells and Coal-Fired Heat Engine Conference, Aug., Morgantown, WV, pp. 3–15.

[2] Mukavetz, D. W., 1994, ''Advanced Turbine System (ATS) Turbine Modification for Coal and Biomass Fuels,'' in Proceedings of the Advanced Turbine System Annual Program Review Meeting, Nov. 9–11, ORNL/Arlington, VA, pp. 91–95.

[3] Guo, T., Wang, T., and Gaddis, J. L., 2000, ''Mist/Steam Cooling in a Heated Horizontal Tube, Part 1: Development of the Experimental Program,'' ASME J. Turbomach., **122**, pp. 360–365.

[4] Li, X., Gaddis, J. L., and Wang, T., 2001, ''Modeling of Heat Transfer in a Mist/Steam Impingement Jet,'' ASME J. Heat Transfer, **124**, pp. 1086–1092.

[5] Wachters, L. H. J., Smulders, L., Vermeulen, J. R., and Kleiweg, H. C., 1966, ''The Heat Transfer from A Hot Wall to Impinging Mist Droplets in The Spheroidal State,'' Chem. Eng. Sci., **21**, pp. 1231–1238.

[6] Goodyer, M. J., and Waterston, R. M., 1973, ''Mist-Cooled Turbines,'' Conf. of Heat and Fluid Flow in Steam and Gas Turbine Plant, Proc. of Institution of Mechanical Engineers, pp. 166–174.

[7] Yoshida, H., Suenaga, K., and Echigo, R., 1988, ''Turbulence Structure and Heat Transfer of A Two-Dimensional Impinging Jet with Gas-Solid Suspensions,'' NHTC, **2**, pp. 461–467.

[8] Buyevich, Yu. A., and Mankevich, V. N., 1995, ''Interaction of Dilute Mist Flow with a Hot Body,'' Int. J. Heat Mass Transf., **38**, pp. 731–744.

[9] Buyevich, Yu. A., and Mankevich, V. N., 1996, ''Cooling of a Superheated Surface with a Jet Mist Flow,'' Int. J. Heat Mass Transf., **39**, pp. 2353–2362.

[10] Fujimoto, H., and Hatta, N., 1996, ''Deformation and Rebounding Processes of a Water Droplet Impinging on a Flat Surface above Leidenforst Temperature,'' ASME J. Fluids Eng., **118**, pp. 142–149.

[11] Hatta, N., Fujimoto, H., Kinoshita, K., and Takuda, H., 1997, ''Experimental Study of Deformation Mechanism of a Water Droplet Impinging on Hot Metallic Surfaces Above Leidenfrost Temperature,'' ASME J. Fluids Eng., **119**, pp. 692–699.

[12] Nirmalan, N. V., Weaver, J. A., and Hylton, L. D., 1998, ''An Experimental Study of Turbine Vane Heat Transfer with Water-Air Cooling,'' ASME J. Turbomach., **120**(1), pp. 50–62.

[13] Guo, T., Wang, T., and Gaddis, J. L., 2000, ''Mist/Steam Cooling in a Heated Horizontal Tube, Part 2: Results and Modeling,'' ASME J. Turbomach., **122**, pp. 366–374.

[14] Guo, T., Wang, T., and Gaddis, J. L., 2001, ''Mist/Steam Cooling in a 180° Tube Bend,'' ASME J. Heat Transfer, **122**, pp. 749–756.

[15] Li, X., Gaddis, J. L., and Wang, T., 2000, ''Mist/Steam Heat Transfer of Confined Slot Jet Impingement,'' ASME J. Turbomach., **123**, pp. 161–167.

[16] Li, X, Gaddis, J. L., and Wang, T., 2001, ''Mist/Steam Heat Transfer of Circular Confined Impinging Jets,'' ASME Paper 2001-GT-0151.

[17] Rayleigh, J. W. S., 1917, ''On the Dynamics of Revolving Fluids,'' Proc. R. Soc. London, Ser. A, **93**, Serial A, pp. 148–154.

[18] Hrycak, P., 1982, ''Heat Transfer and Flow Characteristics of Jets Impinging on a Concave Hemispherical Plate,'' Proceedings of the 7th International Heat Transfer Conf., **3**, pp. 357–362.

[19] Metzger, D. E., Yamashita, T., and Jenkins, C. W., 1968, ''Impingement Cooling of Concave Surfaces with Lines of Circular Air Jets,'' ASME Paper 68-WA/GT-1.

[20] Downs, S. J., and James, E. M., 1987, ''Jet Impingement Heat Transfer—A Literature Survey,'' ASME Paper 87-HT-35.

[21] Moffat, R. J., 1985, ''Using Uncertainty Analysis in the Planning of an Experiment,'' ASME J. Fluids Eng., **107**, pp. 173–178.

[22] Li, X., 1999, ''Cooling by a Mist/Steam Jet,'' Ph.D. dissertation, Dept. of Mechanical Engineering, Clemson University, South Carolina, USA.

Simulation of Compressible Micro-Scale Jet Impingement Heat Transfer

Deborah V. Pence
e-mail: pence@engr.orst.edu
Mem. ASME

Paul A. Boeschoten
Graduate Research Assistant

James A. Liburdy
e-mail: liburdy@engr.orst.edu
Mem. ASME

Department of Mechanical Engineering,
Oregon State University,
Corvallis, OR 97331

A computational study is presented of the heat transfer performance of a micro-scale, axisymmetric, confined jet impinging on a flat surface with an embedded uniform heat flux disk. The jet flow occurs at large, subsonic Mach numbers (0.2 to 0.8) and low Reynolds numbers (419 to 1782) at two impingement distances. The flow is characterized by a Knudsen number of 0.01, based on the viscous boundary layer thickness, which is large enough to warrant consideration of slip-flow boundary conditions along the impingement surface. The effects of Mach number, compressibility, and slip-flow on heat transfer are presented. The local Nusselt number distributions are shown along with the velocity, pressure, density and temperature fields near the impingement surface. Results show that the wall temperature decreases with increasing Mach number, M, exhibiting a minimum local value at $r/R=1.6$ for the highest M. The slip velocity also increases with M, showing peak values near $r/R=1.4$ for all M. The resulting Nusselt number increases with increasing M, and local maxima are observed near $r/R=1.20$, rather than at the centerline. In general, compressibility improves heat transfer due to increased fluid density near the impinging surface. The inclusion of slip-velocity and the accompanying wall temperature jump increases the predicted rate of heat transfer by as much as 8–10% for M between 0.4 and 0.8. [DOI: 10.1115/1.1571082]

Keywords: Computational, Forced Convection, Heat Transfer, Impingement, Jets, Laminar, Microscale, Rarefied

Introduction

Impinging jets are capable of providing surface heating and cooling in applications featuring fairly high heat fluxes. Major industrial applications include annealing metal, tempering glass, drying textiles, cooling turbine blades and cooling electronic components. Recently there has been interest in applying jet cooling to very small scale devices. Campbell et al. [1] used a small electromagnetic actuator to provide pulsating air jets for cooling of a laptop computer processor. Allan [2] reported on a newly developed silicon micro-heat exchanger chip using impinging jets.

There have been many investigations of the heat transfer from impinging macro-scale, incompressible, unconfined jets in recent years. Martin [3] presents a comprehensive study providing extensive heat transfer correlations for single jets and jet arrays. Hrycak [4] studied high Reynolds number jets for a range of large impingement distances. Lytle and Webb [5] investigated very low impingement distances, $H/D<1$, indicating that high acceleration effects on the local heat transfer distribution cause off axis peaks of Nusselt number to occur. Arjocu and Liburdy [6] show the effect of non-circular nozzles at low Reynolds numbers identifying some flow and heat transfer instabilities. Faila et al. [7] indicate the effect of cross-flow and enhanced surface effects in jet arrays. Huber and Viskanta [8] show that as the Reynolds number is decreased, secondary peaks of the heat transfer coefficient away from the jet centerline are eliminated. These secondary peaks have been attributed to fluid acceleration, boundary layer thinning and turbulence transition.

Chatterjee and Deviprasath [9] numerically investigated the effect of upstream vorticity diffusion on the heat transfer coefficient distribution for laminar confined jets when the jet exit-to-impingement distance ratio is less than one diameter. They show that for a jet resulting from a fully developed flow exiting a long tube, the velocity near the edges of the jet at the exit plane increases due to upstream diffusion of vorticity that is generated near the impingement surface. This results in a more uniform velocity profile at the jet exit. Consequently, the Nu distribution has an off-axis peak at a point on the surface approximately one jet radius from the axis. They point out that at larger impingement distances, $H/D>1$, this effect does not occur because the upstream diffusion is weak. Other studies that show the existence of this off axis peak include Scholtz and Trass [10] for mass transfer, and Colucci and Viskanta [11] for heat transfer; however, these results extend into the turbulent regime.

The objective of this study is to evaluate the heat transfer performance of a micro-scale compressible jet impinging on a flat heated surface with an embedded, uniformly heated disk. The flow is confined with an upper flat, adiabatic, surface parallel with the impingement surface at the same level as the jet exit. The heated surface is circular with a diameter equal to four jet diameters. Results are given for a jet having a nozzle diameter, D, of 100 μm, at impingement distances divided by jet diameters ratios, H/D, of 2 and 4. The exit Mach numbers range from 0.2 to 0.8 with corresponding jet Reynolds numbers from 419 to 1782.

Beskok and Karniadakis [12] have computationally predicted pressure drops for gas flows in micro-channels using slip-flow boundary conditions as opposed to the traditional no-slip conditions. These findings, when compared to experimental pressure drop results, suggest that gas flows in some micro-scale geometries do not behave according to the continuum hypothesis but rather exhibit characteristics associated with the slip-flow regime. Deviation from a continuum is often measured by the Knudsen number ($\mathrm{Kn}=\lambda/L$), where λ is the molecular mean free path (approximately 10^{-7} m for air at standard conditions) and L is a characteristic length. It has been accepted for most flow geometries that the continuum hypothesis is valid for $\mathrm{Kn}<0.01$. The slip-flow regime is characterized by $0.01\leqslant \mathrm{Kn}<0.1$, where the compressible Navier-Stokes equations are valid, but a slip velocity and temperature jump condition at the surface is used to describe

Contributed by the Heat Transfer Division for publication in the JOURNAL OF HEAT TRANSFER. Manuscript received by the Heat Transfer Division February 12, 2002; revision received January 31, 2003. Associate Editor: S. P. Vanka.

Table 1 Geometry, flow, and thermal parameters

Geometry:				
Nozzle Radius (R) = 50 μm				
Nozzle to Impinging Surface Distance (H) = 200 μm, 400 μm				
Impinging Surface Radius = 500 μm				
Heated Surface Radius = 200 μm				
Flow and Thermal Parameters:				
Flow Parameters	Nozzle Exit Mach Number (M)			
	0.2	0.4	0.6	0.8
T_o (°C)	20	20	20	20
T_{exit} (°C)	18	11	0	−13
V_{exit} (m/s)	68	135	199	259
Re_D	419	851	1310	1782
Boundary Condition Parameters:				
Impinging Surface: $q'' = 50$ kW/m^2				
Slip-Flow: $\sigma_v = \sigma_T = 0.8$				
Outflow: $p_{ref} = 1$ atm, $T_{ref} = 20$°C				

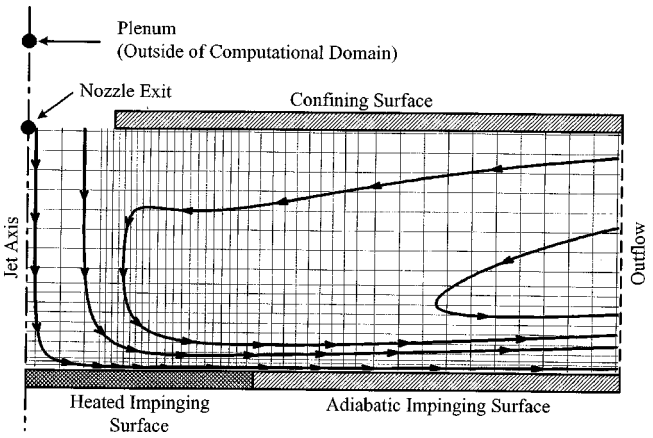

Fig. 1 Illustration of the computational domain indicating the general flow pattern caused by the impinging jet

the local flow and thermal behavior, Schaaf and Chambre [13]. For this study, the value of Kn at the jet exit plane is 0.0013, for air using the nozzle radius as the characteristic length. This is well within the continuum regime.

Although a Kn of 0.0013, based on the jet radius, suggests that slip conditions are minimal, the proper scaling for a representative value of Kn for an impinging jet is not obvious. In the impingement region a more appropriate length scale could be argued to be the viscous boundary layer thickness. As this layer can be considerably smaller than the jet radius, using it to scale the mean free path would result in a larger value of Kn. In fact, as shown for the flow conditions studied, the inner region of the velocity profile is on the order of 0.1 times the jet radius, which puts this flow into the slip flow regime. For the present analysis, λ is based on the exit domain temperature assuming an ideal gas. The absolute temperature does not vary significantly along the wall, and local variation of λ does not alter the local slip velocity, the temperature jump or the heat transfer coefficient beyond the numerical uncertainty of the results.

The present study was undertaken to investigate a micro-scale, confined impinging jet flow geometry with: (i) variations in impingement distance, (ii) relatively large Knudsen numbers which is shown to warrant using a slip-flow boundary condition and (iii) relatively low Reynolds numbers resulting in laminar flow coupled with Mach numbers large enough to cause significant compressibility effects. All cases deal with moderate jet impingement distances of two and four jet diameters.

Model Description

The geometric, flow, and thermal parameters are given in Table 1. The geometry is based on representative micro-scale applications for cooling and is shown schematically in Fig. 1. The jet plenum conditions are set as shown, and the exit conditions calculated for an ideal, isentropic flow from a large plenum. The flow impinges normally onto the heated surface. Ambient fluid is allowed to entrain radially inward, where the ambient pressure is held constant. Nozzle exit Mach numbers vary over a range of incompressible and compressible flow regimes so that compressibility effects on the heat transfer can be assessed. It should be noted that the Mach number and Reynolds number are not varied independently of each other. The heated portion of the impingement surface is centered under the jet and extends radially four jet radii. The surface beyond four jet radii is adiabatic, as is the top boundary. All results are given in the heated region, but the extent of the impingement surface is ten nozzle radii.

Heat transfer results are presented in terms of the local Nusselt number, based on the adiabatic wall temperature (T_{aw}) and jet diameter (D):

$$Nu = \frac{hD}{k} = \frac{q''}{(T_w - T_{aw})}\frac{D}{k} \tag{1}$$

The adiabatic wall temperature was determined for each case by running numerical experiments with adiabatic conditions along the entire impinging surface.

Typically, impinging jets used for macro-scale cooling are rarely laminar. However, Polat et al. [14] concluded that for impinging jets with relatively small H/D, the flow field can be considered laminar up to a Re_D of approximately 2500. Due to the small characteristic length, the largest Re_D encountered in this study is 1782; hence, results are obtained assuming laminar flow. Tests were run using a turbulence model for the highest Re_D, or M, case with no observable change in the output. Results are presented for compressible flows using the ideal gas equation of state. For comparison purposes, incompressible results were also obtained, where the density is considered independent of both pressure and temperature.

Slip Flow Model. In the slip-flow regime, the Navier-Stokes equations are applied with velocity-slip and temperature-jump boundary conditions imposed. The forms of these boundary conditions used in this study are [13]:

$$u_g - u_w = \left(\frac{2-\sigma_v}{\sigma_v}\right)\lambda\frac{\partial u}{\partial n} \tag{2a}$$

$$T_g - T_w = \left(\frac{2-\sigma_T}{\sigma_T}\right)\left(\frac{2\gamma}{\gamma+1}\right)\frac{\lambda}{\mathrm{Pr}}\frac{\partial T}{\partial n} \tag{2b}$$

The formulation of Eq. (2*a*) does not account for thermal creep effects along the surface. These terms were included in trial runs and found to be insignificant since the wall temperature gradients are relatively small. The accommodation coefficients, σ_v and σ_T, are assumed to be constant with a value of 0.8, where a value of 1.0 is representative of a molecularly diffuse surface, Kennard [15]. Depending on the gas and the surface material, a range of values for σ_v and σ_T may be possible, see Karniadakis and Beskok [16] for a discussion.

Beskok and Karniadakis [12] proposed a higher order velocity-slip boundary condition to improve pressure drop predictions for compressible micro-channel flows with very large pressure and temperature changes. Since this higher order term is proportional to the product of Kn^2 and $\partial^2 u/\partial n^2$, neglecting this term in the present study has little consequence on the calculated slip magnitude.

Numerical Model. The jet flows were assumed to be steady, axisymmetric, laminar, and compressible, with slip-flow boundary conditions applied at the impinging surface. Numerical solutions

were obtained for the dimensional discretized form of the compressible form of the Navier-Stokes and energy equations. The second order MARS scheme was used with the SIMPLE finite-volume algorithm of the commercial code STAR-CD. A non-uniform axial by radial grid of 79×118 was employed for all $H/D=2$ cases. Individual control volumes ranged from 0.4×0.6 microns in the regions of high shear to 10×5 microns in the recirculation region. For the $H/D=4$ cases, a 149×118 grid was used. Results were obtained at both low and high Mach numbers using a grid with twice this resolution with no discernable change in the reported results. The convergence criteria were satisfied when the sum of the normalized residuals was reduced to less than 1×10^{-4}, which resulted in typical errors in the velocity and temperature on the order of 1×10^{-4} m/s and 1×10^{-8} K for most of the flow domain. A few localized errors near the edge of the impinging jet and the edge of the jet exit were noted to be 0.1% and 0.1 K, respectively, for velocity and temperature at the highest M case. Based on a sensitivity analysis, these errors are anticipated to result in an error in local Nu on the order of 2 percent.

The computational domain took advantage of axisymmetric conditions, illustrated in Fig. 1, which is not drawn to scale. The flow region was bounded by the plane of the nozzle exit defined by the upper confining plate, the outflow free boundary, the impinging plate and the jet centerline axis. Temperature, density and velocity at the exit plane of the jet were calculated from the selected jet Mach number, for a prescribed plenum temperature of 293 K, using isentropic compressible flow through the nozzle to the exit plane of the jet. The velocity profile specified at the nozzle exit boundary was uniform from the nozzle centerline to 90% of the nozzle radius. A cosine velocity profile taper was matched at $r=0.9R$, with zero velocity at the nozzle edge, $r=R$. This was shown to accurately represent the velocity from a large plenum through a short nozzle by Pelfrey and Liburdy [17]. The average velocity across the entire nozzle exit was used to calculate the jet Reynolds number. The exit plane temperature was assumed to be uniform.

Constant stagnation pressure and temperature boundary conditions were applied at the outflow boundary, which allowed flow to both enter and exit the computational domain. These values, coupled with static pressures extrapolated from the interior of the solution domain, are used to determine the velocity and temperature at the pressure boundary. Polat et al. [14] recommended this constant pressure boundary condition, and it has been used more recently by Morris et al. [18] to accurately predict flow and temperature fields for impinging jets.

A constant heat flux boundary condition was applied at the impinging surface for $r^*<4$, where $r^*=r/R$. Beyond $r^*=4$, the impinging surface was adiabatic. The slip-flow boundary conditions represented by Eqs. (2*a*) and (2*b*) were applied over the entire impinging surface ($0\leqslant r^*\leqslant10$).

Results and Discussion

Details of the effects of compressibility for micro-scale impinging jet heat transfer with wall boundary slip effects are presented in terms of wall temperatures, vector and scalar fields, Nusselt number distributions and average Nusselt number over the heated surface. The results are discussed for two impingement distances ($H/D=2$ and 4) and a range of Mach numbers ($M=0.2,0.4,0.6,0.8$).

The heated surface temperature, T_w, and adiabatic wall temperature, T_{aw}, distributions, on the heated portion ($r^*<4$) of the impinging surface are presented as a function of Mach number in Fig. 2 for both values of H/D. These temperatures are nondimensionalized by dividing by the plenum temperature. This form of normalization is used instead of a reference temperature difference to illustrate the magnitude of temperature variations which directly affects the density, as will be discussed later. At the stagnation point T_{aw} is 293 K for all conditions, which is consistent with the prescribed plenum temperature (T_o) of 293 K. The T_{aw}

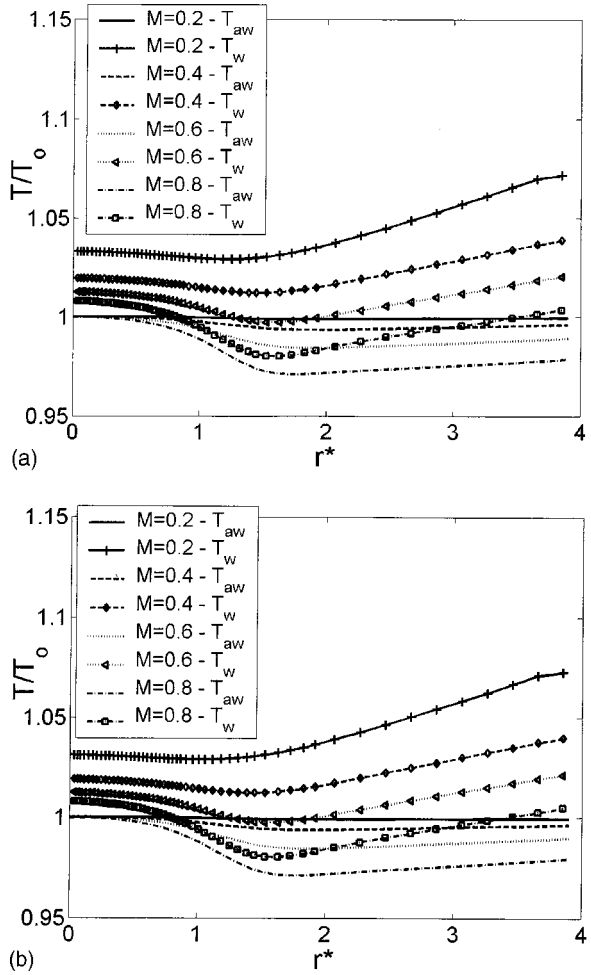

Fig. 2 Nondimensionalized wall and adiabatic wall temperature (T/T_o) versus radial position for (*a*) $H/D=2$ and (*b*) $H/D=4$

distributions are essentially identical, in both trend and local minima, for both H/D values. However, a local minimum of T_w appears for $M=0.2$ near $r^*=1.25$ for $H/D=2$ and $r^*=1.05$ for $H/D=4$. This minimum progresses away from the jet axis with increasing Mach number; at $M=0.8$, the minimum is at $r^*=1.6$ for both H/D. A local maximum of T_w can be observed at the stagnation point ($r^*=0$) for each Mach number. Other than the difference in location of the local minimum of T_w at lower M, there is virtually no change in the shape of the wall temperature distribution when H/D is increased from 2 to 4. In all cases, the local minima for the incompressible flow cases are further from the jet centerline than those for the compressible flow cases.

The off-axis heated wall temperature minima observed in Fig. 2 are seen to be dependent on the Mach number. At $M=0.2$ the reduction of temperature away from the centerline value is very small. As M increases the reduction of the wall temperature becomes more prevalent and the location of the minima move toward larger values of r^*. The adiabatic wall temperature shows evidence of the minimum at larger M, but it is less pronounced than the heated wall temperature. This effect is associated with the flow acceleration which is very strong in this micro-scale geometry at these Reynolds numbers because the corresponding exit velocities are very large. This is true even for the larger values of H/D, when compared to the macro-scale effects. This acceleration is apparently sufficient to induce an off-axis peak in the local heat transfer coefficient; this has not been previously reported for the values of H/D as large, or Re as low, as reported here.

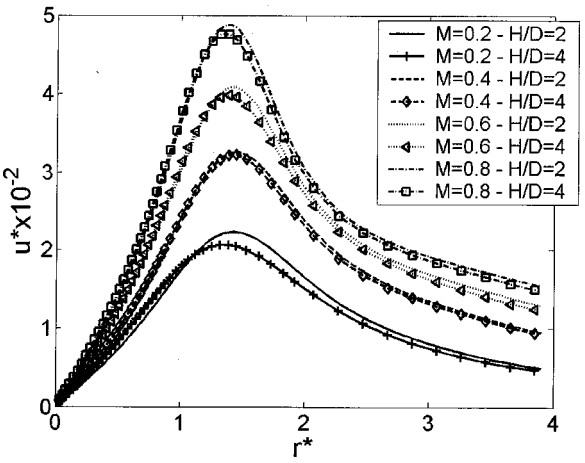

Fig. 3 Nondimensional radial slip velocity distribution along impinging surface

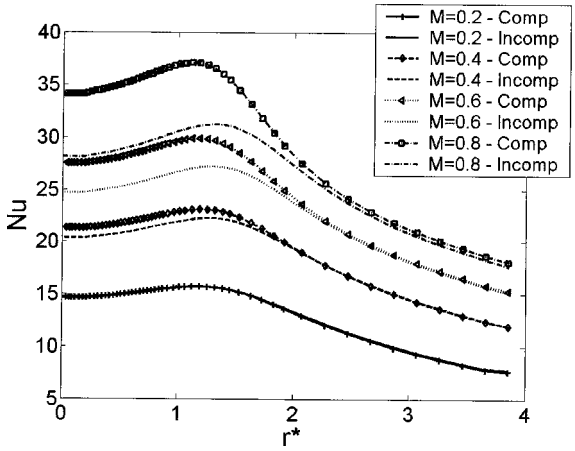

Fig. 4 Local Nusselt number distribution along impinging surface for $H/D=2$ for both compressible and incompressible solutions

Figure 3 shows the radial distribution of the normalized slip-velocity, $u^*=u_g/V_{\text{exit}}$, at the impinging surface for all Mach numbers, and the two impingement distances. The slip-velocity reaches a peak near the same locations of the temperature minima in Fig. 2 (approximately $r=1.4^*$). This peak increases significantly with Mach number. Because the stagnation region has high static pressure, which causes the flow to rapidly accelerate along the wall in the radial direction, the flow continues to accelerate in the impingement region until there is sufficient interaction with the outer region fluid, through entrainment, to establish a decelerating wall jet. According to Eq. (2*a*), the position of maximum slip velocity corresponds to a region of high shear. This is in a region of high acceleration, and its location is found to be a weak function of both impingement distance and Mach number.

Average Nusselt number results were computed by integrating the surface heat transfer coefficient over the heated surface area and are presented in Table 2. Since most recent studies of impinging jets compare reasonably well to those of Martin, results of this study will be contrasted to the correlation given by Martin [3]:

$$\frac{\overline{\text{Nu}}}{\text{Pr}^{0.42}}=2A_r^{1/2}\frac{1-2.2A_r^{1/2}}{1+0.2(H/D-6)A_r^{1/2}}F(\text{Re}_D) \tag{5}$$

where

$$F(\text{Re}_D)=2\ \text{Re}_D^{1/2}(1+0.005\ \text{Re}_D^{1/2})^{1/2} \tag{6}$$

and A_r is the ratio of the nozzle exit area to the heated surface area. This correlation is valid for $2000\leqslant \text{Re}_D\leqslant 400{,}000$, $2\leqslant H/D\leqslant 12$, and $0.04\geqslant A_r\geqslant 0.004$. It should be noted that in the present study $A_r=0.0625$, which is somewhat outside of the range of the above correlation and the values of Re are somewhat lower than those recommended.

Table 2 Computed $\overline{\text{Nu}}$ results compared to correlation by Martin [3]

Mach Number	Reynolds Number	H/D	$\overline{\text{Nu}}$ Martin (1977)	$\overline{\text{Nu}}$ Present study	Difference (%)
0.2	419	2	11.37	11.0	−3.3
0.2	419	4	10.11	10.8	+6.8
0.4	851	2	15.22	16.5	+8.4
0.4	851	4	13.53	16.4	+21.2
0.6	1310	2	19.21	20.9	+8.8
0.6	1310	4	17.07	20.9	+22.4
0.8	1782	2	23.87	24.8	+3.9
0.8	1782	4	21.21	24.8	+16.9

From Table 2 it is seen that the predicted results for $H/D=2$ are within approximately 8% of those of Martin; however, for $H/D=4$ these results are consistently higher than Martin's correlation, by as much as 20%. This trend does not show better agreement as the Reynolds numbers come closer to Martin's recommended range. Interestingly, the approximately 10% decrease in Nu with increasing jet-to-plate spacing from 2 to 4, predicted by Martin, does not occur in this study. Rather, there is little change of the average heat transfer from H/D of 2 to 4. This apparent insensitivity to H/D is contrary to Colucci and Viskanta [11] who concluded that confined jets are more sensitive to variations of H/D than unconfined macro-scale jets. It might be concluded that at the micro-scale, the correspondingly small scales do not result in the same geometric dependence as at the macro-scale when compared at the same Reynolds numbers.

In addition to the seemingly poor agreement of the average Nusselt number with the correlation given by Martin, the form of the local Nusselt number distribution for these results is unique. The magnitude of the local Nusselt number distribution varies as a function of Mach number and is shown in Fig. 4 for $H/D=2$. Although not shown, results for $H/D=4$ have the same shape and, as indicated in Table 2, have essentially the same average magnitude as for $H/D=2$. The Nusselt number is observed to increase with increasing Mach number (and Re_D), and local off-axis maxima are observed between $r^*=1.13$ and 1.33. Uncertainty in r^* is on the order of ± 0.015, due to the grid resolution in this region. Also shown are incompressible flow results indicating reductions of Nu by as much as 15% for the higher M case when compared to the compressible flow results. As M increases the off-axis peak of Nu for the incompressible cases is shifted slightly further away from the centerline compared to the compressible flow cases. This outward shift can be attributed to higher local velocities and flow acceleration caused by a lower fluid density when treated as incompressible. The increases of density due to compressibility effects are discussed later.

The off-axis local Nu maximum has been associated with the local turbulence generation [3], and was found for a variety of nozzle shapes and impingement distances [11]. The impingement distances for the occurrence of the off-axis peak for laminar flows reported in the literature are all very small, less than one jet diameter. In contrast, the present calculations are for laminar flow at larger values of H/D. To help explain these results it should be noted that the jet exit profile assumed in this study is uniform with a cosine taper applied to the outer ten percent of the radius. This profile results in a high acceleration near the impingement surface of the flow near the outer shear layer of the jet, compared to the case of a parabolic profile at the exit. This contributes to the

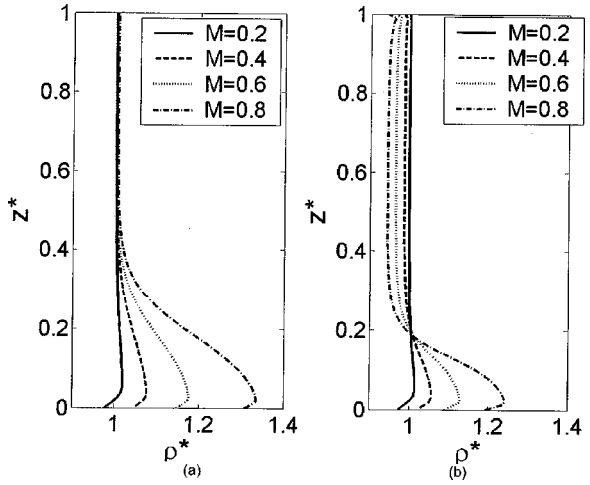

Fig. 5 Nondimensional density distributions normal to the impingement surface for $H/D=2$ at (*a*) $r^*=0.5$ and (*b*) $r^*=1.0$

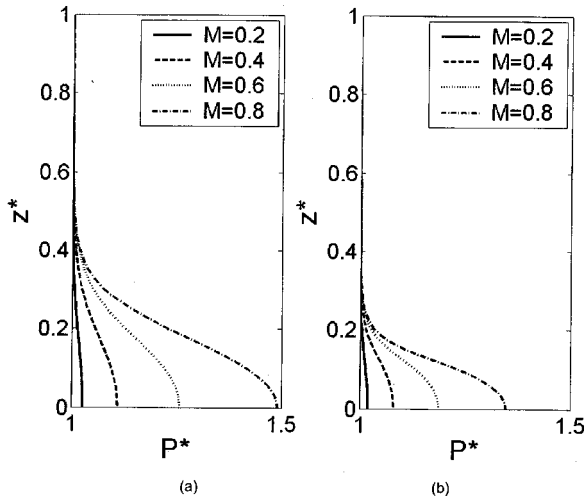

Fig. 6 Nondimensional pressure distributions normal to the impingement surface for $H/D=2$ at (*a*) $r^*=0.5$ and (*b*) $r^*=1.0$

observed off-axis peak even at low values of Re_D and higher H/D values than observed in larger scale flows. Based on these results, it appears that a better indicator of a secondary peak would be a measure of the local acceleration near the wall, at least within micro-scale geometries.

The Nu peak occurs at a smaller radial location than either the minimum T_w in Fig. 2 or the maximum slip velocity in Fig. 3. The Nu peak does not correspond with the T_w minimum because the value of Nu also depends on the distribution of the adiabatic wall temperature, which is found to be a very weak function of H/D and whose minimum location is a weak function of M. The distribution of T_w shows that its minimum shifts away from the centerline for increasing M, and shifts inward as H/D increases. The net effect is the indicated shift of the peak of Nu distribution shown in Fig. 4. The relative location of the Nu and slip velocity peaks implies that the peak wall shear stress occurs further downstream than the peak heat transfer coefficient for the conditions studied.

Improved heat transfer, as a result of compressibility, can be traced to an increase in the fluid density near the surface. This effect is illustrated in Fig. 5, where the density distributions, $\rho^*=\rho/\rho_{\text{exit}}$, are plotted versus the distance from the impingement surface ($z^*=z/H$) at two different radial locations. The corresponding non-dimensional pressure distributions, p^*, are shown in Fig. 6 and the non-dimensional temperature, T^*, in Fig. 7. Note the change in scale of z^* for temperature and the normalization for temperature, which is $T^*=(T-T_{\text{exit}})/(T_o-T_{\text{exit}})$. Within $0.5H$ of the surface the density begins to increase, this is caused by the increase in pressure that occurs within this same region. Very close to the impingement surface, the density decreases as the local temperature rises as shown in Fig. 7, despite the continued rise in pressure in Fig. 6. The layer of increased temperature, and decreased density, near the surface is much thinner than the overall density and pressure layers. This layer is on the order of one tenth of the density and pressure layer thicknesses. The thickness of the reduced density region decreases somewhat with increasing Mach number, as the corresponding temperature layer also decreases with Mach number.

In addition to temperature distributions at $r^*=0.5$ and $r^*=1.0$, Fig. 7 also contains the temperature distribution at $r^*=1.5$ to illustrate that the temperature distribution has a reversal, or local minimum, near the edge of this thin temperature rise layer. The magnitude of this temperature decrease grows in the radial direction and increases with increasing Mach number. Recall that as the flow leaves the plenum it is cooled, as is noted by the exit temperature in Table 1. On the other side of the domain, entrained ambient air warms the outer regions of the flow field, compared to the higher velocity jet regions, particularly in regions away from the jet exit. Outside of the thin layer near the heated wall, the jet flow remains cooler as it is not significantly heated by either the wall or the entrained ambient fluid. This effect increases with M as expected.

It is concluded that the impingement region is marked by two distinctly different scales. In the region $z^*\leqslant 0.4$ there is direct influence of the pressure field on the local density, causing the density to rise as the pressure rises. A thinner layer very near the surface has a decrease in density which is affected by the rise in temperature near the surface. The entrainment of ambient air influences the temperature distribution near the surface, particularly beyond one jet radius. In this region fluid is heated away from the surface while allowing cold flow very near the surface.

Shown in Fig. 8 are velocity profiles at two different radial locations for $H/D=2$, (a) and (b), and at one radial location for $H/D=4$, (c). As the flow is deflected during impingement there is a reduction of the wall jet layer with somewhat thinner layers occuring at high Mach numbers. Comparing Fig. 8(*b*) with 8(*c*) shows that increasing H/D from 2 to 4 results in essentially no change in the thickness of the wall layer since z^* is nondimensionalized by H. Comparison of Figs. 7 and 8 show that for all

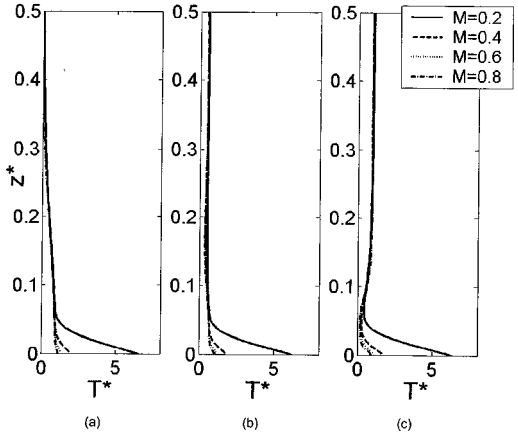

Fig. 7 Nondimensional temperature distributions (T^*) normal to the impingement surface for $H/D=2$ at (*a*) $r^*=0.5$, (*b*) $r^*=1.0$, and (*c*) $r^*=1.5$

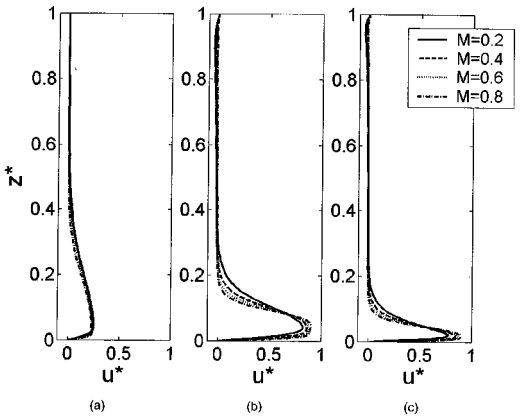

Fig. 8 Nondimensional radial velocity distributions normal to the impingement surface for (*a*) $H/D=2$ at $r^*=0.5$, (*b*) $H/D=2$ at $r^*=1.5$, and (*c*) $H/D=4$ at $r^*=1.5$

cases studied, the thickness of the thermal layer is on the same order as the ''inner'' layer of the velocity field which is defined as the region between the surface and the maximum velocity.

Inclusion of the slip flow condition results in higher velocities near the wall and lower wall shear stress. Also, the temperature jump condition reduces the fluid temperature near the wall during heating. The effects of slip-flow boundary conditions on the Nusselt number distribution are illustrated in Fig. 9 by independently accounting for various slip conditions. Results are contrasted with and without slip in the presence and absence of a temperature jump. When the slip and temperature jump conditions are imposed the heat transfer coefficient is highest. The Nu is reduced when the velocity slip is neglected (no slip), but the temperature jump is included. Retaining the velocity slip but neglecting the temperature jump (no jump) reduces Nu more than if only the slip is neglected. Finally, neglecting both slip and temperature causes an approximate 8% decrease in Nu relative to the slip with temperature jump case for Mach number of 0.8. It should be noted that the magnitudes of these effects will be related to the accommodation coefficients selected.

Conclusions

The heat transfer performance of a compressible micro-scale impinging jet was numerically simulated. The flow was modeled as a steady state, laminar, confined, axisymmetric, submerged impinging jet. Heat transfer results were obtained to study the effects of Mach number, compressibility, and slip conditions for a range of subsonic flows. The main conclusions from this study can be stated as follows. The wall temperature decreases and the Nusselt number increases with increasing Mach number. The wall temperature distribution indicates an off-axis minimum at r^* between 1.05 and 1.60, that persists at relatively large impingement distances with the magnitude dependent on both M and H/D. This is believed to be strongly connected to the flow acceleration near $r^*=1.4$, the strength of which is dependent on the jet exit velocity profile. The acceleration occurs at larger normalized impingement distances compared to macro-scale jets. The averaged Nusselt numbers do not compare well to the standard correlation by Martin [3] for $H/D=4$, tending to be up to 20% higher for the conditions studied. Values of Nu for this micro-scale flow indicate a reduced sensitivity to H/D when compared with larger scale flow results. Accounting for compressibility increases the predicted heat transfer, which is a result of the increased fluid density near the impinging surface. For this confined flow, decreasing H/D thickens the dimensionless near wall region velocity layer, but this has little affect on the local heat transfer. Consequently, at the microscale, it is possible to achieve relatively higher heat transfer rates at larger relative impingement distances compared with those predicted by standard correlations for macroscale flows.

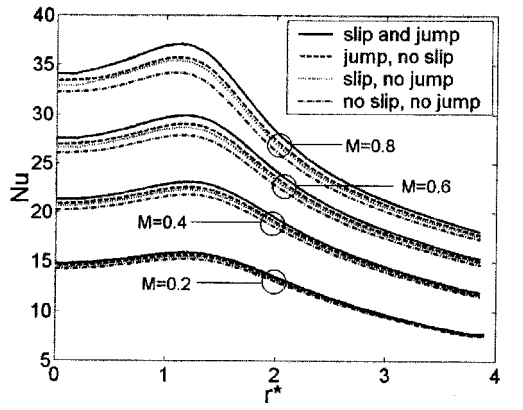

Fig. 9 Local Nusselt number distribution illustrating the effect of slip and temperature jump

Nomenclature

a = acoustic velocity, m/s
A_r = constant in Eq. (5)
D = nozzle diameter, m
h = convection coefficient, W/m^2-K
H = spacing between nozzle exit and impinging surface, m
k = thermal conductivity, W/m-K
Kn = Knudsen Number (λ/R)
L = characteristic length, m
M = Mach number (V/a)
n = coordinate normal to surface, m
Nu = Nusselt number (hD/k)
$\overline{\text{Nu}}$ = Nusselt number averaged over the heated surface
p = pressure, N/m^2
p^* = nondimensional pressure (p/p_o)
Pr = Prandtl number (ν/α)
q'' = heat flux, W/m^2
r = radial distance from jet axis, m
r^* = nondimensional radial distance from the jet axis (r/R)
R = jet radius, m
R_g = gas constant, N-m/kg-K
Re_D = Reynolds number ($V_{\text{exit}}D/\nu$)
T = temperature, K
T^* = nondimensional temperature $[(T-T_{\text{exit}})/(T_o-T_{\text{exit}})]$
u = velocity component tangent to impinging surface, m/s
u^* = nondimensional slip velocity (u/V_{exit})
V = velocity magnitude, m/s
z = axial distance from impinging surface, m
z^* = nondimensional distance from the surface (z/H)

Greek

γ = specific heat ratio
λ = molecular mean free path ($\mu(R_gT\pi/2)^{1/2}/p$), m
μ = dynamic viscosity, N-s/m^2
ν = kinematic viscosity, m^2/s
ρ = density, kg/m^3
ρ^* = nondimensional density (ρ/ρ_{exit})
σ_v = momentum accommodation coefficient
σ_T = thermal accommodation coefficient

Subscripts

aw = adiabatic wall
D = characteristic length equal to nozzle diameter

exit = nozzle exit condition
g = gas condition, adjacent to wall
o = total or stagnation condition in plenum
ref = reference condition at domain exit
w = wall condition

References

[1] Campbell Jr., J. S., Black, W. Z., Glezer, A., and Hartley, J. G., 1998, ''Thermal Management of a Laptop Computer With Synthetic Air Microjets,'' *Proceedings of the 1998 6th Intersociety Conference on Thermal and Thermomechanical Phenomena in Electronic Systems*, IEEE, pp. 43–50.

[2] Allan, R., 1999, ''MEMS Micro Heat Exchanger Employ Impinging Jets to Boost Cooling Efficiency,'' Electronic Design, **47**(7), pp. 29–30.

[3] Martin, H., 1977, ''Heat and Mass Transfer between Impinging Gas Jets and Solid Surfaces,'' *Advances in Heat Transfer*, J. P. Hartnett and T. F. Irvine, Jr., eds., **13**, Academic Press, New York.

[4] Hrycak, P., 1983, ''Heat Transfer from Round Impinging Jets to a Flat Plate,'' Int. J. Heat Mass Transf., **26**(12), pp. 1857–1865.

[5] Lytle, D., and Webb, B. W., 1994, ''Air Jet Impingement Heat Transfer at Low Nozzle-Plate Spacings,'' Int. J. Heat Mass Transf., **37**(12), pp. 1687–1697.

[6] Arjocu, S. C., and Liburdy, J. A., 2000, ''Identification of Dominant Heat Transfer Modes Associated with the Impingement of an Elliptic Jet Array,'' ASME J. Heat Transfer, **122**, pp. 240–247.

[7] Failla, G., Bishop, E., and Liburdy, J. A., 2000, ''Enhanced Jet Impingement Heat Transfer with Crossflow at Low Reynolds Numbers,'' Journal of Electronics Manufacturing, **9**(2), pp. 167–178.

[8] Huber, A. M., and Viskanta, R., 1994, ''Effect of Jet-Jet Spacing on Convective Heat Transfer to Confined, Impinging Arrays of Axisymmetric Jets,'' Int. J. Heat Mass Transf., **37**(18), pp. 2859–2869.

[9] Chatterjee, A., and Deviprasath, L. J., 2001, ''Heat Transfer in Confined Laminar Axisymmetric Impinging Jets at Small Nozzle-Plate Distances: The Role of Upstream Vorticity Diffusion,'' Numer. Heat Transfer, Part A , **39**, pp. 777–800.

[10] Scholtz, M. T., and Trass, O., 1970, ''Mass Transfer in a Nonuniform Impinging Jet: Part II. Boundary Layer Flow-Mass Transfer,'' AIChE J., **16**, pp. 90–96.

[11] Colucci, D. W., and Viskanta, R., 1996, ''Effect of Nozzle Geometry on Local Convective Heat Transfer,'' ASME J. Heat Transfer, **13**, pp. 71–80.

[12] Beskok, A., and Karniadakis, G. E., 1994, ''Simulation of Heat and Momentum Transfer in Complex Microgeometries,'' J. Thermophys. Heat Transfer, **8**(4), pp. 647–655.

[13] Schaaf, S. A., and Chambre, P. L., 1961, *Flow of Rarefied Gases*, Princeton University Press, Princeton, NJ.

[14] Polat, S., Huang, B., Mujumdar, A. S., and Douglas, W. J. M., 1989, ''Numerical Flow and Heat Transfer Under Impinging Jets: A Review,'' Annu. Rev. Numer. Fluid Mech. Heat Transfer, **2**, pp. 157–197.

[15] Kennard, E. H., 1938, *Kinetic Theory of Gases*, McGraw-Hill Book Co. New York.

[16] Karniadakis, G. E., and Beskok, A., 2001, *Microflows Fundamentals and Simulation*, Springer-Verlag, New York.

[17] Pelfrey, J. R. R., and Liburdy, J. A., 1986, ''Mean Flow Characteristics of a Turbulent Offset Set,'' J. Fluids Eng., **108**, pp. 82–88.

[18] Morris, G. K., Garimella, S. V., and Amano, R. S., 1996, ''Prediction of Jet Impingement Heat Transfer Using a Hybrid Wall Treatment With Different Turbulent Prandtl Number Functions,'' ASME J. Heat Transfer, **118**, pp. 562–569.

Scalable Multi-Group Full-Spectrum Correlated-*k* Distributions for Radiative Transfer Calculations

Hongmei Zhang[1]

Michael F. Modest
e-mail: mfm6@psu.edu
Fellow ASME

Department of Mechanical and Nuclear Engineering,
Penn State University,
University Park, PA 16802

A new full-spectrum k*-distribution method has been developed, in which spectral locations are sorted into* M *spectral groups, according to their absorption coefficient dependence on (partial) pressure and temperature. Calculating correlated-*k *full-spectrum* k*-distributions for each of the* M *groups, LBL accuracy can be obtained with* $M \leqslant 32$*. Database values have been assembled for* CO_2 *mixtures at atmospheric pressure. The method is fully scalable, i.e., spectral groups from the database can be combined to obtain coarser group models (*$M = 1,2,4, \ldots$*) for greater numerical efficiency (accompanied by slight loss in accuracy).* [DOI: 10.1115/1.1560156]

Keywords: Computational, Gaseous, Heat Transfer, Radiation

Introduction

Radiative transfer in absorbing-emitting gas mixtures can be most accurately predicted using the line-by-line approach, but LBL calculations require large computer resources and computational time. It has been known for some time that, for a narrow spectral range (i.e., a range over which the Planck function $I_{b\eta} \simeq$ const) in a homogeneous medium (i.e., absorption coefficient κ_η is not a function of spatial location), the absorption coefficient may be reordered into a monotonic *k*-distribution, which produces exact results at a fraction of the computational cost [1,2]. As with other narrow band models, treatment of nonhomogeneous media was somewhat problematic. Two methods have been commonly used to address nonhomogeneity: the *scaling approximation* and the assumption of a *correlated k-distribution*. The Correlated-*k* method has been shown to be accurate primarily for low temperature meteorological applications [1,3,4].

More recently, the reordering concept has also been applied to the full spectrum. Denison and Webb [5,6] developed the Spectral-Line-Based Weighted-Sum-of-Gray-Gases (SLW) model, in which line-by-line databases are used to calculate weight factors for the popular WSGG model [7,8]; for nonhomogeneous gases they assumed a correlated absorption coefficient. A similar method, called the Absorption Distribution Function (ADF) approach, was developed by Rivière et al. [9,10].

Very recently, Modest and Zhang [11] demonstrated how *k*-distributions can be obtained for the entire spectrum, calling it the FSCK method. Their approach differs from the SLW and ADF approaches in two respects: (1) they obtained a continuous *k*-distribution, rather than the stepwise WSGG method [showing that the SLW/ADF/WSGG methods are crude step implementations of the full-spectrum *k*-distribution (FSCK) method]; and (2) they used the scaling approximation, to make a clear mathematical development of the method possible for inhomogeneous media. In addition, they introduced a somewhat more elaborate scheme for establishing a reference state, which further improves accuracy.

These full-spectrum methods can achieve LBL accuracy for homogeneous media, but at a tiny fraction of the computational cost. However, substantial inaccuracies can occur in nonhomogeneous media, because the assumptions of a correlated or scaled absorption coefficient are violated, particularly in the presence of extreme temperature changes and/or changing mole fractions. To overcome this limitation, Pierrot et al. [10] developed the fictitious-gas-based ADF, in which the individual lines comprising the absorption coefficient were placed into separate groups based on their temperature dependence. While improving accuracy, the method becomes computationally more expensive by a factor of M^2, where M is the number of fictitious gases or groups, in order to deal with line overlap from different fictitious gases. Similarly, Zhang and Modest [12] extended their FSCK method to such fictitious gases, called the (multi-scale) MSFSCK method. This method greatly improves the accuracy, while increasing computational time by only a factor of M, since fictitious-gas overlap is treated in an approximate fashion.

The subtle differences between correlated and scaled absorption coefficients were recently detailed by Modest [13]: an absorption coefficient attains a value $\kappa_\eta(\eta, \underline{\phi}_{\text{ref}}) = k_{\text{ref}}$ many times across the spectrum, where k_{ref} is some fixed value, and the composition variables $\underline{\phi} = (T, p, x)$ are evaluated at a reference condition. A correlated absorption coefficient has to satisfy the following two conditions: (i) at every one of these spectral locations, the absorption coefficient at a different state also has a unique specific value $\kappa_\eta(\eta, \underline{\phi}) = k(\underline{\phi}, k_{\text{ref}})$, i.e., k may be a function of k_{ref}, but not of η directly; and (ii) k is a monotonically increasing function of k_{ref}. The absorption coefficient is scaled if this k is independent of k_{ref}. Thus, we may write

$$\text{correlated:} \qquad \kappa_\eta(\eta, \underline{\phi}) = \kappa_{\eta,\text{ref}}(\eta, \underline{\phi}_{\text{ref}}) u(\underline{\phi}, \underline{\phi}_{\text{ref}}, \kappa_{\eta,\text{ref}}) \quad (1)$$

$$\text{scaled:} \qquad \kappa_\eta(\eta, \underline{\phi}) = \kappa_{\eta,\text{ref}}(\eta, \underline{\phi}_{\text{ref}}) u(\underline{\phi}, \underline{\phi}_{\text{ref}}) \quad (2)$$

It follows that scaling is more restrictive, i.e., a scaled absorption coefficient is always correlated, but not vice versa. The FSCK method of Modest and Zhang [11] can be used with either model, and should then be more properly called FSSK (full-spectrum scaled *k*-distribution) and FSCK methods.

It is the purpose of the present paper to introduce a new full-spectrum method, in which spectral positions (with absorption coefficients consisting of contributions from many different lines) are placed into spectral groups according to their dependence on temperature and (partial) pressure (as opposed to the ADFFG and MSFSCK methods, which place spectral lines into groups according to the lower level energies, with each of the lines affecting the

[1]Now with General Electric Corp., Schenectady, NY

Contributed by the Heat Transfer Division for publication in the JOURNAL OF HEAT TRANSFER. Manuscript received by the Heat Transfer Division May 20, 2002; revision received November 6, 2002. Associate Editor: R. Skocypec.

absorption coefficient over many different wavenumbers). Such a model avoids the problem of overlap between different groups. It also allows the consideration of partial pressure dependence during the grouping process. In addition, the HITEMP database [14] will be used to build up a multigroup database. As indicated by Modest and Bharadwaj [15], HITEMP displays some questionable behavior in the band wings of CO_2 at temperatures above 1500 K. However, the model can be used with any other databases. Total pressure variations could be incorporated as well, and will be considered in follow-up work.

Theoretical Development

Spectral Grouping. Consider the top frame of Fig. 1, which shows the absorption coefficient of CO_2 for a small part of its 4.3 μm band, for a temperature of 300 K, a total pressure of 1 bar, and a mole fraction of 10 percent. This absorption coefficient contains the contributions from about 1500 lines (at 300 K). Also shown is the ratio $u=\kappa_\eta(2000\text{ K, }1\text{ bar, }10\text{ percent})/\kappa_\eta(300\text{ K, }1\text{ bar, }10\text{ percent})$ (now with contributions from more than 5000 lines at 2000 K due to the emergence of ''hot lines''). Clearly, for such temperature differences, the absorption coefficient is neither scaled ($u=$const, which is not the case in Fig. 1), nor is it correlated [u is a function of $\kappa_\eta(300\text{ K})$ only]. As shown in Fig. 1, u does not have the same value for the same absorption coefficient at different spectral locations. To obtain an absorption coefficient that more closely follows the rules of ''scaling'' or ''correlation,'' we may want to break up the spectrum into two groups, throwing all wavenumbers with $u>10$ into ''Group 1'' and the rest into ''Group 2,'' as indicated in the bottom frames of Fig. 1. Such simple grouping of the absorption coefficient substantially improves the accuracy of the FSSK and FSCK models, although reaching LBL accuracy will require more sophisticated grouping. This is demonstrated in Fig. 2, which depicts nondimensional heat loss from the cold end of a two-temperature mixture of 10 percent CO_2-90 percent nitrogen. The slab consists of a $l_h=50$ cm hot layer at $T_h=2000$ K, and a cold layer at 300 K of varying width l_c; both sides are bounded by cold, black walls [11,12]. The figure shows that, without grouping, the FSCK method makes a maximum error of 10.3 percent for a large cold layer. The FSSK method considerably outperforms the FSCK results with a maximum error of 4.4 percent. The reason is that, without grouping, the assumption of a correlated k-distribution is a bad one in the presence of such large temperature differences, while the u-function can be optimized for this problem in the FSSK method [11]. The simple two-group model indicated in Fig. 1 results in substantial improvement, reducing the maximum error to about 2.5 percent. It is interesting to note the 2GFSCK and 2GFSSK models perform about equally well: apparently, simply separating absorption coefficients governed by hot lines from those present at low temperature, results in a fairly well correlated distribution.

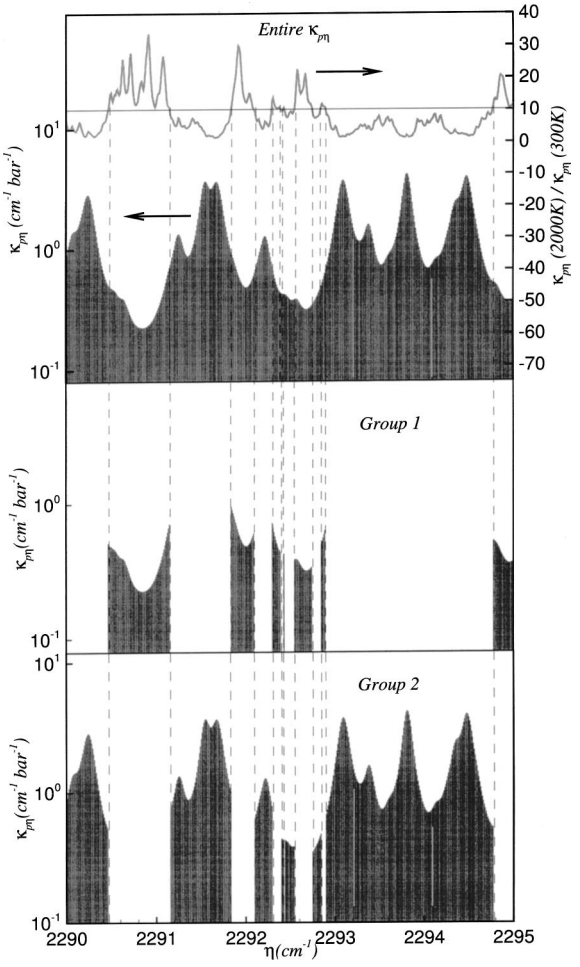

Fig. 1 A small portion of the 15 μm CO_2 band broken up into two groups using Multi-Group approach

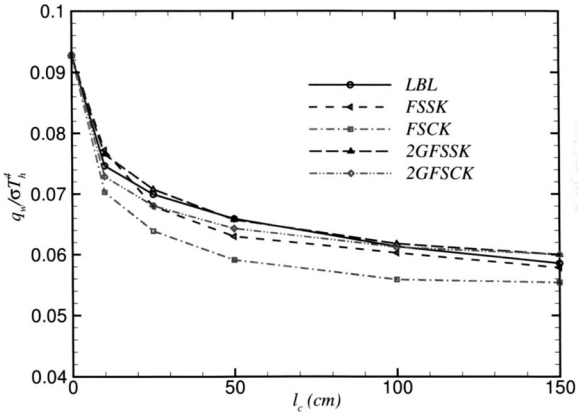

Fig. 2 Two-Group results for the heat flux exiting from the cold column of a two-column CO_2-nitrogen mixture at different temperatures ($T_{hot}=2000$ K, $l_{hot}=50$ cm; $T_{cold}=300$ K, l_{cold} variable; uniform $p=1$ bar, $x_{CO_2}=0.1$, cold and black bounding walls)

To achieve accuracies close to those of line-by-line calculations for arbitrary, nonhomogeneous fields, a wide range of temperatures needs to be considered, and a large number of spectral groups needs to be established (variations with mole fractions tend to be much weaker, especially for CO_2, and will be treated as a secondary effect.)

The Multi-Group FSCK Approach. The multi-group versions of the FSSK and FSCK methods can essentially be developed in the same way as the underlying single group models that were developed by Modest and Zhang [11]. Consider the spectral radiative transfer equation (RTE) for an absorbing, emitting and scattering medium [16]

$$\frac{dI_\eta}{ds}=\kappa_\eta(\underline{\phi},\eta)[I_{b\eta}(T)-I_\eta]-\sigma_s\left[I_\eta-\frac{1}{4\pi}\int_{4\pi}I_\eta(\hat{s}')\Phi(\hat{s},\hat{s}')d\Omega'\right], \quad (3)$$

subject to the restriction that scattering properties σ_s and Φ (as well as bounding wall reflectance) are gray. The RTE is now multiplied by the Dirac-delta function $\delta(k_m-\kappa_\eta(\underline{\phi}_{\text{ref}},\eta))$, and inte-

grated across the m-th spectral group $[\eta_m]$ (containing all the wavenumbers for that group). Assuming the absorption coefficient for the m^{th} group to be correlated, this leads to

$$\frac{dI_{km}}{ds} = k(\underline{\phi}, k_m)[f_m(T, \underline{\phi}_{\text{ref}}, k_m) I_b(T) - I_{km}] - \sigma_s \left[I_{km} - \frac{1}{4\pi} \int_{4\pi} I_{km}(\hat{s}') \Phi(\hat{s}, \hat{s}') d\Omega' \right], \quad (4)$$

where

$$I_{km} = \int_{\eta \in [\eta_m]} I_\eta \delta(k_m - \kappa_\eta(\underline{\phi}_{\text{ref}}, \eta)) d\eta, \quad (5)$$

$$f_m(T, \underline{\phi}_{\text{ref}}, k_m) = \frac{1}{I_b(T)} \int_{\eta \in [\eta_m]} I_{b\eta}(T) \delta(k_m - \kappa_\eta(\underline{\phi}_{\text{ref}}, \eta)) d\eta, \quad (6)$$

is the full-spectrum k-distribution for the m-th group, which depends on local temperature through the Planck function, and a reference state $\underline{\phi}_{\text{ref}}$ through the choice of state for $\kappa_\eta(\underline{\phi}_{\text{ref}}, \eta)$. The first term on the right-hand-side of Eq. (4) uses the assumption of a correlated absorption coefficient, since the absorption coefficient can only be removed from the integral

$$\int_{\eta \in [\eta_m]} \kappa_\eta(\underline{\phi}, \eta) I_{b\eta}(T) \delta(k_m - \kappa_\eta(\underline{\phi}_{\text{ref}}, \eta)) d\eta = k(\underline{\phi}, k_m) \int_{\eta \in [\eta_m]} I_{b\eta}(T) \delta(k_m - \kappa_\eta(\underline{\phi}_{\text{ref}}, \eta)) d\eta, \quad (7)$$

if $\kappa_\eta(\underline{\phi}, \eta)$ attains identical values for each wavenumber in the spectral group $[\eta_m]$, where $\kappa_\eta(\underline{\phi}_{\text{ref}}, \eta) = k_m$. As for the single group model, the development is completed by replacing the inconvenient k_m-variable (which leaves the ill-behaved k-distribution f_m in the RTE) by the cumulative k-distribution evaluated at a reference temperature T_{ref},

$$g_m(T_{\text{ref}}, \underline{\phi}_{\text{ref}}, k_m) = \int_0^{k_m} f_m(T_{\text{ref}}, \underline{\phi}_{\text{ref}}, k_m) dk_m. \quad (8)$$

This is achieved by dividing Eq. (4) by $f_m(T_{\text{ref}}, \underline{\phi}_{\text{ref}}, k_m)$, leading to

$$\frac{dI_{gm}}{ds} = k_m(T_{\text{ref}}, \underline{\phi}, g_m)[a_m(T, T_{\text{ref}}, g_m) I_b(T) - I_{gm}] - \sigma_s \left[I_{gm} - \frac{1}{4\pi} \int_{4\pi} I_{gm}(\hat{s}') \underline{\phi}(\hat{s}, \hat{s}') d\Omega' \right], \quad (9)$$

with

$$I_{gm} = \int_{\eta \in [\eta_m]} I_{b\eta}(T) \delta(k_m - \kappa_\eta(\underline{\phi}_{\text{ref}}, \eta)) d\eta \Big/ f_m(T_{\text{ref}}, \underline{\phi}_{\text{ref}}, k_m), \quad (10)$$

$$a_m(T, T_{\text{ref}}, g_m) = \frac{f_m(T, \underline{\phi}_{\text{ref}}, k_m)}{f_m(T_{\text{ref}}, \underline{\phi}_{\text{ref}}, k_m)}. \quad (11)$$

While f_m varies over many orders of magnitude with thousands of maxima and minima, the weight function $a_m(T, T_{\text{ref}}, g_m)$ is much better behaved [11,13], facilitating integration. Note that the correlated $k(\underline{\phi}, k_m)$ was rewritten as [13]

$$k(\underline{\phi}, k_m) = k(T_{\text{ref}}, \underline{\phi}, g_m), \quad (12)$$

where $k(T_{\text{ref}}, \underline{\phi}, g_m)$ is the inverse of $g_m(T_{\text{ref}}, \underline{\phi}, k_m)$ given by Eq. (8). This is a consequence of the assumption of correlated

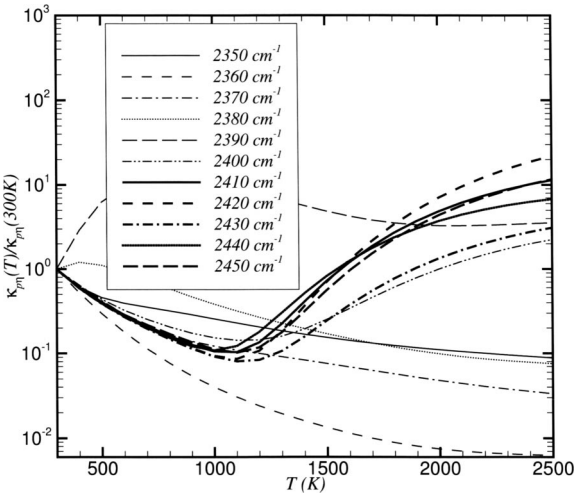

Fig. 3 The scaling function u_η for several spectral locations across the 2350–2450 cm^{-1} spectral range of CO_2, where, $\underline{\phi}_0$ = (300 K, 1 bar, 10 percent)

k-distributions, postulating that $f_m(T, \underline{\phi}, k_m)$ and $f_m(T, \underline{\phi}_{\text{ref}}, k_m)$ have identical cumulative k-distributions g_m (for any Planck function temperature). Therefore, evaluation of I_{gm} requires the precalculation of two sets of full-spectrum k-distributions for each of the M spectral groups: (i) k-distributions $f_m(T, \underline{\phi}_{\text{ref}}, k_m)$, evaluated for the absorption coefficient taken at reference conditions and for all Planck function temperatures (for the determination of a_m), and (ii) k-distributions $f_m(T_{\text{ref}}, \underline{\phi}, k_m)$, with the absorption coefficient evaluated at local conditions, but the Planck function only at the reference temperature [for the evaluation of $k(T_{\text{ref}}, \underline{\phi}, g_m)$]. Once I_{gm} has been found using any arbitrary RTE solution method; total intensity is determined by summing over all spectral groups and integrating over g-space, i.e.,

$$I = \int_0^\infty I_\eta \, d\eta = \sum_{m=1}^{M} \int_0^1 I_{gm} dg. \quad (13)$$

Note that the reference state $\underline{\phi}_{\text{ref}}$ is the only state where the absorption coefficient is taken in its exact form and that a correlated absorption coefficient is assumed for all other states. Therefore, it is important to choose an optimal reference state for each problem at hand. While any arbitrary value can be used for the reference Planck function temperature, it is usually set to the same value as the temperature for the reference state $\underline{\phi}_{\text{ref}}$. The proper choice of the reference state has been discussed by Modest and Zhang [11] and the same methodology has been followed in this paper.

Databasing of Spectral Groups. To aid with the grouping of spectral location it is of advantage to observe the typical behavior of the scaling function

$$u_\eta(\underline{\phi}, \underline{\phi}_0, \eta) = \frac{\kappa_\eta(\underline{\phi}, \eta)}{\kappa_\eta(\underline{\phi}_0, \eta)}, \quad (14)$$

as it varies across the spectrum, where $\underline{\phi}_0$ is any arbitrary standard state to be compared with (and is not related to the reference state of the previous section). Some typical results are shown in Figs. 3 and 4 for a CO_2-air mixture containing 10 percent CO_2, for a few selected spectral locations across the 2350–2450 cm^{-1} (4.3 μm band) and 3400–3500 cm^{-1} (2.7 μm band) ranges. This behavior is seen to be consistent for all spectral locations, and also consistent with theoretical predictions for the absorption coeffi-

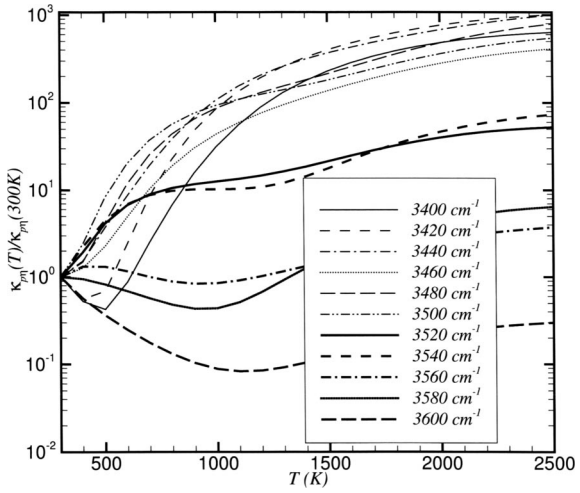

Fig. 4 The scaling function u_η for several spectral locations across the 3400–3500 cm^{-1} spectral range of CO_2, where $\underline{\phi}_0$ =(300 K, 1 bar, 10 percent)

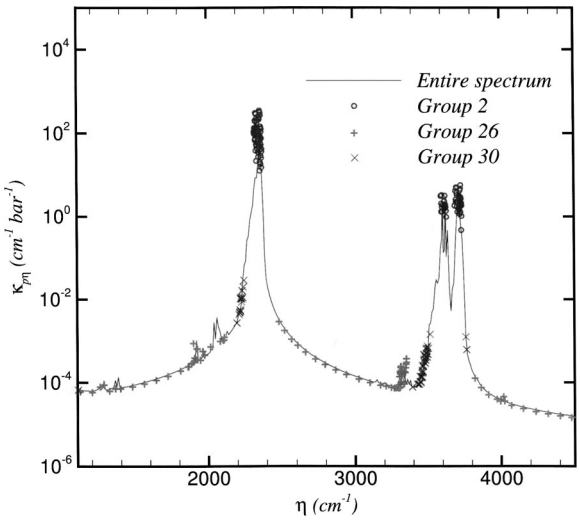

Fig. 6 The absorption coefficient spectrum of CO_2 at 300 K and 1 bar, together with three typical spectral groups for CO_2

cient: for a spectral location dominated by cold lines at 300 K, the scaling function first decreases as predicted from the temperature dependence of the rotational and vibrational partition function and of line widths [17]. At some elevated temperature ''hot lines'' with large lower-level energies wake up, causing a strong increase in u. Based on a thorough investigation of CO_2 scaling function behavior, a set of 32 scaling functions were chosen as

$$u_m(T,x;T_0,x_0) = \frac{1+bx\sqrt{\frac{T_0}{T}}+A_m\left[1+bx\left(\frac{T_0}{T}\right)^2\right]e^{-E_m/T}}{1+bx_0\sqrt{\frac{T_0}{T}}+A_m\left[1+bx_0\left(\frac{T_0}{T}\right)^2\right]e^{-E_m/T_0}}\left(\frac{T_0}{T}\right)^{n_m}, \tag{15}$$

and are shown in Fig. 5 (here arbitrarily normalized with T_0 =300 K and x_0=0.1 for better discernibility). Each of the scaling functions is defined by the three parameters A_m, E_m, and n_m, and a self broadening-to-air broadening coefficient is defined as

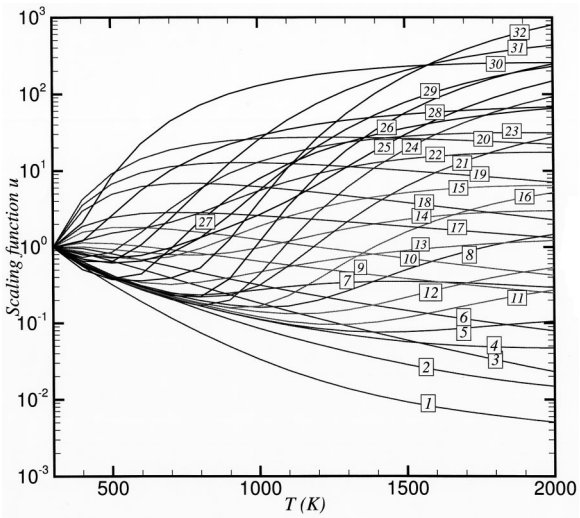

Fig. 5 Standard scaling functions for CO_2

$$b=\frac{b_{\text{self}}}{b_{\text{air}}}-1, \tag{16}$$

where b_{self} is line width due to self broadening, and b_{air} the one due to air broadening. This ratio is fairly constant across the entire spectrum for all gases. For CO_2, it is approximately 0.3, which was chosen for all 32 groups here. With the group of scaling functions defined, a scan is made across the entire spectrum (in steps of $\Delta\eta$=0.01 cm^{-1}), evaluating the absorption coefficient from the HITEMP database [14] at a standard mole fraction of x_0=0.1, for a large set of J (=23) temperatures 300 K$\leqslant T_j \leqslant$2500 K. The spectral group into which wavenumber η_i is placed, $m(\eta_i)$, is found by obtaining the group m, which minimizes

$$\sum_{j=1}^{J}\left[u(T_j,x_0;T_0,x_0;\eta_i)-u_m(T_j,x_0;T_0,x_0)\right]^2=\min. \tag{17}$$

Figure 6 shows the 2.7 and 4.3 μm CO_2 bands at 300 K and 1 bar, together with which spectral locations are sorted into three typical spectral groups for CO_2 (low resolution spectral data were used for better visualization). The circle symbols are the absorption coefficients of Group 2, which is a group dominated by ''cold'' lines, usually making up the center of a band. Group 30 is shown as $\times$ symbols in Fig. 6, representing a group dominated by ''hot'' lines, generally located in the band wings. Finally, the + symbols are the absorption coefficients of Group 26, which is dominated by ''cold'' lines at low temperatures, with ''hot'' lines waking up at an intermediate temperature, as shown in Fig. 5; such behavior is found in the low-absorption regions between bands. Note that, once determined, all spectral locations stay in their specific group, independent of the local state of the gas, $\underline{\phi}$. The same scheme for spectral grouping can be applied to other absorbing gases [18].

The full-spectrum k-distributions and their inverse $k_m(T_0,\underline{\phi},g_m)$ may now be calculated for each group and all states $\underline{\phi}$. Making the assumption of correlated absorption coefficients, these distributions may be compared with those evaluated at the standard state $\underline{\phi}_0$, leading to

$$u_{mg}(\underline{\phi},\underline{\phi}_0,g_m)=\frac{k_m(T_0,\underline{\phi},g_m)}{k_m(T_0,\underline{\phi}_0,g_m)}. \tag{18}$$

As an example, these scaling functions, for $\underline{\phi}$ =(2000 K, 1 bar, 10 percent) and $\underline{\phi}_0$=(300 K, 1 bar, 10 percent), are shown in Fig. 7 for all 32 spectral groups of CO_2. Note

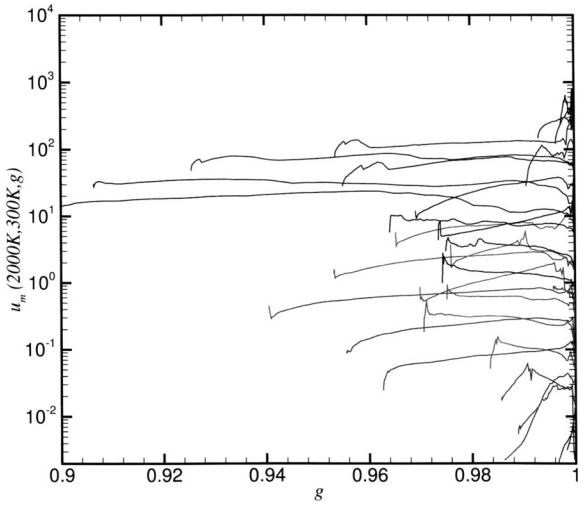

Fig. 7 Variation of scaling function u_m(2000 K,300 K, g) with cumulative k-distribution g for CO_2 base groups

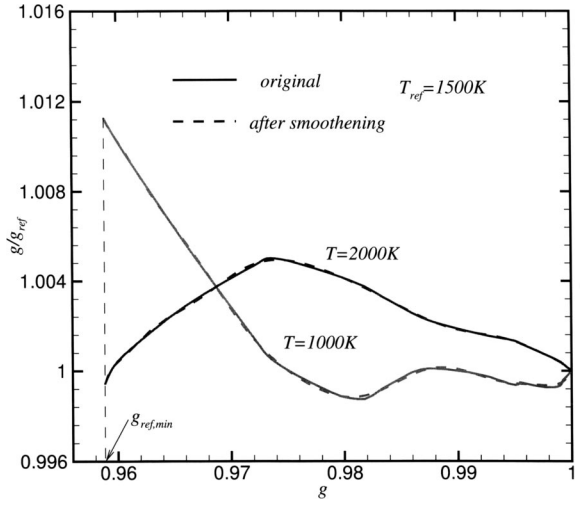

Fig. 8 Original and smoothened cumulative k-distribution stretching factor g/g_{ref}

that, for each spectral group, the cumulative k-distribution ranges from a $g_{m,\min}$ to 1. A large range of $(1-g_{m,\min})$ indicates that group m occupies a large part of the (Planck function weighted) spectrum. All ranges summed together must add to unity. Not surprisingly, the g-dependence of these scaling functions is weak: because of grouping criteria, the scaling function for each wavenumber comprising group m should have a scaling function closely following $u_m(\phi,\phi_0)$, i.e., should be independent of g_m. Therefore, at the 32-group level, we may assume the absorption coefficient not only to be correlated, Eq. (1), but scaled, obeying Eq. (2),

$$\kappa_\eta(\underline{\phi},\eta)=\kappa_\eta(\underline{\phi}_0,\eta)u_m(\underline{\phi},\underline{\phi}_0),\eta\in[\eta_m]. \tag{19}$$

This will allow the construction of a much more compact database with little additional loss of accuracy. The standard state for the database is taken as $\underline{\phi}_0=(T_0=1500\ \mathrm{K},p_0=1\ \mathrm{bar},x_0=0.1)$ simply for convenience, and should not be confused with the reference state (ϕ_{ref}) needed in Eq. (9) to recast the RTE as a function of cumulative k-distribution. Since the absorption coefficient is databased as scaled values at the 32-group level, the choice of reference state for 32GFSCK model is arbitrary. However, when groups are combined, the resulting absorption coefficient is no longer scaled, and an optimal choice for a reference state becomes important.

With 32 groups for CO_2 and the Planck function temperature ranging from 300K to 2500K (23 temperatures), 32×23 k-distributions, $k_m(T_j,\underline{\phi}_0,g_m)$ $(j=1,\cdots,23;m=1,\cdots,32)$ have been evaluated and databased. The k-distributions at any nonstandard state $\underline{\phi}$ can then be calculated as

$$k_m(T_j,\underline{\phi},g_m)=k_m(T_j,\underline{\phi}_0,g_m)u(\underline{\phi},\underline{\phi}_0) \tag{20}$$

For most groups, the preassigned values for A_m, E_m, and n_m are sufficient for use in Eq. (19); however, for a few groups the differences between u_{mg} [from Eq. (18)] and u_m [from equation (15)] were large enough to call for slight adjustments. This was done by first finding average scaling functions

$$\langle u_m\rangle(\underline{\phi},\underline{\phi}_0)=\frac{\int_{g_{m,\min}}^{1}u_{gm}(\underline{\phi},\underline{\phi}_0,g_m)w(g_m)dg_m}{\int_{g_{m,\min}}^{1}w(g_m)dg_m}, \tag{21}$$

where $w(g_m)$ is a weight function (set to unity in our calculations). This is followed by adjusting the values for A_m, E_m, and n_m to minimize the function

$$\int_T\int_x(u_m-\langle u_m\rangle)^2dxdT=\min. \tag{22}$$

Weight Function *a*. For each of the 32 spectral groups for CO_2, the full-spectrum k-distributions can be calculated and databased. The required number of data points and, thus, the efficiency of the database is greatly affected by the smoothness of the weight function a defined in Eq. (11). This function is the ratio of two k-distributions, or, the ratio of the slopes of two cumulative k-distributions (evaluated at Planck function temperatures of T and T_{ref}, respectively). Therefore, the weight function is very sensitive to the structure of the k-distributions, (even though its behavior is much better than that of f itself [11]). While Modest and Zhang [11] have discussed the evaluation of the weight function, this becomes critical for the construction of a database. Noisy weight functions will have detrimental effects on quadrature efficiency, in particular for groups with holes (ranges of absorption coefficient not present in the spectral group under consideration) in their k-distributions. Therefore, the k-distributions were smoothened, in order for them to produce smoothly varying weight functions a. This was achieved by first smoothening $g_m(T,\underline{\phi}_0,k)/g_{m,0}(T_0,\underline{\phi}_0,k)$, since a in Eq. (11) is evaluated as $dg_m/dg_{m,\mathrm{ref}}$ (at identical values of k), where $\underline{\phi}_0=(T_0=1500\ \mathrm{K},p_0=1\ \mathrm{bar},x_0=0.1)$ is the database standard state. Since the weight functions a are stretching factors for the cumulative k-distribution at different Planck function temperatures, it is important to preserve the following integral during the smoothening process:

$$\int_{g_{m,0,\min}}^{1}adg_{m,0}=\int\frac{dg_m}{dg_{m,0}}dg_{m,0}=\int_{g_{m,\min}}^{1}dg_m=1-g_{m,\min} \tag{23}$$

Figure 8 shows the original and smoothened $g_{14}(2000\ \mathrm{K},\underline{\phi}_0,k)/g_{14,0}(1500\ \mathrm{K},\underline{\phi}_0,k)$ and $g_{14}(1000\ \mathrm{K},\underline{\phi}_0,k)/g_{14,0}(1500\ \mathrm{K},\underline{\phi}_0,k)$ for Group 14 of CO_2, whose unsmoothened

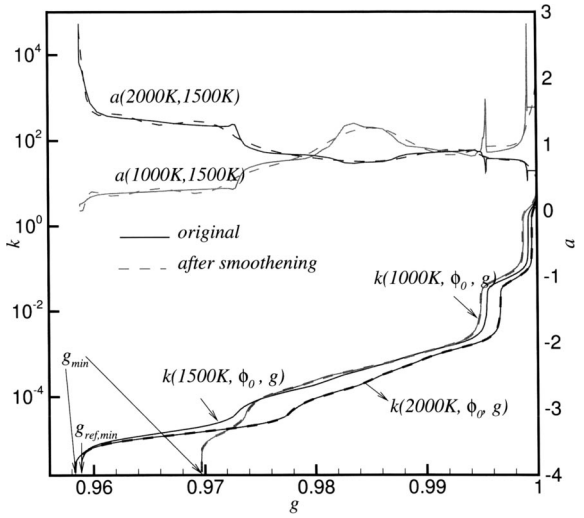

Fig. 9 Original and smoothened weight functions *a* and cumulative *k*-distributions

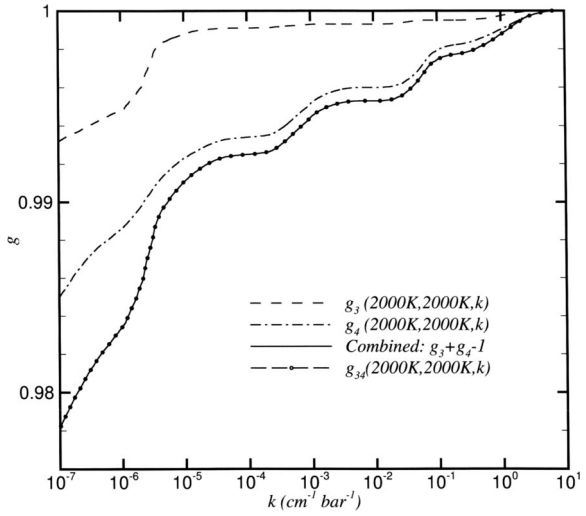

Fig. 10 Combination of two spectral groups into one (CO_2 groups 3 and 4)

a function is very noisy, especially near holes in the *k*-distribution. A smoothened *k*-distribution, for nonstandard conditions, can then be calculated from the standard *k*-distribution as

$$g_m^{(s)}(T,\underline{\phi}_0,k)=g_{m,0}(T_{\text{ref}},\underline{\phi}_0,k)\left(\frac{g_m}{g_{m,0}}\right)^{(s)}, \tag{24}$$

where (s) stands for ''smoothened values.'' Figure 9 shows the *k*-distributions at different Planck function temperature and the corresponding *a* function for Group 14 of CO_2, with the absorption coefficient evaluated at $\underline{\phi}_0$. It can be seen that a very small change in the *k*-distribution function (nearly indiscernible) results in a much smoother *a* function.

Since different absorption coefficient regions may become important at different optical thicknesses, the database for the 32 groups of CO_2 was constructed with 100 *k*-boxes (values), allowing the user to choose proper quadrature points, depending on the problem at hand. With 32 groups, and 23 Planck function temperatures and 100 *k*-boxes (values) for each group, the size of the database is about 1 Megabyte.

Combination of Spectral Groups. For greater numerical efficiency (accompanied by a slight loss of accuracy), the spectral groups from the database can be combined to obtain coarser group models ($N=1,2,4,\cdots$). While the absorption coefficient can be assumed to be scaled at the 32 group level, this is clearly not true after combining groups, unless a new scaling function is determined after each grouping, following the guidelines of Modest and Zhang [11]. However, if we simply assume that each group has a correlated absorption coefficient, then, since there is no overlap between different spectral groups, the *k*-distributions are additive, and one obtains

$$f_n(T,\underline{\phi},k)=\sum_{m=m_{\min}(n)}^{m_{\max}(n)} f_m(T,\underline{\phi},k), \tag{25}$$

where *n* is the new group resulting from combining a number of basic groups. Since each nonoverlapping group is populated only across $g_{\min}<g<1$, the cumulative *k*-distribution for the combined group becomes

$$\int_k^\infty f_n(T,\underline{\phi},k)dk=\int_k^\infty \sum_m f_m(T,\underline{\phi},k)dk=\sum_m \int_k^\infty f_m(T,\underline{\phi},k)dk \tag{26}$$

or

$$1-g_n=\sum_m (1-g_m)=N_n-\sum_m g_m,$$

$$N_n=m_{\max}(n)-m_{\min}(n)+1 \tag{27}$$

i.e.,

$$g_n(T,\underline{\phi},k)=\sum_m g_m(T,\underline{\phi},k)-N_n+1. \tag{28}$$

This relation may be inverted to give k_n as a function of the combined group's cumulative *k*-distribution *g*,

$$k_n(T,\underline{\phi},g_n)=g_n^{-1}(T,\underline{\phi},k_n). \tag{29}$$

This is demonstrated in Fig. 10, where Groups 3 and 4 were combined and the combined *k*-distribution essentially coincides with the *k*-distribution calculated directly from the HITEMP database [the only errors coming from the scaling in Eq. (20) and the smoothening of equation (24)].

Use of the Database. Solving a general radiation problem using *N* different spectral groups requires the solution of the RTE, Eq. (9), for each of the *N* spectral groups. This in turn, requires (i) definition of an optimal global reference state $\underline{\phi}_{\text{ref}}$, at which the absorption coefficient and its *k*-distribution are calculated ''exactly''; (ii) precalculation of a set of *k*-distributions $k_n(T_{\text{ref}},\underline{\phi},g_m)$ for each group, i.e., absorption coefficient evaluated at local state $\underline{\phi}$, Planck function at T_{ref}, and (iii) precalculation of a set of *k*-distributions $k_n(T,\underline{\phi}_{\text{ref}},g_m)$ for each group, i.e., absorption coefficient evaluated at the reference state $\underline{\phi}_{\text{ref}}$, Planck function at local temperature *T* (for the evaluation of the weight function *a*). These distributions are extracted from the database as follows:

Step 1. A global reference state is chosen along the guidelines of Modest and Zhang [11], i.e., the Planck mean temperature as reference temperature and the volume-averaged mole fraction as reference mole fraction.

Step 2. Keeping in mind that the database uses a standard state of $\underline{\phi}_0=$(1500 K, 1 bar, 10 percent), one finds for each of the 32 groups

$$k_m(T,\underline{\phi},g)=k_m(T,\underline{\phi}_0,g)u_m(\underline{\phi},\underline{\phi}_0). \tag{30}$$

At this point $k_m(T,\underline{\phi},g)$ is available for all Planck function temperatures (including T_{ref}) and local states $\underline{\phi}$ (including $\underline{\phi}_{\text{ref}}$) in the form of 100 pairs of points $(k_{m,i},g_{m,i})$.

Step 3. If groups are to be combined into an N-group model for greater numerical efficiency, this is now done through the use of Eq. (28). In the database, groups are numbered in such a way that groups with similar scaling function u_m are always next to each other, so adjacent groups should be combined. This results in 100 pairs of points $(k_{n,i},g_{n,i})$ for the N combined groups.

Step 4. For all Planck function temperatures T, the weight functions $a_n(T,T_{\text{ref}},g_n)$ are calculated from the smoothened k-distributions as

$$a_{n,i}=\left.\frac{dg_n(T,\underline{\phi}_{\text{ref}})}{dg_n(T_{\text{ref}},\underline{\phi}_{\text{ref}})}\right|_{k=k_{n,i}}\approx\frac{g_{n,i+1}(T,\underline{\phi}_{\text{ref}})-g_{n,i-1}(T,\underline{\phi}_{\text{ref}})}{g_{n,i+1}(T_{\text{ref}},\underline{\phi}_{\text{ref}})-g_{n,i-1}(T_{\text{ref}},\underline{\phi}_{\text{ref}})}. \tag{31}$$

Step 5. A set of J quadrature points, say $J=10$, is chosen for the problem at hand to eventually carry out the integration in Eq. (13) as

$$I=\sum_n I_n=\sum_n \int_{g_{n,\min}}^{1} I_{g,n}dg_n\approx\sum_n\sum_{j=1}^{J} w_j I_{g,n}(g_{n,j}), \tag{32}$$

where the w_j and $g_{n,j}$ are quadrature weights and points, respectively. For this operation, the data sets for $k_n(T_{\text{ref}},\underline{\phi},g_n)$ and $a_n(T,T_{\text{ref}},g_n)$ are reduced to the corresponding J values each.

Step 6. Given the necessary set of k_n and a_n values, the RTEs for each of the n groups are solved and results collected according to Eq. (32).

Sample Calculations

The Multi-Group approach and the 32-group database for CO_2 are tested in this section by considering several one-dimensional slabs of gas mixtures with varying temperatures and mole fractions. A uniform mixture of 10 percent CO_2-90 percent N_2 (by volume) at 1 bar, confined between two infinite, parallel, cold and black plates, is considered first to test the validity of the model in situations of extreme temperature changes. An isothermal hot layer of 2000 K with a fixed width of 50 cm is adjacent to an isothermal cold layer at 300 K of varying width. The radiative heat flux exiting the cold column is studied and is shown in Fig. 11, with LBL calculations serving as benchmark. For simplicity, a simple trapezoidal rule was used in the LBL calculations (with a resolution of 0.01 cm^{-1}) and the accuracy of the LBL results should be expected to be within $\approx$1 percent. The Multi-Group FSCK results calculated directly from the HITEMP database are shown by lines, while the symbols represent results using the 32-group database for CO_2, which assumes a scaled absorption coefficient at the 32 group level. The 32-group model, with its scaled absorption coefficient, is independent of the choice of reference state, while for combined groups, the reference state recommended by Modest and Zhang [11] was used. As can be seen from Fig. 11, the direct FSCK results and those from the database are in very good agreement. Note that there is a substantial improvement when going from a single group model (FSCK) to a 2GFSCK model, with the maximum error changing from 11 percent to less than 4 percent. The improvement from 2GFSCK to 4GFSCK is not as large and LBL accuracy can essentially be achieved with 8 or more groups (within the limits of quadrature error for both LBL and FSCK).

The next example considers a CO_2-N_2 gas mixture with both a step in temperature and a step in mixture ratio. The medium is again a one-dimensional slab with a hot layer (2000 K, 20 percent CO_2, 50 cm width) adjacent to a cold layer (300 K, 50 percent CO_2, with varying cold layer l_c). The wall next to the hot layer is at 1000 K and that next to the cold layer is at 0 K, with both walls

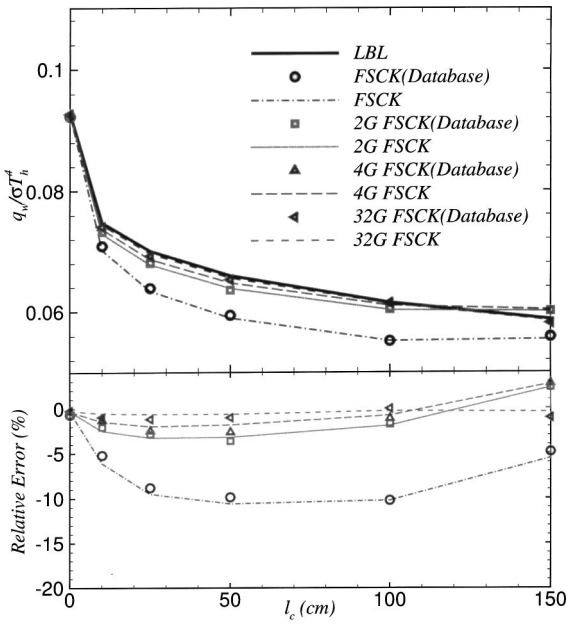

Fig. 11 Radiative flux exiting from the cold column of a two-column CO_2-nitrogen mixture at different temperatures ($T_{\text{hot}}=2000$ K, $l_{\text{hot}}=50$ cm; $T_{\text{cold}}=300$ K, l_{cold} variable; uniform $p=1$ bar, $x_{CO_2}=0.1$, cold and black walls on both sides) and their relative error compared with the LBL benchmark

black. The radiative heat flux exiting the cold column of this mixture is shown in Fig. 12, leading to the same conclusions as the results of Fig. 11. A number of other cases were studied and the same conclusions can be drawn: a substantial improvement occurs when going from a single group model to a 2GFSCK model; LBL accuracy can be approached with 8 groups. However, combining groups using the assumption of correlatedness makes the 8-group model dependent on the chosen reference state, $\underline{\phi}_{\text{ref}}$, and thus

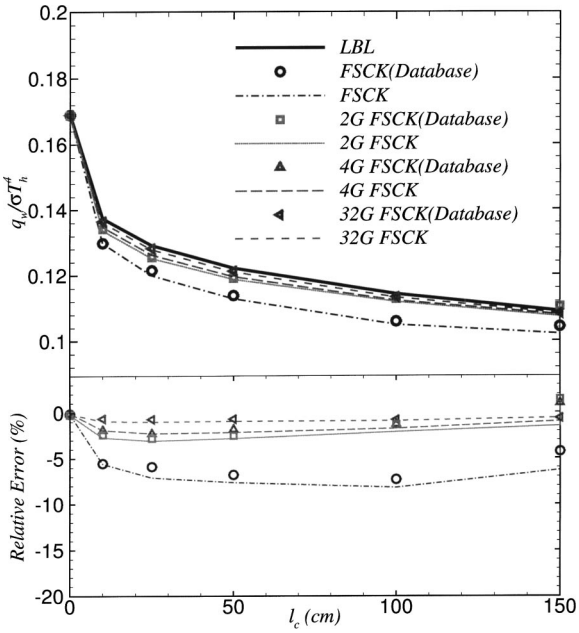

Fig. 12 Same as Fig. 11, except that $x_{\text{hot}}=0.2$, $x_{\text{cold}}=0.5$ and the left wall is at 1000 K

cannot be databased efficiently (in contrast to the 32-group model, which uses a scaled absorption coefficient and is, thus, independent of the reference state).

Summary and Conclusions

A multi-Group Full-Spectrum Correlated *k*-distribution model (MGFSCK) has been developed, in which the spectral locations are broken up into N spectral groups, based on their absorption coefficient dependence on (partial) pressure and temperature. Like all *k*-distribution based methods, the MGFSCK model can be used with any desired RTE solution method. Like all global models, the MGFSCK method is limited to gray scattering and gray walls. And, like with the 1-group full-spectrum *k*-distribution method (FSK), mixing gases through the multi-group *k*-distributions is problematic, requiring further investigation. A 32-group database based on HITEMP was built for CO_2 and tested for problems with large temperature gradients and sharp mole fraction changes. It was found that the MGFSCK model and the CO_2 database provides very accurate results for radiative heat transfer calculations and LBL accuracy can be approached at very affordable cost. While LBL calculations may need 1 million spectral calculations, the Multi-Group approach needs only 10–15 [spectral calculations]$\times N$ [number of groups used]. The database for CO_2 has a size of 1 Megabyte and is available upon request.

Acknowledgment

The authors gratefully acknowledge the financial support of the National Science Foundation under the contract CTS-0112423.

Nomenclature

a = weight function for FSCK method
A = parameter in the scaling function
b = self broadening-to-air broadening coefficient
b_{self} = self-broadening line half-width, cm^{-1}
b_{air} = air-broadening line half-width, cm^{-1}
E = parameter in the scaling function, K
f = *k*-distribution function, cm
g = cumulative *k*-distribution
I = radiative intensity, $\text{W/m}^2\text{sr}$
k = absorption coefficient variable, cm^{-1}
k_η = spectral absorption coefficient at reference state, cm^{-1}
l = geometric length, m
n = scaling function parameter
p = pressure, bar
q = radiative heat flux, W/m^2
s, s' = distance along path, m
T = temperature, K
u = scaling function for absorption coefficient
w = weight function
$x, \underline{x}$ = mole fraction (vector)

Greek Symbols

η = wavenumber, cm^{-1}
$\underline{\phi}$ = composition variable vector
Φ = scattering phase function
κ = absorption coefficient, cm^{-1}
Ω = solid angle, sr
σ_s = scattering coefficient, cm^{-1}

Subscripts

0 = standard state for database
b = blackbody emission
j = line or bin
m = spectral group
max = maximum
min = minimum
P = Planck Mean
ref = reference condition for problem at hand
w = wall
η = spectral

References

[1] Lacis, A. A., and Oinas, V., 1991, "A Description of the Correlated-*k* Distribution Method for Modeling Nongray Gaseous Absorption, Thermal Emission, and Multiple Scattering in Vertically Inhomogeneous Atmospheres," J. Geophys. Res., **96**(D5), pp. 9027–9063.

[2] Goody, R. M., and Yung, Y. L., 1989, *Atmospheric Radiation-Theoretical Basis*, 2nd ed., Oxford University Press, New York.

[3] Goody, R. M., West, R., Chen, L., and Crisp, D., 1989, "The Correlated *k* Method for Radiation Calculations in Nonhomogeneous Atmospheres," J. Quant. Spectrosc. Radiat. Transf., **42**, pp. 539–550.

[4] Fu, Q., and Liou, K. N., 1992, "On the Correlated *k*-Distribution Method for Radiative Transfer in Nonhomogeneous Atmospheres," J. Atmos. Sci., **49**(22), pp. 2139–2156.

[5] Denison, M. K., and Webb, B. W., 1993, "A Spectral Line Based Weighted-Sum-of-Gray-gases Model for Arbitrary RTE Solvers," ASME Journal of Heat Transfer , **115**, pp. 1004–1012.

[6] Denison, M. K., and Webb, B. W., 1995, "The Spectral-Line-Based Weighted-Sum-of-Gray-Gases Model in Nonisothermal Nonhomogeneous Media," ASME Journal of Heat Transfer , **117**, pp. 359–365.

[7] Hottel, H. C., and Sarofim, A. F., 1967, *Radiative Transfer*, McGraw-Hill, New York.

[8] Modest, M. F., 1991, "The Weighted-Sum-of-Gray-Gases Model for Arbitrary Solution Methods in Radiative Transfer," ASME Journal of Heat Transfer , **113**(3), pp. 650–656.

[9] Rivière, Ph., Soufiani, A., Perrin, M. Y., Riad, H., and Gleizes, A., 1996, "Air Mixture Radiative Property Modelling in the Temperature Range 10000–40000 K," J. Quant. Spectrosc. Radiat. Transf., **56**, pp. 29–45.

[10] Pierrot, L., Rivière, Ph., Soufiani, A., and Taine, J., 1999, "A Fictitious-Gas-Based Absorption Distribution Function Global Model for Radiative Transfer in Hot Gases," J. Quant. Spectrosc. Radiat. Transf., **62**, pp. 609–624.

[11] Modest, M. F., and Zhang, H., 2002, "The Full-Spectrum Correlated-*k* Distribution For Thermal Radiation from Molecular Gas-Particulate Mixtures," ASME Journal of Heat Transfer , **124**(1), pp. 30–38.

[12] Zhang, H., and Modest, M. F., 2002, "A Multi-Level Full-Spectrum Correlated-*k* Distribution For Radiative Heat Transfer in Inhomogeneous Gas Mixtures," J. Quant. Spectrosc. Radiat. Transf., **73**(2–5), pp. 349–360.

[13] Modest, M. F., 2003, "Narrow-Band and Full-Spectrum *k*-Distributions for Radiative Heat Transfer—Correlated-*k* versus Scaling Approximation," J. Quant. Spectrosc. Radiat. Transf., **76**(1), pp. 69–83.

[14] Rothman, L. S., Camy-Peyret, C., Flaud, J.-M., Gamache, R. R., Goldman, A., Goorvitch, D., Hawkins, R. L., Schroeder, J., Selby, J. E. A., and Wattson, R. B., 2000, "HITEMP, the High-Temperature Molecular Spectroscopic Database," available through http://www.hitran.com.

[15] Modest, M. F., and Bharadwaj, S. P., 2002, "High-Resolution, High-Temperature Transmissivity Measurements and Correlations for Carbon Dioxide-Nitrogen Mixtures," J. Quant. Spectrosc. Radiat. Transf., **73**(2–5), pp. 329–338.

[16] Modest, M. F., 2003, *Radiative Heat Transfer*, 2nd ed., Academic Press, New York.

[17] Taine, J., and Soufiani, A., 1999, "Gas IR Radiative Properties: From Spectroscopic Data to Approximate Models," in *Advances in Heat Transfer*, **33**, Academic Press, New York, pp. 295–414.

[18] Zhang, H., and Modest, M. F., 2003, "Multi-Group Full-Spectrum *k*-Distribution Database for Water Vapor Mixtures in Radiative Transfer Calculations," *International Journal of Heat and Mass Transfer*, under review.

Radiative Properties of Semitransparent Silicon Wafers With Rough Surfaces

Y. H. Zhou
e-mail: yihui@ufl.edu
Department of Mechanical Engineering,
University of Florida,
Gainesville, FL 32611

Z. M. Zhang
e-mail: zzhang@sununo.me.gatech.edu
George W. Woodruff School of Mechanical Engineering,
Georgia Institute of Technology,
Atlanta, GA 30332

This paper presents a Monte Carlo model for prediction of the radiative properties of semitransparent silicon wafers with rough surfaces. This research was motivated by the need of accurate temperature measurement in rapid thermal processing (RTP) systems. The methods developed in this paper, however, can be applied to various semitransparent materials, such as diamond films. The numerically obtained bidirectional reflectance distribution function (BRDF) showed a similar trend as the experimental data. Furthermore, a higher angular resolution can be achieved by simulation than by experiments. The bidirectional transmittance distribution function (BTDF) can also be computed in the same run for semitransparent wafers. Other spectral radiative properties (such as the directional-hemispherical transmittance and reflectance, the emittance and the absorptance) under various surface conditions were computed at various temperatures. The results can help gain a deeper understanding of the radiative behavior of semitransparent materials and may be applied to various fields. [DOI: 10.1115/1.1565089]

Keywords: Heat Transfer, Microstructures, Monte Carlo, Properties, Radiation, Roughness

Introduction

Optical properties of materials have been extensively studied, especially for some industrial materials and theories have been well established. Silicon is one of such materials because of its unique physical and chemical properties, and its application in microelectronics technology and other areas. The temperature and wavelength-dependent optical constants can be obtained through the semi-empirical relations, as summarized in the review by Timans [1]. For a silicon wafer (or film) with parallel smooth surfaces, the radiative properties can be computed theoretically and the results agree with the measured emittance in a broad wavelength region at elevated temperatures [1,2]. On the other hand, the radiative properties of silicon wafers with rough surfaces are still undergoing extensive research, mainly on the emittance and reflectance [3–9].

For a rough surface, both the emission and reflection are related to the roughness parameters. The reflection can be described by the bidirectional reflectance distribution function (BRDF). The BRDF generally consists of three components, i.e., a specular peak, an off-specular lobe, and a diffuse component. Many research groups have measured the emittance and BRDF of rough surfaces. Vandenabeele and Maex [3] and Abedrabbo et al. [4] investigated the effects of backside roughness on the emittance and used a one-parameter model to predict the effective transmittance. Drolen [5] reported the BRDF measurement results for twelve spacecraft thermal control materials. Germer and Asmail [6] and Murray-Colemann and Smith [7] described their goniometric tables for measuring BRDF and surface scattering. Shen et al. [8] measured the BRDF of several silicon wafers, whose root mean square (rms) roughness varies from 0.1 to 1 μm. Shen and Zhang [9] described a bidirectional reflectometer and used it to obtain the in-plane and out-of-plane BRDFs of silicon wafers.

The empirical and physical BRDF models have been applied extensively in computer graphics and machine vision [10,11]. The BRDFs have also been used in the description of earth surface for remote sensing and in the reflectance modeling of LCD displays [12,13]. Numerical and theoretical models have been developed based on either the wave optics or geometrical optics [14,15]. Koenderink et al. [16] derived a BRDF model by assuming that a rough surface is composed of spherical cavities. The so-called ''lunation curve'' can be explained by this kind of pitted surface model. Tang and Buckius [17] developed a statistical model without using ray tracing. Hebb et al. [18] discussed the effect of surface roughness on the radiative properties of patterned silicon wafers assuming that thin-film optics is applicable when the wavelength is long enough.

Rapid thermal processing (RTP) is a promising technique to replace the conventional batch furnace used in the microelectronic fabrication [1]. Lightpipe radiation thermometers (LPRTs) are commonly used to monitor the wafer temperature during the processing. The (intrinsic) emittance, ε, or the effective emittance, ε_{eff}, of the wafer must be determined in advance to correct the thermometer reading [19,20]. At temperatures below about 600°C, lightly doped silicon wafers are semitransparent at wavelengths greater than about 1.2 μm. The wafer emittance not only depends on the doping level and thickness but also depends on surface roughness.

Semitransparent materials also find applications in other areas. Diamond films formed by chemical vapor deposition were used as a protective coating for optical windows [21,22]; semitransparent masks were used in photolithography [23]; semitransparent crystalline silicon solar cells opened new markets in solar architecture and automobile industry for glass sliding roofs [24]. Montecchi et al. [25] studied the transmittance of a slightly inhomogeneous thin film with rough unparallel interfaces. Andersen et al. [26] developed a bidirectional photogoniometer based on digital imaging techniques to measure the BTDF of advanced fenestration materials for building daylight design.

The present work deals with the effects of surface roughness on the radiative properties of silicon wafers. Most available BRDF models are only applicable to opaque (or semi-infinite) media and for radiation incident from an optical sparse medium to an optical dense medium. For a semitransparent wafer, however, one needs to consider the reflection for radiation from the silicon wafer to the interface. To accomplish this task, a statistical model is employed with a random (Gaussian) surface roughness. This model

Contributed by the Heat Transfer Division for publication in the JOURNAL OF HEAT TRANSFER. Manuscript received by the Heat Transfer Division June 26, 2002; revision received November 20, 2002. Associate Editor: G. Chen.

can be applied to various surface roughness profiles including the pitted surface. It is assumed that the global roughness characteristics can be used to represent the local ones. A Monte Carlo method is applied to trace the ray path between the interfaces to simulate the radiative processes in the wafer with one or both surfaces being rough. The radiative properties, including emittance, reflectance, transmittance, BRDF, and BTDF, can be obtained in the same run. The method used here is similar to that used in deriving the BRDF models from geometric optics [15], hence is subject to the same limitation as geometric optics. Tang et al. [27] illustrated the domain of validity (within 20% error) of the geometric optics approximation to be $0.2\lambda/\cos\theta_i<\sigma<2a$, where σ is the rms roughness height, a the surface autocorrelation length, λ the incident radiation wavelength, and θ_i the incidence angle. The interference and polarization effects are not included in the simulation. The effect of wave interferences between two surfaces of the wafer is often negligible with the presence of surface roughness, except when the wavelength is much greater than the rms roughness height. For semitransparent materials, the resulting BRDF and BTDF will have a lateral extent around the illuminating point. It is necessary to ensure that the standard deviation of the distribution radius is small compared with the observation spot [28]. For the lightly doped silicon with $T_w=500°C$, the refractive index is about 3.5. The corresponding critical angle is about 16.6° so that most rays with large polar angles will be absorbed inside the wafer, resulting in a small distribution radius.

The Ray-Tracing Method for the Radiative Properties

For a typical silicon wafer, the rms roughness height σ is much smaller than the wafer thickness, and the diameter of the wafer is much greater than its thickness. As shown in Fig. 1, at the macroscale the wafer surface is flat, at the mesoscale it is articulated, and at the microscale the surface (or micro-facet) is considered flat again. From now on, the term of ''surface'' will be reserved consistently for the macroscale and mesoscale, and the term of ''micro-facet'' for the microscale. It is assumed that the radiation ray is reflected specularly on each micro-facet.

As shown in Fig. 2, the inclination of the micro-facet is denoted by the angle δ between the normal direction of micro-facet and the surface normal of the wafer (macroscale). The slope of the micro-facet is $\tan\delta$, whose statistical distribution is assumed to be a Gaussian function. The probability can then be expressed as

$$p(\tan\delta)=\frac{1}{b\sqrt{\pi}}\exp\left(-\frac{\tan^2\delta}{b^2}\right) \tag{1}$$

where $b/\sqrt{2}$ is the standard deviation of micro-facet slope, or rms slope. The rms roughness, rms slope, and autocorrelation length are related by [14]

$$b=2\sigma/a \tag{2}$$

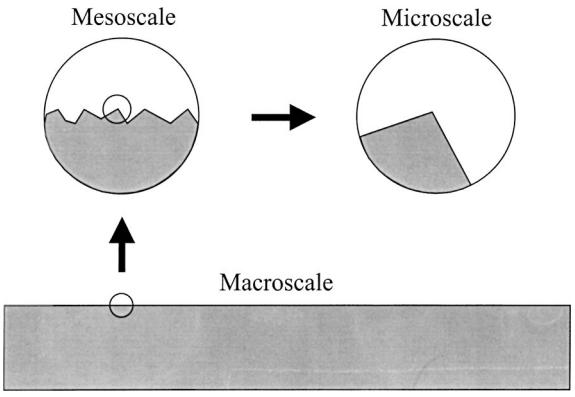

Fig. 1 Surface at different scales

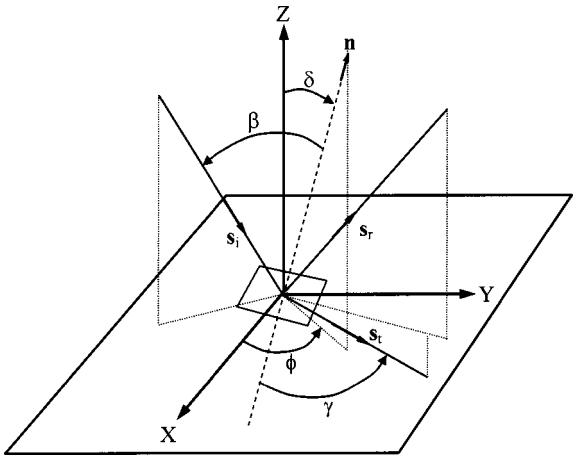

Fig. 2 Reflection and refraction at a micro-facet, where n is the unit normal of the micro-facet. Notice that s_i, s_r, and s_t are the unit directional vectors for the incidence, reflection, and transmission (refraction), respectively.

The specular reflectance is a function of the incidence angle, refractive index, and extinction coefficient. For an unpolarized radiation ray, the specular reflectance can be expressed as

$$\rho=(\rho_p+\rho_v)/2 \tag{3}$$

where ρ_p and ρ_v are the reflectances for parallel and perpendicular-polarized radiation, respectively. Without a coating, ρ_p and ρ_v can be computed from Fresnel's equations by neglecting the small extinction coefficient of lightly doped silicon [29]. In the case when there exists a thin layer of oxide, nitride, or a metallic coating, thin-film optics can be used to compute ρ_p and ρ_v, as in the work of Tang et al. [30]. Coating effects, however, are not included in the present paper, because the emphasis here is on semitransparent wafers.

The statistical model developed by Tang and Buckius [17] based on geometric optics does not require ray-tracing and can be used to calculate the first-, second-, and higher-order scattering for an opaque surface with two-dimensional random roughness. However, this method cannot be easily extended to semitransparent wafers with internal absorption because of the difficulty in handling multiple reflections. The application of ray-tracing method to obtain scattering distribution often starts with the generation of a random rough surface; the reflection at the interface is determined based on the local curvature of the striking point [31]. When both sides of the wafer are rough, the generation of random rough surfaces and the determination of the path length and shadowing functions can be very complicated. In the present study, we present a ray-tracing method that does not require the development of surface profiles. In addition to the assumption that geometric optics is valid, two more assumptions, as discussed above, are also needed for this model to be applicable: (1) the rms roughness height is much smaller than the thickness of the wafer; (2) the lateral extent of multiply reflected rays is much smaller than the beam diameter. In the computation, all the rays are incident on the origin, as shown in Fig. 2, while the orientation of the micro-facet is randomly generated for each ray to simulate the surface roughness.

The procedure begins with illuminating a large number of radiation rays at one surface of the wafer from a specific incident direction (θ_i,ϕ_i). Since the surface is assumed to be isotropic, ϕ_i is set to zero in all calculations. The slope distribution of the micro-facet at the striking point is determined by Eq. (1). There are several ways to deal with a Gaussian distribution, including the rejection technique, look-up table by inverting the cumulative standardized Gaussian distribution, and summation technique ap-

plying the ''central limit theorem'' in probability theory. However, one of the simple ways to calculate the slope is by using two (uniform) random numbers (R_1 and R_2) from

$$\tan \delta = b\sqrt{-\ln R_1}\cos(2\pi R_2) \tag{4}$$

It has been shown in Ref. [32] that $\tan\delta$ obtained from Eq. (4) obeys the Gaussian distribution described by Eq. (1). The absolute value of Eq. (4) is used here to ensure that δ is always positive. Another random number R_3 is used to choose the azimuthal angle of the micro-facet, i.e., $\phi = 2\pi R_3$. As will be discussed later, the azimuthal angle is further limited by the constraint prescribed by shadowing and masking.

After the orientation of the micro-facet is obtained, a new random number R_4 is generated to determine whether ray is reflected. If R_4 is less than the reflectance ρ calculated from Eq. (3), the ray is reflected; otherwise, it will pass through the interface and enter the other medium. Because the micro-facet can be treated as a smooth surface, the reflection angle is equal to the incidence angle and the refraction angle is related to the incidence angle by Snell's law. The direction of reflection or refraction is obtained by a vector analysis. The unit vector of the reflection direction ($\mathbf{s}_r$) is determined from those of the incidence direction ($\mathbf{s}_i$) and the micro-facet normal ($\mathbf{n}$) by

$$\mathbf{s}_r = \mathbf{s}_i + 2\mathbf{n}\cos\beta \tag{5}$$

where β is the incidence angle ($\cos\beta = -\mathbf{s}_i \cdot \mathbf{n}$) as shown in Fig. 2. The unit vector of the refraction direction ($\mathbf{s}_t$) can be expressed as

$$\mathbf{s}_t = \frac{\sin\gamma}{\sin\beta}\mathbf{s}_i + \left(\frac{\sin\gamma}{\tan\beta} - \cos\gamma\right)\mathbf{n} \tag{6}$$

where γ is the refraction angle ($\cos\gamma = -\mathbf{s}_t \cdot \mathbf{n}$). Eqs. (5) and (6) can also be applied to the rays that impinge on the surface from inside the wafer, by reversing the angles of incidence and refraction.

Multiple reflections between micro-facets and the effects of masking and shadowing are considered in the present study. Among all requirements for masking, appropriate values of δ and ϕ must be taken such that the resulting β is less than $\pi/2$. The consideration of shadowing is much more involved. As shown in Fig. 3(*a*), if a radiation ray illuminates a micro-facet and is reflected downward (i.e., the reflection direction still points towards the opposite medium at the interface), then the ray will restrike another micro-facet at the interface from the same medium as before. The associated re-striking probability is unity. Therefore, the preceding process must be repeated, and the micro-facet orientation and the incidence angle need to be updated accordingly for the re-striking ray. On the other hand, Fig. 3(*b*) indicates that a ray is reflected upward and points towards the same medium as the incident ray. In this case, the ray may hit another micro-facet. This phenomenon can be described by a shadowing function, which determines the probability that a reflected ray does not re-strike another micro-facet. The shadowing function introduced by Smith [33] is utilized here, i.e.,

$$p(\theta_r, b) = \left[\frac{b}{\sqrt{\pi}\mu}\exp\left(-\frac{\mu^2}{b^2}\right) - \mathrm{erfc}\left(\frac{\mu}{b}\right) + 1\right]^{-1} \tag{7}$$

where θ_r is the reflection polar angle with respect to the wafer surface, $\mu = \tan(90° - \theta_r)$, and ''*erfc*'' denotes the complementary Gaussian error function. The corresponding re-striking probability is $1-p$, which is plotted in Fig. 3(*c*) as a function of the polar angle of the re-striking ray for several values of a/σ. If the reflected ray does not re-strike another micro-facet, it is counted in the first-order BRDF and reflectance. Otherwise, the ray may be reflected or absorbed by a local micro-facet at the re-striking location. If then the ray is reflected, the preceding process for a ray reflected upward will be repeated until it does not re-strike another micro-facet or is absorbed. An assumption has to be made for the absorption. For an opaque medium with a large absorption coefficient, it is reasonable to assume that a ray is absorbed if the generated random number is greater than the local reflectance. For a semitransparent medium, which is the case in the present study, an appropriate value of thickness of the rough peak in the direction of propagation is needed to compute the absorption probability as discussed in the following paragraph. Here we assume 10 μm as an average thickness. The error caused by this assumption is usually in the high-order scattering and has little effect on the calculated BRDF and reflectance.

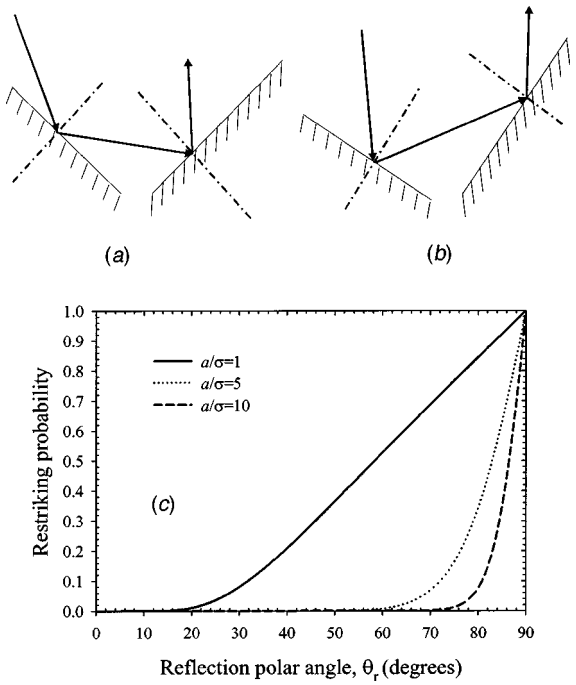

Fig. 3 Re-striking probability: (*a*) rays reflected downward, (*b*) rays reflected upward, and (*c*) re-striking probability for upward reflected rays.

If a ray enters the medium (silicon wafer), it may bounce up and down between the two surfaces of the wafer. The probability for the ray to be absorbed by the medium can be calculated from the actual travel distance d and the absorption coefficient by $1-\exp(-\alpha d)$, keeping in mind that the height of the roughness peak is neglected as compared with the thickness of the wafer. The loss due to scattering is assumed to be negligible because the crystalline wafer can be treated as a homogeneous medium. If a generated random number is greater than the probability of absorption, the ray will travel through the medium and strike the opposite surface. The treatment of the reflection and refraction is similar to those as the ray is incident from the outside. However, total internal reflection must be considered since the ray is from an optically dense medium to an optically sparse medium. The process continues until the ray is absorbed by the medium or leaves either surface of the wafer. The rays leaving from the top surface contribute to the second-order BRDF and reflectance. Those escaped from the bottom surface are counted to the BTDF and transmittance.

As demonstrated in Fig. 3, the rough valleys will entrap some radiation rays outside and inside the medium. The refraction and internal reflection by the rough surface will cause certain rays to be scattered into larger polar angles inside the medium, and therefore, these rays will take a longer path inside the medium. Total internal reflection will trap some rays inside the medium until they are absorbed. As a result, the probability that the ray is absorbed will increase due to surface roughness. The absorptance, which is the ratio of the number of the absorbed rays to the number of incident rays, will therefore be enhanced. The spectral-directional emittance is equal to the spectral-directional absorptance, according to Kirchhoff's law.

The BRDF, defined as the ratio of the reflected radiance (intensity) to the incident irradiance (radiant power flux) [8,9] can be computed by

$$f_r(\theta_i,\phi_i;\theta_r,\phi_r)=\frac{1}{N_i}\frac{\Delta N_r}{\cos\theta_r\Delta\omega_r}, \tag{8}$$

where ΔN_r is the number of rays, reflected at the incidence interface (first-order) and escaped from the medium at same interface (second-order), in the direction (θ_r,ϕ_r) within a solid angle $\Delta\omega_r$, and N_i is the number of incident rays in the direction (θ_i,ϕ_i). The (directional-hemispherical) reflectance is obtained by dividing the total number of rays reflected at the incidence interface and escaped from the medium at the same interface by the total number of incident rays. The BTDF and (directional-hemispherical) transmittance can also be defined and computed using the same method for a semitransparent medium.

Due to the statistic characteristics of the Monte Carlo method, the simulation results cannot be smooth curves or surfaces. The variation is small around the mirror-reflection direction since a large amount of bundle rays are concentrated at this direction. Therefore, the obtained BRDF or BTDF must be post-processed by a low pass filter such as moving average filter to remove noises.

Refractive Index and Absorption Coefficient of Silicon

Although the above ray-tracing method is not limited to silicon materials, the aim of the present paper is to study the radiative properties of semitransparent silicon wafers in rapid thermal processing systems. For lightly doped silicon, there exist different absorption mechanisms that affect the absorption coefficient in different spectral regions. In the near-infrared region, high-energy photons can create electron-hole pairs. Since silicon has an indirect band gap, the transition of electrons is accompanied by phonon emission or absorption [1,34]. The absorption coefficient increases as the photon energy increases. An absorption edge occurs near the band gap with a very low absorption coefficient. Impurities coupled with thermally excited electrons are responsible for the absorption in the mid-infrared. Lattice vibrations also cause some absorption between 6 and 25 μm. The band-gap energy E_g in eV is temperature dependent, and for silicon up to 800°C, it can be expressed as [35]

$$E_g(T)=1.155-4.73\times10^{-4}\frac{T^2}{635+T} \tag{9}$$

where T is in K. The corresponding band-gap wavelength, $\lambda_g=1.24/E_g$ [μm], varies from 1.12 μm at room temperature to 1.43 μm at 1000 K. Various equations for calculating the refractive index and absorption coefficient of lightly doped silicon (dopant concentration less than 10^{15} cm^{-3}) were summarized in the review given by Timans [1]. The calculated refractive index and absorption coefficient as functions of wavelength at different temperatures are shown in Fig. 4 for wavelengths from 1 to 5 μm. The refractive index was obtained using the equation given by Jellison and Modine [36] for $0.4\ \mu\text{m}<\lambda<\lambda_g$ and the equation given by Li [37] for $\lambda_g<\lambda<5\ \mu$m. Extrapolations are made to extend the temperature range to 700°C for both equations. An extension of the wavelength ranges is made for both equations to cover the region around the band gap. Timans [1] showed that these extrapolations agree with experimental data reasonably well. For wavelengths from 0.4 to 0.95 μm, the absorption coefficient is obtained from the equation for calculating the extinction coefficient given by Jellison and Modine [36]. For wavelengths from 0.95 to 5 μm, the absorption coefficient can be calculated as a superposition of the contributions of band-gap absorption and free-electron absorption, since lattice vibration is negligible [3,38].

Notice that the radiation penetration depth is the inverse of the absorption coefficient, i.e., the penetration depth will equal to 0.8 mm (typical wafer thickness) when $\alpha=12.5$ cm^{-1}. One can see from Fig. 4(*b*) that, at wavelengths beyond the absorption edge, lightly doped silicon wafers are essentially transparent at room temperature and semitransparent at temperatures below 700°C. On the other hand, silicon wafers are opaque at wavelengths shorter than 1 μm.

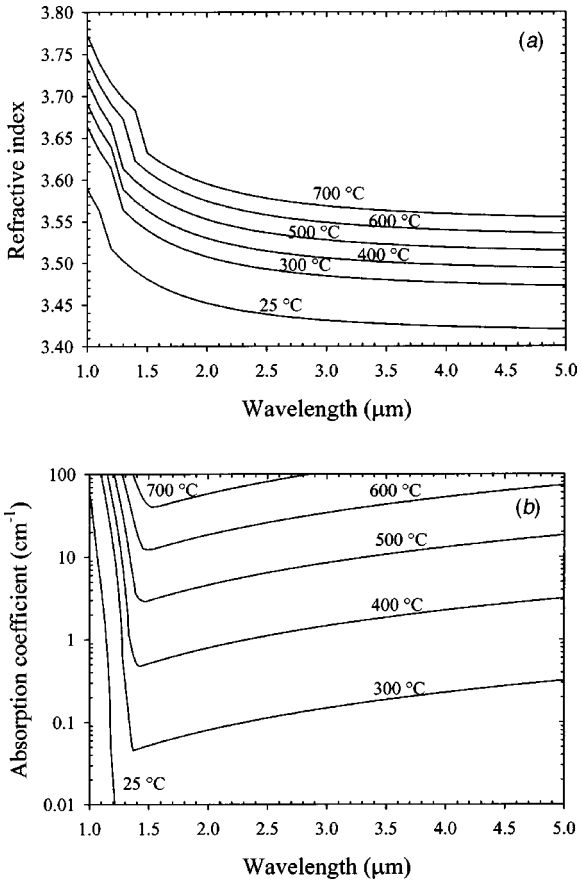

Fig. 4 Calculated (*a*) refractive index and (*b*) absorption coefficient of lightly doped silicon, using equations from Timans [1]

Results and Discussion

The simulation is based on bare silicon wafers with a thickness of 625 μm. The convergence has been carefully tested to ensure meaningful statistical results. For the computation of emittance, reflectance, and transmittance, a total number of one million radiation rays are necessary to achieve a relative error of 0.1%. As to BRDF and BTDF, however, at least 100 million rays must be illuminated to obtain a relative error of 5% when the absolute value is under 0.1. The corresponding relative error of BRDF at the mirror-reflection direction is less than 0.5%, and the computation time is from one to two hours, depending on the values of absorption coefficient and the surface conditions.

The calculated BRDF for a slightly rough and opaque silicon surface at room temperature is shown in Fig. 5 at a wavelength $\lambda=635$ nm. At this wavelength, the refractive index of Si is 3.85. The absorption coefficient is sufficiently large ($\approx$4,000 cm^{-1}) for the wafer to be opaque but the extinction coefficient ($\approx$0.02) is sufficiently small to be neglected in the computation of reflectance by Fresnel's equations. The surface roughness parameter b ($=2\sigma/a$) is 0.2, corresponding to an rms inclination of 8°. The incidence angle θ_i is 45°. A clear specular peak appears at the mirror-reflection direction ($\theta_r=45°$ and $\phi_r=180°$) with a BRDF value of 31.5 sr^{-1}. The angular resolution used for this figure is 1° for polar angle and azimuthal angle, therefore $\Delta\omega_r=(\pi/180)^2\sin\theta_r$, which is a function of θ_r. Because the silicon

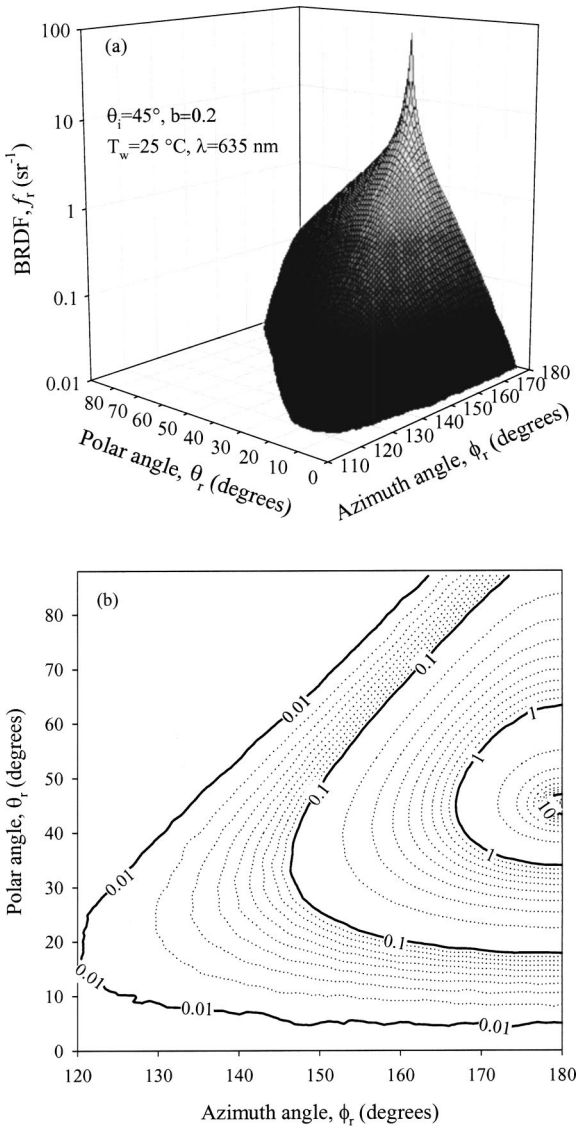

Fig. 5 Calculated BRDF of an opaque surface for incidence angle $\theta_i = 45°$

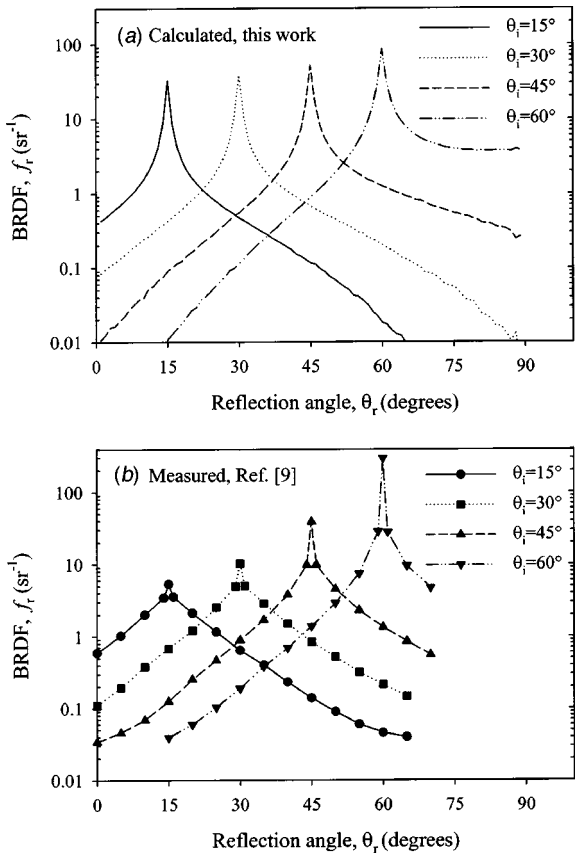

Fig. 6 The in-plane ($\phi_r = 180°$) BRDF for different incidence angles at $\lambda = 635$ nm and for $a/\sigma = 8.7$: (*a*) numerical results; and (*b*) experimental data from Shen and Zhang [9]

surface is isotropic, the BRDF is symmetric about the plane of incidence ($\phi_r = 180°$). The small rms slope contributes to a sharp specular peak. For a one-dimensional random surface, it can be verified that the BRDF has a shape of Gaussian distribution. The portion of BRDF where its values are below about 1 sr^{-1} represents the off-specular lobe.

The calculated in-plane BRDF (i.e., the reflection direction is in the incidence plane or $\phi_r = 180°$) is shown in Fig. 6(*a*) at $\lambda = 635$ nm and for $a/\sigma = 8.7$, as compared with Fig. 6(*b*) the experimental data from Shen and Zhang [9] for a silicon wafer with similar rms roughness slope at the same wavelength. Since the experiments were done with a constant detector area, a constant solid angle, independent of θ_r, must be applied. Corresponding to the half cone angle of 0.5°, the solid angle of 2.39×10^{-4} sr^{-1} is applied only for this figure. The trend of computed BRDF agrees well with the experimental data. For example, the peak values increase with incidence angles. The reciprocity rule of BRDF, which states that $f_r(\theta_i, \phi_i; \theta_r, \phi_r)$ should always equal $f_r(\theta_r, \phi_r; \theta_i, \phi_i)$, can be observed approximately from the curves. The predicted peak BRDF values, however, are greater than measured data at small incidence angles but smaller at large incidence angles. The discrepancies between the predicted and experimental results may be associated with the assumption of this statistical model, that is, it does not completely describe the characteristics of a rough surface. In the present modeling, only one parameter *b* is employed and, as a result, the roughness profile is not fully reserved. Two roughness parameters such as the combination of the standard deviation of height σ and the autocorre-

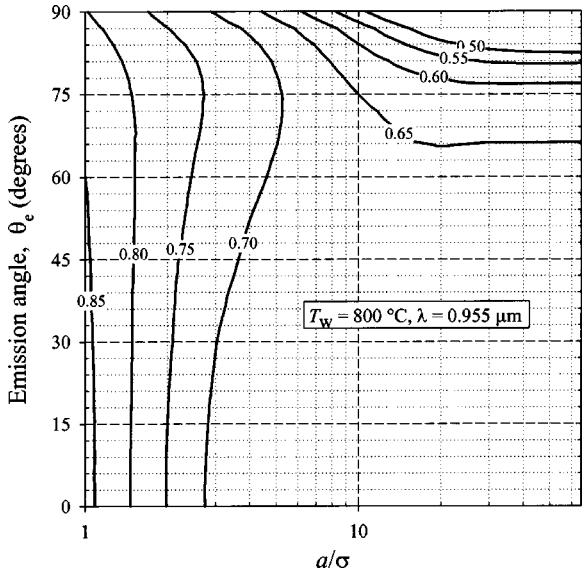

Fig. 7 Contour plot of the emittance of opaque silicon surfaces versus emission angle and the parameter a/σ

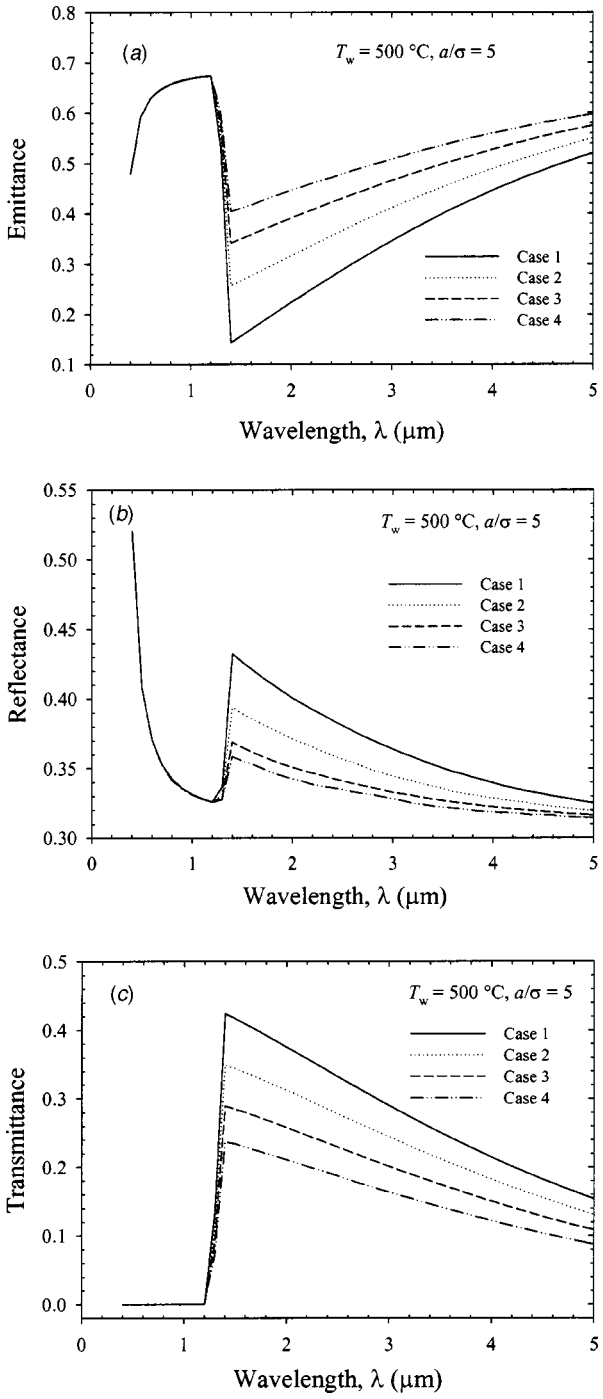

Fig. 8 The spectral radiative properties of 0.625-mm-thick silicon wafer: (*a*) emittance; (*b*) reflectance; and (*c*) transmittance. Case 1. Both surfaces are smooth; Case 2. Only one surface is smooth, the ray is incident on the rough surface; Case 3. Only one surface is smooth, the ray is incident on the smooth surface; Case 4. Both surfaces are rough.

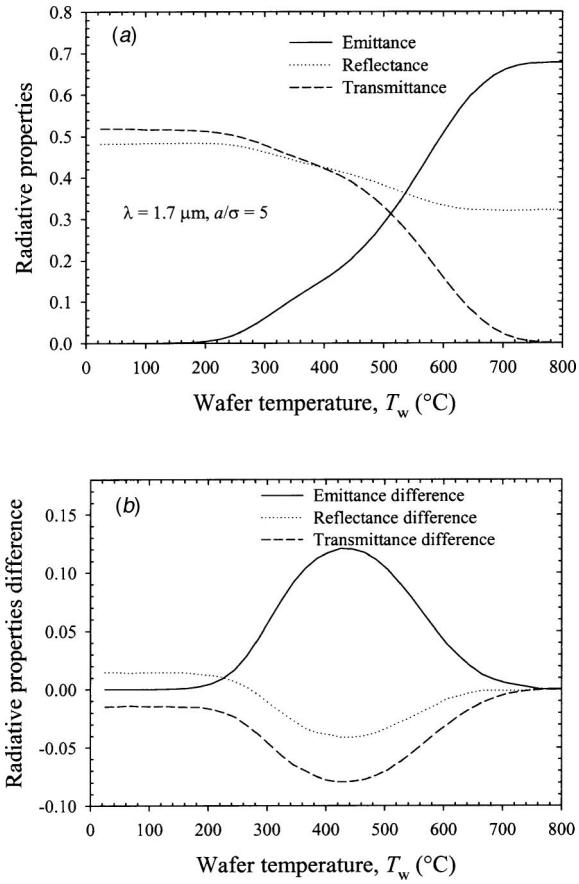

Fig. 9 (*a*) Radiative properties of a 0.625-mm-thick silicon wafer versus wafer temperature, where the radiation is incident on the rough side and the other side is smooth (Case 2); and (*b*) The difference between the radiative properties of Case 2 and Case 1 defined in Fig. 8

lation length a may be needed to better describe the surface microstructure. Distribution functions other than the Gaussian function given in Eq. (1) may be needed to better characterize the micro-facet slope distribution. Note that the measured σ for the test wafer surface is 0.26 μm [9]. Hence, the geometric-optics assumption may be problematic at large incidence angles. At $\theta_i = 60°$, $0.2\lambda/\cos\theta_i = 0.254 \approx \sigma$.

Figure 7 shows the calculated emittance at $\lambda = 0.955$ μm and for a wafer temperature $T_w = 800°C$ for a large range of a/σ values. These conditions are the same as those used in the RTP test bed at NIST [19]. A larger a/σ corresponds to a more specular surface. As a radiation ray impinges on a smooth surface, the reflectance can be obtained from Eq. (3) and the absorptance (or emittance) for an opaque surface equals one minus the reflectance. A nearly constant portion of unpolarized radiation will be absorbed for different incidence angles. Beyond Brewster's angle (about 75°), the emittance will decrease rapidly to zero. The results for large a/σ agree with the theoretically calculated emittance for an opaque medium with a smooth surface. Within a large range of incidence angles and values of a/σ, the emittance varies little, between 0.65 and 0.7. As the surface gets rougher, more radiation will be entrapped in the rough valleys, resulting in a larger emittance. If the surface rough valleys can be viewed as black cavities, the emittance will approach unity. Special attention should be paid to emission angles close to 90° where the geometric optics approximation is not valid.

The emittance, reflectance, and transmittance spectra for normally incident radiation are given in Fig. 8(*a*), (*b*), and (*c*), respectively, with different surface conditions. Specifically, four cases are considered here. Case 1: both surfaces are smooth; Case 2: only one surface is smooth; the radiation is incident on the rough surface; Case 3: only one surface is smooth; the radiation is incident on the smooth surface; Case 4: both surfaces are rough. The roughness parameter a/σ is set to 5. As the wavelength increases, the refractive index decreases, while the absorption coefficient decreases until 1.4 μm and then increases. As seen from these figures, the wafer is opaque at wavelengths shorter than 1.2 μm. In this opaque region, the emittance goes up but the reflectance

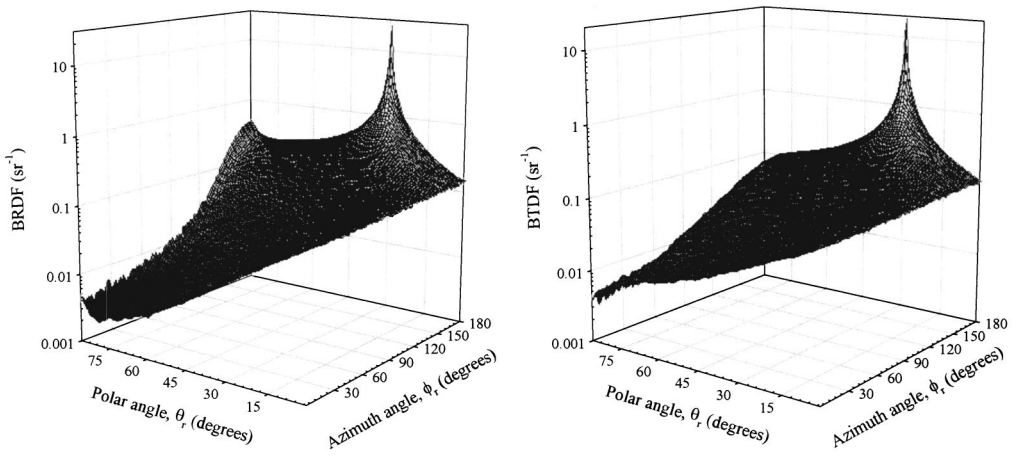

(*a*) Incident on rough surface, the other side is smooth.

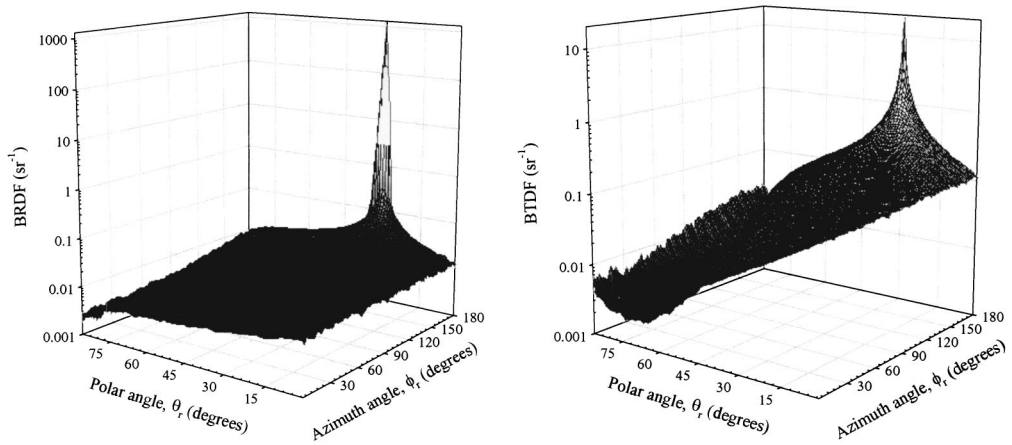

(*b*) Incident on smooth surface, the other side is rough.

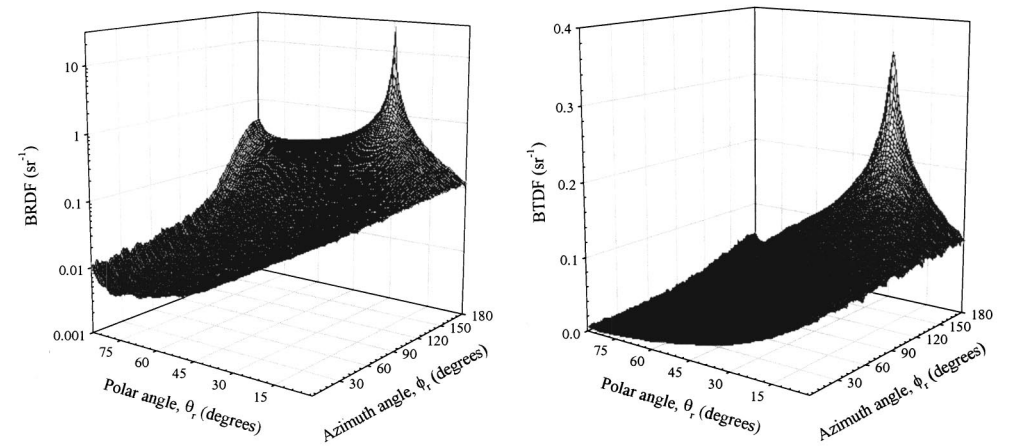

(*c*) Both surfaces are rough.

Fig. 10 The BRDF and BTDF of a semitransparent silicon wafer at $\lambda=1.7$ μm and $\theta_i=30°$, for $T_w=500°C$ and $a/\sigma=5$: (*a*) incident on rough surface, the other side is smooth; (*b*) incident on smooth surface, the other side is rough; and (*c*) both surfaces are rough

goes down as the wavelength increases, due to a decrease in the refractive index. It can also be seen that, in the opaque region, the reflectance and emittance change little for such a slightly rough surface, because shadowing and masking have essentially no effect.

In the wavelength region between 1.2 μm and 1.4 μm, the emittance decreases sharply and the corresponding transmittance increases rapidly. Hence, the wafer becomes semitransparent. As the wavelength further increases beyond 1.4 μm, the emittance goes up again, whereas both the reflectance and transmittance go down. The effect of internal absorption is clearly demonstrated since the extinction coefficient is negligible in computing the micro-facet reflectance using Fresnel's equations. For Case 1, the reflectance, transmittance, and emittance can be computed from geometric optics. The Monte Carlo simulation results agree with the exact solution within a relative error of 0.1% for the emittance. In the semitransparent region, the emittance is enhanced by the surface roughness, especially when both surfaces are rough (i.e., the emittance for Case 4 is the highest). Notice that the emittance for Case 2 is lower than that for Case 3. The reason is explained as follows. Notice that the incident rays are normal to the macro-surfaces of the wafer. When a ray enters the wafer from the rough surface, as in Case 2, the refracted ray is inclined by an angle δ' equal to $\sin^{-1}(\sin \delta/n)$, where δ is the inclination of the micro-facet and n is the refractive index of silicon. This inclined ray impinges on the smooth surface with an incidence angle equal to $\delta-\delta'$. On the other hand, when a ray enters the wafer from the smooth surface, as in Case 3, it will reach the rough side without inclination and hit a micro-facet. Assuming the micro-facet slopes are the same, then the incidence angle is equal to δ. The probability of total internal reflection will be greater in Case 3 than in Case 2. Even without total reflection, the reflected rays in general will travel a longer distance in Case 3 because of the larger inclinations of the reflected rays as compared to those in Case 2. Therefore, the internal traveling distances and the absorption probability are greater in Case 3, resulting in a larger absorptance (emittance) but smaller transmittance and reflectance than those in Case 2. Thorpe et al. [39] measured the directional-hemispherical transmittance of one-side smooth and one-side rough diamond films, and observed that the normal transmittance is greater when the smooth side faces the incoming beam. For oblique incidence, the difference would be smaller.

As $\lambda=1.7$ μm and for $a/\sigma=5$, the relationship between the radiative properties and the wafer temperature is plotted in Fig. 9(*a*) at normal incidence on the rough side of a one-side smooth wafer (Case 2). As expected, the emittance, reflectance and transmittance change little below 200°C, when the absorption is negligibly small at this wavelength. The emittance will increase from zero to 0.68 at above 700°C when the wafer becomes opaque. In contrast, the transmittance will reduce from its room-temperature value of 0.52 to zero. The corresponding reflectance decreases slightly from 0.48 to 0.32. Figure 9(*b*) demonstrates the effects of the roughness by showing the differences in the radiative properties between wafers with one-side rough surface (Case 2) and both smooth surfaces (Case 1). These figures indicate that the roughness has less influence on the reflectance than on the emittance and the transmittance. At wafer temperature T_w near 440°C, the roughness has the largest effect.

Figure 10 shows the BRDF and BTDF for a semitransparent silicon wafer at temperature $T_w=500$°C for three surface conditions. The incident radiation wavelength $\lambda=1.7$ μm, roughness parameter $a/\sigma=5$, and incidence angle $\theta_i=30°$. Compared with the BRDFs of an opaque wafer, the BRDF of semitransparent wafer appears more uniform in the hemisphere due to multiple reflections inside the wafer. A higher specular BRDF peak can be observed for radiation incident on a smooth surface, even though the opposite surface is rough. The BTDF with both rough surfaces appears most uniform, although the BRDF looks almost the same as that with ray incident on the rough surface of a one-side smooth wafer. This indicates that BRDF is more sensitive to the rough parameters of incident surface, whereas BTDF depends on both surfaces. Notice that the figure of BTDF in Fig. 10(*c*) has a linear-scale BTDF axis and the difference of the transmittance between these two cases is about 0.1. The BRDFs in Figs. 10(*a*) and (*c*) have an unreasonable peak at graze angles. This is due to the nearly-zero cosine term in Eq. (8) and the shadowing function of Eq. (7) cannot completely prevent the rays coming out at those angles. As a result, a small uncertainty in the number of rays at these angles can yield a large uncertainty in the computed BRDF. With a more reasonable surface profile instead of a statistical model, this kind of ''ghost''peak may be avoided.

Conclusions

A Monte Carlo model is developed using the micro-facet concept and ray-tracing technique to compute the radiative properties of an opaque or semitransparent silicon wafer with rough surfaces. Rather than applying a BRDF model, the radiation rays are traced directly in the rough valley as well as inside the wafer. One of the advantages is that the specular BRDF peak, the important component of surface reflection is reserved. Multiple reflections between micro-facets, masking and shadowing, and total internal reflection are considered in the present study. The optical properties of lightly doped silicon are obtained from the literature. Silicon wafers are semitransparent at wavelengths beyond the band gap when the temperature is below 700°C.

The radiative properties (including emittance, reflectance, transmittance, BRDF, and BTDF) and their dependence upon the wavelength of the incident radiation, incidence angle, and the wafer temperature and thickness are exploited based on the Monte Carlo model. The trend of computed BRDF is consistent with the experimental data. The BRDF peak values increase with incidence angles. The simulation results demonstrate that rough surfaces can enhance the emittance, while reducing the reflectance and transmittance. With only one rough surface and at normal incidence, the case when rays are incident on the rough surface has lower emittance but higher reflectance and transmittance than the case when rays are incident on the smooth surface. The effect of the wafer temperature on the radiative properties is the strongest when the silicon wafer is neither opaque nor completely transparent (i.e., in the semitransparent region). The BRDF is mainly influenced by the surface on which rays are incident; on the contrary, the BTDF is sensitive to the conditions of both surfaces and becomes nearly uniform when both surfaces are rough.

The disadvantages and limitations of this statistical model have been carefully examined, as well as the convergence and computation accuracy. Concerning the algorithm, the shadowing function is the central part on which further research work would be needed, especially for semitransparent materials. Another issue to be resolved is the absorption probability as the optical ray restrikes a rough micro-facet, i.e., when the multiple reflections need to be considered. Despite of these problems, the methods developed here can help understand the radiative behavior of various semitransparent materials and may also be applied to other application areas.

Acknowledgments

This work was funded by the National Science Foundation (CTS-9875441, 0236831) and the NIST Optical Technology Division. The authors thank Drs. Paul J. Timans, Yu-Jiun Shen, Benjamin K. Tsai, and David P. DeWitt for valuable discussions, and Professor Richard O. Buckius for providing a copy of his Ph.D. student's dissertation that is very useful for the present study.

Nomenclature

a = surface autocorrelation length, μm
b = standard deviation of the micro-facet slope divided by $\sqrt{2}$

E_g = energy band gap, eV
f_r = bidirectional reflectance distribution function (BRDF), sr^{-1}
n = refractive index
$\mathbf{n}$ = unit normal of the micro-facet
p = probability
R = random number
$\mathbf{s}$ = unit directional vector
T = temperature, K

Greek Symbols

α = absorption coefficient, cm^{-1}
β = half angle between the incidence and reflection directions, deg
γ = refraction angle, deg
δ = inclination of a micro-facet, deg
ε = (spectral) emittance
θ = polar angle, deg
λ = wavelength, μm
λ_g = wavelength corresponding to the band gap, μm
μ = $\tan(90° - \theta_r)$ in Eq. (7)
ν = radiation frequency, Hz
ρ = (spectral) reflectance
σ = rms roughness, μm
ϕ = azimuthal angle, deg
ω = solid angle, sr

Subscripts

dh = directional-hemispherical
i = incidence
p = parallel-polarized radiation
r = refraction direction
t = refraction direction
v = perpendicular-polarized radiation
λ = spectral property

References

[1] Timans, P. J., 1996, ''The Thermal Radiative Properties of Semiconductors,'' *Advances in Rapid Thermal and Integrated Processing*, F. Roozeboom, ed., Kluwer Academic Publishers, Dordrecht, Netherlands, pp. 35–102.
[2] Sato, T., 1967, ''Spectral Emissivity of Silicon,'' Jpn. J. Appl. Phys., **6**, pp. 339–347.
[3] Vandenabeele, P., and Maex, K., 1992, ''Influence of Temperature and Backside Roughness on the Emissivity of Si Wafers during Rapid Thermal Processing,'' J. Appl. Phys., **72**(12), pp. 5867–5875.
[4] Abedrabbo, S., Hensel, J. C., Fiory, A. T., Sopori, B., Chen, W., and Ravindra, N. M., 1998, ''Perspectives on Emissivity Measurements and Modeling in Silicon,'' Materials Science in Semiconductor Processing **1**, pp. 187–193.
[5] Drolen, B. L., 1992, ''Bidirectional Reflectance and Secularity of Twelve Spacecraft Thermal Control Materials,'' J. Thermophys. Heat Transfer, **6**(4), pp. 672–679.
[6] Germer, T. A., and Asmail, C. C., 1999, ''Goniometric Optical Scatter Instrument for Out-of-Plane Ellipsometry Measurements,'' Rev. Sci. Instrum., **70**(9), pp. 3688–3695.
[7] Murray-Colemann, J. F., and Smith, A. M., 1990, ''The Automated Measurement of BRDFs and Their Application to Luminaire Modeling,'' J. Illum. Eng. Soc., **19**, pp. 87–99.
[8] Shen, Y. J., Zhang, Z. M., Tsai, B. K., and DeWitt, D. P., 2001, ''Bidirectional Reflectance Distribution Function of Rough Silicon Wafers,'' Int. J. Thermophys., **22**(4), pp. 1311–1326.
[9] Shen, Y. J., and Zhang, Z. M., 2002, ''Design and Characterization of a Bidirectional Reflectometer,'' Proc. 12th International Heat Transfer Conference, J. Taine ed., Elsevier, Paris, **1**, pp. 615–620.
[10] Glassner, A. S., 1995, *Principles of Digital Image Synthesis*, Morgan Kaufmann Publishers, San Francisco, CA.
[11] Nayar, S. K., Ikeuchi, K., and Kanade, T., 1991, ''Surface Reflection: Physical and Geometrical Perspectives,'' IEEE Trans. Pattern Anal. Mach. Intell., **13**(7), pp. 611–634.
[12] Li, X. W., and Strahler, A. H., 1992, ''Geometric-Optical Bidirectional Reflectance Modeling of the Discrete Crown Vegetation Canopy: Effect of Crown Shape and Mutual Shadowing,'' IEEE Trans. Geosci. Remote Sens., **30**(2), pp. 276–292.
[13] Becker, M. E., 1998, ''Evaluation and Characterization of Display Reflectance,'' Displays, **19**, pp. 35–54.
[14] Beckmann, P., and Spizzichino, A., 1963, *The Scattering of Electromagnetic Waves From Rough Surfaces*, Pergamon, Oxford, UK, Appendix D.
[15] Torrance, K. E., and Sparrow, E. M., 1967, ''Theory for Off-Specular Reflection from Roughened Surfaces,'' J. Opt. Soc. Am., **57**(9), pp. 1105–1114.
[16] Koenderink, J. J., Van Doorn, A. J., Dana, K. J., and Nayar, S., 1999, ''Bidirection Reflection Distribution Function of Thoroughly Pitted Surfaces,'' Int. J. Comput. Vis., **31**(2/3), pp. 129–144.
[17] Tang, K., and Buckius, R. O., 2001, ''A Statistical Model of Wave Scattering From Random Rough Surfaces,'' Int. J. Heat Mass Transf., **44**(21), pp. 4059–4073.
[18] Hebb, J. P., Jensen, K. F., and Thomas, J., 1998, ''The Effect of Surface Roughness on the Radiative Properties of Patterned Silicon Wafers,'' IEEE Trans. Semicond. Manuf., **11**(4), pp. 607–614.
[19] Zhou, Y. H., Zhang, Z. M., Tsai, B. K., and DeWitt, D. P., 2001, ''Effects of Radiative Properties of Surfaces on Radiometric Temperature Measurement,'' *Proc. 9th International Conference on Advanced Thermal Processing of Semiconductors (RTP'2001)*, Anchorage, Alaska, pp. 179–188.
[20] Zhou, Y. H., Shen, Y. J., Zhang, Z. M., Tsai, B. K., and DeWitt, D. P., 2002, ''A Monte Carlo Model for Predicting the Effective Emissivity of the Silicon Wafer in Rapid Thermal Processing Furnaces,'' Int. J. Heat Mass Transf., **45**(9), pp. 1945–1949.
[21] Ko, H., Chen, C. K., and Liu, C. J., 1996, ''Optical Scattering of Diamond Films,'' Diamond Relat. Mater., **5**, pp. 861–865.
[22] Petrich, R., and Stenzel, O., 1994, ''Modeling of Transmittance, Reflectance and Scattering of Rough Polycrystalline CVD Diamond Layers in Application to the Determination of Optical Constants,'' Opt. Mater., **3**, pp. 65–76.
[23] Wengelink, J., and Engel, H., 1996, ''Fabrication of Waveguide Tapers by Semitransparent Mask Photolithography,'' Microelectron. Eng., **30**, pp. 137–140.
[24] Boueke, A., Kühn, R., Fath, P., Willeke, G., and Bucher, E., 2001, ''Latest Results on Semitransparent POWER Silicon Solar Cells,'' Sol. Energy Mater. Sol. Cells, **65**, pp. 549–553.
[25] Montecchi, M., Montereali, R. M., and Nichelatti, E., 2001, ''Reflectance and Transmittance of a Slightly Inhomogeneous Thin Film Bounded by Rough, Unparallel Interfaces,'' Thin Solid Films, **396**, pp. 262–273.
[26] Anderson, M., Michel, L., Roecker, C., and Scartezzini, J. L., 2001, ''Experimental Assessment of Bi-directional Transmission Distribution Functions Using Digital Imaging Techniques,'' Energy Build., **33**, pp. 417–431.
[27] Tang, K., Dimenna, R. A., and Buckius, R. O., 1997, ''Regions of Validity of the Geometric Optics Approximation for Angular Scattering from Very Rough Surfaces,'' Int. J. Heat Mass Transf., **40**(1), pp. 49–59.
[28] Tsai, B. K., DeWitt, D. P., and Shaffe, G. H., 1994, ''Macroscopic Spread Function Analysis for Subsurface Scattering of Semitransparent Materials,'' J. Thermophys. Heat Transfer, **8**(2), pp. 202–207.
[29] Zhang, Z. M., 1999, ''Optical Properties of a Slightly Absorbing Film for Oblique Incidence,'' Appl. Opt., **38**(1), pp. 205–207.
[30] Tang, K., Kawka, P. A., and Buckius, R. O., 1999, ''Geometric Optics Applied to Rough Surfaces Coated with an Absorbing Thin Film,'' J. Thermophys. Heat Transfer, **13**(2), pp. 169–176.
[31] Tang, K., and Buckius, R. O., 1998, ''The Geometric Optics Approximation for Reflection From Two-Dimensional Random Rough Surfaces,'' Int. J. Heat Mass Transf., **41**(13), pp. 2037–2047.
[32] Press, W. H., Teukolsky, S. A., Vetterling, W. T., and Flannery, B. P., 1992, *Numerical Recipes in Fortran*, 2nd ed., Cambridge University Press, Cambridge, UK, Chap. 7.
[33] Smith, B. G., 1967, ''Geometrical Shadowing of a Random Rough Surface,'' IEEE Trans. Antennas Propag., **15**, pp. 668–671.
[34] Zhang, Z. M., Fu, C. J., and Zhu, Q. Z., 2003, ''Optical and Thermal Radiative Properties of Semiconductors Related to Micro/Nanotechnology,'' Adv. Heat Transfer, **37**, pp. 179–296.
[35] Jellison, G. E., Jr., and Lowndes, D. H., 1982, ''Optical Absorption Coefficient of Silicon at 1.152 μ at Elevated Temperatures,'' Appl. Phys. Lett., **41**, pp. 594–596.
[36] Jellison, G. E., Jr., and Modine, F. A., 1994, ''Optical Functions of Silicon at Elevated Temperatures,'' J. Appl. Phys., **76**, pp. 3758–3761.
[37] Li, H. H., 1980, ''Refractive Index of Silicon and Germanium and Its Wavelength and Temperature Derivatives,'' J. Phys. Chem. Ref. Data, **9**, pp. 561–601.
[38] Timans, P. J., 1993, ''Emissivity of Silicon at Elevated Temperatures,'' J. Appl. Phys., **74**, pp. 6353–6364.
[39] Thorpe, T. P., Morrish, A. A., Hanssen, L. M., Butler, J. E., and Snail, K. A., 1990, ''Growth, Polishing, and Optical Scatter of Diamond Thin Films,'' Proc. SPIE, **1325**, pp. 230–237.

Temperature Measurements Using a High-Temperature Blackbody Optical Fiber Thermometer

David G. Barker
e-mail: dbarker@byu.edu

Matthew R. Jones
e-mail: mrjones@et.byu.edu

Department of Mechanical Engineering,
Brigham Young University, 435 CTB,
PO Box 24201, Provo, UT 84602-4201

A blackbody optical fiber thermometer consists of an optical fiber whose sensing tip is given a metallic coating. The sensing tip of the fiber forms an isothermal cavity and the emission from this cavity is approximately equal to the emission from a blackbody. When a short length of the fiber is exposed to a high temperature environment, the temperature at the sensing tip can be inferred using the standard two-color approach. If, however, more than a short length of the fiber is exposed to elevated temperatures, emission by the fiber will result in erroneous temperature measurements. This paper presents experimental results that show it is possible to use additional spectral measurements to eliminate errors due to emission by the fiber and measure the tip temperature. In addition, the technique described in this paper can be used to obtain an estimate of the temperature profile along the fiber. [DOI: 10.1115/1.1571085]

Keywords: Heat Transfer, High Temperature, Inversion, Measurement Techniques, Radiation

Introduction

Blackbody optical fiber thermometers (OFT) are created by coating the tip of an optical fiber with a highly conductive, opaque material. This creates an isothermal cavity at the tip of the fiber that emits like a blackbody. Based on measurements of the emission exiting the opposite end of the fiber, the temperature of the tip can be estimated using Planck's law [1]. Compared to thermocouples or other temperature measurement methods, OFT are more stable, have a wider dynamic range, and are more capable of withstanding harsh environments [2].

In many applications only the sensing tip and a small length of the fiber are exposed to the high temperature environment. In these situations, it is acceptable to assume that all radiation detected is emitted by the blackbody cavity [1]. However, it has been shown that when a significant portion of the fiber is exposed to elevated temperatures, the measurements are corrupted due to emission by the fiber [3–4].

Currently, applications where a significant portion of the fiber is exposed to elevated temperatures are avoided. One way to accomplish this is to cool the fiber and only expose the sensing tip to the elevated temperatures [4]. When it is not possible to cool the fiber, it is necessary to perform calibrations in the environment where the temperature is to be measured. Since the calibration procedure must be performed under conditions nearly identical to the operating conditions, this approach is highly restrictive.

In previous studies, numerical simulations indicated that measurements of the spectral intensity emitted by a blackbody fiber at several wavelengths can be used to infer the temperature at the tip of the fiber and estimate the temperature profile along the fiber when exposure to a high temperature environment prevents the use of the standard two-color approach [5–7]. The purpose of this paper is to present the results from preliminary experiments which were conducted to verify these numerical results.

This paper presents a detailed model of the measurement system used in the preliminary experiments. Given the temperature profile existing along the fiber and the properties of the fiber and the cavity, this model predicts the spectral intensity existing the fiber and the irradiance incident on the detector. An equation referred to as the signal measurement equation (SME) provides a relationship between the temperature profile along the fiber and the output of the detector. The SME accounts for emission by the fiber and attenuation in both the fiber and the optical system as the light travels from the blackbody cavity to the detector. An uncertainty analysis was preformed to quantify the precision of the predictions based on the SME. Spectral intensity measurements were obtained while the fiber was inserted into a laboratory furnace, and a conjugate gradient algorithm was used to determine the tip temperature and to estimate the temperature profile along the heated portion of the fiber.

Signal Measurement Equation

The following discussion of the SME is specific to the current problem. General principles relevant to the development of an SME can be found in the literature [8–10].

A schematic of a typical blackbody OFT is shown in Fig. 1 [1]. Normally two optical fibers, a high-temperature fiber and a low-temperature fiber, are coupled together; however, a single fiber was used in this experiment. Since the temperature profile along the heated portion of the optical fiber is of interest, the heated and non-heated portions are treated separately. The following analysis deals with the heated portion of the fiber, and the low temperature portion is treated as part of the detection system.

The objective of the SME is to relate the temperature profile along the fiber to the output of the detector. Development of the SME requires that spectral irradiation incident on the detector be calculated. The spectral irradiation incident on detection system is equal to the product of the spectral intensity exiting the fiber and the solid angle subtended by the fiber when viewed from aperture of the light detection system.

$$G_\nu = I_\nu(L)\,\omega_d \tag{1}$$

Contributed by the Heat Transfer Division for publication in the JOURNAL OF HEAT TRANSFER. Manuscript received by the Heat Transfer Division September 25, 2002; revision received February 4, 2003. Associate Editor: S. T. Thynell.

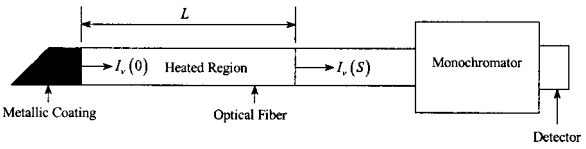

Fig. 1 Schematic of a typical blackbody optical fiber thermometer

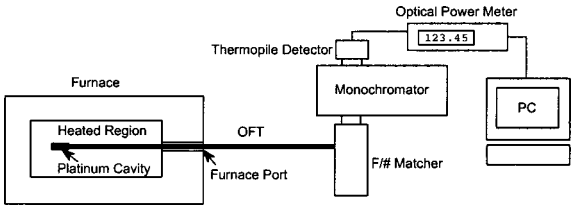

Fig. 3 Schematic of the experimental apparatus

Since the refractive index varies as the light is transmitted from the fiber to the detection system, it is convenient to begin with frequency as the spectral variable. Modeling the fiber as an emitting, absorbing and non-scattering medium yields the following differential equation for the spectral intensity in the fiber [11].

$$\frac{dI_\nu}{ds} = -K_{a\nu}I_\nu + K_{a\nu}I_{b\nu}(T(s)) \tag{2}$$

The emissivity of the cavity can be estimated by approximating the cavity as an isothermal enclosure [12], and the initial condition for Eq. (2) is given by Eq. (3)

$$I_\nu(0) = \varepsilon_\nu I_{b\nu}(T_o) \tag{3}$$

where s is the path length traveled by the light. As illustrated in Fig. 2, the light path is longer than the length of the fiber, and the effect of the difference in the lengths of the various possible light paths are included in the uncertainty analysis. Solving Eq. (3) gives

$$\varepsilon_\nu I_{b\nu}(T_o) = I_\nu(t_{\nu S})\exp\{t_{\nu S}\} - \int_0^{t_{\nu S}} I_{b\nu}(T(t_\nu))\exp\{t_\nu - t_{\nu S}\}dt_\nu \tag{4}$$

where the independent variable has been transformed from s to the optical depth, $t_\nu = K_{a\nu}s$. The upper limit of integral in Eq. (4) is the optical depth for the average of the possible light paths. The effect of the uncertainty in the absorption coefficient has also been included in the uncertainty analysis. The term on the left of the equal sign in Eq. (4) represents intensity exiting the isothermal cavity. The first term on the right accounts for attenuation in the signal due to absorption in the fiber. The integral represents an increase in the intensity exiting the fiber due to emission by the fiber. If the temperature along the fiber is low, emission by the fiber is insignificant compared to emission by the cavity, and the integral can be neglected.

If the optical properties of the fiber and the temperature profile were known, Eq. (4) could be solved for the spectral intensity existing the fiber. In the current problem, however, measurements of spectral intensity exiting the fiber are available, and the temperature profile is unknown. Since the temperature profile cannot be solved for explicitly, an iterative solution is required. This type of problem is typically referred to as an inverse problem.

Equation (4) may be simplified as follows. Wien's limit can be used to approximate the spectral intensity of a blackbody for the frequencies and temperatures of interest.

$$I_{b\nu}(T) = \frac{2h\nu^3 n_\nu^2}{c_o^2[\exp\{h\nu/kT\} - 1]} \approx \frac{2h\nu^3 n_\nu^2}{c_o^2[\exp\{h\nu/kT\}]} \tag{5}$$

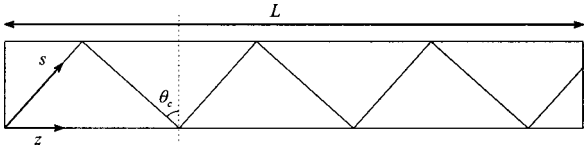

Fig. 2 Path length due to internal reflection

Since the spectral intensity is measured as a function of wavelength, it is convenient at this point to convert the spectral variable from frequency to wavelength. After exiting the fiber, the radiation propagates through air until reaching the detector, so the appropriate conversion is [11]

$$I_\lambda(T) = \frac{c_o}{\lambda^2} I_\nu(T) \tag{6}$$

with $\lambda = c_o/\nu$, $C_1 = 2\pi h c_o^2$, $C_2 = hc_o/k$ and Eq. (1), Eq. (4) becomes

$$G_\lambda = \frac{C_1 n_\lambda^2 \omega_d}{\pi\lambda^5}\left[\varepsilon_\lambda \exp\left\{-t_{\lambda S} - \frac{C_2}{\lambda T_o}\right\} + \int_0^{t_{\lambda S}} \exp\left\{t_\lambda - t_{\lambda S} - \frac{C_2}{\lambda T(t_\lambda)}\right\} dt_\lambda\right] \tag{7}$$

Equation (7) provides a relationship between the temperature profile along the fiber, $T(t_\lambda)$, and the spectral irradiance incident on the detection system, G_λ.

Once the light leaves the optical fiber, it is transferred through an optical system to a detector. The output from the detector may be related to spectral irradiance incident on the detection system by accounting for the attenuation in the system. The following paragraphs provide a detailed description of the detection system and the factors that contribute to the attenuation in the detection system.

Experimental Apparatus. Figure 3 shows a diagram of the apparatus used in the experiments. The OFT is similar to the schematic in Fig. 1. It is made of single crystal sapphire (Al_2O_3), which is 0.5 mm in diameter and 1.0 m in length. The cavity at the tip was created using a thin-walled platinum tube with an inside diameter (1.2 mm) slightly larger than the optical fiber and a length to diameter ratio of 15. One end was crimped to form a cavity and the optical fiber was inserted in the other end leaving approximately a one-fiber-diameter gap at the end of the tube. The fiber is placed in a cylindrical resistance furnace capable of reaching a temperature of 1366 K. Characterization of the furnace temperature profile at several temperature settings (1331 K, 1344 K, and 1366 K) was performed using a multipoint thermocouple inserted through the furnace port (as shown in Fig. 2 for the optical fiber). The temperature profile measured with the furnace set at 1344 K was used in the calibration procedure described in the following section. The temperature was measured at 5 points spaced 5 cm apart in the heated zone of the furnace with the first point's location corresponding to the location of the tip of the OFT. The heated portion of the optical fiber was the distance from the tip of the fiber to the point where the temperature of the fiber was equal to room temperature. At steady state, the standard deviation of the temperature variations with time within the furnace was less than 0.5 K. The accuracy of the reconstructed temperature profiles will be assessed by comparing them with these thermocouple measurements.

The light exiting the fiber passes through a monochromator. To maximize throughput, an $F/\#$ matcher is used to match the lower $F/\#$ of the optical fiber with the higher $F/\#$ of the monochromator. Reflection losses in the $F/\#$ matcher were specified by the

manufacturer and are less than would be experienced by the difference in $F/\#$'s of the fiber and monochromator.

The monochromator is an Oriel 1/8 m monochromator with a micrometer-driven entrance slit and a fixed-width exit slit. The manufacturer specified the mirror reflection efficiency of 88 percent for each of the four mirrors in the monochromator. A single grating is used with the blaze wavelength at 2.0 μm and a line density of 300 lines/mm. The usable wavelength region is from 1.0 μm to 4.0 μm. This yields a grating bandwidth of 22 nm. An approximate spectral efficiency plot of the grating was provided, but the grating was not calibrated. Therefore, the grating efficiency was treated as an unknown, and is accounted for in the calibration procedure that will be discussed in the following section.

After the light is separated into wavelength bands, a thermopile detector is used to measure the radiant flux exiting the monochromator. A thermopile uses an array of thermocouples to measure the temperature rise due to the incident radiant flux. Since a thermopile measures temperature rise, the response is approximated as constant over all wavelengths. The detector was calibrated by the manufacturer, and the responsivity was given as 0.765 nA/(mW/cm^2). The detector window is made of sapphire and the spectral transmissivity of sapphire was provided by the manufacturer. However, the transmissivity data is not specific to the window used, so the transmissivity of the window is accounted for in the calibration procedure.

The signal from the thermopile detector was read by an Oriel Optical Power Meter capable of reading a signal of 1.0 pA. This is slightly less than the noise level of the thermopile so the limiting factor on the signal is the detector. This signal was read into a PC using a LabVIEW® program. Fifty measurements were taken with the monochromator shutter closed to provide a dark reading, 50 measurements were taken with the shutter open and then 50 were again taken with the shutter closed. This process was repeated at each wavelength. The data presented in this paper represent an average of the difference between the light and dark signals, which eliminates bias errors in the measurements. The variance was calculated to quantify the precision in the measurements, and it was found that the standard deviation of the 50 measurements was approximately 0.003 nA at each wavelength.

Attenuation in the Detection System. With knowledge of the apparatus used to measure the spectral intensity exiting the fiber, it is possible to relate the output of the detector to the irradiance incident on the detection system.

$$\psi_\lambda = A\alpha R\,\eta_{F/\#}\eta_m^4\eta_{G_\lambda}\tau_\lambda\Delta\lambda G_\lambda \tag{8}$$

Equation (8) describes the light attenuation after it exists the heated portion of the optical fiber and travels to the detector, as well as the conversion of the incident irradiation to an electrical current by the detector. This equation includes absorption in the low temperature portion of the fiber, the efficiency of the $F/\#$ matcher, the efficiency of the mirrors in the monochromator, the grating efficiency, and the detector window transmissivity. The irradiance incident on the detector is then multiplied by the detector responsivity and the amplifier gain to give the output signal.

Combining Eqs. (7) and (8) gives the SME, which relates the current output by the detector to the temperature profile along the fiber.

$$\psi_\lambda = A\alpha R\,\eta_{F/\#}\eta_m^4\eta_{G_\lambda}\tau_\lambda\Delta\lambda\,\frac{C_1 n_\lambda^2\omega_d}{\pi\lambda^5}\left[\varepsilon_\lambda\exp\left\{-t_{\lambda S}-\frac{C_2}{\lambda T_o}\right\}+\int_0^{t_{\lambda S}}\exp\left\{t_\lambda-t_{\lambda S}-\frac{C_2}{\lambda T(t_\lambda)}\right\}dt_\lambda\right] \tag{9}$$

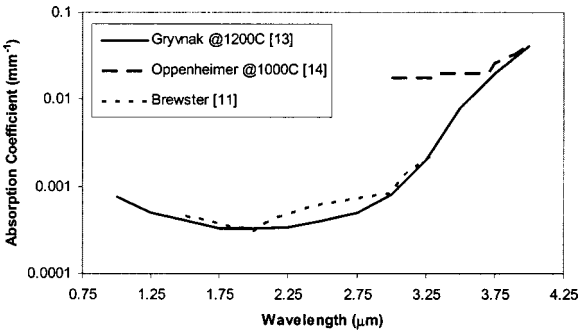

Fig. 4 Available data on the spectral absorption coefficient for sapphire

Experimental Method

The experimental method consisted of four parts: calibration, uncertainty analysis, measurements, and reconstruction of the temperature profile.

Calibration. Introducing a spectral calibration coefficient, κ_λ, simplifies the SME to

$$\psi_\lambda = \kappa_\lambda\left[\varepsilon_\lambda\exp\left\{-t_{\lambda L}-\frac{C_2}{\lambda T_o}\right\}+\int_0^{t_{\lambda L}}\exp\left\{t_\lambda-t_{\lambda L}-\frac{C_2}{\lambda T(t_\lambda)}\right\}dt_\lambda\right] \tag{10}$$

where

$$\kappa_\lambda = A\alpha R\,\eta_{F/\#}\eta_m^4\eta_{G_\lambda}\tau_\lambda\Delta\lambda\,\frac{C_1 n_\lambda^2\omega_d}{\pi\lambda^5} \tag{11}$$

Note that all of the parameters included in the definition of the spectral calibration coefficient are associated with the detection system, and none these parameters depend on the temperature profile along the fiber. Therefore, the spectral calibration coefficients may be used when the fiber is exposed to any arbitrary temperature profile if the detection system is well characterized and all the parameters in Eq. (11) are known. However, many of these parameters are poorly characterized for the detection system used in the preliminary experiments reported here, so it necessary to determine the spectral calibration coefficients using Eq. (12)

$$\kappa_\lambda = \frac{\psi_{m\lambda}(T_c(t_{\lambda S}))}{\varepsilon_\lambda\exp\left\{-t_{\lambda S}-\frac{C_2}{\lambda T_o}\right\}+\int_0^{t_{\lambda S}}\exp\left\{t_\lambda-t_{\lambda S}-\frac{C_2}{\lambda T(t_\lambda)}\right\}dt_\lambda} \tag{12}$$

where $T_c(t_\lambda)$ is the temperature profile existing along the heated portion of the fiber during the calibration procedure (3:6) and $\psi_{m\lambda}(T_c(t_{\lambda S}))$ are the spectral measurements obtained during the calibration procedure.

The use of Eq. (12) also requires knowledge of the spectral emissivity of the cavity and the spectral optical depth. Modeling the platinum tube as a diffuse-gray enclosure with a length to diameter ratio of 15, the emissivity of the cavity is estimated to be 0.92 [12]. The spectral optical depth is equal to the product of the spectral absorption coefficient and the light path length. The light path length can be characterized using the average path length for the fiber, but determining the spectral absorption coefficient is more problematic. Data on the absorption coefficient of sapphire available in the literature as a function of temperature are inconsistent. Figure 4 shows the data available for the spectral absorption coefficient at an unspecified temperature [11], 1200C [13] and 1000C [14]. Brewster [11] actually lists the imaginary part of

the refractive index for sapphire, so the absorption coefficients shown in Fig. 4 are calculated using this data and Eq. (13).

$$K_{a\lambda}=\frac{4000\pi k}{\lambda} \tag{13}$$

Due to the uncertainty regarding the variation in the spectral absorption coefficient with temperature, it was necessary to perform an in-situ calibration similar to the procedure used to calibrate blackbody OFT for the two-color approach [1]. The temperature profile measured with the furnace set at 1344 K was taken as the calibration temperature profile. The spectral calibration coefficients were calculated using Eq. (12) and the estimated spectral emissivity of the cavity and the spectral absorption coefficients at 1200 C [13]. This approach neglects the dependence of the spectral absorption coefficient on temperature, so the resulting calibration coefficients are only valid at temperatures close to the calibration temperature profile. This restriction could be eliminated if the dependence of the spectral absorption coefficient on temperature was known, and a program to obtain these measurements is currently being planned.

Uncertainty Analysis. The objective of the uncertainty analysis is to determine the precision of the predicted signals based on the SME. The sources of uncertainty in the SME are

- The emissivity of the cavity, ε_λ
- The fiber tip temperature, T_o
- The fiber temperature profile, $T(t_\lambda)$
- The optical depth, t_λ
- The spectral calibration coefficient, κ_λ

The first step in calculating the predicted uncertainty is to take the partial derivative of Eq. (10) with respect to each unknown parameter. The partial derivatives are then multiplied by the uncertainty for each parameter. The squares of these products are then summed, and the square root of the sum gives the uncertainty in the predicted signals,

$$u_p(\lambda)=\left[\sum_{i=1}^{N}\left(\frac{\partial\psi_\lambda}{\partial[x_i(\lambda)]}\right)^2 u^2(x_i(\lambda))\right]^{1/2} \tag{14}$$

where the x_i represent each of the unknown parameters and u represents the uncertainty associated with each unknown parameter.

The following is a list of the estimated uncertainty in each of the unknown parameters

- $u_{\varepsilon_\lambda}=0.03$ [12]
- $u_{T_o}=0.5$ K From steady-state thermocouple readings
- $u_{T(t_\lambda)}=0.5$ K From steady-state thermocouple readings
- u_{t_λ} varies with wavelength and is discussed below
- u_{κ_λ} varies with wavelength. Calculated by dividing the standard deviation of the measurements obtained during the calibration procedure at each wavelength by the square-root of the number of measurements at each wavelength.

The predicted uncertainty in the optical depth is calculated by the following expression

$$u_{t_\lambda,p}=\left[\left(\frac{\partial t_\lambda}{\partial K_{a\lambda}}u_{K_{a\lambda}}\right)^2+\left(\frac{\partial t_\lambda}{\partial s}u_s\right)^2\right]^{1/2} \tag{15}$$

The uncertainty in the spectral absorption coefficient as given in [13] is 30 percent, and the uncertainty in the length of the light path at the end of the heated portion of the fiber is 0.175 m.

Figure 5 shows the normalized product of the partial derivative and the uncertainty squared for each of the unknown parameters at several wavelengths.

Measurements. The optical fiber was inserted the desired distance through the furnace port (see Fig. 3). The platinum tube was then placed on the tip of the optical fiber and the tip was rested on a wire stand. The furnace door was closed and sufficient time was allowed for the furnace to reach steady state.

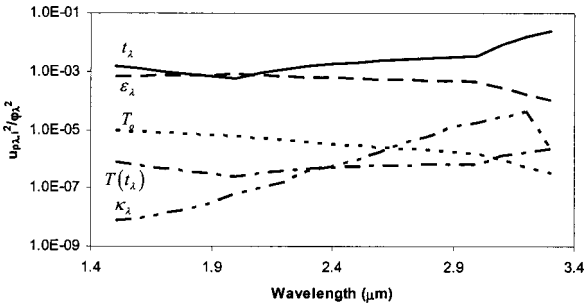

Fig. 5 Normalized squared i^{th} component of the predicted uncertainty

Once the furnace reached steady state, spectral measurements were obtained in the manner described previously. Two measured temperature profiles (furnace settings of 1366 K and 1331 K) were used, and multiple sets of measurements were obtained at each temperature setting. The standard deviation was used to quantify the precision of the measurements at each wavelength.

Reconstruction. Once the spectral calibration factors and the spectral measurements are available, the SME can be inverted to reconstruct the temperature profile along the fiber. Briefly, the reconstructed temperature profile is obtained by assuming an initial temperature. Predicted signals are calculated by substituting the assumed temperature profile into the SME. The assumed temperature profile is then adjusted until the predicted signals match the measurements to within the uncertainty of the measurements and the precision of the predicted signals. The temperature profile that results in predicted signals that most closely match the measurements is taken as the reconstructed temperature profile. Temperature profiles have been reconstructed using both gradient based optimization methods and random search methods [5–7,12], but only the conjugate gradient algorithm was used in this study. Complete details regarding the algorithm used to reconstruct the temperature profile are available elsewhere [7,12,15–18].

Results and Discussion

Two data sets were obtained with the furnace set at 1366 K and with the furnace set at 1331 K. The tip temperatures were obtained by reconstructing the temperature profile for each data set. For comparison purposes, tip temperatures were also obtained using the standard two-color method. The two-color approach is arrived at by neglecting absorption and emission by the fiber [1,19]. These approximations give

$$\psi_\lambda=\kappa_\lambda\varepsilon_\lambda\exp\left\{-\frac{C_2}{\lambda T_{2C}}\right\} \tag{16}$$

Taking the ratio of measurements at two wavelengths and solving Eq. (16) for T_{2C} gives

$$T_{2C}=\frac{\dfrac{C_2}{\lambda_2}-\dfrac{C_2}{\lambda_1}}{\ln\left(\dfrac{\psi_{\lambda_1}\kappa_{\lambda_2}\varepsilon_{\lambda_2}}{\psi_{\lambda_2}\kappa_{\lambda_1}\varepsilon_{\lambda_1}}\right)} \tag{17}$$

When using the two-color approach, it is desirable to choose closely spaced wavelengths to the left of the peak signal where the sensitivity to changes in the measurements is greatest [1,19]. The spectral measurements used to obtain T_{2C} were selected from the set of spectral measurements used for the reconstructions. Using

Table 1 Comparison of the tip temperature measured using a thermocouple (T_{TC}) with the reconstructed tip-temperature (T_R) and the tip-temperature calculated using the two-color method (T_{2C})

Furnace Temperature Setting (K)	T_{TC} (K)	T_R (K)	T_{2C} (K)
1366 (Run 1)	1340.6	1337.3	1221.0
1366 (Run 2)	1340.6	1347.1	1600.6
1331 (Run 1)	1318.8	1327.6	1354.5
1331 (Run 2)	1318.8	1323.8	878.0

the data from Run 1 at each furnace temperature setting, the combination of wavelengths that resulted in a value for T_{2C} that most closely matched the thermocouple reading was determined. For the 1366 K furnace setting, $\lambda_1=1.6$ and $\lambda_2=1.7$ μm. For the 1331 K furnace setting, $\lambda_1=2.0$ and $\lambda_2=2.1$. The same two wavelengths were then used to obtain the two-color temperature based on the measurements for Run 2, and the results are listed in Table 1. In each case, the reconstructed tip-temperature was significantly more accurate than the two-color temperature. Despite the high level of noise in the measurements and the large uncertainty in the predicted signal, the reconstructed tip-temperature agreed with the thermocouple readings to within 0.7%. This is because the reconstruction algorithm uses several wavelengths, and the error in the measurement at one wavelength is frequently offset by the error in the other measurements. Since the two-color method only uses two measurements, it is much more unstable in the presence of error.

Figure 6 shows the reconstructed temperature profile obtained using the data from Run 1 at a furnace setting of 1366 K, and Fig. 7 shows the reconstructed temperature profile obtained using the data from Run 1 at a furnace setting of 1331 K. The reconstructed

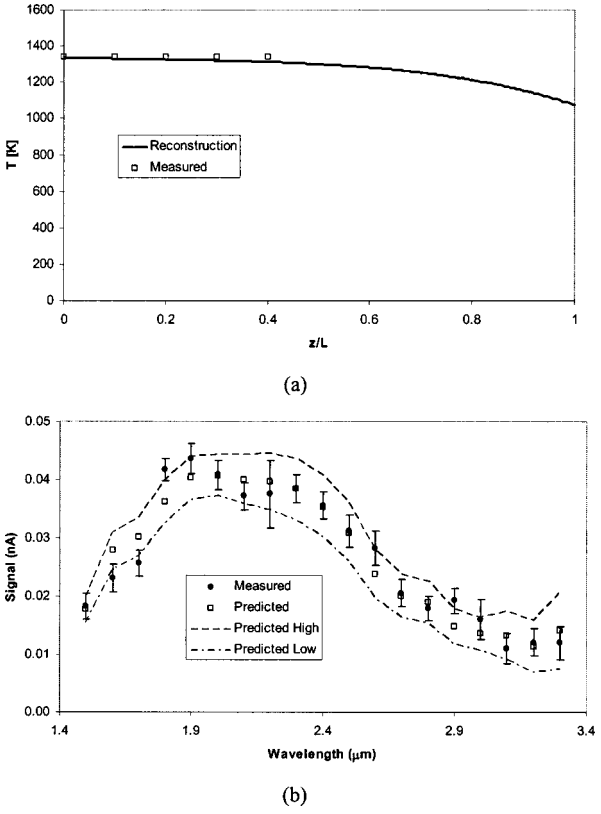

Fig. 6 (*a*) Temperature profile reconstruction and (*b*) predicted and measured spectral signal values for a furnace setting of 1366 K (Run 1)

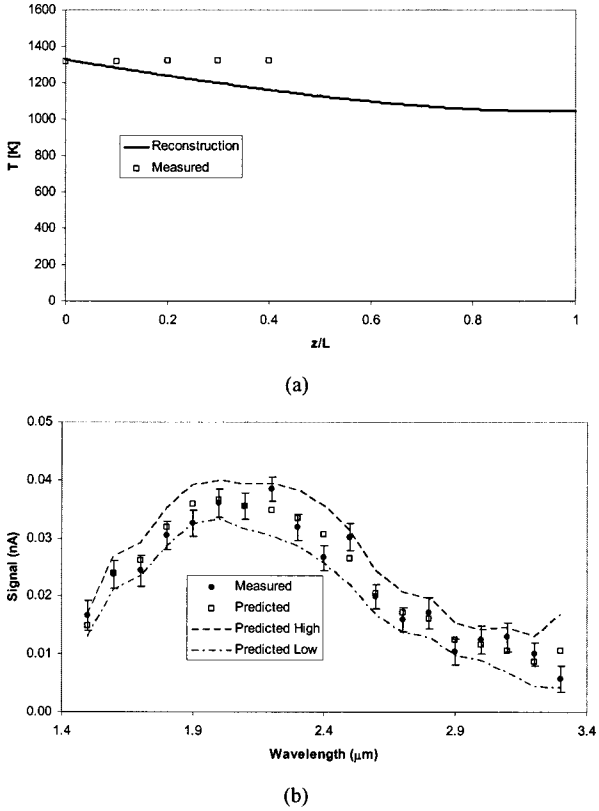

Fig. 7 (*a*) Temperature profile reconstruction and (*b*) predicted and measured spectral signal values for a furnace setting of 1331 K (Run 1)

temperature profiles are compared with the temperature points measured using thermocouples. In addition, the predicted signals obtained when the reconstructed temperature profiles are substituted into Eq. (10) are compared with the measured signals in Figs. 6 and 7.

While the reconstructed temperature profile shown in Fig. 6 is in good agreement with the thermocouple measurements, the reconstructed temperature profile shown in Fig. 7 only matches the thermocouple measurement at the tip of the fiber. These results highlight the fact that the measured signal is dominated by the emission from the cavity, and the measurements are much more sensitive to changes in the tip temperature than to changes in the temperature profile along the fiber. Due to the relatively low sensitivity of the measurements to variations in the temperature profile, a high level of noise in the measurements prevents consistently accurate reconstruction of the entire temperature profile.

The effects of measurement noise and uncertainty in the predicted signals have been studied using numerical simulations [12]. This study shows that consistently accurate reconstruction of the temperature profile can be obtained by increasing the signal-to-noise ratio and decreasing the uncertainty in the predicted signal. The strength of the signal can be increased by using a larger fiber, and the noise can be reduced by using a detector more suitable than a thermopile. A more appropriate detector would be a lead-sulfide photon detector, which covers the required spectral range (1.5 to 4.0 μm) and has a noise equivalent power that is one to three orders of magnitude less than that of the thermopile. Better characterization of the optical system and more accurate measurements of the spectral absorption coefficient of sapphire would reduce the uncertainty in the predicted signals.

As an example, simulated measurements were generated using a fourth-order polynomial fit to the temperature points measured with the thermocouple with the furnace set at 1331 K (see Figs. 6

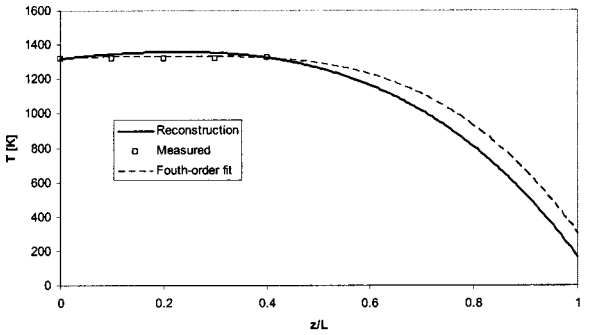

(a)

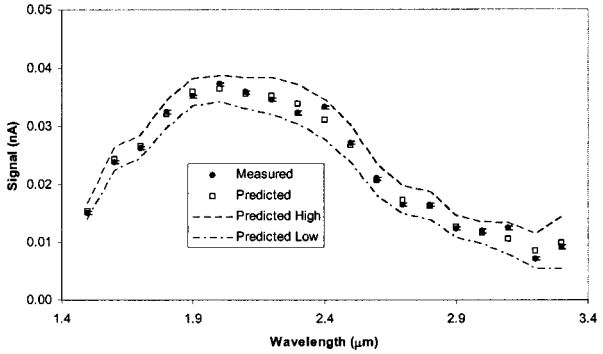

(b)

Fig. 8 (*a*) Simulated temperature profile reconstruction and (*b*) predicted and measured spectral signal values for a furnace setting of 1331 K with an increased signal-to-noise ratio and decreased SME uncertainty

and 7). By implementing the improvements to the optical system discussed above, it is estimated that the signal-to-noise ratio in the measurements can be increased by a factor of 10 using a more suitable detector, and the uncertainty in the predicted signals can be reduced by 30 percent [12]. This is accomplished by reducing the uncertainty in the absorption coefficient to 10% and reducing the uncertainty in the cavity emissivity to 0.02. The reconstructed temperature profile obtained with this level of noise in the measurements and uncertainty in the predicted signals is shown in Fig. 8.

Summary and Conclusions

Optical fiber thermometers are an alternative temperature measurement technique that can provide accurate temperature measurements and have advantages over other temperature measurement methods. If, however, a significant portion of the optical fiber is exposed to elevated temperatures, emission by the fiber will corrupt measurements obtained using the standard two-color method.

Based on an analysis of the optical detection system, a relationship between the temperature profile and the spectral measurements was obtained. This relationship was inverted to find the temperature profile using a conjugate gradient algorithm. The results presented in this paper show that this method can be used to measure the tip temperature and obtain an estimate of the temperature profile along the optical fiber thermometer when the fiber is exposed to a high temperature environment. The measured tip temperatures are more accurate than values obtained using the standard two-color approach. The accuracy of the reconstructed temperature profiles can be improved by reducing the noise in the measurements and the uncertainty in the predicted signals.

Acknowledgment

This research was funded by the College of Engineering and Technology at Brigham Young University.

Nomenclature

A = amplifier gain
C = trial functions
C_1, C_2 = blackbody radiation constants
c_o = speed of light
G = irradiation
h = Planck's constant
I = intensity
K_a = absorption coefficient of Al_2O_3
k = Boltzmann constant, Imaginary part of the refractive index for Al_2O_3
L = length of the heated portion of the optical fiber
N = number of parameters in the conjugate gradient algorithm, and number of uncertainty contributors.
n = refractive index
P = expansion coefficients for the reconstructed temperature profile
R = detector responsivity
S = path length of the light down the heated portion of the optical fiber
s = light path length down the heated portion of the optical fiber
T = temperature
T_o = fiber tip temperature
t = optical depth of the optical fiber, $K_{av}s$
u = uncertainty
z = distance along the heated portion of the optical fiber
α = absorption in the low-temperature portion of the optical fiber
$\Delta\lambda$ = monochromator bandwidth
ε = emissivity
κ = spectral calibration coefficient
$\eta_{F/\#}$ = $F/\#$ matcher efficiency
η_G = grating efficiency
η_m = monochromator mirror efficiency
θ_c = critical angle for total internal reflection
λ = wavelength of measured emission
ν = frequency of measured emission
ω = solid angle
ψ = detector signal
τ = detector window transmissivity

Subscripts

b = blackbody
c = combined
d = detector
j = index for the trial functions and the expansion coefficient
S = light path length of the heated portion of the fiber
m = measured
p = predicted
λ = wavelength
ν = frequency

References

[1] Dils, R. R., 1983, "High-Temperature Optical Fiber Thermometry," J. Appl. Phys., **54**, p. 1198.
[2] Fang, X., May, R. G., Wang, A., and Claus, R. O., 1994, "A Fiber-Optic High-Temperature Sensor," Sens. Actuators A, **44**(1), pp. 19–24.
[3] Jones, M. R., Farmer, J. T., and Breeding, S. P., 1999, "Evaluation of the Use of Optical Fiber Thermometers for Thermal Control of the Quench Module Insert," *Proceedings of the Thermal & Fluids Analysis Workshop*, NASA/CP-2002-21 pp. 1–16.
[4] Tsai, B. K., Meyer, C. W., and Lovas, F. J., 2000, "Characterization of Light-pipe Radiation Thermometers for the NIST Test Bed," *8th International Con-*

ference on Advanced Thermal Processing of Semiconductors, Gaithersburg, MD, pp. 83–93.
[5] Jones, M. R., and Barker, D. G., 2002, ''Use of Blackbody Optical Fiber Thermometers in High Temperature Environments,'' AIAA. Thermophys. Heat Transfer, **16(3)**, pp. 306–312.
[6] Barker, D. G., and Jones, M. R., ''A Hybrid Inverse Method for Predicting the Temperature Profile Along a Blackbody Optical Fiber Thermometer,'' *Proceedings of IMECE: 2002 International Mechanical Engineering Conference and Exposition*, November 17–22, 2002, New Orleans, LA., IMECE2002-39551.
[7] Barker, D. G., and Jones, M. R., 2002, ''Inversion of Spectral Emission Measurements to Reconstruct the Temperature Profile Along a Blackbody Optical Fiber Thermometer,'' to appear in Inverse Probl. Eng. .
[8] McCluney, W. R., 1994, *Introduction to Radiometry and Photometry*, Artech House, Boston, MA.
[9] DeWitt, D. P., and Nutter, G. D., 1988, *Theory and Practice of Radiation Thermometry*, John Wiley and Sons, New York.
[10] National Institute of Standards and Technology, 2002, *Radiation Thermometry Short Course*, Gaithersburg, MD.
[11] Brewster, M. Q., 1992, *Thermal Radiative Transfer and Properties*, John Wiley & Sons, New York, pp. 218–249, Chap. 7.
[12] Barker, D. G., 2003, ''Reconstruction of the Temperature Profile Along a Blackbody Optical Fiber Thermometer,'' M.S. thesis, Brigham Young University, Provo, UT.
[13] Gryvnak, D. A., and Burch, D. E., 1965, ''Optical and Infrared Properties of Al_2O_3 at Elevated Temperatures,'' J. Opt. Soc. Am., **55**(6), pp. 625–629.
[14] Oppenheimer, U. P., and Even, U., 1962, ''Infrared Properties of Sapphire at Elevated Temperatures,'' J. Opt. Soc. Am., **52**(9), pp. 1078–1079.
[15] Özişik, M. N., and Orlande, H. R. B., 2000, *Inverse Heat Transfer*, Taylor & Francis, New York, pp. 1–111, Chap. 1–2.
[16] Polak, E., 1971, *Computational Methods in Optimization*, Academic Press, New York.
[17] Stoer, J., Bulirsch, R., 1980, *Introduction to Numerical Analysis*, Springer-Verlag, New York.
[18] Press, William H., et al., 1999, *Numerical Recipes in C*, Second Edition, Cambridge University Press.
[19] Krieder, K. G., 1985, ''Fiber-Optic Thermometry,'' *Applications of Radiation Thermometry*, ASTM STP 895, Philadelphia, pp. 151–161.

Mechanism of Annular Two-Phase Flow Heat Transfer Enhancement and Pressure Drop Penalty in the Presence of a Radial Electric Field—Turbulence Analysis

Y. Feng

J. Seyed-Yagoobi

Heat Transfer Enhancement and Two-Phase Flow Laboratory, Department of Mechanical, Materials, and Aerospace Engineering, Illinois Institute of Technology, Chicago, IL 60616

The mechanism of heat transfer enhancement and pressure drop penalty in the presence of a radial electric field for the two-phase (liquid/vapor) annular flow is presented. The turbulence spectral theory shows that the radial electric field fluctuation changes the turbulent energy distribution, especially in the radial direction. Consequently, the Reynolds stresses are directly affected by the applied electric field. The analysis reveals that the influence of the applied electric field on the turbulence distribution in an annular two-phase flow leads to the changes in the heat transfer and the pressure drop. The magnitudes of the heat transfer enhancement and the pressure drop penalty are strongly related to the ratio of the radial pressure difference generated by the EHD force to the axial frictional pressure drop. The existing experimental data agree with the predictions of the analysis presented in this paper. The analysis developed here can be a valuable tool in properly predicting the two-phase annular flow heat transfer enhancement and pressure drop penalty in the presence of a radial electric field for both convective boiling and condensation processes. [DOI: 10.1115/1.1571089]

Keywords: Annular Flow, Electric Fields, Enhancement, Heat Transfer, Turbulence, Two-Phase

1 Introduction

Applying an electric field to enhance the heat transfer is potentially an effective approach to improve the effectiveness and reduce the heat exchanger size in various processes pertinent to industries such as automotive, refrigeration, air-conditioning, aircraft, and space. This technique also has many other advantages, including low noise, light weight, simple design, easy to control, no vibration, and low energy consumption.

The research on the effects of strong electric field on single-phase and two-phase (liquid/vapor) heat transfer can be tracked back to a half century ago. Before 1980, many researchers had already applied DC or AC electric fields in the natural convection, boiling, and condensation to enhance the heat transfer. In 1978, Jones [1] reviewed the electrohydrodynamically (EHD) enhanced heat transfer in a comprehensive paper, which included the heat transfer enhancement due to the EHD instability and electroconvection. Though significant progress was made in the EHD field, Jones pointed out that forced convection heat transfer with electric fields had not received the theoretical attention of natural convection.

Later, Yabe [2] listed the heat transfer enhancement techniques utilizing electric fields and discussed the corresponding mechanisms. He focused mainly on the external phase change and EHD extraction phenomenon, which can be observed as the EHD forces tend to destabilize the liquid/vapor interface and pull the liquid towards the more intense electric field. Recently, significant work has been carried out on the internal convective two-phase flow in the presence of a radial electric field based on the EHD extraction phenomenon. Singh [3], Singh et al. [4], Bryan and Seyed-Yagoobi [5,6], and Cotton et al. [7] showed that the radial electric field could, under the proper operating conditions, increase the convective boiling and condensation heat transfer coefficient significantly. They also showed that while the presence of the radial electric field enhances the heat transfer, it could also result in a significant pressure drop penalty.

Although it was rather clear that applying the electric field to the convective two-phase flow could lead to significant enhancement in heat transfer, its mechanism has not been completely understood. The interactions among the two-phase flow field, the electric field, and the temperature field increase the unexpected complexities, which make the prediction of the heat transfer enhancement difficult. Bryan and Seyed-Yagoobi [5] calculated the ratio of the radial EHD pressure to the axial momentum flux rate and they found that this ratio had a similar trend as the experimental data in terms of the heat transfer enhancement ratio as well as the pressure drop penalty. Cotton et al. [7] used the electric Rayleigh and Reynolds numbers to predict the flow redistribution due to the EHD force. They determined the condition under which the EHD effect may be significant. Feng and Seyed-Yagoobi [8] qualitatively predicted the transition region between the EHD-enhanced heat transfer and the EHD-suppressed heat transfer based on the linear instability theory. These above methods are helpful in providing insight, however, the theoretical understanding of the convective two-phase flow heat transfer enhancement with electric field is still not complete.

Based on the literature, the possible mechanisms of EHD-enhanced convective two-phase heat transfer in annular regime could be classified as: (a) electro-convection or EHD induced flow, (b) instability due to the EHD force leading to a way surface, (c) reduced liquid thermal resistance due to the EHD extraction phenomenon, (d) complete redistribution of the flow, and/or (e) change in the surface tension in the presence of electric field.

Contributed by the Heat Transfer Division for publication in the JOURNAL OF HEAT TRANSFER. Manuscript received by the Heat Transfer Division October 1, 2001; revision received February 11, 2003. Associate Editor: P. S. Ayyaswamy.

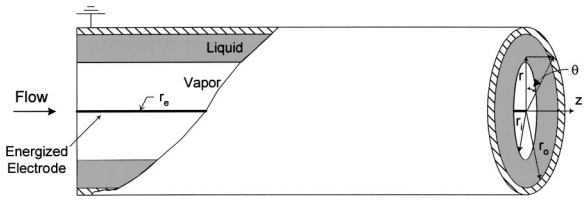

Fig. 1 Two-phase annular flow with the electric field

However, these mechanisms can not be used to successfully explain the associated pressure drop penalty in the presence of electric field.

Among the above suggested mechanisms, one important factor—turbulence—has been ignored. However, turbulence can play a determining role in both the heat and the momentum exchanges, which are directly related to the heat transfer and the pressure drop. Some researchers have pointed out the important role of turbulence in heat transfer in the presence of electric field. Atten et al. [9] experimentally and theoretically studied the electro-convection in a dielectric liquid layer due to the Coulomb force exerted by an electric field and its effect on the heat transfer. They achieved up to fifteen-fold increases in Nusselt number and concluded that the agitation of the liquid by the exerted electric force leads to the enhancement in heat transfer. Balancing the inertial term and the electric force in the Navier-Stokes equation for the fully turbulent regime, Atten et al. [9] evaluated the turbulent kinetic energy and the velocity fluctuation based on the electric force. They proposed a qualitative Nusselt number expression revealing the influence of the resulting turbulence on heat transfer. Yabe and Maki [10] conducted experiments on convective heat transfer enhanced by the EHD jet. Their measurements showed that the turbulent intensities were increased in proportional to the applied voltages. They also found that the theoretical analysis neglecting the turbulent effects failed to quantitatively explain the measured heat transfer enhancement.

Since the flow turbulence is also a critical parameter in the convective two-phase flow, its significant influence on the heat transfer and pressure drop is also expected. When the electric field is coupled with the convective two-phase flow, the turbulence in the flow and temperature fields leads to the fluctuations of the electric properties (such as the permittivity) and the interfacial configuration, and finally results in the fluctuations in the electric field distribution. Meanwhile, the electric forces also affect the turbulence fluctuations and thus the heat transfer and the pressure drop associated with the flow. In this paper, the turbulence analysis is carried out for a typical shear-controlled internal convective two-phase flow (i.e., the two-phase annular flow) in the presence of a radial electric field. The analytical predictions are compared to the existing experimental data.

2 Effects of a Radial Electric Field on Annular Two-Phase Flow Pressure Drop

2.1 Electric Field Distribution and EHD Force. Configuration of the annular two-phase flow coupled with the electric field is shown in Fig. 1. The liquid and vapor flow through the pipe simultaneously, while the liquid layer wraps the vapor core. An electrode, connected to a high voltage power supply, is suspended in the center of the vapor core and the pipe wall is grounded. Thus, the electric field is established in the radial direction only.

For simplicity, it is assumed that the liquid film thickness is uniform circumferentially and that there is no free electric charge in the bulk phases as well as at their corresponding interface. Thus, the electric potential satisfies the Laplace equation, $\nabla^2\Phi_l = \nabla^2\Phi_v = 0$. The electric boundary conditions are

$$\Phi_l = \Phi_v \quad at \quad r = r_i \tag{1}$$

$$\varepsilon_l \frac{d\Phi_l}{dr} = \varepsilon_v \frac{d\Phi_v}{dr} \quad at \quad r = r_i \tag{2}$$

$$\Phi_l = 0 \quad at \quad r = r_o \tag{3}$$

$$\Phi_v = V \quad at \quad r = r_e . \tag{4}$$

Solving for Φ_l and Φ_v gives the following classical electric field distributions:

$$\vec{E}_l = -\nabla\Phi_l = \frac{V}{[\varepsilon_l/\varepsilon_v \cdot \ln(r_i/r_e) + \ln(r_o/r_i)]r}\vec{r}, \quad r_i \leqslant r \leqslant r_o \tag{5}$$

and

$$\vec{E}_v = -\nabla\Phi_v = \frac{(\varepsilon_l/\varepsilon_v)V}{[\varepsilon_l/\varepsilon_v \cdot \ln(r_i/r_e) + \ln(r_o/r_i)]r}\vec{r}, \quad r_e \leqslant r < r_i . \tag{6}$$

Since the generated electric field is non-uniform, the Kelvin EHD body force (Melcher [11]), $\vec{f}^K_{\rm EHD} = q_e\vec{E} + (\varepsilon - \varepsilon_0)\vec{E}\cdot\nabla\vec{E}$, will be present and the corresponding Maxwell stresses will be in the following form:

$$T_{ij} = \varepsilon E_i E_j - \frac{1}{2}\delta_{ij}\varepsilon_0 E_k E_k . \tag{7}$$

From the above Maxwell stresses, the EHD force density, which exists only in the radial direction, becomes:

$$f_{\rm EHD} = \frac{1}{r}\frac{\partial}{\partial r}(rT_{rr}) + \frac{1}{r}\frac{\partial}{\partial\theta}T_{r\theta} - \frac{1}{r}T_{\theta\theta} + \frac{\partial T_{rz}}{\partial z}$$

$$= -\frac{1}{r}(\varepsilon - \varepsilon_0)E_r E_r . \tag{8}$$

Notice that the radial EHD force pulls the fluids with the higher permittivity than the vacuum towards the more intense electric field, which results in a radial pressure gradient. On the liquid side, by substituting Eq. (5) into Eq. (8), the pressure gradient due to the radial EHD force becomes

$$\frac{\partial P}{\partial r} = -(\varepsilon_l - \varepsilon_0)\cdot\frac{V^2}{[\varepsilon_l/\varepsilon_\nu \cdot \ln(r_i/r_e) + \ln(r_o/r_i)]^2}\cdot\frac{1}{r^3}, \quad r_i \leqslant r \leqslant r_o . \tag{9}$$

Similarly, the pressure gradient due to the radial EHD force on the vapor side is

$$\frac{\partial P}{\partial r} = -(\varepsilon_\nu - \varepsilon_0)\cdot\frac{(\varepsilon_l/\varepsilon_\nu)^2 V^2}{[\varepsilon_l/\varepsilon_\nu \cdot \ln(r_i/r_e) + \ln(r_o/r_i)]^2}\cdot\frac{1}{r^3}, \quad r_e \leqslant r < r_i . \tag{10}$$

The radial EHD pressure difference can be obtained by integrating the pressure gradients given above over the corresponding radius:

$$P_{\rm EHD} = P_e - P_o = \left[\frac{1}{2}(\varepsilon_\nu - \varepsilon_0)\cdot E_\nu^2\Big|_{r_i}^{r_e} + \frac{1}{2}(\varepsilon_l - \varepsilon_0)\cdot E_l^2\Big|_{r_o}^{r_i}\right], \tag{11}$$

which indicates the radial pressure difference generated by the electric body force at a given axial location. Note that the interfacial electric force is not taken into account.

2.2 Relation Between Electric Field and Reynolds Stresses. The steady Navier-Stokes equations in the presence of the electric field become

$$(\vec{u}\cdot\nabla)\vec{u} = -\frac{1}{\rho}\nabla P + \nu\nabla^2\vec{u} + \frac{\varepsilon - \varepsilon_0}{\rho}\vec{E}\cdot\nabla\vec{E}. \tag{12}$$

Assuming that the electric field exists only in the radial direction, then the z-direction momentum equation in the presence of the electric field will be of the same form as that in the absence of the electric field:

$$u_r\frac{\partial u_z}{\partial r}=-\frac{1}{\rho}\frac{\partial P}{\partial z}+\nu\frac{1}{r}\frac{\partial}{\partial r}\left(r\frac{\partial u_z}{\partial r}\right), \tag{13}$$

which indicates that the radial electric field indirectly affects the axial pressure drop. The effects of the radial electric field on the axial pressure drop can be determined through the Fourier transform of the Navier-Stokes equations. It is assumed that the turbulence is initially homogeneous, per given fluid phase, in the presence of the electric field to allow for simple Fourier transform analysis. Fluctuation of the electric field is also introduced due to the fluctuations in the electric properties (such as the permittivity) and the interfacial configuration. The turbulent fluctuation $\vec{e}'$ of the electric field is small compared to the applied electric field, $\vec{\bar{E}}$. The governing equations for the fields $\vec{u}'$, P, $\vec{\bar{E}}$, and $\vec{e}'$ are written as:

$$\nabla\cdot\vec{u}'=\nabla\cdot\vec{\bar{E}}=\nabla\cdot\vec{e}'=0 \tag{14}$$

$$\frac{\partial\vec{u}'}{\partial t}+(\overline{u}'\cdot\nabla)\overline{u}'=-\frac{1}{\rho}\nabla P+\nu\nabla^2\overline{u}'+\frac{\varepsilon-\varepsilon_0}{\rho}\vec{\bar{E}}\cdot\nabla\overline{e}'. \tag{15}$$

For the homogeneous turbulence in the presence of the electric field, the Fourier transform of the Navier-Stokes equations becomes:

$$\frac{\partial\hat{u}_i'}{\partial t}+\nu k^2\hat{u}_i'=i(\vec{k}\cdot\vec{\bar{E}})\frac{\varepsilon-\varepsilon_0}{\rho}\hat{e}'-ik_mP_{ij}(k)\times\int_{\vec{p}+\vec{q}=k}\hat{u}_i'(\vec{p},t)\hat{u}_m'(\vec{q},t)d\vec{q}. \tag{16}$$

In the above equation, $\vec{k}$ is the wave vector, and its absolute value indicates the wave number. When the wave number increases, the eddy size decreases. Normally, the turbulence energy is transported from the larger eddies (small wave numbers) to the smaller eddies (large wave numbers), and at the same time for the eddies of the same size the turbulent energy is redistributed among different directions. When the eddies keep reducing in size, the viscosity dissipation turns important, which is represented by $\nu k^2\hat{u}_i'$. Eventually, the turbulent energy is dissipated by the viscosity. If there is no more turbulent energy to be extracted from the main flow, the flow becomes laminar. In the above equation, it is shown that the fluctuation of the electric field takes a role in the distribution of the turbulent energy. As indicated by the term $i(\vec{k}\cdot\vec{\bar{E}})\varepsilon-\varepsilon_0/\rho\hat{e}'$ in Eq. (16), there is a preferred direction (i.e., in the direction of the applied electric field) in the energy distribution. The resulting turbulence will have the non-homogeneous characteristics. In this case, the applied electric field is in the radial direction. Especially, the radial turbulent fluctuation will be intensified, and $|u_r'|_{\text{EHD}}|>|u_r'|_{\text{non-EHD}}|$. Since the axial turbulent fluctuation is orthogonal to the radial applied electric field, it will not be directly influenced by the fluctuation of the radial electric field. Thus, it can be assumed that $-\overline{u_z'u_r'}|_{\text{EHD}}>-\overline{u_z'u_r'}|_{\text{non-EHD}}$. This conclusion agrees with Yabe and Maki's [10] experimental results that the turbulent intensities were increased with the applied voltage when a ring electrode was used to enhance the heat transfer by generating the EHD liquid jet.

Estimating the magnitude of the EHD effect on the turbulence is necessary for the investigation of the heat transfer and the pressure drop in the presence of the electric field. It is assumed that a fluctuating unit volume in the turbulent EHD flow experiences both the inertial force and the radial EHD force. These two forces will influence the magnitude of the intensification of the Reynolds stress. Since the inertial force per unit volume is $f_{inert}\sim\rho U_\tau^2/D_o$ and the radial EHD force per unit volume is $f_{\text{EHD}}\sim(\varepsilon-\varepsilon_0)E^2/r$, then it can be assumed that:

$$\frac{(-\overline{u_z'u_r'})|_{\text{EHD}}}{(-\overline{u_z'u_r'})|_{\text{non-EHD}}}\sim\frac{f_{\text{EHD}}}{f_{\text{inert}}}=\frac{(\varepsilon-\varepsilon_0)E^2/r}{\rho U_r^2/D_o}, \tag{17}$$

where $U_r=\sqrt{\tau_w/\rho}$ indicates the characteristic turbulent fluctuation velocity.

2.3 Evaluation of Pressure Drop Penalty in the Presence of a Radial Electric Field. For a two-phase turbulent pipe flow, the velocity and pressure fields can also be assumed as the summation of the mean values and the fluctuations: $u_z=U_z+u_z'$, $u_r=U_r+u_r'$ and $P=\overline{P}+p'$. After being time-averaged, Eq. (13) becomes:

$$0=-\frac{1}{\rho}\frac{\partial\overline{P}}{\partial z}+\nu\frac{1}{r}\frac{\partial}{\partial r}\left(r\frac{\partial U_z}{\partial r}\right)-\frac{1}{r}\frac{\partial(r\overline{u_z'u_r'})}{\partial r}. \tag{18}$$

Let $U_z^*=U_z/U_o$, $u_z'^*=u_z'/U_o$, $u_r'^*=u_r'/U_o$, $r^*=r/D_o$, $z^*=z/D_o$, $\overline{P}^*=\overline{P}/\rho U_o^2$, where D_o is the inner pipe diameter and U_o is the fluid characteristic velocity, $U_o=2\pi\int_{r_e}^{r_o}U_z r dr/(\pi D_o^2/4)$. Here, the inner pipe diameter is used as the equivalent diameter due to the relatively small electrode size. Equation (18) in the non-dimensional form becomes

$$\frac{\partial}{\partial r^*}\left(r^*\frac{1}{\text{Re}}\frac{\partial U_z^*}{\partial r^*}-r^*\overline{u_z'^*u_r'^*}\right)=\frac{\partial\overline{P}^*}{\partial z^*}r^*, \tag{19}$$

where $\text{Re}=U_oD_o/\nu$.

Integrating the above equation twice from r_e^* to an arbitrary r^* yields

$$\frac{U_z^*}{\text{Re}}=\frac{1}{4}\frac{\partial\overline{P}^*}{\partial z^*}(r^{*2}-r_e^{*2})-\int_{r_e^*}^{r^*}(-\overline{u_z'^*u_r'^*})dy^*+c\ln\left(\frac{r^*}{r_e^*}\right), \tag{20}$$

where c is the integration constant. Equation (20) corresponds to the axial velocity profile along the pipe cross section. The dimensionless volumetric flow rate can be expressed as

$$\frac{2\pi\int_{r_e}^{r_o}U_z r dr}{U_oD_o^2}=2\pi\int_{r_e^*}^{r_o^*}\text{Re}\left[\frac{1}{4}\frac{\partial\overline{P}^*}{\partial z^*}(r^{*2}-r_e^{*2})-\int_{r_e^*}^{r^*}(-\overline{u_z'^*u_r'^*})dy^*+c\ln\left(\frac{r^*}{r_e^*}\right)\right]r^*dr^*. \tag{21}$$

The third term on the right hand side of Eq. (21) indicates the influence of the electrode on the volumetric flow rate. Since the diameter of the electrode is small compared with the pipe diameter and the electrode is intentionally designed with a minimal influence on the net axial flow, it is reasonable to assume that the presence of the electrode does not significantly influence the pressure gradient and the Reynolds stress distribution. Thus, the third term is neglected. According to the definition of the fluid characteristic velocity, U_o, Eq. (21) can be simplified as

$$2\pi\int_{r_e^*}^{r_o^*}\int_{r_e^*}^{r^*}(-\overline{u_z'^*u_r'^*})dy^*r^*dr^*=2\pi\int_{r_e^*}^{r_o^*}\frac{1}{4}\frac{\partial\overline{P}^*}{\partial z^*}(r^{*2}-r_e^{*2})r^*dr^*-\frac{\pi}{4}\frac{1}{\text{Re}}. \tag{22}$$

The above equation shows that the pressure drop $\partial\overline{P}^*/\partial z^*$ is affected by the molecular viscosity (absorbed in Re) and the turbulence (i.e., $-\overline{u_z' u_r'}$). Since the molecular viscosity is not affected by the presence of the electric field, then the effects of the electric field on the turbulence will be mainly discussed here. Also, the molecular viscosity will be ignored in the analysis given below, since it is small compared with the turbulent viscosity for high Re number. Combined with Eq. (17), the ratio of the frictional pressure gradient with EHD to that without EHD becomes

$$\frac{\left.\dfrac{\partial\overline{P}^*_{fr}}{\partial z^*}\right|_{\text{EHD}}}{\left.\dfrac{\partial\overline{P}^*_{fr}}{\partial z^*}\right|_{\text{non-EHD}}} \cong \frac{\left.2\pi\displaystyle\int_{r_e^*}^{r_o^*}\int_{r_e^*}^{r^*}(-\overline{u_z'^* u_r'^*})dy^* r^* dr^*\right|_{\text{EHD}}}{\left.2\pi\displaystyle\int_{r_e^*}^{r_o^*}\int_{r_e^*}^{r^*}(-\overline{u_z'^* u_r'^*})dy^* r^* dr^*\right|_{\text{non-EHD}}} \sim \frac{\displaystyle\int_{r_e^*}^{r_o^*}\int_{r_e^*}^{r^*}\frac{(\varepsilon-\varepsilon_0)E^2}{y^*}dy^* r^* dr^*}{\tau_w\displaystyle\int_{r_e^*}^{r_o^*}\int_{r_e^*}^{r^*}dy^* r^* dr^*}, \tag{23}$$

where E is a function of r, while τ_w can be taken out of the integration since it is independent of r. Inserting the electric field distributions in both the liquid and vapor phases (Eqs. (5) and (6), respectively) into Eq. (23) yields

$$\begin{aligned}
&\frac{\displaystyle\int_{r_e^*}^{r_o^*}\int_{r_e^*}^{r^*}\frac{(\varepsilon-\varepsilon_0)E^2}{y^*}dy^* r^* dr^*}{\tau_w\displaystyle\int_{r_e^*}^{r_o^*}\int_{r_e^*}^{r^*}dy^* r^* dr^*} \\
&\quad= \frac{\dfrac{1}{\tau_w D^2}\left[\displaystyle\int_{r_e^*}^{r_i^*}\int_{r_e^*}^{r^*}\frac{(\varepsilon_\nu-\varepsilon_0)E_\nu^2}{y^*}dy^* r^* dr^* + \int_{r_i^*}^{r_o^*}\left(\int_{r_i^*}^{r^*}\frac{(\varepsilon_l-\varepsilon_0)E_l^2}{y^*}dy^* + \int_{r_e^*}^{r_i^*}\frac{(\varepsilon_\nu-\varepsilon_0)E_\nu^2}{y^*}dy^*\right)r^* dr^*\right]}{\dfrac{1}{3}(r_o^{*3}-r_e^{*3})-\dfrac{1}{2}(r_o^{*2}-r_e^{*2})r_e^*} \\
&\quad= \frac{3}{\tau_w D^2}\cdot\frac{V^2}{[\varepsilon_l/\varepsilon_\nu\cdot\ln(r_i/r_e)+\ln(r_o/r_i)]^2}\cdot\left\{(\varepsilon_\nu-\varepsilon_0)\left(\frac{\varepsilon_l}{\varepsilon_\nu}\right)^2\left[\frac{1}{2}\left(\frac{1}{r_e^{*2}}-\frac{1}{r_i^{*2}}\right)r_o^{*2}\right.\right. \\
&\qquad\left.\left.-\ln\left(\frac{r_i^*}{r_e^*}\right)\right]+(\varepsilon_l-\varepsilon_0)\left[\frac{1}{2}\left(\frac{1}{r_i^{*2}}-\frac{1}{r_o^{*2}}\right)r_o^{*2}-\ln\left(\frac{r_o^*}{r_i^*}\right)\right]\right\}
\end{aligned} \tag{24}$$

Generally, the electrode radius r_e is rather small compared with the pipe radius r_o, indicating that $(\varepsilon_\nu-\varepsilon_0)(\varepsilon_l/\varepsilon_\nu)^2 1/2(1/r_e^{*2}-1/r_i^{*2})r_o^{*2}+(\varepsilon_l-\varepsilon_0)1/2(1/r_i^{*2}-1/r_o^{*2})r_o^{*2}$ is significantly larger than $(\varepsilon_\nu-\varepsilon_0)(\varepsilon_l/\varepsilon_\nu)^2\ln(r_i^*/r_e^*)+(\varepsilon_l-\varepsilon_0)\ln(r_o^*/r_i^*)$. Thus, Eq. (24) reduces to

$$\begin{aligned}
&\frac{\displaystyle\int_{r_e^*}^{r_o^*}\int_{r_e^*}^{r^*}\frac{(\varepsilon-\varepsilon_0)E^2}{y^*}dy^* r^* dr^*}{\tau_w\displaystyle\int_{r_e^*}^{r_o^*}\int_{r_e^*}^{r^*}dy^* r^* dr^*} \\
&\quad\cong \frac{3r_o^{*2}}{(2r_o^*+r_e^*)(r_o^*-r_e^*)^2} \\
&\qquad\cdot\frac{\dfrac{1}{2}(\varepsilon_\nu-\varepsilon_0)E_\nu^2\big|_{r_i}^{r_e}+\dfrac{1}{2}(\varepsilon_l-\varepsilon_0)E_l^2\big|_{r_o}^{r_i}}{\tau_w}.
\end{aligned} \tag{25}$$

Finally, from Eqs. (23) and (25) the pressure gradient ratio can be evaluated as:

$$\begin{aligned}
\frac{\left.\dfrac{\partial\overline{P}^*_{fr}}{\partial z^*}\right|_{\text{EHD}}}{\left.\dfrac{\partial\overline{P}^*_{fr}}{\partial z^*}\right|_{\text{non-EHD}}} &\sim \frac{3r_o^{*2}}{(2r_o^*+r_e^*)(r_o^*-r_e^*)^2} \\
&\cdot\frac{\dfrac{1}{2}(\varepsilon_\nu-\varepsilon_0)E_\nu^2\big|_{r_i}^{r_e}+\dfrac{1}{2}(\varepsilon_l-\varepsilon_0)E_l^2\big|_{r_o}^{r_i}}{\tau_w}.
\end{aligned} \tag{26}$$

Substituting Eq. (11) into the above equation and with $\tau_w = -D_o/4\partial P_{fr}/\partial z|_{\text{non-EHD}}$, Eq. (26) becomes

$$\frac{\left.\dfrac{\partial\overline{P}^*_{fr}}{\partial z^*}\right|_{\text{EHD}}}{\left.\dfrac{\partial\overline{P}^*_{fr}}{\partial z^*}\right|_{\text{non-EHD}}} \sim \frac{12r_o^{*2}}{(2r_o^*+r_e^*)(r_o^*-r_e^*)^2 D_o}\cdot\frac{P_{\text{EHD}}}{-\left.\dfrac{\partial\overline{P}_{fr}}{\partial z}\right|_{\text{non-EHD}}}. \tag{27}$$

The effects of the electric field on the total frictional pressure loss over given pipe length, L, can be reasonably evaluated as

$$\frac{\Delta P_{fr}|_{\text{EHD}}}{\Delta P_{fr}|_{\text{non-EHD}}} = \frac{\left.\int_0^{L^*} \frac{\partial \overline{P}^*_{fr}}{\partial z^*} dz^*\right|_{\text{EHD}}}{\left.\int_0^{L^*} \frac{\partial \overline{P}^*_{fr}}{\partial z^*} dz^*\right|_{\text{non-EHD}}}. \tag{28}$$

From the above two equations, the following relation is deduced

$$\frac{\Delta P_{fr}|_{\text{EHD}}}{\Delta P_{fr}|_{\text{non-EHD}}} \sim \frac{\int_0^L P_{\text{EHD}} dz \Big/ L}{\Delta P_{fr}|_{\text{non-EHD}}}. \tag{29}$$

In a horizontal constant cross sectional pipe, the internal convective two-phase flow pressure drop consists of two components. One component is due to the friction and the other component is due to the momentum exchange caused by the phase change. The effects of the electric field on the frictional pressure drop are shown in Eq. (29). The momentum exchange in the presence of the electric field depends on the amount of the phase change, which is affected by the heat transfer rate. In the next section, it will be shown that the heat transfer coefficient is also related to $\int_0^L P_{\text{EHD}} dz/L/\Delta P_{fr}|_{\text{non-EHD}}$. Thus, the total pressure drop for the annular flow in the presence of the electric field can be assumed as follows

$$\frac{\Delta P_{\text{EHD}}}{\Delta P_0} = \text{function}\left(\frac{\int_0^L P_{\text{EHD}} dz \Big/ L}{\Delta P_{fr}|_{\text{non-EHD}}} \right). \tag{30}$$

3 Effect of a Radial Electric Field on Annular Two-Phase Flow Heat Transfer

Since the heat and momentum in a fluid are transferred in a similar way, the analogy between the heat transfer and the momentum exchange exists in the internal pipe flow. As stated by Colburn [12], the relationship between the convection heat transfer coefficient and the frictional pressure gradient in the single-phase turbulent channel flow can be in the following form:

$$h \sim \left(\frac{dP_{fr}}{dz} \right)^{(n-1)/n}. \tag{31}$$

The quasi-equilibrium two-phase flow in the annular flow regime can also be treated similarly since there are continuous liquid layer along the pipe wall and continuous vapor phase at the core. Altman et al. [13], Kosky and Staub [14], and Yesin [15] suggested that the forced convection heat transfer coefficient in a two-phase annular flow could be expressed as:

$$h|_{\text{two-phase}} \sim \left. \left(\frac{dP_{fr}}{dz} \right)^{(n-1)/n} \right|_{\text{two-phase}}. \tag{32}$$

Altman et al. [13] and Kosky and Staub [14] assumed $n=2.0$ in Eq. (32) for convective condensation in the annular flow regime, while Yesin [15] recommended $n=1.75$. If the two-phase annular flow, either in the presence or absence of the electric field, satisfies Eq. (32), then the magnitude of the heat transfer enhancement in the presence of the electric field can be evaluated as

$$\frac{h_{\text{EHD}}}{h_0} \sim \left(\frac{dP_{fr}|_{\text{EHD}}}{dP_{fr}|_{\text{non-EHD}}} \right)^{(n-1)/n}. \tag{33}$$

Similarly, the ratio of the average convection heat transfer coefficients over the given pipe length, L, can be approximated as:

$$\frac{h_{\text{EHD}}}{h_0} \sim \left(\frac{\Delta P_{fr}|_{\text{EHD}}}{\Delta P_{\text{fr}}|_{\text{non-EHD}}} \right)^{(n-1)/n} = \left(\frac{\int_0^L P_{\text{EHD}} dz \Big/ L}{\Delta P_{fr}|_{\text{non-EHD}}} \right)^{(n-1)/n}. \tag{34}$$

4 Experimental Verification and Discussion

Equations (30) and (34) show that the pressure drop penalty and the heat transfer enhancement for an annular flow in the presence of the electric field can both be predicted as a function of $(\int_0^L P_{\text{EHD}} dz/L)/\Delta P_{fr}|_{\text{non-EHD}}$. Based on this conclusion, two simple expressions are assumed to predict the pressure drop penalty and the heat transfer enhancement in the presence of the electric field:

$$\frac{\Delta P_{\text{EHD}}}{\Delta P_0} = A_p \cdot \frac{\int_0^L P_{\text{EHD}} dz \Big/ L}{\Delta P_{fr}|_{\text{non-EHD}}} + B_p \tag{35}$$

and

$$\frac{h_{\text{EHD}}}{h_0} = A_h \cdot \left(\frac{\int_0^L P_{\text{EHD}} dz \Big/ L}{\Delta P_{fr}|_{\text{non-EHD}}} \right)^{0.5} + B_h, \tag{36}$$

where A and B are constants to be determined and n is assumed to be equal to 2.0. This value of n gives a reasonable agreement between the experimental data and the predictions presented below. Here, the frictional pressure gradient correlation defined as

$$-\frac{dP_{fr}}{dz} = \left(\frac{2 f_{lo} G^2}{\rho_l D_o} \right) \phi_{lo}^2 \tag{37}$$

is recommended for estimating the axial frictional pressure drop in the absence of the electric field (i.e., $\Delta P_{fr}|_{\text{non-EHD}}$). Friedel [16] correlation is selected to calculate the two-phase multiplier ϕ_{lo}^2. The void fraction, α, is calculated using the correlation of Thom [17]. With Eqs. (11) and (37), Friedel correlation, void fraction, given applied voltage, mass flux, pipe dimensions, and corresponding fluids properties, $(\int_0^L P_{\text{EHD}} dz/L)/\Delta P_{fr}|_{\text{non-EHD}}$ can be numerically calculated.

The existing experimental data from four different sources, Singh [3], Singh et al. [4], Bryan and Seyed-Yagoobi [5], and Feng [18], are used to correlate the coefficients in Eqs. (35) and (36). The experimental data provided by Bryan and Seyed-Yagoobi [5] and Feng [18], respectively, correspond to the convective boiling and the convective condensation of R-134a flowing inside a smooth copper tube of $D=14$ mm. The data by Singh [3] and Singh et al. [4] give the pressure drop penalty and heat transfer enhancement during the convective condensation of R-134a inside a smooth cooper tube of $D=11$ mm. Coaxial cylindrical electrodes of 3.2 mm outside diameter were used by Singh [3] and Singh et al. [4], while Bryan and Seyed-Yagoobi [5] and Feng [18] applied the coaxial cylindrical electrodes of 1.6 mm outside diameter. For the data from Singh [3] and Singh et al. [4], the uncertainty in the measured pressure drop was 0.029 kPa and the uncertainty in the calculated heat transfer enhancement was between 12% and 24%. For the data from Bryan and Seyed-Yagoobi [5], the average uncertainty of the pressure drop measurement was 0.056 kPa and the average uncertainty in the calculated heat transfer coefficient was 13.4%. For the data from Feng [18], the average uncertainty of the pressure drop measurement was 0.045 kPa and the average uncertainty in the calculated local heat transfer coefficient was between 24.1% and 30.3%.

Figures 2 and 3, respectively, present the pressure drop penalty and the heat transfer enhancement data against the pressure ratio of the radial pressure difference generated by the EHD force to the axial frictional pressure drop, $(\int_0^L P_{\text{EHD}} dz/L)/\Delta P_{fr}|_{\text{non-EHD}}$. Equations (35) and (36) after regression become

$$\frac{\Delta P_{\text{EHD}}}{\Delta P_0} = 0.93 \cdot \frac{\int_0^L P_{\text{EHD}} dz \Big/ L}{\Delta P_{fr}|_{\text{non-EHD}}} + 1.27 \quad \text{with} \quad R^2 = 0.77 \tag{38}$$

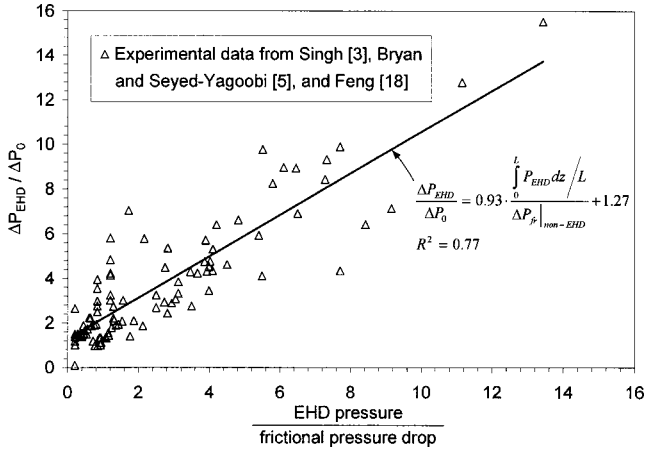

Fig. 2 Regression of pressure drop penalty experimental data in the presence of electric fields

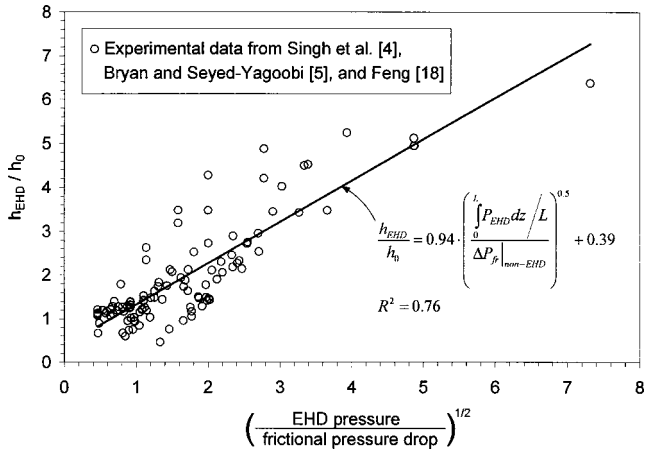

Fig. 3 Regression of heat transfer enhancement experimental data in the presence of electric fields

and

$$\frac{h_{\mathrm{EHD}}}{h_0} = 0.94 \cdot \left(\frac{\int_0^L P_{\mathrm{EHD}} dz \,/\, L}{\Delta P_{fr}|_{\text{non-EHD}}} \right)^{0.5} + 0.39 \quad \text{with} \quad R^2 = 0.76. \tag{39}$$

The above determination coefficients show that the pressure drop penalty and the heat transfer enhancement in the presence of the electric field are closely dependent on the ratio of radial EHD pressure difference to the axial frictional pressure drop. When the applied high voltage increases and the mass flow rate decreases, the heat transfer enhancement and pressure drop penalty go up. The above two equations also indicate that the refrigerants with higher permittivity values can have more significant heat transfer enhancement and pressure drop penalty during the EHD-affected annular two-phase flow. Equations (38) and (39) are obtained based on both the convective boiling data and the convective condensation data. Normally, it would be more reasonable to determine the convective boiling correlation and convective condensation correlation separately considering the different heat transfer directions. Figures 4–7 individually show the pressure drop penalty and the heat transfer enhancement data against the pressure ratio, $(\int_0^L \Delta P_{\mathrm{EHD}} dz/L)/\Delta P_{fr}|_{\text{non-EHD}}$ for the EHD-enhanced convective boiling and condensation. Equation (35) becomes

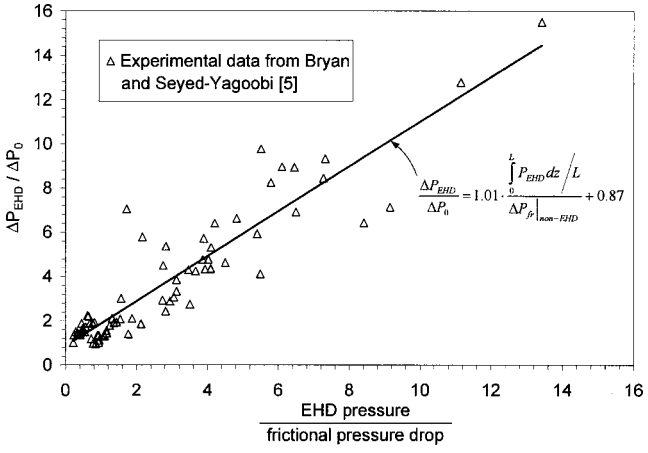

Fig. 4 Regression of boiling pressure drop penalty experimental data in the presence of electric fields

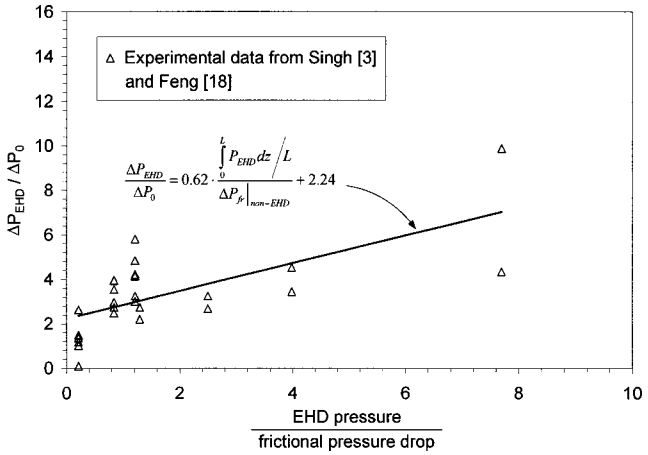

Fig. 5 Regression of condensation pressure drop penalty experimental data in the presence of electric fields

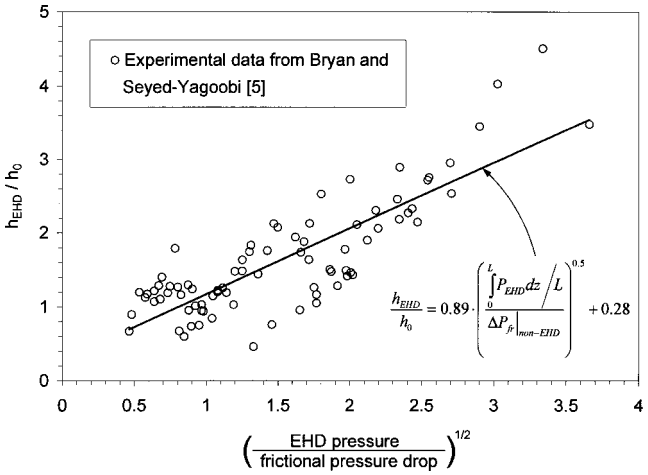

Fig. 6 Regression of boiling heat transfer enhancement experimental data in the presence of electric fields

$$\left. \frac{\Delta P_{\mathrm{EHD}}}{\Delta P_0} \right|_{\text{Boiling}} = 1.01 \cdot \frac{\int_0^L P_{\mathrm{EHD}} dz \,/\, L}{\Delta P_{fr}|_{\text{non-EHD}}} + 0.87 \tag{40}$$

and

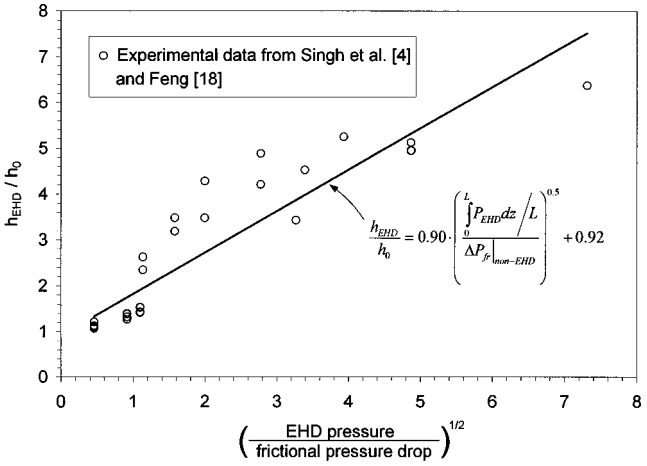

Fig. 7 Regression of condensation heat transfer enhancement experimental data in the presence of electric fields

$$\left.\frac{\Delta P_{\mathrm{EHD}}}{\Delta P_0}\right|_{\mathrm{Condensation}} = 0.62 \cdot \frac{\int_0^L P_{\mathrm{EHD}} dz \Big/ L}{\Delta P_{fr}|_{\text{non-EHD}}} + 2.24, \quad (41)$$

while Eq. (36) becomes

$$\left.\frac{h_{\mathrm{EHD}}}{h_0}\right|_{\mathrm{Boiling}} = 0.89 \cdot \left(\frac{\int_0^L P_{\mathrm{EHD}} dz \Big/ L}{\Delta P_{fr}|_{\text{non-EHD}}} \right)^{0.5} + 0.28 \quad (42)$$

and

$$\left.\frac{h_{\mathrm{EHD}}}{h_0}\right|_{\mathrm{Condensation}} = 0.90 \cdot \left(\frac{\int_0^L P_{\mathrm{EHD}} dz \Big/ L}{\Delta P_{fr}|_{\text{non-EHD}}} \right)^{0.5} + 0.92. \quad (43)$$

Figures 8–13 show that Eqs. (40)~(43) successfully predict the trends of pressure drop penalty and heat transfer heat enhancement in the presence of a radial electric field for both convective boiling and convective condensation processes under various operating conditions. The agreement between the existing data and the predictions also confirms the role of turbulence in the EHD pressure drop penalty and heat transfer enhancement.

In general, the analysis given in this paper properly predicts the experimental data under various operating conditions. However, the discrepancies at high flow quality values between the predicted heat transfer enhancement and the experimental data for convective boiling are partially due to the change of flow regime from annular flow to mist flow. In the mist flow regime, the non-uniform electric field in the two-phase flow is inclined to pull the liquid drops away from the pipe wall towards the electrode. The consequent dry-out on the pipe wall suppresses the convective boiling heat transfer as described by Feng and Seyed-Yagoobi [8]. The analysis provided here does not take the annular-to-mist flow regime transition into account.

At low flow quality values, the two-phase flow may fall into the gravity-controlled flow regime (stratified or intermittent). The disagreement between the experimental data and the theoretical predictions is partially due to the flow regime being different from the assumed annular regime. In the gravity-controlled flow regime, the electro-convection takes an important role in heat transfer of the two-phase flow in the presence of electric field. Thus, ignoring the effects of the electro-convection may lead to the under-prediction of heat transfer enhancement at low flow quality values. The similar problem will possibly be faced if the mass flux is low (i.e., $G = 50\ \mathrm{kg/m^2\ s}$). The horizontal internal convective condensation of low mass flux can be in the gravity-controlled or the transition flow regimes and its heat transfer enhancement will not completely follow the predictions based on the turbulence analysis for annular flow regime. Most importantly, the significant uncertainty of the data of the two-phase flow at any flow quality values along with the effects of the electric field on the void fraction and two-phase multiplier makes the accurate predictions of the experimental data difficult.

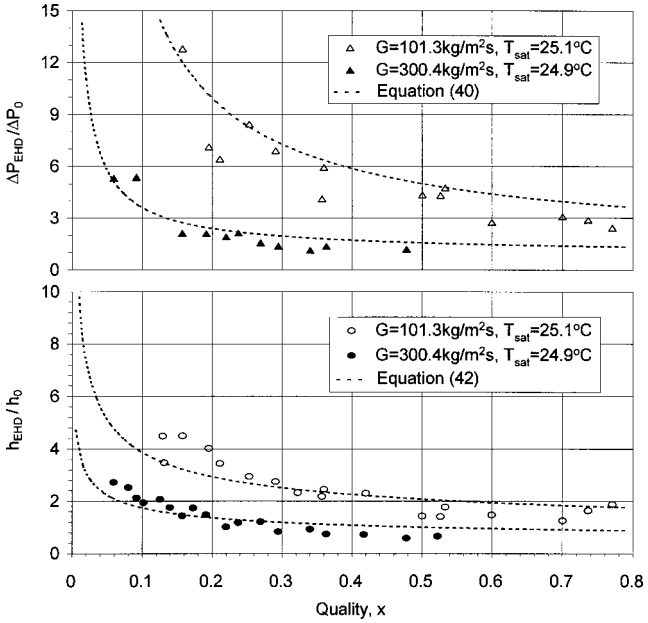

Fig. 8 Comparison of the predictions and the experimental data for R-134a convective boiling at $T_{sat} \cong 25°C$ and applied voltage=15 kV from Bryan and Seyed-Yagoobi [5]

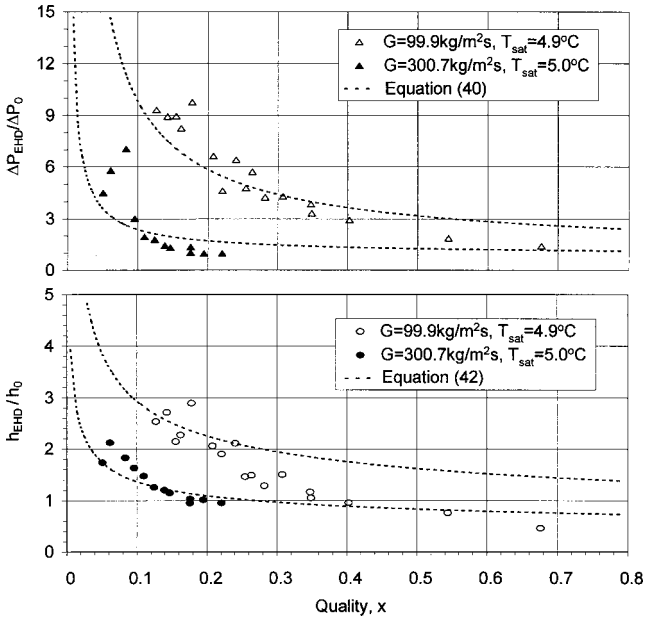

Fig. 9 Comparison of the predictions and the experimental data for R-134a convective boiling at $T_{sat} \cong 5°C$ and applied voltage=15 kV from Bryan and Seyed-Yagoobi [5]

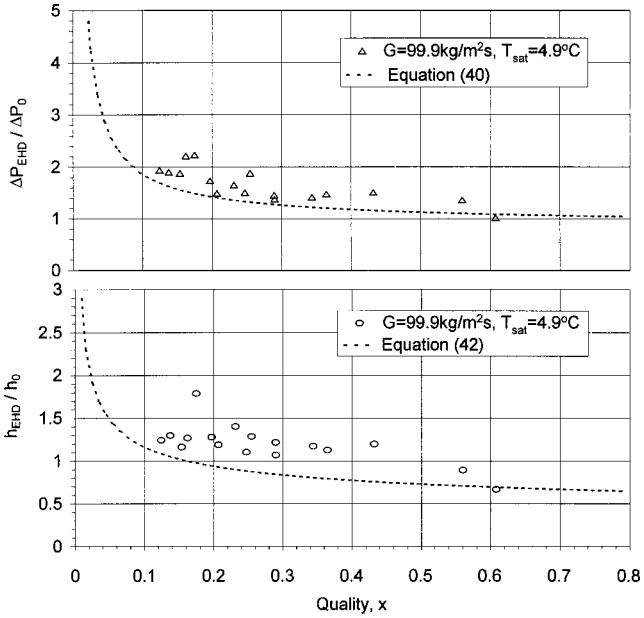

Fig. 10 Comparison of the predictions and the experimental data for R-134a convective boiling at $T_{sat} \cong 5°C$ and applied voltage=5 kV from Bryan and Seyed-Yagoobi [5]

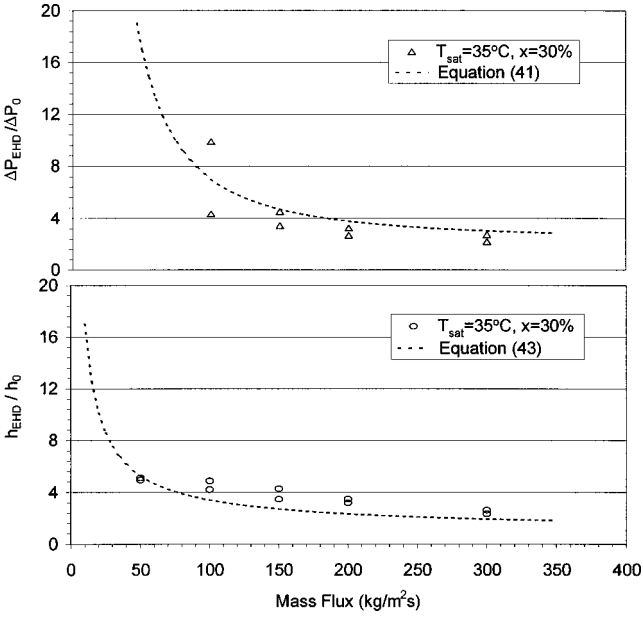

Fig. 12 Comparison of the predictions and the experimental data for R-134a convective condensation at $T_{sat} \cong 35°C$ and applied voltage=15 kV from Singh [3]

5 Conclusions

The effects of the electric field on the heat transfer and pressure drop in an annular two-phase flow were analyzed. Based on the turbulence spectral theory, the fluctuation of the electric field influences the distribution of the turbulent energy, especially in the radial direction. The analysis revealed that the heat transfer enhancement and the pressure drop penalty are strongly related to the ratio of the radial pressure difference generated by the EHD force to the axial frictional pressure drop. The theoretical predictions agreed with the experimental data of the horizontal internal convective boiling as well as the horizontal internal convective condensation processes at high mass fluxes. The analysis presented in this paper can be a valuable tool for properly predicting the heat transfer enhancement and the pressure drop penalty of the horizontal annular two-phase flow in the presence of a radial electric field.

Acknowledgment

This work was partially supported by the NASA Microgravity Fluid Physics Program.

Nomenclature

A = constant
B = constant
c = constant
D = inner diameter, m
E, e = electric field strength, V/m
Fr = Froude number, $U_{sv}^2/(gD)$

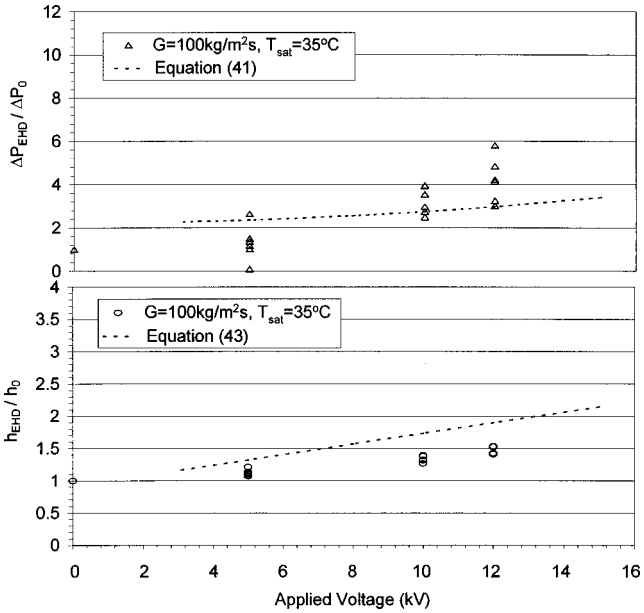

Fig. 11 Comparison of the predictions and the experimental data for R-134a convective condensation at $T_{sat} \cong 35°C$ and G=100 kg/m²s from Feng [18]

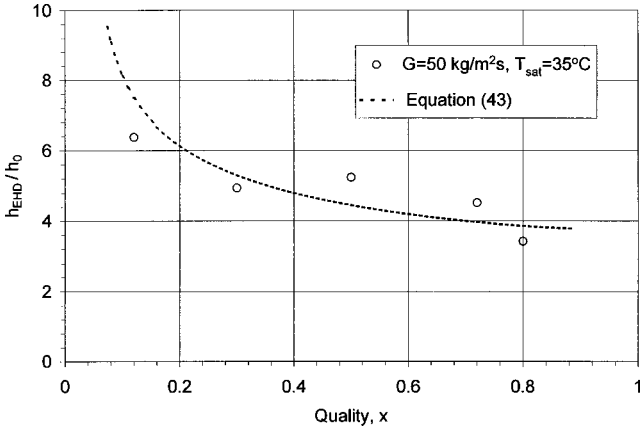

Fig. 13 Comparison of the predicted heat transfer enhancement and the experimental data for R-134a convective condensation at $T_{sat} \cong 35°C$, G=50 kg/m²s, and applied voltage =15 kV from Singh et al. [4]

F = force density, N/m^3
f = friction factor
G = mass flux, $kg/m^2\,s$
h = heat transfer coefficient, $W/m^2\,K$
j = superficial velocity, s/m
k = wave number, m^{-1}
$\vec{k}$ = wave vector
L = pipe length, m
n = coefficient
P, p = pressure, Pa
$\vec{p}$ = wave vector
$\vec{q}$ = wave vector
r = radius, m or r-axis coordinate
$\vec{r}$ = unit radial vector
R^2 = correlation coefficient
Re = Reynolds number
T = temperature, °C or second order tensor, N/m^2
t = time, s
U, u = velocities, m/s
x = quality
y = radius, m
z = z-axis coordinate

Greek Symbols

α = void factor
ε = permittivity, F/m
Φ = electric potential, V
ϕ_{lo} = two-phase multiplier
θ = θ-axis coordinate
ρ = density, kg/m^3
τ = shear force, N/m^2

Subscripts

EHD = electrohydrodynamical
non-EHD = without electric field
e = electrode or electric
fr = frictional
h = heat transfer
i = interfacial or index
inert = inertial
j = index
l = liquid
lo = liquid phase only
m = index
o = pipe
p = pressure drop
r = radial
sat = saturation
tot = total
two-phase = two-phase
v = vapor
vl = difference between liquid and vapor
w = wall
0 = vacuum
1,2,3 = coefficient index
τ = characteristic turbulent velocity

Superscripts

$'$ = fluctuation
$-$ = average
$\dagger$ = in wave number space
$*$ = nondimensional

References

[1] Jones, T. B., 1978, "Electrohydrodynamically Enhanced Heat Transfer in Liquids—A Review," Adv. Heat Transfer, **14**, pp. 107–148.
[2] Yabe, A., 1991, "Active Heat Transfer Enhancement by Applying Electric Fields," *Proceedings of ASME/JSME Thermal Engineering Conference*, **3**, pp. 15–23.
[3] Singh, A., 1995, "Electrohydrodynamic (EHD) Enhancement of In-Tube Boiling and Condensation of Alternate (non-CFC) Refrigerants," Ph.D. dissertation, University of Maryland, College Park, MD.
[4] Singh, A., Ohadi, M. M., and Dessiatoun, S., 1997, "EHD Enhancement of In-Tube Condensation Heat Transfer of Alternate Refrigerant R-134a in Smooth and Microfin Tubes," ASHRAE Trans., **103**, part 1, pp. 813–823.
[5] Bryan, J. E., and Seyed-Yagoobi, J., 2000, "Electrohydrodynamically Enhanced Convective Boiling: Relationship between Electrohydrodynamic Pressure and Momentum Flux Rate," ASME J. Heat Transfer. , **122**, pp. 266–277.
[6] Bryan, J. E., and Seyed-Yagoobi, J., 2001, "Influence of Flow Regime and Heat Flux on Electrohydrodynamically Enhanced Convective Boiling," ASME J. Heat Transfer , **123**, pp. 355–367.
[7] Cotton, J. S., Chang, J. S., Shoukri, M., and Smith-Pollard, T., 2000, "Electrohydrodynamic (EHD) Flow and Convective Boiling Augmentation in Single-component Horizontal Annular Channels," 2000 ASME International Mechanical Engineering Congress & Exposition, HTD (Am. Soc. Mech. Eng.), **366-4**, pp. 177–184.
[8] Feng, Y., and Seyed-Yagoobi, J., 2002, "Linear Instability Analysis of a Horizontal Two-phase Flow in the Presence of Electrohydrodynamic Extraction Force," ASME J. Heat Transfer , **124**, pp. 102–110.
[9] Atten, P., McCluskey, F. M. J., and Perez, A. T., 1988, "Electroconvection and Its Effect on Heat Transfer," IEEE Trans. Electr. Insul., **23**(4), pp. 659–667.
[10] Yabe, A., and Maki, H., 1988, "Augmentation of Convective and Boiling Heat Transfer by Applying an Electro-Hydrodynamical Liquid Jet," Int. J. Heat Mass Transf., **31**, pp. 407–417.
[11] Melcher, J. R., 1981, *Continuum Electromechanics*, MIT Press, Cambridge, MA.
[12] Colburn, A. P., 1933, "A Method of Correlating Forced Convection Heat Transfer Data and a Comparison with Fluid Friction," Trans. Am. Inst. Chem. Engrs., **29**, pp. 174–245.
[13] Altman, M., Staub, F. W., and Norris, R. H., 1960, "Local Heat Transfer and Pressure Drop for Refrigerant-22 Condensing in Horizontal Tubes," Chem. Eng. Prog., Symp. Ser., **56**, pp. 151–159.
[14] Kosky, P. G., and Staub, F. W., 1971, "Local Condensing Heat Transfer Coefficients in the Annular Flow Regime," AIChE J., **17**, pp. 1037–1043.
[15] Yesin, O., 1979, "Relation between Heat Transfer Coefficient and Frictional Pressure Drop in Annular Two-phase Flow," *Proceedings of the Multi-Phase Flow and Heat Transfer Symposium—Workshop*, **2**, pp. 1177–1190.
[16] Friedel, L., 1979, "Improved Friction Pressure Drop Correlations for Horizontal and Vertical Two-phase Pipe Flow," *The European Two-phase Flow Group Meeting*, Ispra, Italy, Paper 2.
[17] Thom, J. R., 1964, "Prediction of Pressure Drop During Forced Circulation Boiling of Water," Int. J. Heat Mass Transf., **7**, pp. 709–724.
[18] Feng, Y., 2002, "Effects of Electric Field on Internal Convective Two-Phase Flow Heat Transfer and Pressure Drop," Ph.D. dissertation, Texas A&M University, College Station, TX.

Dae Hoon Lee
Division of Aerospace Engineering,
Korea Advanced Institute of Science and Technology,
373-1 Kusung-dong, Yusung-Gu,
Taejon 305-701,
Korea

Dae-Eun Park

Euisik Yoon

Division of Electrical Engineering,
Korea Advanced Institute of Science and Technology,
373-1 Kusung-dong, Yusung-Gu,
Taejon 305-701,
Korea

Sejin Kwon
e-mail: melody@kaist.ac.kr
Department of Mechanical Engineering,
Division of Aerospace Engineering,
Korea Advanced Institute of Science and Technology,
373-1 Kusung-dong, Yusung-ku,
Taejon 305-701,
Korea

A MEMS Piston-Cylinder Device Actuated by Combustion

Combustion measurement in a cylindrical micro combustor, the construction procedure and test run of a MEMS reciprocating device are described. The sizing of the MEMS device was based on the findings of combustion measurements. Thermodynamic analysis of the pressure measurement resulted in available work up to 2.4 Joules in a combustor height of 2 mm and more with combustion efficiency of 0.6~0.7. With combustor height less than 2 mm, combustion was incomplete due to excessive heat loss to the wall. In order to achieve the chamber height imposed by the combustion measurement, a fabrication process and wafer material that allow deeper etching was used.
[DOI: 10.1115/1.1565095]

Keywords: Combustion, Combustors, Heat Transfer, Internal, Microscale, Reacting

1 Introduction

As the demand for power sources to actuate mobile micro systems increases, micro scale heat engines have been tested as an alternative to batteries. Particularly when micro systems are required to perform mechanical work as in a micro air vehicle and micro spacecraft, the drain of energy is too quick for batteries to be a viable energy source. Although the power requirement of micro system is substantially less than macro scale devices, mobile micro systems have stringent weight and packaging limitations for power sources. In general, the energy density of batteries is too low for use where mechanical power is needed. On the other hand, the smallest existing engines in model aircraft are still too bulky and unreliable for applications in micro systems. The energy density of hydrocarbon liquid fuel is approximately 1000 times that of batteries. Even if we take into account the low thermal efficiency caused by reducing the scale of the device, power generation using a micro combustor may be an attractive alternative.

In recent years, several research groups started working on concepts of micro scale combustion devices. Fu et al. [1] described work on a MEMS rotary engine and Mehra et al. [2] tested a prototype MEMS turbine engine that was fabricated by wafer bonding and Deep RIE. Sitzki et al. [3] reported an experiment on a micro scale excess enthalpy burner. While the fabrication processes of MEMS devices have matured, combustion phenomena at micro scale have not yet been explored, partly because need for research has arisen recently.

We expect that a variety of constraints in a millimeter or submillimeter scale combustion chamber have been ignored in a macro scale heat engine, when combustion occurs. Firstly, the sizing of a combustor is dictated by combustion in a micro scale environment. As noted above, literature is scarce in this area. Except the quenching distance measured between two discs, data on the lower limit of a combustor scale that allows burning are not adequate for design and evaluation of such devices. As the combustor size is reduced to a scale comparable to or less than quenching distance, processes that have been ignored in a macro scale combustion become significant. Increased heat transfer through the combustor wall affects both the flame propagation and the cooling of burnt gases after burning is completed. Secondly, the small-scale combustor volume has adverse effects on the ignition of the fuel and air mixture. For stable initiation of combustion, a relatively large heat input is required in terms of electric discharge or catalytic reaction in some cases. When electric spark discharge is used for ignition, electrical insulation must be provided between the electrodes and the combustor walls without increasing the overall volume of the device, common silicon wafer material is not a good insulator and not suitable as a base plate material in an electrically ignited combustor as a result. Work on ignition by micro scale electric discharge, thermal heating and catalytic reaction have been reported by different research groups [4–6]. Thirdly, a practical micro engine requires a number of micro fluidic devices to meter and calibrate fuel and oxidizer flows. Due to the progress in MEMS devices in the past decades, there is a wide variety of available technology in micro fluidic devices including valves and pumps [7]. Lastly, we need an estimate of available work from combustion in a micro combustor. The theoretically available work in terms of the second law of thermodynamics must be sufficiently high for the combustor to produce work.

In order to solve all the technical problems in the development of a micro engine, a systematic investigation involving many different disciplines is necessary. Two of the most pressing tasks in the design of a micro engine are the understanding the combustion process in a micro scale volume and developing fabrication pro-

Contributed by the Heat Transfer Division for publication in the JOURNAL OF HEAT TRANSFER. Manuscript received by the Heat Transfer Division April 12, 2002; revision received December 26, 2002. Associate Editor: R. Skocypec.

cesses to materialize such a device. Past research on micro combustion devices placed emphasis on the fabrication processes and performance verification of subsystems and overlooked the importance of the thermo-fluidic phenomena of micro combustion. In the present study, combustion phenomena in a micro cylinder with variable depth were investigated experimentally and simple model was derived to predict the quenching. The results of the combustion study were applied to the design of a micro-reciprocating device powered by combustion for sizing and performance estimation. A micro machining process was established to accommodate the scale requirement imposed by the combustion experiment and modeling. Finally, a prototype device was constructed and a single stroke operation was tested successfully.

2 Design and Feasibility

2.1 Combustion Experiment. A miniature closed vessel combustion chamber with a cylindrical inside volume was designed and fabricated with a variable depth from 0.4 to 4 mm [8]. A stoichiometric mixture of hydrogen and air was supplied to the combustor. A piezoelectric pressure transducer inserted through the chamber wall picked up the instantaneous pressure hike after ignition and the subsequent pressure drop after completion of reaction.

The ratio of the peak pressure to the initial pressure is plotted in Fig. 1 for the cases tested. Eight realizations of each test condition were made to obtain statistically significant results. The scatter of individual measurement ranged from 3 to 17% around the mean values and has an average of 7% with a significance, tested by significance level of 5%. The deviations are represented by error bars on the plot. This ratio represents a measure of the mean effective pressure of the burnt gases and has significance in evaluating the available work. Also, the value is used for the determination of the heat transfer coefficient for thermal analysis. The plot shows that the pressure ratio is nearly independent of the initial pressure for a combustion chamber height less than 2.0 mm. With bigger combustion chamber volumes, the pressure ratio responded favorably to higher initial pressure.

The effect of heat loss to the surroundings is related to the shape parameter, which is defined as the ratio of surface to volume of the cylinder. Figure 2 shows the effect of the shape parameter on the pressure ratios that is averaged over each initial pressure ratio in Fig. 1. The error bars on this plot represent the extent of deviation of the ratio of peak pressure to initial pressure. The deviation decreases and the pressure ratio becomes independent of initial pressure as the combustor size decreases. The vertical dotted line, toward the higher value of shape parameter, is the surface to volume ratio evaluated from existing data of quenching distance [9]. The horizontal dotted line represents a pressure ratio of unity, implying no combustion. The measured pressure ratio starts high at low shape parameter and decreases toward unity as the shape parameter increases. This figure qualitatively demonstrates combustion efficiency is significantly lower in a micro scale combustion chamber than in a macro scale. However, pressure data alone are inadequate for the quantitative estimation of the combustion efficiency.

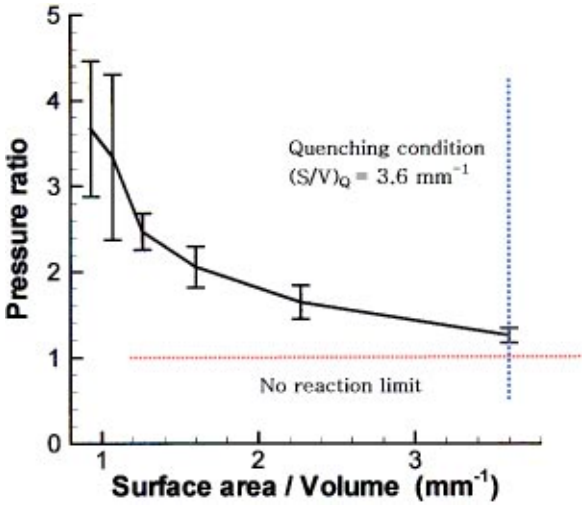

Fig. 2 Pressure ratio plotted against shape factor

2.2 Quenching Prediction. The present calculation employs a simple theoretical model rather than a direct numerical simulation to predict quenching and combustion efficiency. It is based on energy balance equation within closed vessel combustor [10]. In the modeled MEMS combustor, the flame is assumed to propagate in a shallow cylindrical volume with a depth of a few millimeters at most. The flame propagates in a radial direction while the dominant heat transfer is towards the top and bottom walls. Unlike combustion in a macro scale volume, the heat loss actively affects the flame propagation and must be accounted for in the integration of the equation that governs the flame motion.

The flame propagation is divided into many small consecutive steps. Upon completion of each propagation step, the system is adjusted by the heat loss during the step. Assumptions made for the modeling follow Lee and Kwon [11]. Figure 3 shows the

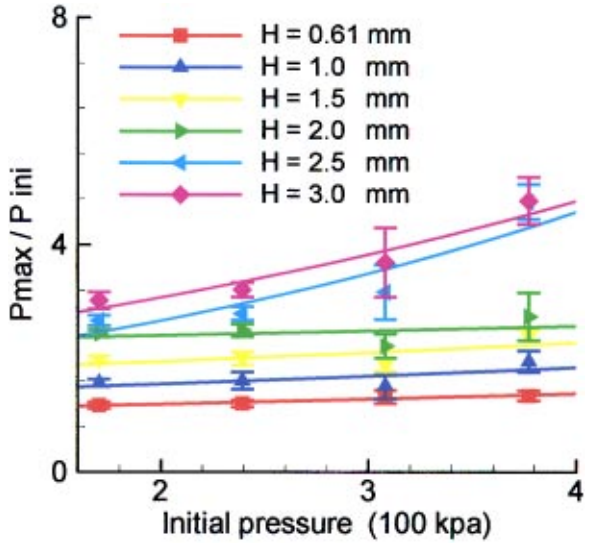

Fig. 1 Maximum to initial pressure ratio in each test condition

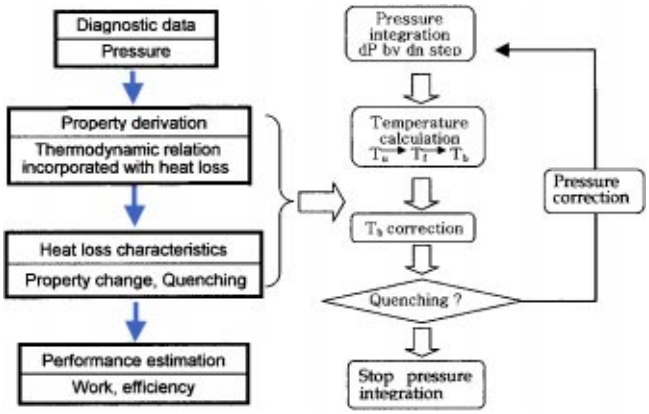

Fig. 3 Schematic diagram for solution procedure

calculation procedure of the model. For each small step of flame propagation, the pressure and temperature are corrected by the adiabatic compression and the heat loss to the wall. The step size of the flame propagation was about the scale of the flame thickness to ensure the convergence of calculation. For each step, the heat generated by the combustion is compared to the heat loss to the wall to test the quenching condition. The total heat loss is the sum of wall heat transfer and conduction to the unburned region and is expressed as $(2n/H)Vh(T_b-T_\infty)+A_fk\Delta T_f/\delta_f$. If heat production from the advancement of the flame is less than the total loss, quenching has occurred. The simplified equations to be solved simultaneously are as follow [10].

Pressure-burned fraction relation

$$\frac{dP}{dn}=\frac{(\beta(P/P_i)^{1/\gamma_u}-1)\cdot P}{1/\gamma_b\cdot(P/P_i)^{1/\gamma_u}-(1/\gamma_b-1/\gamma_u)(1-n)} \tag{1}$$

Pressure-temperature relation

$$T_u=T_i\left(\frac{P_u}{P_i}\right)^{1-1/\gamma_u} \tag{2}$$

$$m_ec_{p(b)}T_f=\lfloor m_ic_{p(u)}\cdot T_u+m_i\cdot\chi_{H_2}\hbar_{H_2}\rfloor \tag{3}$$

$$T_{bj}=T_{fk}\left(\frac{P_k}{P_j}\right)^{1-1/\gamma_b} \tag{4}$$

Where, j is an index for an arbitrary spatial location in the burnt region, while k is an index of the flame location.

Equation (1)–(4) are normalized by initial temperature and pressure in the following Eqs. (5)–(8), The cooling step and quenching condition, also expressed in normalized form, are presented in Eqs. (9)–(10)

$$\frac{d\pi}{dn}=\frac{(\beta\pi^{1/\gamma_u}-1)\cdot\pi}{1/\gamma_b\cdot\pi^{1/\gamma_u}-(1/\gamma_b-1/\gamma_u)(1-n)} \tag{5}$$

$$\theta_u=\pi^{1-1/\gamma_u} \tag{6}$$

$$\theta_f=\left[\frac{m_iC_{p(u)}}{m_eC_{p(b)}}\cdot\theta_u+\frac{m_i}{m_eC_{p(b)}T_i}\cdot\chi_{H_2}\hbar_{H_2}\right] \tag{7}$$

$$\theta_b=\theta_f\cdot\left(\frac{\pi}{\pi_f}\right)^{1-1/\gamma_b} \tag{8}$$

$$[\theta_b-\theta_f]=\frac{2nh}{m_eC_{\nu(b)}H}(\theta_b-\theta_\infty)+\frac{A_fk}{Vnm_eC_{\nu(b)}\delta_f}(\theta_f-\theta_u) \tag{9}$$

$$\delta_Lm_i\chi_{H_2}\hbar_{H_2}\leqslant\frac{2nVhT_i}{H}(\theta_b-\theta_\infty)+\frac{A_fkT_i}{\delta_f}(\theta_f-\theta_u) \tag{10}$$

Equation (1) is the relationship between pressure and burned volume fraction inside the cylinder. Equation (2) to (4) are relationships between gas properties assuming ideal gas and instantaneous isentropic compression due to flame propagation substeps. Equation (4) is the expression of frozen isentropic relation between any location in burned region and flame [12]. Equation (9) represents the conservation of energy including the heat loss to the combustor wall as well as to the unburnt region. Equation (10) is the quenching condition that will be tested upon completion of each flame propagation step. Equation (5)–(9) constitute a system of equations and solved simultaneously for π, θ_f, θ_u, θ_n, n with a known heat transfer coefficient.

Figure 4(a) shows the pressure-burnt fraction relationship obtained by integrating Eq. (5) and Fig. 4(b) is the ratio of the heat loss (the right hand side of Eq. (10)) to the heat of combustion (the left hand side of Eq. (10)) as a function of burnt fraction for various values of h. Flame is quenched when this ratio reaches unity and pressure attains its peak at that burnt fraction. The procedure for determination of the heat transfer coefficient from the measured peak pressure is as follows: (1) guess h, (2) find burnt fraction at quenching from Fig. 4(b), (3) find peak pressure from

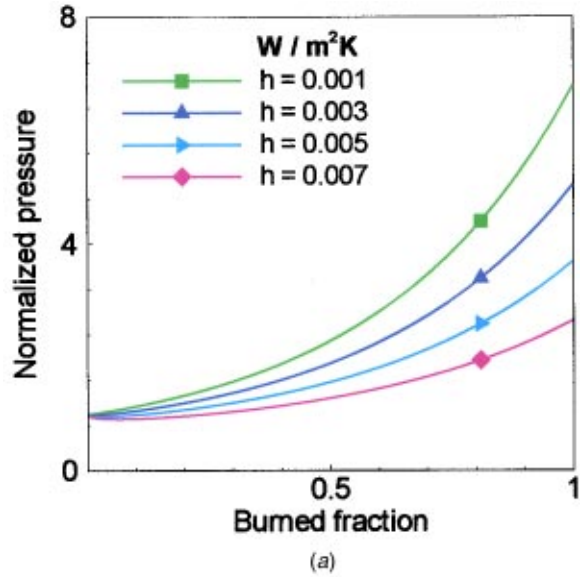

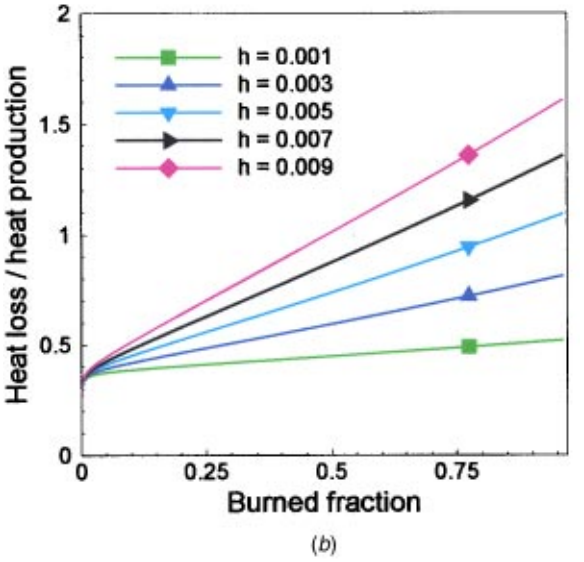

Fig. 4 Heat loss effect on pressure buildup and heat loss to heat production ratio: (*a*) pressure change for the assigned *h* value; and (*b*) the ration of heat loss to production for the assigned *h* value.

Fig. 4(a) with the same h and burnt fraction, and (4) if the resulting peak pressure is largely different from the measured peak pressure, correct h and repeat (2) and (3) until the discrepancy between the calculated and measured peak pressures fall within a tolerance limit. The procedure is illustrated in Fig. 5.

The numerical integration was performed by the second order Runge-Kutta method which has a numerical uncertainty of the order of $(dn)^3$, where dn is the integration step size. We used 0.01 for dn, which resulted in the computational uncertainty with an order of 10^{-6}.

Figure 6 shows the temperature profiles as a function of burnt fraction at two typical instances during the flame propagation. In Fig. 7, the heat transfer coefficients determined at different test conditions are presented as a function of the initial pressure with the cylinder depth as a parameter. Figure 7 shows the dependence of heat transfer coefficient on the combustor height and initial pressure.

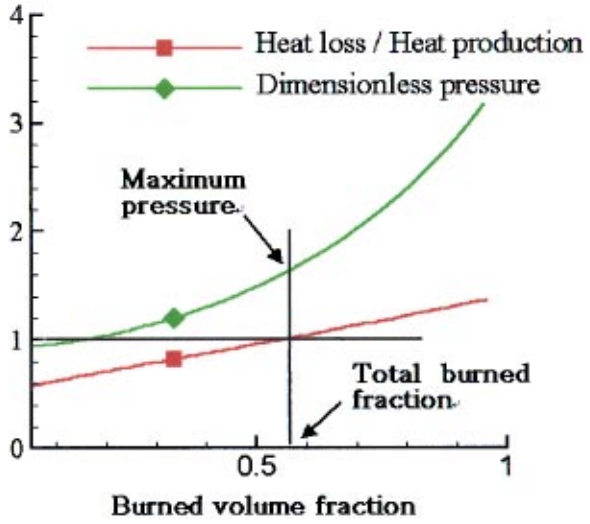

Fig. 5 Determination of total burned fraction in experiment case

2.3 Second Law Analysis. Total burned fractions that were obtained from the quenching calculation at all test cases are presented in Fig. 8. From the result of total burned fraction quenching is observed in most cases. The result can be used to calculate heat produced by the combustion process which experiences quenching. Also it can be used as design parameter as upper limit of device dimension to prevent quenching in combustor. The work available from a hot gas system is estimated from the gas properties in a closed system undergoing a quasi-equilibrium process from the peak pressure to quenching [13] by

$$m_{\text{Total}} = m_e + m_u$$

$$W_{\text{rev}} = (m_{eb}u_e - m_{ib}u_i) + (m_{iu}u_e - m_{iu}u_i) - T_\infty\{(m_{eb}s_e - m_{ib}s_i) + (m_{iu}s_e - m_{iu}s_i)\} \quad (11)$$

Where, subscript i denotes the initial state and subscript e the state at the instant the flame stops. The available work is plotted in Fig. 9. With chamber depth greater than 2 mm, the hot gas generated by combustion can theoretically produce 0.5 to 2.4 J per

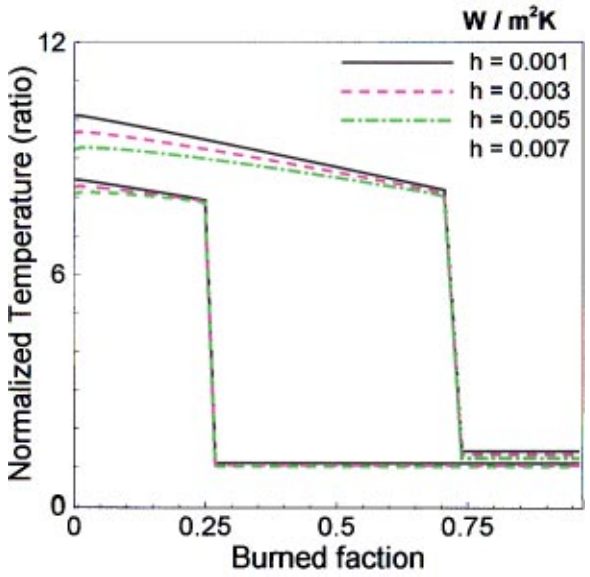

Fig. 6 Heat loss effect on temperature propagation

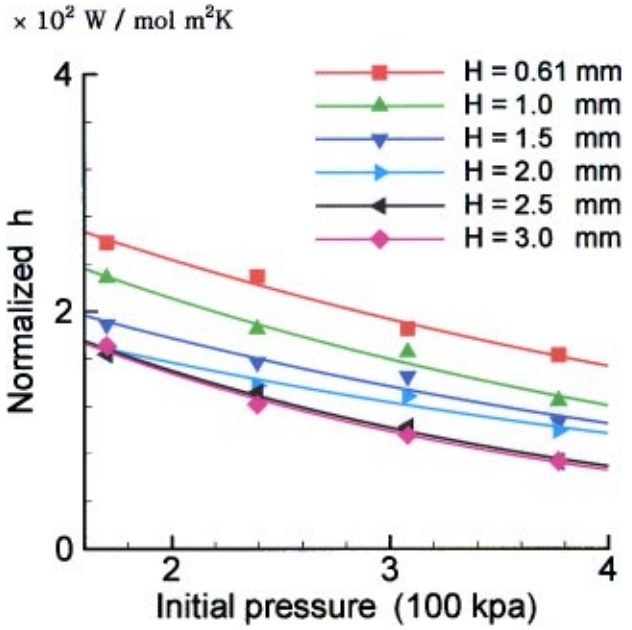

Fig. 7 Heat transfer coefficient normalized by initial molar mass

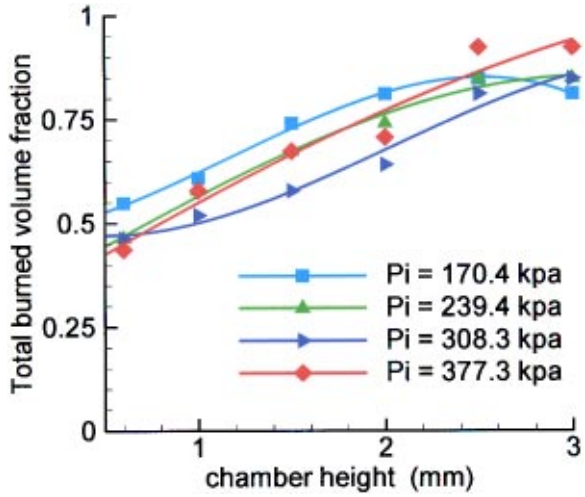

Fig. 8 Total burned fraction of all test cases

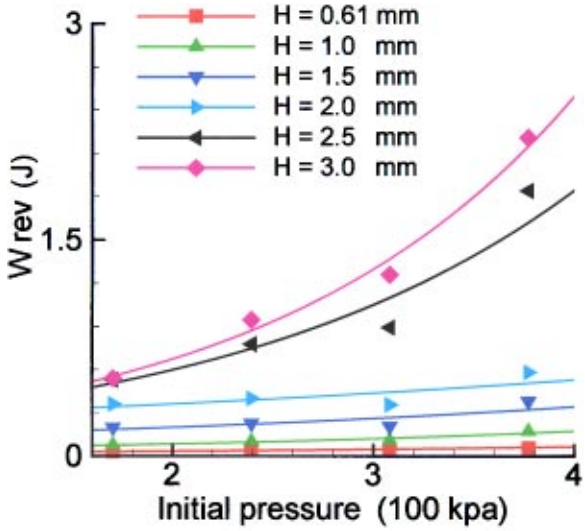

Fig. 9 Estimated reversible work

cycles. From comparison of the estimated reversible work, the combustion efficiency is evaluated. Combustion efficiency is defined by

$$\eta = \frac{W_{\text{rev}}}{\hbar_{H_2} m_i \chi_{H_2}} \tag{12}$$

For all experimental conditions, the combustion efficiency was between 0.6 and 0.7, which is lower than macro scale combustors as expected.

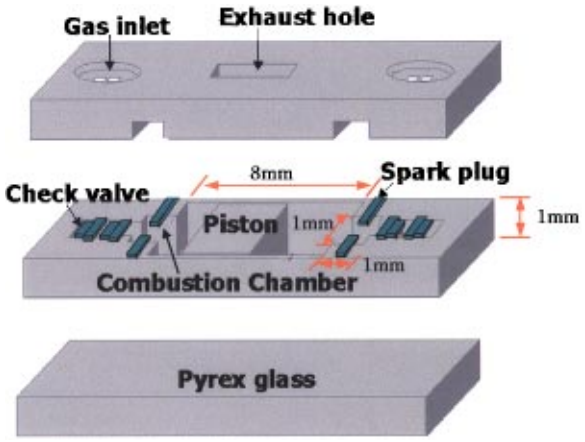

Fig. 10 Proposed structure of MEMS engine

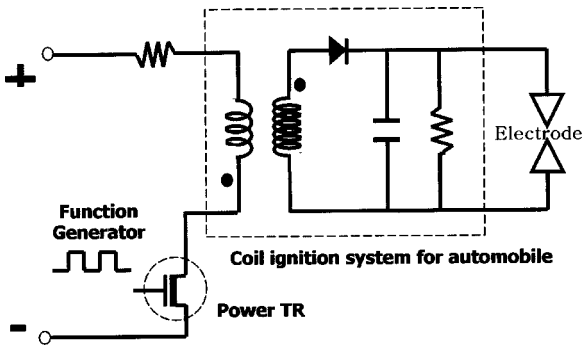

Fig. 11 Schematic of coil ignition system

3 Micro Fabrication of the Device

3.1 Proposed Design. The experimental data were used in the design of a micro reciprocating device. In this part, the design, fabrication process and actual combustion test of a prototype reciprocating device are described. The design concept tested here can be further developed and incorporated into a micro engine system. The engine structure consists of three wafer layers bonded together. Photosensitive glass was selected as base material for two reasons: glass wafer itself is a good electrical insulator than Si wafer and anisotropic etching produces better result with a photosensitive glass. The middle layer is also made of photosensitive glass wafer and the cylinder and the combustion chamber are engraved on this layer. The bottom layer is made of Pyrex glass wafer and serves as a base plate of the assembly. The schematic of the device is illustrated Fig. 10. The initial combustor volume was 1 mm$\times$1 mm$\times$1 mm with a stroke length of 8 mm. The design is a result of compromise between competing requirements of the fabrication and the combustion. The smaller the chamber height, the easier and cheaper the fabrication process becomes, because the device can be built on an off-the-shelf wafer that are usually available in thickness of 1 mm.

3.2 Ignition. Ignition is required to initiate combustion in the device. In the present study, an electric spark was used to accurately calibrate the ignition energy. The ignitor circuitry is integrated onto the wafer on which the device is built during the micro machining process of the overall device. The construction of the ignitor should take into account the minimum ignition energy for the given gas mixture and integration with the overall device. We used Ni electroplating to build the ignition circuitry and electrodes on the wafer material [14]. The electroplated Ni layer on the base plate was 40 μm high and 20$\sim$200 μm wide. A schematic of an inductance type ignition system used in the experiment is shown in Fig. 11. The ignition energy of 1.7 $\sim$1.8 mJ was sufficient to ignite the combustible gas and much smaller than the available work.

Effects of electrode geometry on the discharge voltage are shown in Fig. 12. The endurance of the electrodes was tested by discharging an electric spark at a frequency of 1 kHz. The test result in Fig. 13 shows growth of erosion at the tip of the electrodes. However, the spark discharge did not show further deterioration up to 10^6 operations.

3.3 Fabrication Process. The fabrication process for each layer is described below, beginning with the middle layer. Photosensitive glass of thickness 1 mm is exposed to UV light and thermally treated. UV intensity was controlled to 8J/cm^2 at a wavelength of 350 nm. The wafer was then etched slightly to make a depth coverage that could be used as an align key. A

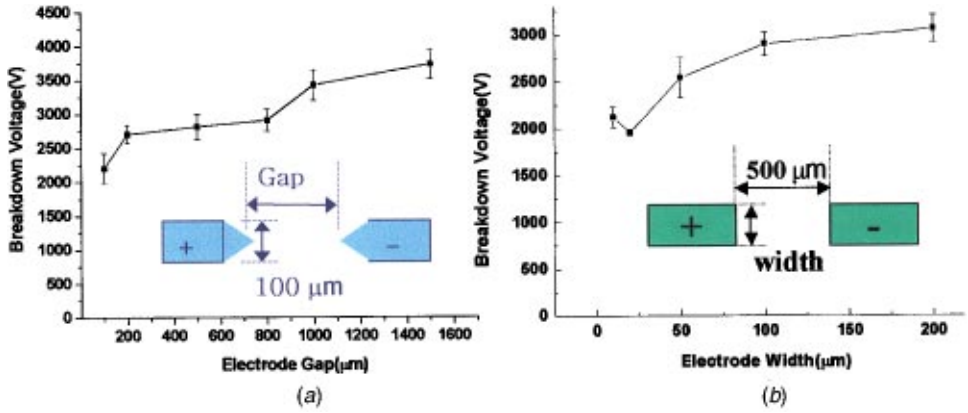

Fig. 12 Discharge voltage according to electrode gap: (*a*) gap versus discharge voltage; and (*b*) width versus discharge voltage

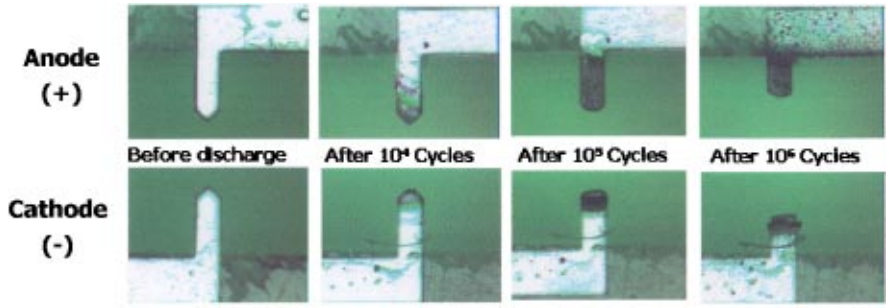

Fig. 13 Result of reliability test of fabricated electrode

Cr/Au seed layer was deposited for the electroplating process with a thermal evaporator with a thickness of 250 Å/2500 Å. A thick PR (AZ9260) mold was formed on top of the wafer with a thickness of 45 μm. A 40 μm deep Ni layer was electroplated on top of it. The UV-exposed and thermally treated glass was etched in an HF solution with 10% of HF concentration by volume. The use of an ultrasound washing device accelerated the etching to 20 μm/min. The glass wafer was etched from the backside to protect the seed layer and Ni structure during the etching process. For additional protection, the front side was coated with a paraffin layer. After completion of etching, paraffin and AZ 9260 PR are stripped by boiling in TCE(Trichloroethylene), acetone, and methanol solutions, in that order.

The same process is used for the top layer with a reduced UV intensity of 3J/cm^2, as the etching depth for the top layer is approximately half the thickness of the wafer. This is because the upper and lower halves are patterned differently.

The bottom and middle layers were bonded together and a piston made of photosensitive glass was inserted into the cylinder. Lastly, the top layer was bonded to the middle layer with epoxy glue. Since the piston must remain free, fusion bonding of the middle layer and the top layer is not suitable in this structure. This process is not complex but causes the problem of gas leakage through a gap resulting from the epoxy bonding. Although not used in the present study, fusion bonding is expected to result in better seal against gas leakage. Aside from the unsealed gap of tens of microns caused by bonding of the different layers, there is also a gap between the side face of the piston and the cylinder wall. Gas leakage through these gaps undermines the performance of a heat device. For better construction, better bonding methods with possible lubricant on the sidewall of the cylinder can be considered.

Fig. 14 Fabricated result

3.4 Results. The final fabricated device is shown in Fig. 14. A combustion test was carried out with the prototype device. Test was performed with stoichiometric mixture of hydrogen and air at atmospheric pressure. The results suggest proper ignition and flame propagation within the cylinder. Analyzing the piston displacements of consecutive video images, piston velocity was derived. Image analysis of the video clip taken at a framing rate of 9000 fps by a digital motion analyzer resulted in the piston speed of approximately 10 cm/stion gas. Relatively low piston speed is partly anticipated due to incomplete sealing of the cylinder. For the temperature measurement, monolithically implanted micro resistance appears promising but was not tried in the present study.

4 Conclusion

A MEMS combustion device was built and its operation was demonstrated. The design was based on data obtained from a combustion experiments in a micro combustor. Simple pressure measurement and visualization of the test combustor resulted in data for sizing and prediction of performance of the device. When the combustion chamber had a height less than 2 mm, quenching and increased heat loss prevented stable ignition and completion of combustion. Partial flame propagation and subsequent pressure rise was observed even in a combustor depth slightly less than the quenching distance. Theoretical analysis based on the measured pressure data resulted in thermal energy release up to a few Joules in a combustor height of 2 mm and more. Combustion efficiency was about 0.6~0.7, which is lower than in a macro scale combustor. In order to achieve higher efficiency, additional measures such as preheating and/or insulation of the wall may prove effective.

Based on the findings of the micro combustion experiment and the theoretical analysis, a MEMS reciprocating device was designed and a fabrication process was established. Photosensitive glass was proven to be suitable for the reciprocating combustion device for its favorable material properties, namely, high electric resistance, anisotropic etching characteristics and low thermal conductivity.

A combustion test of the reciprocating device showed piston displacement by hot gases. Although plagued with the leakage problem aforementioned, the test demonstrated that a micro-scale reciprocating device can be built and power can be generated. The findings of the present study warrant further research on micro combustion phenomena and different concepts of micro engines.

Nomenclature

A = area
C_p = specific heat
H = combustor height
h = heat loss coefficient
$\hbar$ = heating value
k = thermal conductivity
m = mole number
n = burned fraction
P = pressure
s = entropy
T = temperature
u = internal energy
V = combustor volume
W = work

Subscripts

b = burned
e = after completion of combustion
f = flame surface, at flame
i = initial
L = laminar
u = unburned
∞ = surrounding

Greek

β = ratio of burned region temperature after and before compression
χ = mole fraction
δ = thickness
γ = specific heat ratio
η = combustion efficiency
π = non dimensional pressure
θ = nondimensional temperature

References

[1] Fu, K., Knobloch, A. J., Cooley, B. A., Walter, D. C., Fernandez-Pello, C., Liepmann, D., and Miyaska, K., 2001, ''Microscale Combustion Research for Application to MEMS Rotary IC Engine,'' *Proc. ASME 35th National Heat Transfer Conference*, NHTC2001-20089.

[2] Mehra, A., Ayon, A. A., Waitz, I. A., and Schmidt, M. A., 1999, ''Microfabrication of High-Temperature Silicon Devices Using Wafer Bonding and Deep Reactive Ion Etching,'' J. Microelectromech. Syst., **9**(2), pp. 152–160.

[3] Sitzki, L., Borer, K., Schuster, E., Maruta K., Ronney, P. D., and Wussow, S., 2001, ''Combustion in Microscale Heat-Recirculating Burners,'' *Proc. 3rd Asia-Pacific Conference on Combustion*, pp. 473–476.

[4] Ono, T., Sim, D. Y., and Esashi, M., 2000, ''Imaging of Micro-Discharge in a Micro-Gap Electrostatic Actuator,'' *Proc. 13th IEEE International Micro Electro Mechanical Systems Conference, MEMS'00*, pp. 651–654.

[5] Kercher, D. S., Seriburi, P., and Allen, M. G., 1999, ''An Experimental Study of Microfabricated Nickel Spark Plugs,'' *Proc. Solid State Sensors and Actuators Transducers '99*, pp. 1412–1415.

[6] Srinivasan, R., Firebaugh, S. L., Hsing, I-M., Ryley, J., Harold, M. P., Jensen, K. F., and Schmidt, M. A., 1997, ''Chemical Performance and High Temperature Characterization of Micromachined Chemical Reactors,'' *Proc. Solid State Sensors and Actuators, Transducers '97*, pp. 163–166.

[7] Kovacs, G. T. A., 1998, *Micromachined Transducers-Sourcebook*, McGraw-Hill.

[8] Lee, D. H., Choi, K. H., and Kwon, S., 2001, ''Measurement and Modeling of Combustion in a Microcombustor,'' *Proc. AIAA 36th Thermophysics Conference*, AIAA 2001–3077.

[9] S. R., Turns, 1996, *An Introduction to Combustion*, McGraw Hill, Singapore.

[10] Lewis, B., and von Elbe, G., Combustion, *Flames and Explosions of Gases*, Academic Press, London, Chap. V. 15.

[11] Lee, D. H., and Kwon, S., 2002, ''Heat Transfer and Quenching Analysis of Combustion in a Micro Combustion Vessel,'' J. Micromech. Microeng., **12**(5), pp. 670–677.

[12] Takeno, T., and Iijima, T., 1985, ''A Theoretical Analysis of Flame Propagation in Closed Vessel,'' Trans. Japan Soc. Aero. Space Sci., **28**(79), pp. 1–15.

[13] Cengel, Y. A., and Boles, M. A., 1989, *Thermodynamics—An Engineering Approach* 2nd ed., McGraw-Hill, p. 335.

[14] Kercher, D. S., Seriburi, P., and Allen, M. G., 1999, ''An Experimental Study of Microfabricated Nickel Spark Plugs,'' Transducers '99 Sendai, Japan, pp. 1412–1415.

Heat Transfer Coefficients and Film-Cooling Effectiveness on a Gas Turbine Blade Tip

Jae Su Kwak
Senior Researcher,
Aeropropulsion Department,
Korea Aerospace Research Institute
e-mail: jskwak@kari.re.kr

Je-Chin Han
M. C. Easterling Endowed Chair
Turbine Heat Transfer Laboratory,
Department of Mechanical Engineering,
Texas A&M University,
College Station, TX 77843-3123
e-mail: jchan@mengr.tamu.edu

The detailed distributions of heat transfer coefficient and film cooling effectiveness on a gas turbine blade tip were measured using a hue detection based transient liquid crystals technique. Tests were performed on a five-bladed linear cascade with blow-down facility. The Reynolds number based on cascade exit velocity and axial chord length was 1.1 $\times 10^6$ *and the total turning angle of the blade was 97.7°. The overall pressure ratio was 1.2 and the inlet and exit Mach numbers were 0.25 and 0.59, respectively. The turbulence intensity level at the cascade inlet was 9.7%. The blade model was equipped with a single row of film cooling holes at both the tip portion along the camber line and near the tip region of the pressure side. All measurements were made at the three different tip gap clearances of 1.0%, 1.5%, and 2.5% of blade span and the three blowing ratios of 0.5, 1, and 2. Results showed that, in general, heat transfer coefficient and film effectiveness increased with increasing tip gap clearance. As blowing ratio increased, heat transfer coefficient decreased, while film effectiveness increased. Results also showed that adding pressure side coolant injection would further decrease the blade tip heat transfer coefficient but increase film-cooling effectiveness.* [DOI: 10.1115/1.1565096]

Keywords: Cooling, Film Cooling, Heat Transfer, Measurement Techniques, Rotating, Turbines

Introduction

In modern gas turbines, there is a continuing trend towards higher gas turbine inlet temperatures in order to increase power and efficiency. This, however, has resulted in a higher heat load on turbine components. Blade tips are one of the regions susceptible to failure due to the large thermal load and difficulty in cooling. For the typical gas turbine rotor blade, there is a gap between the rotating blade tip and the stationary shroud surface called the tip gap. Blade tip failure is caused primarily by hot gas flow through the tip gap. Hot gas leaks through the tip gap because of pressure differences between the blade pressure and the suction side, causing a thin boundary layer and a high heat transfer coefficient. Therefore, sophisticated cooling techniques must be employed to cool the blade tip in order to maintain performance requirements.

Figure 1 shows typical cooling methods for the modern gas turbine blade with a plane tip. Impingement cooling, pin-fin cooling, and rib turbulated cooling are employed to remove heat from blade's interior. Outside of the blade, one common method for reducing the heat transfer from the hot gas to the blade components is the film-cooling method. The film-cooling method cools blades by ejecting cooler air from the blade's internal coolant passages through discrete holes to provide a protective film on the surface exposed to hot gas. Due to the decreased film-to-wall temperature, heat transfer rates can be substantially reduced. However, few papers have been presented about blade tip cooling. Thus, it is important to investigate the heat transfer and film-cooling effectiveness of a film-cooled blade tip. Detailed turbine cooling methods are described by Han et al. [1].

Recently, many researchers have paid attention to turbine blade tip heat transfer. Mayle and Metzger [2] studied heat transfer in a two-dimensional rectangular tip model with and without a rotating shroud. They noted that the effect of blade rotation could be neglected to access the blade tip heat transfer over the entire range of parameters considered in the study. Metzger et al. [3] and Chyu et al. [4] studied heat transfer for both flat and grooved rectangular tip models. They confirmed that relative motion had little effect on the averaged tip heat transfer, though some local effects were observed.

There are some data in the open literature on blade tip heat transfer in a cascade environment. Metzger et al. [5] used heat flux sensors to measure local heat flux in a rotating turbine rig with two different tip gaps. Bunker et al. [6] investigated the detailed distributions of heat transfer coefficient on the blade tip surface using hue detection based liquid crystals technique. They measured the heat transfer coefficients at three tip gaps and two free-stream turbulence levels with both sharp and rounded edges. Azad et al. [7,8] studied the flow and heat transfer on the first stage blade tip of an aircraft engine turbine (GE-E^3). They presented the effects of tip gap clearance and free-stream turbulence intensity level on the detailed heat transfer coefficient distributions for both plane and squealer tips under engine representative flow conditions. They used the transient liquid crystals technique and found that the overall heat transfer coefficients on the squealer tip were lower than those of the plane tip. Teng et al. [9] measured heat transfer coefficients and static pressure distributions on a tur-

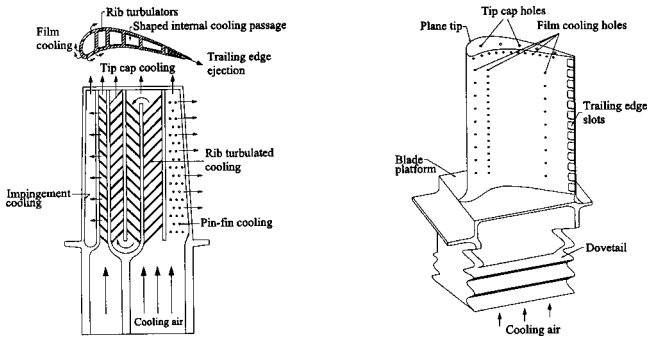

Fig. 1 The schematic of a modern gas turbine with common cooling techniques

Contributed by the Heat Transfer Division for publication in the JOURNAL OF HEAT TRANSFER. Manuscript received by the Heat Transfer Division May 17, 2002; revision received December 27, 2002. Associate Editor: K. S. Ball.

bine blade tip in a large-scale low-speed wind tunnel facility using the transient liquid crystals technique. They showed that major leakage flow existed in the mid-chord region and that the unsteady wake effect increased the Nusselt number at a large tip gap (3%), but the effect diminished with the decrease of tip gaps. Dunn and Haldeman [10] measured time averaged heat flux at the recessed blade tip for a full-scale rotating turbine stage at transonic vane exit conditions. They found that the Nusselt number on the floor of the recess near the leading edge of the blade and on the suction side lip was in excess of the blade stagnation value.

Some researchers carried out numerical investigations to predict blade tip heat transfer. Ameri and Steinthorsson [11,12] predicted the heat transfer on the tip of the SSME (Space Shuttle Main Engine) rotor blade. Ameri et al. [13] computed flow and heat transfer on the tip of a GE-E^3 first stage rotor blade for both smooth and recessed tips. Ameri et al. [14] also predicted the effects of tip clearance and casing recess on heat transfer and stage efficiency for several squealer blade tip geometries. Ameri and Bunker [15] performed a computational study to investigate detailed heat transfer distributions on blade tip surfaces for a large power generation turbine and compared with the experimental data of Bunker et al. [6].

There are a few papers available on blade tip film-cooling experiments. Kim et al. [16] and Kim and Metzger [17] used a two-dimensional rectangular tip model to simulate the leakage flow. They studied the heat transfer coefficients and film cooling effectiveness using transient liquid crystals technique with various cooling configurations.

The present study used hue detection based transient liquid crystals technique to measure the heat transfer coefficients and film-cooling effectiveness on a blade tip. The test section used for this study was a five-bladed linear cascade, and the blade profile was a first stage rotor blade tip of the modern aircraft gas turbine engine (GE-E^3). Measurements were performed for the tip clearances of 1.0%, 1.5%, and 2.5% of blade span with the averaged blowing ratios of 0.5, 1, and 2. In the authors' knowledge, this study is the first experimental data available in the open literature for the blade tip film-cooling test. The results presented in this paper could be used for the CFD code validation.

Experimental Setup

Figure 2 shows the schematic of the test facility. The test section consisted of a stationary blow-down facility with a five-bladed linear cascade. Compressed air stored in tanks entered a high flow pneumatic control valve. The controller received feedback from the downstream and could maintain the downstream velocity within $\pm 3\%$ of the desired setting value. The cascade inlet dimensions were 31.1 cm wide and 12.2 cm high. The test section's top, bottom, and sides were made of 1.27 cm thick polycarbonate plate for the pressure measurement test. For the heat transfer test, however, the top was replaced with a 1.27 cm thick

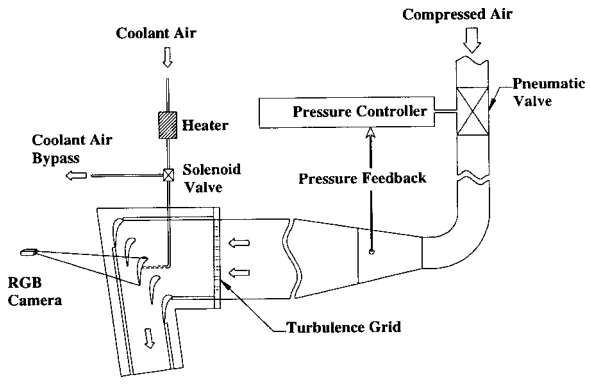

Fig. 2 The schematic of a blow-down facility

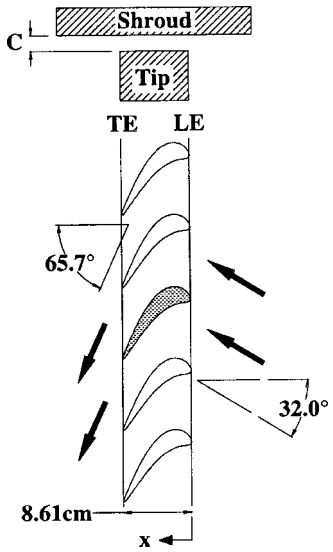

Fig. 3 Definition of blade tip clearance and the inflow and outflow angles

clear acrylic plate for best optical access to the blade tip. Two adjustable trailing edge tailboards were used to provide identical flow conditions through the two passages adjacent to the center blade. For the heated coolant air test, coolant air was bypassed until the desired temperature was achieved. After the coolant air temperature reached the desired value, heated coolant air was diverted to the film-cooling measurement blade by a 3-way solenoid valve. A turbulence-generating grid of 57% porosity was placed 26.7 cm upstream of the center blade. The turbulence intensity was measured 6 cm upstream of the center blade with a TSI IFA-100 unit. In this test, turbulence intensity with a turbulence-generating grid was 9.7%. The turbulence length scale was estimated to be 1.5 cm, which is slightly larger than the grid size. Figure 3 shows the definition of the blade tip clearance and the inflow and outflow angles. The tip gaps used for this study were 1.31 mm, 1.97 mm, and 3.29 mm, which correspond to about 1.0%, 1.5%, and 2.5% of the blade span (12.2 cm). Hard gaskets of desired thickness were placed on top of the side walls, the trailing edge tailboard, and two outer guide blades to create tip gaps of desired height.

During the blow-down test, the inlet air velocity was set at 85 m/s and the exit velocity at 199 m/s. The Reynolds number based on axial chord length and exit velocity was 1.1×10^6. Detailed flow conditions, such as the flow periodicity in cascade and the pressure distribution along the blade, are described in Azad et al. [7].

The blades were made of aluminum and finished with EDM machine. Each blade had a 12.2 cm span and 8.61 cm axial chord length. These were three times enlarged dimension of a GE-E^3 blade tip profile. Each blade had a constant cross section for the entire span. Figure 4 represents the film-cooling measurement blade. The lower portion of the blade was made of aluminum and had two holes for supplying coolant air and one hole for a cartridge heater. The upper portion had an inner aluminum rim with a cavity and an outer shell that was made of black polycarbonate with low thermal conductivity. One cartridge heater was inserted into the aluminum blade. The cartridge heater provided heat to the aluminum core, which heated the outer polycarbonate shell. Thirteen film-cooling holes were instrumented on both the blade tip and pressure side, respectively. On the tip, holes were located along the camber line. Film-cooling holes on the pressure side had a 30° angle with respect to the blade pressure surface. Each hole

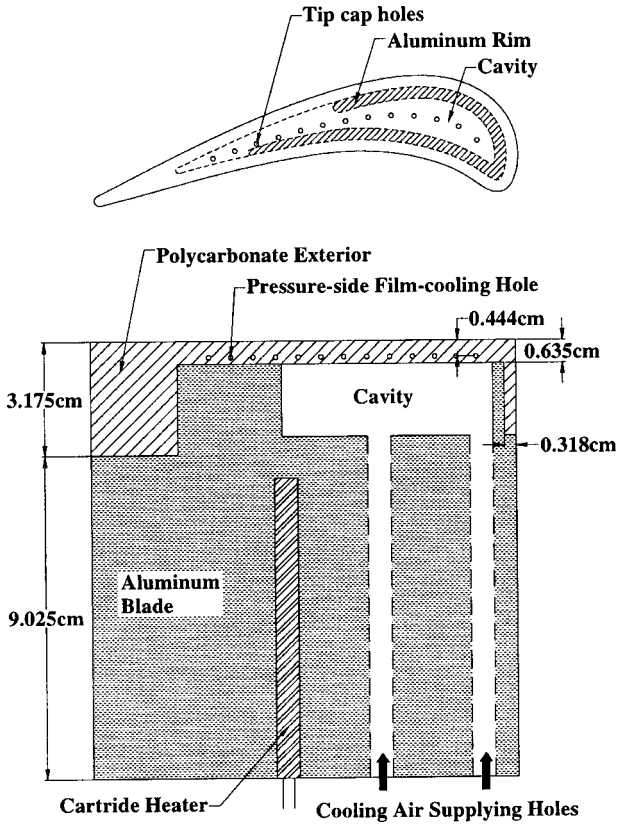

Fig. 4 Film-cooling measurement blade

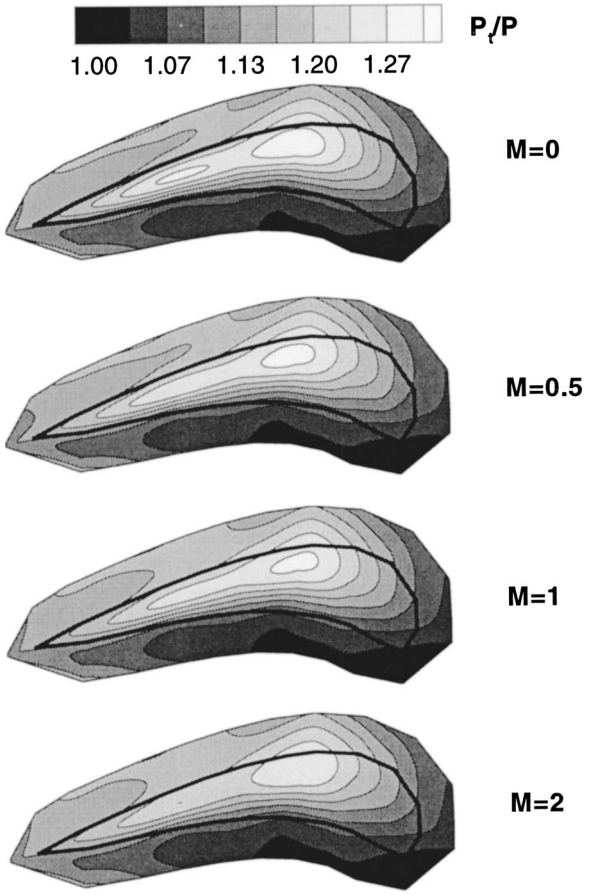

Fig. 6 Pressure distributions on the shroud surface for $C = 1.5\%$ and injection from tip holes only

had a diameter (d) of 0.127 cm and the distance between each hole was 0.635 cm (5d). Figure 5 shows the geometry of film-cooling holes on the pressure side and the tip.

Three different blowing ratios (M) of 0.5, 1, and 2 were tested. Because the actual velocity of leakage flow and coolant air could vary with location and blowing ratio, blowing ratio was defined as $M = \rho_c V_c / \rho_m V_{\text{avg}}$. Here, V_c is the averaged coolant air velocity, V_{avg} is the averaged velocity of cascade inlet and exit velocity, and ρ_m and ρ_c are the densities of mainstream and coolant air, respectively.

Pressure Measurement and Results

A total of 46 pressure taps were instrumented on the shroud surface opposite to the blade tip surface. Pressures were recorded with a 48-channel Scanivalve system with Labview software. Measurements were repeated 18 times for each blowing ratio case and averaged. The estimated uncertainty was less than 2%.

Figure 6 shows the total pressure to local static pressure ratio (P_t/P) distributions on the shroud surface for four different blowing ratios. The pressure side holes were covered with duct tape and coolant air was injected from the tip holes only. A higher value of P_t/P corresponds to a lower static pressure (high velocity), while a lower value corresponds to a higher static pressure (low velocity). The pressure distributions in Fig. 6 could explain the heat transfer results on the tip surface to be presented in the later part of the paper. The black curves in the contours indicate blade location under the shroud. The P_t/P distributions show the possible paths of leakage flow. The lower P_t/P near the pressure side leading edge portion indicates that leakage flow enters the tip gap at this region, while the higher P_t/P near the suction side indicates where the leakage flow exits. Results show that overall P_t/P decreases as blowing ratio increases (overall leakage flow decreases as blowing ratio increases). A possible reason for this trend is that leakage flow may be blocked by injected coolant. Injected jets to the narrow tip gap may work as flow resistance and increase local static pressure, which results in the reduced flow leakage through the tip gap. As blowing ratio increases from $M=0$ to $M=2$, P_t/P decreases by 6% at the highest P_t/P region located at the suction side near 30–40% of the chord. At the pressure side edge near 40% of the chord, P_t/P decreases by about 10% as blowing ratio increases from $M=0$ to $M=2$.

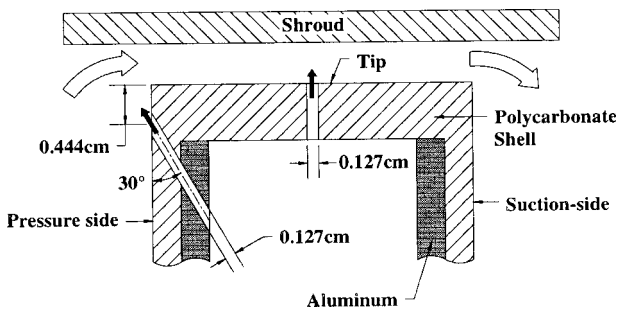

Fig. 5 Geometry of film-cooling holes

The Heat Transfer Measurement Theory

A hue detection based transient liquid crystals technique was used to measure heat transfer and film-cooling effectiveness on the blade tip. The local heat transfer coefficient over a liquid crystals coated surface without film injection can be obtained using a one-dimension semi-infinite solid assumption for the test surface. The one-dimensional transient conduction equation, the initial condition, and the convective boundary condition are:

$$k\frac{\partial^2 T}{\partial x^2}=\rho c_p\frac{\partial T}{\partial t} \tag{1}$$

$$at\ \ t=0,\ \ T=T_i \tag{2}$$

$$at\ \ x=0,\ \ -k\frac{\partial T}{\partial X}=h(T_w-T_m);\ \ \text{as}\ \ x\to\infty,\ \ T=T_i \tag{3}$$

The solution of the above equation at the convective boundary surface ($x=0$) is the following:

$$\frac{T_w-T_i}{T_m-T_i}=1-\exp\left(\frac{h^2\alpha t}{k^2}\right)\text{erfc}\left(\frac{h\sqrt{\alpha t}}{k}\right) \tag{4}$$

By knowing the initial temperature (T_i) of the test surface, the mainstream temperature (T_m) at cascade inlet and the test surface color change temperature (T_w) at time t, the local heat transfer coefficient (h) can be calculated from Eq. (4). For the film-cooling test, the mainstream temperature (T_m) in Eq. (4) is replaced by the local film temperature (T_f), which is a mixture of the coolant (T_c) and mainstream temperature (recovery temperature) (T_m). The film temperature is defined in terms of the film-cooling effectiveness η.

$$\eta=\frac{T_f-T_m}{T_c-T_m}\quad\text{or}\quad T_f=\eta T_c+(1-\eta)T_m \tag{5}$$

Then, Eqs. (4) and (5) can be combined as follows:

$$\frac{T_w-T_i}{T_f-T_i}=\frac{T_w-T_i}{\eta T_c+(1-\eta)T_m-T_i}=\left[1-\exp\left(\frac{h^2\alpha t}{k^2}\right)\text{erfc}\left(\frac{h\sqrt{\alpha t}}{k}\right)\right] \tag{6}$$

Two similar transient tests were run to obtain the heat transfer coefficient (h) and the film-cooling effectiveness (η). In the first test, the surface of the test model was heated while the coolant was not. For the second test, both the surface and the coolant air were heated. Because both mainstream and coolant air temperature changed with time, the gradual change of the temperatures was recorded on the chart recorder. In this study, the temperature of the mainstream at the cascade inlet varied from 20°C to 24°C; the temperature of the heated coolant case varied from 26°C to 55°C. The varying temperatures were represented as a series of time step changes (τ_i, $i=1,2\ldots N$). Using Duhamel's superposition theorem (Ekkad et al. [18]), Eq. (6) can be written as follows:

$$\begin{aligned}T_{w1}-T_{i1}&=\{\eta(T_{c1,0}-T_{m1,0})+T_{m1,0}-T_{i1}\}\times F\left(\frac{h\sqrt{\alpha t_1}}{k}\right)\\&\quad+\sum_{i=1}^{n}\left[\{\eta(\Delta T_{c1,i}-\Delta T_{m1,i})+\Delta T_{m1,i}\}F\left(\frac{h\sqrt{\alpha(t_1-\tau_i)}}{k}\right)\right]\end{aligned} \tag{7}$$

$$\begin{aligned}T_{w2}-T_{i2}&=\{\eta(T_{c2,0}-T_{m2,0})+T_{m2,0}-T_{i2}\}\times F\left(\frac{h\sqrt{\alpha t_2}}{k}\right)\\&\quad+\sum_{i=1}^{n}\left[\{\eta(\Delta T_{c2,i}-\Delta T_{m2,i})+\Delta T_{m2,i}\}F\left(\frac{h\sqrt{\alpha(t_2-\tau_i)}}{k}\right)\right]\end{aligned} \tag{8}$$

where, $F(x)=1-\exp(x^2)\text{erfc}(x)$

ΔT_m and ΔT_c are step changes in the mainstream and coolant air temperatures, respectively. Subscript 1 and 2 indicate the separate tests

Equations (7) and (8) were solved iteratively at each pixel to obtain the detailed heat transfer coefficient and film effectiveness distributions.

The experimental uncertainty was calculated by the methods of Kline and McClintock [19]. Note that the blade tip material (polycarbonate) has a very low thermal conductivity of 0.18 W/mK. The liquid crystals color change transition occurs at the surface which is kept at a uniform initial temperature. Test duration is smaller (10–30 sec) than the time required for the temperature to penetrate the full thickness of the blade tip material. Thus a one-dimensional transition, semi-infinite solid assumption is valid throughout the surface, except near the tip edges. The individual uncertainties in the measurement of the time of color change ($\Delta t=\pm 0.5$ sec), the mainstream temperature ($\Delta T_m=\pm 0.5$°C), the coolant temperature ($\Delta T_c=\pm 0.5$°C), the color change temperature ($\Delta T_w=\pm 0.2$°C), the initial temperature ($\Delta T_i=\pm 1$°C), and the blade tip material properties ($\Delta\alpha/k^2=\pm 5\%$) were included in the calculation of the overall uncertainty of heat transfer coefficient and film cooling effectiveness. The uncertainty for the local heat transfer coefficient and film-cooling effectiveness was estimated to be $\pm 8\%$ and $\pm 10\%$, respectively. However, the uncertainty near the blade tip edge and the film-hole edge might be much greater than 10% due to the two-dimensional conduction effect. Also, the uncertainty in the high heat transfer region might be greater than 10% due to the short color change time.

Heat Transfer Measurement and Results

Two different liquid crystals were used in this study. The 20°C bandwidth liquid crystals (R34C20W, Hallcrest) were used to measure the initial temperature of the tip surface and the 5°C bandwidth liquid crystals (R30C5W, Hallcrest) were used to measure the color change time.

Calibration was performed to find the hue versus temperature relation. A foil heater was placed at the bottom of a 0.635 cm thick copper plate. Above the copper plate, a 0.32 cm thick black polycarbonate plate was attached with high conductivity glue. Because the color display of liquid crystals depends on background color, the same black polycarbonate material was used for both the calibration and heat transfer tests. Input voltage was set properly in order to increase the surface temperature by 0.6°C, and enough time was allowed for the temperature to be steady at each temperature step. The surface temperature was then read by a thermocouple that was attached at the surface of the black polycarbonate and the color of the liquid crystals was recorded to the computer. At each temperature step, the hue was calculated from the stored image and relation between hue and temperature was established for both 20°C and 5°C bandwidth liquid crystals as shown in Fig. 7(*a*).

Before the transient test, the 20°C bandwidth liquid crystals was sprayed uniformly on the blade tip, which was then heated for about two hours. After the surface temperature reached the desired temperature (about 70°C), the color of the liquid crystals on the tip surface was recorded by a RGB color CCD camera with 24-bit color frame grabber board. From every pixel of stored image, the hue was calculated using the single hex cone color model (Foley et al. [20]), and the initial temperature of the blade tip was determined using the pre-calibrated hue versus the temperature relation. Figure 7(*b*) shows the distribution of the initial temperature for the $C=1.5\%$ case.

After the initial temperature measurement on the blade tip, the 20°C bandwidth liquid crystals was removed and the 5°C bandwidth liquid crystals was sprayed. The blade tip was heated for about two hours until the reference temperatures became the same as those of the initial temperature measurement test. Reference temperatures were measured by two thermocouples located at the blade trailing edge surface and the inside of the cavity to ensure the same temperature conditions for both the initial temperature measurement and the transient test. After temperatures reached the

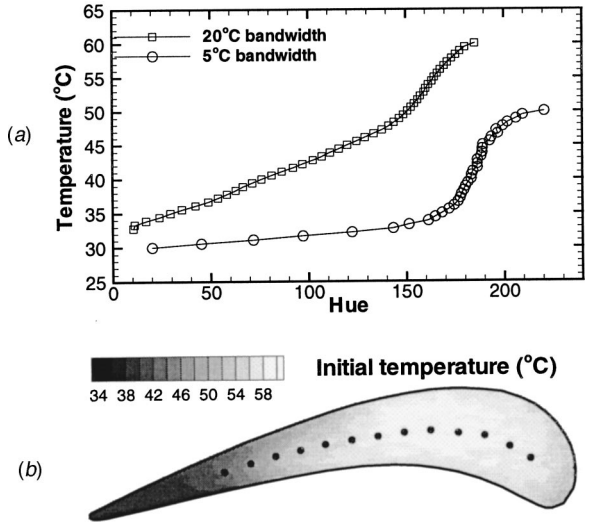

Fig. 7 (*a*) The relation between hue and temperature; and (*b*) Initial temperature distribution for $C=1.5\%$

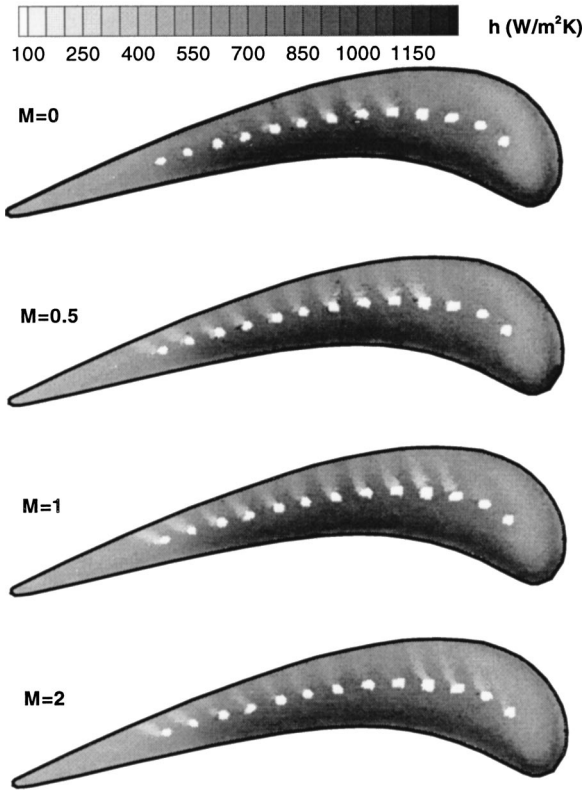

Fig. 8 Heat transfer coefficient for $C=1.5\%$ and coolant injection from tip holes only

desired value, compressed air was allowed to flow by turning on the flow controller and the color change of the liquid crystals was recorded at the speed of 30 frames per second. The test duration time was small enough (10–30 sec) to make a semi-infinite solid assumption. From every pixel at each stored image, the hue was evaluated and used to calculate the time from the initial condition (about 50°C–65°C, depending on location) to the given hue value (50), which corresponded to 30.6°C in this test. Two similar tests were done with different coolant air temperatures. The local heat transfer coefficient and film-cooling effectiveness on every pixel were then calculated using Eqs. (7) and (8).

Heat Transfer Coefficient Results for Coolant Injection From Tip Holes Only. Figure 8 shows the heat transfer coefficient distributions for $C=1.5\%$ and the coolant injection from tip holes only. All cases show a high heat transfer coefficient near the pressure side tip to the camber line at 30~40% of the blade chord. This high heat transfer coefficient region corresponds to the maximum tip leakage flow at this region due to the large pressure difference between the blade pressure side and the suction side as shown in Fig. 6.

As the blowing ratio increases, the heat transfer coefficient between the pressure side edge and the camber line decreases. This trend corresponds to the static pressure measurement results shown in Fig. 6. As blowing ratio increases, the potential blockage effect may increase, which reduces leakage flow and the heat transfer coefficient. The overall averaged heat transfer coefficient decreases by about 8% as the blowing ratio increases from $M=0$ to $M=2$.

At the pressure side edge, a relatively low heat transfer region exists due to the separation of leakage flow. After the separation region, the flow reattaches and the heat transfer coefficient gradually increases towards the camber line where the film-cooling holes are located.

For all cases, a low heat transfer region exists near the leading edge suction side. Azad et al. [7] also found a low heat transfer region near the leading edge suction side. Heat transfer near the trailing edge is lower than that of the other region due to the low velocity of leakage flow. These trends correspond with the results of Azad et al. [7].

For the $M=0$ case, the heat transfer coefficient downstream of the mid-chord holes is smaller than that between the holes. Because the velocity of the leakage flow at the mid-chord is higher than that of the leading or trailing side (Fig. 6), the leakage flow with the higher velocity may go around the film-cooling holes. As the blowing ratio increases, however, the heat transfer coefficients downstream of the mid-chord holes increases, while the heat transfer coefficients downstream of the leading and trailing edge holes decrease. These trends may be induced from the nonuniform actual blowing ratio through each hole. Due to the complicated leakage flow field on the tip with coolant injection, the local blowing ratio may vary from hole to hole. This difference in actual blowing ratios would give different interactions between the film-cooling jets and the leakage flow, and may result in different trends in the heat transfer coefficient distribution after the holes.

Effects of the Pressure Side Injection. Figure 9 presents the heat transfer coefficient distribution for $C=1.5\%$ and the coolant injection from both the tip and pressure side holes. As blowing ratio increases, this case again shows the trend of decreasing heat transfer coefficient between the pressure side edge and the camber line due to the potential blockage effect from both the pressure side and tip hole injections. As the blowing ratio increases, however, the heat transfer coefficients downstream of all tip holes increase. This can be explained by the increased turbulent mixing of the leakage flow and the injected coolant from the pressure side holes. Pressure side injected coolant may enhance flow disturbance and result in a relatively uniform distribution of heat transfer coefficients downstream of the tip holes.

Figure 9 shows that the heat transfer coefficient between the pressure side edge and the camber line becomes lower as the blowing ratio increases. For the high blowing ratios, the pressure side injected coolant may be carried over to the tip and may increase interaction with the leakage flow. However, the additional blockage effect of the injected coolant from the pressure side holes may reduce the heat transfer coefficient as blowing ratio increases. Therefore, for injection from both the pressure side and tip holes, the net result is to reduce heat transfer coefficients as

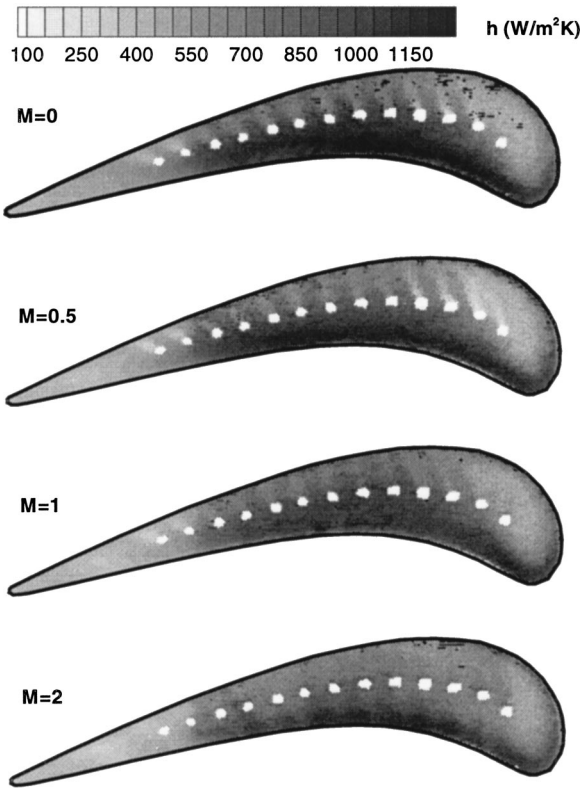

Fig. 9 Heat transfer coefficient for $C=1.5\%$ and coolant injection from both tip and pressure side holes

blowing ratio increases. As blowing ratio increases from $M=0$ to $M=2$, the overall averaged heat transfer coefficient decreases by about 11%.

Figures 10 and 11 show the averaged heat transfer coefficient for $C=1.5\%$, the coolant injection from the tip holes only and the coolant injection from both the tip and pressure side holes, respectively. The local heat transfer coefficients on the tip are averaged from the pressure side to the suction side at a given x/C_x location. Both cases show that the maximum heat transfer occurs near $x/C_x=0.6$. Results show that the averaged heat transfer coefficient decreases with increasing blowing ratio for the injection from tip hole injection only. However, there is no monotonic trend for the injection from both tip and pressure side holes. For both cases, however, the overall averaged heat transfer coefficient on the entire blade tip surface shows a decreasing trend with increasing blowing ratio. Compared to the injection from the tip holes only (Fig. 10), the injection from both the tip and pressure side holes (Fig. 11) shows slightly reduced heat transfer coefficients at each blowing ratio. This trend is possibly caused by an additional blockage effect due to the pressure side injection. As the blockage effect increases, the leakage flow and the heat transfer coefficient decrease.

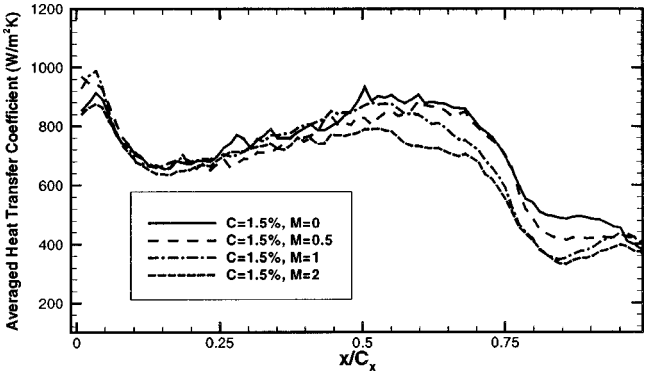

Fig. 11 Averaged heat transfer coefficient for $C=1.5\%$ and coolant injection from both tip and pressure side holes

Effects of Tip Gap Clearance. Figures 11, 12, and 13 present the averaged heat transfer coefficient for $C=1.5\%$, 1.0%, and 2.5%, respectively. All cases have injection from both tip and pressure side holes.

For the $C=1.0\%$ case (Fig. 12), the averaged heat transfer coefficient shows a decreasing trend as blowing ratio increases. As blowing ratio increases from $M=0$ to $M=2$, the overall averaged heat transfer coefficient decreases by 13%. The averaged heat transfer coefficients are slightly smaller than the $C=1.5\%$ case (Fig. 11). Depending on the blowing ratio, the overall heat transfer coefficients are 6–9% smaller than $C=1.5\%$ with the same injection conditions.

For the $C=2.5\%$ case (Fig. 13), generally, the averaged heat transfer coefficient decreases as blowing ration increases. The overall heat transfer coefficient is slightly larger than $C=1.5\%$ case.

It seems that the effect of blowing ratio ($M=0.5\sim2$) on heat transfer coefficients is relatively large for the smaller tip gap ($C=1.0\%$), with a reduced effect on the large tip gap ($C=2.5\%$). For the small tip gap case, due to the small amount of leakage flow, the coolant injection has relatively large effect on heat transfer coefficients. However, for the larger tip gap case, because the amount of leakage flow is larger, the effect of coolant injection on heat transfer coefficients is less important.

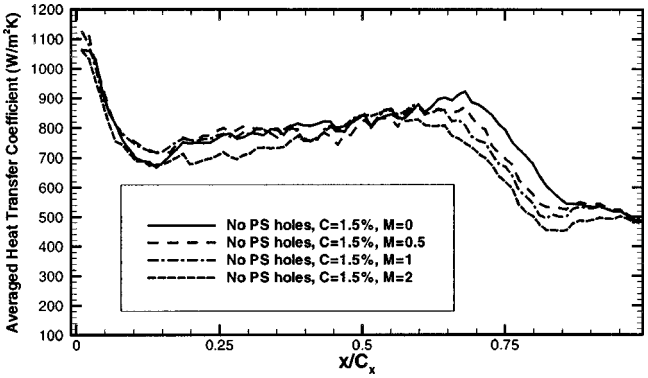

Fig. 10 Averaged heat transfer coefficient for $C=1.5\%$ and coolant injection from tip holes only

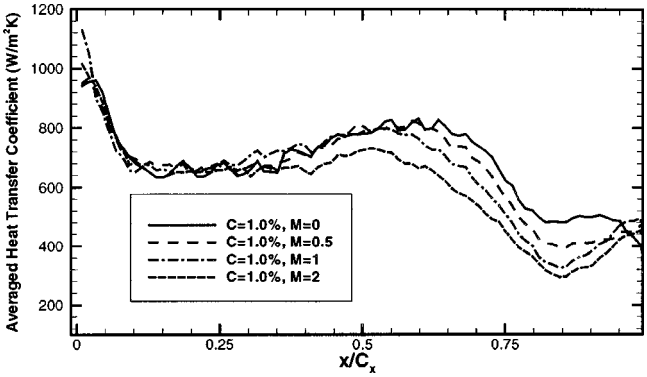

Fig. 12 Averaged heat transfer coefficient for $C=1.0\%$ and coolant injection from both tip and pressure side holes

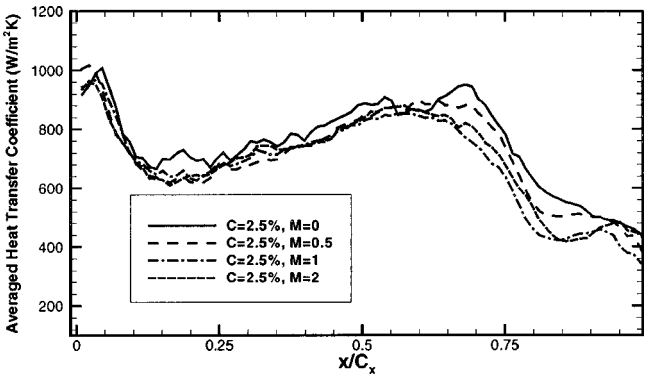

Fig. 13 Averaged heat transfer coefficient for $C=2.5\%$ and coolant injection from both tip and pressure side holes

Film-Cooling Effectiveness Results

Film-cooling effectiveness was calculated simultaneously using the Eqs. (7) and (8). Film-cooling effectiveness was calculated for three tip gap cases with three blowing ratios.

Film-Cooling Effectiveness Results for Coolant Injection From Tip Holes Only. Figure 14 shows the film-cooling effectiveness distributions for $C=1.5\%$ and coolant injection from tip holes only. Because tip holes have 90° injection angles, coolant may dilute well with the leakage flow and result in a low film-cooling effectiveness on the blade tip. For all three blowing ratios, the maximum film-cooling effectiveness is less than 0.2 and appears immediately downstream of the holes.

As blowing ratio increases from $M=0.5$ to $M=2$, the overall film-cooling effectiveness also increases. For the $M=0.5$ case, film-cooling effectiveness can be seen only immediately downstream of the holes, and the film covered area is small. However, as blowing ratio increases, the film covered area is extended further downstream, and maximum film-cooling effectiveness also increases. The most significant increase occurs at the blade's leading and trailing edge, where the amount of leakage flow is relatively small. However, because of the larger amount of leakage flow at the 30~40% of chord region, the injected coolant can be diluted well with the leakage flow. This may result in a less increase in the film-cooling effectiveness as blowing ratio increases.

Effects of Pressure Side Injection. Figure 15 shows the distributions of film-cooling effectiveness for $C=1.5\%$ and coolant injection from both pressure side and tip holes.

This case again shows that overall film-cooling effectiveness increases as blowing ratio increases. As blowing ratio increases to $M=2$, the traces of the pressure side injection can be seen between the pressure side edge and the camber line due to the potential carrying over of the pressure side coolant to the tip surface. Film-cooling effectiveness downstream of the camber line holes increases due to the film coolant cumulating effect. Film-cooling effectiveness is highest near the trailing edge region due to the film coolant cumulating effect at the trailing edge region.

For the $M=0.5$ case, the effect of pressure side injection is not observed. However, compared to the tip holes injection only case (Fig. 14), the traces of the injection from tip holes appear differently. This case shows clear traces near the blade leading edge portion, while the injection from tip holes only does not. This may be caused by the different local blowing ratios. The different configuration of injection (injection from tip holes only or injection from both pressure side and tip holes) may change the pressure distribution inside the cavity, which results in different local blowing ratios. Different local blowing ratios would give different mixing between coolant and leakage flow, and may result in different trends in film-cooling effectiveness.

Figure 16 presents the averaged film-cooling effectiveness for the $C=1.5\%$ and coolant injection from tip holes only. Film-cooling effectiveness is averaged from the pressure side to the suction side tip at a given x/C_x location. Results show that the averaged film-cooling effectiveness increases as blowing ratio increases. However, the overall film-cooling effectiveness for all cases is very small.

Figure 17 shows the averaged film-cooling effectiveness for $C=1.5\%$ and coolant injection from both tip and pressure side holes. Results clearly show that averaged film-cooling effectiveness increases as blowing ratio increases. Compared to the injection from tip holes only (Fig. 16), the averaged film-cooling effectiveness increases significantly for all blowing ratios. This trend clearly demonstrates that injection from both tip and pres-

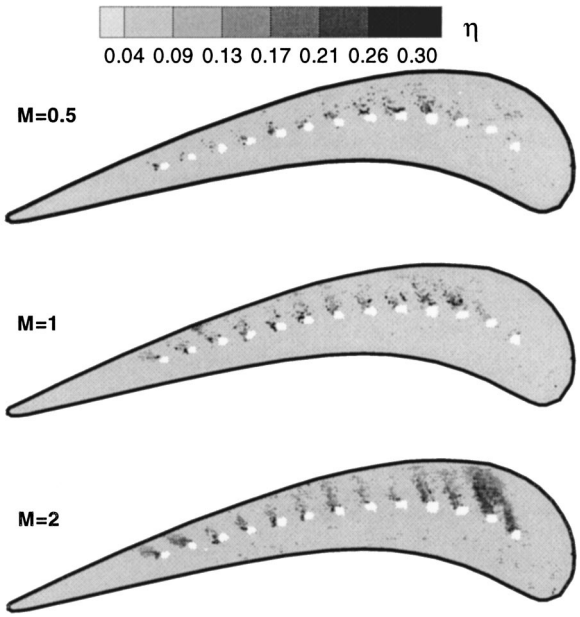

Fig. 14 Film-cooling effectiveness for $C=1.5\%$ and coolant injection from tip holes only

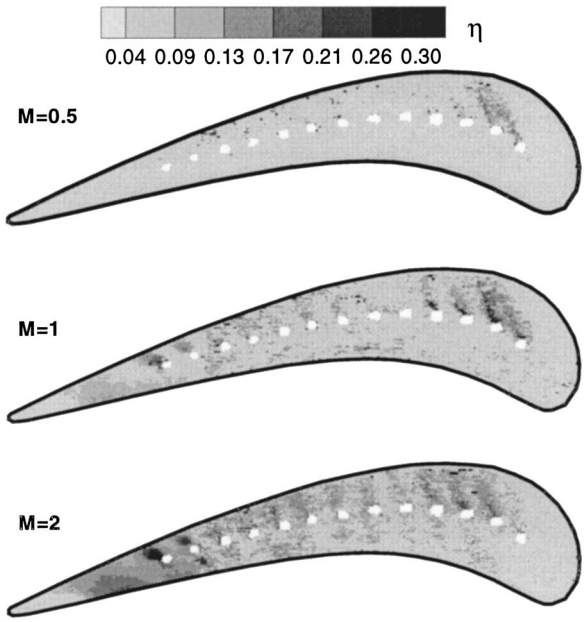

Fig. 15 Film-cooling effectiveness for $C=1.5\%$ and coolant injection from both tip and pressure side holes

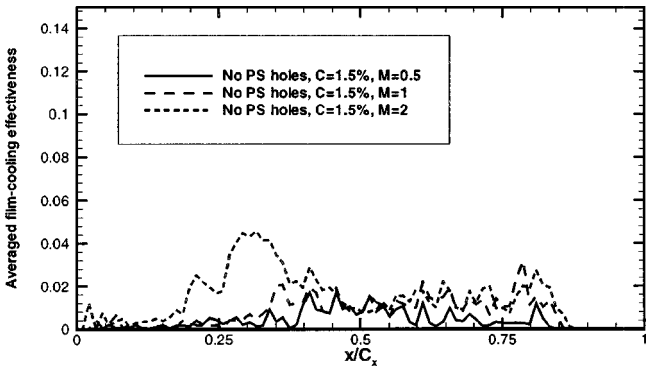

Fig. 16 Averaged film-cooling effectiveness for $C=1.5\%$ and coolant injection from tip holes only

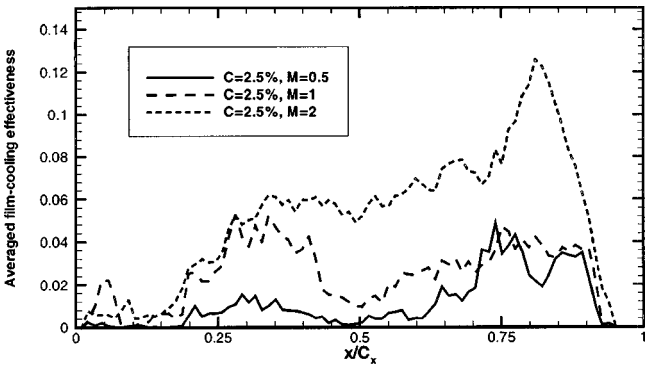

Fig. 19 Averaged film-cooling effectiveness for $C=2.5\%$ and coolant injection from both tip and pressure side holes

sure side holes results in a much better film-cooling effectiveness compared to injection from tip holes only. This is due to the coolant cumulating effect of the coolant from the pressure side and tip holes.

Effects of Tip Gap Clearance. Figures 17, 18, and 19 show the averaged film-cooling effectiveness for $C=1.5\%$, $C=1.0\%$, and $C=2.5\%$, respectively. All cases have injection from both tip and pressure side holes. All cases show that averaged film-cooling effectiveness increases as blowing ratio increases. The $M=0.5$ and $M=1$ cases show lower averaged film-cooling effectiveness. For the $M=2$ case, averaged film-cooling effectiveness is higher and local peaks of the averaged film-cooling effectiveness appear near $x/C_x=0.8$ due to increased local film-cooling effectiveness by the pressure side coolant carrying over.

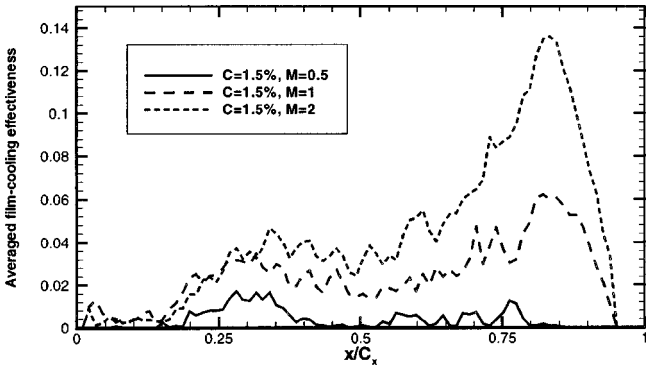

Fig. 17 Averaged film-cooling effectiveness for $C=1.5\%$ and coolant injection from both tip and pressure side holes

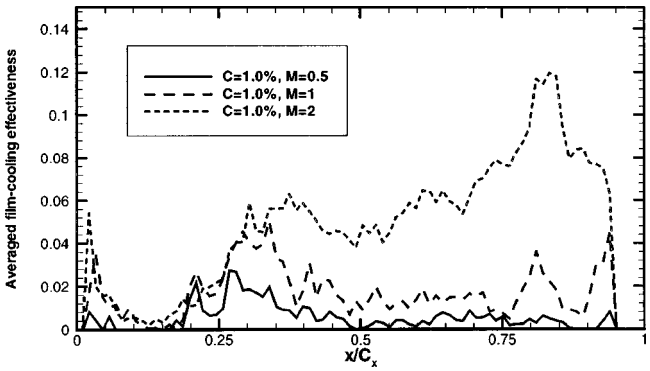

Fig. 18 Averaged film-cooling effectiveness for $C=1.0\%$ and coolant injection from both tip and pressure side holes

As tip gap clearance increases, generally, the overall film-cooling effectiveness also increases. This trend may be caused by the different interactions of injected coolant with the shroud and the leakage flow. At a small tip gap clearance, injected coolants may impinge on the shroud and dilute well with the leakage flow, which results in relatively small film-cooling effectiveness. As tip gap clearance becomes larger, however, injected coolant may be relatively easily deflected and would provide better film coverage.

Conclusions

The detailed heat transfer coefficients and film-cooling effectiveness distributions on a blade tip were measured in a 5-bladed linear cascade with blow-down facility using a hue detection based transient liquid crystals technique. The mainstream Reynolds number based on cascade exit velocity and axial chord length was 1.1×10^6. The blade tip model was a two-dimensional profile of a GE-E^3 blade of an aircraft gas turbine engine. Measurements were performed with three tip gap clearances of about 1.0%, 1.5%, and 2.5% of blade span, a mainstream turbulence level of 9.7%, and three blowing ratios of 0.5, 1, and 2. Major findings based on the experimental results are as follows:

1) As blowing ratio increased, static pressure on the shroud increased and the heat transfer coefficient on the tip slightly decreased due to a possible blockage effect of the injected coolant.
2) Film-cooling effectiveness increased as blowing ratio increased for all cases.
3) The coolant injection from both tip and pressure side holes case showed a slightly reduced heat transfer coefficient compared with the injection from tip holes only case, due to the additional blockage effect of pressure side injected coolant.
4) Compared with the injection from tip holes only case, film-cooling effectiveness for the coolant injection from both tip and pressure side holes case was higher potentially due to the pressure side injected coolant carrying over the tip surface.
5) Generally, the overall averaged heat transfer coefficients and film-cooling effectiveness increased as tip gap clearance increased.

Acknowledgment

This work was prepared with the support of the NASA Glenn Research Center under grant number NAG3-2002. The NASA technical team is Mr. Robert Boyle and Dr. Raymond Gaugler. Their support is greatly appreciated. Technical discussions with Dr. C. Pang Lee of GE Aircraft Engines, Dr. Ron Bunker of GE R&D Center, and Dr. GM S. Azad of Siemens-Westinghouse were helpful and are acknowledged. Dr. C. Pang Lee also provided us with the E^3 profile for the plane and squealer tips. His help is also appreciated.

Nomenclature

C = tip clearance gap (% of the blade span or mm)
C_x = axial chord length of the blade (8.61 cm)
d = diameter of film-cooling holes (0.127 cm)
h = local convective heat transfer coefficient ($W/m^2 K$)
k = thermal conductivity of blade tip material (0.18 W/m K)
M = average blowing ratio ($=\rho_c V_c / \rho_m V_{avg}$)
LE = leading edge of the blade
P = local static pressure (kPa)
P_t = total pressure at the cascade inlet (kPa)
PS = blade pressure side
t = transition time for liquid crystals color change (second)
TE = trailing edge of the blade
T_c = Coolant air temperature (°C)
T_i = initial temperature of the blade tip surface (°C)
T_m = temperature of the mainstream at the cascade inlet (recovery temperature) (°C)
T_w = color change temperature of the liquid crystals (°C)
Tu = turbulence intensity level at the cascade inlet (%)
x = axial distance (cm)
V_{avg} = averaged velocity of mainstream air between cascade inlet and exit (m/s)
V_c = averaged velocity of coolant air from all film cooling holes (m/s)
α = thermal diffusivity of blade tip material (1.25×10^{-7} m^2/s)
η = local film-cooling effectiveness
ρ_c = density of coolant air (kg/m^3)
ρ_m = density of mainstream air (kg/m^3)
τ_i = step change of time (second)

References

[1] Han, J. C., Dutta, S., and Ekkad, S. V., 2000, *Gas Turbine Heat Transfer and Cooling Technology*, Taylor & Francis, New York.
[2] Mayle, R. E., and Metzger, D. E., 1982, ''Heat Transfer at the Tip of an Unshrouded Turbine Blade,'' Proc. Seventh Int. Heat Transfer Conf., Hemisphere Pub., pp 87–92.
[3] Metzger, D. E., Bunker, R. S., and Chyu, M. K., 1989, ''Cavity Heat Transfer on a Transverse Grooved Wall in a Narrow Flow Channel,'' ASME J. Heat Transfer, **111**, pp. 73–79.
[4] Chyu, M. K., Moon, H. K., and Metzger, D. E., 1989, ''Heat Transfer in the Tip Region of Grooved Turbine Blades,'' ASME J. Turbomach., **111**, pp. 131–138.
[5] Metzger, D. E., Dunn, M. G., and Hah, C., 1991, ''Turbine Tip and Shroud Heat Transfer,'' ASME J. Turbomach., **113**, pp. 502–507.
[6] Bunker, R. S., Baily, J. C., and Ameri, A. A., 2000, ''Heat Transfer and Flow on the First Stage Blade Tip of a Power Generation Gas Turbine: Part 1: Experimental Results,'' ASME J. Turbomach., **122**, pp. 272–277.
[7] Azad, G. M. S., Han, J. C., Teng, S., and Boyle, R., 2000, ''Heat Transfer and Pressure Distributions on a Gas Turbine Blade Tip,'' ASME J. Turbomach., **122**, pp. 717–724.
[8] Azad, G. M. S., Han, J. C., and Boyle, R., 2000, ''Heat Transfer and Pressure Distributions on the Squealer Tip of a Gas Turbine Blade,'' ASME J. Turbomach., **122**, pp. 725–732.
[9] Teng, S., Han, J. C., and Azad, G. M. S., 2001, ''Derailed Heat Transfer Coefficient Distributions on a Large-Scale Gas Turbine Blade Tip,'' ASME J. Heat Transfer, **123**, pp. 803–809.
[10] Dunn, M. G., and Haldeman, C. W., 2000, ''Time-Averaged Heat Flux for a Recessed Tip, Lip, and Platform of a Transonic Turbine Blade,'' ASME J. Turbomach., **122**, pp. 692–697.
[11] Ameri, A. A., and Steinthorsson, E., 1995, ''Prediction of Unshrouded Rotor Blade Tip Heat Transfer,'' ASME Paper 95-GT-142.
[12] Ameri, A. A., and Steinthorsson, E., 1996, ''Analysis of Gas Turbine Rotor Blade Tip and Shroud Heat Transfer,'' ASME Paper 96-GT-189.
[13] Ameri, A. A., Steinthorsson, E., and Rigby, L. David, 1998, ''Effect of Squealer Tip on Rotor Heat Transfer and Efficiency,'' ASME J. Turbomach., **120**, pp. 753–759.
[14] Ameri, A. A., Steinthorsson, E., and Rigby, L. David, 1999, ''Effects of Tip Clearance and Casing Recess on Heat Transfer and Stage Efficiency in Axial Turbines,'' ASME J. Turbomach., **121**, pp. 683–693.
[15] Ameri, A. A., and Bunker, R. S., 2000, ''Heat Transfer and Flow on the First Stage Blade Tip of a Power Generation Gas Turbine: Part 2: Simulation Results,'' ASME J. Turbomach., **122**, pp. 272–277.
[16] Kim, Y. W., Downs, J. P., Soechting, F. O., Abdel-Messeh, W., Steuber, G. D., and Tanrikut, S., 1995, ''A Summary of the Cooled Turbine Blade Tip Heat Transfer and Film Effectiveness Investigations Performed by Dr. D. E. Metzger,'' ASME J. Turbomach., **117**, pp. 1–11.
[17] Kim, Y. W., and Metzger, D. E., 1995, ''Heat Transfer and Effectiveness on Film Cooled Turbine Blade Tip Model,'' ASME J. Turbomach., **117**, pp. 12–21.
[18] Ekkad, S. V., Zapata, D., and Han, J. C., 1995, ''Heat Transfer Coefficients over a Flat Surface With Air and CO2 Injection through Compound Angle Holes Using a Transient Liquid Crystal Image Method,'' ASME J. Turbomach., **119**, pp. 580–586.
[19] Kline, S. J., and McClintock, F. A., 1953, ''Describing Uncertainties in Single Sample Experiments,'' Mech. Eng. (Am. Soc. Mech. Eng.), **75**, pp. 3–8.
[20] Foley, J. D., van Dam, A., Feiner, S. K., and Huyghes, J. F., 1990, *Computer Graphics: Principles and Practice*, Addison-Wesley Publishing Company, pp. 592.

Heat Transfer Enhancement Caused by Sliding Bubbles

Baris B. Bayazit

D. Keith Hollingsworth
e-mail: hollingsworth@uh.edu

Larry C. Witte
e-mail: witte@uh.edu

Heat Transfer and Phase Change Laboratory,
Department of Mechanical Engineering,
University of Houston,
Houston, TX 77204

Measurements that illustrate the enhancement of heat transfer caused by a bubble sliding under an inclined surface are reported. The data were obtained on an electrically heated thin-foil surface that was exposed on its lower side to FC-87 and displayed the output of a liquid crystal coating on the upper (dry) side. A sequence of digital images was obtained from two cameras: one that recorded the response of the liquid crystal and one that recorded images of the bubble as it moved along the heated surface. With this information, the thermal imprint of the bubble was correlated to its motion and position. A bubble generator that produced FC-87 bubbles of repeatable and controllable size was also developed for this study. The results show that both the microlayer under a sliding bubble and the wake behind the bubble contribute substantially to the local heat transfer rate from the surface. The dynamic behavior of the bubbles corresponded well with studies of the motion of adiabatic bubbles under inclined plates, even though the bubbles in the present study grew rapidly because of heat transfer from the wall and the surrounding superheated liquid. Three regimes of bubble motion were observed: spherical, ellipsoidal and bubble-cap. The regimes depend upon bubble size and velocity. A model of the heat transfer within the microlayer was used to infer the microlayer thickness. Preliminary results indicate a microlayer thickness of 40–50 μm for bubbles in FC-87 and a plate inclination of 12 deg. [DOI: 10.1115/1.1565090]

Keywords: Boiling, Enhancement, Heat Transfer, Phase Change, Thin Films

Introduction

Boiling heat transfer occurs in a wide variety of engineering applications including energy conversion systems, manufacturing processes, and cooling of advanced electronic systems. Nucleate boiling provides an attractive means of cooling temperature-sensitive, high heat-flux devices because it can sustain a large heat flux over a small and relatively stable temperature difference. Modern developments in high-density computer chips and compact heat exchangers are requiring reliable predictions of the initiation of boiling and of the heat transfer rate that follows for a variety of surfaces and convective fields. Assuring that a surface designed to operate in boiling is in fact doing so is of extreme importance. For example, it is well known that boiling can be delayed on heat-flux-controlled surfaces so that potentially damaging overshoots in surface temperature can occur. There is a need for flows that combine convection and boiling so that heat transfer is enhanced beyond the rates that occur in boiling alone. There are many convective situations where bubbles that have been formed at one place in a device will, after detachment, move along adjacent surfaces. This motion history has become known as the sliding bubbles phenomenon. There is evidence that sliding bubbles can dramatically increase the local heat transfer rate from the surface on which they slide. One of the first devices in which sliding bubbles were observed to enhance heat transfer was a shell-and-tube heat exchanger that experiences boiling over some or all of its tubes. Cornwell [1] produced a surprising result during a study of a tube bank. With all the tubes at the same heat flux, the upstream tubes were in nucleate flow-boiling while the downstream tubes experienced no boiling at all. Clearly the heat transfer coefficient on the downstream tubes had to be high enough to hold the surface temperature below that required for the onset of boiling—while supporting a heat flux that should have resulted in boiling.

Cornwell postulated that the heat transfer coefficient on the downstream tubes resulted from heat transfer into bubbles that nucleated on the upstream tubes and slid around the walls of the downstream tubes. Furthermore, at higher heat flux levels, boiling initiated on the downstream tubes with no reported temperature overshoot. This observation implies that for higher fluxes the downstream heat transfer coefficients are so high that little change is experienced once boiling initiates.

A sliding bubble can induce at least two significant mechanisms that enhance heat transfer. Because the bubble displaces liquid and acts almost like a bluff body moving through the liquid, a local enhancement in convection around the bubble can certainly take place. Also it has been known for decades [2,3] that a sliding bubble can create a thin liquid microlayer under the bubble as it slides along the heated surface. As the bubble slides, the microlayer evaporates and is replenished by liquid trapped under the upstream edge of the bubble. This is much the same mechanism that occurs as bubbles are nucleated and grow outward from a nucleation site. Addlesee, Cornwell, and coworkers [4–6] have examined the fluid dynamics of sliding bubbles and the accompanying heat transfer implications, and the velocity of bubbles that rise under an inclined plate along with the film thickness that separates the bubble from the surface. Yan, Kenning, and coworkers [7,8] have also undertaken studies that seek to explain the enhancement mechanisms of sliding bubbles. Kenning was the first to apply liquid crystal thermography to the measurement of surface temperature fields that develop around sliding bubbles. The most recent research from this group [9] involved mapping the surface temperature underneath a bubble sliding through saturated water. Because the liquid was saturated, the heat transfer rate to the bubble could be estimated from the observed volume increase of the bubble. Kenning found that the microlayer could account for only a small fraction of energy transferred to the bubble. The thickness of the microlayer was estimated to be about 60 μm.

Qiu and Dhir [10] studied heat transfer enhancement under a sliding bubble on a silicon test surface heated by micro-gage heaters and instrumented with thermocouples. Vapor bubbles of PF-5060 were created from an artificial cavity. Silvered glass particles were added to the fluid to enable flow visualization. They observed a transition from spherical to elliptical bubbles, and they

Contributed by the Heat Transfer Division for publication in the JOURNAL OF HEAT TRANSFER. Manuscript received by the Heat Transfer Division June 26, 2002; revision received November 14, 2002. Associate Editor: D. B. R. Kenning.

found that vortices in the bubble wake enhanced the heat transfer continuously by bringing cooler liquid from the pool nearer to the surface.

Thorncroft and Klausner [11] examined the effect of a gas bubble sliding during forced convection boiling. The flow facility was vertical with a transparent test section. They concluded that sliding bubbles enhance heat transfer significantly, up to 52%, even during single-phase convection. They also showed that the turbulence induced by bubble injection was a significant heat transfer enhancement mechanism.

Previous studies have illuminated several problems in investigating the behavior of sliding bubbles. It is unclear whether microlayer evaporation or wake mixing is the dominant enhancement mechanism for a given arrangement of system parameters. The difficulty, and necessity, of co-locating the bubble and its surface temperature field through independent, simultaneous measurements is apparent. Attempts to infer the microlayer thickness through the development and application of microlayer models of varying sophistication has produced a broad range of results. The research described in this paper is directed toward providing further insight into these questions.

Methodology

Apparatus. Figure 1 shows a schematic of the apparatus developed to investigate sliding bubble heat transfer. It consisted of a rectangular chamber (approximately $40\times20\times19$ cm) made of thin aluminum plates. The chamber could be rotated about a pivot point to give different heater inclination angles relative to the horizontal. The test fluid is FC-87, a perfluorocarbon fluid manufactured by the 3M Corporation. FC-87 has a boiling point of 30.0°C at 1 atmosphere.

Two sidewalls and the bottom were equipped with glass windows for lighting and photography. Openings in the chamber allowed injection of vapor bubbles, removal of vapor produced in the chamber, and placement of pressure transducers and thermocouples. Bubbles of FC-87 vapor were injected just below the lower end of the heated surface by a vapor generation system designed to allow control of the frequency and size of the bubbles. The ability to produce a single bubble of a consistent and substantial size, as opposed to an uncontrolled stream of bubbles, is a nontrivial technical issue. Vapor was created by electrically heating a small quantity of the test fluid. The vapor flowed to a conical plastic injection head through a precision metering valve. Bubble size was controlled in part by the exit diameter of the injector.

Test Surface. A 51 μm thick by 21.0×16.8 cm stainless steel foil served as the electrically heated test surface and was mounted on top of the chamber. The test fluid touched the bottom face of the test surface, and a thermochromic liquid crystal (TLC) was applied to the upper (dry) face of the heater. The application was by airbrush: a layer of black paint followed by a layer of microencapsulated thermochromic liquid crystals from Hallcrest, Inc.

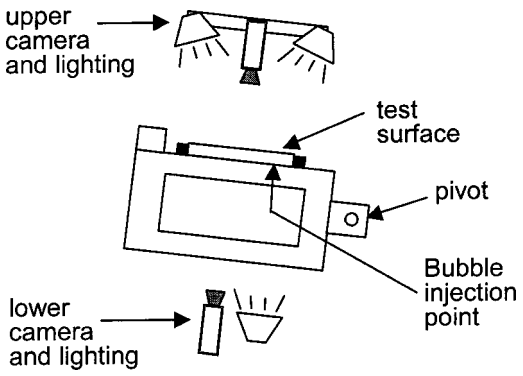

Fig. 1 Schematic drawing of the test apparatus

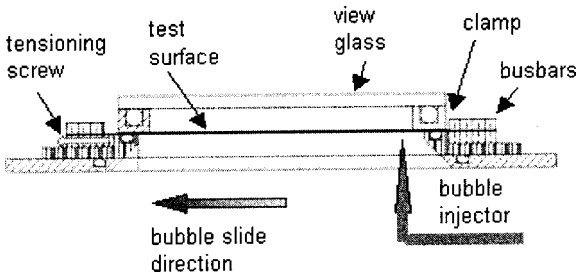

Fig. 2 Detailed sketch of test surface

The foil was heated by a dc power supply capable of 12 volts and 200 amps. Further details of the design can be found in Bayazit [12].

Figure 2 shows a side view of the assembly with the various components labeled. Those include a tensioning mechanism to hold the foil relatively flat, and a sealing system to prevent leakage to the outside of the chamber. This system included an aluminum frame that clamped the edges of the foil. The frame was water-cooled to remove the energy generated within the clamped edges of the foil. A glass window attached to the frame allowed viewing of the TLC surface as well as providing a stagnant air gap above the test surface to minimize heat losses to the atmosphere.

Imaging Technique and Data Acquisition. In the UH Heat Transfer Laboratory, various experiments have employed wideband calibrated liquid crystal thermography. For examples see Hay and Hollingsworth [13,14], Dukle and Hollingsworth [15], and Dalrymple, Dukle, and Hollingsworth [16]. The TLC used here was calibrated according to the procedure of Hay and Hollingsworth over a range of 30.2–40.6°C. The first-order, 95% confidence, uncertainty was less than ±0.5°C below 33°C, rose to ±0.8°C at 35°C, and was ±1.2°C at 40.6°C.

Two 15 W fluorescent light bulbs were used to light the TLC surface; while a single 15 W bulb lighted the lower surface (bubble view). An upper light stand, fixed to the pivot arms of the chamber, held the upper camera and lights at a fixed position relative to the test surface regardless of the inclination angle. The data acquisition system consisted of a Matrox Meteor MC II dual-camera color frame grabber board and a Matrox G-4 video card installed in an Intel Pentium computer. A pair of digital video sequences was acquired from the bottom and the top of the heated surface by alternating image acquisition from two cameras. Software was developed for grabbing the images and sequencing them in time. A Pulnix charge-coupled device (CCD) color camera with a Navitar lens acquired the TLC images. The bottom camera was

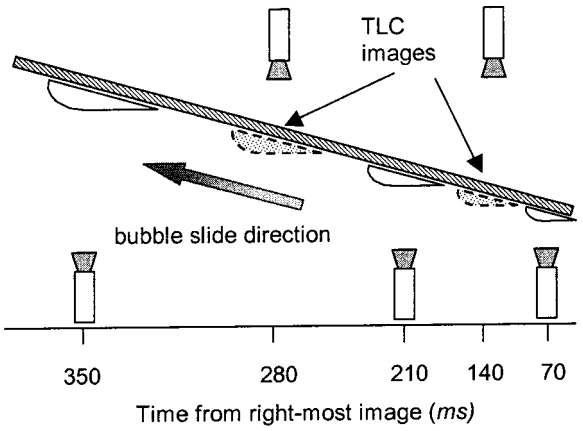

Fig. 3 Timing of lower and upper image sequences. The positions of the bubbles drawn in dashed line are interpolated.

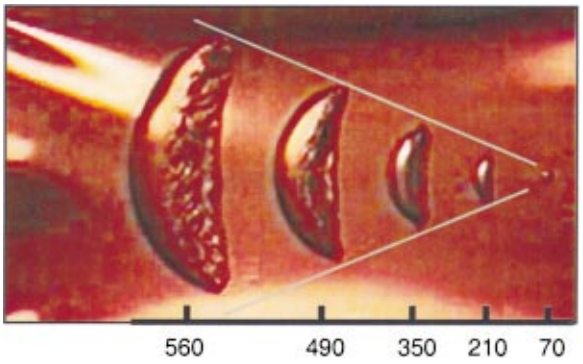

Fig. 4 Collage of bubble images. The frame timing is in ms.

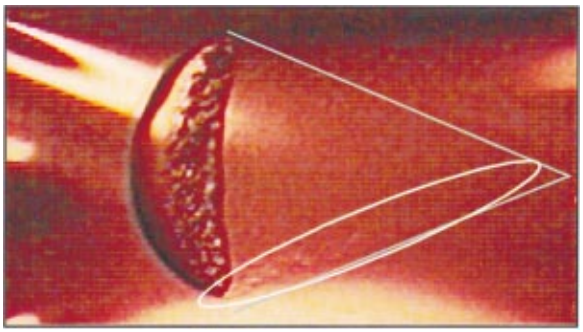

Fig. 5 Large cap-shaped bubble with a shear layer at the lower extremity

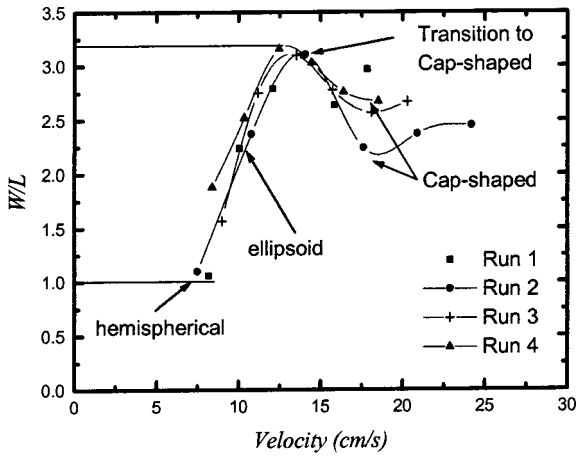

Fig. 6 Width to length ratio versus velocity

a Pulnix CCD unit with Fujinon lens and an external shutter control. The bottom camera was synchronized with a signal generated by the top camera. The field size in pixels for the digitized images from both cameras was 640×480. The dimensions for the square pixels were 217 μm/pixel for the TLC surface and 231 μm/pixel for the bubble images.

The image sequencing produced an interlaced TLC image from the upper camera followed by an interlaced bubble image from the lower camera at a net framing rate of 14.29 frames/sec-less than the nominal 30 frames/sec because of latency in the acquisition board and the control software. As shown in Fig. 3, the result is two digital video sequences, each sequence having frames separated by 140 ms. The sequences are offset in time by 70 ms. To co-locate the bubble with its TLC temperature, the position of the bubble (as given by three points on the bubble surface) for every bubble image in a run was mapped from the lower to the upper

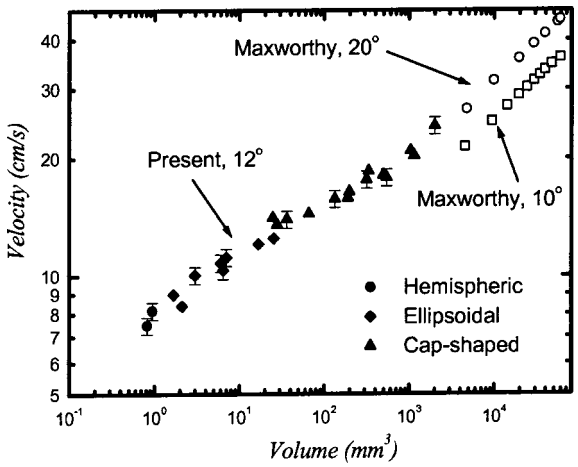

Fig. 7 Velocity versus volume

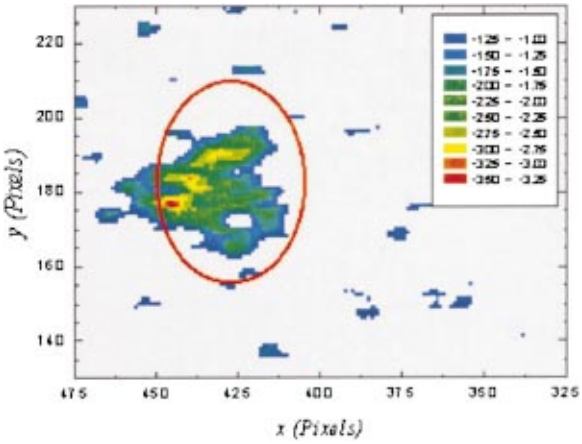

Fig. 8 Contour plot of the change in T_w caused by the passage of the bubble: $T_w(t=140\ \text{ms}) - T_w(t=0\ \text{ms})$. The bubble first contacts the plate near $x=516$ pixels.

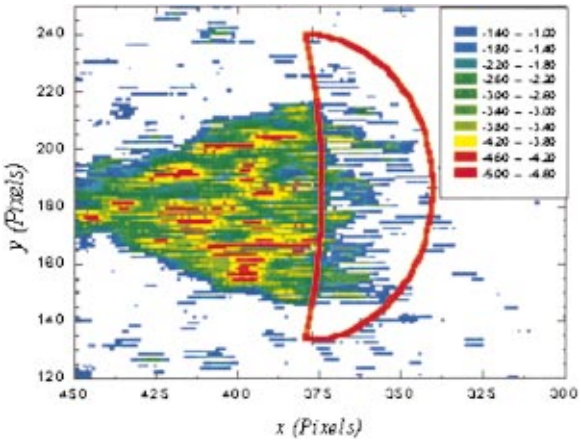

Fig. 9 Contour plot of the change in T_w caused by the passage of the bubble: $T_w(t=280\ \text{ms}) - T_w(t=0\ \text{ms})$. The bubble first contacts the plate near $x=516$ pixels.

surface, and the position of the bubble for each TLC image in the run was computed from a nonlinear interpolation of the known mapped points. Typical uncertainty for locating the bubble in the TLC image was ±5 pixels, or ±1.09 mm.

Additional data acquisition equipment included a pressure transducer connected to the upper wall of the apparatus to ensure

the pressure there remained atmospheric, and a thermocouple probe with a true ice-bath junction to measure the bulk fluid temperature far from the test surface.

Experimental Results

For the present results, the test surface inclination was 12 deg from horizontal. Greater inclination angles produced bubbles that moved too fast to be imaged clearly at the present framing rate. Bubble velocities ranged up to 20 cm/s, and volumes grew to 2000 mm^3. For the run presented here, the surface heat flux based on the ohmic heating rate was 1.6 kW/m^2, the bulk fluid temperature was $25 \pm 0.5°C$, (subcooling of 5°C) and the pressure at the test surface was atmospheric.

Bubble Shape and Motion. In addition to capturing the surface temperature as a bubble passed a given location, the images allowed the determination of the bubble shapes and velocities as the bubbles slid along the surface. Some insight into the bubble shapes that could be encountered was provided by Maxworthy [17] from work in which gas bubbles of fixed volume were introduced below an unheated inclined surface. In the current research, hemispherical, ellipsoidal and cap-shaped bubbles were observed, and they grew rapidly due to evaporation. Figure 4 is a collage of bubbles from the featured run along with the timing of the images. The collage was created while preserving the position and size of the bubbles. Here, a small hemispherical bubble quickly grows and transforms to a cap-shaped bubble. While a clearly ellipsoidal bubble is not present, the small cap-shaped bubble at 210 ms is evolving from an elliptic shape. The cap-shaped bubbles exhibit a smooth, rounded front, and a rough, slanted rear surface. The slant results from a skewing of the shape as the portion of the bubble near the test surface is slowed by the presence of the surface. Once a cap-shaped bubble formed, it tended to grow linearly with distance: a sequenced collage of images nest within a constant angle as shown. The large cap-shaped bubble at 560 ms is shown again in Fig. 5, and the angled lines are shown in the positions taken from Fig. 4. The wake behind these bubbles lies within the lines shown and is marked by a shear layer which forms at the extremities of the bubble. The shear layer appears to contain small-scale turbulent structures made visible by the high gradients in index of refraction they create near the heated surface.

The transverse width, W, of the bubbles and their streamwise length, L, were measured from the bubble images. Figure 6 illustrates how the width to length ratio, W/L, behaved with bubble velocity. The three regimes of bubble shape are distinct, and the results are consistent between experimental runs. Figure 7 shows measured velocity and estimates of volume obtained from several runs [12]. Also included are the data from [17] for air bubbles in water at higher velocities and different inclinations. Even though the vapor bubbles in our study were growing rapidly, their behavior agrees well with the adiabatic observations of Maxworthy.

Surface Temperature Distributions. Prior to the injection of a bubble, the wall temperature field, T_w, is that produced by a natural convection boundary layer on a uniform-heat-flux surface. As a result, T_w increases in the downstream direction. The passage of the bubble alters this field. The interval between the bubbles, as controlled by the injector, was very long compared to the time of bubble passage beneath the surface. Thus the test surface temperature recovered to a level controlled by natural convection. To isolate the effect of the bubble from this natural convection precursor, the undisturbed T_w field at $t=0$ ms was subtracted from the data in subsequent TLC frames. The result is shown as a contour plot in Figs. 8 and 9 for the TLC images at 140 ms and 280 ms, respectively. The bubble is moving from left to right in these figures.

The bubble location was determined by the co-location procedure described above. We chose to examine bubbles toward the upstream half of the test surface because T_w there was within the optimum response range of the TLC. The bubble in Fig. 8 is approximately elliptic is shape; it lies between the hemispherical and cap-shaped bubble in Fig. 4. The lateral extremes of the bubble do not produce a significant depression in T_w, and a short wake can be seen behind the central portion of the bubble. Figure 9 is the result of a typical cap-shaped bubble—between the second and third bubbles in Fig. 4. The triangular thermal wake is consistent in position and size with the structure seen in Figs. 4 and 5. The maximum T_w depression in Fig. 9 is 4–5°C, or approximately one-third of the surface-to-bulk temperature difference typical to this location. The image shows that the T_w depression starts beneath the bubble and continues to form the triangular wake. As in the preceding figure, the depression does not extend to the transverse extremities, and the lateral extremes of the wake are sharply defined. This observation may indicate that the bubble curves away from the wall towards its transverse end so that an effective microlayer does not form.

Some amount of the temperature depression measured in the wake is caused by the passage of the microlayer over this area as the bubble approached its present location, and some is caused by the direct action of the wake from the bubble in the present location. The fact that the largest temperature depression is in the wake and not at the trailing edge of the bubble suggests that the mixing in the wake is strong enough, at a subcooling of 5°C, to further depress the surface temperature after the microlayer departs.

A Model for Sliding Bubble Heat Transfer

A numerical model was developed to analyze the heat transfer through the microlayer. A sketch of the model system is given in Fig. 10. A number of simplifying assumptions were made. The microlayer thickness, δ, is uniform. The coordinate system is attached to the bubble: the bubble is stationary and the surface is moving with the measured bubble velocity, U. The velocity profile is linear across the microlayer, $u(y)=Uy/\delta$, and does not change with x (fully developed). This velocity profile assumes that the bubble surface supports a shear stress such that the no-slip condition applies. While this assumption is applied here with no supporting evidence, the opposite (and simpler) assumption, that the bubble surface supports no stress is equally unsupported and not required in the present formulation. The bubble length is fixed at a measured value. The entrance temperature profile is linear with limits T_w and T_{sat}, and the slope is consistent with the measured steady-state heat flux, $\dot{q}''_e$. The bubble surface is assumed at saturation temperature, T_{sat}. The steady-state energy generation rate, $\dot{q}''_e$, is uniform in the foil; however, the capacity of the foil to locally store energy is modeled so that the total local heat flux from the foil to the fluid may vary with x. The upper surface of the foil is adiabatic, and the foil has no conduction in the x-direction. By defining a reference frame that moves with the bubble, the flow in the microlayer is steady-state, and the temporal response of the foil to the passing of the bubble translates into a spatial (streamwise) variation of heat flux.

The energy equation for a two-dimensional steady flow with no viscous dissipation is

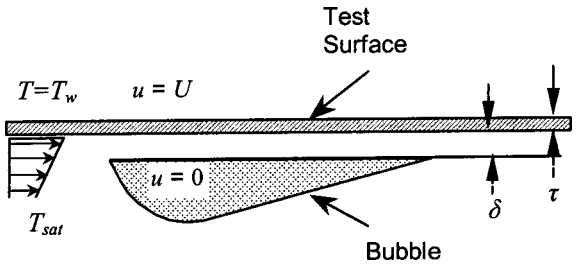

Fig. 10 Sketch of the model system for computation of heat transfer across the microlayer

$$u\frac{\partial T}{\partial x}+v\frac{\partial T}{\partial y}=\alpha\left[\frac{\partial^2 T}{\partial x^2}+\frac{\partial^2 T}{\partial y^2}\right]. \tag{1}$$

Using δ as the length scale, and U as the velocity scale, Eq. 4.25 was made dimensionless by using

$$u^*\equiv\frac{u}{U}, \tag{2}$$

$$v^*\equiv\frac{v}{U}, \tag{3}$$

$$x^*\equiv\frac{x}{\delta}, \tag{4}$$

$$y^*\equiv\frac{y}{\delta}, \tag{5}$$

$$\mathrm{Pe}\equiv\frac{U\delta}{\alpha}, \tag{6}$$

to produce

$$u^*\frac{\partial T}{\partial x^*}+v^*\frac{\partial T}{\partial y^*}=\frac{1}{\mathrm{Pe}}\left[\frac{\partial^2 T}{\partial x^{*2}}+\frac{\partial^2 T}{\partial y^{*2}}\right].$$

The continuity equation for this flow is

$$\frac{\partial u}{\partial x}+\frac{\partial v}{\partial y}=0. \tag{7}$$

For fully developed flow

$$\frac{\partial u}{\partial x}=0. \tag{8}$$

From Eq. 7, $\partial v/\partial y=0$, and $v=\mathrm{const}=0$. In dimensionless form,

$$v^*=0. \tag{9}$$

Using the assumption of a fully developed linear velocity profile,

$$u(y)=\frac{Uy}{\delta}, \tag{10}$$

$$u^*=y^*. \tag{11}$$

Assuming no streamwise conduction, $\partial^2 T/\partial x^{*2}=0$, the energy equation becomes

$$y^*\frac{\partial T}{\partial x^*}=\frac{1}{\mathrm{Pe}}\frac{\partial^2 T}{\partial y^{*2}}. \tag{12}$$

The dimensionless temperature, T^* is defined as

$$T^*\equiv\frac{T(x,y)-T_{\mathrm{sat}}}{\Delta T_{\mathrm{ref}}}, \tag{13}$$

where

$$\Delta T_{\mathrm{ref}}\equiv\frac{\dot{q}_e''\delta}{k}. \tag{14}$$

The final form of the governing equation becomes

$$y^*\frac{\partial T^*}{\partial x^*}=\frac{1}{\mathrm{Pe}}\frac{\partial^2 T^*}{\partial y^{*2}}. \tag{15}$$

The boundary condition at the bubble surface is

$$T^*=0 \quad \text{at} \quad y^*=0. \tag{16}$$

At the foil surface, $y^*=1$, the local heat flux is governed by the unsteady response of the foil,

$$-m''c\frac{\partial T_w}{\partial t}+\dot{q}_e''=\dot{q}_w''=k\left.\frac{\partial T}{\partial y}\right|_{\mathrm{fluid}}, \tag{17}$$

where m'' is the mass of the foil per unit wetted area, and the minus sign is absent from the Fourier term due to the defined direction of y. If the density of the foil is ρ_w, and the thickness is τ_w, then

$$-(\rho\tau c)_w\frac{\partial T_w}{\partial t}+\dot{q}_e''=\dot{q}_w''=k\left.\frac{\partial T}{\partial y}\right|_{\mathrm{fluid}}. \tag{18}$$

Using $\Delta T_{\mathrm{ref}}=\dot{q}_e''\delta/k$, and $dT=\Delta T_{\mathrm{ref}}dT^*$ and $T_w=T|_{y^*=1}$, Eq. 17 becomes

$$\left.\frac{\partial T^*}{\partial y^*}\right|_{y^*=1}=-\frac{\delta}{k}(\rho\tau c)_w\left.\frac{\partial T^*}{\partial t}\right|_{y^*=1}+1. \tag{19}$$

The speed of the surface moving above the stationary bubble is $U=dx/dt|_{y^*=1}$.

Therefore $dt=dx/U|_{y^*=1}=\delta/Udx^*|_{y^*=1}$. Substituting this variable change into Eq. 19 produces

$$\left.\frac{\partial T^*}{\partial y^*}\right|_{y^*=1}=-\frac{U}{k}(\rho\tau c)_w\left.\frac{\partial T^*}{\partial x^*}\right|_{y^*=1}+1. \tag{20}$$

A dimensionless group, γ, is defined as

$$\gamma\equiv\frac{U}{k}(\tau c\rho)_w, \tag{21}$$

and Eq. 20 becomes

$$\left.\frac{\partial T^*}{\partial y^*}\right|_{y^*=1}=-\gamma\left.\frac{\partial T^*}{\partial x^*}\right|_{y^*=1}+1. \tag{22}$$

Eq. 22 is the boundary condition at $y^*=1$.

At the inlet to the microlayer, $x^*=0$, the fluid temperature is assumed to vary linearly with a slope, $dT/dy|_{\mathrm{inlet}}=\dot{q}_e''/k$, across the entire microlayer.

This condition assumes the foil is in steady-state upstream of the bubble. In dimensionless variables, the temperature profile at the inlet is

$$T^*|_{x^*=0}=T_w^*|_{x^*=0}+y^*-1, \tag{23}$$

where $T_w^*|_{x^*=0}$ is taken from measurements immediately upstream of the bubble.

The system to be solved is:

$$y^*\frac{\partial T^*}{\partial x^*}=\frac{1}{\mathrm{Pe}}\frac{\partial^2 T^*}{\partial y^{*2}}, \tag{24}$$

$$T^*|_{y^*=0}=0, \tag{25}$$

$$\left.\frac{\partial T^*}{\partial y^*}\right|_{y^*=1}=-\gamma\left.\frac{\partial T^*}{\partial x^*}\right|_{y^*=1}+1 \tag{26}$$

$$T^*|_{x^*=0}=T_w^*|_{x^*=0}+y^*-1. \tag{27}$$

The system has four parameters, Pe, γ, $T^*|_{x^*=0}$, and L_{bubble}. The Peclet number represents the ratio of the bubble speed to the speed of the temperature diffusion across the microlayer. The parameter γ controls the relative importance of stored energy to generated energy in the foil, and $T^*|_{x^*=0}$ captures both the local strength of the natural convection field in the absence of the bubble and the subcooling of the bulk liquid. The bubble length, L_{bubble}, sets the streamwise length of the microlayer.

Equation 24 is descretized as:

$$y^*\frac{T_{i,j}^*-T_{i-1,j}^*}{\Delta x^*}=\frac{1}{\mathrm{Pe}}\frac{T_{i,j+1}^*+T_{i,j-1}^*-2T_{i,j}^*}{(\Delta y^*)^2}, \tag{28}$$

so that

$$T^*_{i,j}=\frac{\frac{1}{\mathrm{Pe}(\Delta y^*)^2}(T^*_{i,j+1}+T^*_{i,j-1})+y^*\frac{T^*_{i-1,j}}{\Delta x^*}}{\frac{y^*}{\Delta x^*}+\frac{2}{\mathrm{Pe}(\Delta y^*)^2}}. \quad (29)$$

The boundary condition at the wall is descretized as

$$\left.\frac{T^*_{i,j}-T^*_{i,j-1}}{\Delta y^*}\right|_{y^*=1}=-\gamma\left.\frac{T^*_{i,j}-T^*_{i-1,j}}{\Delta x^*}\right|_{y^*=1}+1, \quad (30)$$

so that

$$T^*_{i,j}|_{y^*=1}=\frac{\left.\frac{\gamma}{\Delta x^*}T^*_{i-1,j}+\frac{1}{\Delta y^*}T^*_{i,j-1}\right|_{y^*=1}+1}{\frac{1}{\Delta y^*}+\frac{\gamma}{\Delta x^*}}. \quad (31)$$

Microsoft Excel was used to solve the resulting set of coupled algebraic equations using the implicit iteration system embodied in its ''circular reference'' format of operation. To implement the geometry, a rectangular array of cells are defined such that the top row of the array is defined by the wall boundary condition, Eq. 31, the bottom row is defined by the bubble surface boundary condition, Eq. 25, and the first ''up-stream'' column of cells is defined by the entrance condition, Eq. 27. The remaining ''internal'' cells are defined by Eq. 29. Values for the parameters Pe, γ, and $T^*|_{x^*=0}$ are taken from TLC frames $t=0.27$ sec and $t=0.40$ sec from Run 2. Table 1 gives the parameters for these two cases along with the δ and Pe determined from the analysis.

To allow comparison to the data, the measured temperature ($T_w-T_{w,\text{natural convection}}$) was determined by averaging across five pixel rows in each image. The model assumes that the microlayer is developing in a precursor field with a uniform wall temperature of $T_{w,\text{inlet}}$. Therefore, the value of $T_{w,\text{inlet}}$ at the beginning of each bubble is uniformly added to the measured difference values.

The model results are shown along with measured data in Fig. 11. The visual reference for the figure is the saturation temperature, 30°C. The measurements have been filtered by a 9-pixel local area average and have a resulting uncertainty of $\approx\pm0.67$°C. The data show a wavy structure that is most likely due to spatial variations in the natural convection boundary layer through which the bubble slides. The smaller bubble (280 ms) begins near a trough in a wave, while the trace from the larger bubble (420 ms) displays a peak toward the center of the bubble. Two model predictions are shown for each bubble in order to bracket reasonable values of δ. For the small bubble, $T_{w,\text{inlet}}$ was chosen to be either at the trough or near the center of the temperature wave, and values of δ were found to fit the overall trend. For the larger bubble, $T_{w,\text{inlet}}$ was held constant and values of δ were found to bracket the wavy structure in the downstream portion of the bubble. This technique gave $\delta=40\pm5$ μm for the smaller bubble and $\delta=50\pm7$ μm for the larger example. The lengths of the computed temperature traces correspond to the measured bubble lengths.

Table 1 Parameters used in the model of the microlayer

	Bubble at 280 ms	Bubble at 420 ms
U	12.5 cm/s	16.07 cm/s
L_{bubble}	5.0 mm	8.7 mm
α	3.16×10^{-8} m^2/s	3.16×10^{-8} m^2/s
k	0.056 W/mK	0.056 W/mK
τ_w	50.8 μm	50.8 μm
ρ_w	8000 kg/m^3	8000 kg/m^3
c_w	470 kJ/kgK	470 kJ/kgK
$T_w\|_{\text{inlet}}$	38.6°C	40.2°C
γ	425	548
δ	40 μm	50 μm
Pe	158	254

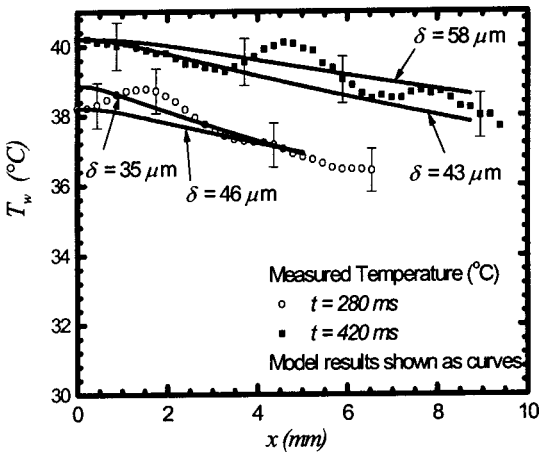

Fig. 11 Comparison of the calculated and measured wall temperature. The lengths of the computed temperature traces correspond to the measured bubble lengths.

The present values for FC-87 are near Kenning's result of $\delta=50$ μm for saturated water. The short horizontal section at the entrance to the microlayer is the length required for the temperature disturbance created by the bubble to diffuse across the microlayer. For the bubble lengths modeled, the microlayer did not become thermally fully developed as would be indicated by a streamwise-uniform T_w consistent with pure conduction across the microlayer. The wall heat flux has two sources: the uniform electrical generation and the local, unsteady depletion of foil's internal energy. The present results show that the energy storage term dominates the wall heat flux: it is roughly five times the steady generation flux over most of the bubble's length.

Concluding Remarks

The present facility allows the co-location of the bubble with its surface thermal trace through the acquisition of two digital image sequences: one of the bubble itself and one of the TLC surface. It is interesting to note that experiments of this type carry the technique of full-field wide-band liquid crystal thermography away from ''snapshots'' of steady or almost-steady thermal fields and into the world of truly transient, multiple-frame imaging. Computer power and digital imaging hardware now make it possible to create ''liquid crystal movies'' indexed to other video streams, in this case, a digital movie of the bubble's history.

Our measurements of velocity and volume for growing vapor bubbles agree surprisingly well with those of Maxworthy [17] for adiabatic gas bubbles. Vapor bubbles in FC-87 quickly obtained a cap-shaped geometry, grew rapidly, and created a triangular thermal wake with sharp lateral edges. Thin, apparently turbulent, shear layers were observed shedding from the lateral extremes of the caps; they cant inward at the same angle as the triangular thermal trace left by the bubble. In laboratory coordinates, these shear layers may be a train of relatively stationary small-scale vortices shed at the extremes of the bubble. As the bubble grows, these vortices dissipate slowly and form a triangular boundary around the wake. The bubbles created substantial surface temperature depressions on a uniform heat-generation surface: roughly 1/3 of the total temperature drop from the wall to the bulk fluid in the images shown here. The temperature depression continues into the wake of the bubble. The T_w field does not recover quickly downstream of the trailing edge of the bubble; instead, T_w continues to drop in the triangular region well behind the bubble. We hypothesis that as the bubble rescales linearly with distance, the length of the wake region (fed by bulk-temperature fluid from around and

above the bubble) rescales accordingly. The net effect is a wake thermal depression that persists long after the bubble has passed a given location.

The present thermal and hydrodynamic model of the microlayer allows the thermal profile within the microlayer to evolve down the length of the bubble, and it includes a simple model for the thermal response of the test surface. Preliminary results show that both elements are extremely important: the microlayer does not come to a fully developed state by the end of the bubble, and the transient response of the test surface is a critical issue. Because of the latter observation, a statement of the magnitude of the augmentation in the heat transfer coefficient by a sliding bubble is not a simple issue: the local heat flux used in that computation is not the steady-state heat flux.

Acknowledgments

The authors appreciate the support of the Advanced Research Program of the Texas Higher Education Coordinating Board.

Nomenclature

c = specific heat of foil (kJ/kgK)
k, α = conductivity and diffusivity of the liquid
L_{bubble} = measured bubble length (mm)
m'' = mass of foil per wetted area (kg/m^2)
Pe = Peclet number for the microlayer; $\equiv U\delta/\alpha$
$\dot{q}''_e$ = heat flux based on electrical heating rate (kW/m^2)
T = local temperature (°C)
T_w = temperature of the heated wall (°C)
T_{sat} = saturation temperature of fluid (30°C at 1 atm)
T^* = dimensionless temperature; $\equiv (T(x,y)-T_{\text{sat}})k/\dot{q}''_e\delta$
t = time (sec)
U = local bubble velocity, and velocity scale for the microlayer model (cm/s)
u = streamwise velocity in the microlayer (cm/s)
u^* = dimensionless velocity; $\equiv u/U$
v = transverse velocity in the microlayer (cm/s)
v^* = dimensionless velocity; $\equiv v/U$
W = bubble width (mm)
x = streamwise position coordinate (mm)
x^* = dimensionless streamwise position; $\equiv x/\delta$
y^* = dimensionless position across microlayer; $\equiv y/\delta$
y = position coordinate across the microlayer, beginning at the bubble surface (μm)
δ = microlayer thickness, and length scale for the microlayer model (μm)
γ = dimensionless group where $(\tau c\rho)_w$ is the product of the thickness, specific heat, and density of the heated foil; $\equiv U(\tau c\rho)_w/k$

References

[1] Cornwell, K., 1991, "The Influence of Bubbly Flow on Boiling From a Tube Bundle," Int. J. Heat Mass Transf., **33**, pp. 2579–2584.
[2] Cooper, M. G., and Lloyd, A. J. P., 1969, "The Microlayer in Nucleate Pool Boiling," Int. J. Heat Mass Transf., **12**, pp. 895–913.
[3] Koffman, L. D., and Plesset, M. S., 1983, "Experimental Observations of the Microlayer in Vapor Bubble Growth on a Heated Solid," ASME J. Heat Transfer, **105**, pp. 625–632.
[4] Addlesee, A. J., Cornwell, K., and Peace, D. G., 1989, "Fluid Dynamics of Sliding Bubbles and Heat Transfer Implications," *Proc. Eurotherm Seminar 8, Pool Boiling*, Paderborn, pp. 57–64.
[5] Addlesee, A. J., and Cornwell, K., 1997, "Liquid Film Thickness Above a Bubble Rising Under an Inclined Plate," Chem. Eng. Res. Des., **75**, pp. 663–667.
[6] Addlesee, A. J., and Cornwell, K., 1999, "The Velocity of Bubbles Rising Under an Inclined Plate," ImechE Conf. Trans., *6th UK National Conf. on Heat Transfer*, pp. 231–236.
[7] Yan, Y., and Kenning, D. B. R., 1994, "Heat Transfer Near Sliding Vapor Bubbles in Boiling," *Proc., 10th International Heat Transfer Conference*, pp. 195–200.
[8] Yan, Y., Kenning, D. B. R., Grant, I. A., and Cornwell, K., 1996, "Heat Transfer to Sliding Bubbles Under Plane and Curved Surfaces," Fourth UK National Conf. On Heat Transfer, Manchester, IMechE, C510/118, pp. 295–299.
[9] Kenning, D. B. R., Bustnes, O. E., and Yan, Y., 2000, "Heat Transfer to a Sliding Vapor Bubble," *Proc. ASME Boiling 2000 Conf.*, **104**, pp. 82–89.
[10] Qiu, D. M., and Dhir, V. K., 1999, "An Experimental Study of Heat Transfer During Sliding of Bubbles on Inclined Surfaces," *Proc. 5th ASME/JSME Joint Thermal Engineering Conference*, San Diego, Paper AJTE99/6279.
[11] Thorncroft, G. E., and Klausner, J. F., 1999, "The Influence of Vapor-Bubble Sliding on Forced Convection Boiling Heat Transfer," ASME J. Heat Transfer, **121**, pp. 73–79.
[12] Bayazit, B. B., 2000, "A Thermographic Analysis of the Heat Transfer Mechanisms Generated by a Sliding Bubble," Masters thesis, University of Houston, Houston, TX.
[13] Hay, J. L., and Hollingsworth, D. K., 1996, "A Comparison of Trichromic Systems for Use in the Calibration of Polymer-Dispersed Thermochromic Liquid Crystals," J. Exp. Thermal and Fluid Sci., **12**, pp. 1–12.
[14] Hay, J. L., and Hollingsworth, D. K., 1998, "Calibration of Micro-Encapsulated Liquid Crystals Using Hue Angle and a Dimensionless Temperature," J. Exp. Thermal and Fluid Sci., **18**, pp. 251–257.
[15] Dukle, N. M., and Hollingsworth, D. K., 1996, "Liquid Crystal Images of the Transition from Jet-Impingement Convection to Nucleate Boiling, Part 1: Monotonic Distribution of the Convection Coefficient," and "Part 2: Non-monotonic Distribution of the Convection Coefficient," J. Exp. Thermal and Fluid Sci., **12**, pp. 274–297.
[16] Dalrymple, N. E., Dukle, N. M., and Hollingsworth, D. K., 1995, "The Behavior of a Boiling Front in Jet-Impingement Boiling," *Proc. of ASME/JSME Thermal Engineering Conference*, **2**, pp. 339–346.
[17] Maxworthy, T., 1991, "Bubble Rise Under an Inclined Plate," J. Fluid Mech., **229**, pp. 659–674.

Nejla Mahjoub Said
e-mail: Nejla.Mahjoub@fsm.rnu.tn

Hatem Mhiri

Salem El Golli

Laboratoire de Mécanique des
fluides et thermique,
Ecole Nationale d'Ingénieurs de Monastir,
route de Ouardanine 5020
Monastir, Tunisie

Georges Le Palec
e-mail: Lepalec@unimeca.univ-mrs.fr

Philippe Bournot

Unimeca,
60 rue Joliot-Curie,
Technopôle de Château-Gombert,
13453 Marseille Cedex 13, France

Three-Dimensional Numerical Calculations of a Jet in an External Cross Flow: Application to Pollutant Dispersion

The paper presents a three-dimensional numerical simulation of a circular turbulent jet issuing transversely into a uniform air stream. In the first part an air-helium jet is considered and the three-dimensional structure of the flow field is discussed. Then, a comparison between the numerical results of four turbulence closure models (three first-order models and a second-order one) are presented and compared with the experimental data given by Crabb et al. [7] and Andreopoulos et al. [9]. Although the different models render identical results in the upstream and far downstream regions of the jet, only the second order model is shown to give good results in the exit region and in the trailing zone of the jet. Based on this last model, the dynamic and scalar fields of a fume turbulent jet issuing transversely with velocity v_0 *into a uniform air flow with velocity* u *are then examined as functions of the ratio* $R = v_0/u_\infty$ *in order to simulate pollutant dispersion from industrial chimneys.* [DOI: 10.1115/1.1560158]

Keywords: Dispersion, Heat Transfer, Jets, Modeling, Three-Dimensional

Introduction

Researches concerning jets mixing into transverse flows are motivated by their great relevance to industrial applications in, such as, emission of pollutants by chimneys of factories. The turbulent phenomena produced by this type of flow are thus of practical interest. According to the ratio of the set velocity and the transverse flow velocity, numerous examples of applications can be found in various domains (injection, mixture, V/STOL planes with vertical take off, air pollution . . .). Therefore, because of their big practical meaning, numerous experimental and theoretical studies about this subject were undertaken.

Some fundamental characteristics associated with the largest values of R ($R = v_0/u_\infty$, v_0 and u being respectively the velocity in the exit section of the chimney and the velocity of ambient air) were experimentally studied by Komotani et al. [1], Fearn et al. [2], Keffer et al. [3] and Moussa et al. [4]. They experimentally determined the velocity and temperature fields, notably in the median plane of the jet.

Ramsey et al. [5] and Bergeles et al. [6] reported measurements of the efficiency of the film-cooling process on jets. They so determined the velocity distributions and proved that, for weak values of R, the velocity profile through the perpendicular plane to the exit section of the jet cannot be considered uniform. A more complete experimental study on the average flow field is found in the work of Crabb et al. [7]. They measured the velocity field of a jet in a transverse flow for the whole region of the mixture with R varying between 1.15 and 2.3. They used the LDA (Laser Doppler Anemometry) in the upflow region ($x/D < 0.6$) where the turbulence intensity is high and the HWA (Hot Wire Anemometry) in the backflow region. They showed that the obtained measurements by HWA are valid in regions where the turbulence is weak; on the other hand, for regions where the intensity of turbulence is higher than 30 percent, there is a probability of inversion of the flow which can not be determined with the HWA method. The LDA technique was thus used for the zone ranging from 0 to 6D. Beyond this region, the levels of turbulence are weak enough to allow the use of a hot wire anemometer to determine the average velocities and characteristics of the turbulent flow. They also determined the scalar field, resulting from the injection of tracks of gas in the jet flow.

Andreopoulos [8] studied experimentally an incompressible jet issuing in a transverse duct flow. He analyzed the effect of the transverse upstream flow near the region from which the jet arises. He showed that the initial interaction between the jet and the transverse flow strongly depends on flow conditions inside the duct. This study was undertaken for values of R which vary from 0.25 to 3. These measurements show that for low values of R, the deformation of the jet by a transverse stream is important. The experimental results of Andreopoulos et al. [9] gave a quantitative image of the complex three-dimensional structure of a jet of air issuing in a transverse turbulent flow in a duct. They determined the wall static pressure, the average and fluctuating velocities by the HWA technique and they measured the concentration field. They showed that for high values of R, the velocity field close to the jet in a cross flow is controlled by the dynamic aspect, and the effect of turbulence on the development of the flow in this region is limited. While downstream, the flow is always influenced by turbulence. For low values of R, they showed that the flow field close to the jet is dominated by turbulence.

This configuration was also considered by Fric et al. [10] who studied the interaction of a round jet with a transverse flow. They defined the various swirling structures, which develop during this interaction. They described the origin and formation of whirlwinds in the trail zone of the jet and showed that this phenomenon is fundamentally different from that observed around a solid obstacle. Blanchard [11] performed measurements on the dynamic parameters of this flow and showed that the various structures described by Fric et al. also exist for a rectangular jet. In particular, the forming of a pair of vortices in the limits of the jet are observed.

Contributed by the Heat Transfer Division for publication in the JOURNAL OF HEAT TRANSFER. Manuscript received by the Heat Transfer Division April 24, 2002; revision received November 6, 2002. Associate Editor: A. F. Emery.

In the present study, we numerically analyze a jet subjected to a transverse turbulent flow. The first objective consists in examining the efficiency of the various usual turbulence closure models (the k-ε standard model, the k-ε R.N.G model, the realizable k-ε model and the second-order model) in describing the behavior of the flow in its various regions. This is done by comparing the obtained numerical results with those experimentally determined by Crabb et al. [7] and Andreopoulos et al. [9]. The second objective consists in studying the flow behavior and examining the influence of R on the dispersion of the jet.

2 Presentation of the Problem

When a jet is deviated under the action of a transverse flow, its section becomes deformed and the flow is dominated by a pair of very intense contrarotating vortices (see region II on Fig. 1). The early researches concentrated on mixing efficiency and the properties of dispersion of the jet, and so privileged the trajectory of the deviated jet (line where velocities are maximum) and the line of maximum vorticity (points where rotational velocity projected on *xy* plane is maximum). More detailed studies highlighted three secondary swirling systems:

- a ''horseshoe'' swirl similar to that which appears near the junction of a wing and a plane plate (I).
- a strongly three-dimensional wake resembling a Von Karman street downstream of a circular cylinder (III). The physical analogy between these two phenomena is only very partial because, in addition to the curvature of the jet, there is no production of vorticity on the boundary between the jet and the transverse flow, contrary to the wall of a cylinder (where the condition of no-slip implies a production of vorticity).
- swirls of the sheared layer all around the jet.

The swirls of the sheared layer and the swirls of the wake are unstable. Whereas the two other swirls (horseshoe swirls and the pair of contrarotating swirls) behave as an average flow although they can also have unstable components.

3 Mathematical Formulation

Consider a circular round jet of a pollutant containing air-heluim of diameter d emitted through a wall with an ejection velocity v_0, and a temperature T_0. This jet is subjected to a transverse flow with a uniform velocity u_∞ and a temperature T_∞. The ratio between the two velocities, $R=v_0/u_\infty$ is obtained by varying v_0 whereas u is maintained constant. Consideration is given to a steady, three-dimensional, compressible and turbulent flow. The equations describing this flow are obtained in a system of cartesian coordinates, the origin of which is situated in the center of the section of ejection of the jet (Fig. 1). We have:

$$\frac{\partial(\overline{\rho}\widetilde{u}_i)}{\partial x_i}=0 \tag{1}$$

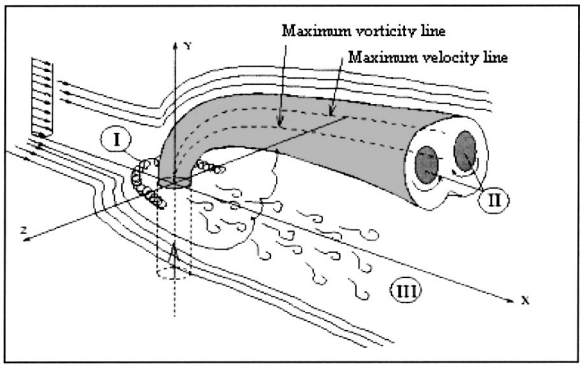

Fig. 1 Steady flow topology (according to Boris et al. [12])

$$\frac{\partial(\overline{\rho}\widetilde{u}_i\widetilde{u}_j)}{\partial x_j}=-\frac{\partial\overline{p}}{\partial x_i}+\frac{\partial}{\partial x_j}\left(\mu\frac{\partial\widetilde{u}_i}{\partial x_j}-\overline{\rho u_i'' u_j''}\right)+(\overline{\rho}_\infty-\overline{\rho})g\,\delta_{ij} \tag{2}$$

with

$$-\overline{\rho u_i'' u_j''}=\mu_t\left(\frac{\partial\widetilde{u}_i}{\partial x_j}+\frac{\partial\widetilde{u}_j}{\partial x_i}-\frac{2}{3}\delta_{ij}\frac{\partial\widetilde{u}_k}{\partial x_k}\right)-\frac{2}{3}\overline{\rho}k\,\delta_{ij}$$

$$\frac{\partial(\overline{\rho}\widetilde{u}_j\widetilde{T})}{\partial x_j}=\frac{\partial}{\partial x_j}\left[\left(\frac{\mu}{\mathrm{Pr}}+\frac{\mu_t}{\sigma_t}\right)\frac{\partial\widetilde{T}}{\partial x_j}\right] \tag{3}$$

$$\frac{\partial(\overline{\rho}\widetilde{u}_j\widetilde{f})}{\partial x_j}=\frac{\partial}{\partial x_j}\left[\left(\frac{\mu}{\mathrm{Sc}}+\frac{\mu_t}{\sigma_f}\right)\frac{\partial\widetilde{f}}{\partial x_j}\right] \tag{4}$$

The introduction of the fluctuating functions and variables requires the use of a turbulence closure model. In this study, we have compared two types of closure models: first-order models (k-ε standard model, k-ε R.N.G model, the realizable k-ε model) and a second-order model (RSM: Reynolds Stress Models).

3.1.1 First-Order Models. All the three first-order models use a linear correlation between the turbulent diffusion, the turbulent viscosity and the rate of average deformation and so yield an isotropic turbulent viscosity. These models are the standard K-ε model proposed by Launder and Spalding [13], the k-ε RNG model (Yakhot and Orszag [14]) and the realizable k-ε model (Chen & Kim [15]). Equations associated to each of them are:

For the Standard k-ε Model. The equation of conservation of the turbulent kinetic energy is

$$\frac{\partial(\overline{\rho}\widetilde{u}_j k)}{\partial x_j}=\frac{\partial}{\partial x_j}\left[\frac{(\mu+\mu_t)}{\sigma_k}\frac{\partial k}{\partial x_j}\right]+P_k+G_k-\overline{\rho}\varepsilon \tag{5}$$

and the equation of conservation of its dissipation rate is

$$\frac{\partial(\overline{\rho}\widetilde{u}_j\varepsilon)}{\partial x_j}=\frac{\partial}{\partial x_j}\left[\frac{(\mu+\mu_t)}{\sigma_\varepsilon}\frac{\partial\varepsilon}{\partial x_j}\right]+C_{\varepsilon 1}\frac{\varepsilon}{k}(P_k+G_k)-C_{\varepsilon 2}\frac{\overline{\rho}\varepsilon^2}{k} \tag{6}$$

with

$$P_k=\mu_t\left[\frac{\partial\widetilde{u}_i}{\partial x_j}\left(\frac{\partial\widetilde{u}_i}{\partial x_j}+\frac{\partial\widetilde{u}_j}{\partial x_i}\right)\right];\quad G_k=\beta g_j\frac{(\mu+\mu_t)}{\sigma_t}\frac{\partial\widetilde{T}}{\partial x_j};$$

$$\mu_t=C_\mu\overline{\rho}\frac{k^2}{\varepsilon} \tag{7}$$

The difference between the standard K-ε model and the two other first-order models is that an additional term is considered in Eq. (6). This term describes the production of dissipation rate and is written as follows:

for the k-ε RNG model

$$\frac{\eta(1-\eta/\eta_0)}{1+\beta\eta^3}\frac{\varepsilon P_k}{k} \quad \text{and} \quad \eta=\frac{Sk}{\varepsilon} \quad \text{with} \quad S=(2S_{ij}\times S_{ij})^{1/2} \tag{8}$$

and for the realizable k-ε model

$$C_{\varepsilon 3}\frac{P_k^2}{k} \tag{9}$$

The above-cited authors proposed the following values of constants, which are summarized in Table 1.

3.2 The Second-Order Model. In the second-order model, the following equation is solved:

$$\underbrace{\frac{\partial}{\partial x_k}(\bar{\rho}\tilde{u}_k\overline{u_i''u_j''})}_{C_{ij}}=\underbrace{\frac{\partial}{\partial x_k}\mu\frac{\partial}{\partial x_k}(\overline{u_i''u_j''})}_{D_{ij}^L}-\underbrace{\bar{\rho}\left[\overline{u_i''u_k''}\frac{\partial\tilde{u}_j}{\partial x_k}+\overline{u_j''u_k''}\frac{\partial\tilde{u}_i}{\partial x_k}\right]}_{P_{ij}}+D_{ij}^T+G_{ij}+\phi_{ij}+\varepsilon_{ij} \tag{10}$$

Table 1 Constants used in the first-order models

Model	c_μ	$C_{\varepsilon 1}$	$C_{\varepsilon 2}$	σ_k	σ_ε	η_0	β	$C_{\varepsilon 3}$
Standard k-ε	0.09	1.44	1.92	1.0	1.17	-	-	-
k-ε RNG	0.085	1.42	1.68	0.718	0.718	4.38	0.012	-
Realizable k-ε	0.09	1.15	1.9	0.75	1.15	-	-	0.25

Table 2 Constants of the first-order models

$C_{\varepsilon 1}$	$C_{\varepsilon 2}$	σ_k	σ_ε
1.44	1.92	0.82	1.0

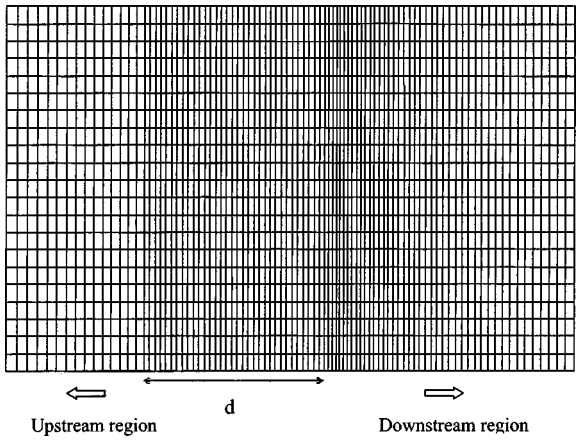

Fig. 2 Schematic presentation of the grid at the symmetry plane

C_{ij} being the convective term. D_{ij}^L, P_{ij}, D_{ij}^T, G_{ij}, ϕ_{ij}, ε_{ij} are, respectively, the molecular diffusion, the stress production, the turbulent diffusion, the buoyancy production, the pressure strain and the dissipation rate [16].

Equations of turbulent kinetic energy (k) and dissipation rate of kinetic energy (ε) associated with the second-order model are defined as

$$\frac{\partial(\bar{\rho}\tilde{u}_j k)}{\partial x_j}=\frac{\partial}{\partial x_j}\left[\frac{(\mu+\mu_t)}{\sigma_k}\frac{\partial k}{\partial x_j}\right]+\frac{1}{2}(P_{ii}+G_{ii})-\bar{\rho}\varepsilon \tag{11}$$

$$\frac{\partial(\bar{\rho}\tilde{u}_j\varepsilon)}{\partial x_j}=\frac{\partial}{\partial x_j}\left[\frac{(\mu+\mu_t)}{\partial_\varepsilon}\frac{\partial\varepsilon}{\partial x_j}\right]+C_{\varepsilon 1}\frac{1}{2}\frac{\varepsilon}{k}P_{ii}-C_{\varepsilon 2}\frac{\bar{\rho}\varepsilon^2}{k} \tag{12}$$

The used constants are defined in Table 2.

The boundary conditions associated with the above system of differential equations are summarized in Table 3.

4 Numerical Procedure

Several important problems arise from the numerical simulation of this last system of equations. The topology of the flow requires a very fine meshing in a great part of the domain. In order to describe exactly any temperature or mass fraction variations, particularly near the jet, we adopted a non-uniform meshing, strongly tightened near the jet.

The variation of the mesh size is described by the following relation: $x_{i+1}=x_i+\alpha_x\Delta$. Indeed, the step of calculation and the rate of extension of the grid in the longitudinal direction are taken equal to $\Delta=0.08$ and $\alpha_x=0.98$, upstream to the jet, respectively. Near the jet, these are reduced to $\Delta=0.03$ and $\alpha_x=1$ (Fig. 2). Downstream of the jet, values of $\Delta=0.13$ and $\alpha_x=0.98$ are adopted. This grid, which is refined around the jet, allows to cap-

Table 3 Boundary conditions

Boundaries	Velocity	Temperature	Mass fraction	Kinetic energy	Rate of dissipation
Nozzle section	$\tilde{u}=0$, $\tilde{v}=v_0$, $\tilde{w}=0$	$\tilde{T}=T_0$	$\tilde{f}=f_0$	$k=k_0=10^{-3}v_0^2$ [17]	$\varepsilon=k_0^{3/2}/0.5d$ [17]
Transverse flow	$\tilde{u}=u_\infty$, $\tilde{v}=0$, $\tilde{w}=0$	$\tilde{T}=T_\infty$	$\tilde{f}=0$	$k=0$	$\varepsilon=0$
wall	$\tilde{u}=0$, $\tilde{v}=0$, $\tilde{w}=0$	$\frac{\partial\tilde{T}}{\partial y}=0$	$\frac{\partial\tilde{f}}{\partial y}=0$	$\frac{\partial k}{\partial y}=0$	$\frac{\partial\varepsilon}{\partial y}=0$
Other boundaries of the domain	$\frac{\partial\tilde{u}}{\partial n}=0$, $\frac{\partial\tilde{v}}{\partial n}=0$, $\frac{\partial\tilde{w}}{\partial n}=0$	$\frac{\partial\tilde{T}}{\partial n}=0$	$\frac{\partial\tilde{f}}{\partial n}=0$	$\frac{\partial k}{\partial n}=0$	$\frac{\partial\varepsilon}{\partial n}=0$

ture vortices and recirculating zones induced by the interaction of the two flows. In the transverse and lateral directions, the mesh size is uniform with a constant step equal to 0.08. For all directions, the number of points is chosen so that the boundary conditions far from the interaction are satisfied.

The computation were carried out with a $83\times40\times40$ grid in the x, y, and z directions in all cases. This grid was chosen after calculations with a much coarser $63\times33\times33$ grid and grid dependency tests had been performed. The maximum concentration deviation of the $83\times40\times40$ fine grid and $63\times33\times33$ grid is less than 5 percent.

The discretized equations are solved by means of a finite volume method. The numerical resolution uses the Patankar and Spalding's algorithm ''SIMPLE'' for the correction of the pressure [18]. The convergence of the calculations is obtained when the sum of normalized residues is equal to 10^{-5}.

5 Results and Discussion

In this part, we first of all discuss the validity of the turbulence models generally used to modelize the interaction between a jet and a cross flow. Then, based on the experimental results of Crabb et al. [7] and Andreopoulos et al. [9], we determine the dynamic characteristics of an air jet containing traces of helium in a transverse flow of air. Lastly, the heat and mass transfer characteristics of a jet of hot fumes interacting with a transverse airflow are presented and discussed.

5.1 Choice of the Turbulence Closure Model. Among the physical characteristics of turbulent flows, one can note, for trailing bodies, the true representation of the regions of longitudinal vorticity and the effects of the surface curvature on the intensification or damping of turbulence. Several turbulence models were developed in the past. The simplest being the ⟪mixture length⟫ model, while the most complex is the Reynolds stress model (RSM). The main goal of all these models is the determination of the dynamic turbulent field.

In order to choose the suitable model of turbulence, we compared our numerical results with experimental ones. Figure 3, presents the variation of the normal velocity in the symmetry plane ($z=0$) for a velocity ratio of $R=2.3$, at $y/d=0.25$ and for the various models of turbulence (the standard k-ε model, the k-ε R.N.G. model, the realizable k-ε model, and, finally, the RMS second-order model). This figure shows a slight difference between the results given by the various closure models in the region $-0.23\leqslant x/d\leqslant0.45$. In this zone, the results obtained by the second-order model are closer to those found in experiments by Crabb et al. [7], while the first-order models seem to slightly underestimate the normal velocity in this zone.

We also analyzed the efficiency of the closure model in predicting the evolution of the flow in the area $-1\leqslant x/d\leqslant5$ by comparing the longitudinal velocity with that given in experiments of Crabb et al. [7] (Fig. 4). The difference between the results provided by the various models becomes significant in the exit section of the jet and in the wake close to the jet. That is seen especially for the k-ε R.N.G. model. The RMS second-order model seems to approach a little better the experimental results in the upstream region of the jet ($-1<x/d<-0.5$) and downstream of the jet ($x/d\geqslant2$).

Figure 5 shows how the longitudinal mean velocity $\tilde{u}/u_\infty$ varies with distance y at various downstream positions x. This figure gives the profiles for the velocity ratio $R=0.5$ at $z/d=0$. The first three profiles correspond to x-positions above the exit and indicate a deceleration of the streamwise velocity while the last three profiles correspond to stations downstream of the exit and indicate accelerating flow in the wake region. The numerical calculation is compared with those of Andreopoulos et al. [9]. For the position $x/d=2$, the data of Bergeles et al. [6] are included for comparison. The agreement with the present calculations and the experimental measurements can be seen to be quite good, even though Bergeles et al. used a single wire to measure $\tilde{u}$, a method that is not very accurate in general three-dimensional flows. That the single-wire measurements agree quite well with the Andreopoulos et al. [9] three-sensor measurements is due to the fact that at $x/d=2$ the $\tilde{v}$-component is small (the component $\tilde{w}$ is zero at the centerplane anyway) so that the flow is predominantly in the x-direction and the velocity $\tilde{u}$ could be obtained quite satisfactorily with a single sensor.

Therefore it is possible to say that the strong curvature effects during the deflection of the jet as well as the swirling movements in the wake region located very close to the exit section of the jet illustrate the limitations of the first-order turbulence models in this zone.

The center-plane helium trace profiles are presented in Fig. 6 for a velocity ratio of $R=2.3$, at locations $x/d=4$, 6, 8, 10 and for the various models of turbulence (the standard k-ε model, the k-ε

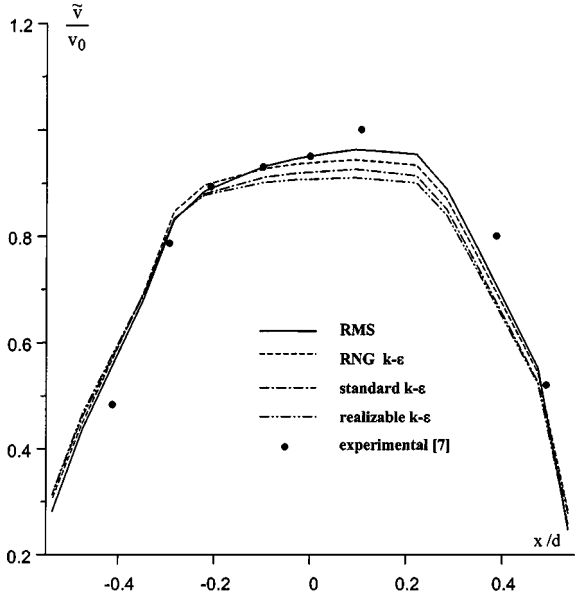

Fig. 3 Mean $\tilde{v}$-velocity profiles at the plane of symmetry $z/d=0$ and $R=2.3$ at $y/d=0.25$ with different turbulent models

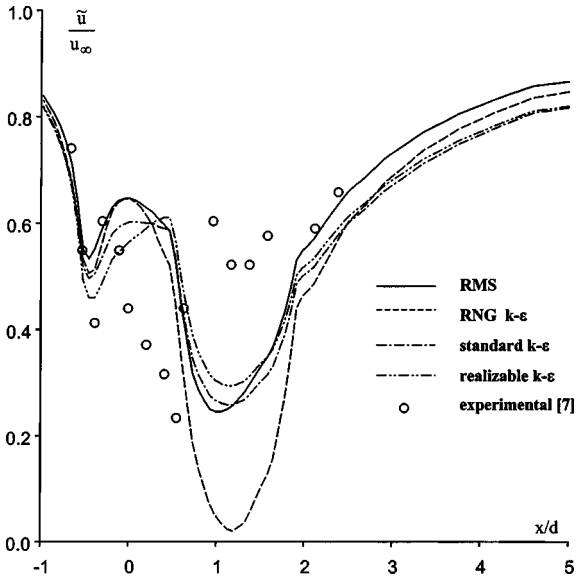

Fig. 4 Mean $\tilde{u}$-velocity profiles at the plane of symmetry $z/d=0$ and $R=2.3$ at $y/d=0.75$ with different turbulent models

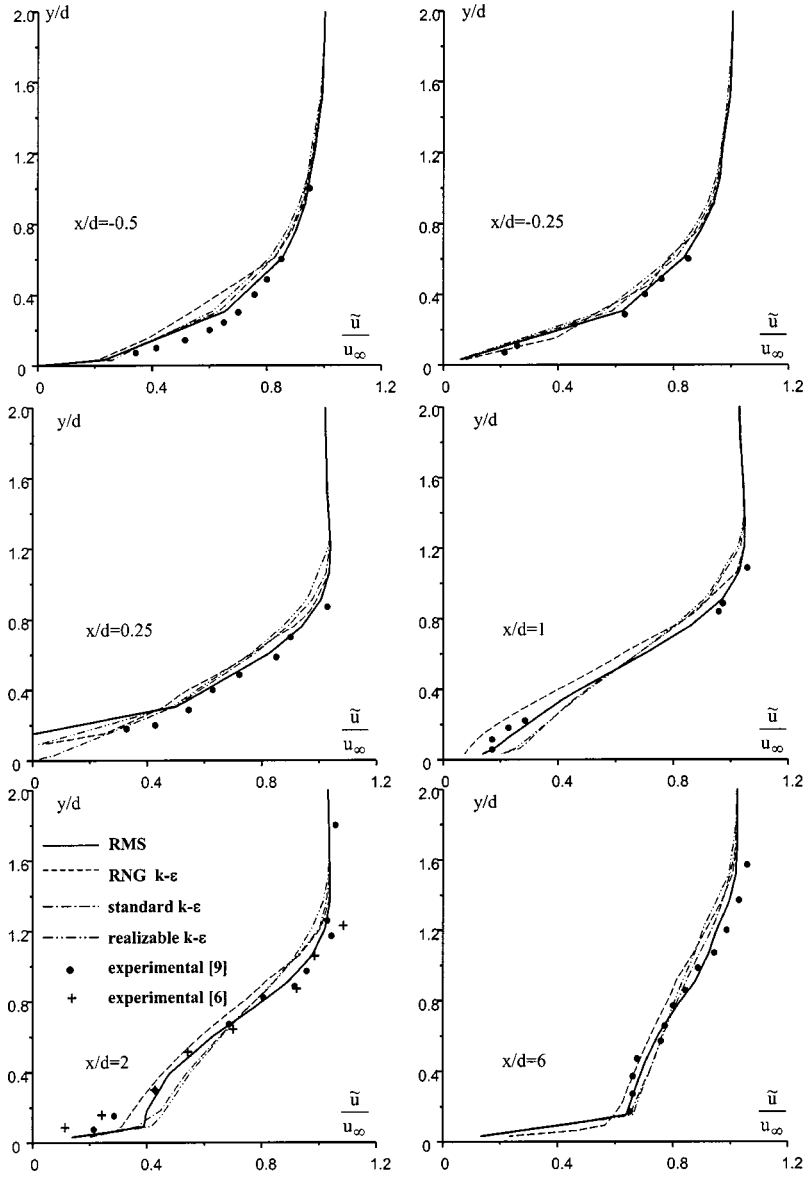

Fig. 5 Mean $\tilde{u}$-velocity profiles at the plane of symmetry $z/d=0$ for $R=0.5$

R.N.G. model, the realizable k-ε model, and, finally, the RMS second-order model). This figure shows that the results obtained by the second-order model are closer to those found in experiments by Crabb et al. [7]. In the wake region, the helium mass fraction is overestimated by the two models: standard k-ε model and realizable k-ε model whereas it is underestimated by the k-ε R.N.G. model. Beyond this region, the reverse is observed.

Thus, with respect to the previous results, the RMS second-order model is chosen for the remainder of this work.

5.2 Study of the Mean Velocity Profiles. Figure 7 presents the normal mean velocity $\tilde{v}/v_0$ for vertical planes corresponding to $y/d=0.25$ and 0.75. It shows the development of the jet near its exit section. When no transverse flow occurs ($u_\infty=0$), the velocity profile appears uniform and symmetrical with respect to the vertical axis. Once the jet is subjected to a transverse flow ($R=1.15$ and 2.3), the deformation of the potential core of the jet starts, even at $y=0.25d$. For $y=0.75d$, the deformation is quite obvious. For both values of R ($R=2.3$ and $R=1.15$), one observes that the profile is not symmetric with regards to the $x/d=0$ plane, which is due to the superposition of the jet flow with the transverse flow. The acceleration of the y-velocity component for $x>0$ is also more evident for low values of R., which shows the relative effect of inertia forces.

Figure 8 presents the variation of the normal velocity component $\tilde{v}/v_0$ compared with that experimentally obtained by Crabb et al. [7] for the height $y/d=0.75$. This figure shows the good agreement between our results and the experimental ones especially for the distance $z/d=1$. This figure also features two significant characteristics of the jet in its initial stages of development. The pair of vortices starts to develop as indicated by the negative values of $\tilde{v}$ for $z/d=1$ and $-0.5<x/d<0$. The vortex begins to develop for $x/d=-0.5$, its center being located between $z/d=0.5$ and $z/d=1$. The center of the vortex moves forward, outside, and beyond the distance $z/d=1$, then returns in the wake because of the low pressure zone occurring at $x/d=2$. The center remains at $z/d=1$ (as indicated by the zero average value of $\tilde{v}$) until $x/d=3.25$, from which the velocity starts to increase.

In the plane located at $y/d=1.35$, we traced the evolution of the average normal velocity component $\tilde{v}/v_0$ for $z/d=0.5$ and $z/d=1.5$ (Fig. 9). We notice that for $z/d=1.5$, there is an agreement

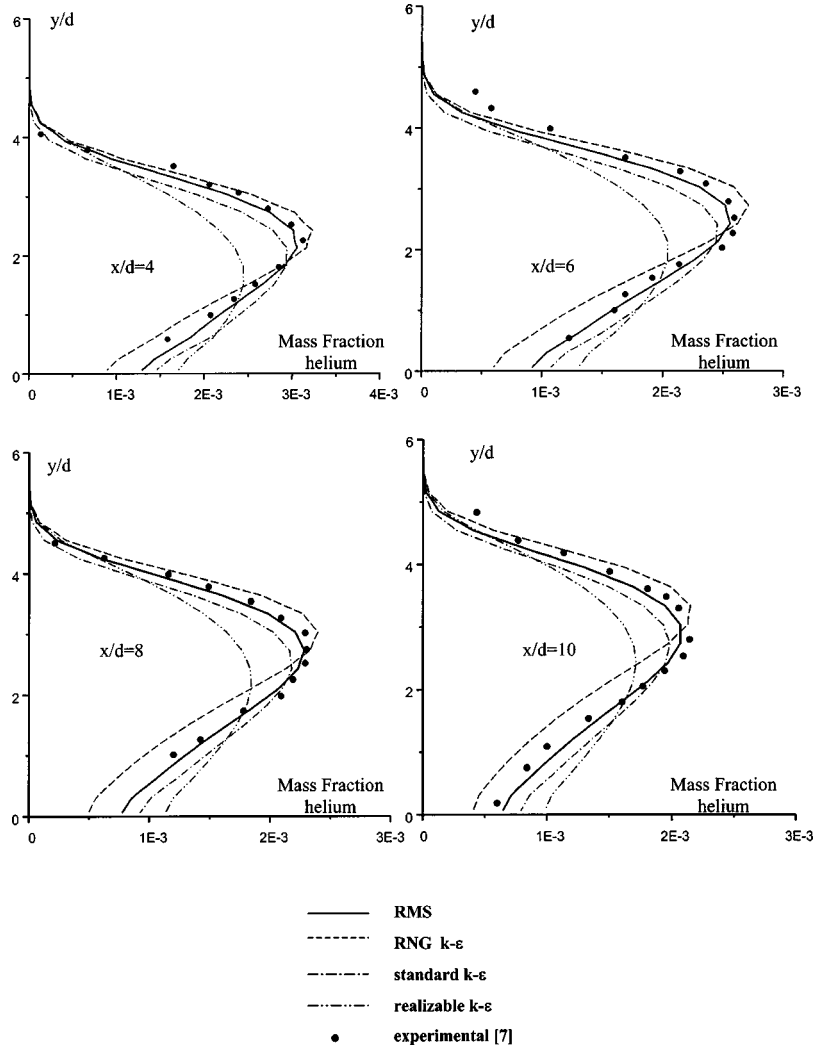

Fig. 6 Centerplane helium mass fraction for $R=2.3$

between our results and those found in experiments by crabb et al. [7]. The vortex structure is still clearly indicated by the negative normal component at the distance $z/d=1.5$.

Figure 10 proves that in the symmetry plane ($z/d=0$), for $y/d=2.5$, the jet lost the major part of its vertical momentum component and the maximum velocity is reduced only to 45% of its average normal velocity component at the exit section of the jet (40% in the experiments reported in reference [7]). For $y/d=3.5$, the vertical momentum vanishes and the profile shows only one low positive normal velocity component which is due to the main stream circulating around the obstruction caused by the jet. In the $z/d=1.5$ plane, and for $y/d=2.5$, the average normal velocity component is very low and approaches zero near $x/d=3$ ($x/d=3.5$ in reference [7]) where it is influenced by the vortex. This profile shows a good agreement with the experiment.

Figure 11 presents the evolution of the average longitudinal velocity component $\tilde{u}/u_\infty$ for $y/d=0.75$ and $y/d=3.5$ and for various planes along to z axis ($z/d=0$, $z/d=0.5$ and $z/d=1$). The main flow in the symmetry plane ($z=0$) and $y/d=0.75$ shows a minimum longitudinal velocity equal to $0.49\,u_\infty$ (in experiments this minimum is equal to $0.42\,u_\infty$), but the reduction of the normal velocity in the area $-0.5\leqslant x/d\leqslant 0$ is accompanied by an increase in the longitudinal component up to a value of $0.62\,u_\infty$ ($0.61\,u_\infty$ in experiments). Downstream, and near the jet, the minimum value of $\tilde{u}$ is equal to $0.13\,u_\infty$ (the experimental value being $0.14\,u_\infty$ [7]) and no recirculation occurs, indicating that the flow is very different from that associated with the wake of a solid body. The region immediately located behind the jet ($z/d=0.5$) is filled with the transverse flow which mixes with that of the fluid being in the recirculating region. This figure also shows a good agreement with the experimental data of Crabb et al. [7].

Figure 12 presents the evolution of $\tilde{u}/u_\infty$ in two planes ($z/d=0.5$ and $z/d=1.5$) for $y/d=1.5$. It is noticed that for $z/d=1.5$, there is an agreement between our results and the experiments whereas in the $z/d=0.5$ plane a great difference is observed. The maximum of the normal velocity component of the jet is considerably reduced (as depicted in Fig. 7) with an accompanying development of the longitudinal component. This phenomenon is obvious because of the strong aerodynamic curvature effects in this region.

Figure 13 shows the profiles of $\tilde{w}/u_\infty$ for different planes x/d ($x/d=1,2,4,6,10$), $y/d=2$ and for $R=2$. This velocity component decreases with x/d, which reveals that the further one moves away from the jet, the less the transverse stream influences the flow. The average transverse velocity is equal to zero in the symmetry plane. The curve shows a symmetry point at $z/d=0$.

Figures 14 and 15 compare the calculated Reynolds stress $\overline{v''v''}/v_0$ with the experimental data. The profiles at $y/d=0.25$ and $y/d=0.75$ planes are dominated by two maximum values, the peak upstream being higher than the downstream one. The Reynolds stresses at the exit section of the jet ($-0.5\leqslant x/d\leqslant 0.5$) in-

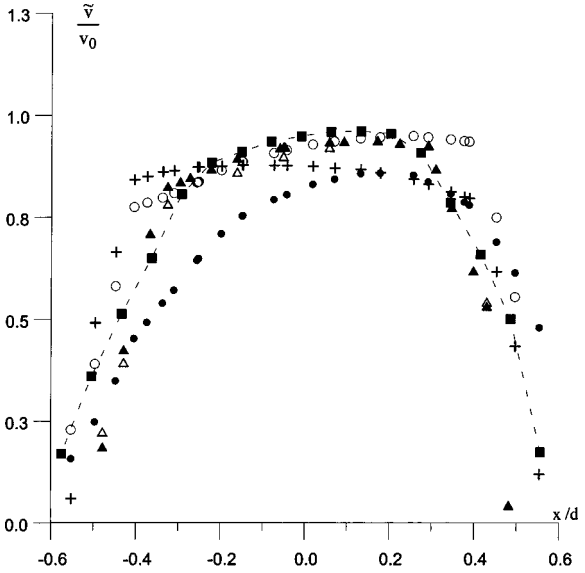

Fig. 7 Mean $\tilde{v}$-velocity profiles

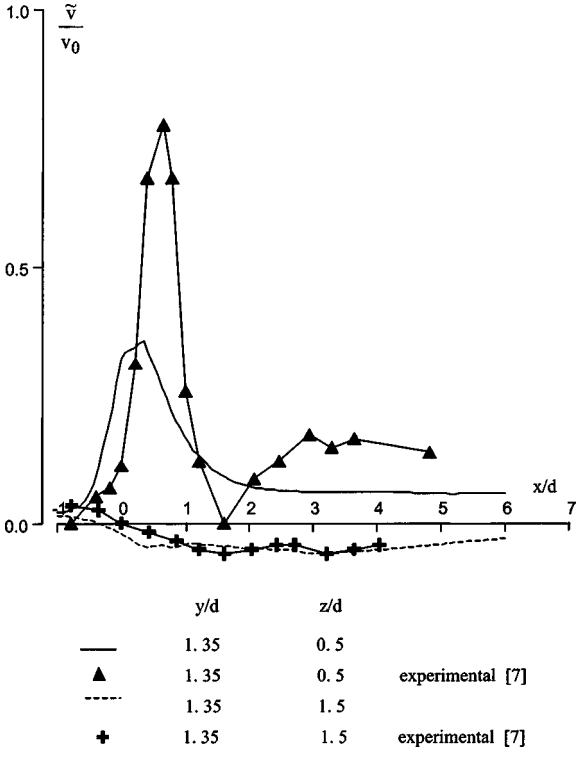

Fig. 9 Mean $\tilde{v}$-velocity profiles for $R=2.3$

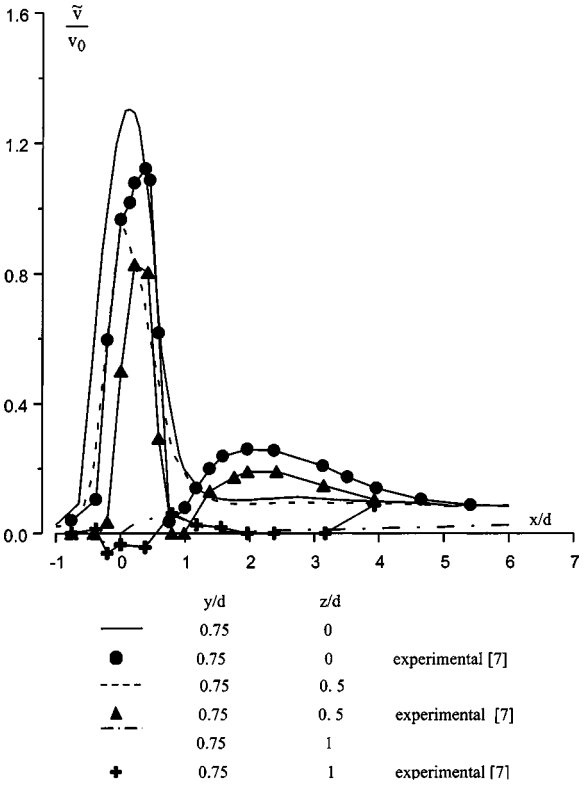

Fig. 8 Mean $\tilde{v}$-velocity profiles for $R=2.3$

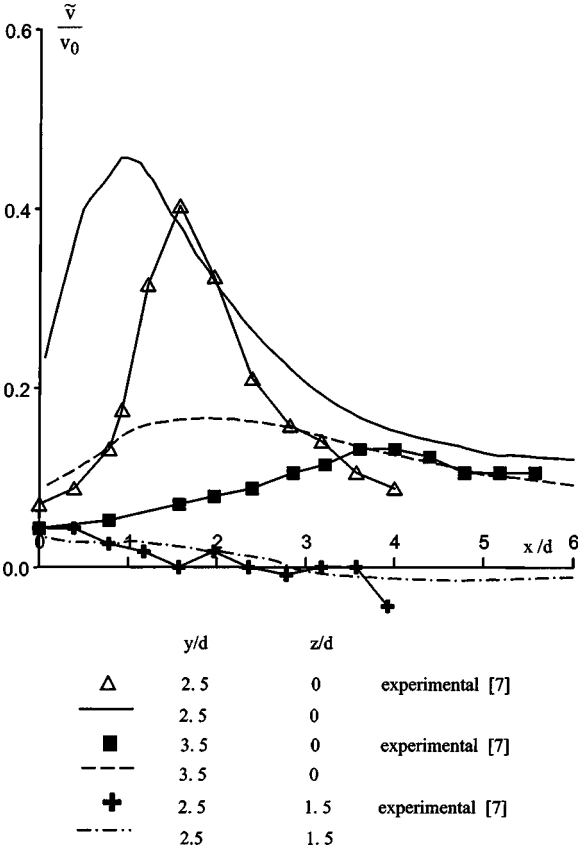

Fig. 10 Mean $\tilde{v}$-velocity profiles for $R=2.3$

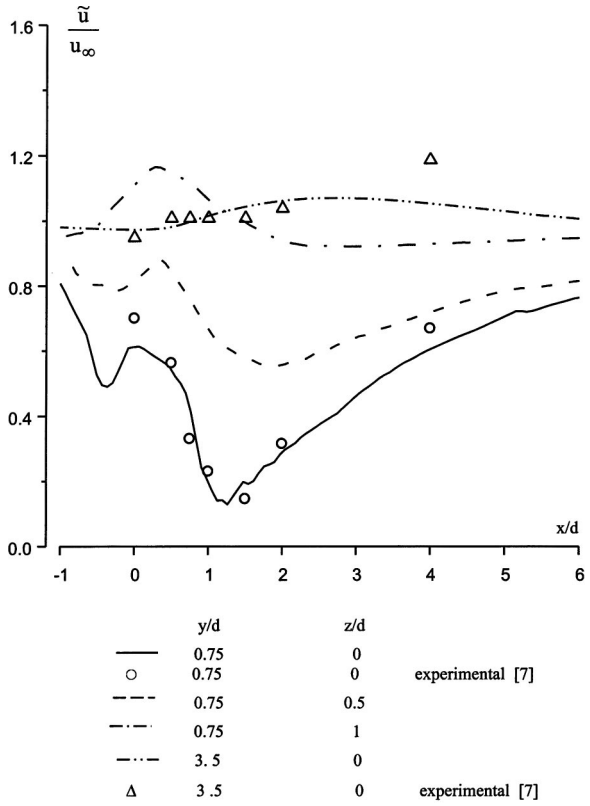

Fig. 11 Mean $\tilde{u}$-velocity profiles for $R=2.3$

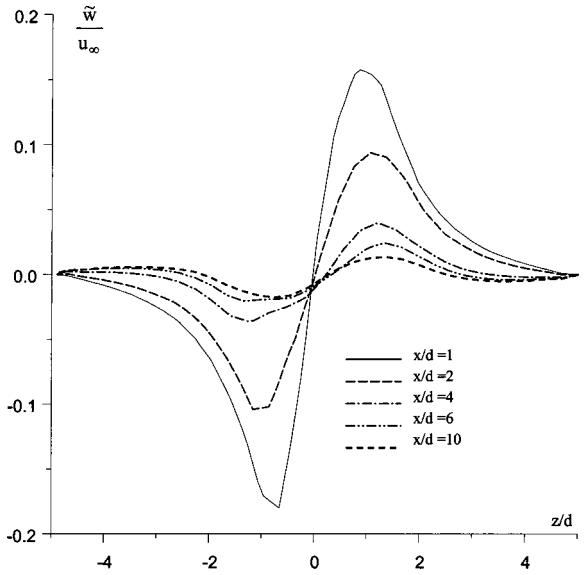

Fig. 13 Mean $\tilde{w}$-velocity profiles for $R=2$ at $y/d=2$

crease in amplitude with y/d up to the value $y/d=2.5$. Downstream of the jet, the Reynolds stresses are high for all values of y/d, and decrease slowly as one moves away from the jet. The larger is the height y/d, the further the position of the maximum Reynolds stress moves far downstream from the jet.

Figure 16 features the evolution of the Reynolds stress in the

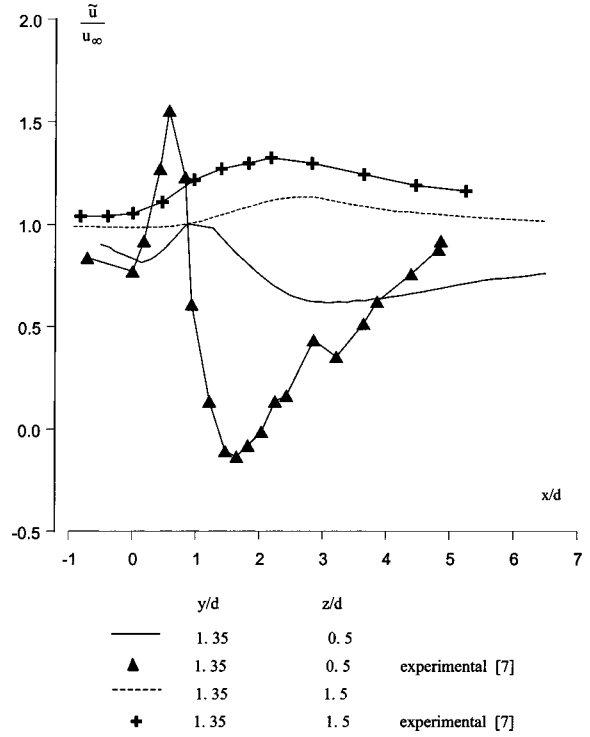

Fig. 12 Mean $\tilde{u}$-velocity profiles for $R=2.3$

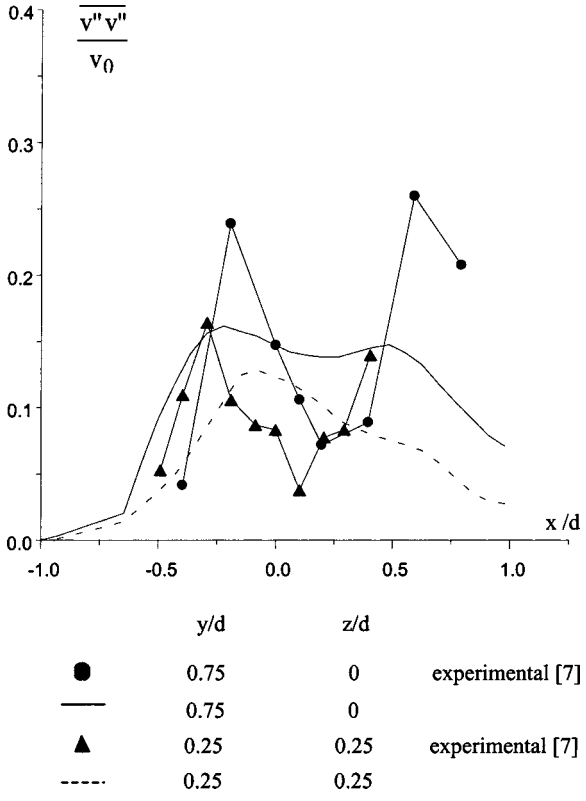

Fig. 14 Normal stress profiles $\overline{v''v''}$ for $R=2.3$

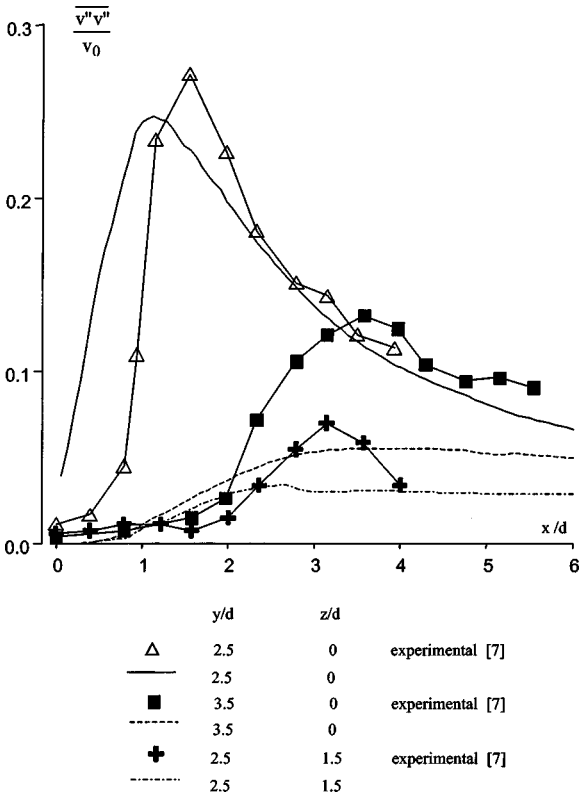

Fig. 15 $\overline{v''v''}$**-normal-stress profiles for** $R=2.3$

symmetry plane for several values of x/d and for $R=2$. It is noticed that the profile of the Reynolds stress presents a maximum and a minimum values. The values of $\overline{u''v''}$ are larger in the external area of the sheared layer, but they are also rather strong in the area located close to the wall. When the area of the wake starts to disappear downstream, and far enough far from the jet, the profile of the Reynolds stress ceases a changing sign and evolves to a typical profile of a boundary layer type of flow. On this figure we also compared our results with those obtained in experiments of Andreopoulos et al. [9] and a good enough agreement is noticed for $z/d=1.5$.

5.3 Thermal Characteristics of the Flow. In this part, consideration is given to the study of a smoke jet ejected at a temperature of 130°C in an air cross flow with a temperature of 30°C. The composition of the smoke is as follows: 20.9 percent carbon dioxide (CO_2), 76.9 percent nitrogen (N_2), 1.8 percent oxygen (O_2) and 0.4 percent sulfur dioxide (SO_2). Then, note that a species conservation equation, as Eq. (5), should be written for each constituant of the fume.

Figure 17 presents the temperature profiles in the symmetry plane as functions of the distance z/d for various sites y/d, at $x/d=8$ and for $R=5$. The distortion of the temperature profile has the shape of a kidney, which is caused, by the longitudinal vortices. The presence of a pair of swirls is remarkable for $y/d=5$. The two peaks attenuate and disappear at the distance $y/d=7$. Beyond this location, the temperature decreases.

On Fig. 18, the temperature iso-valeurs are presented, for three heights ($y/d=0.5$, 1, 2), in the xz plane and for $R=2$. This figure shows that when the height y/d increases, the maximum of temperature moves far downstream from the jet. Indeed, one notices on the curvature induced by the transverse flow a bending of the jet on its two sides, which is caused by the three-dimensional nature of the flow. Furthermore, the dispersion of the temperature is faster for the three-dimensional case than it would be for a two-dimensional model because of the additional mixture induced by the transverse vortices.

Figure 19 presents the isotherms in the central plane ($z=0$), for $R=2$. This figure shows the well-known Gaussian distribution and the effect of transport of the jet by the external transverse flow. Although the velocity of the jet is twice that of the external flow, it is noted that the thermal plume extends rather far downstream from the ejection section (see, for example, the shape of the isotherm 323 deg). However, the thermal diffusion process remains very significant since one can note a fall of 30 deg on a distance of about the diameter of the section of ejection. This behavior is characteristic of the turbulent mixing of the flow.

Figure 20, shows the influence of R ($R=0.5$, 2, 1) on the temperature distribution in the $z/d=0$ plane for a height $y/d=0.25$. It is noticed that the temperature of the air resulting from the mixture of the two flows is lower as the rate of the transverse flow is higher ($R=0.5$.). Indeed, in this case, the external flow becomes prevalent in front of the jet and this last is strongly deviated as it exits from the chimney.

5.4 Mass Transfer Characteristics of the Flow. The most obvious characteristic of interaction between the jet and a transverse flow is the mutual deviation of the jet and the cross flow. The jet is deformed by the impact of the transverse flow, then pulled by this last, and this is clearer as R is higher. Figure 21 shows the contours of the mass fraction of air in the median plane for $R=2$. The jet is slightly affected close to the exit section, because the inertia force induced by the jet prevails in front of that of the cross flow. This force becomes weaker as y increases and the jet is curved by the transverse flow when the two inertia forces have the same magnitude. Because of the turbulent structure of the flow mixture, a velocity of wind twice that of the ejection velocity of the pollutants allows a great dilution, i.e., a high mass fraction of air close the injection section. This phenomenon is also seen on Fig. 22, where contours of the mass fraction of the carbon dioxide in the central plane are plotted for $R=2$. The maximum concentration is observed in the vicinity of the jet, while very far downstream from the jet the mass fraction of CO_2 is weak. This figure shows a Gaussian distribution near the exit section of the jet.

In the absence of chemical reaction, no new information is added by showing results for multiple species, in fact all species should diffuse together. So we present on Fig. 23 only the distribution of the mass fractions of CO_2 as well as the mass fraction of air according to the longitudinal position x/d. These distributions are drawn in the symmetry plane ($z=0$) for $y/d=0.25$ and $R=0.5$ as functions of the longitudinal position x/d. The maximum concentration of the pollutant is observed at the exit section of the jet. In the vicinity of the jet, the mass fraction of the air is more significant than that of the pollutant which decreases quickly downstream from the jet. For $R=0.5$, the flow is very attached to the wall and therefore the maximum concentration is observed near the wall.

Figure 24 examines the influence of R ($R=0.5$, 2, 1) on the mass fraction of CO_2 in the central plane ($z=0$) and $y/d=0.25$. It is shown that the dispersion of the pollutants is stronger as the rate of the transverse flow is higher ($R=0.5$). Indeed, for this last case, the air flow is sufficiently significant to allow a better dilution of the pollutant. On the other hand, Fig. 25 presents the profiles of the air mass fraction for various values of R. The lower R is, the more the mass fraction of air on the jet section is significant. The mass fraction of air at the distance $x/d=-0.5$ is more significant than that located at the distance $x/d=0.5$, this is due to the deflection of the jet under the transverse flow.

Figure 26 represents the distribution of the mass fraction of carbon dioxide for $R=2$, at $y/d=1.35$ and for various values of z/d. One notices that this parameter decreases as one moves away from the exit section of the jet along the z direction. In the x direction, one also notes that the distance from the chimney, for

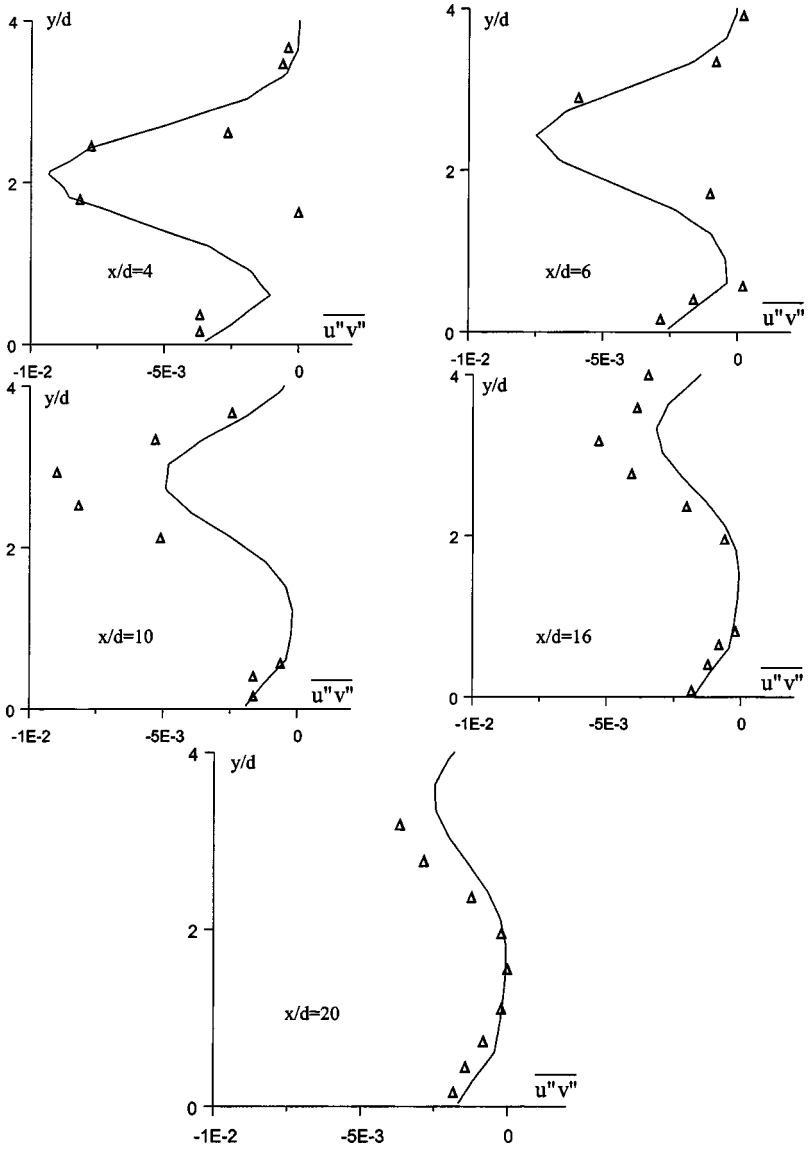

Fig. 16 $\overline{u''v''}$**-shear stress profiles for** $R=2$ **at** $z/d=0$ **Δ experimental [9]**

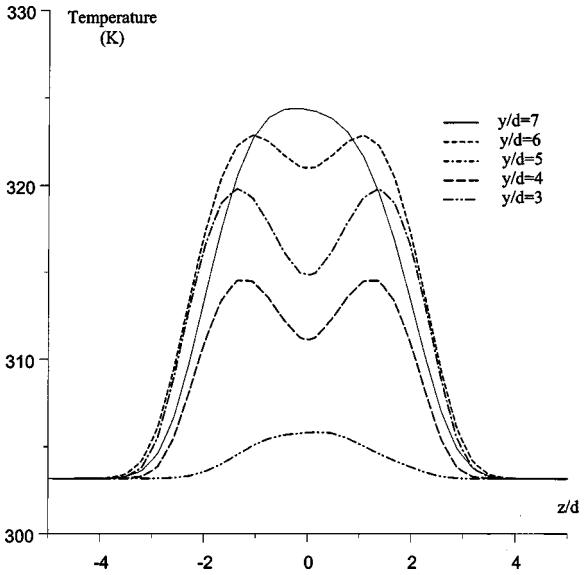

Fig. 17 Profiles of the temperature at $x/d=8$**, for** $R=5$

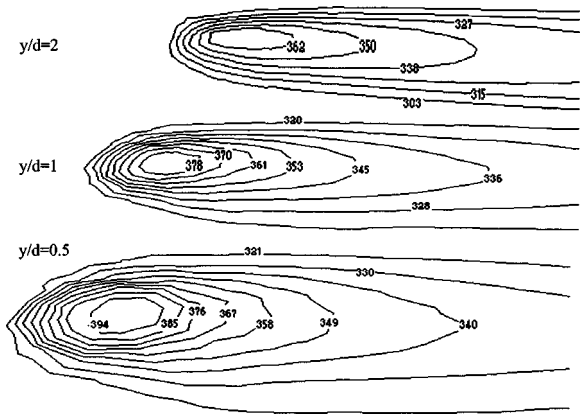

Fig. 18 Cross-sectional contours of the temperature at three planes and $R=2$

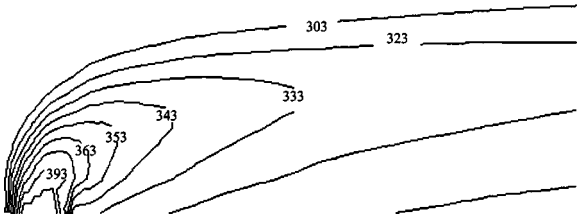

Fig. 19 Temperature contours at the plane of symmetry $z/d=0$ and $R=2$

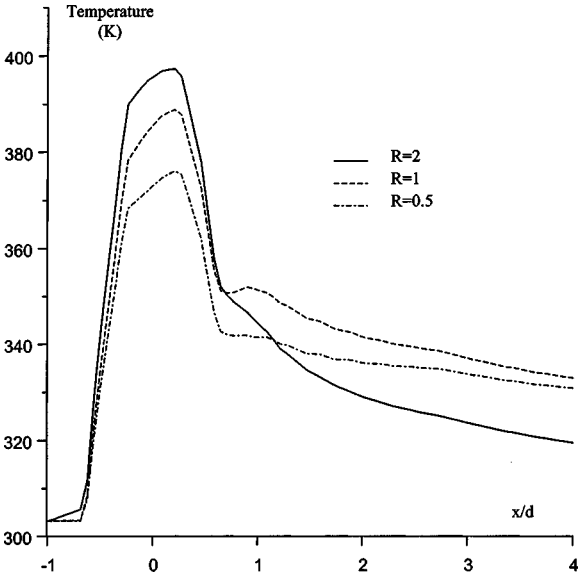

Fig. 20 Profiles of the temperature at $y/d=0.25$ and $z/d=0$ for various velocity ratios

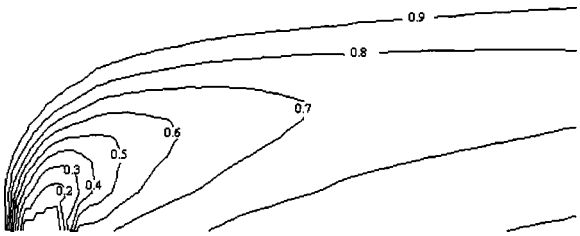

Fig. 21 Air mass fraction contours at the plane of symmetry $z/d=0$ and $R=2$

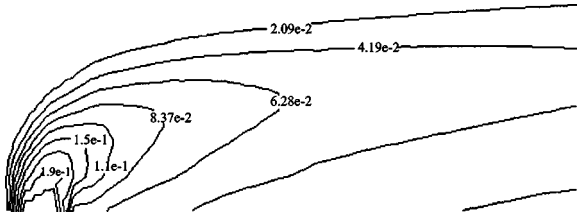

Fig. 22 CO_2 mass fraction contours at the plane of symmetry $z/d=0$ and $R=2$

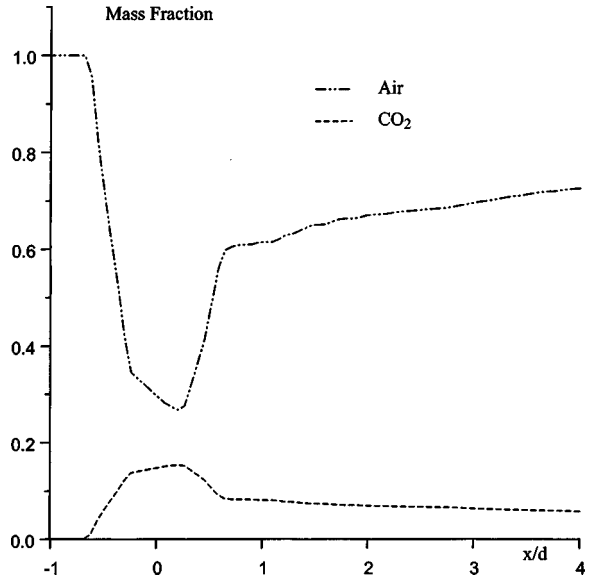

Fig. 23 Various species mass fraction profiles at $y/d=0.25$ for $R=0.5$, in the symmetry plane ($z/d=0$)

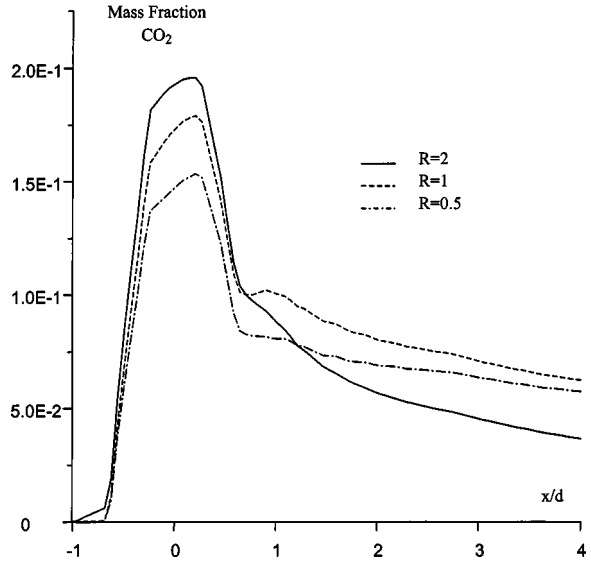

Fig. 24 CO_2 mass fraction profiles at $y/d=0.25$ and $z/d=0$ for various velocity ratios

Table 4 Position of maximal values of the mass fraction according to x and z directions

z/d	x/d	Maximal mass fraction
0	0.484848	0.122
0.5	0.767677	0.089
1	1.9697	0.048
1.5	2.60606	0.021

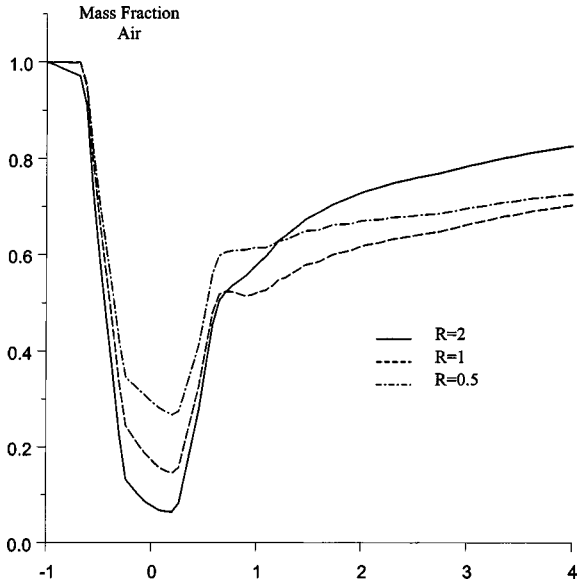

Fig. 25 Air mass fraction profiles at $y/d=0.25$ and $z/d=0$ for various velocity ratios

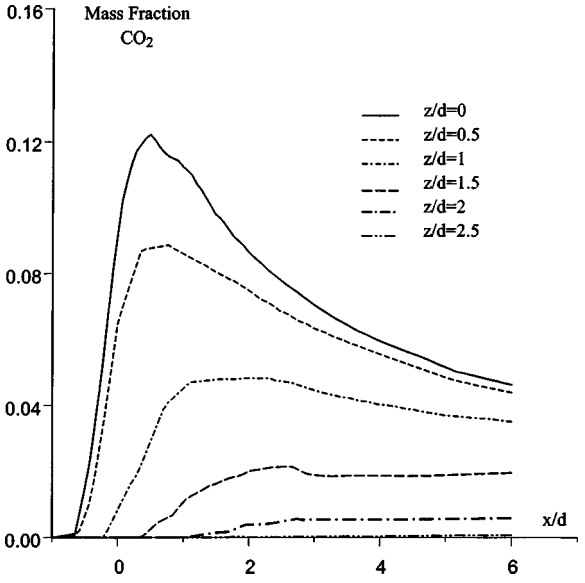

Fig. 26 CO_2 mass fraction profiles at $y/d=1.35$ for $R=2$

which the mass fraction is maximum increases for increasing z/d (see Table 4). For $z/d=2$ and $z/d=2.5$, the mass fraction of carbon dioxide is weak.

Finally, Fig. 27 presents the distribution of the mass fraction of carbon dioxide (CO_2) in the symmetry plane according to the distance z/d for various sites y/d. The values of x/d and R are respectively 8 and 5. This figure shows that the pair of vortices starts to appear at $y/d=4$, just where the formation of the second peak is noticed. Indeed, this later is also pronounced for the heights $y/d=5$ and $y/d=6$. The CO_2 mass fraction maximum is located at the center of each vortex. From the height $y/d=6$ (that is for $y/d=7$ and higher values), the contrarotating pair of vortices starts to disappear and consequently the mass fraction decreases.

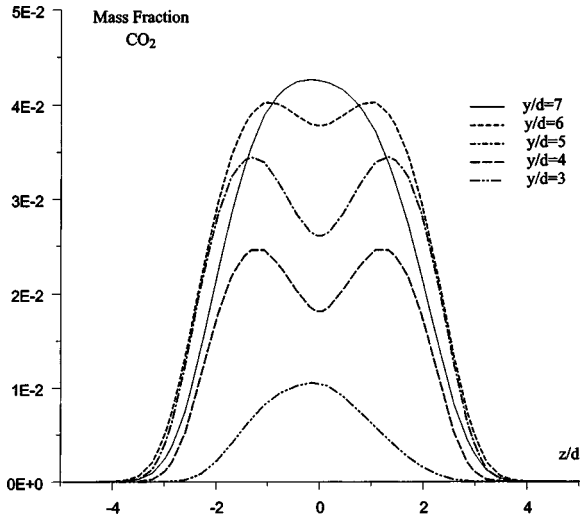

Fig. 27 CO_2 mass fraction profiles at $x/d=8$, for $R=5$

Conclusion

In this work, we have studied the momentum, heat and mass transfer exchanges related to the interaction between a circular jet and a transverse flow. The variable curvature of jets emerging transversely in a cross flow renders their determination particularly delicate. The different results confirm the formation of a pair of contrarotating vortices downstream of the exit section of the jet. The profiles of mean velocity in the median plane of the jet are not uniform and the development of the jet is characterized by a strong anisotropy and an acceleration of the free flow around the jet and in its wake. By comparing numerical results with experimental data of Bergeles et al. [6], Crabb et al. [7] and Andreopoulos et al. [9] we could first justify the choice of the RMS second-order turbulence closure model. We could also determine the distribution of temperature and mass fraction near the jet and downstream from it and examine the dispersion of a hot pollutant under the influence of the velocity ratio $R=v_0/u_\infty$. The obtained results show mainly that the temperature of the pollutants is low when the velocity of the transverse flow is high because, in this case, the cross flow prevails in front of the jet flow and high temperature gradients are observed near the exit section of the jet. Moreover, turbulence is sufficiently significant to allow a better dilution of pollutants.

Nomenclature:

d = diameter of the jet (nozzle diameter)
g = gravitational acceleration
k = kinetic energy of turbulence
T = temperature
f = mass fraction
R = velocity ratio v_0/u_∞
$\tilde{u}$, $\tilde{v}$, $\tilde{w}$ = velocity components along x, y, and z directions
x, y, z = coordinates
S_{ij} = mean strain rate
P_k = term of production due to the mean gradients
G_k = term of production due to buoyancy forces
$\overline{u_i'' u_j''}$ = Reynolds stress

Greek Symbols

Δ = step size
α_x = the rate of grid streching in direction x
β = thermal expansion coefficient
ε = rate of dissipation of turbulence kinetic energy
μ_t = turbulent (or eddy) viscosity

σ_t = turbulent Prandtl number
σ_f = turbulent schmidt number

Subscripts

∞ = condition in crossflow
$\circ$ = exit section of the jet

Superscripts

$-$ = Reynolds average
$\sim$ = Favre average

References

[1] Kamotani, Y., and Greber, I., 1972, ''Experiments on a Turbulent Jet in a Cross Flow,'' AIAA J., **10**, pp 1425–1429.
[2] Fearn, R., and Weston, R. P., 1974, ''Vorticity Associated With a Jet in a Crossflow,'' AIAA J., **12**, pp. 1666–1671.
[3] Keffer, J. F., and Baines, W. D., 1963, ''The Round Turbulent Jet in a Cross-wind,'' J. Fluid Mech., **15**, pp. 481–496.
[4] Moussa, Z. M., Trischka, J. W., and Eskinazi, S., 1977, ''The Near Field in the Mixing of a Round Jet With a Cross Stream,'' J. Fluid Mech., **15**, pp. 481–496.15, 481–496.
[5] Ramsey, J. W., and Goldstein, R. J., 1971, ''Interaction of a Heated Jet With a Deflecting Stream,'' ASME C, J. Heat Transfer , **94**, pp. 365–372.
[6] Bergeles, G., Gosman, A. D., and Launder, B. E., 1976, ''The Near Field Character of a Jet Discharged Normal to a Main Stream,'' ASME C, J. Heat Transfer , **98**, p. 373.
[7] Crabb, D., Durao, D. F. G., and Whitelaw, J. H., 1981, ''A Round Jet Normal to a Cross Flow,'' ASME J. Fluids Eng., **103**, pp. 142–152.
[8] Andreopoulos, J., 1982, ''Measurements in a Jet-Pipe Flow Issuing Perpendicularly Into a Cross Stream,'' ASME J. Fluids Eng., **104**, pp. 493–499.
[9] Andreopoulos, J., and Rodi, W., 1984, ''Experimental Investigation of Jets in a Crossflow,'' J. Fluid Mech., **138**, pp. 93–127.
[10] Fric, T. F., and Roshko, A., 1994, ''Vortical Structure in the Wake of a Transverse Jet,'' J. Fluid Mech., **279**, pp. 1–47.
[11] Blanchard, J. N., 1996, ''Etude d'une interaction d'un jet 2 D avec un écoulement transversal perpendiculaire et confine,'' thèse de l'université de Lille.
[12] Boris Papin, Calcul numérique de l'interaction d'un jet et d'un écoulement transversal sur plaque plane, Division Modélisation numérique pour la mécanique des fluides.
[13] Launder, B. E., and Spalding, D. B., 1975, ''The Numerical Computation of Turbulent Flows,'' Comput. Methods Appl. Mech. Eng., **3**, pp. 269–282.
[14] Yakhot, V., Orszag, S. A., Thengam, S., Gatki, T. B., and Speciale, G., 1992, ''Development of Turbulent Models for Shear Flows by a Double Expansion Technique,'' Phys. Fluids A, **4**(7), pp. 1510–1520.
[15] Chen, Y. S., and Kim, S. W., 1987, ''Computation of Turbulent Flows Using an Extended k-ε Turbulence Closure Model,'' NASA Contractor Report n° CR-179204.
[16] Roland Schieste, 1993, Modélisation et simulation des écoulements turbulents, Hermès, Paris.
[17] Demuren, A. O., and Rodi, W., 1987, ''Three Dimensional Numerical Calculations of Flow and Plume Spreading Past Cooling Towers,'' J. Heat Transfer , **109**, pp. 113–119.
[18] Patankar, S. V., and Spalding, D. B., 1972, ''A Calculation Procedure for Heat, Mass and Momentum Transfer in Three Dimensional Parabolic Flows,'' Int. J. Heat Mass Transf., **15**, pp. 1787–1806.

Journal of Heat Transfer

Technical Notes

This section contains shorter technical papers. These shorter papers will be subjected to the same review process as that for full papers.

Nodal Integral and Finite Difference Solution of One-Dimensional Stefan Problem

James Caldwell
e-mail: majimca@cityu.edu.hk

Svetislav Savović

Yuen-Yick Kwan

Department of Mathematics,
City University of Hong Kong,
Kowloon, Hong Kong, People's Republic of China

The nodal integral and finite difference methods are useful in the solution of one-dimensional Stefan problems describing the melting process. However, very few explicit analytical solutions are available in the literature for such problems, particularly with time-dependent boundary conditions. Benchmark cases are presented involving two test examples with the aim of producing very high accuracy when validated against the exact solutions. Test example 1 (time-independent boundary conditions) is followed by the more difficult test example 2 (time-dependent boundary conditions). As a result, the temperature distribution, position of the moving boundary and the velocity are evaluated and the results are validated. [DOI: 10.1115/1.1565091]

Keywords: Finite Difference, Heat Transfer, Melting, Moving Boundaries, Numerical Methods, Phase Change

1 Introduction

Moving boundary Stefan problems involving heat conduction in conjunction with change of phase arise in many physical processes, such as melting of ice, recrystallization of metals, evaporation of droplets, oxygen diffusion problem, particle dissolution in solid media, binary alloy melting and solidification induced by pulsed-laser irradiation, etc. Such a process covers a wide range of applications in which phase changes from solid, liquid or vapor states. The material is assumed to undergo a phase change, where the position of the boundary is always moving. So, the boundary is not known in advance and must be determined as part of the solution. Owing to the unknown location of the phase change interface and the nonlinear form of the thermal energy balance equation at the interface, analytical solutions are difficult to obtain except for a limited number of special cases.

Due to difficulties in obtaining analytical solution, various numerical techniques are often employed [1]. Numerical techniques are specially known to have difficulties with time-dependent boundary conditions and very fine mesh size and small time steps are often needed for accurate solutions. Because these are often computer intensive—only a few results for the Stefan problem with time-dependent boundary conditions are available in the literature. Solutions of such Stefan problems include linear, exponential and periodical variation of the surface temperature or the flux with time [2–4]. A comparative study of various numerical methods for moving boundary problems has been made by Furzeland [3].

Various numerical methods have been applied to the Stefan problem including finite element, finite difference and integral methods. Several finite element methods have been developed and successfully applied to the Stefan problem with various boundary and initial conditions (see e.g., [5–8]). Solutions reported in the literature using the finite difference (FD) methods for solving the moving boundary problem include the one-dimensional Stefan problem describing the evaporation processes [9,10], the process of melting of solid [11], oxygen diffusion problem [12] and the dissolution of stoichiometric multi-component particles in ternary alloys [13]. On the other hand, a coupling integral equation approach has been used by Mennig and Özişik [2] for solving the Stefan problem describing the melting/solidification process as well as the nodal integral (NI) approach applied by Rizwan-uddin [14] to the Stefan problem describing the melting of solids, where both phase-change problems involve time-dependent boundary conditions. Generally, in terms of accuracy and efficiency, the choice between various finite element, finite difference and integral methods for the solution of a particular Stefan problem is not always clear, due to their specific advantages and limitations. Clearly there is a need for benchmarking in the area.

In this paper we consider the one-dimensional Stefan problem describing the melting process. We use two independent methods, namely, the nodal integral and finite difference approaches in order to determine the evolution of the temperature distribution and phase boundary during the process. Our aim is to produce highly accurate results which can be validated against the exact solution. This will result in benchmark cases involving two test examples.

2 Formulation of the Problem

The dimensionless formulation of the Stefan problem for the liquid region of a melting solid at the phase change temperature in an invariant domain $(0 \leqslant x \leqslant 1)$ is [14]

$$\frac{\partial^2 T(x,t)}{\partial x^2} + xR(t)\frac{dR(t)}{dt}\frac{\partial T(x,t)}{\partial x} = R^2(t)\frac{\partial T(x,t)}{\partial t}, \quad 0 \leqslant x \leqslant 1, \tag{1}$$

$$R(t)\frac{dR(t)}{dt} = -\,\mathrm{Ste}\frac{\partial T(x,t)}{\partial x}, \quad x = 1, \tag{2}$$

Contributed by the Heat Transfer Division for publication in the JOURNAL OF HEAT TRANSFER. Manuscript received by the Heat Transfer Division July 3, 2002; revision received November 27, 2002. Associate Editor: C. Amon.

subject to the initial and boundary conditions

$$R=0, \quad t\leqslant 0,$$
$$T=f(t), \quad x=0, \quad t>0,$$
$$T=0, \quad x=1, \quad t>0, \tag{3}$$

where $T(x,t)$ is the temperature distribution, R is the position of the moving boundary, Ste is the Stefan number given by $(C_l\Delta T_{\text{ref}})/h_{sl}$, where C_l is the liquid specific heat, h_{sl} is the latent heat and ΔT_{ref} is a reference temperature [15].

As the solid melts with time, the moving boundary $R(t)$ moves to the right. If the temperature in the solid region $(x>1)$ is assumed to be spatially uniform and constant in time, equal to the phase change temperature, as here, then the problem is usually referred to as the single-phase Stefan problem. In order to solve the Stefan problem defined by Eqs. (1–3) we employ the nodal integral and finite difference methods.

3 Nodal Integral Method

A semianalytical nodal method to solve the one-dimensional Stefan problem was recently developed [14]. We give a brief description of the method here. The space-time domain $(0\leqslant x \leqslant 1;\ 0\leqslant t\leqslant t_{\text{final}})$ is first discretized into space-time nodes. Each node is identified by the subscript (i,j), where $1\leqslant i\leqslant N_x$, $0\leqslant j \leqslant N_j$, and N_x and N_j are the number of nodes in the spatial direction and the total number of time steps, respectively. The space-averaged, time-dependent temperature and time-averaged, space-dependent temperature for each node are respectively defined as

$$\overline{T}_i^x(t)\equiv \frac{1}{\Delta x}\int_{x_i}^{x_i+\Delta x} T(x,t)\,dx, \quad \overline{T}_j^t(x)\equiv \frac{1}{\Delta t}\int_{t_{j-1}}^{t_i} T(x,t)\,dt. \tag{4}$$

First, Eq. (2) is integrated over the time step $t_{j-1}\leqslant t\leqslant t_j$ to yield

$$R^2(t)=R^2(t_{j-1})-2\,\text{Ste}\,\frac{d\overline{T}_j^t(x=1)}{dx}(t-t_{j-1}), \quad t_{j-1}\leqslant t\leqslant t_j. \tag{5}$$

Next, for each space-time node, a time-step-averaged, second-order ODE is obtained for $\overline{T}_j^t(x)$ by operating on Eq. (1) with $1/\Delta t\int_{t_{j-1}}^{t_j} dt$, and a space-averaged, first-order ODE for $\overline{T}_i^x(t)$ is obtained by operating on Eq. (1) with $1/\Delta x\int_{x_i}^{x_i+\Delta x} dx$. After introducing some simplifying assumptions, the second-order ODE in space is solved using Dirichlet boundary conditions at the left and right edge of the node, leading to a solution of the form

$$\overline{T}_j^t(x)=C_1+C_2x+g(e^{-C_3x}), \tag{6}$$

where C_m $(m=1,2,3,\ldots)$ are constants. On the other hand, the first-order ODE in time is solved using the initial condition at the beginning of the time step, leading to a solution of the form

$$\overline{T}_i^x(t)=\overline{T}_{i,j-1}^x+C_4\ln[1-C_5(t-t_{j-1})] \tag{7}$$

4 Finite Difference Method

In the present paper we also employ an explicit FD method. Using a forward difference scheme for the time derivative and a central difference scheme for the space derivative, then Eq. (1) in discretized form can be expressed as

$$T_{i,m+1}=T_{i,m}+\frac{kx_i\dot{R}_m}{2hR_m}(T_{i+1,m}-T_{i-1,m}) + \frac{k}{h^2R_m^2}(R_{i+1,m}-2R_{i,m}+R_{i-1,m}), \tag{8}$$

where $T_{i,m}\equiv T(x_i,t_m)$, $h(\equiv\Delta x)$ is the constant space grid size such that $x_i=ih$, with $i=0,1,\ldots,N$, $(x_0=0, x_N=1)$, $t_m=t_0+mk$ where $k(\equiv\Delta t)$ is the time step and t_0 is the time at which the numerical process is initialized. A truncation error for this scheme is $O(k)+O(h^2)$.

The temperature history at the origin $(x=0)$ is easily obtained using Eq. (3), which in discretized form is

$$T_{i,m}=f(t_m), \quad i=0, \ m=0,1,2,\ldots. \tag{9}$$

For the temperature distribution at $0<x<1$ $(i=1,2,\ldots,N-1, m=0,1,2,\ldots,)$ Eq. (8) is to be used. The temperature history at $x=1$ according to (3) is

$$T_{i,m}=0, \quad i=N, \ m=0,1,2,\ldots. \tag{10}$$

The Stefan condition (2) at $x=1$ $(i=N)$ in discretized form is

$$R_{m+1}=R_m-\frac{k\,\text{Ste}}{2hR_m}(3T_{N,m}-4T_{N-1,m}+T_{N-2,m}), \quad m=0,1,2,\ldots, \tag{11}$$

where the following three point backward scheme [3,10] is used for the temperature gradient at the moving interface $(x=1=N\Delta x)$:

$$\left.\frac{\partial T}{\partial x}\right|_{x=R}=\frac{3T_N-4T_{N-1}+T_{N-2}}{2\Delta x}+O(\Delta x^2). \tag{12}$$

Initial condition (3) in discretized form is

$$R_0=0. \tag{13}$$

5 Benchmark Results and Discussion

In this section we present the computational results obtained by using the NI and FD approaches applied to the one-dimensional Stefan problem describing the melting process of a solid. It should be noted that $\overline{T}$ has been used in Section 3 (NI method) to represent the temperature distribution as it has been space-averaged or time-averaged, whereas T has been used in Section 4 (FD method). In this section we adopt the common notation $T(x,t)$ for the numerical results obtained by both methods for the temperature distribution.

5.1 Test Example 1. In order to have a validation of the accuracy of both the NI and FD methods, we first present the computational results for the Stefan problem defined by Eqs. (1–3) with time-independent boundary condition $T(x=0,t)=1$, for which the exact solution is [16]

$$T(x,t)=1-\frac{\text{erf}(x\lambda)}{\text{erf}(\lambda)}, \qquad R(t)=2\lambda\sqrt{t}, \tag{14}$$

where the exact value of λ is determined from the solution of the following transcendental equation:

$$\sqrt{\pi}\lambda e^{\lambda^2}\,\text{erf}(\lambda)=\text{Ste}. \tag{15}$$

For both the NI and FD methods the initial time $t_{in}=0.01$ is used. In the FD approach a constant grid size $h(\equiv\Delta x=1/N)=0.1$ (number of grid points $N=10$ is adopted) and the time step $k(\equiv\Delta t)=0.000002$ are used. One should mention here that a larger grid size and time steps, e.g., $h=0.2$ and $k=0.0001$, also guarantee stability of our difference schemes applied. But such a choice of smaller time step and finer grid size has been made in order to improve on the accuracy of previous published results.

Table 1 Temperature distribution for test example 1 (Ste = 0.2, t = 1.6)

	$T(x,t)$				
x	Nodal integral (N_x = 10)	Error (%)	Finite differences	Error (%)	Exact
0.0	1.0	0.0	1.0	0.0	1.0
0.1	0.896893	0.000000	0.896891	0.000223	0.896893
0.2	0.793979	0.000126	0.793976	0.000504	0.793980
0.3	0.691451	0.000145	0.691446	0.000868	0.691452
0.4	0.589498	0.000339	0.589493	0.001187	0.589500
0.5	0.488309	0.000410	0.488303	0.001638	0.488311
0.6	0.388066	0.000515	0.388060	0.002061	0.388068
0.7	0.288945	0.000692	0.288940	0.002423	0.288947
0.8	0.191120	0.000523	0.191115	0.003139	0.191121
0.9	0.094752	0.001055	0.094750	0.003166	0.094753
1.0	0.0	0.0	0.0	0.0	0.0

Applying the NI approach, number of nodes $N_x = 10$ (it corresponds to node size $\Delta x = 0.1$) and time step $\Delta t = 0.02$ were adopted. The values of λ obtained from the solution of transcendental Eq. (15) are 0.30642 and 0.62006 for Ste = 0.2 and 1.0 [2], respectively, which we have adopted in this work.

The present computational results and exact solution for the temperature distribution, the position of the moving boundary and its velocity together with percent errors are shown in Table 1 and 2, for Stefan number Ste = 0.2, and Table 3 and 4, for Ste = 1.0. Very close agreement between the present results and the exact solution is seen, where somewhat better accuracy is achieved using the NI method. Since the moving boundary moves faster as Ste is increased, the problems with larger Stefan number are more difficult. This can explain the larger percent errors both for temperature distribution and boundary movement seen for Ste = 1.0 compared to those obtained for Ste = 0.2. However, for all the results presented in Tables 1–4 the maximum percentage error is less than 0.05%.

Table 2 Position of moving boundary and its velocity for test example 1 (Ste = 0.2)

	$R(t)$				
t	Nodal integral (N_x = 10)	Error (%)	Finite differences	Error (%)	Exact
0.2	0.27409	0.00730	0.27414	0.02554	0.27407
0.4	0.38763	0.01032	0.38769	0.02580	0.38759
0.6	0.47474	0.00843	0.47482	0.02528	0.47470
0.8	0.54819	0.00912	0.54828	0.02554	0.54814
1.0	0.61289	0.00816	0.61300	0.02611	0.61284
1.2	0.67139	0.00894	0.67150	0.02532	0.67133
1.4	0.72518	0.00827	0.72531	0.02620	0.72512
1.6	0.77525	0.00774	0.77539	0.02580	0.77519
	dR/dt				
t	Nodal integral (N_x = 10)	Error (%)	Finite differences	Error (%)	Exact
0.2	0.68524	0.00876	0.68536	0.02627	0.68518
0.4	0.48454	0.01032	0.48462	0.02683	0.48449
0.6	0.39562	0.00758	0.39569	0.02528	0.39559
0.8	0.34262	0.00876	0.34268	0.02627	0.34259
1.0	0.30645	0.00979	0.30650	0.02611	0.30642
1.2	0.27975	0.01073	0.27979	0.02503	0.27972
1.4	0.25899	0.00772	0.25904	0.02703	0.25897
1.6	0.24227	0.00826	0.24231	0.02477	0.24225

Table 3 Temperature distribution for test example 1 (Ste = 1.0, t = 0.8)

	$T(x,t)$				
x	Nodal integral (N_x = 10)	Error (%)	Finite differences	Error (%)	Exact
0.0	1.0	0.0	1.0	0.0	1.0
0.1	0.887190	0.000789	0.887180	0.001916	0.887197
0.2	0.775245	0.001548	0.775224	0.004257	0.775257
0.3	0.665007	0.002707	0.664978	0.007067	0.665025
0.4	0.557283	0.003948	0.557248	0.010228	0.557305
0.5	0.452822	0.005079	0.452783	0.013691	0.452845
0.6	0.352300	0.006528	0.352260	0.017881	0.352323
0.7	0.256310	0.008193	0.256273	0.022627	0.256331
0.8	0.165350	0.009676	0.165320	0.027817	0.165366
0.9	0.079816	0.011275	0.079798	0.033824	0.079825
0.1	0.0	0.0	0.0	0.0	0.0

Table 4 Position of moving boundary and its velocity for test example 1 (Ste = 1.0)

	$R(t)$				
t	Nodal integral (N_x = 10)	Error (%)	Finite differences	Error (%)	Exact
0.1	0.39224	0.02040	0.39226	0.02550	0.39216
0.2	0.55473	0.02344	0.55474	0.02524	0.55460
0.3	0.67941	0.02503	0.67942	0.02650	0.67924
0.4	0.78451	0.02422	0.78453	0.02677	0.78432
0.5	0.87711	0.02395	0.87713	0.02623	0.87690
0.6	0.96083	0.02394	0.96085	0.02603	0.96060
0.7	1.03782	0.02506	1.03784	0.02699	1.03756
0.8	1.10948	0.02524	1.10950	0.02705	1.10920
	dR/dt				
t	Nodal integral (N_x = 10)	Error (%)	Finite differences	Error (%)	Exact
0.1	1.96140	0.03060	1.96137	0.02907	1.96080
0.2	1.38689	0.02813	1.38688	0.02741	1.38650
0.3	1.13238	0.02738	1.13238	0.02738	1.13207
0.4	0.98066	0.02652	0.98067	0.02754	0.98040
0.5	0.87713	0.02623	0.87714	0.02737	0.87690
0.6	0.80071	0.02748	0.80071	0.02748	0.80049
0.7	0.74131	0.02699	0.74132	0.02834	0.74111
0.8	0.69343	0.02596	0.69344	0.02741	0.69325

The computational times t_c required to achieve the NI results on a Pentium 4, 1 GHz personal computer are as follows:

Table 1 (Ste = 0.2, t = 1.6), t_c = 6 sec

Table 3 (Ste = 1.0, t = 0.8), t_c = 3 sec.

These computational times are shorter than the corresponding times required to achieve the FD results, namely,

Table 1 (Ste = 0.2, t = 1.6), t_c = 14 sec

Table 3 (Ste = 1.0, t = 0.8), t_c = 7 sec,

which are still very reasonable.

5.2 Test Example 2. This problem with exponentially rising temperature on the left surface, is relatively more difficult than the time-independent test example 1. It has an exact solution [3] and for the special case of Ste = 1, the differential Eqs. (1–3) are satisfied by

$$T(x,t) = e^{t(1-x)} - 1, \quad R(t) = t, \tag{16}$$

$$T(x,t) \equiv f(t) = e^{t} - 1, \quad x = 0,$$

$$T(x,t) = 0, \quad x = 1,$$

$$T(x,t) = 0, \quad t = 0. \tag{17}$$

For benchmarking purposes, we compare our computational results with the exact solution and with the computational results obtained previously by Rizwan-uddin [14], who used the NI method. In the present paper the numerical process is initialised using the exact solution (16) of the Stefan problem defined by Eqs. (1–3). The initial time $t_0 = 0.02$ which according to Eq. (16) corresponds to the initial position of the moving boundary $R(t_0)$

Table 5 Temperature distribution for test example 2 (Ste =1.0)

		$T(x,t)$				
t	x	Nodal integral ($N_x=10$)	Error (%)	Finite differences	Error (%)	Exact
1.0	0.0	1.718463	0.010534	1.718282	0.0	1.718282
	0.1	1.459617	0.000959	1.459742	0.009523	1.459603
	0.2	1.225442	0.008078	1.225771	0.018767	1.225541
	0.3	1.013585	0.016572	1.014033	0.027620	1.013753
	0.4	0.821917	0.024571	0.822418	0.036369	0.822119
	0.5	0.648514	0.031909	0.649013	0.045012	0.648721
	0.6	0.491633	0.039038	0.492088	0.053474	0.491825
	0.7	0.349699	0.045733	0.350076	0.062025	0.349859
	0.8	0.221287	0.052393	0.221559	0.070460	0.221403
	0.9	0.105110	0.058001	0.105255	0.079870	0.105171
	1.0	0.0	0.0	0.0	0.0	0.0

$=0.02$, is used to get a solution of the Stefan problem at $t=1.0$. Within the FD approach a constant grid size $h(\equiv\Delta x=1/N)=0.1$ (number of grid points $N=10$ is adopted) and the time step $k(\equiv\Delta t)=0.000002$ are used. Such a choice of time step and grid size guarantees stability of our difference schemes applied. Using the NI approach, number of nodes $N_x=10$ (it corresponds to node size $\Delta x=0.1$) and time step $\Delta t=0.2$ were adopted.

The present computational results and exact solution for the temperature distribution together with percent errors for $t=1.0$ are shown in Table 5. Very close agreement between the present results and exact solution is seen, with higher accuracy resulting from the NI method. The computational time t_c required to achieve the NI results in Table 5 (Ste$=1.0$,$t=1.0$) on a Pentium 4, 1 GHz personal computer is approximately 2 seconds which is an improvement on the corresponding time, namely 8 seconds, required to achieve the FD results. In Table 6 the computational and exact values for boundary position and its velocity are shown together with percent errors. Very good agreement between the present results and the exact solution is seen. Furthermore, the accuracy of the present results for the position of the moving boundary obtained using the NI method with number of nodes $N_x=10$ is better than the accuracy of the results achieved earlier by Rizwan-uddin who use the same method with smaller number of nodes $N_x=4$. The accuracy of the present FD results for boundary position is similar to that obtained previously by Rizwan-uddin [14]. Clearly, from Tables 5 and 6 we can see that the maximum percentage error for both the NI and FD methods is less than approximately 0.2%.

On the basis of the present computational results obtained using the NI and FD methods, the NI method is seen to generate more accurate solutions of the Stefan problem analyzed. Although in order to achieve the stability of our FD schemes small time steps are usually required if compared to those used within the NI method, which makes the FD method applied more computer intensive, it may be assumed sufficiently accurate and efficient for most practical purposes. This is additionally supported by the fact that the FD approach used in the present work has been earlier successfully applied to the Stefan problem with Neumann boundary condition at $x=0$ by Caldwell and Savović [10] describing the evaporation of droplets. The method has also been successfully applied to a more complicated Stefan problems with time-dependent boundary conditions at $x=0$ by Savović and Caldwell [11] describing one dimensional single-phase melting process.

6 Conclusion

We report on the nodal integral and finite difference solution of the Stefan problem describing the melting process of a solid. Good agreement between the present computational results for temperature distribution and boundary movement obtained using the nodal integral and finite difference approaches for two test examples is seen. Furthermore, comparison with the exact solutions show that both the NI and FD schemes are very accurate with higher accuracy being achieved using the NI method. Although the NI method permits the use of relatively large time

Table 6 Position of moving boundary and its velocity for test example 2 (Ste=1.0)

	$R(t)$						
t	Nodal integral ($N_x=4$) Rizwanuddin (1994) [14]	Error (%)	Nodal integral ($N_x=10$)	Error (%)	Finite differences	Error (%)	Exact
0.1			0.099999	0.001000	0.099999	0.001000	0.1
0.2			0.200010	0.005000	0.199994	0.003000	0.2
0.3			0.300007	0.002333	0.299979	0.007000	0.3
0.4			0.400001	0.000250	0.399951	0.012250	0.4
0.5			0.499990	0.002000	0.499906	0.018800	0.5
0.6			0.599974	0.004333	0.599840	0.026667	0.6
0.7			0.699952	0.006857	0.699750	0.035714	0.7
0.8			0.799924	0.009500	0.799632	0.046000	0.8
0.9			0.899888	0.012444	0.899484	0.057333	0.9
1.0	0.99930	0.070	0.999844	0.015600	0.999301	0.069900	1.0

	dR/dt				
t	Nodal integral ($N_x=10$)	Error (%)	Finite differences	Error (%)	Exact
0.1	1.000134	0.013400	0.999976	0.002400	1.0
0.2	1.000033	0.003300	0.999906	0.009400	
0.3	0.999961	0.003900	0.999793	0.020700	
0.4	0.999916	0.008400	0.999641	0.035900	
0.5	0.999869	0.013100	0.999451	0.054900	
0.6	0.999814	0.018600	0.999226	0.077400	
0.7	0.999751	0.024900	0.998966	0.103400	
0.8	0.999680	0.032000	0.998674	0.132600	
0.9	0.999602	0.039800	0.998349	0.165100	
1.0	0.999517	0.048300	0.997994	0.200600	

steps, the FD approach which needs smaller time steps is shown to provide accurate solutions of two test cases of the Stefan problem, one with time-dependent and one with time-independent boundary conditions.

This numerical study has provided benchmarking for the use of both the NI and FD methods. It is important to realize that for most realistic Stefan problems, which may include time-dependent boundary conditions, analytical solutions are generally not available. The high accuracy and agreement produced by both methods for the two test examples presented gives us confidence in the application of these methods to similar problems. One obvious typical example would be an extension of test example 1 where the temperature on the left boundary is not constant but is ramped linearly in the form $T(x=0,t)=F(t)=1-at$.

The numerical results obtained from the two test examples presented show a high level of accuracy and efficiency. Clearly, the accuracy and efficiency of numerical approaches are functions of the time step and grid size, and higher accuracy may be achieved by using finer grid size and time step at the cost of computational time or efficiency. Obviously, further benchmarking is required to draw the conclusion that both the NI and FD approaches may be considered as sufficiently accurate and efficient for a wider class of Stefan problems.

Acknowledgment

The authors would like to thank the reviewers for their helpful comments and to thank City University of Hong Kong for funding this research by Strategic Research Grants (Project No. 7001048 and 7001242).

References

[1] Crank, J., 1984, *Free and Moving Boundary Problems*, Clarendon Press, Oxford.

[2] Mennig, J., and Özişik, M. N., 1985, "Coupled Integral Equation Approach for Solving Melting or Solidification," Int. J. Heat Mass Transf., **28**, pp. 1481–1485.

[3] Furzeland, R. M., 1980, "A Comparative Study of Numerical Methods for Moving Boundary Problems," J. Inst. Math. Appl., **5**, pp. 411–429.

[4] Rizwan-uddin, 1999, "One-Dimensional Phase Change With Periodic Boundary Conditions," Numer. Heat Transfer, Part A, **35**, pp. 361–372.

[5] Asaithambi, N. S., 1997, "A Variable Time-step Galerkin Method for a One-Dimensional Stefan Problem," Appl. Math. Comput., **81**, pp. 189–200.

[6] Finn, W. D., and Voroğlu, E., 1979, "Finite Element Solution of the Stefan Problem," in *The Mathematics of Finite Elements and Applications*, J. R. Whiteman, ed., MAFELAP 1978, Academic Press, New York.

[7] Asaithambi, N. S., 1992, "A Galerkin Method for Stefan Problems," Appl. Math. Comput., **52**, pp. 239–250.

[8] Černý, R., and Přikryl, P., 1999, "Numerical Solution of a Stefan-Like Problem in Laser Processing of Semiconducting Alloys," Math. Comput. Simul., **50**, pp. 165–173.

[9] Gupta, R. S., and Kumar, D., 1980, "A Modified Variale Time Step Method for the One-Dimensional Stefan Problem," Comput. Methods Appl. Mech. Eng., **23**, pp. 101–108.

[10] Caldwell, J., and Savović, S., 2002, "Numerical Solution of Stefan Problem by Variable Space Grid Method and Boundary Immobilisation Method," J. Math. Sciences, **13**, pp. 67–79.

[11] Savović, S., and Caldwell, J., 2002, "Numerical Solution of Stefan Problem with Time Dependent Boundary Conditions by Variable Space Grid Method and Boundary Immobilisation Method," submitted to Numer. Heat Transfer.

[12] Moyano, E. A., and Scarpettini, A., 2000, "Numerical Stability Study and Error Estimation for Two Implicit Schemes in a Moving Boundary Problem," Numer. Methods Partial Differ. Equ., **16**, pp. 42–61.

[13] Vermolen, F., and Vuik, K., 1998, "A Numerical Method to Compute Dissolution of Second Phases in Ternary Alloys," J. Comput. Appl. Math., **93**, pp. 123–143.

[14] Rizwa-uddin, 1999, "A Nodal Method for Phase Change Moving Boundary Problems," Int. J. Comput. Fluid Dyn., **11**, pp. 211–221.

[15] Yao, L. S., and Prusa, J., 1989, "Melting and Freezing," Adv. Heat Transfer, **19**, pp. 1–95.

[16] Özişik, N., *Heat Conduction*, 1993, 2nd Edition, Wiley, New York.

A General Expression for the Determination of the Log Mean Temperature Correction Factor for Shell and Tube Heat Exchangers

Ahmad Fakheri
Assoc. Prof. ASME Mem.
e-mail: ahmad@bradley.edu
Department of Mechanical Engineering,
Bradley University, Peoria, IL

This paper presents a single closed form algebraic equation for the determination of the Log Mean Temperature Difference correction factor (F) for shell and tube heat exchangers having N shell passes and 2M tube passes per shell. The equation and its graphical presentation generalize the traditional equations and charts used for the determination of F. The equation presented is also useful in design, analysis and optimization of multi shell and tube heat exchanger, particularly for direct determination of the number of shells. [DOI: 10.1115/1.1571078]

Keywords: Heat Transfer, Heat Exchangers, Optimization, Ventilation

Introduction

The rate of heat transfer in heat exchangers is given by

$$q = UAF\frac{(\Delta T)_1-(\Delta T)_2}{\ln\dfrac{(\Delta T)_1}{(\Delta T)_2}} = UA\,F\,LMTD \tag{1}$$

where $F(\leqslant 1)$ is interpreted as a geometric correction factor, that when applied to the LMTD (Log Mean Temperature Difference) of a counter flow heat exchanger, provides the effective temperature difference of the heat exchanger under consideration. It is a measure of the heat exchanger's departure from the ideal behavior of a counter flow heat exchanger having the same terminal temperatures.

The Log Mean Temperature Difference is widely used in heat exchanger analysis, particularly for heat exchanger selection (sizing problems) when as a result of the process requirements the temperatures are known (can be determined) and the size of the heat exchanger is required.

Determination of F is primarily based on the breakthrough paper by Bowman et al. [1] in which they compiled the available data, and presented a series of equations and charts to find F for a variety of heat exchangers, including different shell and tube exchangers. The correction factor F is expressed in terms of two nondimensional variables,

$$P = \frac{t_2-t_1}{T_1-t_1} \tag{2}$$

and

$$R = \frac{T_1-T_2}{t_2-t_1} \tag{3}$$

which were later interpreted as the capacity ratio and a measure of heat exchanger effectiveness, respectively [2].

Contributed by the Heat Transfer Division for publication in the JOURNAL OF HEAT TRANSFER. Manuscript received by the Heat Transfer Division August 20, 2003; revision received January 16, 2003. Associate Editor: J. K. Jensen.

To date, a general expression for the determination of F for all shell and tube heat exchangers has not been available in the literature. The values of F have been determined using correlations and charts presented in Ref. [1] who for one shell and two tube pass heat exchangers, Fig. 1, provide the following expression,

$$F=\frac{\sqrt{R^2+1}}{R-1}\frac{\ln\dfrac{1-P}{1-PR}}{\ln\dfrac{\left(\dfrac{2}{P}\right)-1-R+\sqrt{R^2+1}}{\left(\dfrac{2}{P}\right)-1-R-\sqrt{R^2+1}}} \tag{4}$$

for the determination of the *LMTD* correction factor. The same equation was found to be valid [1] for one shell pass and any even number of tube side passes.

To determine the correction factor for shell and tube heat exchangers with two shell and any multiple of four-tube passes, Bowman et al. [1] provided the following expression,

$$F_{2-4}=\frac{\sqrt{R^2+1}}{2(R-1)}\frac{\ln\dfrac{1-P}{1-PR}}{\ln\dfrac{\left(\dfrac{2}{P}\right)-1-R+\dfrac{2}{P}\sqrt{(1-P)(1-PR)}+\sqrt{R^2+1}}{\left(\dfrac{2}{P}\right)-1-R+\dfrac{2}{P}\sqrt{(1-P)(1-PR)}-\sqrt{R^2+1}}} \tag{5}$$

Although, Bowman et al. [1] did not provide closed form solutions for three or more shell passes, Bowman [1,3] showed that Eq. (4) can also be used for this case, provided that in Eq. (4) P is interpreted as $P_{1,2}$ which is related to the P for a multi-shell multi-tube heat exchanger ($P_{N,2N}$) by the following equation.

$$P_{N,2N}=\frac{1-\left[\dfrac{1-P_{1,2}R}{1-P_{1,2}}\right]^N}{R-\left[\dfrac{1-P_{1,2}R}{1-P_{1,2}}\right]^N}, \tag{6}$$

Based on the above, Bowman et al. [1] provided a series of charts for the determination of F for multi-shell and tube heat exchangers. These charts as well as the underlying correlations have proven invaluable in heat exchanger design and analysis and have been reproduced extensively in the heat exchanger literature including basic heat transfer texts [4,5]. The charts are perhaps less frequently used, in recent years, in favor of heat exchanger design computer codes. Also, Tucker [6] recently discovered an error in one of the charts for the cross flow heat exchangers correction factors that apparently had gone unnoticed for over 65 years.

Analysis

The goal of this study is to derive a single equation, and therefore a single chart, for the determination of the *LMTD* correction factor applicable to shell and tube heat exchangers with any number of tube and shell passes.

From Eq. (6), it can be shown that:

$$\frac{1-P_{1,2}R}{1-P_{1,2}}=\left[\frac{1-P_{N,2N}R}{1-P_{N,2N}}\right]^{1/N} \tag{7}$$

from which $P_{1,2}$ can be expressed in terms of $P_{N,2N}$ and R as,

$$P_{1,2}=\frac{1-\left[\dfrac{1-PR}{1-P}\right]^{1/N}}{R-\left[\dfrac{1-PR}{1-P}\right]^{1/N}} \tag{8}$$

where the subscript $N, 2N,$ of P has been dropped to generalize. Substituting $P_{1,2}$ from Eq. (8) for P in Eq. (4) and simplifying, yields the following expression for the determination of F:

$$F_{N,2NM}=\frac{\sqrt{R^2+1}}{R-1}\frac{\ln\left[\dfrac{1-P}{1-PR}\right]^{1/N}}{\ln\dfrac{2\dfrac{R-\left[\dfrac{1-PR}{1-P}\right]^{1/N}}{1-\left[\dfrac{1-PR}{1-P}\right]^{1/N}}-1-R+\sqrt{R^2+1}}{2\dfrac{R-\left[\dfrac{1-PR}{1-P}\right]^{1/N}}{1-\left[\dfrac{1-PR}{1-P}\right]^{1/N}}-1-R-\sqrt{R^2+1}}} \tag{9}$$

It is easy to show that for $N=1$, Eq. (9) reduces to Eq. (4) for single shell multi tube pass heat exchangers,

As mentioned before, Bowman et al. [1] state that by redefining P using Eq. (6), Eq. (4), and therefore Eq. (9), can be used to determine F for shell and tube heat exchangers with any number of shell passes except two. For Two shell passes, they provide Eq. (5) which is identical to Eq. (9) when the latter is evaluated for two shell passes, making Eq. (9) a substitute for Eq. (5) as well. To show the redundancy of Eq. (5), consider Eq. (9) for the special case of $N=2$ (two shell passes)

$$F_{2,4}=\frac{\sqrt{R^2+1}}{2(R-1)}\frac{\ln\dfrac{1-P}{1-PR}}{\ln\dfrac{2\dfrac{R-\sqrt{\dfrac{1-PR}{1-P}}}{1-\sqrt{\dfrac{1-PR}{1-P}}}-1-R+\sqrt{R^2+1}}{2\dfrac{R-\sqrt{\dfrac{1-PR}{1-P}}}{1-\sqrt{\dfrac{1-PR}{1-P}}}-1-R-\sqrt{R^2+1}}} \tag{10}$$

It easy to shown that,

$$2\frac{R-\sqrt{\dfrac{1-PR}{(1-P)}}}{1-\sqrt{\dfrac{1-PR}{(1-P)}}}=\left(\frac{2}{P}\right)+\frac{2}{P}\sqrt{(1-P)(1-PR)} \tag{11}$$

proving that Eqs. (5) and (10) are identical. Therefore, for a shell and tube heat exchanger, with $N=1,2,3,\ldots.$ shell passes and

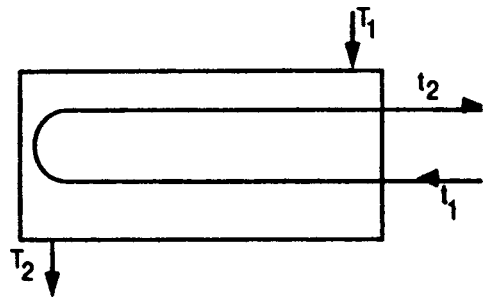

Fig. 1 Shell and tube heat exchanger

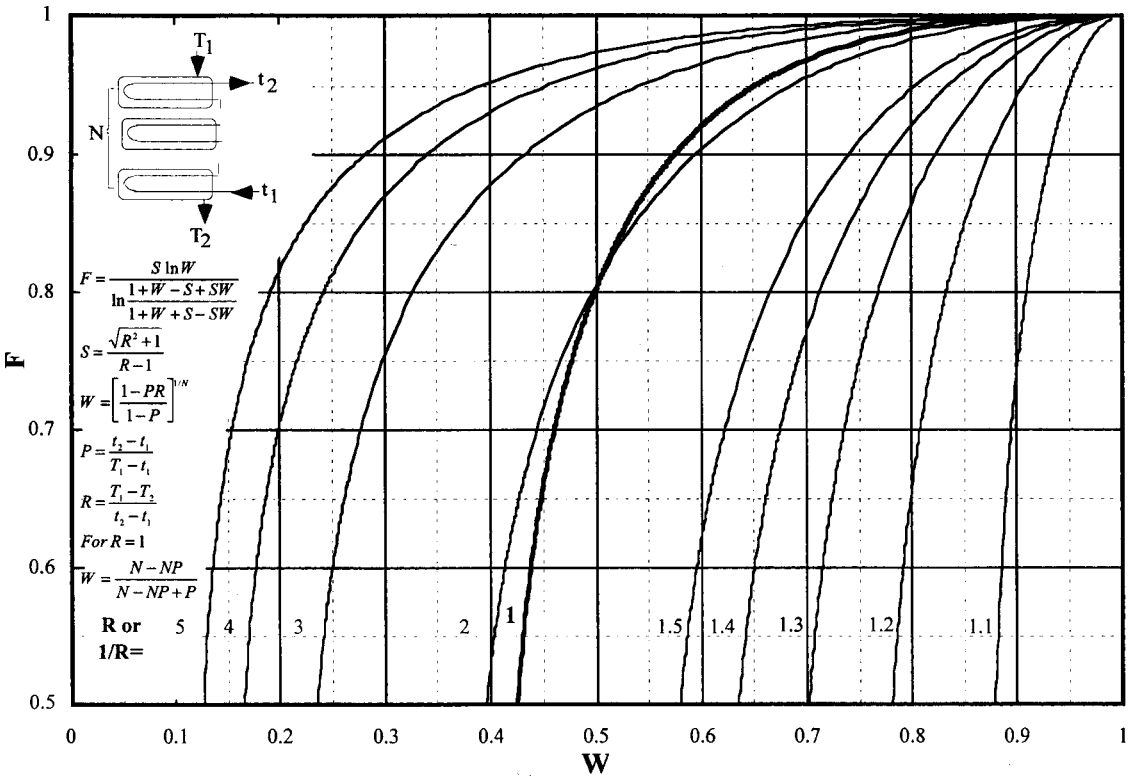

Fig. 2 ***F*** **correction factor for shell and tube heat exchangers with** ***N*** **shell and 2*NM* tube passes**

$2M=2,4,6,8\ldots$ tube passes per shell, the *LMTD* correction factor can be obtained from Eq. (9) which can be further rearranged into

$$F_{N,2NM}=\frac{\dfrac{\sqrt{R^2+1}}{R-1}\ln\left[\dfrac{1-PR}{1-P}\right]^{1/N}}{\ln\dfrac{1+\left[\dfrac{1-PR}{1-P}\right]^{1/N}-\dfrac{\sqrt{R^2+1}}{R-1}+\dfrac{\sqrt{R^2+1}}{R-1}\left[\dfrac{1-PR}{1-P}\right]^{1/N}}{1+\left[\dfrac{1-PR}{1-P}\right]^{1/N}+\dfrac{\sqrt{R^2+1}}{R-1}-\dfrac{\sqrt{R^2+1}}{R-1}\left[\dfrac{1-PR}{1-P}\right]^{1/N}}} \tag{12}$$

As can be seen, F is a function of two parameters $W=[(1-PR)/(1-P)]^{1/N}$ and $S=\sqrt{R^2+1}/(R-1)$. Therefore the *LMTD* correction factor for shell and tube heat exchangers can be determined from the simple expression,

$$F_{N,2NM}=\frac{S\ln W}{\ln\dfrac{1+W-S+SW}{1+W+S-SW}} \tag{13}$$

Figure 2 is a plot of F as a function of W for different values of R. It also turns out that in Eq. (12) $F(P,R)=F(P,1/R)$, and therefore only values of $R>1$ or $R<1$ need to be considered.

For the limiting case of $R=1$, Eq. (4) becomes

$$F=\sqrt{2}\,\frac{P}{1-P}\,\frac{1}{\ln\dfrac{\left(\dfrac{1}{P}\right)-1+\dfrac{1}{\sqrt{2}}}{\left(\dfrac{1}{P}\right)-1-\dfrac{1}{\sqrt{2}}}} \tag{14}$$

and and Eq. (6) reduces to

$$P_{1,2}=\frac{P}{N-NP+P} \tag{15}$$

Substituting for $P_{1,2}$ from (15) into (14) and defining,

$$W'=\frac{N-NP}{N-NP+P}$$

For the special case of $R=1$, Eq. (13) reduces to

$$F=\sqrt{2}\left(\frac{1-W'}{W'}\right)\frac{1}{\ln\dfrac{\dfrac{W'}{1-W'}+\dfrac{1}{\sqrt{2}}}{\dfrac{w'}{1-W'}-\dfrac{1}{\sqrt{2}}}} \tag{16}$$

F as a function of W' is also plotted in Fig. 2. Note that for the special case of a single shell pass, $(N=1)$, W' reduces to $(1-P)$.

Conclusions

The Log Mean Temperature Difference (LMTD) correction factor for shell and tube heat exchangers is traditionally determined using the charts and more recently using computer based heat exchanger design software, as the underlying equations appeared complicated. In this work, it is shown that it is possible to collapse all the available correlations for the determination of the geometric correction factor F into a single simple algebraic equation applicable to the shell and tube heat exchangers with N shell passes and $2M$ tube passes per shell. This equation can then be used in different aspects of shell and tube heat exchanger design and analysis, including determining the number of shells, in a multipass system.

Nomenclature

A = surface area, m^2
F = LMTD correction factor
LMTD = log mean temperature difference; $LMTD=(\Delta T)_1-(\Delta T)_2/\ln(\Delta T)_1/(\Delta T)_2$
N = number of shells
P = $P=t_2-t_1/T_1-t_1$
q = rate of heat transfer; $q=U\ A\ F\ LMTD$
R = $R=T_1-T_2/t_2-t_1$
S = $S=\sqrt{R^2+1}/R-1$
T_1 = shell (hot fluid) inlet temperature
T_2 = shell (hot fluid) exit temperature
t_1 = tube (cold fluid) inlet temperature
t_2 = tube (cold fluid) exit temperature
U = overall heat transfer coefficient, W/m^2K
W = $W=[1-PR/1-P]^{1/N}$
W' = $W'=N-NP/N-NP+P$
$(\Delta T)_1$ = temperature difference at one end of heat exchanger $(\Delta T)_1=T_1-t_2$
$(\Delta T)_2$ = temperature difference at the other end of heat exchanger $(\Delta T)_2=T_2-t_1$

References

[1] Bowman, R. A., Mueller, A. C., and Nagel, W. M., 1940, "Mean Temperature Difference in Design," Trans. ASME, **62**, pp. 283–294.
[2] Taborek, J., 1990, Hemisphere Handbook of Heat Exchanger Design Hemisphere, Bristol, PA.
[3] Bowman, R. A., 1936, "Mean Temperature Difference Correction in Multipass Exchangers" Ind. Eng. Chem. Fundam., **28**, pp. 541–544.
[4] Incropera, F. P., and De Witt, D., *Fundamentals of Heat and Mass Transfer*, 3rd ed., Wiley.
[5] Mills, A. F. 1999, *Heat Transfer*, 2nd Ed., Prentice Hall.
[6] Tucker, A. S., 1996, "The LMTD Correction Factor for Single-Pass Crossflow Heat Exchangers with Both Fluids Unmixed," ASME J. Heat Transfer, **118**, pp. 488–490.

Duality of Heat Exchanger Performance in Balanced Counter-Flow Systems

Ken Ogiso
e-mail: k-og@myad.jp
Professor Emeritus,
Tokyo University of Technology, 1404-1, Katakura-cho, Hachioji-city, Tokyo, 192-0982, Japan

The duality of heat exchangers to act as both heat conductors and insulators when considering heat exchanger performance is studied from the viewpoint of entropy generation. By defining an appropriate index of the entropy generation rate, it is clarified that the performance paradox pointed out by Bejan can be resolved. The case of a balanced counter-flow system was examined and it has been shown that a heat exchanger can be regarded as both a heat conductor and a heat insulator in terms of entropy generation. [DOI: 10.1115/1.1571079]

Keywords: Analytical, Heat Transfer, Heat Exchangers, Second Law, Thermodynamics

Introduction

The macroscopic performance of heat exchanger systems is usually described in terms of heat exchanger effectiveness (ε) and the number of heat transfer units (N_{tu}). The maximum heat exchanger capacity is achieved in the limiting case of $\varepsilon\to 1$ or $N_{tu}\to\infty$. However, such conditions are practically impossible to realize within the constraints of finite size and time. This can be equated to the impossibility of realizing Carnot thermal efficiency in heat engines. In both cases, entropy generation (proportional to available work lost) tends to zero.

In a balanced counter-flow heat exchanger, when the pressure loss is sufficiently small, the entropy generation index N_S defined by Bejan contains only the irreversible heat transfer term, $N_{S,\Delta T}$ (described as N_S in the following). The relationship between N_S and ε (or N_{tu}) is shown in Fig. 1, where the maximum occurs at $\varepsilon=0.5$.

This description of heat exchanger performance is clearly illogical in the $\varepsilon<0.5$ region, a paradox pointed out by Bejan himself [1,2]. In the present report it is shown that by appropriately defining the entropy generation index, the paradox can be resolved.

This treatment of the problem is based on the duality of heat exchanger systems to act as both heat conductors and heat insulators in terms of entropy generation.

Entropy Generation Index and the Performance Paradox

Figure 2 shows a temperature profile for a balanced counter-flow heat exchanger with negligible pressure loss, for which the entropy generation index, defined by Bejan, is

$$N_S=\dot{S}_{\rm gen}/C_{\rm min}=\ln\{[1-T_2/T_1][1+\varepsilon(T_1/T_2-1)]\} \quad (1)$$

The variation of N_S against ε is shown in Fig. 1. The phenomenon has been pointed out as a paradox by Bejan, who explained the paradox as follows. As ε tends to zero, $N_{tu}=AU/C_{\rm min}$ also tends to zero, implying that the heat exchanger stops exchanging heat and hence entropy generation ceases. ("A vanishing heat exchanger" as is termed by Bejan.)

More Appropriate Definition of Entropy Generation Index

N_S is defined as $\dot{S}_{\rm gen}/C_{\rm min}$, in which $C_{\rm min}$ has nothing directly to do with heat exchanger performance. As such, it is quite natural that N_S tends to zero as ε decreases and the heat exchanger ceases to function.

In order to define the entropy generation rate in terms of heat conducting capacity, a quantity $S_{\rm gen}/Au$ (non-dimensional) is introduced, given by

$$\Gamma=\dot{S}_{\rm gen}/AU=(\dot{S}_{\rm gen}/C_{\rm min})/(AU/C_{\rm min})=N_S/N_{tu} \quad (2)$$

The relationship between N_{tu} and ε in the case of a balanced counter-flow system is given by

$$N_{tu}=\varepsilon/(1-\varepsilon) \quad (3)$$

From Eqs. (2) and (3) we obtain

$$\Gamma=\{(1-\varepsilon)/\varepsilon\}\times N_S \quad (4)$$

where, if $\varepsilon\ll 1$, using the approximation

$$\ln(1+x)\fallingdotseq x(\ll 1)$$

we obtain

$$\Gamma\fallingdotseq(T_1-T_2)^2(1-\varepsilon)/T_1T_2 \quad (5)$$

Numerical Examples and Discussion

Examples of numerical calculations using Eqs. (4) and (5) are shown in Fig. 3. As is clear from the figure, Γ increases as ε decreases, and in the limit of $\varepsilon\to 0$, Γ converges to a finite value. This means that irreversible loss increases as heat exchanger per-

Contributed by the Heat Transfer Division for publication in the JOURNAL OF HEAT TRANSFER. Manuscript received by the Heat Transfer Division September 19, 2002; revision received January 16, 2003. Associate Editor: M. K. Jensen.

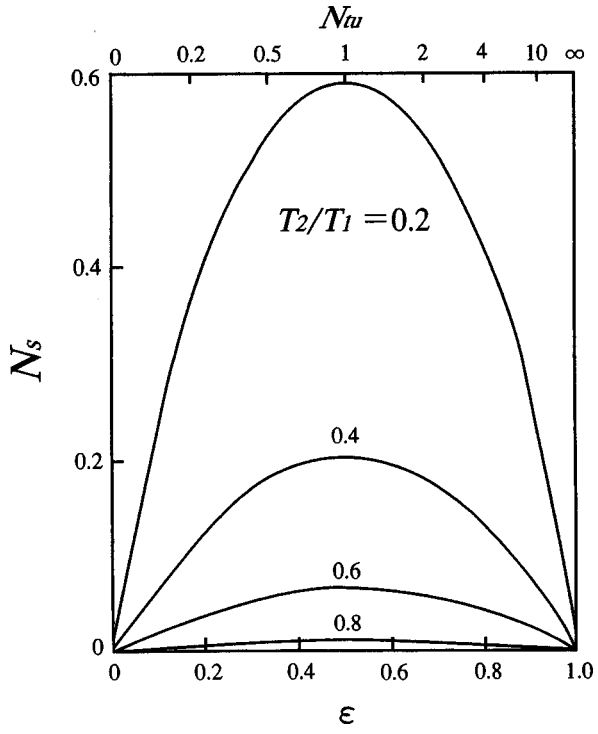

Fig. 1 N_S versus ε and N_{tu}[1][2]

formance deteriorates, effectively eliminating the paradox. In the limit of $\varepsilon \to 0$ (no heat exchange), the heat exchanger would become a perfect heat insulator.

In order to assess the performance of a heat exchanger as a heat conductor for the entire range of ε, N_S should be multiplied by a weighting factor related to the degradation of heat conducting capacity. As $N_{tu}(0 \sim \infty)$ is a direct measure of heat conductor performance, $1/N_{tu}(\infty \sim 0)$ represents a measure of heat insulator performance. Hence, if multiplied by $1/N_{tu}$, N_S/N_{tu} can express the irreversibility index of a heat exchanger for the entire range of ε. Γ in Eq. (2) complies with that definition.

Assessment as a Heat Insulator

From the preceding description, the performance of a heat exchanger in the range of heat insulating behavior can be assessed by multiplying N_S by a weighting factor that represents the degree of heat insulation degradation. The factor is N_{tu}, as is easily understood. $N_{tu} \to 0$ indicates a perfect insulator and $N_{tu} \to \infty$ represents the worst heat insulator. Therefore, from the expression

$$\Gamma' = N_S \times N_{tu}. \tag{6}$$

we can assess the performance of a heat insulator for the entire range of ε. As ε is an index of heat conductor performance, ε'

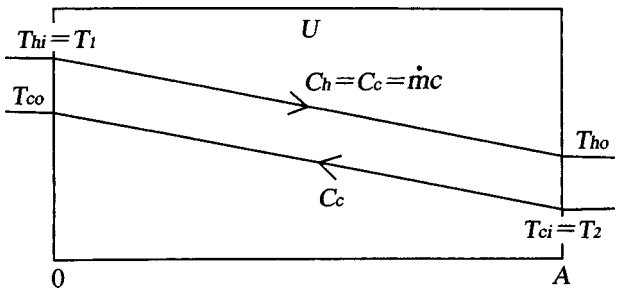

Fig. 2 Balanced counter-flow H.E.

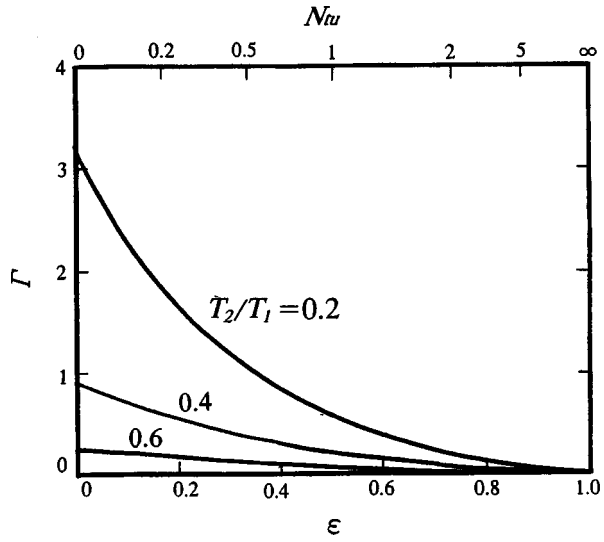

Fig. 3 Γ versus ε

$=1-\varepsilon$ represents the effectiveness of heat insulation. By replacing ε in the abscissa in Fig. 3 with $1-\varepsilon'$ and calculating Γ', we obtain Fig. 4, which is symmetrical to Fig. 3 with relation to $\varepsilon' = \varepsilon = 0.5$.

Furthermore, by replacing ε in Eq. (4) with $1-\varepsilon'$, we can obtain Eq. (6).

Other Type of Heat Exchangers

For other type of heat exchangers than of balanced and counter-flow, similar analysis will be possible because the relationships between ε and N_{tu} are similar in terms of their increase and decrease [3].

Conclusion

We have shown that a heat exchanger can be regarded as both a heat conductor and a heat insulator in terms of entropy generation. The case of a balanced counter-flow system was examined, and it was clarified that by defining an appropriate assessment index, a paradox in heat exchanger theory can be resolved.

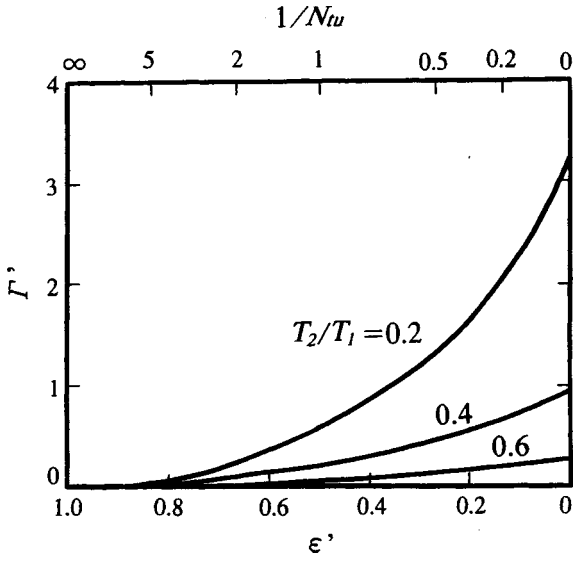

Fig. 4 Γ' versus ε'

Nomenclature

A = heat transfer area (m^2)
C_{max} = maximum heat capacity rate (W/K)
C_{min} = minimum heat capacity rate (W/K)
$\dot{S}_{gen}$ = entropy generation rate (W/K)
T = temperature (K)
T_1 = hot side inlet temperature (K)
T_2 = cold side inlet temperature (K)
U = overall heat transfer rate ($W/(m^2K)$)

Greek Symbols

Δ = difference
Γ = entropy generation rate index (heat conductor); N_S/N_{tu}
Γ' = entropy generation rate index (heat insulator); $N_S \times N_{tu}$
ε = heat exchanger effectiveness
ε' = $1-\varepsilon$

Dimensionless

N_S = entropy generation rate index; $\dot{S}_{gen}/C_{min}$
N_{tu} = number of heat transfer units; AU/C_{min}

References

[1] Bejan, A., 1995, *Entropy Generation Minimization*, CRC Press, Boca Raton, FL, pp. 124–126, Chap. 5
[2] Bejan, A., 1997, *Advanced Engineering Thermodynamics*, John Wiley and Sons, Inc., New York, pp. 604–609, Chap. 11
[3] Kakaç, S., and Liu, H., 1998, *Heat Exchangers: Selection, Rating, and Thermal Design*, CRC Press, New York, pp. 59–61, Chap. 2

Thermal Resistance for Random Contacts on the Surface of a Semi-Infinite Heat Flux Tube

N. Laraqi
e-mail: najib.laraqi@cva.u-paris10.fr
University of Paris 10, LEEE, EA. 387, Heat Transfer Department 1, Chemin Desvallières, 92410 Ville d'Avray, France

Analytical solution is developed to calculate the thermal constriction resistance for contacts randomly distributed on the surface of a laterally insulated semi-infinite square prism. The contacts are modeled by circular spots with different radii and uniform heat flux. We analyze the evolution of the thermal constriction resistance as a function of the number of contacts, the relative contact size, and the dispersion of radii of spots. We show that the thermal constriction resistance for random contacts is a few tens of percents greater than that of the regular contacts.

[DOI: 10.1115/1.1571081]

Keywords: Contact Resistance, Heat Transfer, Interface, Roughness, Tribology

1 Introduction

The thermal contact resistance was widely studied during these last decades. Several works have been conducted to evaluate its evolution according to the geometrical, mechanical and thermal characteristics of materials and the properties of the interstitial fluids. The quality of contact between two solids depends of the technique of realization of surfaces, the loading, and the mechanical properties of material. So when two solids are put in contact, the real contact areas are of complex geometry of which dimensions are different and the positions are random. These areas are difficult to determine experimentally and the resort to statistical models allows to propose theoretical approaches. Among these models, we can mention those of Greenwood and Williamson [1], Cooper, Mikic, and Yovanovich [2], Mikic [3], Bush, Gibson, and Thomas [4] and Whitehouse, and Archard [5]. A review of these contact models is provided by Sridhar and Yovanovich [6]. McCool [7] has proposed a comparative study of different models describing the micro-geometry of contact between rough surfaces. Recently, Leung, Hsieh, and Goswami [8] has developed a predictive model of thermal contact conductance using a statistical mechanics approach. A review of some different approaches is provided by Fletcher [9].

The models proposed in the literature are generally based on idealized contact areas, where the asperities are assumed identical and regularly distributed over the contact plane (Yovanovich [10], Beck [11], Negus, Yovanovich, and Beck [12]). In the practice, the real contact areas are different, and their distribution is random. Experimental studies based on the use of the electric analogy have been performed by Bardon [13] and Cooper [14] to examine the effect of the eccentricity of a contact on the evolution of the constriction resistance. The authors showed that the constriction resistance increases with the increase of the eccentricity, more particularly when the relative size of contact is large. Das and Sadhal [15] developed an analytical solution for the problem of contacts with identical radii randomly distributed on a square region of a semi-infinite medium. The authors showed that in the case of the random contacts, the constriction resistance is more large compared to the one of regular contacts. The difference is of a few ten of percent. More recently, an approached model has been proposed by Laraqi [16] in order to investigate the effect of disorder of contacts and their radii on the thermal constriction resistance. Superposition method has been used with asymptotic expansions. An assumption has been adopted to calculate the temperature due to a macro-constriction phenomenon.

In this paper, an exact solution is developed. The study concerns a semi-infinite square heat flux tube with random spots. We analyze the influence of the number of contacts, the relative contact size, and the dispersion of radii of contacts on the evolution of

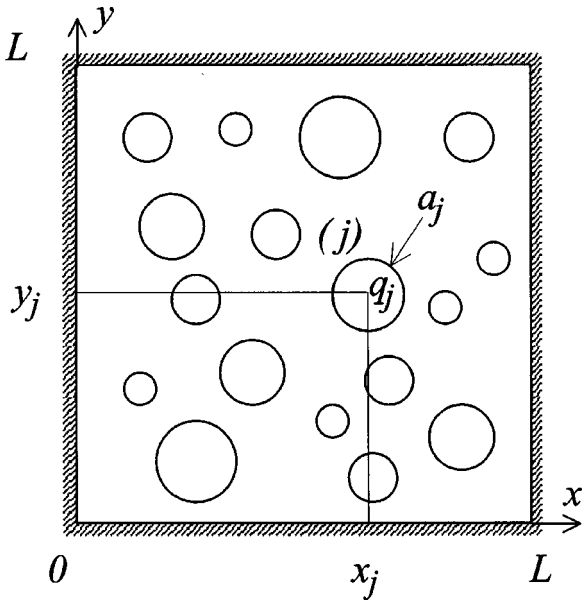

Fig. 1 Random contacts on a semi-infinite square prism

Contributed by the Heat Transfer Division for publication in the JOURNAL OF HEAT TRANSFER. Manuscript received by the Heat Transfer Division March 5, 2002; revision received January 31, 2003. Associate Editor: A. F. Emery.

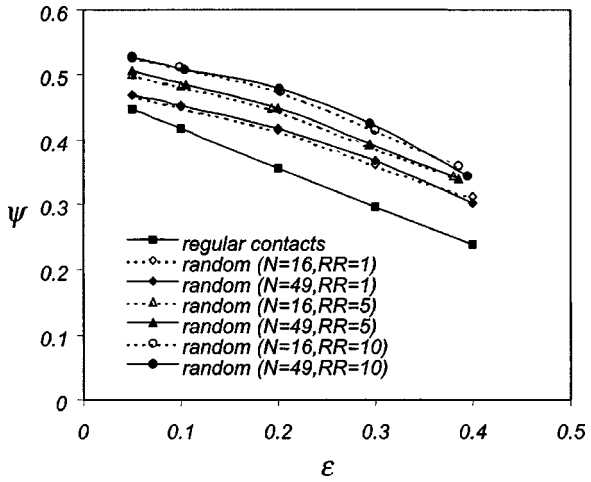

Fig. 2 Evolution of ψ as a function of ε

thermal constriction resistance. These results are compared to those of the regular contacts having the same number of contacts and the same ratio of real contact area to apparent contact area.

2 Formulation of Problem and Solution

We consider a laterally insulated semi-infinite square prism (Fig. 1), with side, L, thermal conductivity, k, and zero reference temperature. The face, $z=0$, is submitted to numerous heat sources, N, with circular shape. Each contact is characterized by its radius, a_j, space coordinates (x_j, y_j), and heat flux, q_j. The remainder of the surface, $z=0$, is insulated.

The governing equations can be written as follows:

Equation of Heat.

$$\nabla^2 T(x,y,z)=0 \tag{1}$$

Boundary Conditions.

$$\left(\frac{\partial T}{\partial x}\right)_{0,y,z}=0,\quad \left(\frac{\partial T}{\partial x}\right)_{L,y,z}=0,\quad \left(\frac{\partial T}{\partial y}\right)_{x,0,z}=0,\quad \left(\frac{\partial T}{\partial y}\right)_{x,L,z}=0$$

$$-k\left(\frac{\partial T}{\partial z}\right)_{x,y,0}=\begin{cases} q_j & : \text{ at contacts} \\ 0 & : \text{ elsewhere} \end{cases},\quad T_{x,y,z\to\infty}=0 \tag{2}$$

To solve this problem we use the double cosine Fourier transform with respect to x and y-directions as:

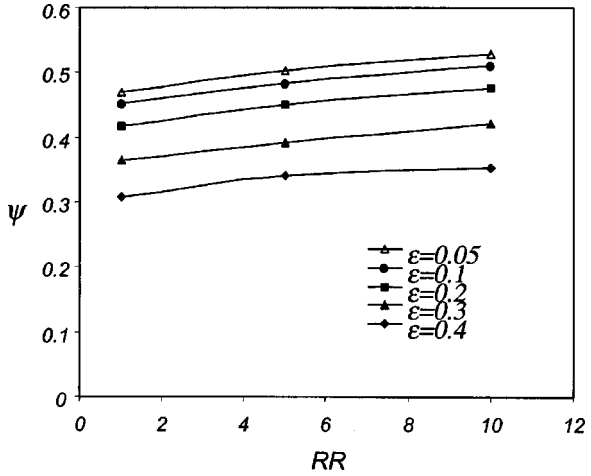

Fig. 3 Evolution of ψ as a function of RR

Table 1 Relative difference between random and regular contacts

RR	1		5		10	
N	16	49	16	49	16	49
ε	$100\times(R_{cs}-R_{cs}^{(u)})/R_{cs}^{(u)}\%$					
0.05	4.8	4.9	11.9	12.9	18.2	17.5
0.1	8.0	8.7	15.7	17.4	22.8	22.8
0.2	16.8	17.4	22.6	28.4	27.3	29.7
0.3	22.2	24.4	30.2	31.9	33.9	42.3
0.4	31.4	26.8	37.6	38.4	46.2	43.0

$$\tilde{\tilde{T}}=\frac{1}{L^2}\int_0^L\int_0^L \cos(m\pi x/L)\cos(n\pi y/L)\,dx\,dy \tag{3}$$

and its inverse:

$$T=\sum_{m=0}^{\infty}\sum_{n=0}^{\infty}\epsilon_m\epsilon_n\cos(m\pi x/L)\cos(n\pi y/L)\tilde{\tilde{T}}$$

$$\begin{cases}\epsilon_{m,\text{or},n}=1 & : m,\text{or},n=0\\ \epsilon_{m,\text{or},n}=2 & : m,\text{or},n\neq 0\end{cases} \tag{4}$$

After calculation, we deduce the expression of the surface temperature as follows:

$$T_{z=0}=\frac{2}{k\pi}\sum_{\substack{m=0\\ n\neq 0}}^{\infty}\sum_{\substack{n=0\\ m\neq 0}}^{\infty}\left[\frac{\epsilon_m\epsilon_n\cos(m\pi x/L)\cos(n\pi y/L)}{[m^2+n^2]}\right.$$

$$\times\sum_{j=1}^{N} q_j a_j\cos(m\pi x_j/L)\cos(n\pi y_j/L)$$

$$\left.\times J_1[(m^2+n^2)^{1/2}\pi a_j/L]\right] \tag{5}$$

The thermal constriction resistance of a contact (i) is defined as:

$$R_{cs}^{(i)}=\frac{\Delta T_c^{(i)}}{q_i\pi a_i^2}=\frac{T_c^{(i)}-T_a}{q_i\pi a_i^2} \tag{6}$$

where $T_c^{(i)}$ and T_a are the average temperatures of the real contact area (i) and the apparent contact area respectively. Considering the boundary condition, $T_{x,y,z\to\infty}=0$, in Eq. (2), we have $T_a=0$. The expression of $T_c^{(i)}$ is obtained by integration of Eq. (5) over the contact area (i) as follows:

Table 2 Relative effect of the disorder of contacts position

RR	5		10	
N	16	49	16	49
ε	$100\times R_{cs}(RR=1)/R_{cs}(RR)\%$			
0.05	40.3	37.6	26.4	27.7
0.1	51.1	50.3	35.1	38.2
0.2	74.2	61.3	61.5	58.6
0.3	73.6	76.6	65.4	57.7
0.4	83.4	69.8	67.8	62.3

$$T_c^{(i)}=\frac{4L}{k\pi^2 a_i}\sum_{\substack{m=0\\ n\neq 0}}^{\infty}\sum_{\substack{n=0\\ m\neq 0}}^{\infty}\left[\frac{\epsilon_m\epsilon_n\cos(m\pi x_i/L)\cos(n\pi y_i/L)}{[m^2+n^2]^{3/2}}\right.$$
$$\times J_1[(m^2+n^2)^{1/2}\pi a_i/L]\sum_{j=1}^{N} q_j a_j\cos(m\pi x_j/L)$$
$$\left.\times\cos(n\pi y_j/L)J_1[(m^2+n^2)^{1/2}\pi a_j/L]\right] \quad (7)$$

In order to calculate the total constriction resistance R_{cs} by the association in parallel of all elementary resistances $R_{cs}^{(i)}$ as:

$$R_{cs}=\left[\sum_{i=1}^{N}\frac{1}{R_{cs}^{(i)}}\right]^{-1} \quad (8)$$

it is necessary that all the contacts have the same temperature over the contact area, i.e., $T_c^{(i)}-T_a=\Delta T_c=Cst$. It is well known that the thermal resistance for uniform heat flux is greater that the one of isothermal contacts. The relative difference for these two boundary conditions varies between 8% and 16% for ε between 0 (unique contact) and 0.4. Actually, the relative contact size ε is less than 0.1 (for metals). In the present study the difference between the two boundary conditions has little importance because we compare the results of random contact to regular contacts for the same boundary condition (i.e., uniform heat flux).

Then, by writing Eq. (7) as:

$$T_c^{(i)}=\sum_{j=1}^{N} G_{ij}q_j \quad (9)$$

where G_{ij} are the other terms of the Eq. (7), which are known, we obtain a linear matrix system of order N of which the unknowns are $(q_j/\Delta T_c)$. This system is written under the following form:

$$\sum_{j=1}^{N} G_{ij}\frac{q_j}{\Delta T_c}=1 \quad (i=1\ \ to\ \ N) \quad (10)$$

Solving this system, we determine $(q_i/\Delta T_c)$ for $(i=1\ to\ N)$, and using Eqs. (6) and (8), we deduce the values of $R_{cs}^{(i)}$ and R_{cs} respectively.

3 Results and Discussion

To validate this model, we consider the particular case of a unique circular contact with radius a centered on a square flux tube [12], with side L. For this configuration, we have $(x_i/L=y_i/L=1/2)$ in Eq. (7). The terms $\cos^2(m\pi/2)$ and $\cos^2(n\pi/2)$ are equal to 1 (only for m and n pairs, i.e., $m=2m'$ and $n=2n'$). Using the expression of the thermal dimensionless constriction resistance $\psi=R_{cs}k\sqrt{A_r}$ (here $A_r=\pi a^2$), we deduce ψ under the following form:

$$\psi=\frac{1}{2\pi^2\sqrt{\pi}a}\sum_{\substack{m'=0\\ n'\neq 0}}^{\infty}\sum_{\substack{n'=0\\ m'\neq 0}}^{\infty}\frac{\epsilon_{m'}\epsilon_{n'}J_1^2[(m'^2+n'^2)^{1/2}2\pi a/L]}{[m'^2+n'^2]^{3/2}} \quad (11)$$

This expression is the same as the one predicted by the authors of reference [12].

The present model is used to calculate the thermal constriction resistance due to a multiple spots which radii are different and positions are randomly distributed over the surface. The data (x_i, y_i, a_i) characterizing the contacts are generated theoretically by a random function. If a generated contact overlaps with an existing contact, it is omitted and replaced by the next one. We continue this procedure until the desirable number of contacts, N, is obtained. For each studied case we fix the relative contact size, $\varepsilon=\sqrt{A_r/A_a}$, the number of contacts, N, and the ratio of the largest disk radius, $Max(a_i)$, to the smallest one, $Min(a_i)$. This ratio is denoted RR, as $RR=Max(a_i)/Min(a_i)$.

In order to compare the random and regular contacts, we consider the number of contact, N, equal to a square number. The thermal constriction resistance of uniform contacts is denoted $R_{cs}^{(u)}$.

We have studied 30 cases combining two values of N (16 and 49), five values of ε (0.05, 0.1, 0.2, 0.3, and 0.4) and three values of RR (1, 5, and 10). The particular case $RR=1$ corresponds to identical spots configuration but randomly distributed. This allows to analyze the effect of contact position only. For each case, we plot the average value of 10 random sets realized in the same conditions. The double series of the analytical solution converges slowly. For contacts with large value of ε (0.1 to 0.4) about 200 terms are sufficient. The required number of terms for $\varepsilon=0.05$ is more important (about 500).

The Fig. 2 presents the evolution dimensionless constriction resistance ψ as a function of ε. For all studied cases, the value of ψ for random contacts is more large than the one of regular contacts. This result is in agreement with the trend obtained by Das and Sadhal [15]. The difference between random and regular contacts increases with the increase of the dispersion of the radii of contacts (i.e., the increase of RR values). This result is inconsistent with the one of Beck [11]. The author has studied the influence of the scattering of spots radii for regular positions of contacts and has shown that the more standard deviation of the scattering of the spots radii is large (i.e., RR value is large) more the constriction resistance increases.

Otherwise, the number of contacts seems to have little influence. Indeed, the results for $N=16$ and $N=49$ are approximately the same. For the small value of ε, all curves converge toward the value of $\psi=0.4789$ (the one of a unique circular contact). Indeed, when contacts have very small dimensions, their interaction is also small, and the disorder has small effect on the results.

The Fig. 3 shows the evolution of ψ as a function of RR (for the case $N=16$). The constriction resistance increases almost linearly with the increase of the value of RR (i.e., the scattering of the spots radii).

The relative differences between the constriction resistance of the random and regular contacts are reported on the Table 1. We note that for the same values of N and RR, these differences increase with the increase of the value of ε. The increase of the value of RR amplifies these differences. However, for the all studied cases, we have obtained that the constriction resistance of random contacts is, in the most unfavorable case, superior of about 46% to the one of the regular contacts.

To analyze the effects of the positions and the scattering of the sizes of spots separately, we reported in the Table 2 the ratio between the constriction resistance for $RR=1$ (all spots having the same size) and the one for $RR=5$ and 10, considering for each case the same values of ε and N. The obtained results show that the effect of the disorder of the positions increases with the increase of the value of ε (i.e. the increase of the ratio of the real contact area to the apparent contact area). On the other hand, for the same value of ε, more the disorder of the radii of spots increases, more the effect of the disorder of the positions decreases. For the studied cases here, the relative effect of the positions disorder varies between 28% and 84%.

The proposed solution provide constriction resistances slightly greater than the one of approximate model given in reference [16]. This difference doesn't exceed 10%.

4 Conclusions

Analytical solution has been developed in this article to calculate the thermal constriction resistance for multiple contacts with

random positions and sizes. It is shown that the constriction resistance of random contacts is systematically more large than the one of the regular contacts having the same number of contacts and surface of spots. In the range of the values of ε investigated in this study, the difference between the results of the random contacts and the regular contacts increase with the increase of the value of ε. This difference is more large than the scattering of the radii of spots is large (i.e., *RR* value increases). The number of contacts seems to have little influence on the evolution of the constriction resistance (considering the same values of ε and *RR*). For all studied cases the value of the relative difference between random and regular contacts is of the order of a few tens percent.

Nomenclature

a = radius of circular contact
A_a = apparent contact area
A_r = real contact area
k = thermal conductivity
L = width of flux tube
N = number of contacts
q = heat flux density
R_{cs} = thermal constriction resistance
RR = ratio of maximum to minimum radii of contacts, $=\mathrm{Max}(a)/\mathrm{Min}(a)$
T = temperature
T_a = average temperature of apparent contact area
T_c = average temperature of real contact area
x, y, z = cartesian coordinates

Greek Symbols

ε = relative contact size, $=\sqrt{A_r/A_a}$
ψ = dimensionless thermal constriction resistance

References

[1] Greenwood, J. A., and Williamson, J. B. P., 1966, ''Contact of Nominally Flat Surfaces,'' Proc. R. Soc. London, Ser. A, **A295**, pp. 300–319.
[2] Cooper, M. G., Mikic, B. B., and Yovanovich, M. M., 1969, ''Thermal Contact Conductance,'' Int. J. Heat Mass Transf., **17**, pp. 205–214.
[3] Mikic, B. B., 1974, ''Thermal Contact Conductance: Theoretical Considerations,'' Int. J. Heat Mass Transf., **12**, pp. 279–300.
[4] Bush, A. W., Gibson, R. D., and Thomas, T. R., 1972, ''The Elastic Contact of Rough Surface,'' Wear, **35**, pp. 87–111.
[5] Whitehouse, D. J., and Archard, J. F., 1970, ''The Properties of Random Surfaces of Significance in Their Contact,'' Proc. R. Soc. London, Ser. A, **A316**, pp. 97–121.
[6] Sridhar, M. R., and Yovanovich, M. M., 1994, ''Review of Elastic and Plastic Contact Conductance Models: Comparison With Experiments,'' J. Thermophys. Heat Transfer, **8**(4), pp. 633–640.
[7] McCool, J. I., 1986, ''Comparison of Models for the Contact of Rough Surfaces,'' Wear, **107**, pp. 37–60.
[8] Leung, M., Hsieh, C. K., and Goswami, D. Y., 1998, ''Prediction of Thermal Contact Conductance in Vacuum by Statistical Mechanics,'' ASME J. Heat Transfer, **120**, pp. 51–57.
[9] Fletcher, L. S., 1988, ''Recent Developments in Contact Conductance Heat Transfer,'' ASME J. Heat Transfer, **110**, pp. 1059–1070.
[10] Yovanovich, M. M., 1976, ''General Expression for Circular Constriction Resistances for Arbitrary Flux Distribution,'' AIAA 13th Aerospace Sciences Meeting, Pasadena, California, pp. 381–396.
[11] Beck, J. V., 1979, ''Effects of Multiple Sources in the Contact Conductance Theory,'' ASME J. Heat Transfer, **101**, pp. 132–136.
[12] Negus, K. J., Yovanovich, M. M., and Beck, J. V., 1989, ''On the Nondimensionalization of Constriction Resistance for Semi-infinite Heat Flux Tubes,'' ASME J. Heat Transfer, **111**, pp. 804–807.
[13] Bardon, J. P., 1965, ''Contribution to the Study of Thermal Contact Resistance,'' (in French), thesis, University of Poitiers, France.
[14] Cooper, M. G., 1969, ''A Note on Electrolytic Analogue Experiments for Thermal Contact Resistance,'' Int. J. Heat Mass Transf., **12**, pp. 1715–1718.
[15] Das, A. K., and Sadhal, S. S., 1999, ''Thermal Constriction Resistance Between two Solids for Random Distribution of Contacts,'' Heat Mass Transfer, **35**, pp. 101–111.
[16] Laraqi, N., and Baïri, A., 2002, ''Theory of Thermal Resistance at the Interface of Solids With Randomly Sized and Located Contacts,'' Int. J. Heat Mass Transf., **45**(20), pp. 4175–4180.

A Parabolic Temperature Profile Model for Heating of Droplets

L. A. Dombrovsky
Institute for High Temperatures, Krasnokazarmennaya 17A, Moscow 111250, Russia

S. S. Sazhin
School of Engineering, The University of Brighton, Brighton BN2 4GJ, UK

A model for convective heating of droplets, which takes into account their finite thermal conductivity, is suggested. This model is based on the assumption of the parabolic temperature profile in the droplets. A rigorous numerical solution, without restrictions on temperature profiles inside droplets, is compared with predictions of the parabolic temperature profile and isothermal models. The comparison shows the applicability of the parabolic approximation to modelling of the heating of fuel droplets in realistic diesel engines. The simplicity of the model makes it particularly convenient for implementation into CFD codes.

[DOI: 10.1115/1.1571083]

Keywords: Conduction, Convection, Droplet, Engines, Evaporation, Heat Transfer

1 Introduction

There has been much progress in the development of the theory of droplet heating [1]. The models actually used in modern multidimensional commercial CFD codes, designed to simulate combustion processes (including those in diesel engines), however, are rather basic. In most cases they are based on the assumption that droplets are under isothermal conditions. The application of more sophisticated models, taking into account the finite thermal conductivity of droplets and internal recirculation in them, has been generally believed to be unpractical. Improvement in the accuracy of modelling of droplet heating might not match the level of accuracy of other parts of the code (e.g. turbulence modelling, chemical reactions). At the same time, some authors have noted that taking into account finite thermal conductivity of droplets gives noticeable improvement in the prediction of diesel spray evaporation processes, when compared with the isothermal model. It has been suggested that a numerical solution of the heat conduction equation inside fuel droplets in diesel engines is added to the solution of gas dynamics, heat transfer and chemical equations for the gas phase [2]. The addition of these calculations would certainly increase the computational requirements of CFD codes. In this paper, an attempt is made to estimate the effect of the temperature gradient inside non-isothermal droplets without solving the heat conduction equation. It is expected that this approach will allow us to reach a reasonable compromise between the accuracy and computational efficiency of simulations of heat transfer and combustion processes involving heating of fuel droplets (e.g., diesel engines).

2 Basic Equations

The transient heat conduction equation inside a spherical droplet can be written as:

Contributed by the Heat Transfer Division for publication in the JOURNAL OF HEAT TRANSFER. Manuscript received by the Heat Transfer Division May 30, 2002; revision received February 6, 2003. Associate Editor: P. S. Ayyaswamy.

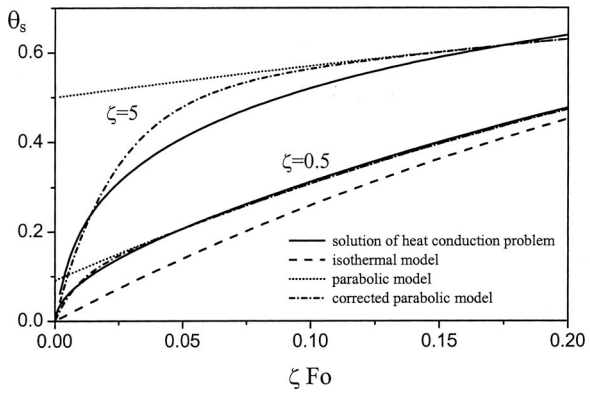

Fig. 1 Plots of dimensionless surface temperature of the droplet θ_s versus dimensionless time ζFo

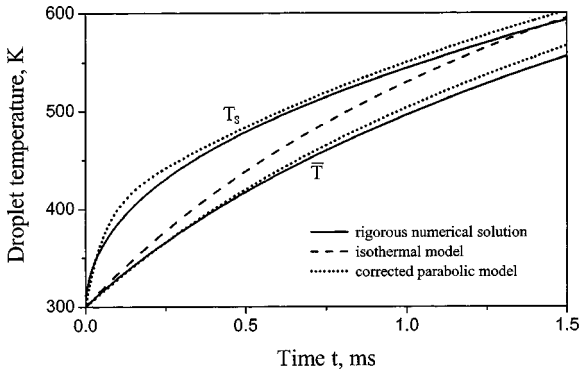

Fig. 2 Plots of surface and average temperatures' evolutions of the moving fuel droplet

$$\rho_l c_l \frac{\partial T}{\partial t} = \frac{k_l}{r^2}\frac{\partial}{\partial r}\left(r^2 \frac{\partial T}{\partial r}\right) + P, \tag{1}$$

where P is the thermal radiation power density absorbed by a semi-transparent droplet [3], k_l is the liquid thermal conductivity assumed to be constant, c_l and ρ_l are the liquid specific heat capacity and density respectively, r is the distance from the center of the droplet. The initial and boundary conditions for the droplet temperature can be written as:

$$T|_{t=0} = T_0(r), \quad \left.\frac{\partial T}{\partial r}\right|_{r=0} = 0, \quad k_l \left.\frac{\partial T}{\partial r}\right|_{r=r_d} = h(T_g - T_s) + \rho_l L \dot{r}_d,$$

where h is the heat transfer coefficient, r_d is the droplet radius, T_s is the droplet surface temperature, T_g is the ambient gas temperature, L is the latent heat of vaporization. Equation (1) can take into account the recirculation inside droplets by replacing k_l by the so called effective thermal conductivity k_{eff} [1]. This approach can be used in most engineering applications when we are interested in an approximate estimate of the influence of the temperature difference between the core and the surface of the droplets on droplet heating and evaporation, rather than in the details of temperature distribution inside droplets. h and $\dot{r}_d$ are time dependant in the general case.

The model suggested in this paper is based on the presentation of the temperature profile inside the droplet in the parabolic form:

$$T(r,t) = T_c(t) + [T_s(t) - T_c(t)](r/r_d)^2, \tag{2}$$

where T_c is the temperature in the center of the droplet. This presentation of $T(r,t)$ takes into account the difference between the temperatures in the center and on the surface of the droplet. The boundary condition at $r=0$ is satisfied. Substitution of Eq. (2) into the boundary condition at $r=r_d$ gives:

$$T_s - T_c = \zeta(T_g - T_s)/2 + \rho_l L r_d \dot{r}_d/(2k_l), \tag{3}$$

where $\zeta = 0.5\text{Nu}k_g/k_l$, $\text{Nu} = 2hr_d/k_g$ is the Nusselt number.

Equation (2) should satisfy the equation of thermal balance, which is obtained from integration of Eq. (1) along the radius:

$$\rho_l c_l \frac{r_d}{3}\frac{d\overline{T}}{dt} = h(T_g - T_s) + q_r + \rho_l \dot{r}_d[L - c_l(T_s - \overline{T})] \tag{4}$$

where:

$$\overline{T} = \frac{3}{r_d^3}\int_0^{r_d} r^2 T(r)\mathrm{d}r, \quad q_r = \frac{3}{r_d^3}\int_0^{r_d} r^2 P(r)\mathrm{d}r.$$

From the definition of $\overline{T}$ and Eqs. (3) it follows:

$$T_s = (\overline{T} + 0.2\zeta T_g)/\psi + 0.2\zeta\rho_l r_d \dot{r}_d(T_s)L/(k_l\psi). \tag{5}$$

where $\psi = 1 + 0.2\zeta$. Equations (4) and (5) give the full solution of the problem of droplet heating in the presence of evaporation. In CFD applications the solution of the coupled ODEs for droplet parcels is performed at each time step by a numerical solver. For each iteration of the solver the droplet surface temperature is calculated from Eq. (5). The values of T_s are used in the subroutines describing droplet heat and mass transfer. All these processes can be accounted for by minor modifications of the existing CFD codes. They will lead to a negligible increase in computational cost.

In the absence of evaporation, Eq. (4) is identical to the equation:

$$\rho_l c_l \frac{r_d}{3}\frac{d\overline{T}}{dt} = h^*(T_g - \overline{T}) + q_r \tag{6}$$

describing droplet heating in isothermal approximation if h^* is found from the modified Nusselt number: $\text{Nu}^* = \text{Nu}(T_g - T_s)/(T_g - \overline{T}) = \text{Nu}/\psi$.

Considering a limiting case when Nu=const, $\dot{r}_d = 0$, $q_r = 0$, and introducing dimensionless variables $\theta = (T - T_0)/(T_g - T_0)$ and $\text{Fo} = k_l t/(\rho_l c_l r_d^2)$ (Fourier number) the analytical solution of Eq. (4) with the initial condition $\overline{T} = T_0$ can be presented as:

$$\theta_s = (\overline{\theta} + 0.2\zeta)/\psi; \quad \overline{\theta} = 1 - \exp(-3\zeta\text{Fo}/\psi), \tag{7}$$

This can be compared with the solution for the isothermal model:

$$\theta_s = \overline{\theta} = 1 - \exp(-3\zeta\text{Fo}). \tag{8}$$

3 Results

In Fig. 1 approximate solutions (7) and (8) are presented alongside the numerical solution of the heat conduction problem for $\zeta = 0.5$ and $\zeta = 5$. The first value of ζ is close to that of a slowly moving droplet. The second value corresponds to a "fast" moving droplet [4]. One can see that for $\zeta = 0.5$ the parabolic model is a good approximation when $\zeta\text{Fo} > 0.02$. In the case of $\zeta = 5$ the parabolic model can be used for $\zeta\text{Fo} > 0.1$ if an error of about 10% can be tolerated. In any case, the accuracy of the parabolic approximation in this range of ζFo is better than the accuracy of the isothermal solution. When looking for a "corrected" parabolic model, valid in the whole range of t, we have found that θ_s determined as:

$$\theta_s = (\overline{\theta} + 0.2\zeta)[1 - \exp(-\xi\text{Fo})]/\psi \tag{9}$$

reduces to that predicted by Equation (7) when $\text{Fo} \gg 1$ and predicts the correct solution $\theta_s = 0$ for $\text{Fo} = 0$. A good fit for the intermediate values of Fo has been achieved for $\xi = 100\sqrt{\zeta}$. As can be seen from Fig. 1, the agreement between the values of θ_s pre-

dicted by Eq. (9) and the numerical solution of the conduction problem is reasonably good in the whole range of ζFo both for $\zeta=0.5$ and $\zeta=5$.

The following results are based on the numerical solution of the equations for droplet velocity and temperature taking into account the actual evolution of the drag coefficient and the Nusselt number along the droplet trajectory in conditions typical for diesel engines. Calculations are based on a scheme similar to the one used in [5]. We ignored the effects of thermal radiation and droplet vaporization and assumed that $r_d=20$ μm and the initial droplet velocity 1 m/s. Following [4] we assumed that $T_g=880$ K, $p=6$ MPa, $\rho_g=23.8$ kg/m^3, $\rho_l=600$ kg/m^3, $\gamma=1.4$, $k_l=0.14$ W/(m·K), $c_l=2.83$ kJ/(kg·K), $k_g=0.061$ W/(m·K), Pr $=0.7$, and $T_0=300$ K. The plots of droplet temperature versus time are shown in Fig. 2. As can be seen from this figure, the parabolic approximation predicts accurately both the surface and the average temperatures of the fuel droplet.

Acknowledgment

Authors are grateful to EPSRC (grant GR/R51711/01) and INTAS (grant 00-0309) for financial support of this project.

References

[1] Sirignano, W. A., 1999, *Fluid Dynamics and Transport of Droplets and Sprays*, Cambridge University Press.

[2] Bertoli, C., and na Migliaccio, M., 1999, ''A Finite Conductivity Model for Diesel Spray Evaporation Computations,'' Int. J. Heat Mass Transf., **20**, pp. 552–561.

[3] Dombrovsky, L. A., 2000, ''Thermal Radiation From Nonisothermal Spherical Particles of a Semitransparent Material,'' Int. J. Heat Mass Transf., **43**, pp. 1661–1672.

[4] Sazhin, S. S., Feng, G., Heikal, M. R., Goldfarb, I., Goldshtein, V., and Kuzmenko, G., 2001, ''Thermal Ignition Analysis of a Monodisperse Spray With Radiation,'' Combust. Flame, **124**, pp. 684–701.

[5] Dombrovsky, L. A., and Ignatiev, M. B., 2001, ''Inclusion of Nonisothermality of Particles in the Calculations and Diagnostics of Two-Phase Jets Used for Spray Coating,'' High Temp., **39**, pp. 134–141.

Journal of Heat Transfer

Errata

Errata: "Inverse Design Model for Radiative Heat Transfer" [Journal of Heat Transfer, 2000, 122, pp. 492–502]

J. R. Howell, O. A. Ezekoye, and J. C. Morales

The integral on the right hand side of Eq. (1) should be preceded by a minus sign.

